Supramolecular soft materials and structural studies of a series of BTA and pyridine-dicarboxamide derivatives with various *d*-metal ions

Amy Danielle Lynes, B. A. (Mod)

September 2018

Based on research carried out under the direction of Prof. Thorfinnur Gunnlaugsson

A thesis submitted to the School of Chemistry, Trinity College Dublin, The University of Dublin, for the degree of Doctor of Philosophy

Declaration

I declare that this thesis has not been submitted as an exercise for a degree at this or any other university and it is entirely my own work, except where duly acknowledged. I agree to deposit this thesis in the University's open access institutional repository or allow the Library to do so on my behalf, subject to Irish Copyright Legislation and Trinity College Library conditions of use and acknowledgement.

Amy Danielle Lynes

Abstract

As will be discussed in the introduction, the control and tuning of the self-assembly of supramolecular soft materials is an area of great current interest and importance. A particularly interesting motif for investigating what governs these processes is the benzene-1,3,5-tricarboxamide (**BTA**) central unit decorated with a variety of different side arm functionalities. The aim of this PhD thesis was to investigate the role of side arm functionality on self-assembly processes and to study the soft materials formed from these various derivatives. Also discussed will be the structural studies of a series of pyridine-3,5-dicarboxamides.

Chapter 2 will discuss the synthesis and characterisation of a family of short alkyl chain ester and carboxylic acid **BTA** derivatives. Investigations into the soft materials formed, using a variety of techniques such as Scanning electron microscopy, X-ray crystallography, powder diffraction and rheology, will also be discussed.

Chapter 3 will then focus on two **BTA** derivatives and their potential as porous materials. Gas adsorption studies will be discussed here along with their solid state structural and thermal properties. Attempts to further extend the aromatic **BTA** derivative with some simple amino acids will then be discussed briefly.

Chapter 4 will introduce attempts to synthesise **BTA**-based polymers, both covalently and non-covalently linked, with a variety of side chains. The main focus will be on a dynamic polymer formed by Schiff-base condensation, with investigation of the materials properties and metal interactions, using techniques including IR, SEM and X-ray crystallography studies.

Chapter 5 will first introduce a new central core, the pyridine-3,5-dicarboxylic acid unit and discuss some related example from the Gunnlaugsson group, followed by the synthesis and characterisation of a number of new derivatives incorporating amino acid-like side chains and their interactions with transition metals. Finally, there will be discussion of the structural, microscopic and thermal studies of the materials formed from these derivatives.

Chapter 6 contains the instrumental and experimental details, followed by references in Chapter 7. Additional information, such as characterisation and supplementary data for all the work described, can be found in the appendix.

Acknowledgements

First and foremost, my sincerest thank you to my supervisor Professor Thorri Gunnlaugsson. I really appreciate the opportunity you gave me to join the group and for all the guidance, research freedom with my project and support when times were tough.

Secondly, I must thank my various collaborators throughout my PhD. Prof Wolfgang Schmitt and Mr Kevin Byrne for their assistance with gas adsorption, Prof John Boland and Dr Chiara Rotella for introducing me to AFM and to Prof Robert Pal and Mr Edward Ward for hosting me in Durham University for a week to carry out some microscopy experiments. Thanks for the help with rheology measurements Prof Matthias Mobius and Dr Ben Haffner.

In a similar vein, I must also thank the Experimental and Technical staff within the School of Chemistry, particularly Dr John O'Brien and Dr Manuel Ruether for all the help when it came to NMR and solving my problems when I couldn't get the TGA or DSC working. Dr Brendan Twamley, Dr Gary Hessman and Dr Martin Feeney for their help with X-ray crystallography and mass spectrometry respectively.

Massive thanks to all the members of the Gunnlaugsson group, past and present, for the support, chats, proof-reading and Friday night drinks throughout the past four years. Chris, thanks for always being willing to help solve my chemistry problems, introducing me to crystallography and proof-reading some of this thesis! Oxana, thanks for all you do, the group wouldn't run without you. Don't worry, I'll be in touch with TV recommendations and all the Royal Family gossip. Thank you for solving all my computer problems and for always being willing to give chemistry guidance since I was an undergraduate student, Sam, I really appreciate it. Dawn, it was lovely to have such a calming desk neighbour during my writing-up time. Thanks for showing me the SEM ropes Sachi! My 4th year buddies, Sandra (aka. Espandra), Dermot (aka. My Dermy-derm), Elena and Anna, it's been a long four years, but we're almost there and I'm glad I got to go through it all with such lovely people. Thanks for being a great friend, flatmate and support Espandra and I'm sorry I haven't found you a farmer yet, but there is still time! Dermy-derm I hope you've got the tequila sorted! Hannah, Isabel and Bruno (What I did?), sorry I have to leave you guys, but don't worry, I'll be back to visit. And Hannah and Isabel (which one is which again?), we must plan our girls weekend soon! Jason, you're a good lad! Best of luck with the rest of your PhD studies June and Emanuele (and Adam). And thanks for the crystallography help June. Fergus, I hope you make it to San Francisco!

To my chemistry and non-chemistry friends, thanks for always being there, no more thesis talk from me! Adriana, I'm so glad we arranged to submit the same day, we started out together in undergraduate, so it's only fitting really! Couldn't have done it without you, now for cocktails! Helen, never more than a message away, thanks for always being there! Also, we must organise that London trip! Nuala, signing up for all those runs kept me from being the size of a house while writing, half marathon next. And we must get you that Copper's high vis vest soon! Thanks for proof-reading some of this thesis Andy, the constant culchie teasing not so much. Those podcast tips really helped keep me sane(ish) while writing other Amy, so thanks a lot! Now that I'm finished Katie, we'll have to have a proper catch-up soon!

Last, but definitely not least, my family. Danielle and Mark, thanks for everything, especially the 20-mile drives just to get ice-cream (culchie problems) and for all the times you've picked me up from the train station! Mom and Dad (aka. Mother Teresa and Heuge) there really aren't adequate words to thank you for everything you do for me, I don't know what I'd do without you. I did see a bumper sticker once that said, 'treat your kids well, they choose your nursing home', well you guys deserve somewhere 5 star!

Abbreviations

AFM	Atomic Force microscopy
Ala	Alanine
API	Active pharmaceutical ingredient
BET	Brunauer-Emmett-Teller
Boc	tert-butyloxycarbonyl
BTA	Benzene-1,3,5-tricarboxamide
Btp	2,6-bis(1,2,3-triazol-4-yl)pyridine
CPL	Circularly polarised luminescence
CPZ	Carbamazepine
Cr-I	Crystalline to isotropic
Cryo	Cryogenic
DBS	Dibenzylidene sorbitol
Dc	Direct current
DCM	Dichloromethane
DMAP	4-Dimethylaminopyridine
DMF	Dimethylformamide
DMSO	Dimethylsulfoxide
DSC	Differential scanning calorimetry
DNA	Deoxyribonucleic acid
DR	Dubinin-Radushkevich
EDA	Ethylenediamine
EDCI	1-ethyl-3-(3-dimethylaminopropyl)carbodiimide
EDX	Energy dispersive X-ray
Et al	et alia
ET_3N	Triethylamine
EtOH	Ethanol
Eq	Equivalent
FIB	Focused ion beam
FTIR	Fourier transform infrared spectroscopy
GPa	Gigapascals
HCl	Hydrochloric acid
H_2O	Water

HOBt	1-Hydroxybenzotriazole hydrate
IBU	Ibuprofen
i.e.	id est
IPA	Isopropanol
I-Cr	Isotropic to crystalline
KCl	Potassium chloride
KI	Potassium iodide
KOH	Potassium hydroxide
LB	Langmuir Blodgett
Leu	Leucine
LMWG	Low molecular weight gelator
MeCN	Acetonitrile
MeOH	Methanol
MOF	Metal organic framework
MRI	Magnetic resonance imaging
MSZ	5-amino-salicylic acid
NaCl	Sodium chloride
$NaHCO_3$	Sodium bicarbonate
NaOH	Sodium hydroxide
NR	Nile red
NPX	Naproxen
OLED	Organic light emitting diode
OPV	Organic photovoltaics
Pa	Pascals
PEG	Polyethylene glycol
PGA	poly(glutamic acid)
Phe	Phenylalanine
POM	Polarised optical microscopy
Ppm	Parts per million
Rt	Room temperature
SCC	Supramolecular coordination compound
SEM	Scanning electron microscopy
SiRNA	Small interfering ribonucleic acid
$SOCl_2$	Thionyl chloride

STP	Standard temperature and pressure
TB	Tröger’s base
TBA	Tetra-butyl ammonium
TEM	Transmission electron microscopy
TES	Triethylsilane
TGA	Thermogravimetric analysis
THF	Tetrahydrofuran
TLC	Thin layer chromatography
UPy	Ureidopyrimidone
UV/Vis	Ultraviolet-visible

Note on Publications

Sections of this work have been published in peer-reviewed journals prior to submission of the thesis.

Chapter 2, most of the work was described in the article 'Benzene-1,3,5-tricarboxamide n-alkyl ester and carboxylic acid derivatives: tuneable structural, morphological and thermal properties' co-authored with Chris S. Hawes, Edward N. Ward, Benjamin Haffner, Matthias E. Möbius, Kevin Byrne, Wolfgang Schmitt, Robert Pal and Thorfinnur Gunnlaugsson, (*CrystEngComm*, 2017, **19**, 1427-1438).

Chapter 3, much of the work described in this chapter featured in the article 'Coordination chemistry of flexible benzene-1,3,5tricarboxamide derived carboxylates; notable structural resilience and vaguely familiar packing motif' co-authored with Chris S. Hawes, Kevin Byrne, Wolfgang Schmitt and Thorfinnur Gunnlaugsson, (*Dalton Trans*, 2018, **47**, 5259-5268).

Chapter 4, a section of this chapter was published in the article 'A Schiff-base cross-linked supramolecular polymer containing diiminophenol compartments and its interaction with copper(II) ions', co-authored with Marcel Klein-Hitßas, Chris S. Hawes, Kevin Byrne, Wolfgang Schmitt and Thorfinnur Gunnlaugsson, (*Supramol. Chem.*, 2018, **30**, 93-102).

Table of Contents

‘Women are like teabags, we don’t know our true strength until we are in hot water.’

Eleanor Roosevelt

1. Introduction

1.1 Supramolecular chemistry and soft materials

Incorporating the principles of supramolecular chemistry into the design and synthesis of new materials, namely soft materials, is a current research area of great curiosity and importance.[1] In particular, the study of supramolecular soft materials and the correlation of their structural features and the chosen self-assembly paths of the constituents with the properties of the bulk materials is a research area of great current significance.[2-6]

Supramolecular chemistry has been defined by Lehn as 'the chemistry beyond the molecule' with its entities being held together by reversible, non-covalent interactions such as hydrogen bonds or metal ion coordination.[7] Whitesides described self-assembly as the 'autonomous organisation of components into patterns or structures without human intervention'[8] and as involving 'association by many weak, reversible interactions to obtain a final structure that represents a thermodynamic minimum'.[9] Self-assembly occurs when molecules interact with one another through a balance of attractive and repulsive interactions and these interactions are usually weak and non-covalent.[10] A major challenge within the area of supramolecular self-assembly lies in the ability to reconcile how small changes in the self-assembly structure can result in the major or minor changes in the supramolecular assembly.[11] It has also been well documented that the materials formed through supramolecular self-assembly can vary significantly in their morphology, from nano-materials[12,13] to gels[14-16] to porous structures[17,18] and is a function of a factors, for example, the monomeric structure,[19] the functional groups present[12] or a pH change[20,21] to name but a few. Soft materials are defined as a transformable, functional class of materials, with moderate mobility and flexibility, which enables them to change their bulk shape and properties depending on the conditions.[22] Examples of soft materials include gels, liquid crystals and colloids.

The objective of this PhD project was to design and develop ligands that could be used in the formation of supramolecular self-assembly structures, with a particular focus on the use of benzene-1,3,5-tricarboxamide **(BTA)**-based ligands. The main objective was to try to devise some new design principles or guidelines so that the behaviour of the resulting materials could be tuned or predicted to obtain materials of interest. With this in mind, the introduction chapter will focus on the development of ligands, that in recent times have been developed and published in the literature, that can generate such soft materials. There will first be a short introduction on various soft-materials and the techniques used to characterise them.

1.1.1 Supramolecular gels and some of their applications

Gels belong to an important class of soft materials in which solvent molecules are entrapped within the network structure provided by the gelator molecules under suitable conditions.[23] A substance is initially designated as being a gel based on its flow characteristics, i.e. gels have solid-like rheological properties and do not flow.[24] Supramolecular gels are often composed of low molecular weight gelators (LMWGs) (molecular weight ≤ 3000) which can self-assemble in a suitable solvent to form nano- or micro-scale network structures, such as fibres, ribbons or sheets.[22,25,26] These structures are held together by reversible interactions such as hydrogen bonding, π-π interactions, van der Waals forces, metal coordination or solvophobic effects to name a few. The dynamic and reversible nature of these non-covalent interactions that hold the networks together allow these supramolecular gels to respond to various external stimuli. A common method to prepare a gel is to warm the gelator in a solvent or solvent mixture until all the solids have completely dissolved to form clear solutions. Upon cooling, the solution undergoes supramolecular self-assembly to form three-dimensional nano- or microstructures, immobilising the solvent molecules and resulting in a gel.[27] A crude test of gelation is the inversion test, in which a vial containing the material is inverted to see if it can support its own weight for an extended period of time (>1 h), an example is shown in Figure 1.1.[24] Other techniques for the characterisation of gels include thermogravimetric analysis (TGA), differential scanning calorimetry (DSC), transmission electron microscopy (TEM), scanning electron microscopy (SEM), atomic force microscopy (AFM), nuclear magnetic resonance (NMR), various spectroscopy techniques and rheological studies.[22,28] TGA is an analytical technique in which the weight of a sample is measured as a function of time or temperature and as such gives a quantitative description of the thermal stability of the material and the amount of the corresponding residue.[29] DSC is another thermoanalytical technique used in the characterisation of gels. The basic principle of this technique is that when a sample undergoes a physical transformation, heat will be needed for the sample than the reference sample to maintain both samples at the same temperature. The amount of heat, more or less, that must be applied to the sample of interest depends on whether an exothermic or endothermic process is occurring. The result of a DSC experiment is a curve of heat flow *vs*. temperature or *vs*. time. The enthalpy of phase transitions can then be calculated by integrating the area under the peak corresponding to the transition of interest.[22] TEM is a microscopy technique in which a beam of electrons interacts with the sample of interest as it passes through the sample. An image of this can be formed from the interaction of the electrons with the sample and this can be magnified and focused onto an imaging device, for example, a fluorescent screen or layer of photographic film. TEM affords resolution on the sub-nanometre scale.[22] SEM is an electron microscopy technique in which an image is obtained by scanning a sample with a focused beam of electrons. The electrons interact with the electrons in the sample and produce a variety of signals that can be detected and contain information about the morphology of the sample under observation. SEM is capable of producing images of high resolution on the nanometre scale.[22] Some typical SEM image of dried gel samples are shown in Figure 1.1. Gels can be classified depending on the conditions in which they form; for example, organogels are those that form in organic solvent, hydrogels gelate water, ionogels are those that gelate in ionic liquids and metallogels are those that contain metals.[22] [30] While SEM and TEM are useful techniques for studying gel morphology, there are some disadvantages, for example, sample preparation requires drying of the sample before imaging. Drying can result in considerable distortion of the samples, thus these techniques do not always result in an accurate representation of the morphology. Cryo-SEM and cryo-TEM offer a more accurate representation of the materials in solution. These cryogenic techniques effectively ‘freeze’ the gel in a rapid step thus preventing any distortion or reorganisation of the samples.[22] AFM is a different type of microscopy technique in which the information is gathered by ‘feeling’ the surface of the sample with a very sensitive cantilever. Attractive or repulsive interactions that influence the tip at the end of the cantilever as it is moved over the sample causes the cantilever to bend, thus providing a mechanical means to probe the sample. One of the advantages of this technique over SEM and TEM is that sample preparation is non-destructive and it does not require any special treatment such as coating that is often required for SEM sample preparation.[22] Rheology is defined as the study of flow and can yield information about the structures of the assemblies. Gels are known to display both solid-like and liquid-like rheological properties and these properties can be investigating using a rheometer.[22,25,31] Soft materials exhibit both elastic and viscous responses to stress and are therefore termed viscoelastic. The response of soft materials to an applied stress

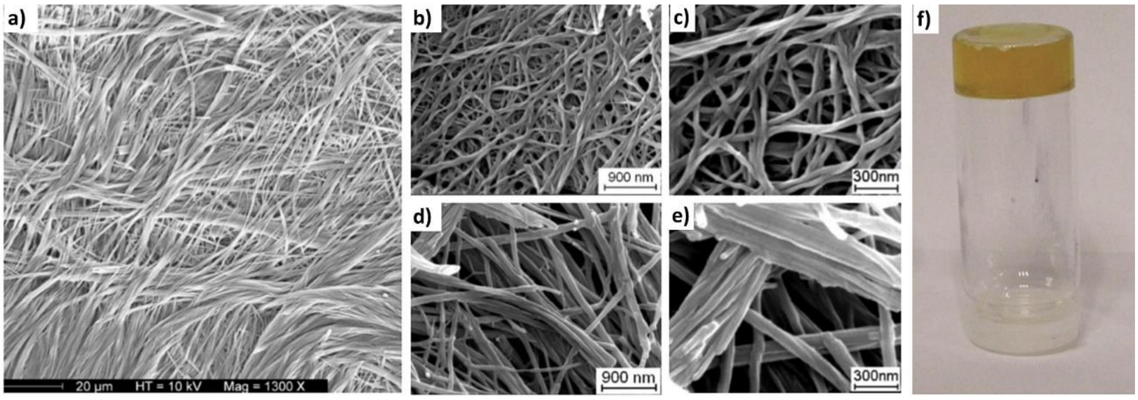

Figure 1.1 (a-e) Some typical SEM images of xerogel samples of supramolecular gels, (f) inversion test of a supramolecular gel. Images reproduced from references 23, 76 and 112.

can be described using the elastic storage modulus, *G′*, which is the contribution of solid-like behaviour and the elastic loss modulus, *G″*, which is the viscous or liquid-like contribution.[25,31] A variety of rheological experiments can be carried out to confirm gel-like behaviour, for example, a typical stress-sweep experiment would show *G′* to be approximately one order of magnitude higher than *G″*, confirming solid-like behaviour. After a certain amount of stress is applied, the material will begin to flow and this is referred to as the yield stress and can be estimated as the point where the straight lines on the plot representing *G′* and *G″* cross-over.[31] Gels have found many applications, for example, use as matrices for cell and tissue engineering, scaffolds for wound healing and drug delivery vehicles.[32,33,34] [35] Other applications and uses include as sensing materials, as materials for printing, media for organic reactions and catalysis and as crystal growth media.[21,36]

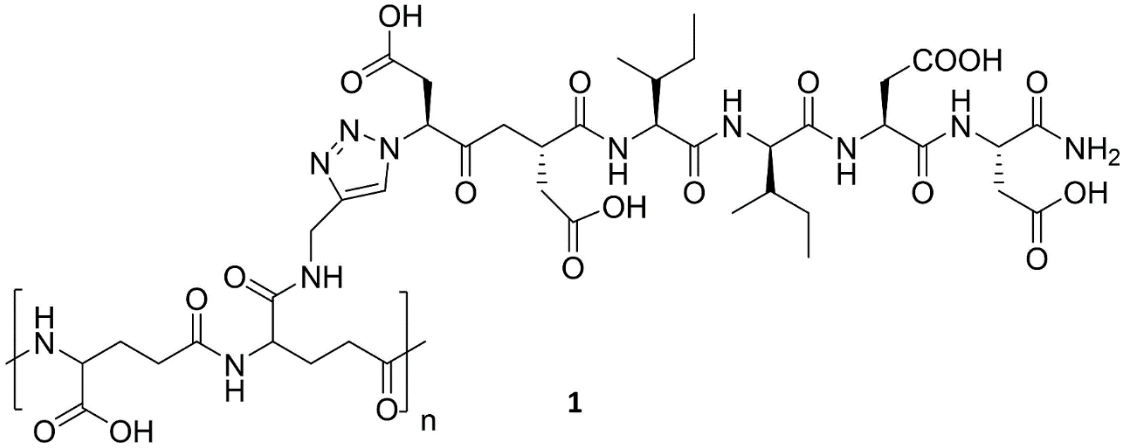

1

Figure 1.2 The structure of the γ-PGA-β sheet conjugate used in the study by Stevens and co-workers. Structure reproduced from reference 34.

An emerging and interesting application of hydrogels is their potential as a platform for tissue engineering. Stevens and co-workers reported a biodegradable polymer-peptide hydrogel that consisted of a poly(glutamic acid) (PGA) polymer network, **1**, that was physically cross-linked by conjugated *β*-sheet peptide sequences and showed potential for use as a platform for future tissue engineering scaffolds and biomedical applications, Figure 1.2.[34] The authors demonstrated that by altering the gelation conditions, for example, the concentration of the hybrid peptide-polymer and the ratio of the covalently coupled versus uncoupled peptide, was possible to tailor the mechanical properties of the gel. The response of the hydrogel to cyclic loading and its recovery following the application of high strain was also evaluated. It was found that the mechanical properties were dependent on the concentration of the hydrogel, the *β*-sheet peptide graft density and the ratio of coupled peptides to free peptides. The authors also reported that the hybrid hydrogels did not lose any mechanical integrity up to a strain of approximately 20%, while also demonstrating a self-healing ability. The hydrogel stiffness could be varied by over an order of magnitude by changing the hydrogel concentration. Further modifications of the hydrogels with peptides and bioactive isotopes was also possible. Self-healing is the ability of a gel to return to its original state after damage.[37] The self-healing and resistance properties, along with the potential for further modification, would suggest this hydrogel's suitability for use in biomedical applications that require recovery after significant deformation, for example, injectable therapies. Human dermal fibroblasts were cultured on the gels and were found to adhere thus further supporting the use of the gel in biomedical applications.[34]

Another report of the use of a supramolecular gel system as a potential tissue engineering scaffold was made by Rowan and co-workers.[38] In this report, the authors used a guanosine-based hydrogelator that was capable of gelating both water and cell media. Studies carried out on the assembly of this gel suggest that the gel forms helical assemblies instead of the more common macrocyclic quartet assemblies usually observed in guanosine hydrogels, as seen in Figure 1.3. The helical arrangement of **2** is presumed to be due to the presence of metal ions, namely Na^+ or K^+, in the aqueous media. This gel was found to be non-toxic to cells, injectable and it was also possible to modulate the modulus and shear sensitivity of the gel over orders of magnitude.

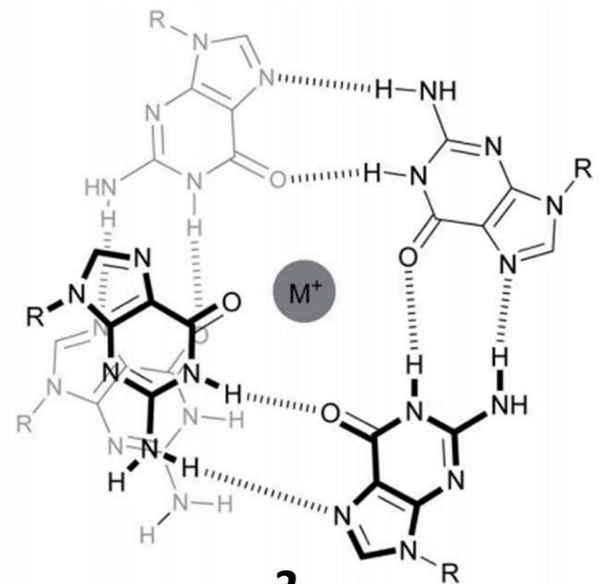

2

Figure 1.3 An illustration of the proposed formed continuous G-helix. Illustration reproduced from reference 38.

In work reported by Smith and co-workers, it was found that gelators based on dibenzylidene sorbitol (DBS) were capable of incapsulating anti-inflammatories, followed by release at the desired pH.[33] DBS, **3**, shown in Figure 1.4 along with the anti-inflammatories

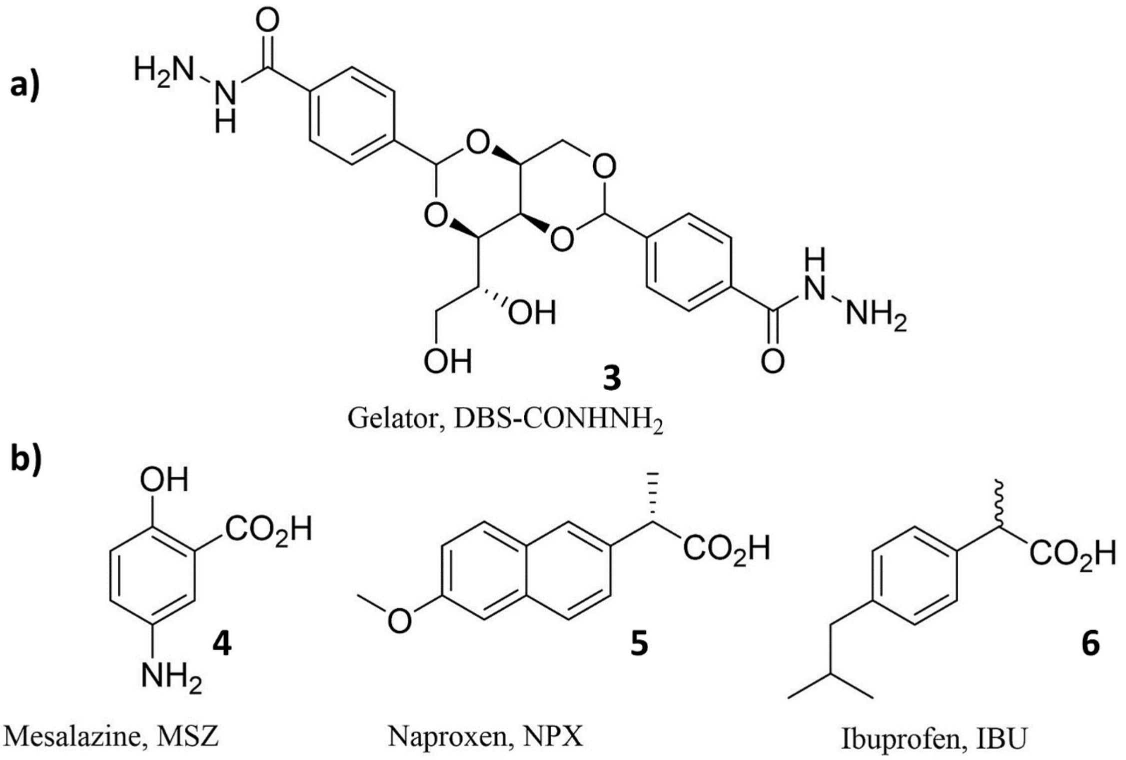

Figure 1.4 (a) Structure of the gelator, **3**, reported by Smith and co-workers and (b) the APIs, **4-6**, used in the study. Figure reproduced from reference 33.

chosen in this work, is widely used in the cosmetics industry and was chosen due to its acceptable toxicity and environmental profile. The active pharmaceutical ingredients (APIs) were encapsulated to form a two-component gel network. The chosen APIs were 5-amino-salicylic acid, **4**, ibuprofen, **6**, and naproxen, **5**, and were encapsulated by mixing the API and gelator as solids then gelating in water. In the case of NPX, the release was monitored using ultraviolet-visible (UV/Vis) absorption spectroscopy. It was found release of the API at 37 °C at pH 7 over a 24 h period was 33%, while at pH 8 the release was 100%. This suggests that deprotonation of the API disrupts the interactions within the gel network and assists release of the API. Release of **5** at pH 8 is useful for delivery in the intestine. The release of MSZ and IBU could not be monitored using the same conditions as those used for NPX due to issues with inconsistent release and solubility. Due to the promising results observed for NPX, the authors proposed this gelator to be a potential tissue engineering scaffold.[33]

Steed and co-workers reported the use of a LMWG as a crystal growth medium[39] Crystal growth in gel media is useful as the gel limits convection and prevents sedimentation thus allowing for continuous, diffusion-limited growth and spatial control of nucleation. The gel environment can influence a number of factors, for example, crystal habit, polymorphism and enantiomorphism.[31,40] Four bis(urea) gelators, **7-10**, shown in Figure 1.5, were used and the crystallisation of a variety of pharmaceutical drug substances within these gel media was investigated. These initial screening experiments were followed by a more detailed study of carbamazepine (CBZ) with all four gelators reported. CBZ is an anticonvulsant and has four known polymorphs, as well as a number of co-crystals, thus it serves as a model compound for studying crystal polymorphism. Clear differences in crystal habit were observed in the gel phase when compared to the crystals grown in solution. In some cases, the gel-phase crystallisation resulted in the formation of different polymorphs when compared to the parallel solution-phase experiments. Recovery of the crystals of CBZ grown in the gels was achieved by adding an excess of solid tetra-butyl ammonium (TBA) acetate to the top of the gel leading to a rapid dissolution of the gel, with the crystals then recovered by filtration. It was noted that this anion recovery method is likely to be limited to compounds that do not themselves compete with the urea gels for anion binding and the effectiveness is limited by the solvent and ability of the crystalline substrate to interact with the anion. Given these results, the authors postulate that supramolecular gels could be used as an important tool for polymorph screening methods, commonly used in several stages of drug development.

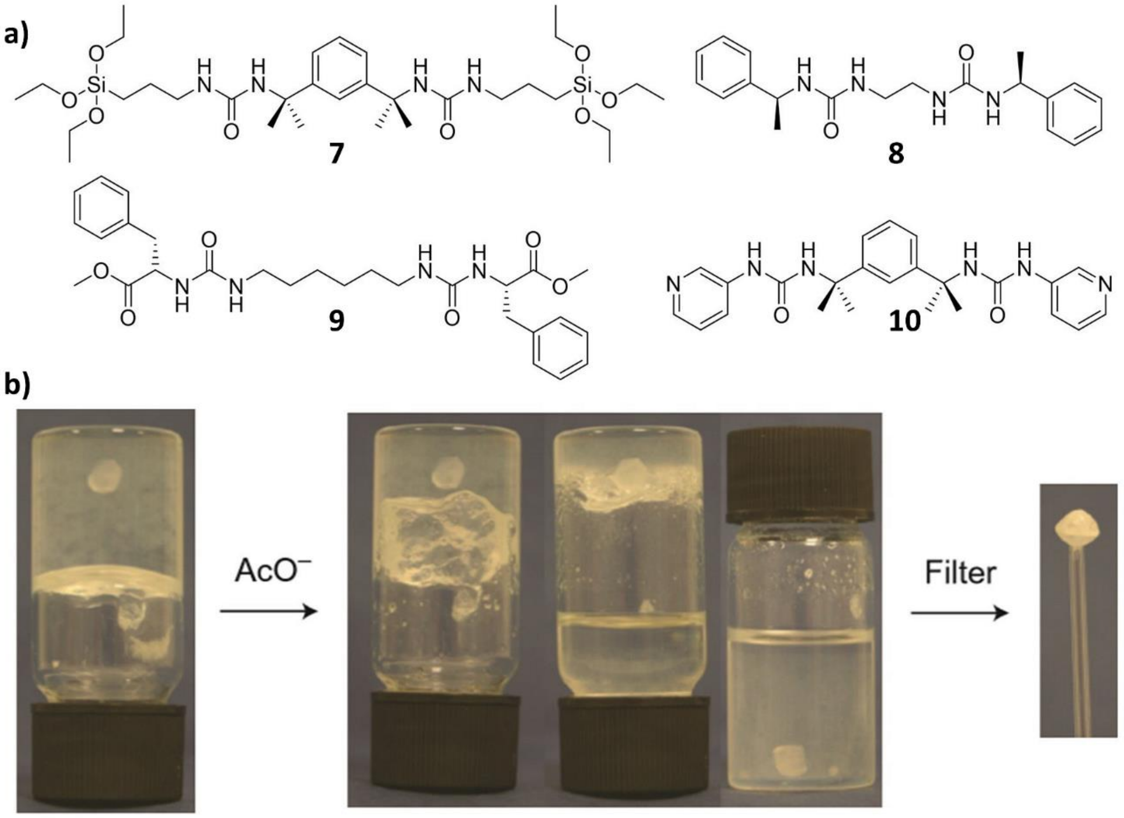

Figure 1.5 (a) The bis(urea) gelators, **7-10**, used in the study and (b) the recovery of a CBZ crystal from the gel by acetate-anion triggered gel dissolution. Structures and gel images reproduced from reference 39.

Adams and co-workers recently detailed the effect of the method of preparation has on the mechanical properties of a LMWG or gel.[41] The authors used a known gelator, the functional dipeptide 2NapFF, **11**, shown in Figure 1.6, and reported the effect of gelation method on the mechanical properties. Three gelation methods were employed here; (i) dissolution at high pH, followed by addition of a divalent salt such as calcium; (ii) dissolution at high pH, followed by a reduction in pH and (iii) dissolution in a water-miscible solvent such as DMSO, followed by the addition of water. The gels formed by different methods were studied using a variety of techniques, for example, SEM, TEM and rheological studies. SEM images of a number of samples of gels generated by each method showed the Ca-triggered gels to look like a mat of fibres, with the acid-triggered samples showing a similar morphology, while the solvent-triggered gels show a more crystalline morphology with the fibres being the largest of those generated. The rheological properties of the gels were also studied with the strain sweeps of the gels revealing them all to behave differently presumably due different types of networks present within the gels. For viscous materials, the strain lags behind the stress by a 90° phase difference (δ), while intermediate viscoelastic materials have a strain lag somewhere between 0 and 90°.[31] The frequency sweeps showed less variation, while the recovery tests showed the gels to respond differently to deformation. The solvent-triggered gel showed the least recoverability performance, with *G*’ only recovering to 10 % after the first deformation, with this value maintained over a further five cycles. Overall, this work demonstrated the effect

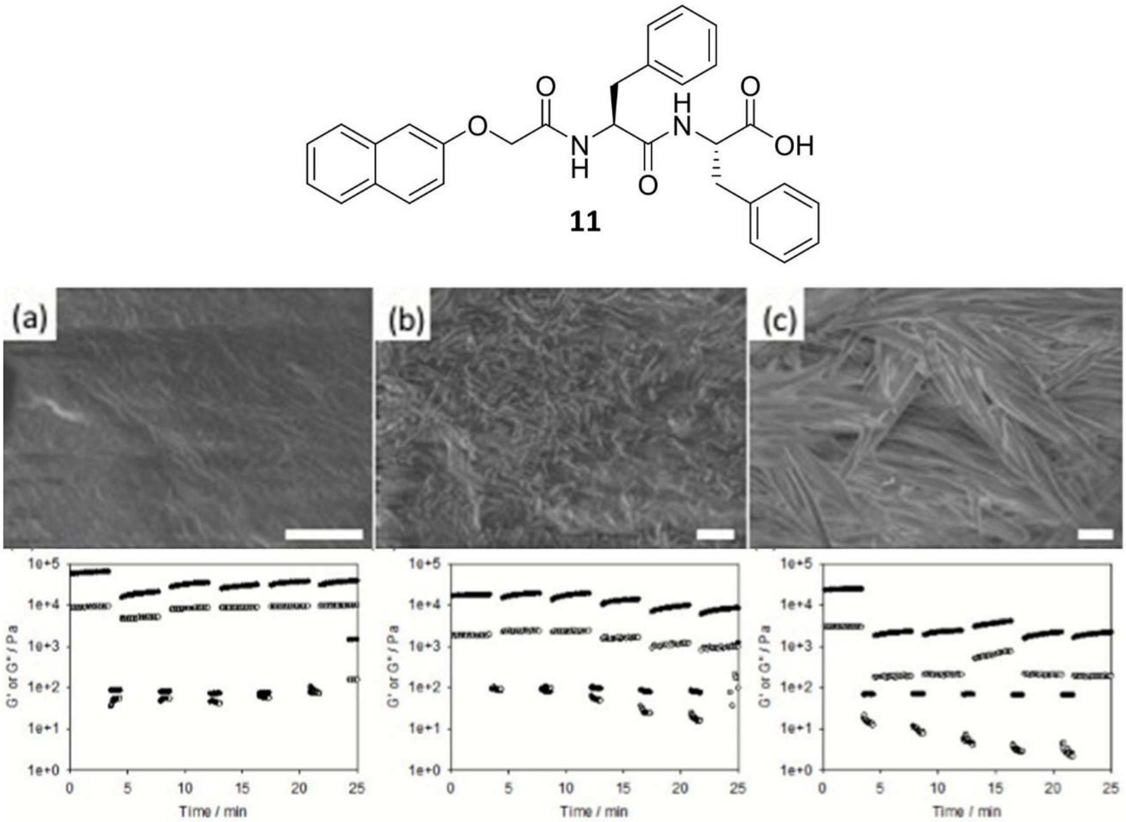

Figure 1.6 (Top) Structure of the gelator used in the study, (middle, a-c) SEM of the Ca-triggered xerogel, acid-triggered xerogel and the solvent-triggered xerogel, scale bar is 1µm in all cases and (bottom, left to right) the recovery tests for the Ca-triggered gel, the acid-triggered gel and the solvent-triggered gel. Images are reproduced from reference 41.

of varying just some of the possible parameters and their effect on gel morphology and mechanical properties.

From these examples, it is clear that varying some of the many parameters involved in gelation can have a large impact on the gel morphology and the mechanical properties of the material. It is also shown that supramolecular gels have a vast array of useful potential applications, however, work to finely tune gelation conditions and the properties of the resulting materials is an ongoing area of research.

1.1.2 Liquid crystals and some of their applications

Supramolecular liquid crystals are a class of soft materials that combine order with fluidity through non-covalent interactions.[42,43] Liquid crystals can be characterised using a number of techniques, such as TGA, DSC and polarised optical microscopy (POM).[44,45] One of the useful aspects of liquid crystal research is that liquid crystals are birefringent, thus polarised optical microscopy can be used to view birefringent textures typical of the organisation of liquid crystals.[46] The liquid crystal state is also known as a mesophase and they are of technological importance,[47] for example, for use in organic light emitting diodes (OLEDs), organic photovoltaics (OPVs) and organic semiconductors.[48] There is an increasing interest in developing novel supramolecular columnar liquid crystals as they form architectures with control at the nanoscale and due to their supramolecular nature, they have the potential to respond to different external stimuli such as temperature, pH or pressure.[43]

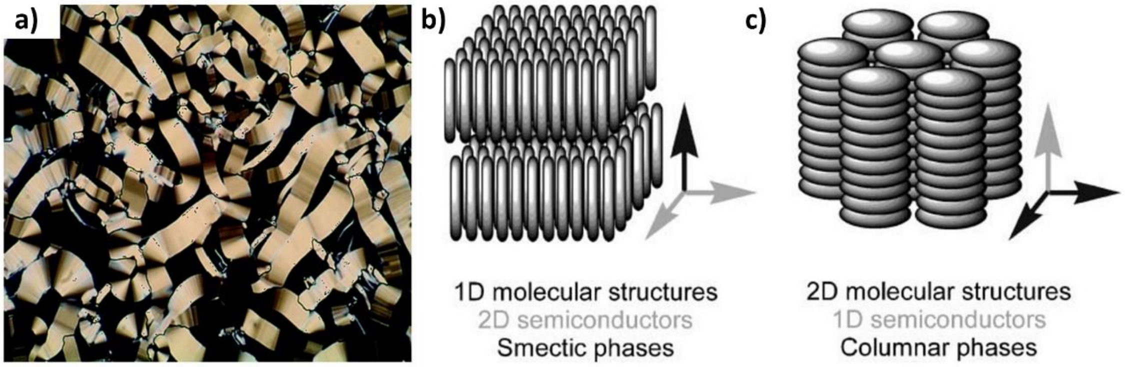

Figure 1.7 (a) An example of the polarised optical microscopy (POM) observed for a discotic liquid crystal and a schematic of a (b) smectic and (c) columnar mesophase. Images reproduced from references 44, 45 and 48.

Liquid crystals that form upon heating a solid mesomorphic compound are known as thermotropic liquid crystals, which can be further divided into sub-categories: (i) columnar/discotic, which align in stacks, (ii) nematic, which have no positional order but tend to align in the same direction and (iii) smectic, which arrange in well-defined layers.[49] An example of the optical texture of a discotic liquid crystal and a schematic of some of the types of liquid crystal are shown in Figure 1.7. Lyotropic crystals are those that form upon addition of a solvent, while metallomesogens are metal-containing liquid crystals.[49] A mesophase is enantiotropic and thermostable if it forms on both heating and cooling cycles, while it is monotropic and metastable if it only appears below the melting point on the cooling cycle.[49] A mesophase that is both thermotropic and lyotropic is known as amphoteric.[49] Materials that display columnar mesophases are of interest as they offer properties such as improved charge transportation, anisotropic ion transportation and photonic functions.[50] They are of interest as potential components for organic electronic and optoelectronic devices. Often, discotic liquid crystals have a π-electron rich aromatic core attached to a flexible alkyl chains and the columnar phases are formed *via* stacking interactions. Some of the reported discotic liquid crystals have consisted of cores based on porphyrins, triphenylenes and coronenes, to name but a few.

Recently, Sijbesma and co-workers reported a method for the preparation of a nanoporous membrane with a pore size of approximately 1 nm derived from polymerisable discotic liquid crystals, shown in Figure 1.8.[51] The authors used a tris-4-methyl-benzimidazoyl benzene which binds three organic acids to form a hydrogen bonded discotic liquid crystal. For fixation of the homeotropic liquid crystal films, a high temperature compatible copolymerisation method of allyl ethers with vinyl esters was used. This method of preparing nanoporous membranes from polymerisable discotic liquid crystals offers ample opportunities for developing functional materials.

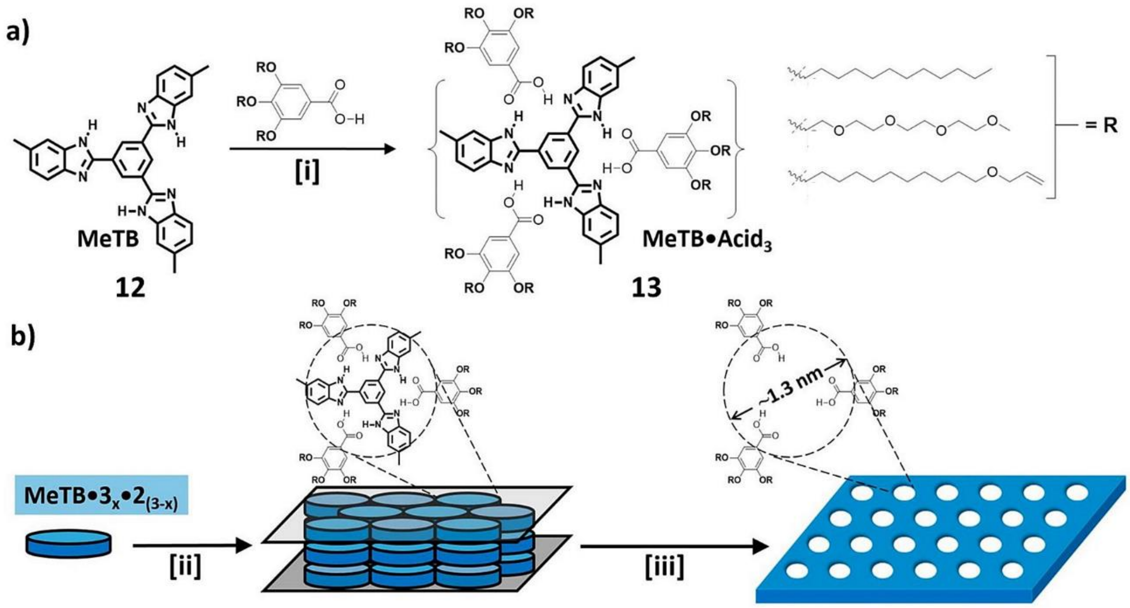

Figure 1.8 (a) Molecular representation of triply hydrogen-bonded discotic liquid crystals based on tris-4-methyl-benzimidazolyl benzene (MeTB) and alkylated gallic acids reported by Sijbesma and co-workers. (i) Self-assembly of the AB_3 hydrogen-bonded discotic liquid crystal. (b) Homeotropic alignment of the MeTB·Acid$_3$ complex by mixing in dopant 2. (ii) Homeotropic alignment of discotic LC phase between glass slides by cooling down from the isotropic phase. (iii) Fixation of the LC its columnar morphology using photoinitiated radical polymerization, followed by formation of nanopores by template removal. Image reproduced from reference 54.

Tanaka and co-workers recently reported the construction of a macrocyclic columnar liquid crystal possessing nanochannels for the development of well-defined molecular nanospaces in flowable media and the functionalisation of the interior of the cavities through the incorporation of metal complexes.[52] A schematic of the macrocyclic ligands used and the scheme for the synthesis for the reported metallo-macrocycle is shown in Scheme 1.1. Designer molecular nanospaces are considered as promising systems for promoting multiple chemical processes such as specific recognition, storage and the reaction of confined molecules.[52] It is generally difficult to synthesise a large macrocylic molecule that has a low phase transition temperature and also challenging to organise macrocyclic molecules into homogenously ordered columnar mesogens over a wide area. The authors managed to overcome these challenges and successfully synthesised imine-based macrocycles composed of alternately linked carbazole and salphen moieties for the construction of the columnar liquid crystal. Metals were also successfully incorporated into the liquid crystal with the potential to interact with guest molecules.

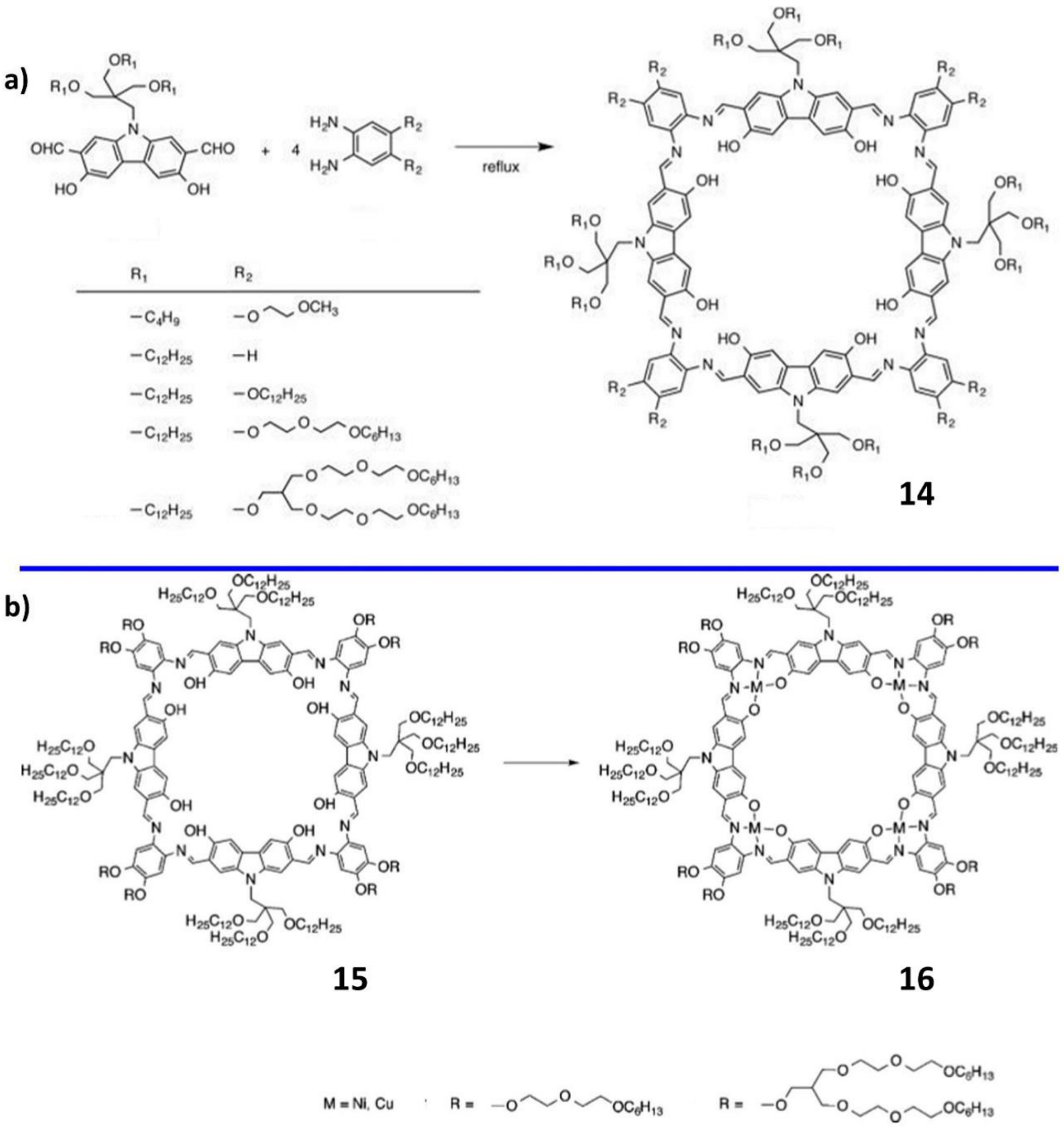

Scheme 1.1 Synthetic scheme of (a) the macrocyclic ligands **14** reported by Tanaka and (b) for the synthesis of the metallo-macrocycle **16** Image reproduced from reference 52.

1.1.3 Supramolecular polymers

Supramolecular polymers are polymers that are based on monomeric units that are held together by directional and reversible non-covalent interactions such as hydrogen bonding, electrostatic and hydrophobic interactions.[53,54] The supramolecular nature of these materials endows them with unique modular and dynamic properties, while the non-covalent interactions allow for fine-tuning of the final properties of the aggregates, along with convenient incorporation of the functionalities without repeated and challenging covalent synthesis steps.[55] Supramolecular polymers differ from conventional polymers in that the self-assembly process of the monomers can result in assemblies that have internal order and therefore completely new functions and persistence lengths that are not observed in covalent polymers.[56] Some reported applications of supramolecular polymers include materials chemistry, organocatalysis, regenerative medicine, protein assembly and drug delivery systems to name a few.[55,57 58]

The group of Meijer have contributed much to the discovery and investigations of supramolecular polymers. One example was their report on a series of supramolecular polymers consisting of polyethylene glycol (PEG) end functionalised with four-fold hydrogen bonding ureidopyrimidone (UPy) moieties and alkyl spacers, shown in Figure 1.9.[59] These micrometer-long hydrophobic nanofibers with tunable macroscopic properties were found to be promising protein delivery carriers and could be administered by a minimally invasive injection.[59]

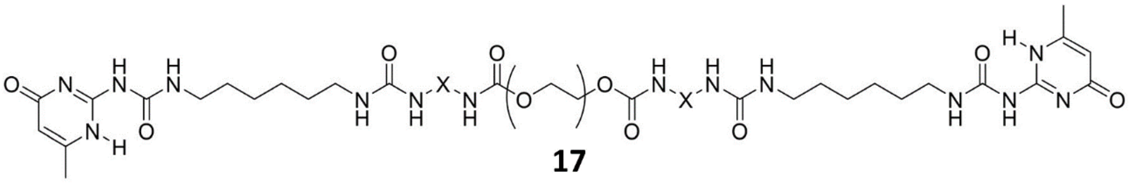

17

Figure 1.9 Structure of the supramolecular UPy-modified PEG hydrogelator reported by Meijer and co-workers. X represents an alkyl chain of lengths between C6 and C12. Structure reproduced from reference 60.

Scherman and co-workers have also made significant contributions to the field of supramolecular polymers. For example, they recently described the construction of supramolecular polymer networks through an *in situ* copolymerisation of a guest, acrylamide, and a host, cucurbit[8]uril, Figure 1.10.[60] This supramolecular polymer network could be stretched more than 100 times its original length and was found to be able to lift more than 2000

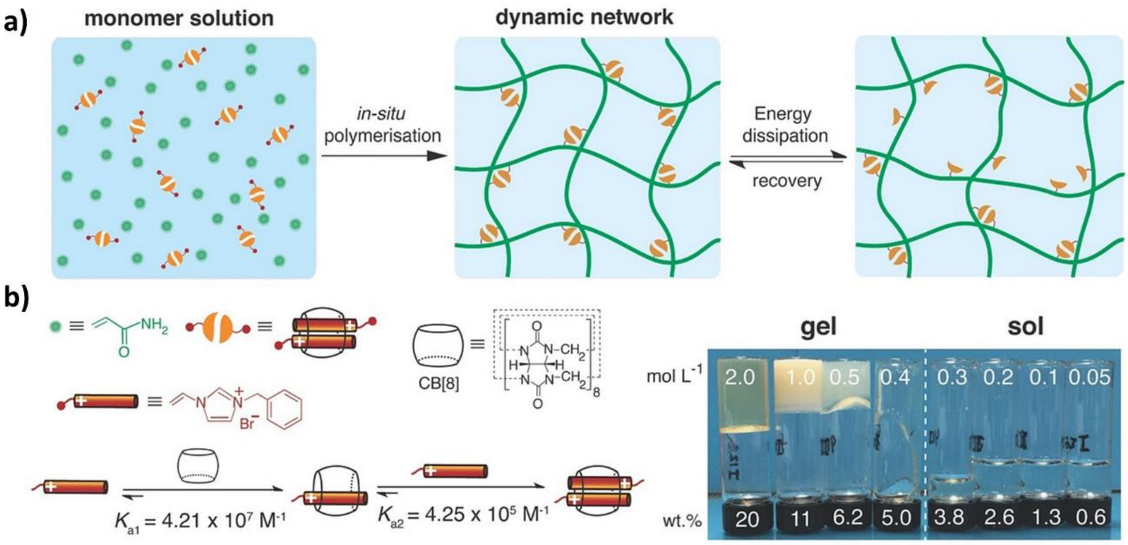

Figure 1.10 (a) In situ polymerisation of supramolecular polymer networks in the presence of macrocyclic host cucurbit[8]uril (CB[8]) and polymerizable guest molecules (1-benzyl-3-vinylimidazolium) and acrylamide. CB[8] supramolecular ternary conjugates act as dynamic crosslinks, leading to a network structure after photoinitiated polymerisation at room temperature. They act as bonds that rupture under deformation and dissipate energy, which can be further reformed, resulting in the self-healing of macroscopic network; (b) stepwise formation of ternary host-guest complexation between CB[8] and guests and (b, right) inversion tests of the polymers at different concentrations. Image reproduced from reference 60.

times its own weight. The authors propose that this polymer could have potential for wearable electronic devices, biomaterials and sensors.

Supramolecular oligomeric systems based on two hetero-complementary subunits, namely a tetrathiafulvalene-functionalised calix[4]pyrrole and a glycol diester-linked bis-2,5,7-trinitrodicyanomethylenefluorene-4-carboxylate, were reported by Sessler and co-workers.[61] Supramolecular aggregation of these units produced a short oligomer that is stabilised by hydrogen bonding and donor-acceptor charge-transfer interactions. This system was proposed to be an attractive platform for the detection of nitro-aromatic explosives and anions, due to a fluorescence quenching effect observed upon exposure to these substrates.

The above examples are a small sample of the various types and uses of supramolecular polymers and demonstrate the utility of supramolecular chemistry in polymer science. Supramolecular polymers based on benzene-1,3,5-tricarboxamides will be discussed in 1.2.2.

1.1.4 Supramolecular coordination complexes, polymers and metal organic frameworks (MOFs)

As is evident from the details in the preceding sections, supramolecular chemistry is a very broad field, with one subset being the area of supramolecular coordination compounds. Coordination polymers are a subgroup of inorganic polymers with metal-ligand bonds as the primary design feature.[62] Similarly to metal organic frameworks, they contain two central components, connectors and linkers, with transition metal ions often utilised as versatile connectors.[63] Two branches of coordination chemistry that have emerged in recent decades are supramolecular coordination compounds (SCCs) and metal organic frameworks (MOFs). SCCs are discrete constructs that are obtained through the mixing of soluble metal and ligand precursors that spontaneously form metal-ligand bonds to generate a thermodynamically favoured product.[62] Some commonly used linkers in coordination polymers are shown in Figure 1.11, along with some of the structural frameworks that can be constructed.[63] MOFs consist of an infinite network of metal centres or inorganic clusters that are bridged by simple organic linkers through metal-ligand coordination bonds.[62] MOFs represent are examples of coordination polymers that make use of extended metal-ligand interactions to form infinite, long-range ordered one-, two-, or three-dimensional structures.[27] Single crystal X-ray diffraction is used to gain an insight into the structural details of MOFs, with powder diffraction and elemental analysis used to determine bulk purity.[64] The term MOF is technically a suitable term to describe any extended array composed of metal nodes (either mono- or polynuclear), however, it is more common to reserve the term for referring to microcrystalline materials, well-defined materials containing polynuclear clusters and those that show permanent porosity.[62]

Modern MOF synthesis is driven by the goal to generate porous materials often accompanied by a large internal surface area, which is often accomplished by a careful selection of the molecular precursors and reaction conditions as these dictate the thermodynamically favoured architectures. The pore size of MOFs can be controlled on the angstrom level through a gradual increase in the number of atoms in the organic linkers.[65] Examples of MOF applications include energy storage, chemical purification, heavy metal removal from water, heterogeneous catalysis, biomedical applications and sensing.[62,66]

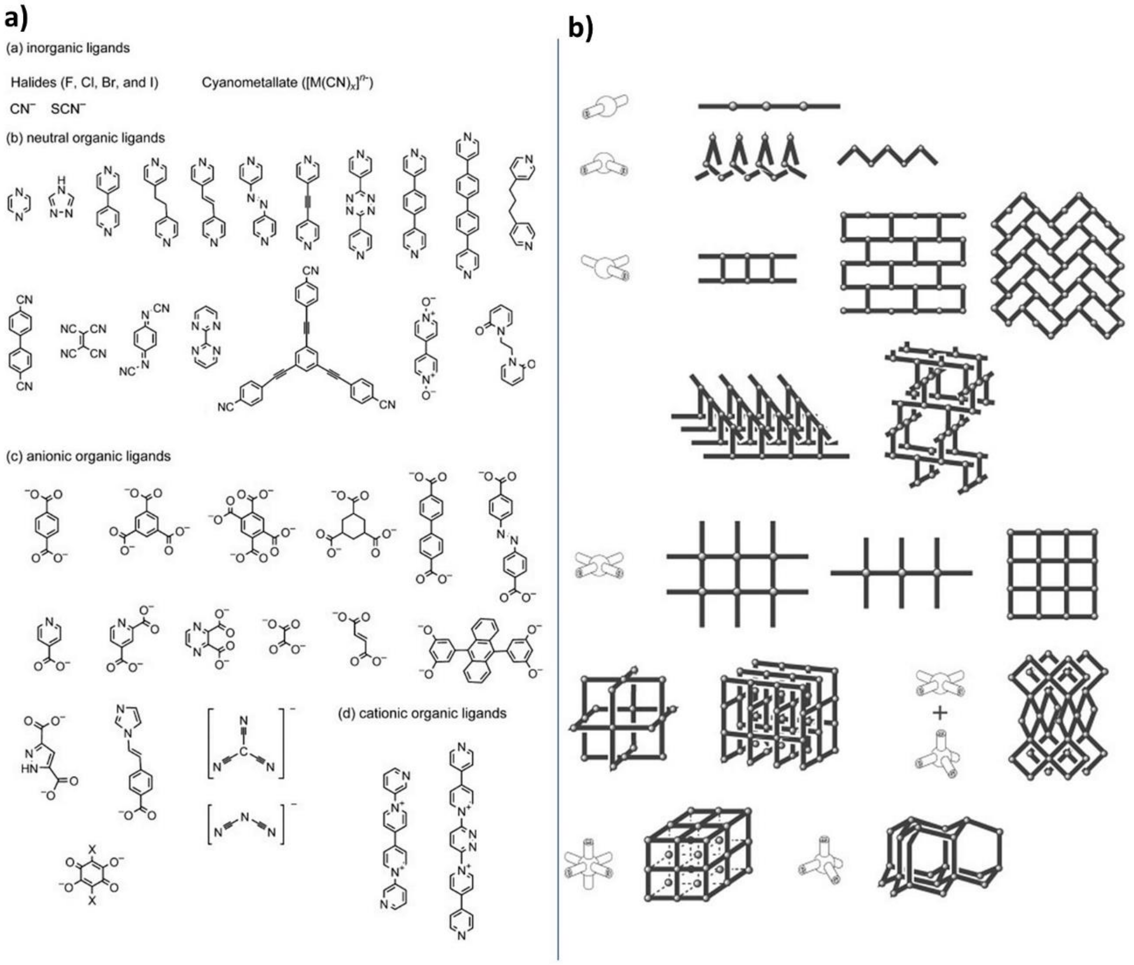

Figure 1.11 (a) Some common linkers used in coordination polymers and (b) the structural frameworks that can be constructed by using different connectors and linkers. Images reproduced from reference 63.

Forgan and co-workers have recently made a number of reports into the use of zirconium-based MOFs as drug delivery systems.[67,68] In order to be an effective drug delivery agent, the MOF needs to be able to penetrate the cells and release its cargo into a precise intracellular location. Zirconium based MOFs are promising as drug delivery systems due to their low toxicity. In one report, Forgan and co-workers reported a series of Zr-based MOFs with a variety of different linkers and investigated their potential as drug delivery systems, Figure 1.12. The authors loaded the various MOFs with the fluorescent molecule calcein and an anti-cancer drug and observed their respective delivery properties.[67] In this report, it was found that the loading values of both the calcein and the anti-cancer drug were higher for the MOFs that contained unfunctionalised linkers. Confocal microscopy showed that all the materials were able to penetrate the cells. It was also reported that the therapeutic effect of the anti-cancer drug on HeLa cells was enhanced when it was loaded on the MOF with the longest linker. Another report by Forgan and co-workers investigated the effect of the linker functionalisation of the MOFs on the endocytosis pathways and efficiency, and then use this information to prepare an optimal MOF drug delivery system that has enhanced endocytosis efficacy and improved ability to avoid lysosomal entrapment. The authors reported that Zr-based MOFs with different sizes and surface chemistries enter the cells *via* different endocytic pathways. They also demonstrated that control of the surface chemistry through linker functionalisation is of critical importance in tuning the pathways in which the cells take up the particles, while the particle size does not seem to have a significant impact on the uptake.[68]

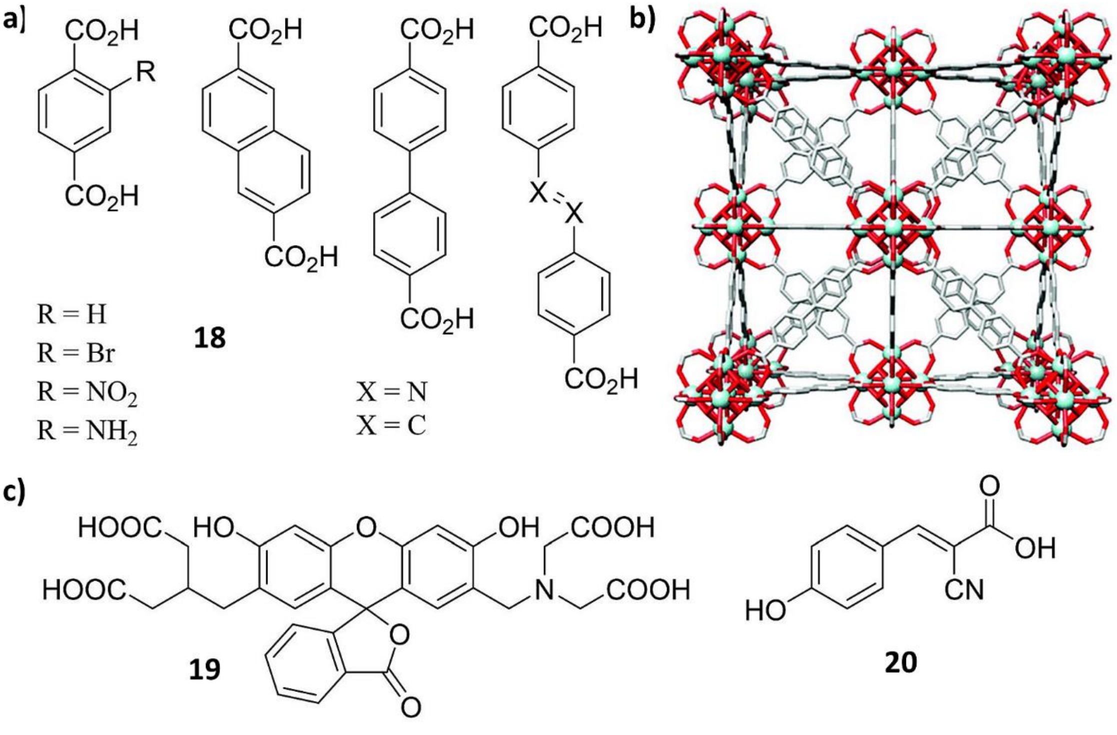

Figure 1.12 (a) Chemical structure of the organic linkers used to synthesise the different zirconium-based MOFs and (b) the packing of Zr-L6 and (c) the structure of the guest molecules, calcein and α-CHC. Image reproduced from reference 67.

One of the main uses and applications of MOFs is for gas storage and separation, thus there has been a large variety of reports of different compounds and their potential as functional MOFs in recent years. For example, Turner and co-workers reported four new coordination polymer materials based on a novel tetracarboxylic acid ligand and zinc, which all displayed CO_2 uptake to various extents.[69] Vaidhyanathan and co-workers recently reported the permanent porosity demonstrated by a hydrogen bonded framework formed by a single tripodal tricarboxylic acid.[70] This material showed a preference for CO_2 adsorption over N_2 adsorption with a very high selectivity.

Owing to the dynamic and reversible nature of the non-covalent interactions that hold the network structures of supramolecular materials together and their potential to respond to external stimuli, such as temperature, pH and solvent, supramolecular soft materials are an especially attractive area of research.[22] A readily and systematically modified core unit, that retains its key modes of interaction, is an attractive platform for studying the relationship between structural features and the chosen self-assembly pathways of the chemical constituents with the properties of the bulk materials.[3,71-73] A suitable motif for this purpose is the benzene-1,3,5-tricarboxamide (**BTA**) motif, as was mentioned previously and which will be discussed in the following section.

1.2 Benzene-1,3,5-tricarboxamides (BTAs)

BTAs consist of a benzene core and three amides connected to the benzene at the 1, 3 and 5 positions. The amide group can either be attached to the benzene ring *via* the nitrogen (*N*-centred **BTA**) or *via* the carbonyl group (*C*-centred **BTA**, Figure 1.13. This thesis work will focus on *C*-centred **BTA**s, which are most commonly synthesised by reacting benzene-1,3,5-tricarbonyl trichloride with the appropriate amine in the presence of a base. The R groups that are connected to the **BTA**s can be aliphatic, aromatic, polar, apolar, etc and if all three are identical, the **BTA** is C_3 symmetric.[74] It has also been well reported that the nature of the R group attached to the **BTA** core has a great influence on the resulting properties of the derivatives, with the self-assembly of **BTA**s being finely tuned by adjusting the groups at the periphery.[74,75,76] **BTA**s can be desymmetrised by introducing different functionalities on the amides.[74] **BTA** derivatives have a tendency to form highly ordered one dimensional hydrogen-bonded superstructures, a property that leads to the formation of many classes of soft

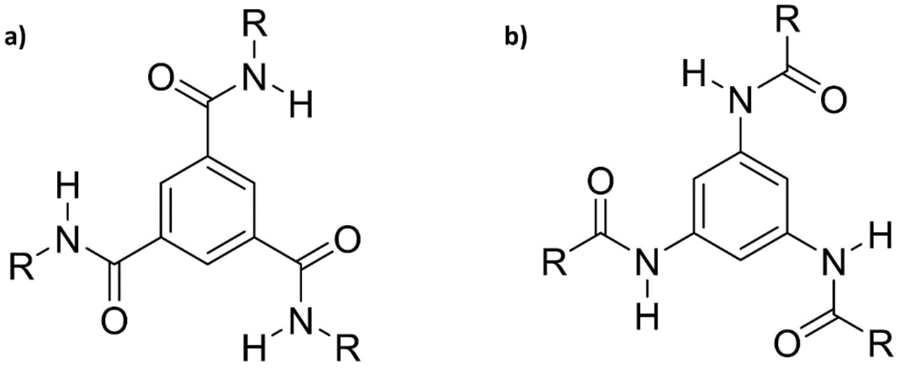

Figure 1.13 (A) General structure of a C-centred **BTA** and (b) N-centred **BTA**

materials.[77] In fact, a large variety of materials based on the **BTA** core have been reported, along with a large range of potential applications. For example, it has been reported that **BTA**s with branched alkyl side chains result in organogel behaviour,[78] while long alkyl chains can give rise to thermotropic liquid crystal behaviour.[79,80] **BTA**s that contain bulky aliphatic side chains are high melting crystalline solids, which crystallise as fibre-like needles.[81] It has also been shown that **BTA**s that contain water-labile groups can be used as microcapsules that hydrolyse over time and release their cargo into the environment, Figure 1.14.[82] Some applications of **BTA** based materials so far include organogels,[78] hydrogels,[83,84] liquid crystals,[79] nanostructures materials,[85] MRI contrast agents[86] and as nucleating agents for polymers.[87] One of the aims of the work described in this thesis was to make minor structural modifications and study this effect on function.

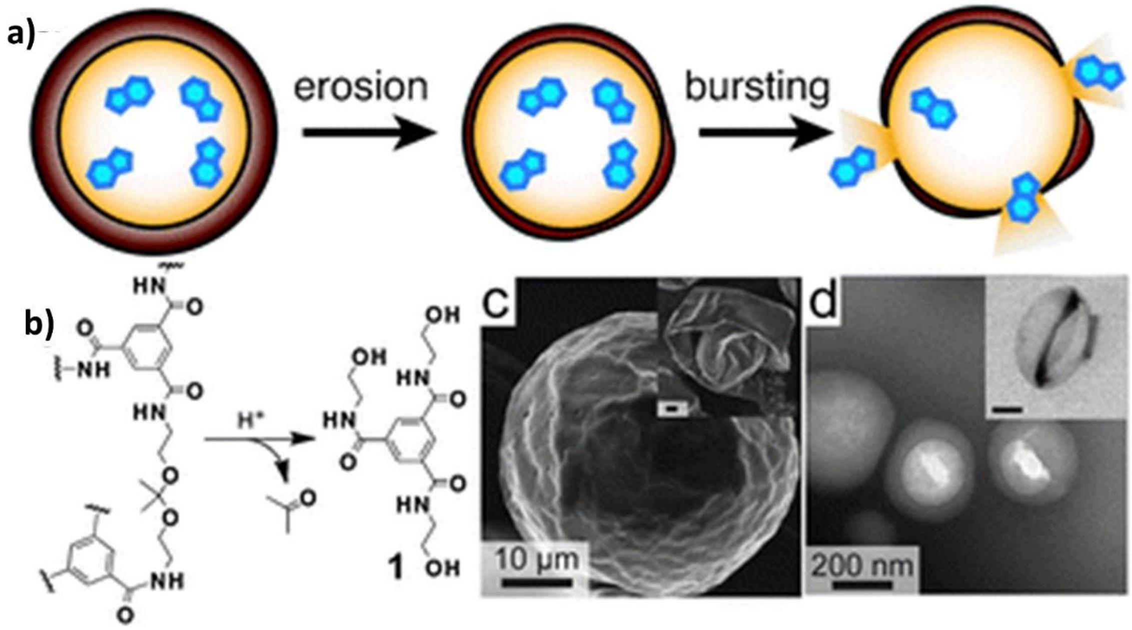

Figure 1.14 Degradation of a **BTA**-based microcapsule leading to the burst-release *via* wall erosion which occurs by (b) acid catalysed ketal hydrolysis and SEM (c) and TEM (d) images reveal smooth spherical capsules at two scales. Images of ruptured or folded capsules (insets) support a liquid-filled architecture. Images reproduced from reference 82.

1.2.1 BTA-based gels

Meijer and co-workers have reported some investigations into **BTA**-based hydrogels and the effect on the strength of the hydrogel of connecting two **BTA** units by a PEG chain.[88] The **BTA**s reported contained various hydrophobic side chains, seen in Figure 1.15, which were all found

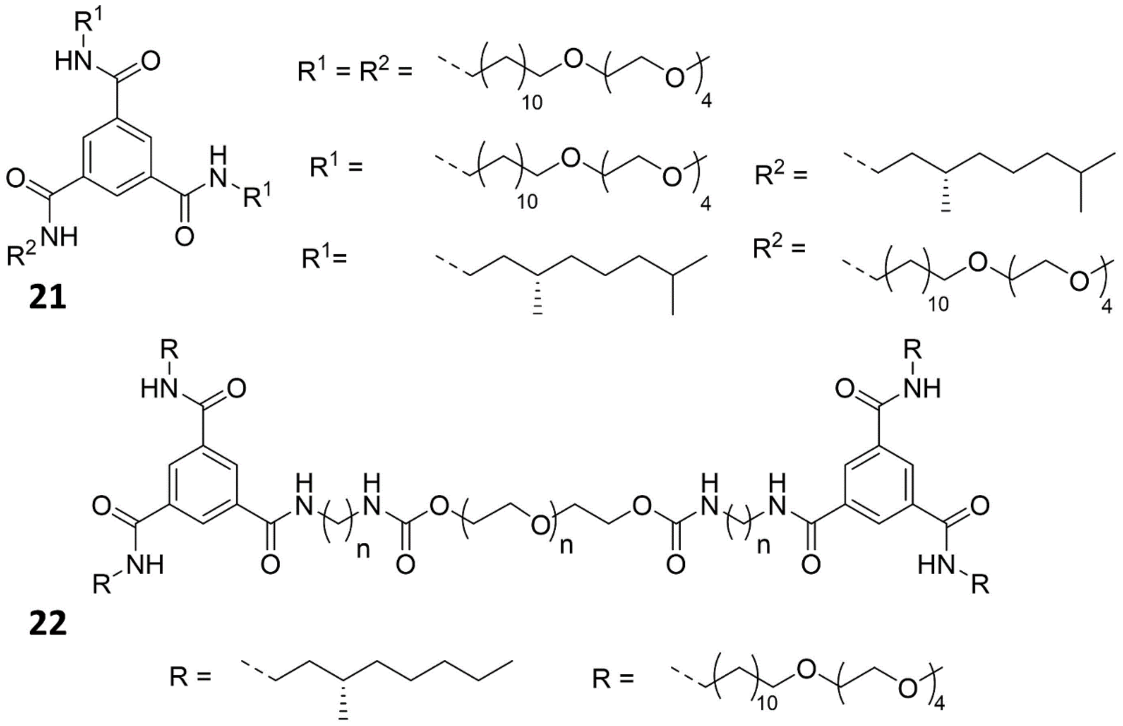

Figure 1.15 Chemical structures of the **BTA**-based compounds, where n = 8, 10 or 12, reported by Meijer to form hydrogels, image reproduced from reference 88.

to form weak hydrogels. Stronger hydrogels were obtained by connecting two **BTA** units by a PEG-based linker.

A number of aromatic carboxylic acid **BTA** derivatives, Figure 1.16, that gelate at low concentrations through the use of a pH trigger were reported by Lloyd *et al*.[14] The compounds synthesised were all insoluble in water, however, were found to dissolve upon the addition of three equivalents of aqueous sodium hydroxide (NaOH) (except for **28a**) Addition of small amounts of hydrochloric acid (HCl) resulted in the gelation of compounds **23a-27a**. **23b** not gelate using these conditions thus implying that hydrogen bonding between the amides is necessary for gel formation. SEM images of the gel fibres revealed them to be 50-200 nm in diameter.

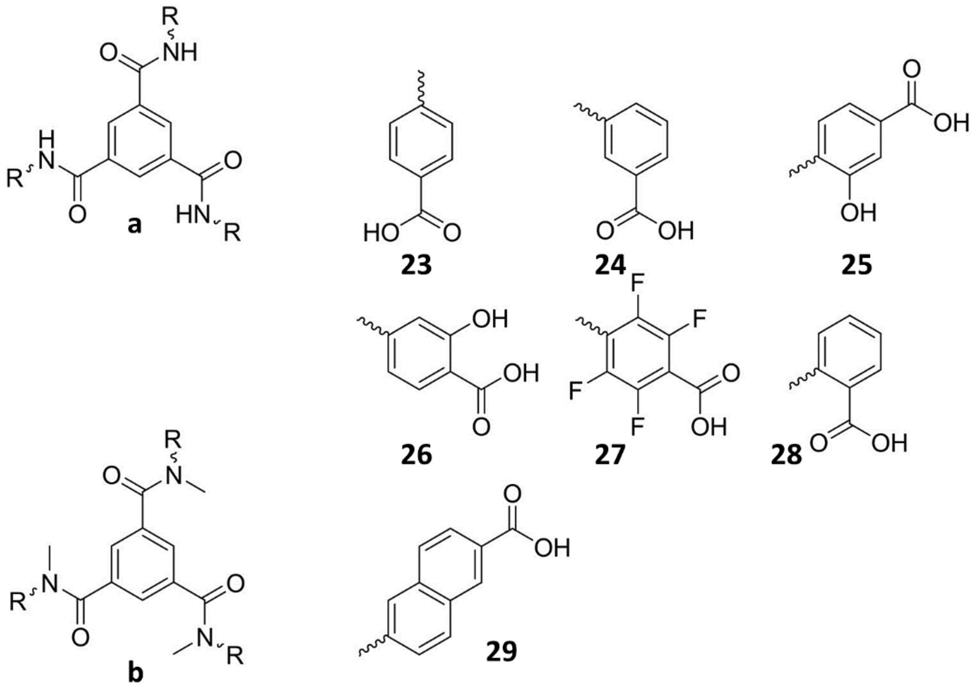

Figure 1.16 Compounds reported by Lloyd and co-workers. Structures reproduced from reference 14.

The kinetics of the pH-induced self-assembly of a model hydrogelator, Figure 1.17, into nanofibers using a microfluidic device were studied by Förster and co-workers.[89] In this study, the formation of the fibre assemblies, in a reaction channel, was accompanied by a blue photoluminescence which was monitored. This was the first time that the association constant of a hydrogel could be determined.

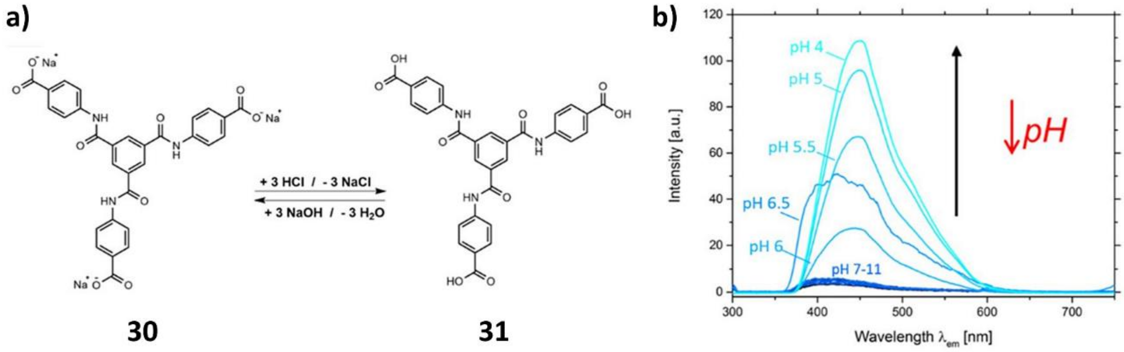

Figure 1.17 (a) The structure of the **BTA** hydrogelator in its charged sodium salt form and its uncharged protonated form and (b) the characteristic fluorescence spectra showing the increase of fluorescence intensity of the aqueous **BTA** solutions with decreasing pH value due to its self-assembly into fibres. Image reproduced from reference 89.

The self-assembly of an achiral **BTA** molecule into a variety of nanostructures was reported by Liu and co-workers, Figure 1.18.[12] The **BTA** compound reported contained peripheral naphthoic acid ethyl ester moieties and was found to self-assemble into structures

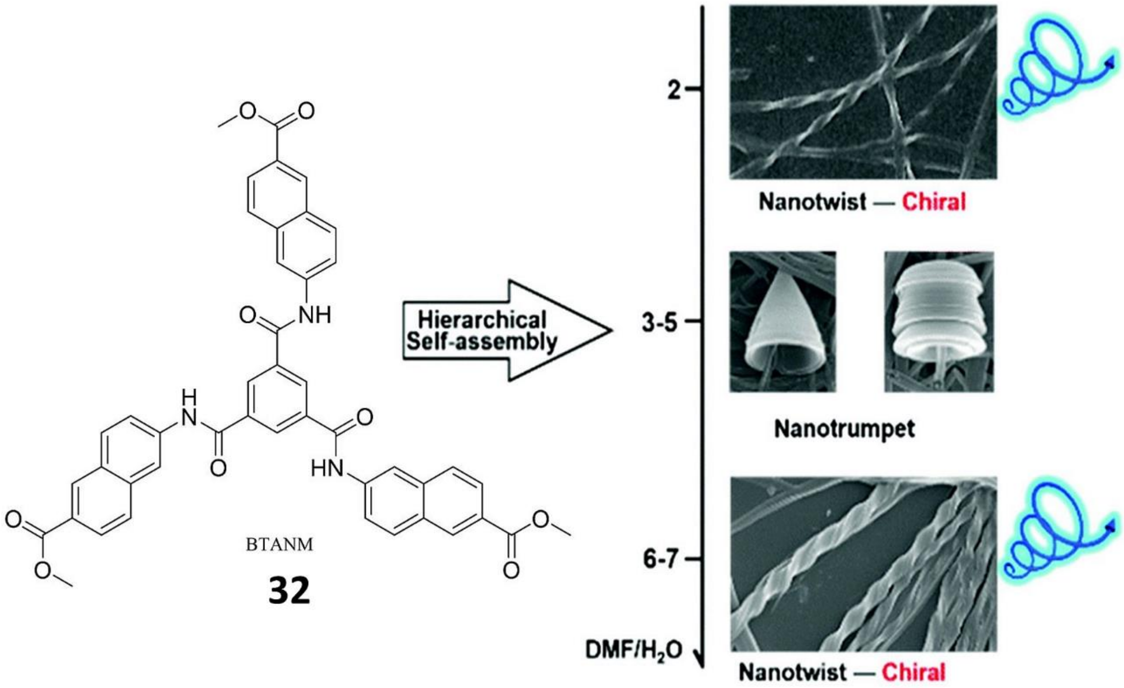

Figure 1.18 Structure of the gelator reported by Liu and co-workers and the various nanostructures formed from different ratios of DMF/H_2O. The nanotwists showed supramolecular chirality and CPL while the nanotrumpets did not. Image reproduced from reference 12.

such as nanobelts, nanotwists and nanotrumpets in a mixture of dimethylformamide (DMF)/H_2O. An interesting feature of these structures was that they displayed supramolecular chirality as well as circularly polarised luminescence signal (CPL) though the component is achiral. Upon gelation of the compound in DMF/H_2O, different structures were formed based on the DMF content. Nanobelts were formed at lower DMF concentrations, while ‘nanotwists’ or ‘nanotrumpets’ were formed at a higher DMF content. This work further enhanced the understanding of the effect of solvent on supramolecular self-assembly and supramolecular chirality emerging from achiral molecules.

BTA-based organogels have also been reported.[3] For example, Feringa *et al*. compared the properties of a cyclohexane core and a benzene-1,3,5-tricarboxamide core substituted with various arms, and showed the effect that these modifications have on the intermolecular interactions. They compared the aggregation properties, thermal stability and morphology of the reported compounds and found that the cyclohexane derivatives in this case displayed better gelation and aggregation properties. The authors state that the sterically demanding R-groups of the **BTA** compounds are presumably the cause of the diminished aggregation and gelation behaviour. Replacing the benzene core with a cyclohexane core resulting in a dramatic increase

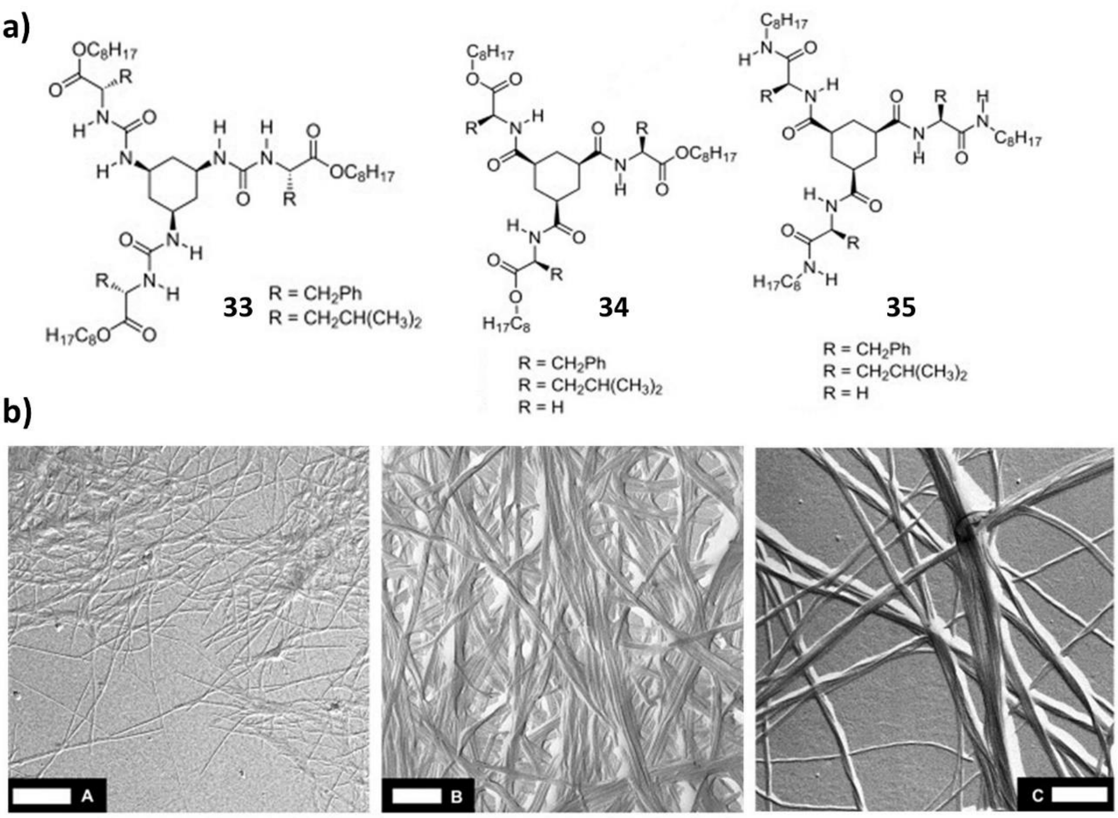

Figure 1.19 (a) Examples of the various cyclohexane structures reported by Feringa and co-workers and (b) TEM of some of the cyclohexane tris amide derivatives in (a) 1-octanol, (b) *n*-hexadecane and (c) 1-octanol. All scale bars represent 500 nm. Image reproduced from reference 3.

in the gelation and aggregation, with all the derivatives found to gelate. This was presumably related to the more favourable orientation of the H-bonding units with respect to the mean plane of the core.

The gelation behaviour of **BTA** decorated on each arm by a pillar[5]arene was recently disclosed by Ning and co-workers, shown in Figure 1.20.[90] Pillar[n]arenes are rigid-like architectures that contain electron donating cavities and are relatively easily functionalised,

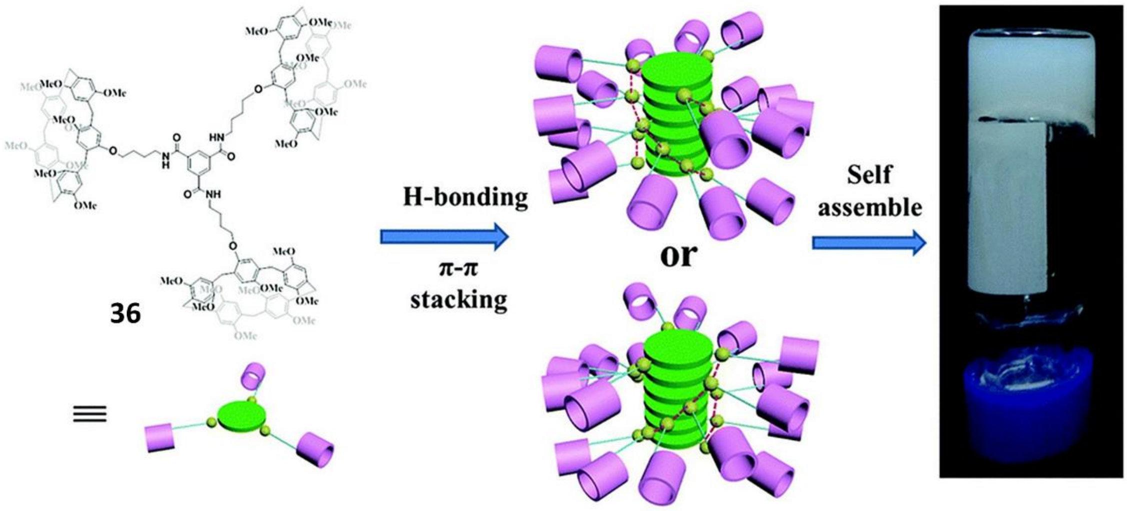

Figure 1.20 One of the pillarene compounds reported by Ning and co-workers, and the formation of an optically active supramolecular gel**.** Image reproduced from reference 90.

making them excellent host molecules for a variety of guests and are also a good adsorption and separation material for gases.[91] Thus it was postulated that incorporating pillar[n]arenes into a gel could endow the gel with some new abilities, for example, gas adsorption. The **BTA**-pillar[5]arene derivative, **36**, reported was found to gelate at low concentrations (0.2 wt%) in acetonitrile upon sonication at room temperature. The authors report the potential of this as a gel featuring a cavity for guest adsorption and further work is ongoing.

Supramolecular gelators for ionic liquids comprised of amino acid benzene-1,3,5-tricarboxamides were developed by Maruyama, thus opening up the possibilities for new types of electrochemical applications for **BTA** molecules.[92] In this report, a number of amino acid based **BTA** methyl esters were reported to gelate a number of ionic liquids at low wt%, with hydrogen bonding found to play a key role in the gelation process. Gelation was also observed in organic solvents however, it was at a higher wt% than for ionic liquids, the morphology of these gels is shown in Figure 1.21. The ionogels obtained possessed reversible thermal transition properties and viscoelastic properties typical of a gel. The intrinsic conductivity of the ionic liquids, even at high gelator concentrations, was retained in the ionogels, thus demonstrating that the characteristics of the ionic liquids were maintained following gelation.

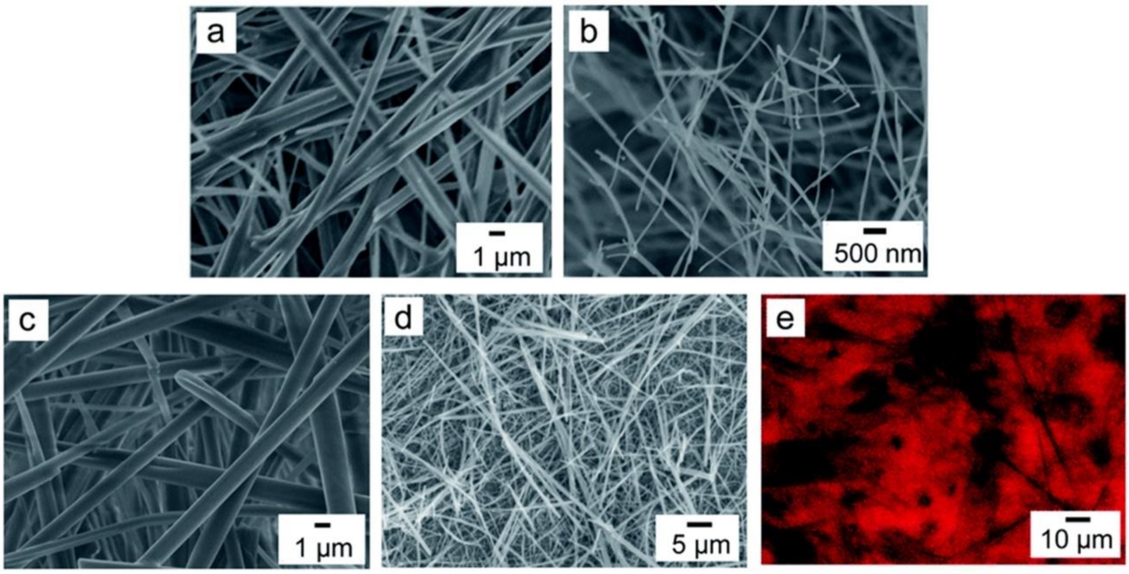

Figure 1.21. (a&b) Field emission SEM (FESEM) of ionogels formed in [BuMeIm][TFSA] and [BuMeIm][CF_3SO_3], (c&d) organogels formed in EtOH and MeCN and (e) confocal laser scanning microscopy of ionogels stained with rhodamine. Image reproduced from reference 92.

Another area of research for **BTA**-based systems is their ability to form supramolecular polymers and the applications of these polymers which will be discussed in the section.

1.2.2 BTA-based polymers

Supramolecular polymers have been defined as ‘polymeric arrays of monomeric units that are held together by highly directional and reversible non-covalent interactions, resulting in polymeric properties in solution and bulk'.[93] Supramolecular polymers differ from conventional covalent polymers as the process of one-dimensional self-assembly of the monomers can create assemblies that have internal order and thus, can have completely new functions and persistence lengths that are not observed in covalent polymers.[56] They offer a new approach to biodegradation and drug delivery as they lack the covalent backbone of traditional polymers. Some current applications of these materials have been found in the area of organic electronics and as biomaterials for drug delivery and tissue engineering.[94] Much work on **BTA**-based supramolecular polymers has been carried out by the group of Meijer and Palmans, as previously mentioned.[57,95]

Meijer reported the use of a **BTA**-based system as a platform for intracellular drug delivery, Figure 1.22.[96] In this report, Nile red (NR) was used as a hydrophobic guest for encapsulation in the interior of the polymer, while a small interfering ribonucleic acid (siRNA) was used for electrostatic binding on the exterior. The authors reported the ability to load NR and siRNA on a modularly prepared cationic multicomponent **BTA** polymer and the delivery of this cargo into living cells. Silencing experiments revealed that the intracellular delivered

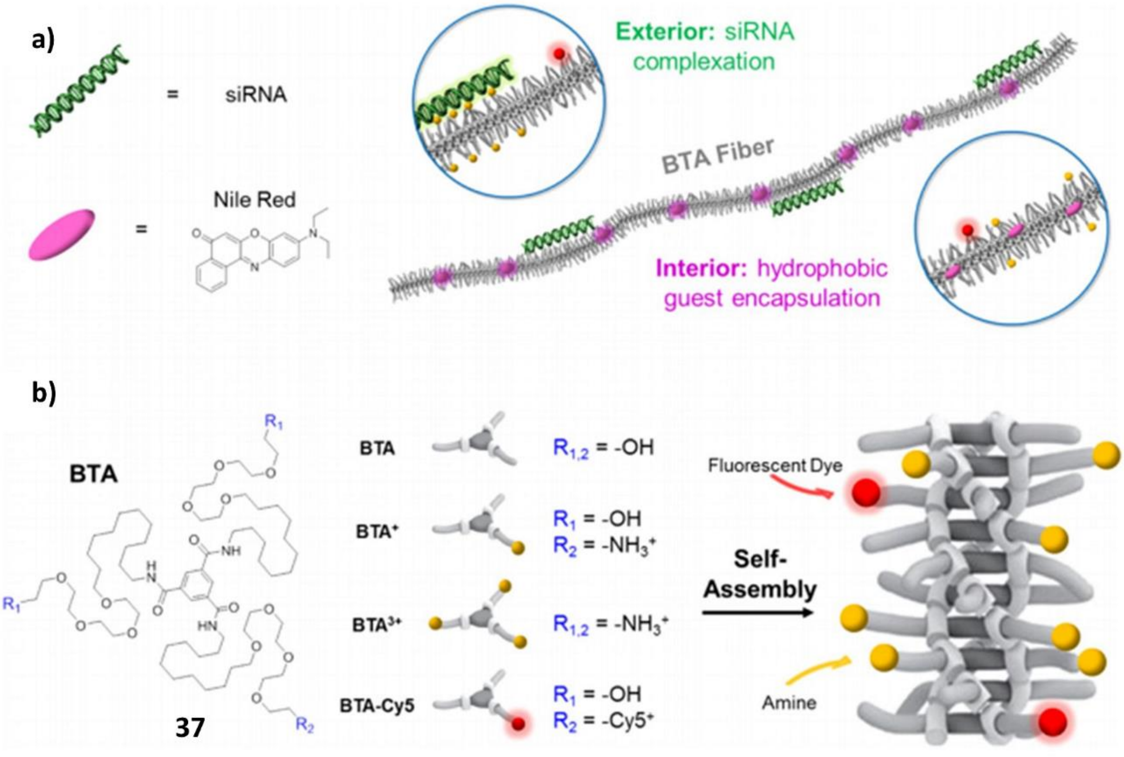

Figure 1.22 (a) **BTA** fibers contain two compartments that can be used for intracellular delivery. Small hydrophobic compounds such as Nile Red can be encapsulated in the lipophilic core and siRNA can be condensed on the hydrophilic exterior through electrostatic interactions and (b) the multicomponent polymers *via* co-assembly of non-functional, positively charged, and fluorescently labelled **BTA** monomers. Image reproduced from reference 96.

siRNA significantly reduced gene expression, thus validating the potential of the supramolecular **BTA** platform for intracellular delivery.

A water-soluble BTA derivative, **38**, functionalised at the periphery with one L-proline moiety shown in Figure 1.23, that self-assembles into a one-dimensional, helical, supramolecular polymer was also reported by Meijer and co-workers.[57] The reported derivative formed micrometre long supramolecular polymers which were stabilised by hydrophobic interactions and directional hydrogen bonds. This polymer was found to display high activity and selectivity as catalysts for the aldol reaction in water using *p*-nitrobenzaldehyde and cyclohexanone as reaction substrates.

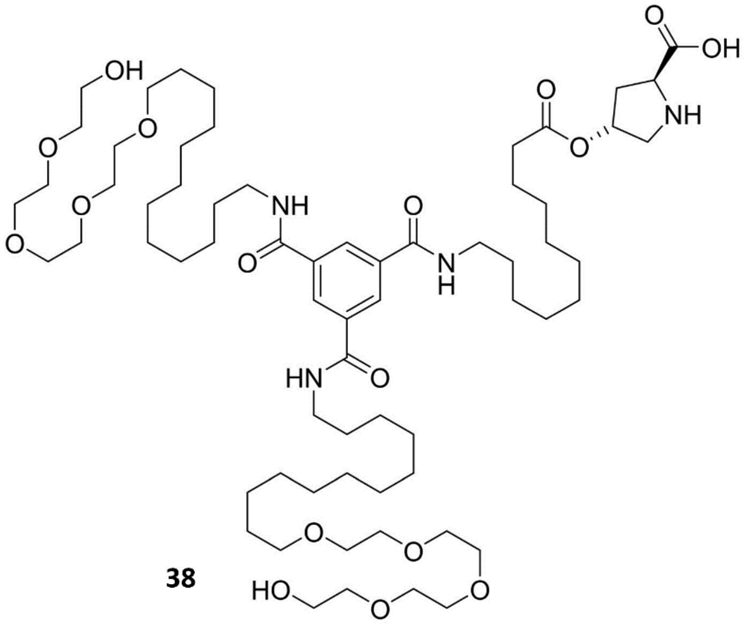

38

Figure 1.23 BTA-proline structure reported by Meijer and co-workers.

1.2.3 BTA-based liquid crystals

It has been previously noted that **BTA**s substituted with long alkyl side chains often result in thermotropic liquid crystal behaviour.[74,79,80] The threefold hydrogen bonding between the amide groups, that is commonly found in **BTA** derivatives, results in columnar structures, with these structures known to form hydrogen bonded columnar liquid crystals.[85,97] In addition, the strong macrodipoles that are present in these **BTA** columnar systems offer the possibility for the alignment of the columnar phase by an electric field. For example, Sijbesma and co-workers reported the polar-switching of three symmetrically substituted **BTA**s, with alkyl chain lengths varying from six to eighteen carbons. It was found that the columnar phases of these three derivatives could be aligned uniformly in a direct current (dc) field, Figure 1.24.[97] Other

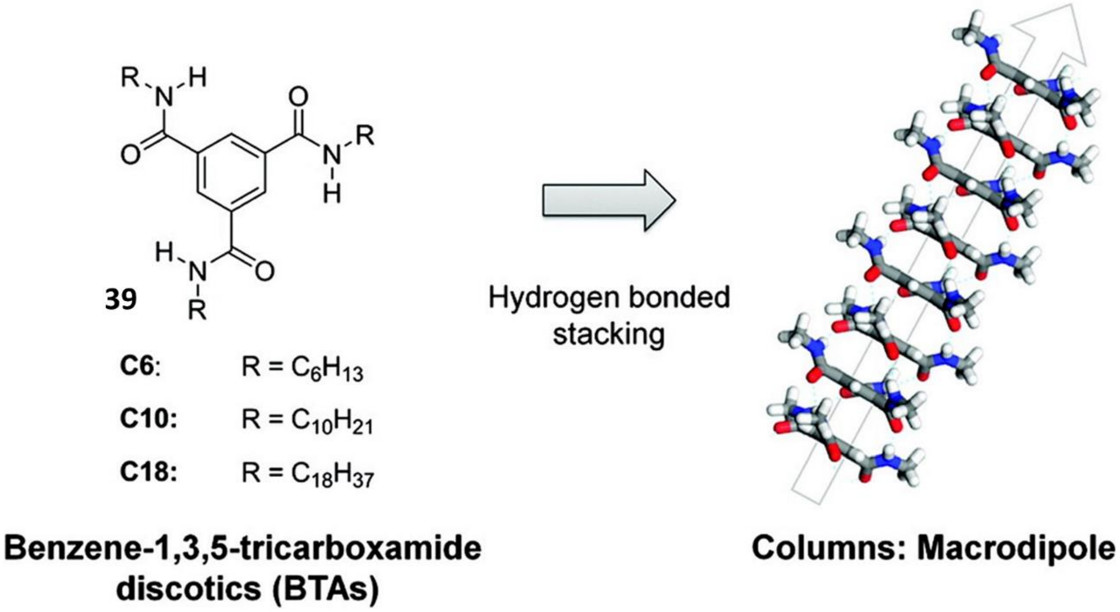

Figure 1.24 The **BTA** derivatives reported by Sijbesma and co-workers and a schematic of their assembly into columnar structures. Image reproduced from reference 97.

reports of **BTA** discotic liquid crystal behaviour include a report of Neier and co-workers of a columnar mesophases formed by a bromo-substituted and alkyloxy substituted **BTA**s,[98] another report by Sijbema and co-workers of a discotic liquid crystal derived from a **BTA** compound and poly(propylene) dendrimer[85] and a **BTA**-azobenzene derivative that formed a mesophase at high temperatures to name a few examples.[99]

Due to the tendency of **BTA** derivatives to crystallise, particularly those with bulky, aliphatic side chains,[74,81,87] they give rise to a variety of solid-state structures which will be discussed in the following section.

1.2.4 BTA-based coordination polymers and porous materials

BTA-based derivatives have a strong tendency to form crystalline materials and as previously discussed with respect to the other types of soft materials. The identity of the side arm functionality greatly influences the structure and behaviour of these materials. In this section, a brief overview of some reported **BTA** compounds and their structural features and potential applications will be given.

The self-assembly of cadmium with a **BTA** derivative, Figure 1.25, resulting in the formation of a two-dimensional polymer was reported by Vittal *et al*.[100] This polymer consisted of two-dimensional sheets that stacked through face to face π-π interactions between the central benzene ring and hydrogen bonds in a bilayer structure. It was presumed that the formation of this bilayer structure was due to the seven-coordinate geometry of the cadmium which forces the pyridyl rings above and below the plane of the benzene ring of the ligand as opposed to the cage structures favoured by Cu(II) and Pd(II) that were previously reported.[101]

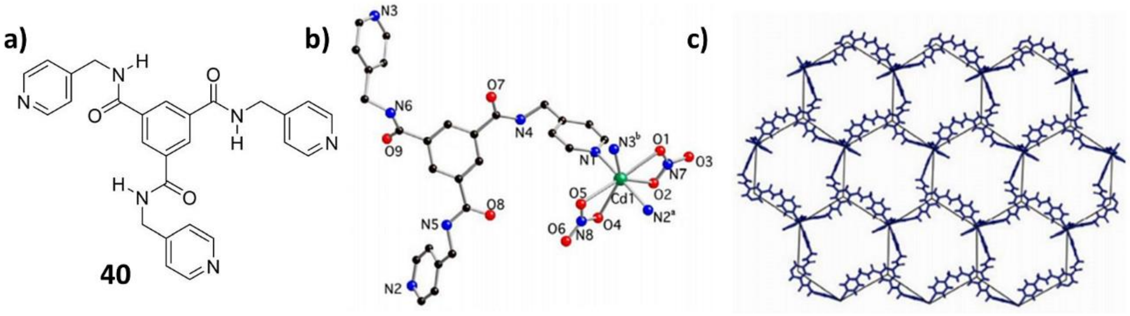

Figure 1.25 (a) Structure reported by Vittal and co-workers, (b) the coordination environment of Cd(II) and (c) a perspective view of the 2D layer with honeycomb structure in the *ab* plane. Image reproduced from reference 100.

Zhao and co-workers reported the self-assembly of a C_3 symmetric ligand, **41**, into an interesting core-rosette structure whose formation was driven by intermolecular hydrogen-bonding interactions.[102] The reaction between **41** and Zn(II), Co(II) or Cd(II) in solvothermal conditions resulted in the formation of four new coordination polymers with a variety of interesting structural motifs, which are shown in Figure 1.26. For example, the solvothermal reaction between **41** and zinc nitrate resulted in a coordination polymer with a twofold

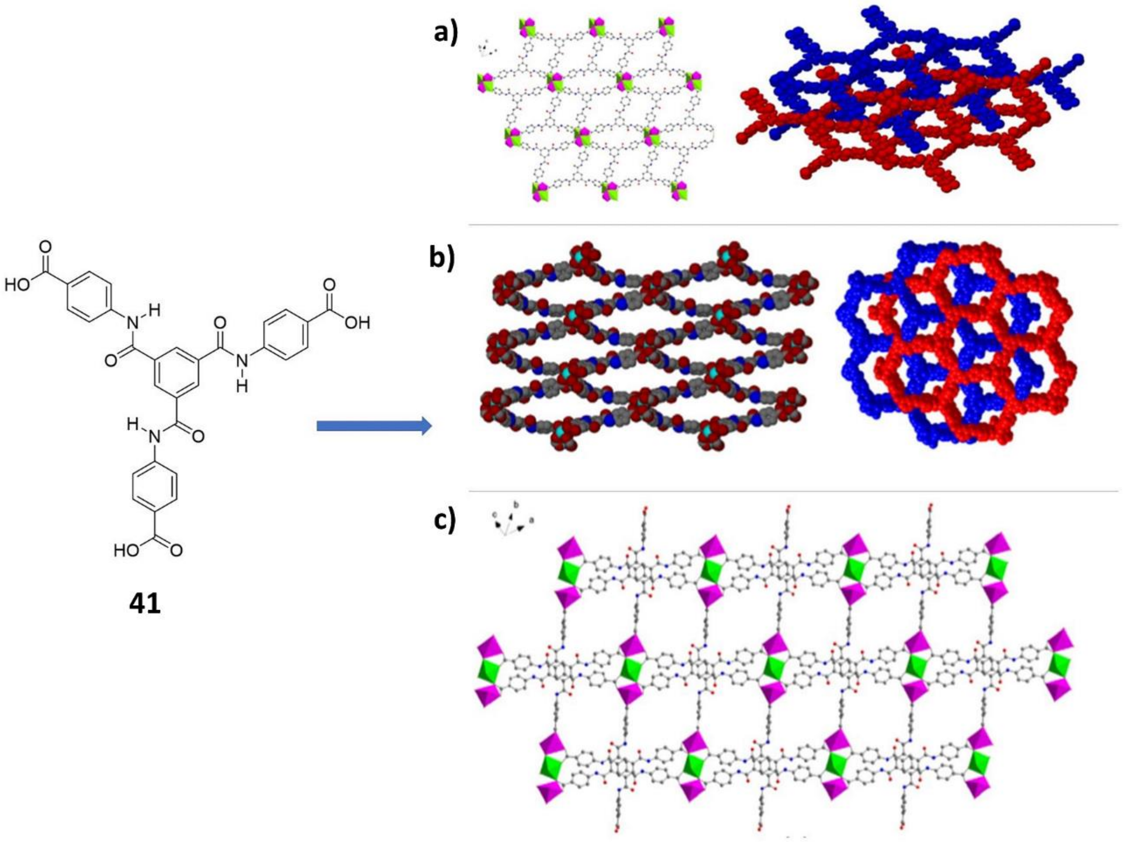

Figure 1.26 (a) Ligand used by Zhao and co-workers, (b) the layer structure of the zinc complex, with the Zn^{2+} atoms shown in polyhedral mode and the doubly interpenetrated framework, (c) space filled model showing the three-dimensional framework of the cobalt chloride complex viewed along the b direction and the twofold interpenetrated network of the zinc complex viewed along the a direction and (d) the polyhedral representation of the two-dimensional network generated from cobalt nitrate and the ligand Image reproduced from reference 102.

interpenetrating architecture, with **41** and cobalt chloride resulting in a twofold interpenetrating three-dimensional architecture. Cobalt nitrate or cadmium nitrate when reacted with **41** gave rise to isomorphous structures that showed a grid layered architecture, while also displaying classical π-π stacking interactions. These results demonstrated the effect of the structural diversity of **41** when reacted with different metals. The authors report that further investigations into the potential applications of these polymers are ongoing.

Structural investigations of a series of halogen derivatives of **BTA** were reported by Biradha and co-workers.[103] The halogens were introduced to the structures in the form of halophenyl side arms as depicted in Figure 1.27. In this report, the derivatives were found to assemble into the triple helical columns, *via* amide bonds, common for **BTA** compounds. In the case of the iodo, chloro and bromo derivatives, the columns were found to assemble into porous materials *via* halogen-halogen interactions. The I_2 uptake of these three compounds was investigated, with the chloro derivative found to display the best uptake, followed by iodo and bromo, respectively. N_2 uptake experiments were also carried out and revealed the same results as the I_2 uptake experiments, while CO_2 uptake was much lower than the uptake of N_2 and I_2. The fluoro derivative was found to assemble into a one-dimensional column through triple helical N–H···O bonds, with the central rings stacking on each other in a staggered fashion, with no contacts between the fluorine observed. Packing between the columns is very compact and the fluorophenyl rings of neighbouring columns are interdigitated. This was a nice example of relatively simple **BTA** structures that displayed potential gas uptake applications.

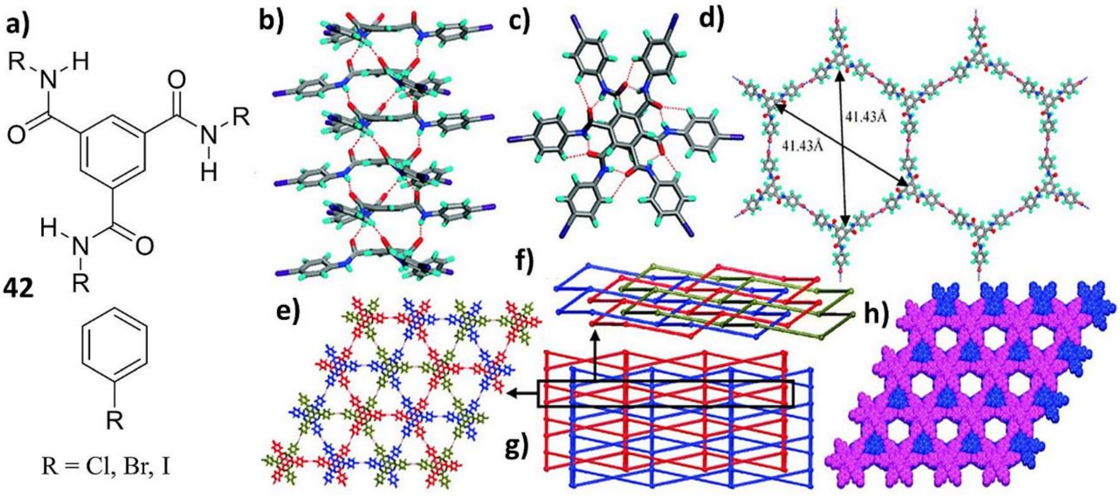

Figure 1.27 (a) Ligand **42** used by Biradha and co-workers where R is an iodophenyl, bromophenyl or chlorophenyl group, (b) side view of the columns formed in the iodo-complex, (c) top view of the columns formed in the iodo-complex, (d) 2D honeycomb layer formed *via* Br···Br interactions in the bromo-complex, (e) top view of the triply interpenetrated honeycomb network, (f) side view by reducing the molecules into nodes and the Br···Br interactions into connections, (g) doubly interpenetrated 2D network with the vertical lines representing one-dimensional hydrogen bonded columns and (h) top view of the two-fold interpenetrated 3D network. Image reproduced from reference 103

Amino-acid based **BTA** derivatives have also shown some promise in the area of porous materials with an example of such being demonstrated by Haldar and co-workers.[17] In this work, a tyrosine and methionine derivative were synthesised, their structures analysed and potential porosity investigated. **43** self-assembled through the classical threefold hydrogen bonding and π-π stacking interactions to form a one-dimensional nanorod type structure. On the other hand, **44**, which contains multiple hydrogen bonding units on the side chains, loses its C_3 symmetry and thus loses its classical threefold amide-amide helical arrangement to result in a porous structure. The resulting structures are shown in Figure 1.28. The lack of a columnar structure of **44** compound was attributed to the competitive intermolecular hydrogen bonding that occurs between the tyrosine phenolic oxygen and the amide hydrogen of the tricarboxamides, combined with a certain amount of steric hindrance imparted by the tyrosine.

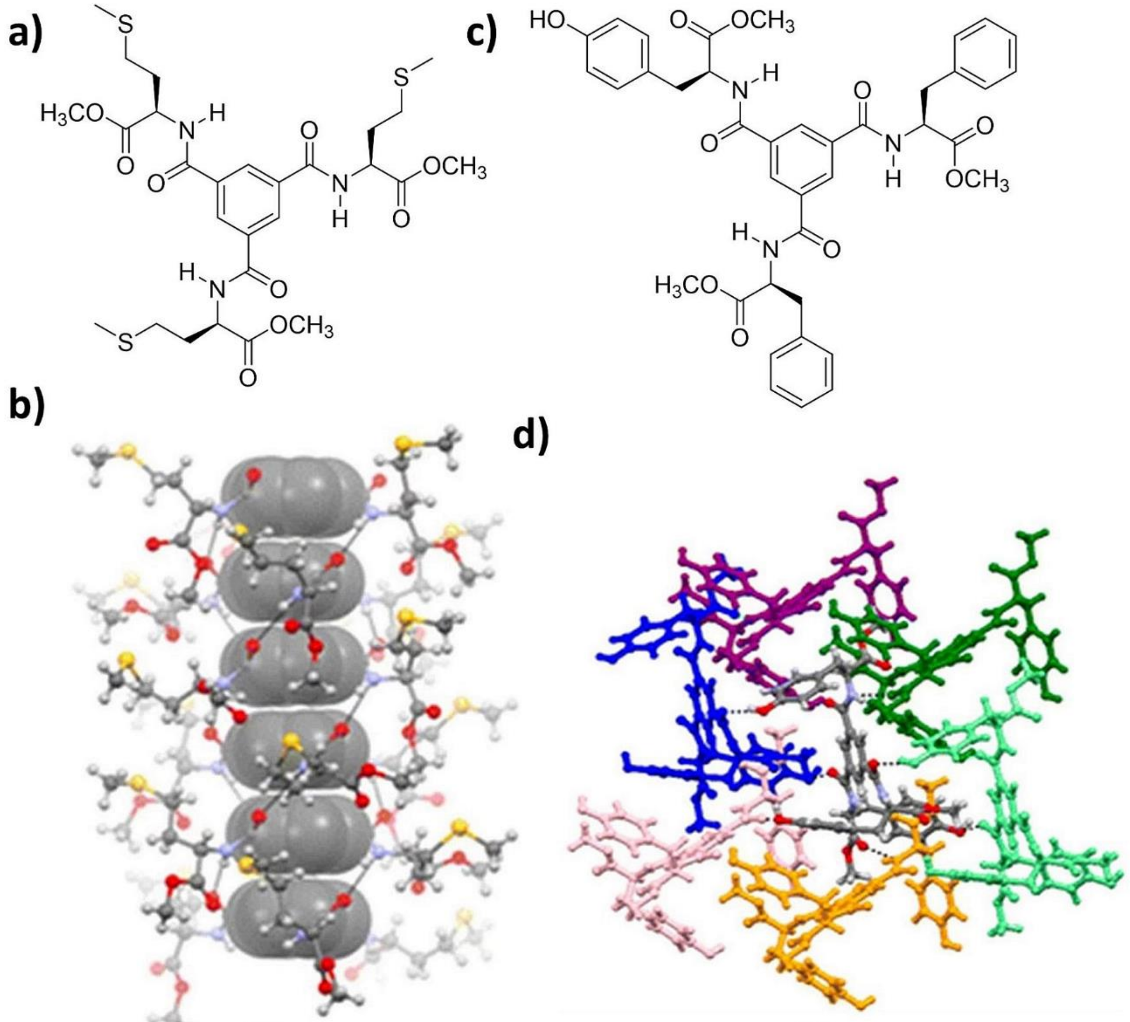

43 **44**

Figure 1.28 (a&b) The methionine derivative, **43**, reported by Haldar and co-workers and its columnar assembly through multiple intermolecular N-H···O hydrogen bonds and π-π stacking interactions and (c&d) the reported tyrosine derivative, **44**, and its cage-like packing in the solid state by multiple N-H···O and O-H···O hydrogen bonds. Image reproduced from reference 17.

The porous tyrosine derivative **44** was found to exhibit ten times N_2 uptake compared to its methionine, **43**, counterpart.

These studies served as an influence for some of the work described in Chapter 3 in which the adsorption properties of an aromatic and amino acid based **BTA** is investigated.

1.2.5 Other niche uses of BTA-based compounds

There have been a number of other, more niche potential applications of **BTA**-based systems, for example, the use of a **BTA**-Gd(III) system as a potential MRI imaging agent reported by Meijer and co-workers.[86] A discotic fluorinated **BTA**, previously reported by the Meijer group which had been shown to polymerise in H_2O into columnar aggregates was used in this study, Figure 1.29.[104] The aggregation was due to a combination of hydrogen bonding, π-π interactions and solvophobic effects The authors proposed that that the addition of charged Gd(III)-diethylenetriaminepentacetic acid (**DTPA**) chelates to the **BTA** would yield supramolecular oligomers of a controlled shape and size due to the balancing of electrostatic charges, while the fluorinated aromatics increased the aggregate stability. Due to the high stability and the hydrodynamic radius in the nanometer range, this system was evaluated as an MRI contrast agent. The high stability and slow clearance rates of the **BTA**-Gd(III) complex, combined with the ideal nanometer size, were all positive indicators of potential use as molecular imaging agents, with the authors stating that further investigations are ongoing.

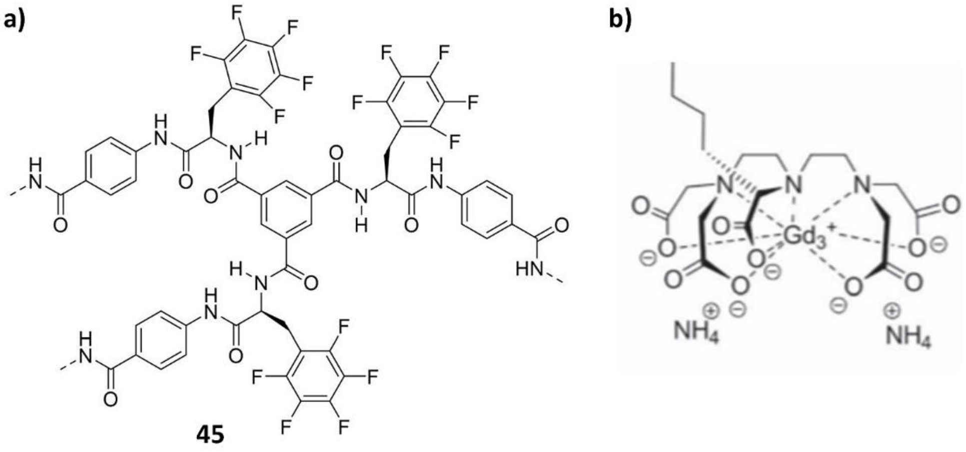

Figure 1.29 (a) The discotic **BTA** compound used by Meijer and (b) the Gd(III)-**DTPA** used. Structures reproduced from reference 104.

In nature, dynamic molecular platforms are used for the recruitment of weakly associating proteins to form higher-order assemblies. These unique abilities and properties of natural supramolecular protein assemblies has inspired scientists to create synthetic systems capable of mimicking these characteristic features of their natural counterparts, for example, supramolecular polymers, vesicles and DNA-origami structures.[105] Nanostructures that emulate these dynamic behaviours require features such as reversibility, specificity and plasticity. Meijer and co-workers recently reported the use of a **BTA** derivative as a synthetic protein recruitment platform.[106] A schematic of this process is shown in Figure 1.30. The **BTA** derivative used consisted of a **BTA** core with a ten-nucleotide receptor strand that assembled into micrometre long supramolecular polymers. It was reported that protein-DNA conjugates could be recruited on the **BTA** polymer with a high degree of specificity and temporal control. The supramolecular interactions between the relatively small **BTA**s were found to be sufficient

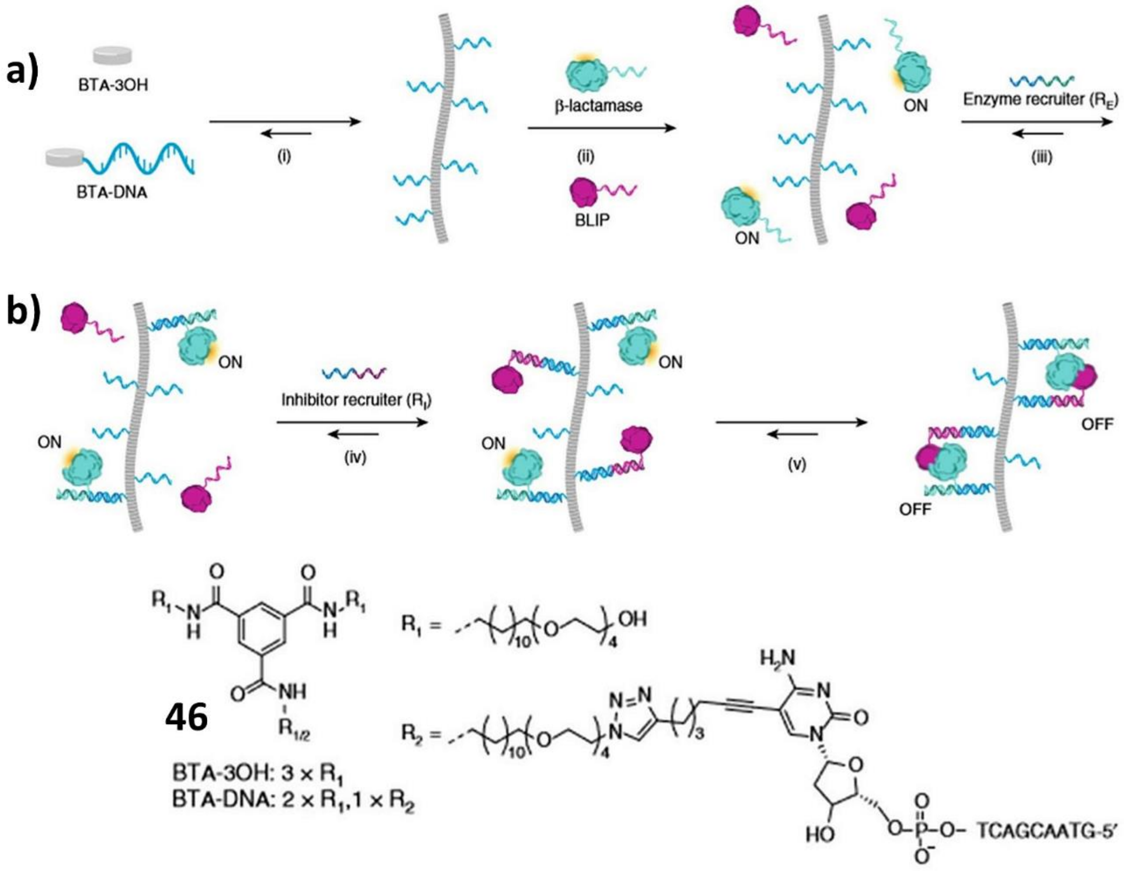

Figure 1.30 (a) Schematic representation of the selective recruitment of proteins to **BTA** polymers, (i) the 10-nucleotide functionalised **BTA** monomers are co-assembled in a desired ratio with inert BTA monomers to result in supramolecular polymers decorated with DNA receptors. (ii) To allow for sequence specific oligonucleotide directed recruitment of the enzyme (β-lactamase) and its inhibitor (BLIP), each protein is functionalised with a unique 21-nucleotide handle strand. (iii) Addition of a specific recruiter oligonucleotide that is complimentary to the handle strand on the **BTA** polymer and the enzyme results in the selective recruitment of the enzyme to the polymer. (iv) Addition of the inhibitor recruiter strand results in the recruitment of the inhibitor to the supramolecular platform. (v) The dynamic nature of the platform enables the rearrangement of the proteins along the polymer to allow an enzyme-inhibitor complex to form, resulting in decreased enzyme activity. (b) The **BTA** structures used in the study. Image reproduced from reference 106.

to coordinate the assembly of protein complexes *via* DNA hybridisation. The ten nucleotide DNA-receptor strand provides adequate recruitment of low nanomolar concentrations of proteins on the **BTA** polymer, while still allowing a rapid exchange of DNA-conjugated proteins along the **BTA** scaffold. In a follow-up publication by a number of the same authors, they reported the use of the same **BTA** derivative as a dynamic scaffold to template DNA-based molecular computing.[107] The authors report that by selectively recruiting DNA circuit components to a supramolecular **BTA** polymer functionalised with ten nucleotide handle strands, the kinetics of strand displacement and strand exchange were accelerated one hundred fold. The strand exchange reactions were also thermodynamically favoured by bivalent interactions between the reaction product and the supramolecular polymer. The ability of the supramolecular polymer to increase the efficiency of DNA-based computing was tested in three well-known and important DNA-computing operations; multi-input AND gates, catalytic hairpin assembly and hybridisation chain reactions and was successful in each case. It was proposed that these polymers could also hold potential in the areas of responsive biomaterials and smart drug delivery systems.

To summarise, **BTA**-based derivatives have a wide range of potential applications and show a variety of interesting structural features. Although there have been many reports of **BTA** materials and the effect of structure on function, there still remains many unknowns on the structural features and their influence on the self-assembly behaviours of supramolecular materials. The effect of very minor structural changes on function will be reported in following chapters, along with the extension of these simple core **BTA** molecules into more extended systems and the effect of this extension.

1.3 Previous work carried out within the Gunnlaugsson group

1.3.1 BTA-based work

In recent years, much of the research carried out within the Gunnlaugsson has focused on the generation of supramolecular soft materials, particularly gels and polymers which will be discussed in the following sections.

Kotova and co-workers reported the use of metal-directed gelation in developing supramolecular structures.[108] In this work, the formation and physical analysis of novel luminescent Eu(III)-based hydrogel formed by the self-assembly of the tripodal **BTA** ligand **47**, shown in Figure 1.31, was analysed. The **BTA** core of **47** facilitates the initial self-assembly of the ligand into the classical **BTA** helices through threefold hydrogen bonding, with the terpyridine end group moieties facilitating the coordination of Ln(III) ions, offering the possibility of the formation of higher-order self-assembly gels. **47** alone was found to gelate in

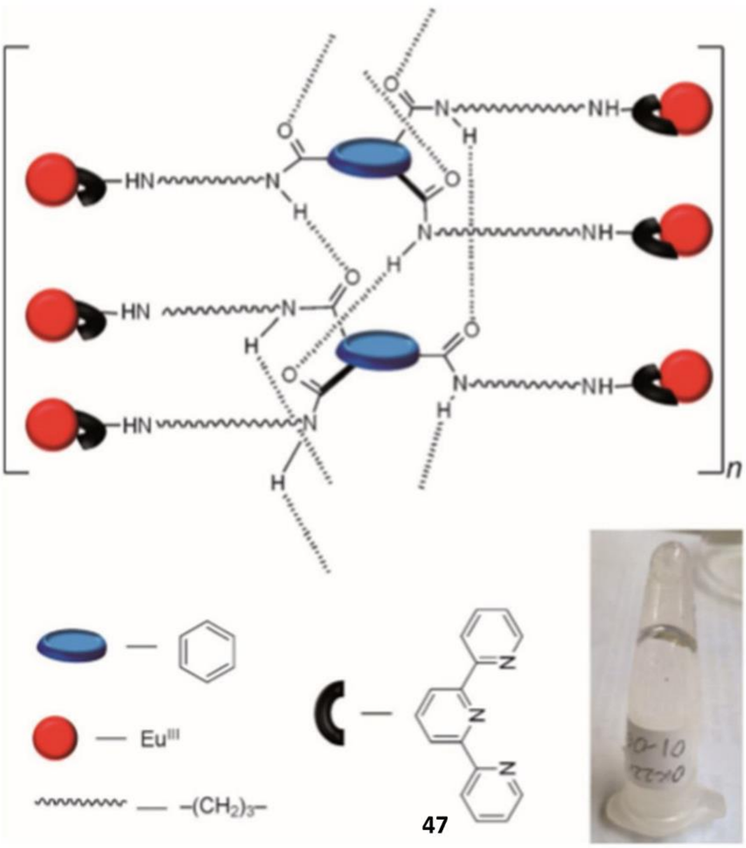

Figure 1.31 Schematic representation of the proposed formation of threefold hydrogen bonding in helices of the terpyridine-based tripodal ligand **47**, showing the europium binding sites on the outside of the helix. Also shown is the inversion test of the transparent $EuCl_3$-L gel in a H_2O/MeOH mixture Image reproduced from reference 108.

a 70:30 H_2O/MeOH mixture at 0.25-0.3 wt% upon slow evaporation. When the ligand was mixed with $EuCl_3.6H_2O$ (in 1:1, 2:1 and 3:1 Eu/L ratios) in a 70:30 H_2O/MeOH mixtures, transparent gels result in all cases upon sitting of the mixtures at ambient conditions. The Eu(III) gels were found to be luminescent, with the coordination of the terpyridine moieties confirmed by the characteristic metal-centred emission. The morphology of these gels was studied using SEM and TEM and were found to be drastically different, as seen in Figure 1.32. The ligand gels consisted of long intertwining bundles of strings, similar to that observed for similar organic **BTA** structures, while the metallogel resulted in more ordered gels, where the strands appear to be locally aligned. Results from TEM studies, along with the diffraction patterns obtained suggested that the initial polymerisation of the ligand takes place and that this allowed for the preorganisation of the ligand in a way that allowed for the Eu(III) ions to act as a type of glue by intermolecularly connecting the polymers through Eu(III) ions to more than one terpyridine unit in neighbouring strands.

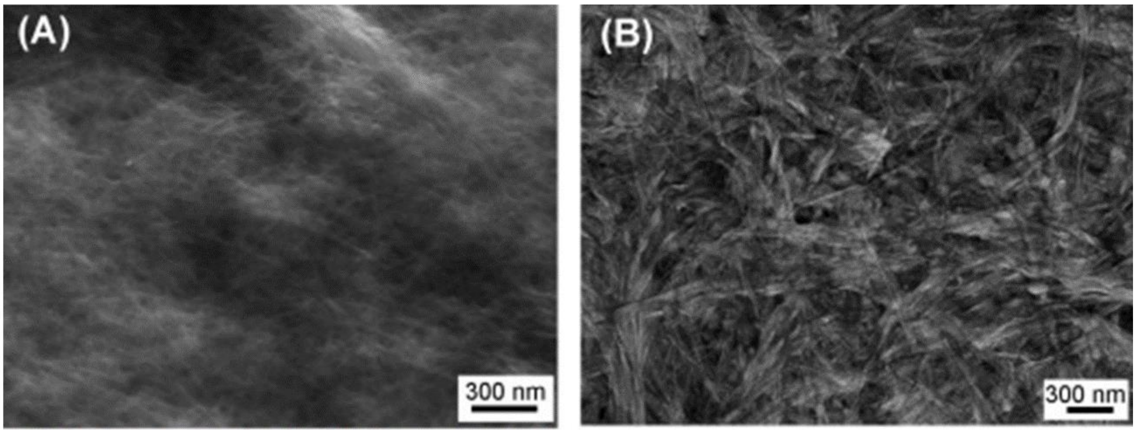

Figure 1.32 (a) SEM of the gel of **47**, scale bar 300 nm and (b) SEM of the Eu(III) gel, scale bar 300 nm, showing it to be more ordered than the ligand gel. Image reproduced from reference 108.

In further work on this ligand, the effect of transition metals on the gel characteristics was investigated.[4] Here, the self-assembly properties of the ligand in MeOH solution with d-block ions was monitored by changes in the ligand-centred absorbance and fluorescence, with the results revealing that the ions interacted with the ligands in all cases. To study the effect of the metals on the gel morphology, ligand gels were formed in a mixture of H_2O/MeOH (70:30) upon slow evaporation at 0.3wt%. SEM analysis, shown in Figure 1.33, revealed the morphology to consist of a fibrous network with the average fibre width being approximately 20-22 nm, with the TEM analysis suggesting that the formation of supramolecular polymer within the gel through extended 1D threefold hydrogen bonding between the **BTA** units. The metallogels were then formed by dissolving the metal salt in water and adding this solution to the top of the preformed gel, and then left to diffuse through the gel structure. In the case of all the metals added (Fe(II), Ni(II), Cu(II), Zn(II) and Ru(III)), the morphology of the gels were

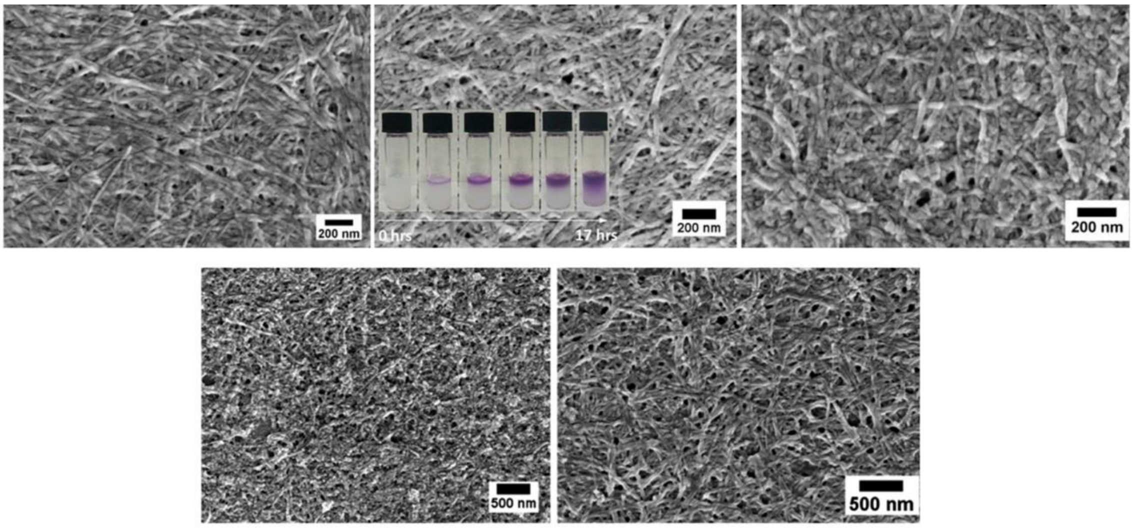

Figure 1.33 (a) SEM of **47**, (b) Fe(II)-**47** gel (inset: diffusion of Fe(II) ions into the ligand gel over a period of 17 h, (c) Zn(II)-**47**gels (all scale bars correspond to 200 nm), (d) Ni(II)-**47** gel and (e) Ru(III)-**47** gel (scale bars correspond to 500 nm). Images reproduced from reference 4.

found to have changed, again indicating that the metals were interacting with the terpyridine moieties. It was found that the fibrous nature of the gel remained, while the width of the fibres increased. Further investigations into these metallogels is ongoing.

A unique use of this **BTA**-terpyridine gel also reported by the Gunnlaugsson group, in which halide salt wire growth occurred was facilitated on the surface of the dried **47** gel, a schematic is shown in Figure 1.34.[5] This was the first example of a single-step technique in which high aspect nanowires are grown from a dropcast supramolecular gel that contains dissolved salt ions of common halide salts. The salts used were NaCl, KCl and KI, with the smallest wire diameters being 130-200 nm in diameter. Halide wires can be used as a model system to test the theories of growth and the electrical and mechanical properties of near perfect materials. In this study, a Eu(III) gel was prepared and this gel contained an NaCl impurity of 1.3 %w/w. SEM imaging of this gel directly after preparation did not reveal the presence of any nanowires, while SEM of a sample that had been left to dry for three to four days showed signs of thin wires growing from the surface of the dried gel. The largest crystals observed were 130-200 nm in diameter and up to 10 μm in length. It is clear that the supramolecular gel plays an important role in the growth of the wires, although a detailed growth mechanism is not yet understood. Further work into understanding this crystal growth is ongoing within the group.

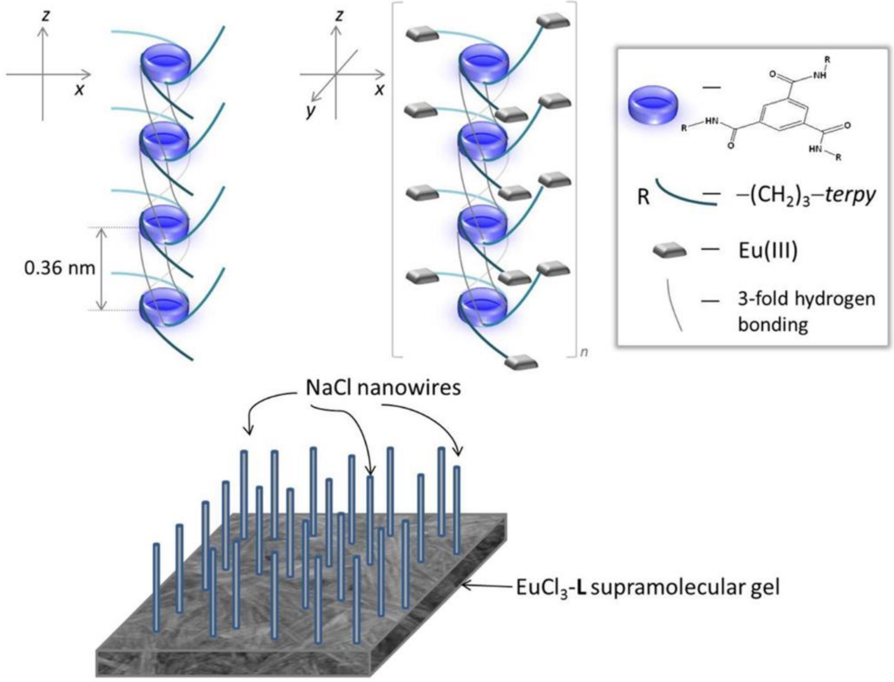

Figure 1.34 Schematic representation of (a) the two-dimensional supramolecular polymers formed through hydrogen bonding between **BTA**-terpyridine molecules and (b) three-dimensional supramolecular network of $EuCl_3$-L along with (c) formation of NaCl nanowires. Image reproduced from reference 5.

The thesis work of Dr Savyasachi AJ further functionalised this **BTA**-terpyridine derivative by incorporating a variety of amino acids into the side arms and studied the effects this had on the self-assembly processes and the resulting materials formed. Here, incorporation of glycine into the arms of the **BTA** resulted in the formation of a gel, similarly to the non-amino acid derivative. The incorporation of chiral amino acids, however, did not result in any gel material but the solutions did appear to be quite viscous. These viscous materials were probed further using a variety of techniques, mainly spectroscopic and microscopic. The SEM revealed the presence of microspheres, with different solvents found to influence the size and distribution of such. In the case of MeOH and EtOH, the spheres were found to vary from approximately 0.5 to 2 µm in diameter, while the spheres prepared in MeCN were found to be approximately 2 µm and more uniform in size. This will be further discussed in Chapter 2. Further microscopy studies, in the form of AFM and Focused ion beam microscopy (FIB) were carried out to investigate the solid-like properties of the materials and the addition of metals to the viscous solutions were found to cross-link the microspheres. FIB is similar to SEM except that the beam is an ion beam rather than an electron beam and is a useful tool for nanomanipulation and fabrication.[109]

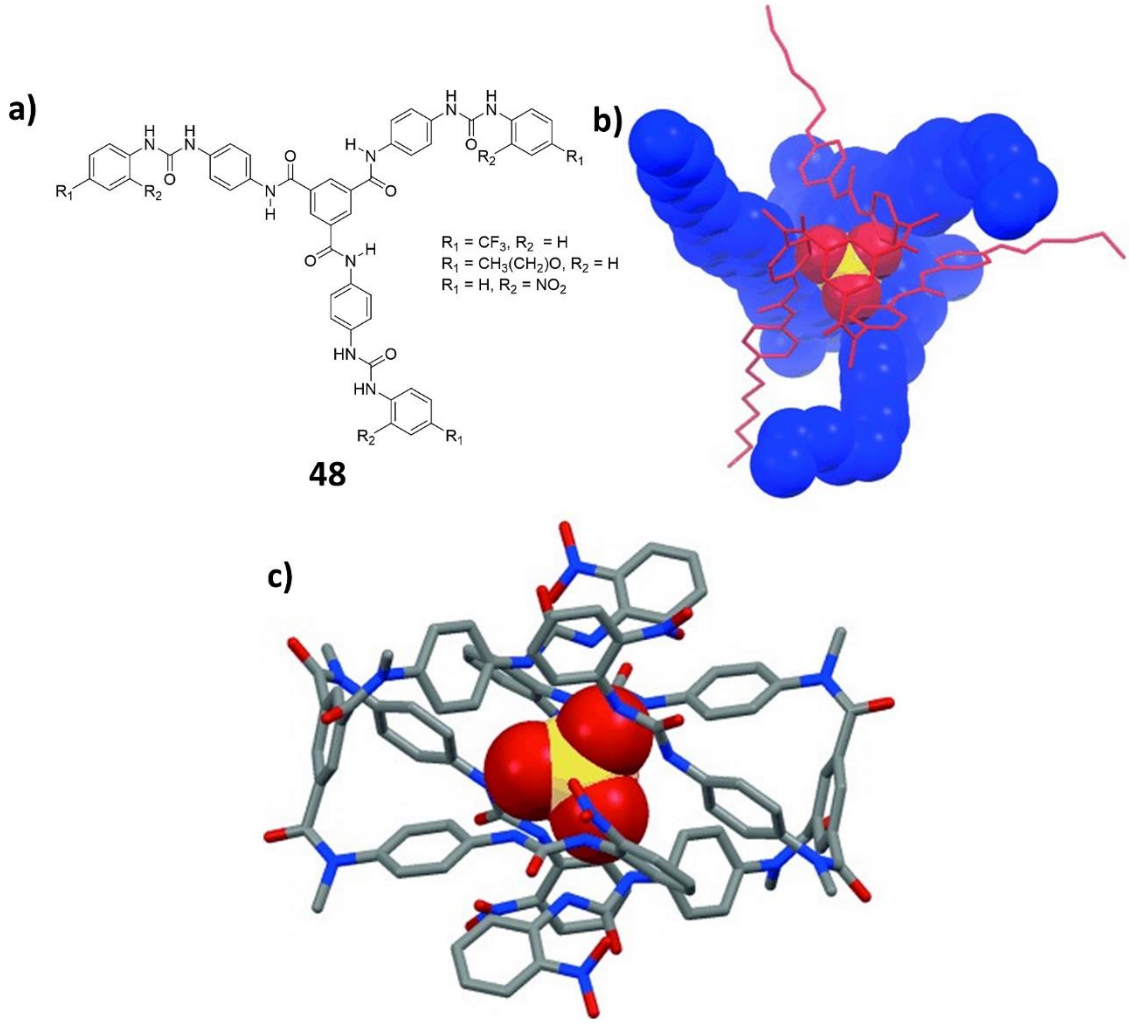

Figure 1.35 (a) Structures reported by Pandurangan and co-workers, (b) Receptor **48b** with sulphate capsule formation in a 2:1 stoichiometry shown through a mixed space-filling and stick representation highlighting both the C_3 symmetry and sulphate template within the cavity, (c) the 2:1 complex of **48c** with sulphate showing the encapsulation of the anion through hydrogen bonding of all twelve N-H urea hydrogen atoms. TBA and solvent molecules are omitted from the structures for clarity. Image reproduced from reference 110.

In another use of **BTA**-based compounds, three different **BTA**s with aryl urea arms was recently reported by Pandurangan and co-workers.[110] The aim of this work was to prepare a number of receptors that possess electron-withdrawing or lipophilic electron-donating substituents and to study the ability of these compounds to bind anions, potentially generating new self-assembled anion capsules. It was found that all three ligands gave highly preorganised and barrel-shaped structures and these cavities require little conformational changes in order to achieve a strong interaction with tetrahedral anions through hydrogen bonding. This preorganisation results in the formation of self-assembled anion capsules with sulfate (SO_4^{2-}) in a 2:1 ligand/anion stoichiometry in solution, while forming a 2:2 stoichiometry with hydrogen phosphate ($H_2PO_4^-$). Crystals of the SO_4^{2-} with the ligand showed there to be multiple hydrogen bonding interactions, while the phosphate-ligand crystals showed the ions to be bridged by a single water molecule. At the time of publication, these ligands were the first examples of ordered anion-driven self-assemblies based on the use of SO_4^{2-} as a templating agent, demonstrating that minor structural changes can have a great effect on the ability of the ligands to self-sort and form highly ordered self-assemblies. Further studies into the anion binding of **BTA**-based systems is being carried out in the thesis work of Anna Aletti.

1.3.2 Other examples of soft materials reported by the Gunnlaugsson group

Moving on from the **BTA** motif, other supramolecular motifs have been used to generate gel materials within the Gunnlaugsson group. For example, a number of aryl-pyridyl urea derivatives, shown in Figure 1.36, were synthesised and some of these were found to form gels with antibacterial properties.[15] The crystal structures of a number of these derivatives were also obtained, with these showing the expected hydrogen bonding and π-π interactions. Three of the derivatives were found to gelate in a variety of solvents at 1 wt% and were all stable to inversion. The gelation was found to be thermoreversible and were found to be fibrous in nature by SEM. Hydrogen bonding plays an important role in many antibacterial agents, as many of these agents work by inhibiting bacterial wall synthesis by forming hydrogen bond interactions with the peptides involved. As these derivatives contained a number of hydrogen bonding

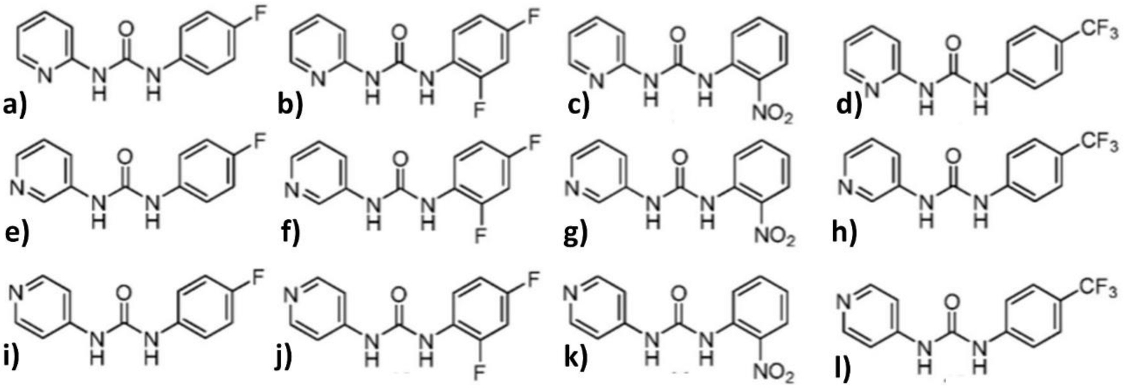

49

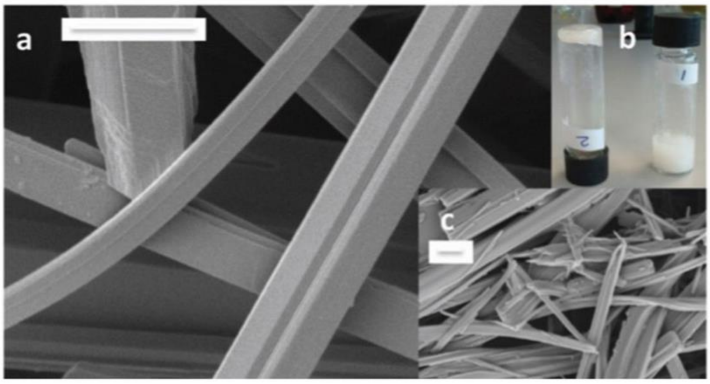

Figure 1.36 (a) The aryl-pyridyl ureas, **49a-l**, reported by Pandurangan and co-workers and (bottom) a) SEM of an organogel of the compound **49a**, that formed after 24 h using a 1%wt concentration in THF, scale bar 10 µm; b) vial labelled 2 contains a gel formed at 1%wt in a toluene/THF/$CHCl_3$ mixture and vial labelled 1 contains a gel formed at 1%wt in MeOH; c) SEM of the organogel in a with $AgNO_3$ in a THF/H_2O mixture, scale bar 2 µm. Image reproduced from reference 15.

groups, there antibacterial properties against common strains were investigated. All the derivatives were found to possess antibacterial properties, although at various strengths. It was proposed that such soft materials would serve as useful antibacterial agents for use in coating implants to prevent bacterial infection.

Another report on the formation of gels involved the development of supramolecular metallogels based on a pyridine-2,6-dicarboxylic acid derivative as a type of polydentate host and lanthanides as guests to generate a soft material.[16] Eu(III) and Tb(III) were used as the lanthanides and gels of each, along with a mixed metal gel, were generated. The Eu(III) gel emitted the characteristic red emission, while the Tb(III) had characteristic green emission. These highly luminescent gels could be mixed to give a variety of different colours depending

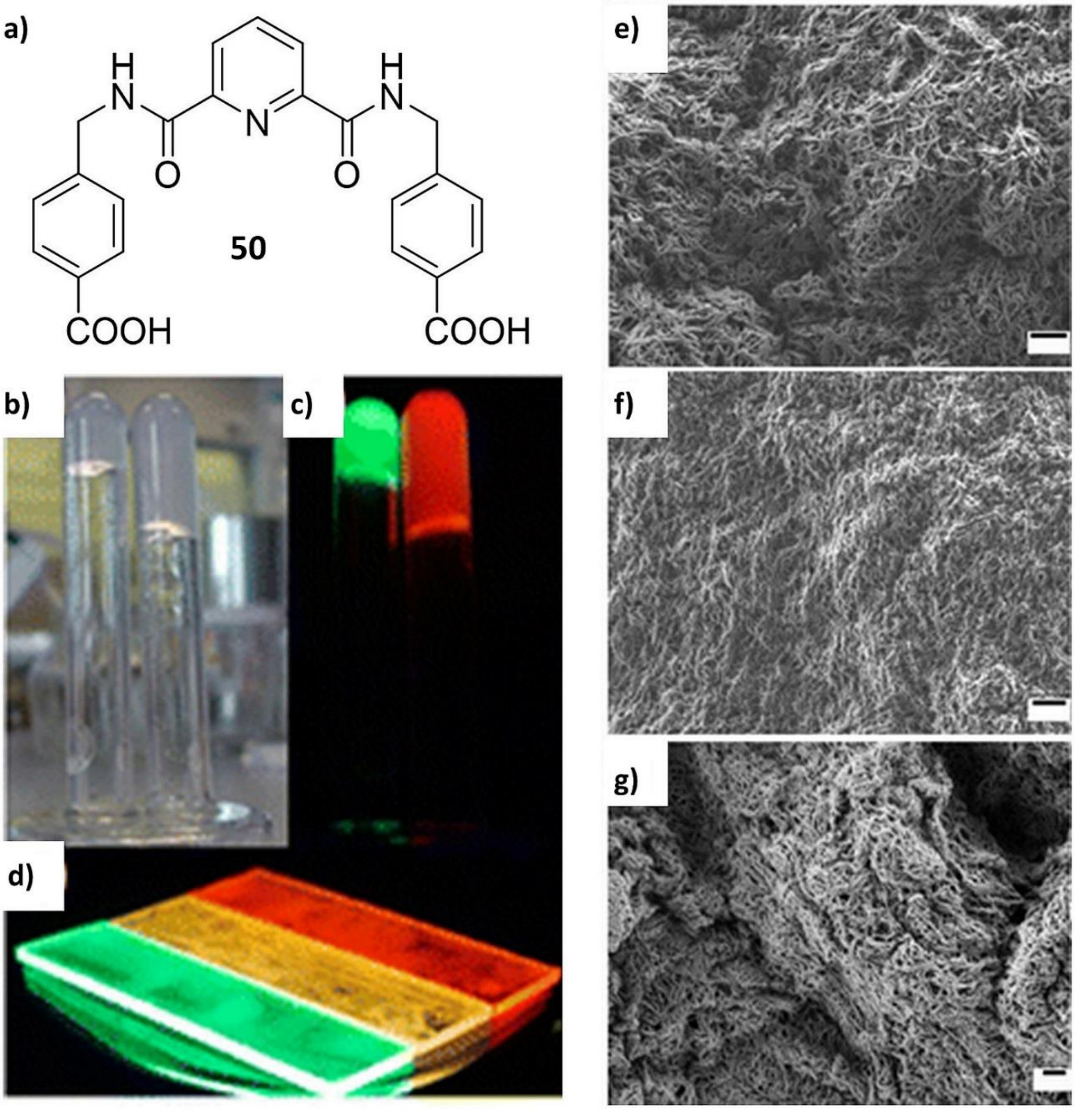

Figure 1.37 (a) Ligand **50** reported by Martinez-Calvo and co-workers, (b) the Eu(III) and Tb(III) gels in daylight and (c) under UV light and the (d) luminescence of the Eu(III) gel, mixed gel and Tb(III) gel on quartz plates and (e-g) SEM of the Eu(III) gel, Tb(III) gel and the mixed gel, scale bars 500 nm. Images reproduced from reference 16.

on the stoichiometric ratio of Eu(III) and Tb(III). The morphology was examined by SEM and showed the two gels to have similar cotton-like fibrous structures, while the Tb(III) gel had a higher density of fibres. The mixed gel was found to have a different morphology to that of the individual gels, as seen in Figure 1.37. All three gels formed were found to display self-healing properties, although to different extents and the mixed gel was found to be much softer and possess a smaller G' than that of the 'pure' gels. It is presumed that there is some sort of self-recognition process occurring in the 'pure' gels that does not take place in the mixed gels and that this is the cause of the lower rheological values obtained for the mixed gel system.

Other gelators reported by the group include a healable lanthanide luminescent gel based on the 2,6-bis(1,2,3-triazol-4-yl)pyridine (**btp**) motif by McCarney,[72] d-metal **btp** based gels by Byrne,[111] and a most recently, the report of the combination of *N*-picolyl-1,8-naphthalimide derivatives and d-block metals to generate a series of metallogels by Lovitt.[112]

Another area of ongoing research within the Gunnlaugsson group is in the area of coordination polymers and porous materials. For example, Hawes reported the synthesis of two novel ditopic naphthalimide-based ligands and their subsequent coordination chemistry, Figure 1.38a&b.[113] The preparation of three new coordination polymers was reported, with π-π interactions dominating the extended structures, resulting in a threefold interpenetrated network in the case of the Ag polymer, while robust and flexible intralayer interactions in the two-dimensional networks of the Cu and Cd polymers were observed. The Cu and Cd polymers were evaluated for CO_2 uptake and were found to display modest guest uptake upon evacuation and both materials could be reverted to their original phases after the uptake studies. [113]

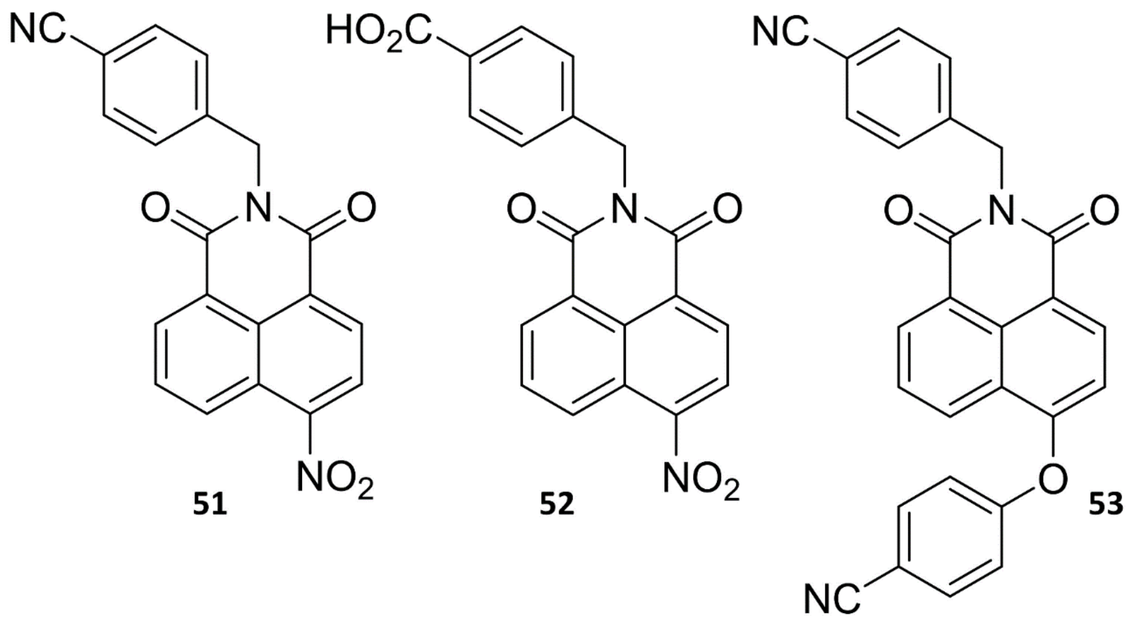

51 **52** **53**

Figure 1.38a The structures reported by Hawes, reference 113.

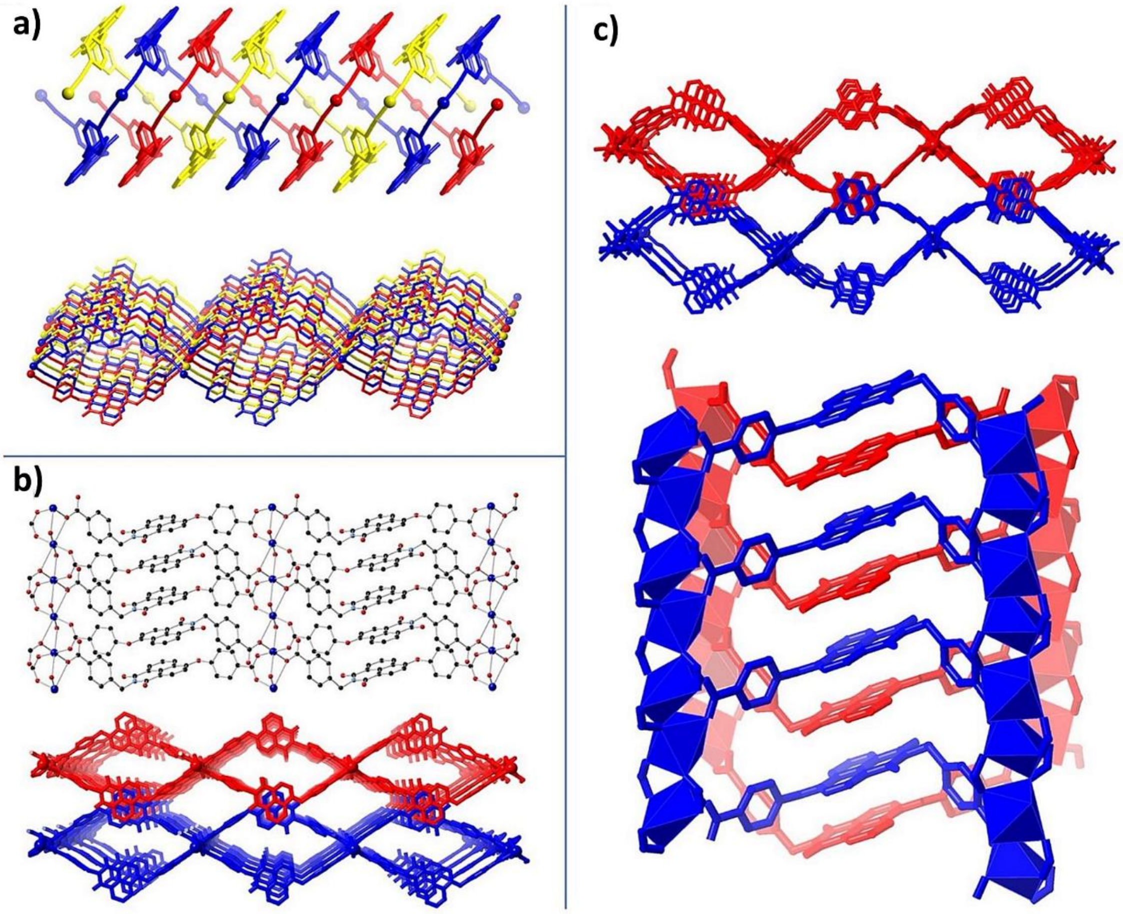

Figure 1.38b (a) Interpenetration of the **51Ag** complex with independent networks coloured separately, showing the π-π interactions between the three interpenetrated networks around a single channel and the overall two-dimensional structure of the assembly; (b) the extended structure of the **52Cu** complex, showing the connectivity of a single layer and the interdigitation of the two adjacent layers with independent networks coloured separately; (c) the extended structure of the **53Cd** complex showing interdigitation between two layers viewed parallel and perpendicular to the one-dimensional solvent channels, independent networks are coloured separately. Hydrogen atoms and lattice solvent are omitted from the bottom left and right images for clarity. Image reproduced from reference 114.

In another example from the group, Shanmugaraju reported the formation of two new coordination polymers from a naphthalimide-Tröger's base (TB) derivative.[114] The design of this ligand was influenced by a number of factors, for example, the fluorescent nature of the naphthalimide could be useful for sensing applications, the Tröger's base motif could result in a cleft-shaped structure, while the flexible picolylamime used can result in unusual coordination topologies. This work resulted in the generation of a Co and Cd based coordination polymers using solvothermal methods, and the X-ray diffraction studies revealed that π-π interactions prevailed in the extended structures resulting in one-dimensional supramolecular polymeric networks, Figure 1.39.

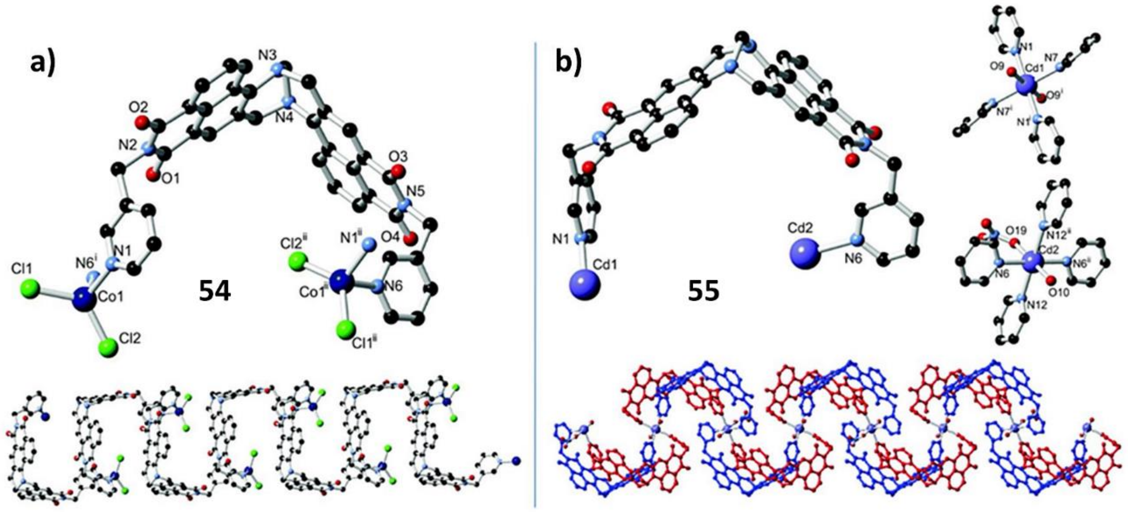

Figure 1.39 (a) The structure of the cobalt-TB coordination polymer and the extended structure for the complex, with the heteroatoms and pyridyl ring disorder omitted for clarity; (b) an example of the ligand geometry in the cadmium-TB coordination polymer and the coordination environment of the two cadmium ions and the extended structure of a single chain of the coordination polymer with the symmetry related ligand groups coloured together showing the two overlapping zig-zag chains present. Images reproduced from reference 114.

Other reports of coordination polymers synthesised within the group include the report by Dalton of eight new coordination complexes based on the coordination of two bipyridine ligands with Cd(II), Co(II) and Co(III)[115] and the work of McCarney in which the synthesis of a three-dimensional MOF material derived from a btp-based ligand and Zn(II) was discussed.[116] These reports are shown in Figure 1.40.

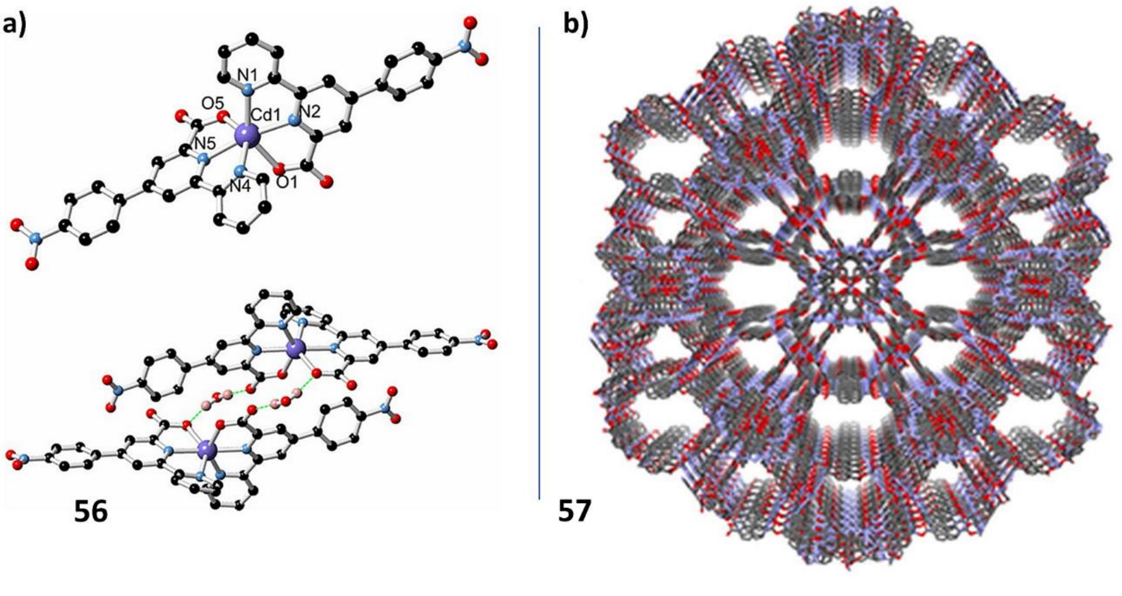

Figure 1.40 (a) One of the complexes reported by Dalton and co-workers with labelling scheme and showing hydrogen bonding interactions between the adjacent complexes through lattice water molecules. Selected hydrogen atoms are omitted for clarity. (b) Perspective view of the solvent channels in the crystal structure of the complex reported by McCarney and co-workers with the hydrogen atoms omitted for clarity Images reproduced from references 115 and 116.

1.4 Work described in this thesis

As discussed above, the control and tuning of the self-assembly of supramolecular soft materials is an area of great current interest and importance. A particularly interesting motif for investigating what governs these processes is the **BTA** central unit decorated with a variety of different side arm functionalities. The aim of this PhD thesis was to investigate the role of side arm functionality on self-assembly processes and to study the soft materials formed from these various derivatives.

Chapter 2 will discuss the synthesis and characterisation of a family of short alkyl chain ester and carboxylic acid **BTA** derivatives. Investigations into the soft materials formed by these compounds will also be discussed.

Chapter 3 will focus mainly on two BTA derivatives and their potential as porous materials. Also briefly discussed will be the attempts to further extend the aromatic **BTA** derivative with some simple amino acids.

Chapter 4 will introduce attempts to synthesise **BTA**-based polymers, both covalently and non-covalently linked, with a variety of side chains.

Chapter 5 will first introduce a new central core unit, the pyridine-3,5-dicarboxylic acid unit and discuss some related example from the Gunnlaugsson group, followed by the synthesis and characterisation of a number of new derivatives. The chapter will then discuss the structural, microscopic and thermal studies of the materials formed from these derivatives.

Chapter 6 contains the instrumental and experimental details, followed by the references and additional information, such as characterisation and supplementary data in the appendices.

‘If you aren’t willing to keep looking for the light in the darkest of places without stopping, even when it seems impossible, you will never succeed.’

Grey’s Anatomy

2. Benzene-1,3,5-tricarboxamide *n*-alkyl ester and carboxylic acid derivatives: tuneable structural, morphological and thermal properties

2.1 Introduction

An area of great interest in supramolecular chemistry is the study of the correlation between structural features and the chosen self-assembly pathways of the chemical constituents with the properties of the bulk materials.[1,2,5,40,108] The benzene-1,3,5-tricarboxamide (**BTA**) motif is an attractive building block for exploring this correlation as its core is readily functionalised with a large variety of side arms, thus imparting a variety of potential structural and behavioural features, while retaining some of the key modes of interaction due to the core.[4,74,108] **BTA**s consist of three amide groups connected to a benzene rigid unit; these amides have the tendency to form columnar structures due to the cooperative three-fold helical hydrogen bonds between the consecutive amide groups of neighbouring molecules and strengthened by π-π interactions between the benzene units.[77] There are a vast range of possibilities for functionalisation at the amide groups, owing to this, the use of **BTA** derivatives in a vast array of fields, from nanotechnology to biomedical applications, has been investigated.[17,55,74] As discussed in the introduction, the nature of the side chains attached greatly influences the form and function of the resulting materials.[88,99,117,118] For example, bulky, aliphatic side chains give rise to high melting crystalline solids which crystallise as fibre-like needles,[74] while long alkyl side chains tend towards thermotropic liquid crystalline behaviour[79,80] and branched alkyl side chains favour organogel behaviour.[78] Other derivatives, such as carboxylic acid terminated **BTA**s[14] and terpyridine terminated **BTA**s have been reported to form hydrogels.[108]

Although it is known that the general type of side chain functionality influences the form and function of **BTA** derivatives, we decided to investigate this phenomenon further by studying a family of **BTA** derivatives and investigating the effect of minor structural differences on the properties of the resulting materials. This was done with the aim of gaining a greater

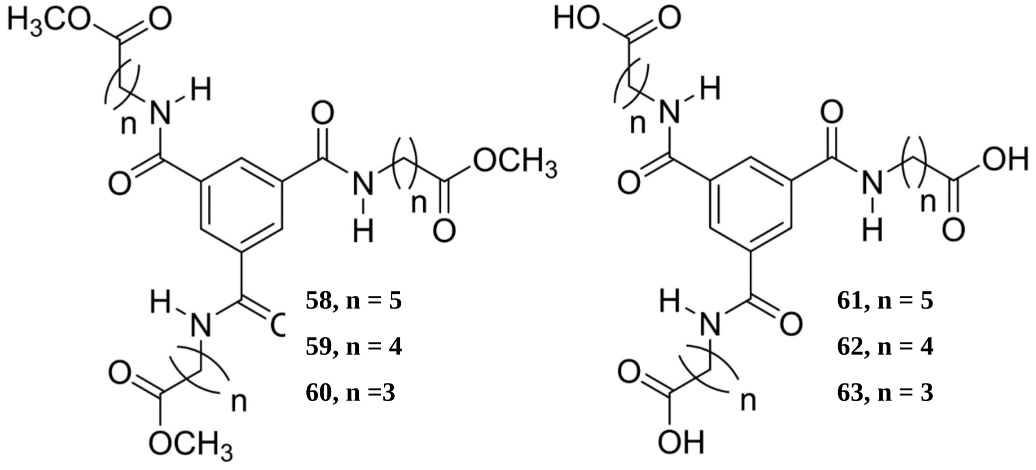

58, n = 5
59, n = 4
60, n =3

61, n = 5
62, n = 4
63, n = 3

Figure 2.1 The compounds of varying alkyl chain length and end group functionality that will be discussed in this chapter.

understanding of the processes involved in the self-assembly behaviour of **BTA** compounds and the factors that influence the resulting materials formed. This chapter will mainly focus on the synthesis, structural, physical and thermal properties of the six **BTA** derivatives shown in Figure 2.1. The synthesis of these derivatives was achieved in two to three steps yielding either ester or carboxylic acid end group moieties. It will be demonstrated that small changes in spacer length ($3 \leq n \leq 5$) and the end group functionality have a great effect on the self-assembly properties of these **BTA** structures. First, however, the synthesis and scanning electron microscopy (SEM) of a related compound previously synthesised within the Gunnlaugsson group will be discussed. This was carried out for a variety of reasons, mainly to become acquainted with the synthesis of tripodal compounds and to use as a model compound for training on the SEM.

2.1.1 Design rationale

The compounds discussed in this chapter are structurally simple alkyl ester and carboxylic acid derivatives with varying lengths of alkyl chain spacers. The inspiration for studying this family of compounds came from previous work carried out within the Gunnlaugsson group and work by other groups such as that of Meijer and Palmans. The group of Palmans and Meijer have made significant contributions to the field of **BTA** chemistry, with much focus on the study of extended alkyl spacer **BTA** supramolecular polymers.[88,96,119,120] In the Gunnlaugsson group, previous efforts have focused on a terpyridine functionalised **BTA** compound and their behaviour, with particular attention being paid to the gelation behaviour, as stand-alone compounds and upon interaction with metals.[4,5,108] The PhD thesis work presented by Dr Savyasachi AJ focused on the incorporation of amino acid linkers as spacers in this **BTA**-terpyridine system.[121] One of these compounds, **66**, as shown in Scheme 2.1 was synthesised at the beginning of this thesis work as a model compound to use for microscopy training. The aim of this work was to study structurally simple **BTA**-alkyl systems and investigate the effect of small structural changes on the self-assembly behaviour of the resulting compounds and to potentially tune this self-assembly. Furthermore, it would be possible to use these structurally simple BTA-alkyl systems as the building blocks for more extended and derivatised systems.

2.2 Synthesis and characterisation of compound 66 and 68

2.2.1 Synthesis and characterisation of 66

As previously mentioned, one of the initial projects undertaken in this thesis work was to reproduce the synthesis of a **BTA** compound containing an amino acid linker and terpyridine end group, previously synthesised by Dr Savyasachi AJ of the Gunnlaugsson group. The purpose of this was to prove the reproducibility of the synthesis of this interesting compound, to become familiar with the synthesis of tripodal compounds and to use as a model compound for microscopy training. The synthetic scheme of **66** is illustrated in Scheme 2.1. The first step in this scheme was the reaction between 4′-chloro-2,2′:-6,2″-terpyridine with 1,3-diaminopropane to yield the amino-terpyridine derivative as shown in the scheme. This was achieved by reacting 4′-chloro-2,2′:-6,2″-terpyridine with 1,3-diaminopropane at 125 °C for 24 h. Upon completion of the reaction, the reaction mixture was quenched with ice cold H_2O resulting in the formation of a white precipitate which was separated by filtration, re-dissolved in DCM and washed with H_2O. The organic layer was then separated and dried over Na_2SO_4, filtered and the solvent was removed under reduced pressure to reveal a white solid in 57 % yield. The amino-terpyridine was then coupled onto an alanine-derivatised **BTA**, using the conditions shown in Scheme 2.1, to result in **66**. The solubility of this compound was investigated in a variety of solvents and then its self-assembly properties were probed using

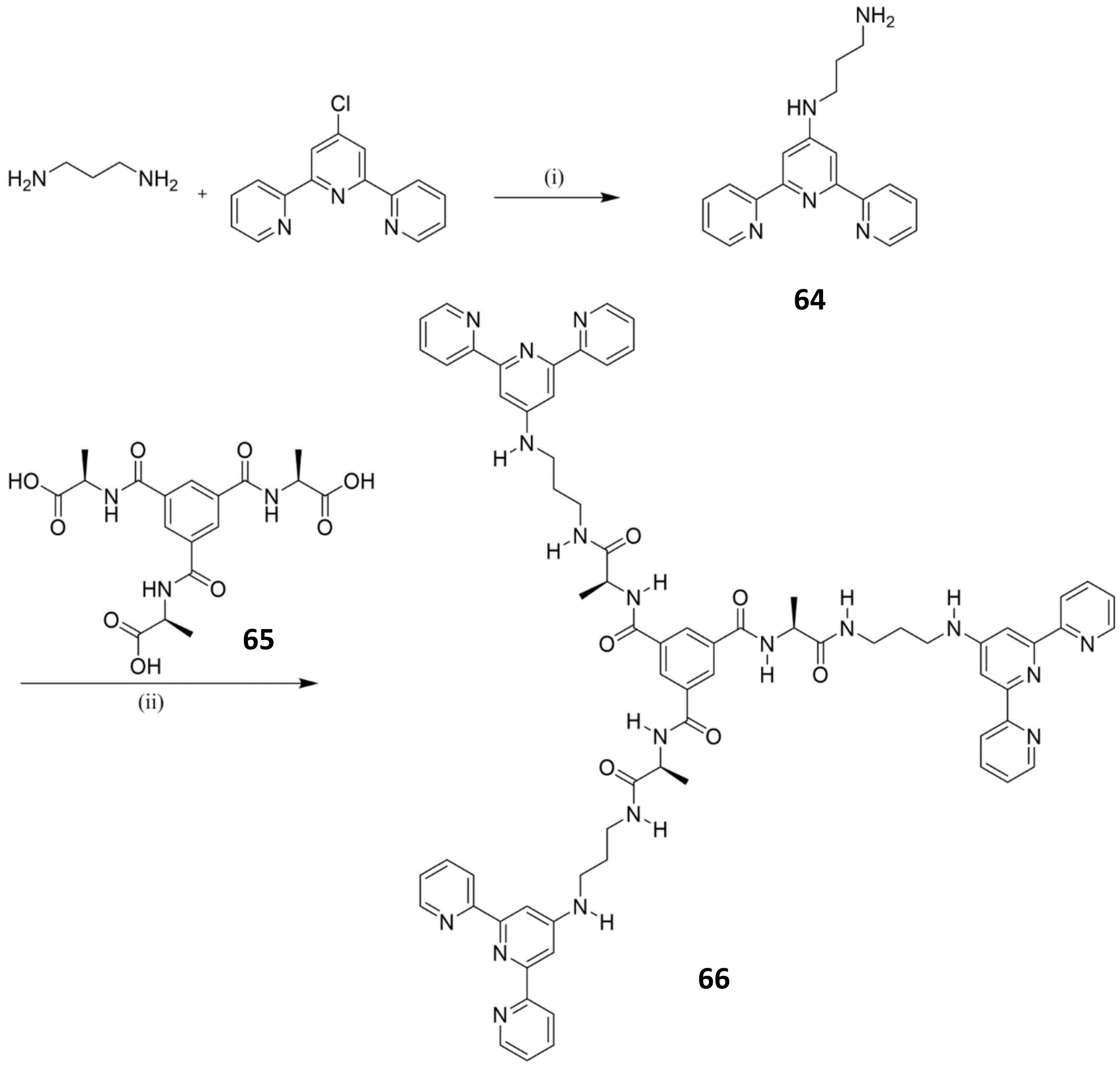

Scheme 2.1 Synthetic scheme for the synthesis of **66**, where (i) reflux at 125 °C for 24 h; (ii) DMF, DCM, EDC.HCl and HOBt, rt, 24 h.

SEM. In the PhD thesis of Dr Savyasachi AJ, he reported the effect of the linker on the self-assembly process of his family of amino acid based **BTA**s. In the case of a glycine linker, the material was found to gelate in a variety of solvents, however the chiral amino acid derivatives did not. They did, however, become viscous solutions when dissolved in various solvents, thus this was investigated further using SEM. These microscopy studies were carried out by drop-casting 5 µl portions of the various viscous solutions onto silica wafers, which were then dried under dynamic vacuum before being coated with a conductive Au/Pd layer and studied under SEM. Instead of the expected fibrous material, Dr Savyasachi observed the presence of microspheres, with different solvents and concentrations found to influence their size uniformity and distribution. This was repeated during this thesis work and the same results were

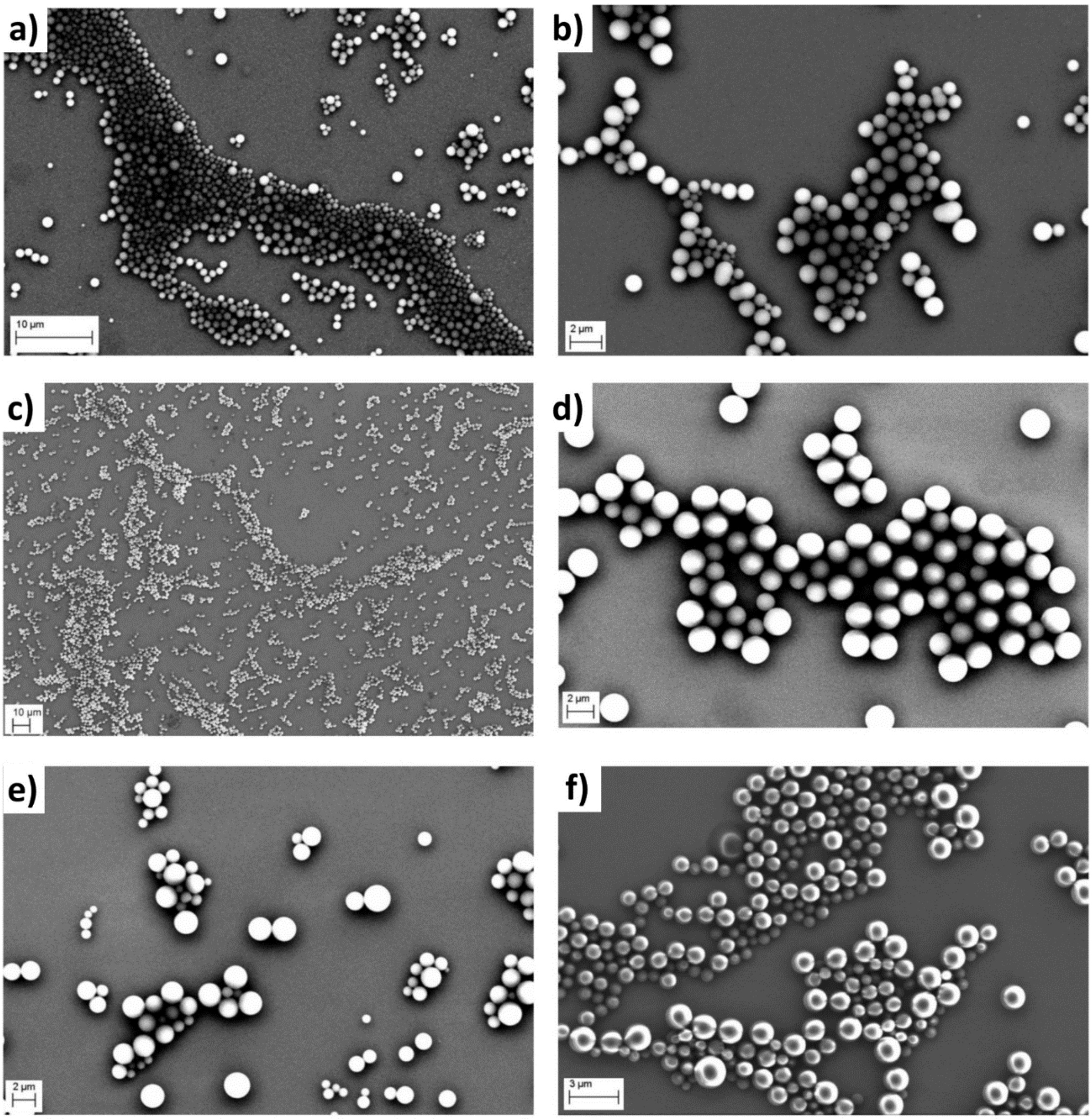

Figure 2.2 (a&b) SEM images of **66** in EtOH (scale bar left 10 µm, scale bar right 2 µm); (c&d) SEM of **66** in MeCN (scale bar left 10 µm, right 2 µm); (e&f) SEM of **66** in EtOH (scale bar left 2 µm, right 3 µm).

obtained as demonstrated in Figure 2.2, where the results of the SEM carried out on dried samples of **66** in EtOH, MeCN and MeOH are presented. In the case of both EtOH and MeOH, the spheres were found to have various sizes, ranging from approximately 0.5 µm to 2 µm in diameter, while the MeCN samples were of more uniform size, approximately 2 µm in diameter. From this, it is clear that interactions with the solvent influence sphere size and that the moderate polarity of MeCN favours the formation of microspheres of a uniform size distribution. This work also illustrated the impact different amino acids can have on the self-assembly processes of related compounds. Further work was carried out by Dr Savyasachi AJ on the influence of a variety of metals on this derivative and other amino acid derivatives, however, this was not repeated during this thesis study.

2.2.2 Synthesis and characterisation of 68

Inspired by the interesting properties of **66**, it was decided to synthesise a phenanthroline analogue, **68**, seen in Scheme 2.2, to investigate if it displayed similar properties to those observed for **66**. Phenanthroline was chosen as it has a different coordination requirement than terpyridine, thus it could potentially react with different metals than those used for the terpyridine derivatives studied by Dr Savyasachi AJ and due to the vast expertise in studying phenanthroline derivatives for a variety of purposes within the Gunnlaugsson group.[122 123]

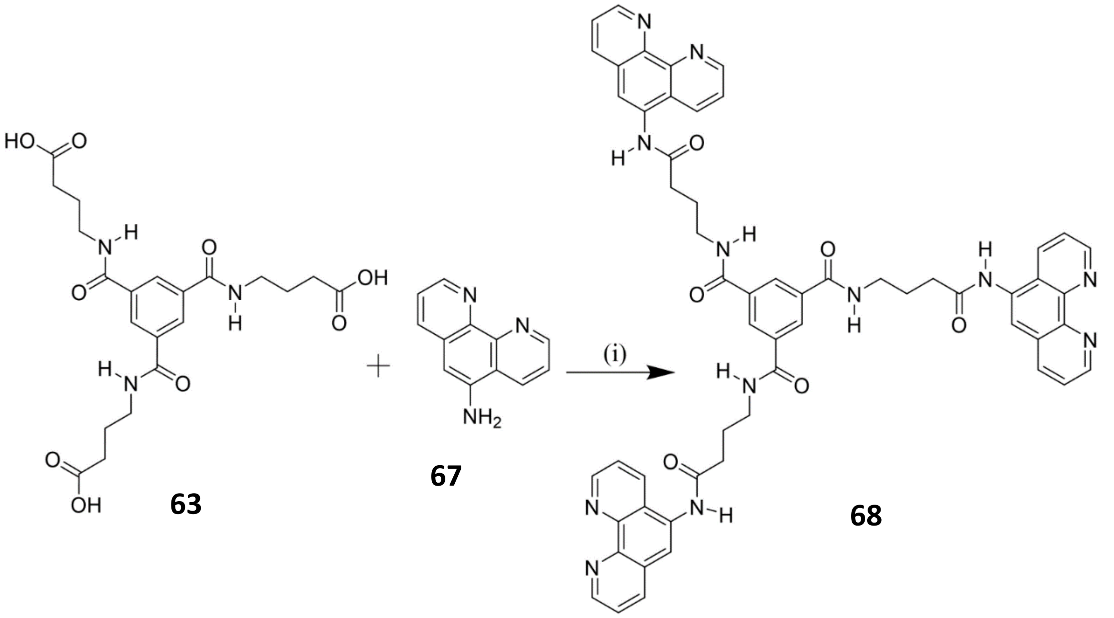

Scheme 2.2 Reaction scheme for the synthesis of **68**, where (i) EDC.HCl, DMAP, DCM, argon, rt, 72 h.

After a number of attempts, **68** was successfully synthesised using a BTA derivative, **63**, will be discussed in the next section, amino phenanthroline, **67**, and the coupling reagents EDC.HCl and DMAP, stirring in DCM at room temperature in an inert atmosphere for approximately 72 h, a procedure adapted from that used by Dr Robert Elmes, previously of the Gunnlaugsson group.[122] Once the reaction was complete, the solvent was removed under reduced pressure to reveal an orange oil, which precipitated to form an orange solid after the addition of H_2O which was isolated by filtration. The product was an orange solid, that was difficult to obtain in high yield and purity and quite insoluble in most common lab solvents, even at low concentrations and with the aid of heat and sonication. Some attempts were made to solubilise **66** in an attempt to gelate or crystallise the compound, however, these attempts were largely unsuccessful as shown in Figure 2.3. The solvents tested included MeOH, EtOH, IPA, H_2O, C_6H_{14}, MeCN and $CHCl_3$ and in most cases resulted in fibrous precipitates. SEM was used to image the precipitates formed in the solvents of various polarities and the results obtained are shown in Figure 2.4. In the case of the one of the more polar solvents used, the morphology of the dried sample of **66** in MeOH looked like a dried film. In the case of the less polar solvents, the dried precipitates had a more fibrous-like precipitate and there was evidence of a small amount of spherical material, however, in most cases these were damaged or broke, as seen in Figure 2.4.Some metal salts were added to these gelation attempts and the effect of the addition of $CuCl_2$ is seen in Figure 2.4, with the metal having very little effect on the morphology of the material and also had no effect on the solubility of the ligand. Due to the synthesis, purification and solubility issues with this compound, further investigations were not pursued and instead we moved onto studying the family of structurally simple **BTA**s shown in Scheme 2.3.

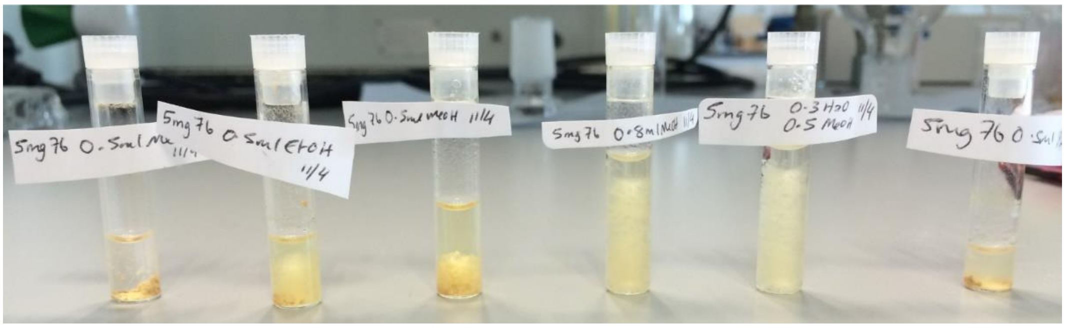

Figure 2.3 Gelation attempts of **68,** left to right, (i) 5mg in 0.5 mL MeOH; (ii) 5mg in 0.5 mL EtOH; (iii) 5mg in 0.5 mL MeOH; (iv) 5mg in 0.8 mL MeOH; (v) 5mg in 0.3 mL MeOH and 0.3 mL H_2O; (vi) 5mg in 0.5 mL IPA.

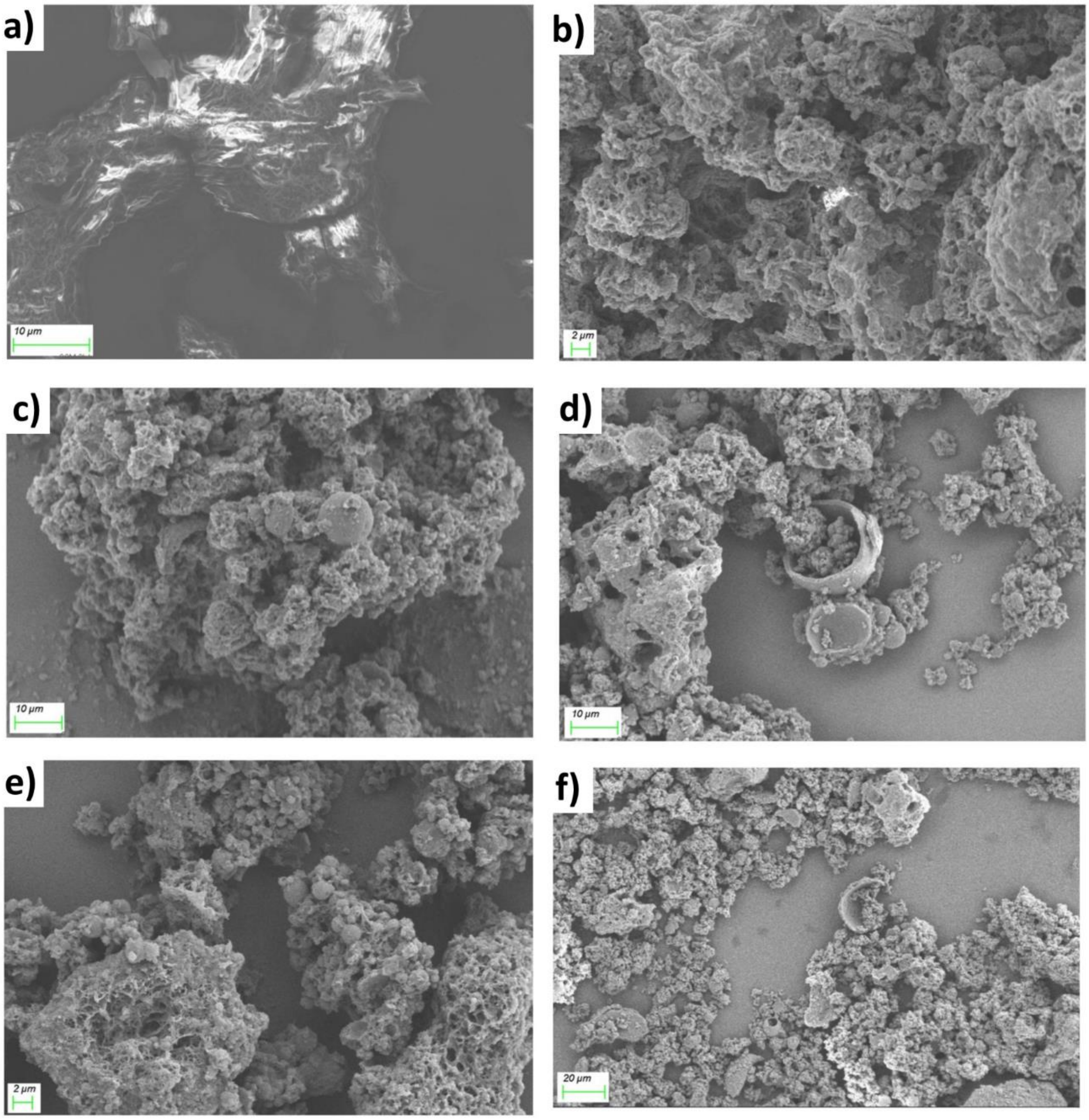

Figure 2.4 SEM of dried sample of **66** in (a) MeOH, scale bar 10 µm; (b&c) MeCN, scale bar 2 µm and 10 µm; (d) hexane, scale bar 10 µm; (e) $CHCl_3$, scale bar 2 µm; (f) in MeOH with $CuCl_2$, scale bar 20 µm.

2.3 Synthesis and characterisation of 58, 59, 61, 62 and 63

The synthetic scheme for compounds **58, 59, 61, 62 and 63** is shown in Scheme 2.3. **60** was also synthesised as the precursor to **63**, however, only thermal studies were conducted, as it has been previously studied and reported by Haldar *et al.*[77] The first step in the synthesis was to ester protect the amino acid chains of the three lengths. This was achieved by stirring the commercially obtained carboxylic acid

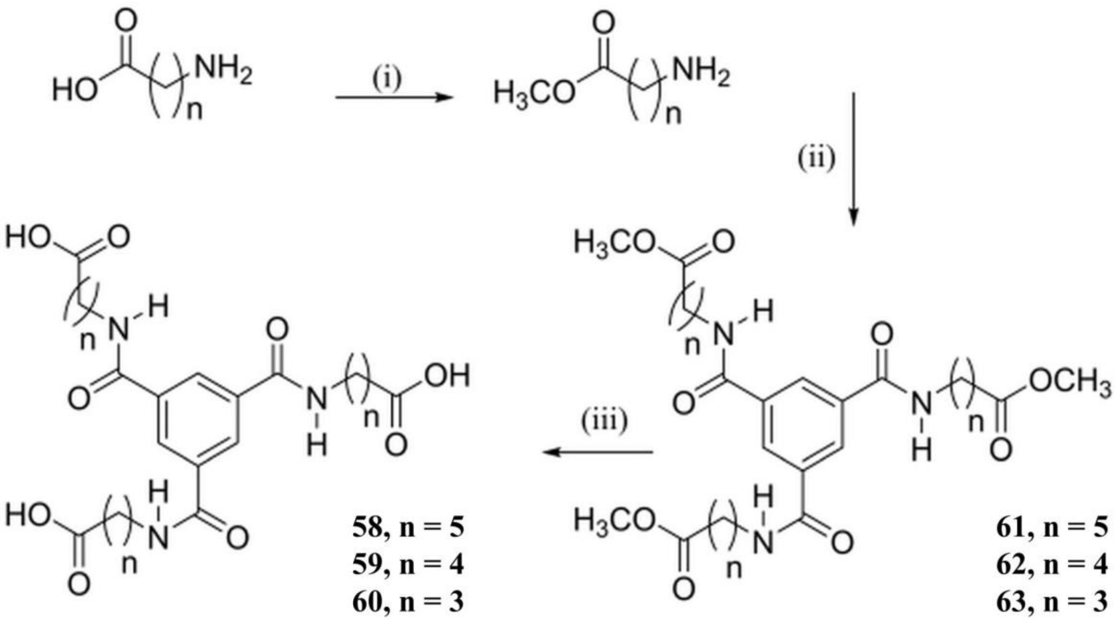

Scheme 2.3 Synthetic scheme for the compounds discussed in this chapter, where n = 3, 4 or 5; (i) rt, MeOH, $SOCl_2$, 12 h; (ii) rt, DCM, argon, Et_3N, 24 h; (iii) NaOH, MeOH, 4 h.

precursors in $SOCl_2$ and MeOH for 12 h at room temperature, followed by removal of the $SOCl_2$ and MeOH using vacuum distillation to reveal the ester protected amino acids, in high yields. The ester **BTA** derivatives **58** and **59** were then prepared in good yields using the established protocols for the symmetric tri-substitution of benzene-1,3,5-tricarbonyl trichloride, using the

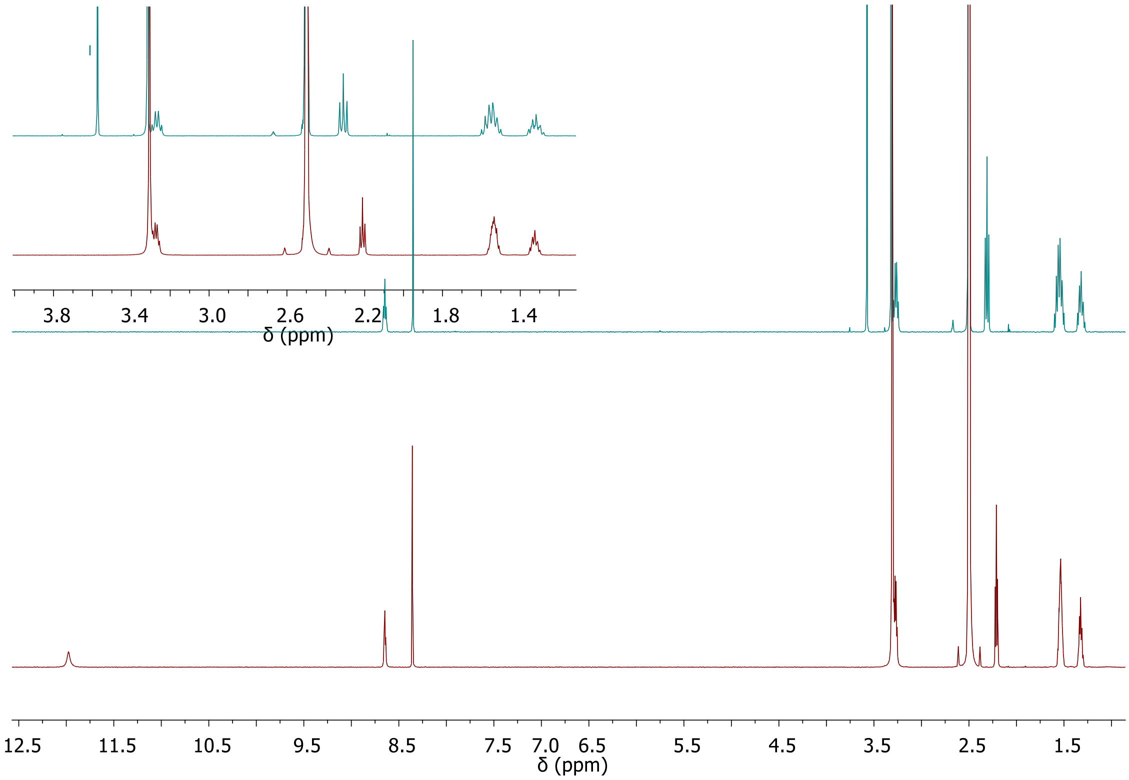

Figure 2.5 ^1H NMR (600 MHz, DMSO-d_6) of (bottom) and **58** (top) showing the disappearance of the ester signals after hydrolysis and (inset) disappearance of ester signal in **58** compared to **61**.

previously prepared ester-protected amino acids in the presence of base, Scheme 2.3. In this case, the reactions were carried out by stirring in dry DCM under an argon atmosphere at room temperature in the presence of Et_3N for 24 h. Following this, the reaction mixture was washed with $NaHCO_3$ solution in H_2O three times, with the organic layer evaporated to reveal the ester derivatives as white solids. Compounds **58** and **59** were purified by automatic silica column chromatography (10:90, MeOH/DCM) to yield crystalline-like white solids in high yields. These ester derivatives were next converted to their corresponding carboxylic acids by base hydrolysis followed by acidification to precipitate the neutral compounds, **61**, **62** and **63** in good to quantitative yields (94%, 87% and 77% respectively). The formation of the acid derivative was confirmed by the disappearance of the characteristic proton resonances of the ester at approximately 3.6 ppm in all cases. The **BTA** aromatic protons appear as a sharp singlet at approximately 8.3 ppm indicative of the C_3 symmetry of the molecules, while the amide proton resonance was at approx. 8.6 ppm in all cases. An example of a typical NMR spectra for the ester and carboxylic acid derivative is shown in Figure 2.5 and agrees with literature reports.[108]

The ester and carboxylic acid derivatives were fully characterised by ^{1}H and $^{13}C\{^{1}H\}$ NMR, along with mass spectrometry, infrared spectroscopy and elemental analysis, see Experimental and Appendix. Further to this, the structures of **58**, **59**, **62** and **63** were also investigated by X-ray diffraction and powder diffraction, the results of which will be discussed in Section 2.4.

2.4 Solid-state structural studies of 58, 59, 62 and 63

Long, needle-like, single crystals of **58**, **59**, **62** and **63** were obtained by slow evaporation of varying solvents (2:1 H_2O/THF, 1:1 H_2O/MeOH, H_2O and 2:1 H_2O/THF respectively). Despite repeated efforts, single crystals of suitable quality of **61** were not obtained, see appendix for further details. The crystallography in this chapter was carried out and the data solved and refined by Dr Chris Hawes (TCD, Keele University).

2.4.1 Structural study of 58

A single crystal of **58** was obtained from a mixture of 2:1 H_2O/THF with the single crystal data being solved and refined in the monoclinic space group $P2_1/c$. The asymmetric unit was found to contain the entire molecule, Figure 2.6, with no associated solvent or guest molecules. It was found that each of the three arms adopts a slightly different conformation, with the three amide groups displaying varying degrees of planarity with the central phenyl ring. The amide-phenyl mean interplanar angles were 21.6°, 7.6° and 39.4° for the three amides defined by N1/O1,

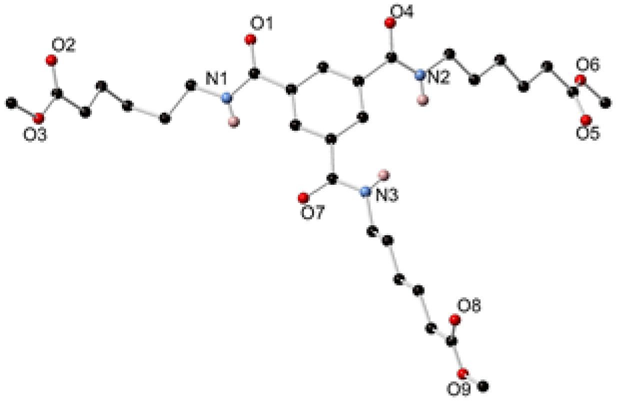

Figure 2.6 Structure of **58** with heteroatom labelling scheme. Selected hydrogen atoms and crystallographic disorder are omitted for clarity.

N2/O2 and N3/O3 respectively. These distortions represent both twisting about the C(amide)–C(phenyl) bonds, related to the three associated dihedral angles of 19.0(8)°, 8.5 (8)° and 36.7(6)° respectively, and folding of the amide group out of the phenyl ring plane.

Two of the aliphatic chains adopt linear fully staggered conformations, while the third, originating from the amide nitrogen atom N1, contains gauche conformers at methylene groups C13 and C14 causing a bent arrangement for the chain. Hydrogen bonds originating from the amide N–H groups, interacting with carbonyl oxygen atoms from adjacent amide or ester functional groups, constitute the majority of the intermolecular interactions within the structure. Figure 2.7 shows the hydrogen bonding of the aliphatic chain originating from amide nitrogen atom N1. Here, it is seen that the aliphatic chain engages in two hydrogen bonding interactions with the same adjacent molecule acting as a hydrogen bond acceptor at both amide and ester oxygen atoms, O1 and O2, from two amide nitrogen atoms N1 and N2. This interaction is considered quite unusual and to be a $R\frac{2}{2}(19)$ loop which spans two amide donors across the width of the central phenyl ring and is accommodated by the bent arrangement of the doubly-accepting amido-ester chain, shown in Figure 2.7.

The remaining amide nitrogen N3 undergoes N–H···O hydrogen bonding with amide oxygen atom O4. Slight positional disorder was encountered on the two ester moieties not engaging in hydrogen bonding interactions, and these groups were modelled, after free variable refinement to determine the occupancy of the disordered contributors, split at 0.75:0.25 and 0.85:0.15 occupancy for O8/O9 and O5/O6, respectively. The hydrogen bonding between the molecules of **58** results in a densely packed network, with there being no void space being detected within the structure. The structure of this **BTA** derivative deviated from the classical columnar structures, arising from threefold hydrogen bonding interactions between the neighbouring amides. This is presumably due to the length of the alkyl chain enabling the loop interaction described above, thus preventing the amide to amide interactions necessary for the columnar arrangement.

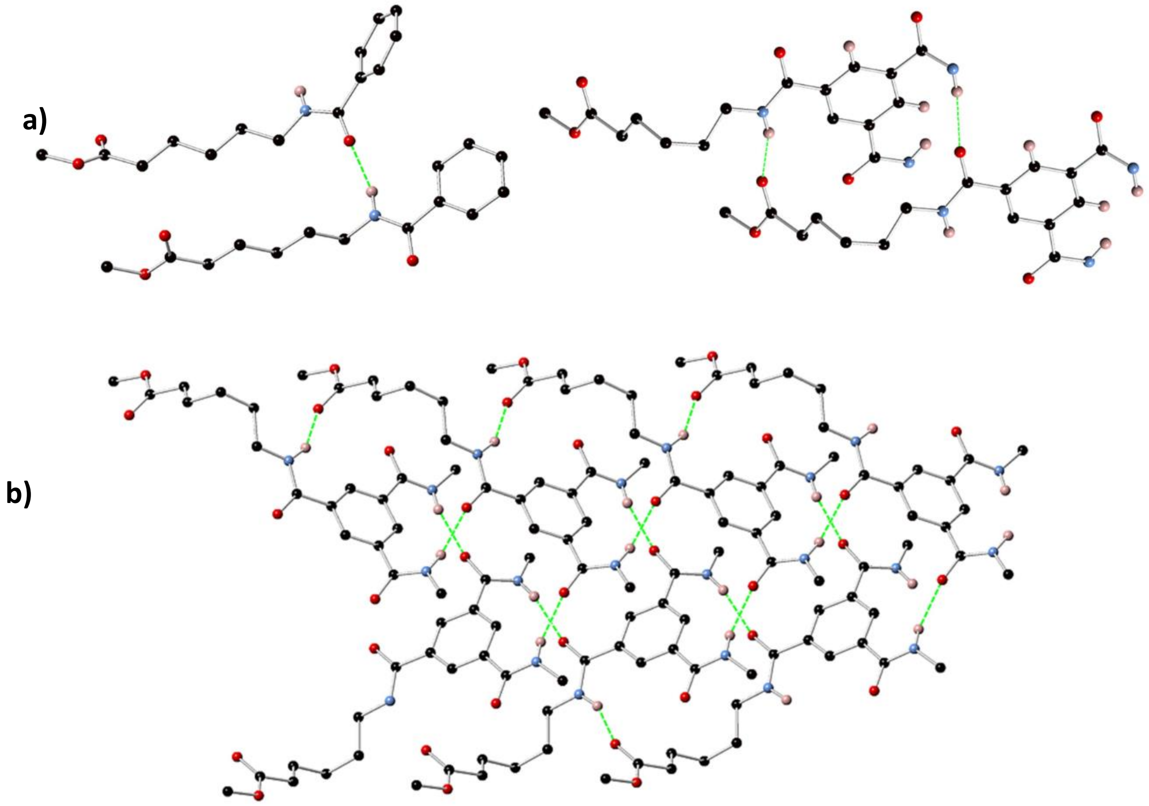

Figure 2.7 (a) The unusual loop interaction of the amide donors of **58** and (b) the extended structure of **58** showing the densely packed structure.

Elemental analysis carried out on a sample of **58** confirmed that the bulk formulation matched that observed in the crystal structure. X-ray powder diffraction is a useful method for the characterisation of crystalline materials and for examining the phase purity of a bulk sample.[124] Unlike single crystal diffraction, a microcrystalline powder sample is used in the analysis rather than a single crystal, thus its utility in phase purity determinations. Practically, the bulk powder sample of interest is subjected to powder diffraction, with the resulting pattern compared to that generated in the single crystal experiment. For a phase pure sample, the diffraction patterns should be the same, though occasionally slight shifts in the peaks are observed due to overlapping reflections and potential thermal expansion of the crystalline material.[125] X-ray powder diffraction on a bulk sample of **58** revealed the presence of a mixture of polymorphs, as depicted in Figure 2.8. The pattern obtained for the as-synthesised material does not agree with the simulated pattern obtained from the single crystal data nor that obtained for **59**, thus indicating it was a different polymorph or multiple polymorphs. Despite a number of crystallisation attempts, it was not possible to obtain suitable single crystals of another polymorph of **58** and characterise these additional polymorphs by single crystal X-ray diffraction, nor was it possible to separate the phases or selectively prepare one phase over another.

The phase behaviour of **58** was further probed using differential scanning calorimetry (DSC), as described in Section 2.6.

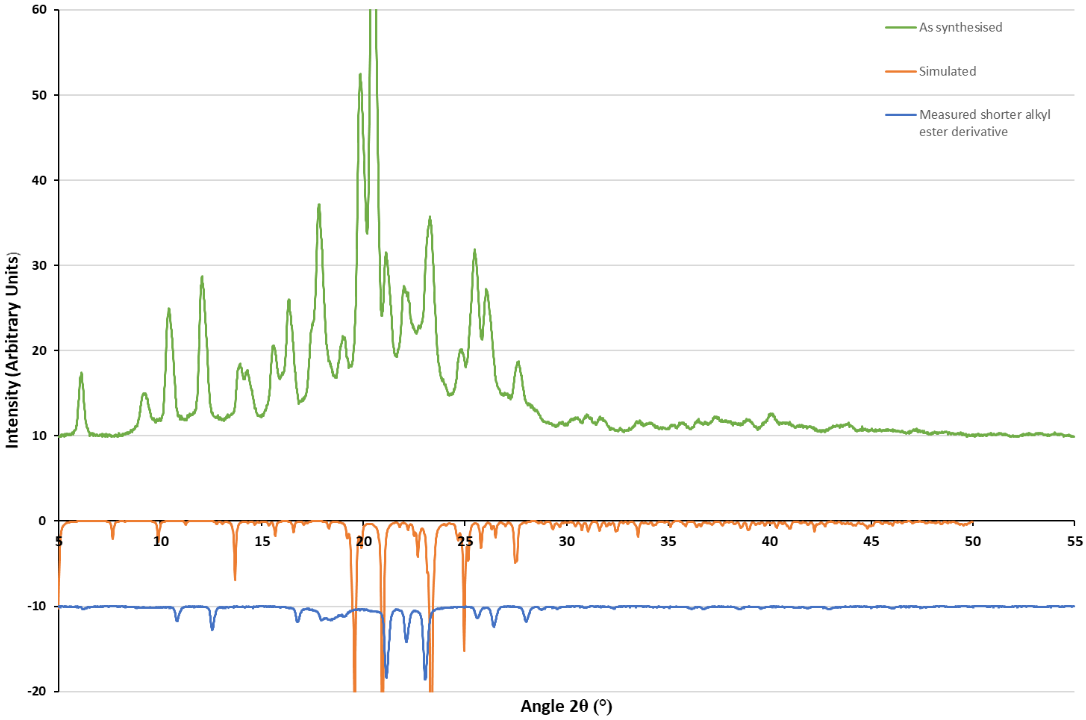

Figure 2.8 X-ray powder diffraction pattern for compound **58** (room temperature), showing the as-synthesised material consisting of multiple crystalline and polycrystalline phases (green); and comparison with the simulated pattern for compound **58** (orange) and the measured pattern for compound **59** (blue).

2.4.4 Structural study of 59

A single crystal of **59** of suitable quality for X-ray diffraction was obtained from a 1:1 H_2O/MeOH mixture. The data was solved and refined in the hexagonal space group *P*6$_3$/*m*, with a unit cell a = b = 15.57 Å, c = 6.87 Å, with the structure obtained shown in Figure 2.9. The

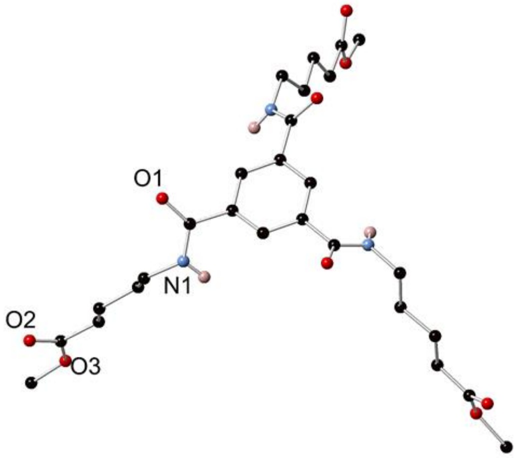

Figure 2.9 The structure of **59** with labelling scheme for unique heteroatoms. Selected hydrogen atoms and crystallographic disorder are omitted for clarity.

asymmetric unit of **59** contains one-third of the molecule, with a crystallographic threefold rotation axis coincident with the centre of the phenyl ring. The alkyl chains in this structure were modelled as being disordered over two orientations, with this disorder originating from two possible symmetry-related orientations of the amide groups from which the aliphatic chains extend in a linear fashion, seen in Figure 2.10. The extended structure of **59** comprises of one-dimensional hydrogen-bonded stacks of aromatic groups, with three equivalent N–H···O hydrogen bonding interactions (N···O distance 2.825(4) Å, angle N–H···O 159 (4)°) supporting each of these pairs, as seen in Figure 2.11 The adjacent phenyl rings are separated by an interplanar distance of 3.4134(3) Å, half the length of the crystallographic c axis. Arising from the inherent disorder in the phenyl-amide torsion angle, the exact nature of the extended hydrogen bonding network is obscured, however, a triple helical arrangement is most likely based on precedence in similar compounds.[77,79] Another piece of supporting evidence in favour of a helical arrangement is the unfavourable geometric mismatch that would occur in the case of a statistical mixture of orientations within a single stack. The adjacent columns were aligned in a hexagonal close packed manner, with the disordered aliphatic chains interdigitated in the interstitial spaces. No solvent or other guest molecules were found within the structure, nor did

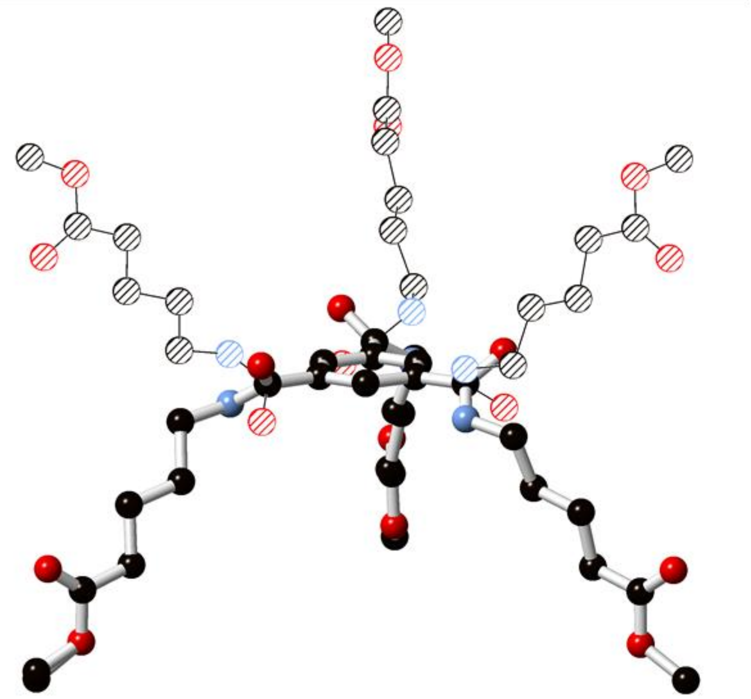

Figure 2.10 The two overlapping disordered orientations of compound **59**, modelled as an average across the entire structure by the mirror plane parallel to the phenyl ring. Selected hydrogens are omitted for clarity.

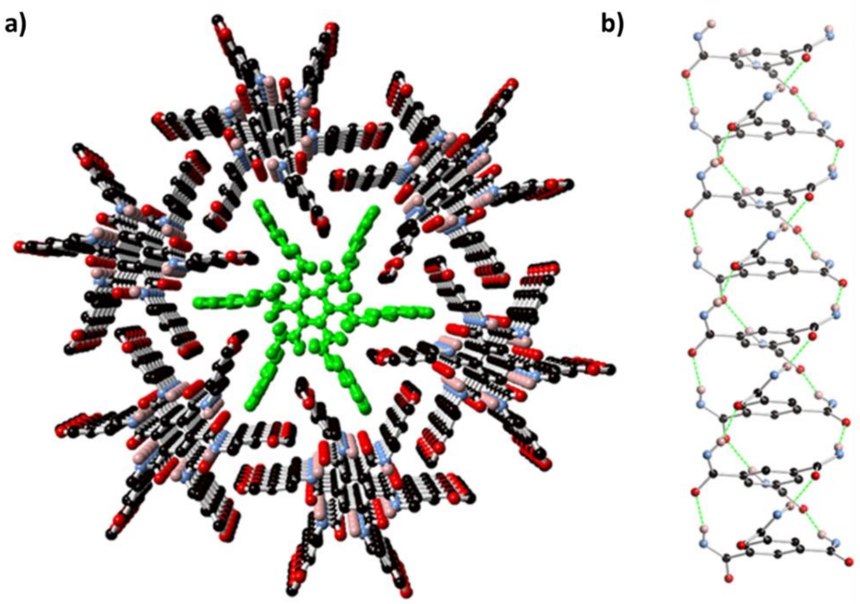

Figure 2.11 (a) The extended structure of **59** showing hexagonal close packing of adjacent columns, with single column highlighted in green. (b) Representation of the helical hydrogen bonding motif present within columns in **59**. C –H hydrogen atoms, crystallographic disorder of amide groups, and alkyl arms are omitted for clarity

elemental analysis indicate the presence of any additional species. The bulk material was found to be phase pure by X-ray powder diffraction, thus there was no obvious evidence of any other polymorphs at room temperature, as shown in Figure 2.12 The difference in structural arrangement between that of the isolated polymorph of **58** and **59** is due to the length of the alkyl chains, with the length of the chain of **59** being of suitable length to allow for the more

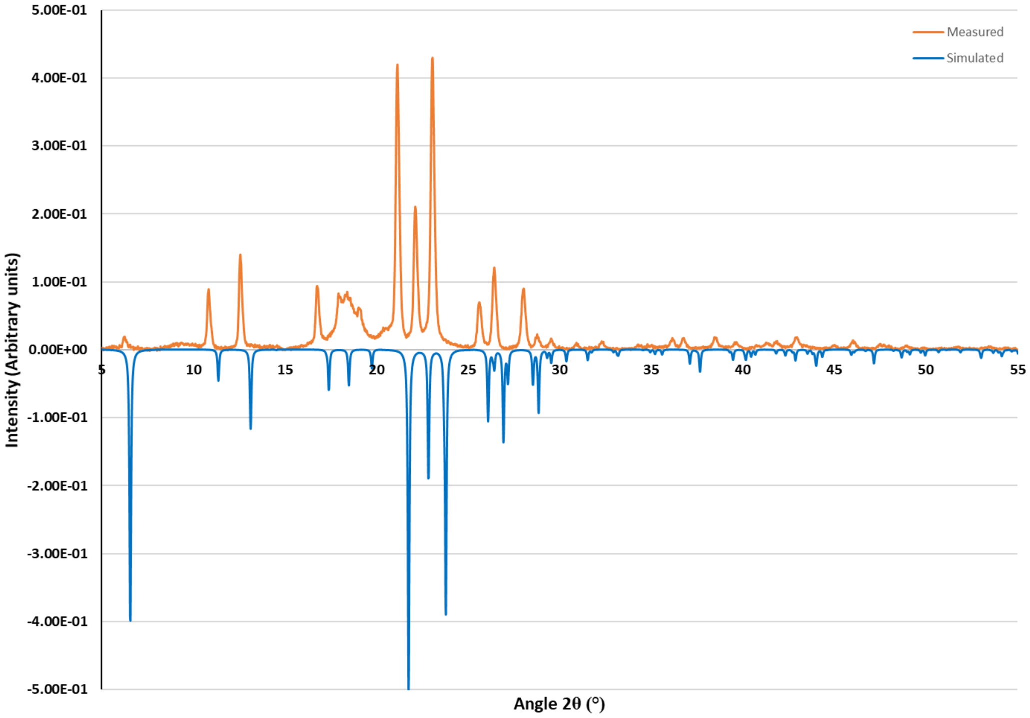

Figure 2.12 Measured (orange) and simulated (blue) X-ray powder diffraction patterns of **59.**

classical triple helical arrangement. As mentioned, the chains of **58** span the central phenyl ring in an unusual loop interaction, however, as seen by powder diffraction the sample is polymorphous, thus one of the other polymorphs could potentially arrange in the helical structure.

Due to the discotic columnar packing motif observed in the crystal structure and inspired by previous reports,[97,126] the potential for **59** to possess additional high-temperature crystalline phases or thermotropic mesophases was investigated and will be discussed in Section 2.6.

2.4.5 Structural study of 62

To study the influence of a carboxylic acid terminal group instead of the ester, a single crystal of suitable quality for diffraction was obtained from a 1:1 H_2O/MeOH mixture, with the resulting data solved and refined in the monoclinic space group *P2/n*. The asymmetric unit was found to contain the molecule in its entirety, along with five unique and well-localised water molecules. In this structure, each of the three arms are crystallographically non-equivalent and each has a folded conformation. One of the amide groups shows a significant torsion to the phenyl ring mean plane (interplanar angle 29.8°), with the remaining two amides are essentially coplanar with the ring as shown in Figure 2.13.

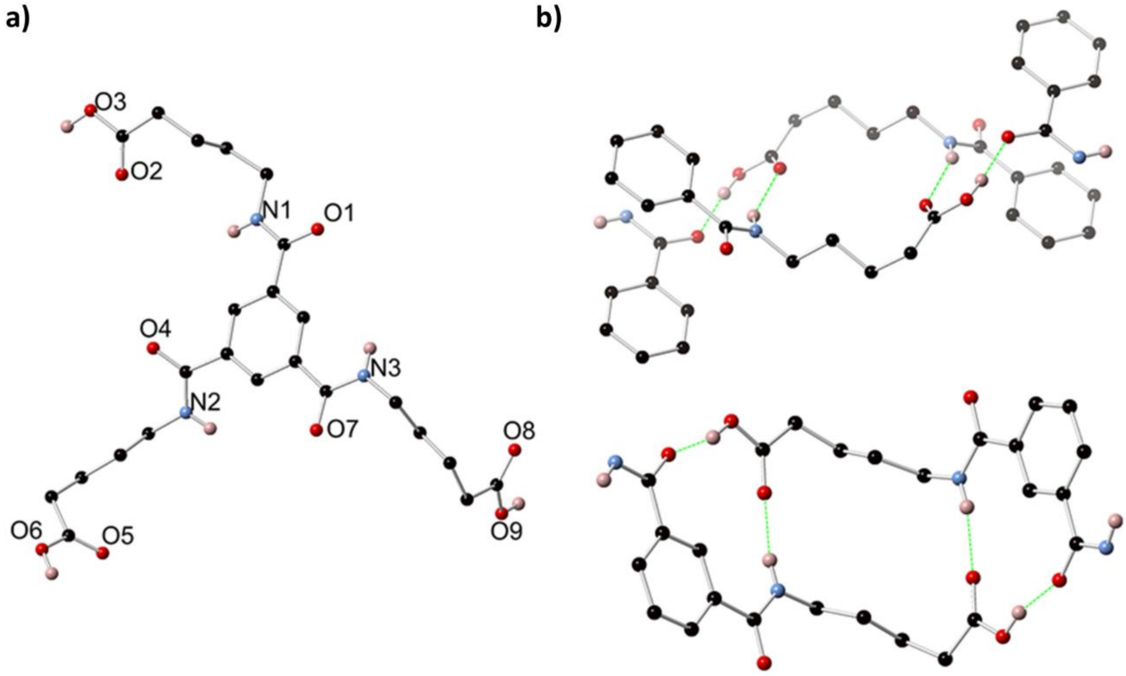

Figure 2.13 (a) Structure of **62** with heteroatom labelling scheme. Selected hydrogen atoms and crystallographic disorder are omitted for clarity. (b) The two unique modes of intermolecular hydrogen bonding present in the structure of **62**.

The extended structure of **62** possesses multiple hydrogen bonding interactions between both the molecules of **62** and involving the lattice water molecules. When analysing these interactions, three unique motifs are observed, the first being the arm originating from N3 undergoes a reciprocated interaction with a symmetry-equivalent arm. This interaction is equivalent to that observed in the structure of **63** while allowing for the increase in chain length, in which each carboxylic acid group donates one hydrogen bond to an amide oxygen atom and accepts one hydrogen bond from the N–H site of a different amide group on the same molecule. A similar interaction is observed from the amido-acid arm originating from nitrogen atom N2. However, the terminal carboxylic acid groups are arranged in a divergent manner, whereby the O–H···O interaction originating from O6 is directed at a different molecule than the N–H···O contact which is received from nitrogen atom N2. N1 and O3, the remaining hydrogen bond donors in the molecule, both donate hydrogen bonds to lattice water molecules.

The linkages due to the hydrogen bonding interactions and the minor amide-phenyl π-π interactions give rise to a three-dimensional assembly of **62**, leaving one-dimensional channels parallel to the crystallographic *b* axis centred on a twofold axis of symmetry, with an approximate (interatomic) diameter of 8.5 Å, as seen in Figure 2.14. Contained within this channel is a one-dimensional hydrogen-bonded water cluster with a repeating unit of five unique water molecules. In total, the five water molecules cumulatively accept eight hydrogen bonds; water molecules O12 and O14 accept one hydrogen bond each from framework atoms N1 (amide) and O3 (carboxylic acid), respectively, and the remaining three water molecules accept six hydrogen bonds both from other and symmetry-related water molecules. The framework atoms O2 (carboxylic acid) and O4 (amide) each accept two hydrogen bonds from lattice water molecules. **62** was the only structure in this study that contained a well-defined water cluster.

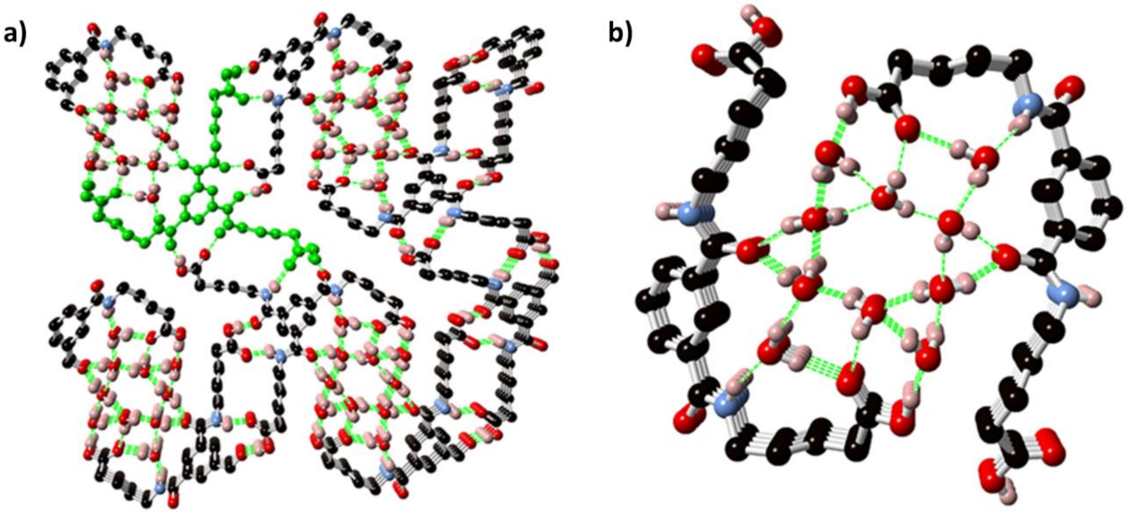

Figure 2.14 (a) The **e**xtended structure of **62** showing linkages through adjacent stacks of molecules via polymeric water clusters. A single molecule of **62** is highlighted in green. (b) A single columnar water cluster in the structure with bordering organic groups. Selected hydrogen atoms are omitted for clarity.

In order to study the role that solvent plays in this structure, a number of further experiments were carried out. A freshly isolated sample of **62** was analysed by TGA and showed a loss of 25 wt% before 80 °C, corresponding to the loss of both surface water and the water present in the channels. TGA on a sample of **62** that had been dried *in vacuo* revealed no mass loss until decomposition began at approximately 200 °C. The elemental analysis also indicated the presence of solvent, with the data indicating that there were 0.4 H_2O and 0.25 MeOH molecules per ligand molecule.

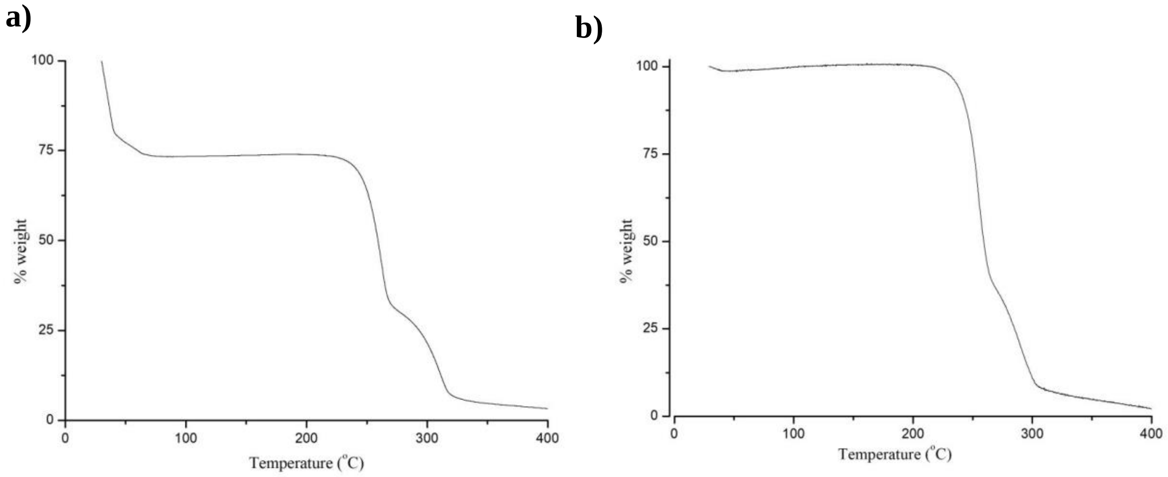

Figure 2.15 (a) TGA of a freshly isolated sample of **62** showing a mass loss of 25 wt% before 80 °C; (b) TGA of a vacuum dried sample of **62** showing no mass loss until the onset of decomposition at approx. 200 °C.

Time course X-ray powder diffraction studies of the crystalline material, seen in Figure 2.16, showed that the peaks due to the original crystalline phase begun to disappear almost immediately upon removal from solvent, and are replaced by new peaks corresponding to a second, unidentified crystalline phase that coincides with the loss of lattice solvent. As can be seen in Figure 2.16, this new phase did not resemble the pattern obtained from the single crystal data. Despite best efforts, it was not possible to collect meaningful single-crystal data on this poorly crystalline desolvated phase and attempts to re-solvate the collapsed material with water lead to an immediate loss of crystallinity, indicating that the first phase transition is irreversible.

Although rare, there are some examples of permanent porosity in hydrogen-bonded molecular crystals, where stability to evacuation is inferred in cases where the pore architectures are supported by multiple strong hydrogen bonding interactions.[127] In collaboration with Mr Kevin Byrne (of Prof. Wolfgang Schmitt's group, School of Chemistry, Trinity College Dublin) a number of gas adsorption experiments were carried out. Adsorption experiments work by evacuating the pores of the sample of interest by heating at a high temperature for several hours

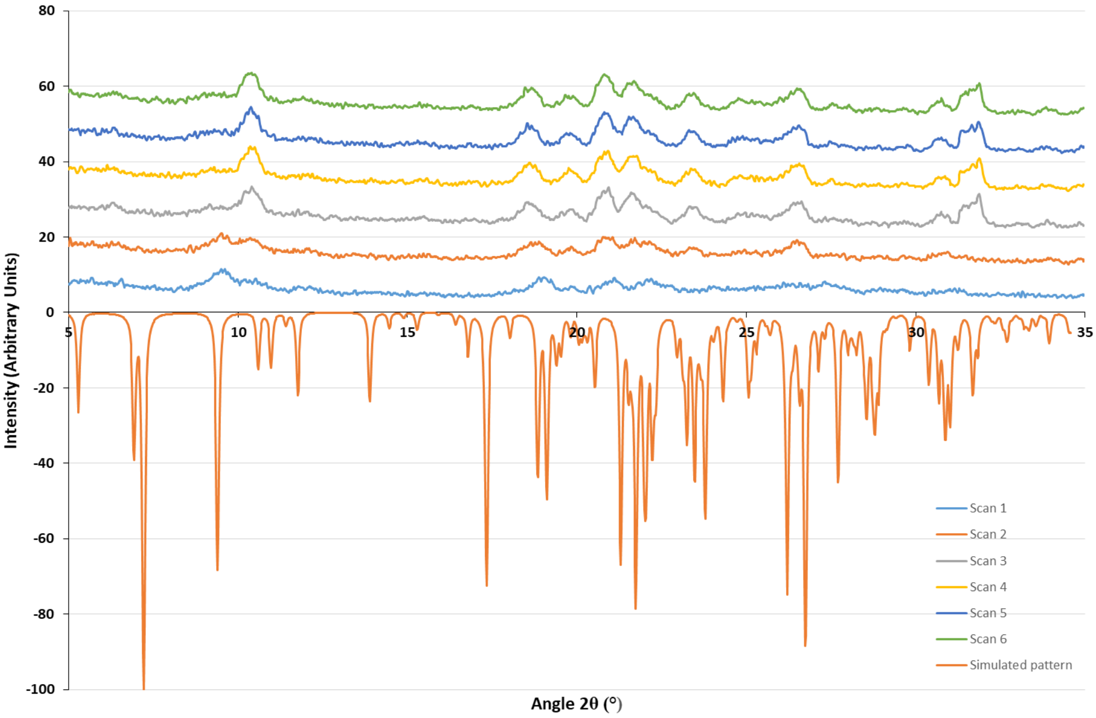

Figure 2.16 Time course X-ray powder diffraction of **62** collected immediately after removal from the recrystallisation solvent, showing the rapid loss of the original poorly-crystalline phase and growth of the collapsed microcrystalline phase. Each of the scans 1 – 6 corresponds to 3 minutes exposure. The dry sample was measured after drying the sample *in vacuo* with a 30 min exposure time. The simulated pattern was obtained from the X-ray data.

under vacuum, with the weight loss after evacuation determined. The N_2 and CO_2 isotherms are obtained by introducing high purity grade gases into the sample chamber with increasing pressure intervals at 77 K for N_2 and 287 K for CO_2 and monitoring the resulting weight changes.[128] A sample of **62** was dried under dynamic vacuum at 100.0 °C and the resulting compressed material was examined for N_2 and CO_2 gas adsorption behaviour. In both cases, 77 K N_2 and 273 K CO_2, the uptake experiments failed to provide any meaningful adsorption above the instrumental detection limit. These results would indicate that **62** immediately transitions to a collapsed, non-porous crystalline phase upon desolvation. Two examples of purely organic **BTA** based materials that survived evacuation and was found to adsorb N_2 were reported by Haldar *et al*.[17] In this report, a methionine and tyrosine derivative were synthesised and subject to adsorption studies, where the tyrosine analogue was found to uptake ten times more N_2 than the methionine analogue. This was attributed to the unusual solid-state packing arrangement of this analogue and highlights the difference in hydrolysing the ester group of **59** to result in the very different packing arrangement of the carboxylic acid analogue **62**.

2.4.6 Structural studies of 63

63 is the shortest alkyl chain carboxylic acid derivative in this family of compounds and single crystals were prepared from a 2:1 H_2O/THF mixture. The data obtained from X-ray diffraction were refined and solved in the triclinic space group $P\overline{1}$, with the asymmetric unit shown in Figure 2.17. The entire molecule is present in the asymmetric unit, with each of the three unique arms exhibiting a slightly different conformation. The arm containing the amide group C7, O1 and N1 displays a slightly twisted configuration with respect to the central phenyl ring (amide-ring interplanar angle 26.9°), compared to the other two unique amides which are effectively coplanar with the central ring. In addition, the arm originating from C17, O3 and N3 has fully staggered dihedral angles which results in an overall linear arrangement, while the remaining two arms have a combination of staggered and *gauche* conformations resulting in non-equivalent twisted arrangements.

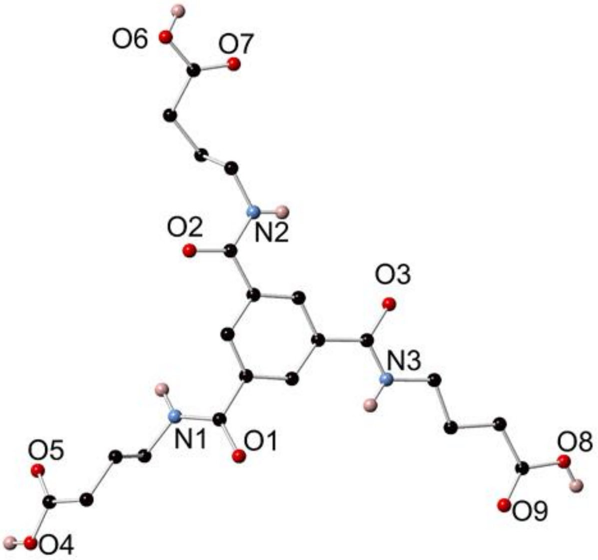

Figure 2.17 The structure of **63** with heteroatom labelling scheme. Selected hydrogen atoms are omitted for clarity.

Hydrogen bonding interactions are the dominant mode of intermolecular interactions within this structure with there being six non-equivalent hydrogen bonding donors and six possible acceptors. The hydrogen-bonded network is quite symmetrical in nature, with each of the three unique arms interacting with its symmetry equivalent to generate four hydrogen bonds per pairing, as shown in Figure 2.18. Arising from the hydrogen bonding interactions, each molecule of **63** interacts with three others to form an extended 2-dimensional hydrogen bonded network. Adjacent layers of the network interact through π-π type interactions, with an overlap of π systems occurring between the phenyl ring and the amide groups from adjacent layers at minimum (interatomic) distance of 3.352(4) Å for C1-C12. One-dimensional hexagonal channels parallel to the crystallographic *a* axis, of approximately 10 Å (interatomic) diameter,

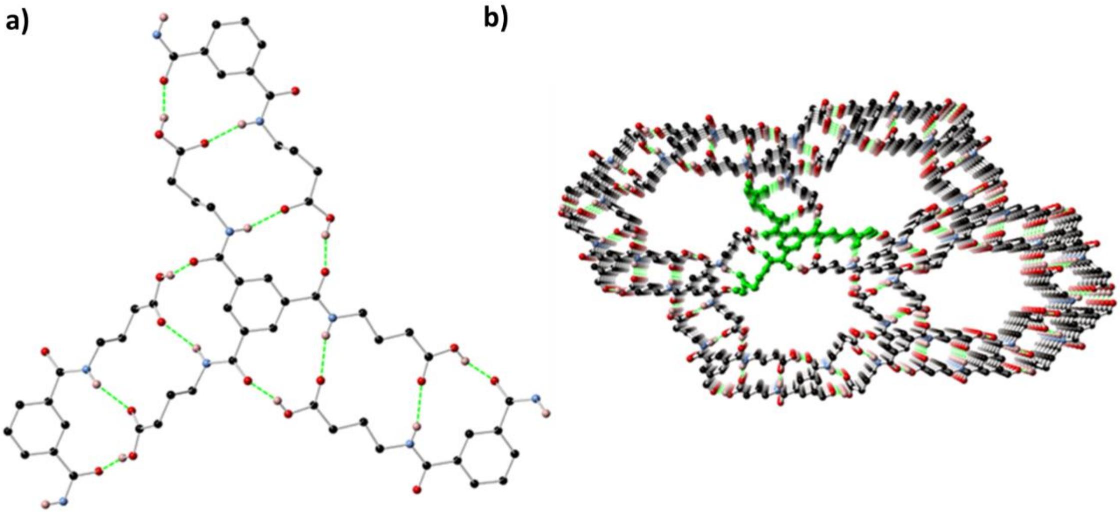

Figure 2.18 (a) Hydrogen bonding interactions between adjacent molecules in the structure of **63**. Hydrogen atoms not involved in hydrogen bonding interactions are omitted for clarity. (b) Extended structure of **63** viewed parallel to the solvent channels

are the by-product of this packing arrangement. Unlike for **62**, it was not possible to sensibly model the contents of these channels from the crystallographic data obtained due to poor ordering of the guest molecules, presumably owing to the lack of strongly interacting groups (hydrogen bond donors or otherwise) directed into the channels. Due to this disorder, the contribution from the disordered guest molecules to the measured structure factors was accounted for using the SQUEEZE routine in PLATON,[129] and elemental analysis was used to determine the solvent content in the channels. For an air-dried sample, elemental analysis revealed the presence of 1.2 H_2O molecules per molecule of **63**. A freshly isolated, crystalline sample of **63** displayed a mass loss of approximately 39% below 100 °C by TGA, with the onset of decomposition occurring at 250 °C, as seen below in Figure 2.19. These results would suggest greater occupancy of the solvent channels immediately after removal from solution,

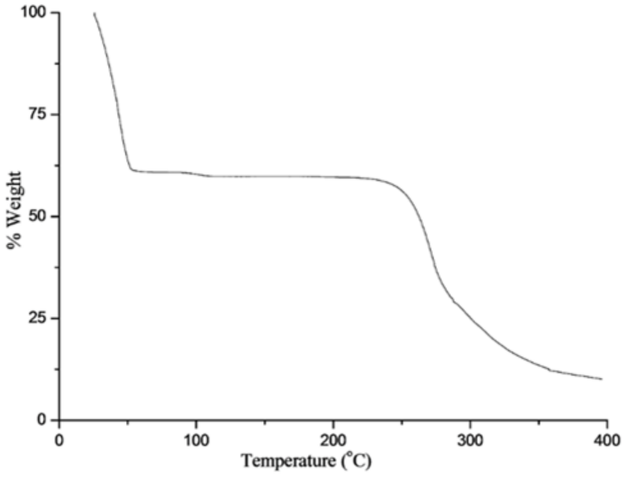

Figure 2.19 TGA of **63** showing a weight loss of 39 wt% before 100 °C, with the onset of decomposition at 250 °C.

with additional guest molecules gradually lost or exchanged for atmospheric water. X-ray powder diffraction analysis of **63** revealed that the phase identified from the single crystal analysis was the predominant in the bulk sample and was unchanged on standing in air, as seen in Figure 2.20. In powder diffraction, a random orientation is usually assumed, however, in some cases such as with plates or needles it can be difficult for the samples to adopt random orientations. The preferred orientations of these samples can cause systematic errors in the peak intensities of the powder patterns, thus, this can be accounted for by applying the March-Dollase parameter for preferred orientations, as was the case for **63** due to its needle-like nature.[130]

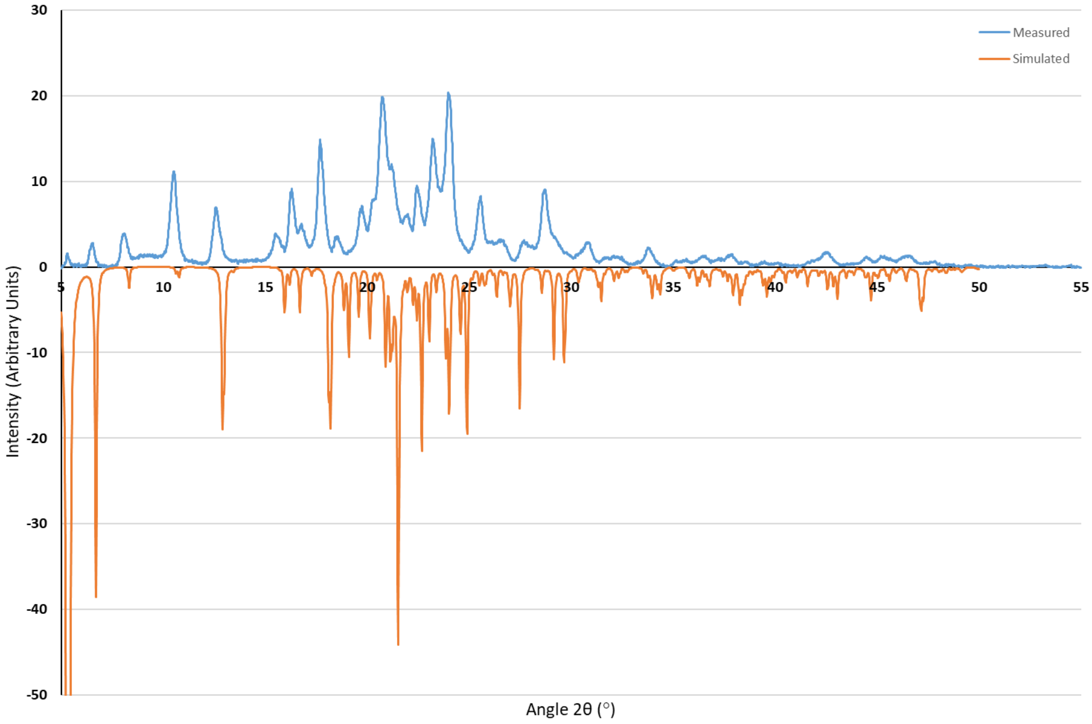

Figure 2.20 X-ray powder diffraction of **63** measured at room temperature compared to the simulated pattern from the single-crystal data collected at 100 K. To account for the preferred orientation caused by the needle-like crystalline morphology, the data were simulated with preferred orientation (011) with a March-Dollase parameter of 2.

To further probe the stability of these pores, some gas adsorption studies were undertaken. A sample of **63** was subjected to exhaustive evacuation by heating at 100 °C under dynamic vacuum overnight, followed by testing for uptake of N_2 at 77 K and adsorption of CO_2 at 273 K. Similarly, to **62**, negligible uptake was recorded in both cases, suggesting that the framework collapsed upon complete desolvation. The crystal structure of the ester analogue of **63** was reported in 2015 by Haldar *et al*,[77] in which **60** was reported to exhibit a supramolecular columnar structure that is stabilized by threefold intermolecular H-bonding interactions in the solid state. The individual discotic molecules stack one on top of another and are connected by intermolecular H-bonding interactions between the neighbouring amides to form a helical columnar assembly along the crystallographic *b* axis. There was also some π-π interactions between adjacent aromatic rings, with the centre-centre distance between the rings being 3.486 Å. A similar type structure was also observed for **59**.

To conclude this section, single crystal X-ray structures were obtained of the two ester derivatives and two of the carboxylic acid derivatives, with the end group functionality and length of alkyl chain having an impact on the solid-state structure. The carboxylic acid derivatives, **62** and **63**, formed crystalline materials that contain well-resolved solvent channels, which were destroyed upon drying under dynamic vacuum. The carboxylic acid derivatives synthesised in this chapter did not form the classical columnar structures associated with **BTA** structures. This is due to the competitive hydrogen bonding interactions that are possible due to the presence of the carboxylic acids and prevent the three-fold amide-amide interactions necessary for the columnar structures. On the other hand, the ester derivatives, **58** and **59**, were found to have weakly associated columnar packing behaviour in the crystalline state. The shorter chain derivative, **59**, forms the classical helical structure common for **BTA** compounds, while the longer chain was found to be polymorphous, with one X-ray crystal structure obtained and found to have be a densely packed network and possess an unusual loop interaction. This loop interaction occurred due to the length of the alkyl chain enabling the chain to engage in two hydrogen bonding interactions with the same adjacent molecule, spanning the width of the central phenyl ring. Thus, the length of the side chains of the **BTA**s has a great impact on structure, with a difference of just one carbon leading to great structural changes. As expected, the shorter chains, both ester and carboxylic acid, have a greater tendency towards crystallinity, with this decreasing as the alkyl chain length increases, with it not being possible to obtain single crystals of suitable quality for diffraction of **61**. Many attempts were made to obtain metal complexes of the carboxylic acid derivatives, with the intention of these being more stable to evacuation and possessing useful adsorption properties. Unfortunately, however, these attempts were fruitless, only resulting in amorphous materials.

2.5 Investigations into the gelation properties of compounds 58, 59, 61, 62 and 63

As mentioned in the introduction, a gel is a type of soft material and is characterised by its lack of flow, *i.e.* its solid-like rheological properties.[31] A gel is a substantially dilute cross-linked system, with these cross links within the fluid giving the gel its structure and contributing to its composition.[22] A crude test of a gelation behaviour is the 'inversion test', in which the potential gel sample is inverted for an extended period of time (> 1 h) to see if it can support its own weight.[31]

Due to the propensity of **BTA** compounds to gelate,[14,108] and given the fibrous nature of the crystals reported in Section 2.4, studies into the potential gelation ability of compounds **58, 59** and **61-63** were undertaken. Gelation tests in a variety of solvent and concentration conditions were carried out, with no gel formation occurring in the case of the ester derivatives **58** and **59**. Instead, gelation tests on these derivatives mostly resulted in the formation of crystalline or micro-crystalline solids upon precipitation.

After test experiments in a wide range of common solvents, it was found that gelation of the carboxylic acids **61** and **63** was most effective by dissolving the appropriate compound at 1 wt% in a 2:1 H_2O/THF mixture with gentle heating, and then allowing the mixtures to set for several hours. Under these conditions, **61** was found to readily gelate, while **63** forms a weak gel. The remaining carboxylic acid derivative, **62**, did not reliably or reproducibly gelate using these conditions, nor was it possible to scale the preparation to useful quantities. Other solvent mixtures and conditions were screened for the gelation of **62**, however, these attempts were fruitless.

As mentioned a crude test of gelation is the 'inversion test',[31] which, when applied to **61** revealed the gel to be able to withstand inversion and appeared to be quite robust. TGA was carried out on this sample and the wt% was determined to be 2.4 wt%. **61** was also found to be thermo-reversible, as is common for supramolecular gels.[23] Compound **63** resulted in visually weaker gels and appeared more crystalline in nature, with TGA results confirming this as the wt% was found to be 5 wt%, Figure 2.22. It was also possible to carry out TGA on a sample of **62,** with the results showing the wt% to be 2.5 wt%, Figure 2.22. These observations agree with

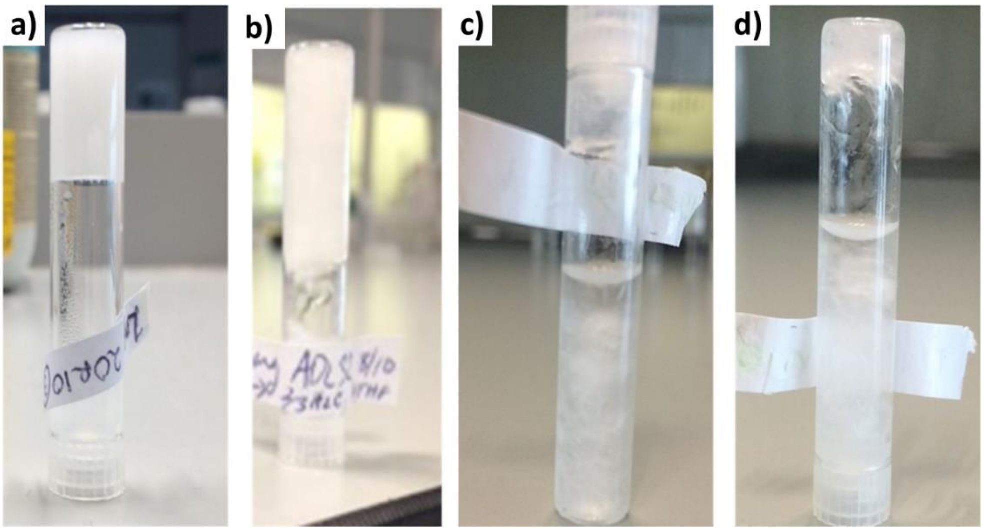

Figure 2.21 Inversion tests of (a) **61**, (b) **62** and (c & d) very weak, more crystalline gel sample and failed inversion test of **63.**

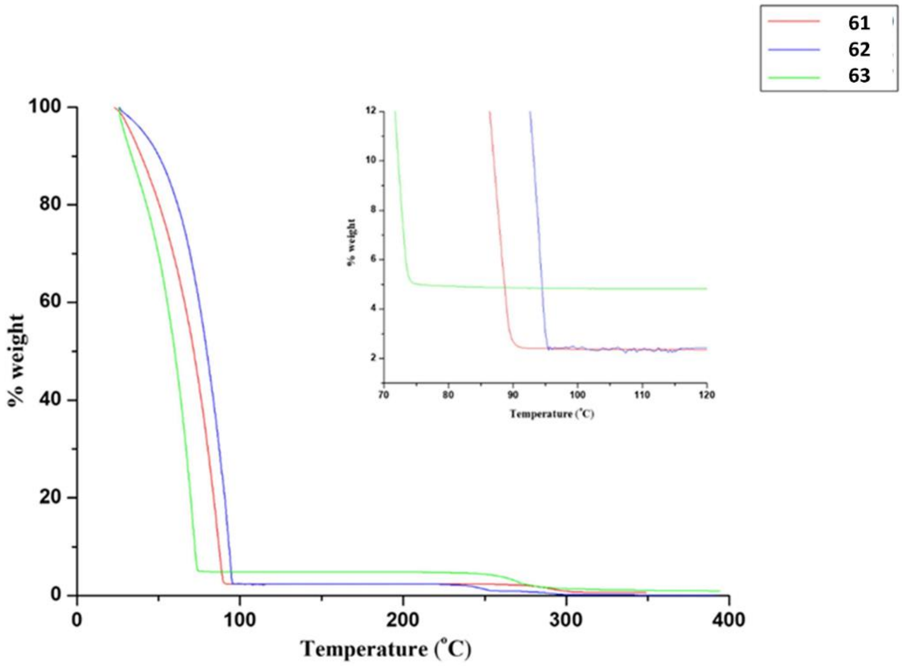

Figure 2.22 TGA thermographs of **61**, **62** and **63** showing weights losses of 97.6 %, 97.5 % and 95 % before 100 °C respectively.

the intuitive expectation that the length of the aliphatic chain influences the gelation behaviour and the strength of the resulting materials.

Xerogels of **61**, **62** and **63** were obtained by drying gel samples under dynamic vacuum, with the morphology of the resulting materials then being studied by SEM. Xerogels were used as the SEM operates under a vacuum and therefore requires the samples to be completely dried before imaging, thus the concentration of the sample being imaged cannot be deduced. Cryo SEM would have been a useful way to study the gel morphology without the collapse of the gel network that drying causes, however, access to this technique was not available at the time of study.[24] These images show the entangled fibrous nature of the materials and show individual fibres to be as small as 500 nm in diameter. This result was similar to the morphology and size reported for related **BTA** based gelators.[92,118] The fibrous nature of the gels was also observed in the bulk scale using optical magnification, as seen in Figure 2.23. In these images, **61** and **62** look fibrous, while **63** looks more crystalline in nature, which is in accordance with the tendency of **63** to form both gel and crystalline materials.

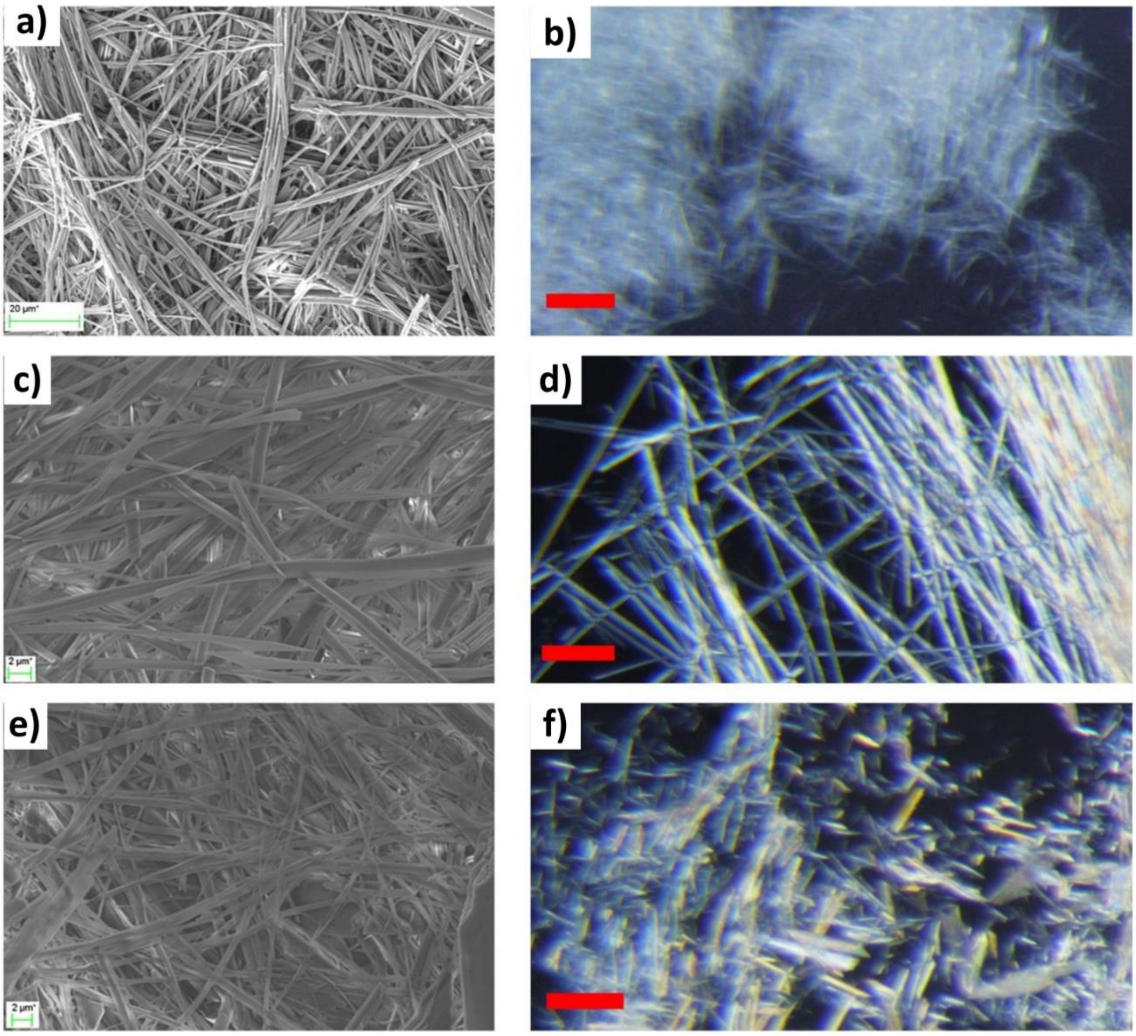

Figure 2.23 (a) SEM images of xerogels of **61** (scale bar 20 µm), (b) **62** (scale bar 2 µm) and (c) **63** (scale 2 µm). (d) Optical microscopy images of (d) **61**, (e) **62** and (f) **63**(red scale bars are equal to 100 µm)

Due to the robust and reproducible nature of the gel material formed from compound **61**, rheological studies were carried out on the material in collaboration with Dr. Benjamin Haffner and Prof. Matthias Möbius (School of Physics, Trinity College Dublin). Rheology is the study of flow, as mentioned previously, and is one of the most useful techniques in gel characterisation. Rheology involves the study of liquids and solids under applied stress conditions, in which the materials flow rather than deform in a classical manner. A rheometer similar to that used in this case is shown in Figure 2.24.[31,131] Gels which have a complex structure have solid like rheological properties.[31] In a rheometer the sample is placed between two parallel plates and a stress is applied by moving one plate relative to the other, with the resulting strain measured using a pressure transducer. To measure the shear stress of the sample, the material to be examined is placed between the two plates, with one applying a shear by oscillating at a constant frequency with increasing applied stress. A frequency sweep experiment is also possible with a constant stress.[31] The rheological response of a material to

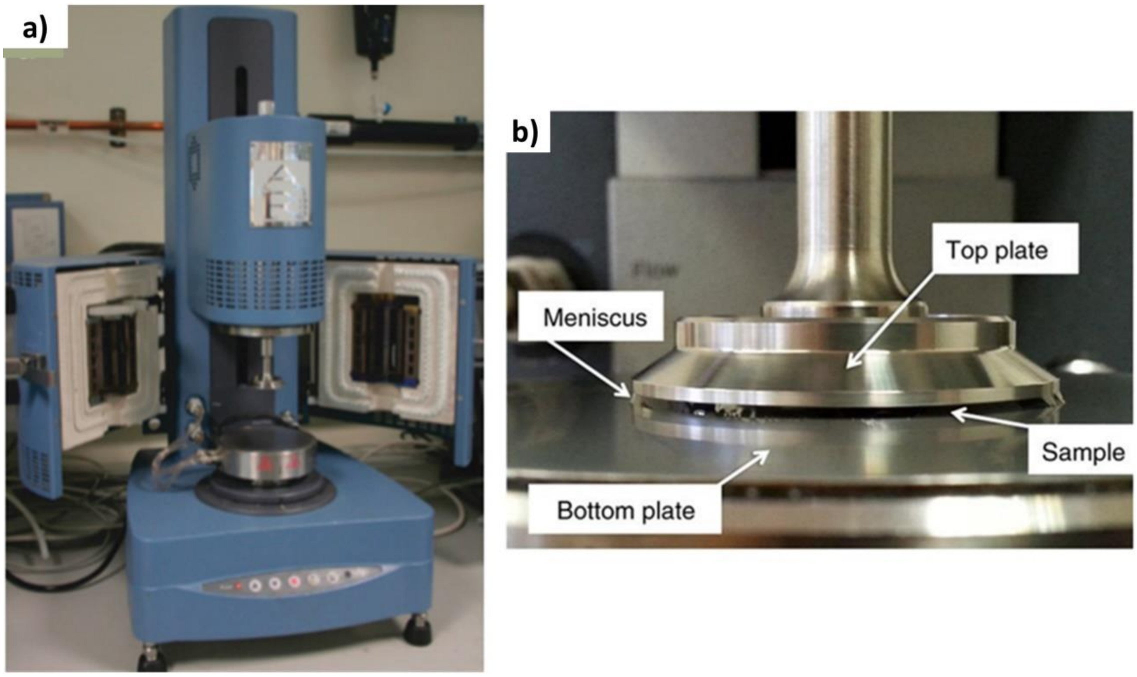

Figure 2.24 (a) a rheometer similar to that used in this expermient and (b) magnified image of the parallel plates. Image reproduced from references 31.

shear stress can be classed as being solid-like or liquid-like in behaviour. A gel is considered as being a complex fluid and as such, its response to an applied stress is described by considering both the contribution of the solid-like behaviour (the elastic storage modulus, G') and the viscous or liquid-like contribution (the elastic loss modulus, G'').[31]

On compression of **61** between the parallel plates of the rheometer, phase separation was observed which resulted in the contraction of the gel matrix and liberation of an amount of the encapsulated solvent. To generate a robust and homogenous gel sample required for the measurements, the original 2.4 wt% gel was compressed until separation of the solvent was no longer observed. TGA was then carried out on this sample to determine the wt%, revealing it to be 25 wt%, as shown in Figure 2.25, where we can see a weight loss of 75 % before 100 °C followed by the onset of decomposition at approximately 250 °C. The results of the stress and frequency sweeps along with the recovery tests are shown in Figure 2.25. The strain experiment shows the storage modulus G' being 3.12×10^6 Pa, which is an order of magnitude greater than the loss modulus, G'', at the same stress amplitude. This is as expected for a solid-like material.

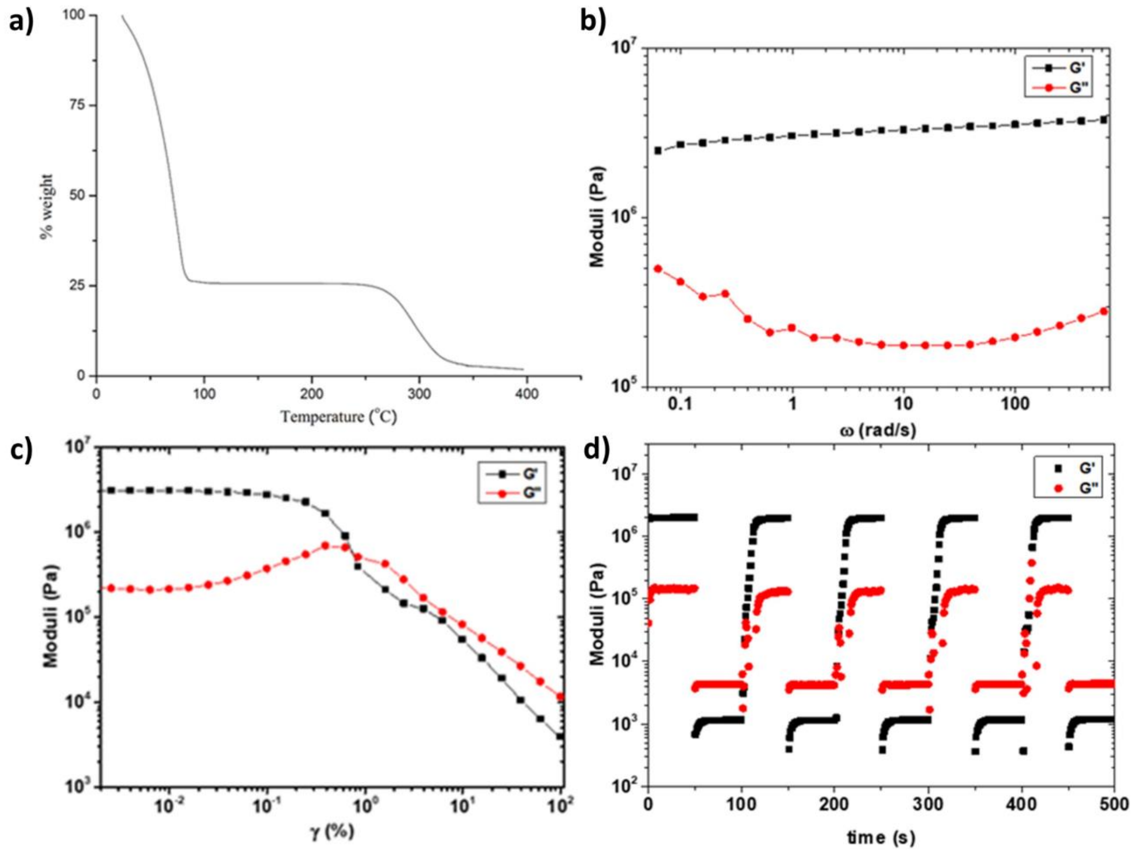

Figure 2.25 (a) TGA of **61** after rheology showing the wt% to be 25 wt% (b) Strain sweep experiment of **61** showing the crossover from solid-like to liquid-like behaviour and (c) Frequency sweep experiment demonstrating that G′ is invariant to frequency, indicative of gel-like behaviour (d) Recovery test revealing the mechanical reversibility of the material. The strain amplitude was alternating between γ = 0.01% (solid-like) and γ = 500% (liquid-like) for 50 seconds each over 5 cycles at ω = 6.28 rad s−1.

Some previous reports of G′ for **BTA**-based gels have included a G′ of 769 Pa for a tris-pyridyl BTA gel reported by Li and co-workers, a G′ of 3950 Pa for a pillar(5)arene derivatised **BTA** synthesised by Ning and co-workers and the G′ of 1040 Pa for a terpyridine functionalised **BTA**, **66**, reported by Savyasachi AJ in his PhD thesis, [90,121,132] thus indicating the strength of the gel. The point at which the material begins to flow is known as the yield strain and for **61** the crossover occurs at the yield strain 0.78% thus indicating a change to liquid-like behaviour. The results of the frequency sweep experiment shows that the elastic response, *G′*, is invariant to frequency, which is indicative of gel-like behaviour.[31] An oscillatory recovery test was carried out which showed the effect on the storage and loss moduli at low strain amplitude in the linear viscoelastic regime after shearing beyond the yield stress. The results showed that **61** rapidly returns to its original strength after shearing and this behaviour is maintained over repeated cycles, thus demonstrating the mechanical reversibility of the gel, a common feature of supramolecular gels.[72,133]

It was also possible to generate gel-like material of compounds **61**, **62** and **63**, through the use of a pH trigger similar to that used by Schimdt and co-workers[83] and Lloyd and co-workers.[14] In this method, the water insoluble carboxylic acid derivatives are dissolved in an aqueous solution of NaOH, followed by addition of aqueous HCl which caused the gelation of the carboxylic acid derivatives with varying degrees of success. In the case of **61**, upon addition of HCl a gel-ish material formed immediately, however it was not robust enough to withstand the inversion test, as seen in Figure 2.26. TGA of material revealed to % weight to be approximately 3 wt%, weaker than its H_2O/THF counterpart, as seen in Figure 2.26. SEM was carried out on xerogels samples of this weak gel material and showed a densely packed fibrous gel network and the presence of a significant amount of NaCl crystals underneath the gel material, Figure 2.26. The presence of this salt may be contributing to the lack of robustness of this material.

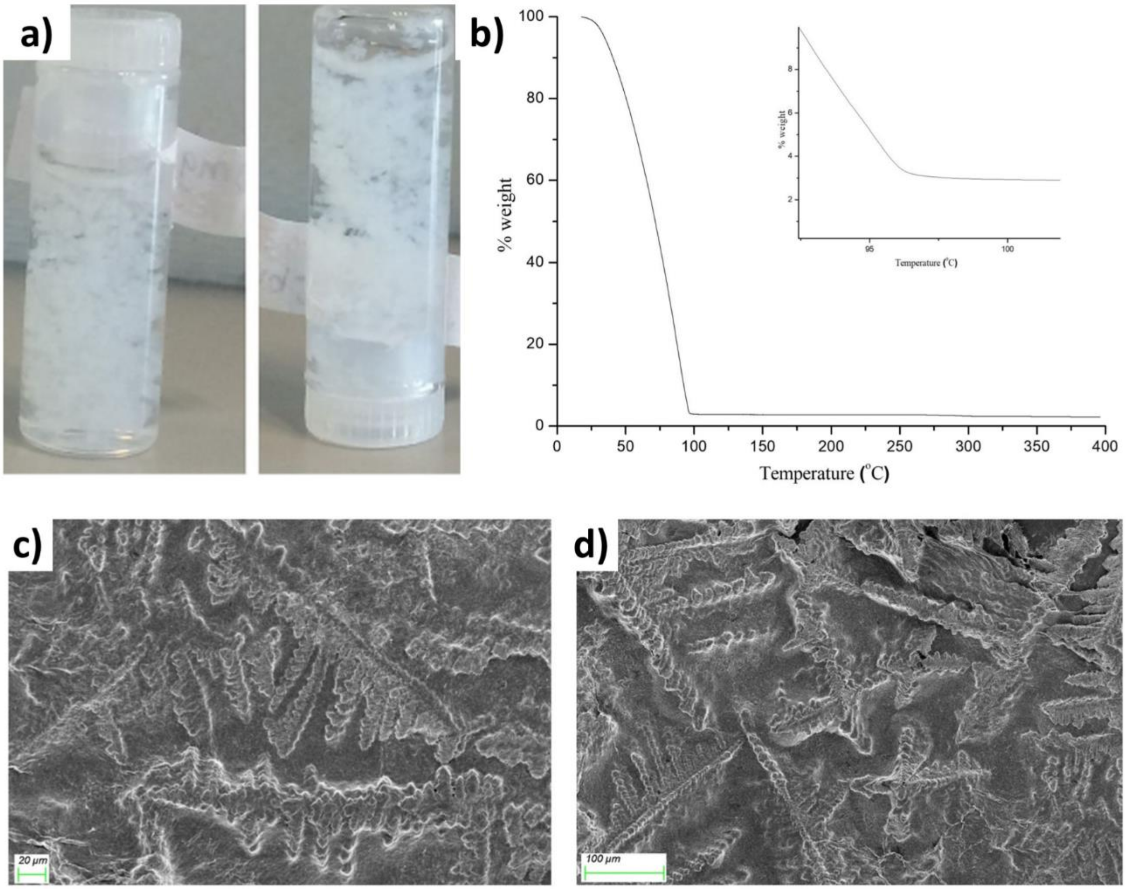

Figure 2.26 (a) Failed inversion test of **61** and (b) TGA of **61** revealing the % weight to be approximately 3 wt% and SEM images of a xerogel sample of **61** (scale bars 20 μm (c) and 100 μm (d)), showing the fibrous gel network and the NaCl crystals

62 formed a slightly more robust gel-like material, however, it too was unable to support its own weight. Shown in Figure 2.27. is the failed inversion test and the TGA of the gel-like material of **62**. The TGA revealed the % weight to be about the same as that of **61** (about 3wt%) generated using the acid/base method. Although the material did not withstand inversion, it was the most reliable method to generate a gel-like material of **62**. Shown in Figure 2.27. are the SEM images of the xerogels of **62** and show the densely fibrous material, with individual fibres approximately 0.5 to 2 µm in diameter and the presence of NaCl crystals amongst the fibres. The morphology of this gel-like material is similar to the gels generated from H_2O/THF.

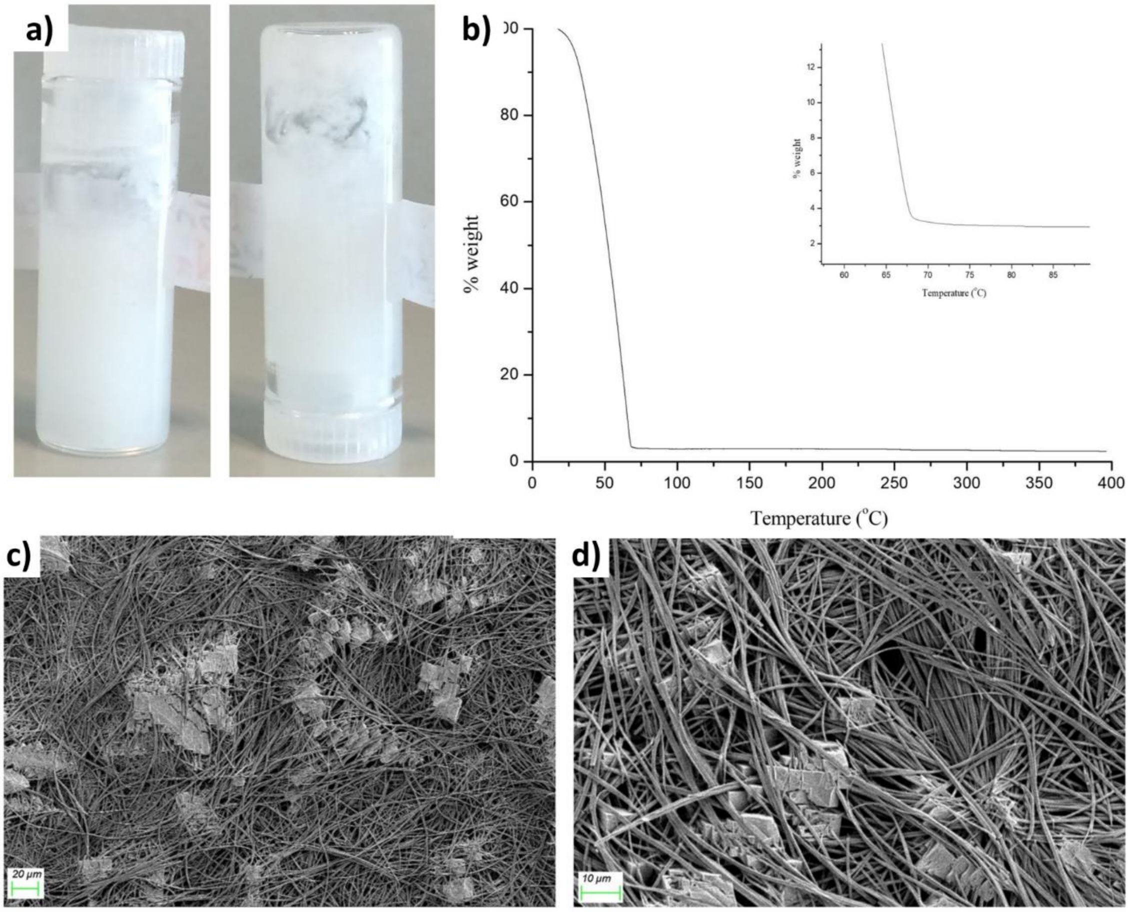

Figure 2.27 (a) Failed inversion test of **62** and (b) TGA of **62** revealing the % weight to be approximately 3 wt% (c) SEM images of a xerogel sample of **62** (scale bar 20 µm) and (d) (scale bar 10 µm) showing the fibrous gel network and NaCl crystals.

For **63**, however, it took a number of hours for any gel/crystal fibres to form, as seen by SEM in Figure 2.28. As with the other gelation method described for **63**, the resulting gel-like material looked more crystalline in nature and again shows that the shorter chain derivatives tend more towards crystalline behaviour rather than gelation.

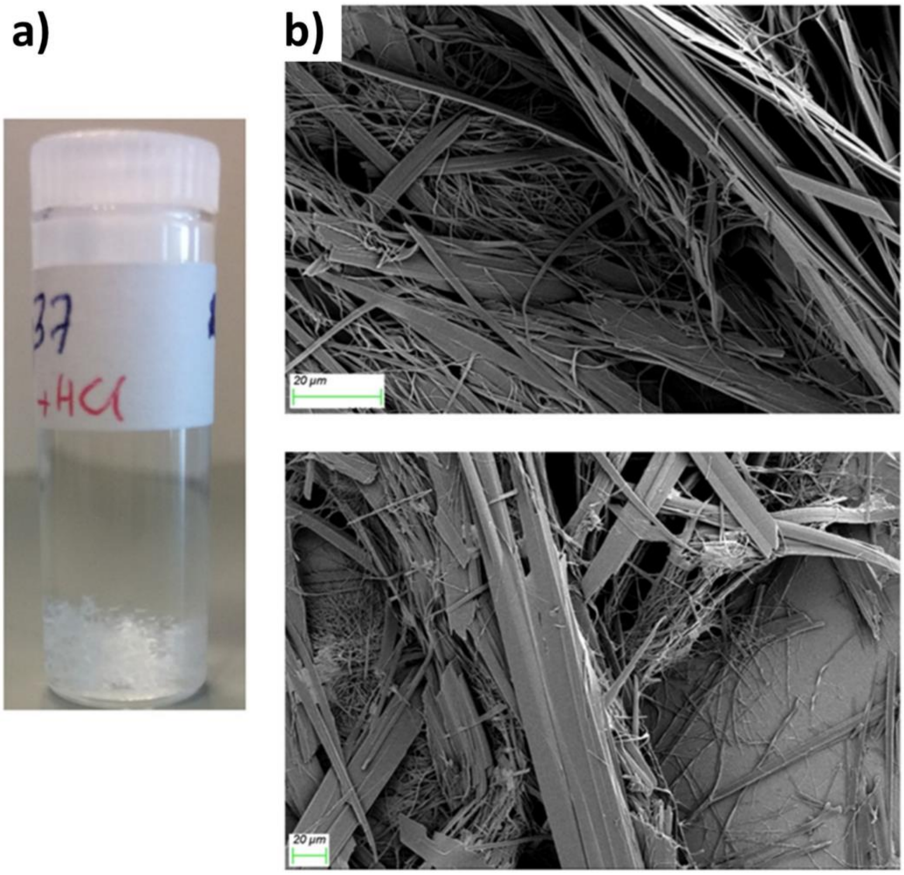

Figure 2.28 (a) vial containing **63** in NaOH and HCl and (b) SEM images of a xero-sample of the material formed by **63** using the acid/base method, showing the sample to be a mixture of gel-like fibres and crystals and NaCl crystals (scale bars 20 µm).

To summarise the gelation behaviours of the derivatives **58**-**63**, it was found that the ester derivatives do not gelate at any reasonable concentration, however, the carboxylic acid derivatives were all found to gelate to varying degrees of success. The longest chain derivative, **61**, was found to be the most robust gelator, with the shorter derivatives **62** and **63** being less reliable and less robust gelators. This is partly intuitive and in line with some previous studies, where longer alkyl chain groups tend to more towards crystallisation.[134,135] Intuitively, the longer chain derivatives have a greater degree of flexibility, thus are less likely to crystallise and instead undergo growth in one dimension to form fibres, which then aggregate to form a gel.[23,134] The shorter derivatives have less flexibility and tend towards highly ordered aggregation resulting in crystals.

2.6 Thermal studies

Due to the discotic columnar packing motif of **59** and inspired by previous reports,[97,126] TGA, differential scanning calorimetry (DSC) and polarised optical microscopy (POM) were used to investigate the existence of additional high temperature crystalline phases or thermotropic mesophases in compounds **58**, **61**, **59**, **62** and **63**. Thermal studies were also carried out on **60** though its synthesis and characterisation has been previously reported by Haldar *et al.*,[77] they did not study the thermal properties. TGA was used first to determine the highest temperatures the compounds were stable up to and this was then used for the DSC measurements. DSC works by heating a sample pan and empty reference pan and maintaining the same temperature in both pans. An image of a similar apparatus to that used in this work is shown in Figure 2.29, along with an image of the double furnace.[136] During a phase transition occurring in the sample pan, there will be a difference in the energy required to keep it at the same temperature as the reference pan, thus exothermic and endothermic transitions can be detected. Polarised optical microscopy is used to observe the texture of liquid crystalline materials at different temperatures. Liquid crystal phases are birefringent, thus highly coloured textures are observed when viewed through crossed polarisers.[44,46] The polarised optical microscopy described in this section was carried out in collaboration with Dr Robert Pal and Mr Edward Ward at the School of Chemistry in Durham University and the microscope used was equipped with a heating stage, seen in Figure 2.30.

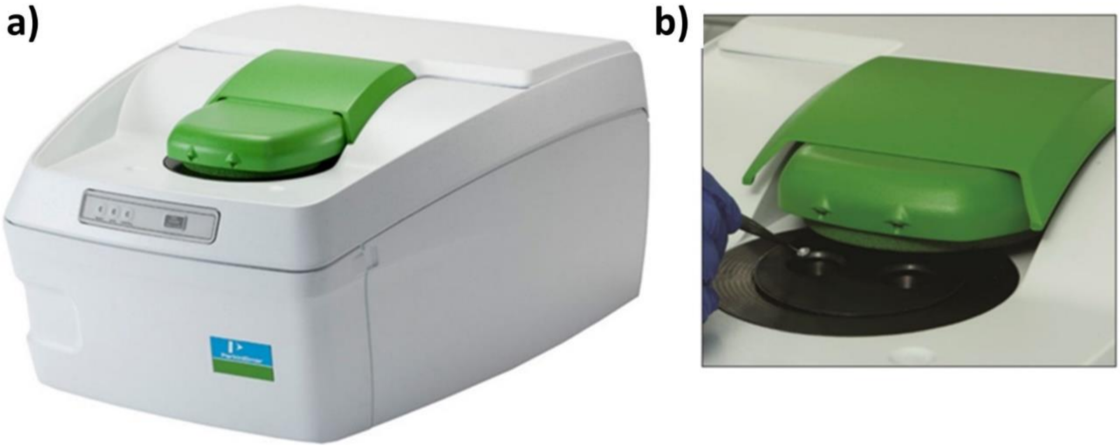

Figure 2.29 (a) A DSC setup similar to that used in this work and (b) magnified image of the double furnace of the DSC. Images reproduced from references 136.

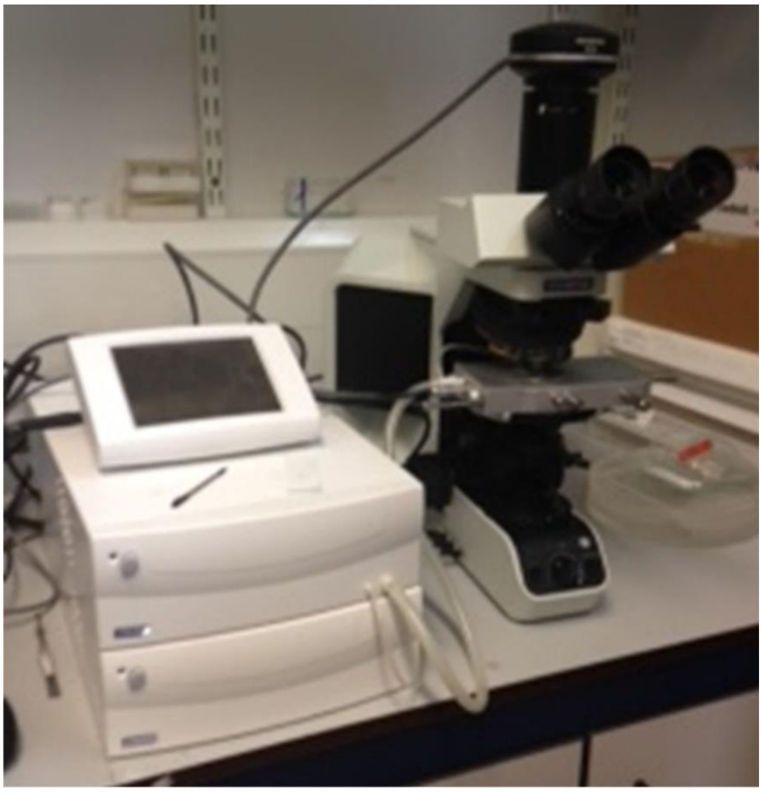

Figure 2.30. The polarised optical microscope equipped with a heating stage used in Durham University as part of the mesophase characterisation discussed in this chapter.

When **60** was subjected to a heating and cooling cycle, it only showed a crystalline to isotropic liquid (Cr-I) and isotropic liquid to crystal (I-Cr) transition on heating and cooling cycles, respectively. There was no evidence of any additional phases, as seen in Figure 2.31.

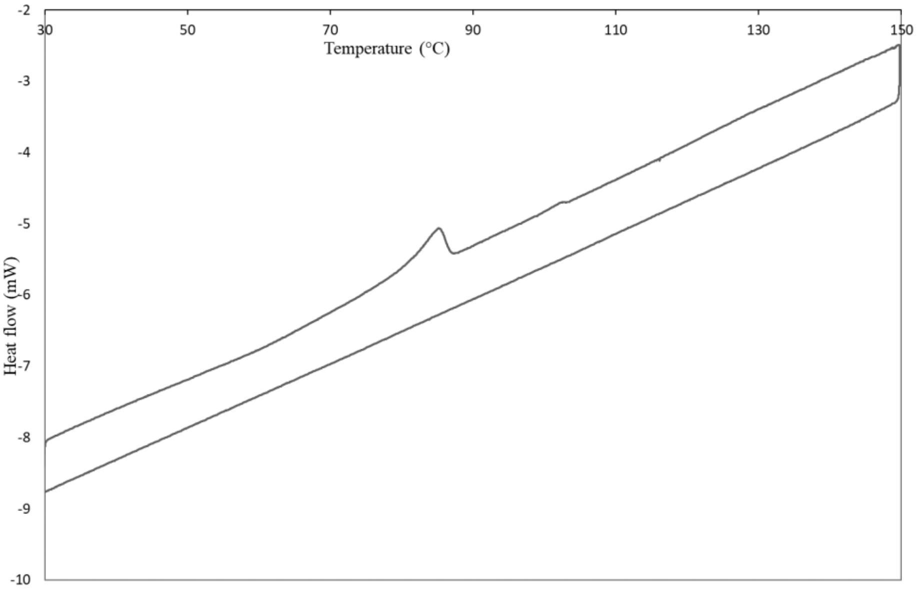

Figure 2.31 Second cycle DSC thermograph of **60** showing the crystalline to isotropic transition.

Additionally, the three carboxylic derivatives, **61**, **62** and **67**, were also analysed by DSC. The DSC thermograph for each of the carboxylic derivatives **61** and **63**, Figure 2.32 and 2.33 revealed a well-resolved melting transition on the first heating cycle, along with the loss of encapsulated solvent, followed by freezing into amorphous phases on the cooling cycle, with no obvious distinct phase transitions evident on further heating and cooling cycles. The DSC thermograph of **62** looked to be quite unremarkable and is thought to undergo a glass transition, which can be a subtle change in the baseline, Figure 2.32.

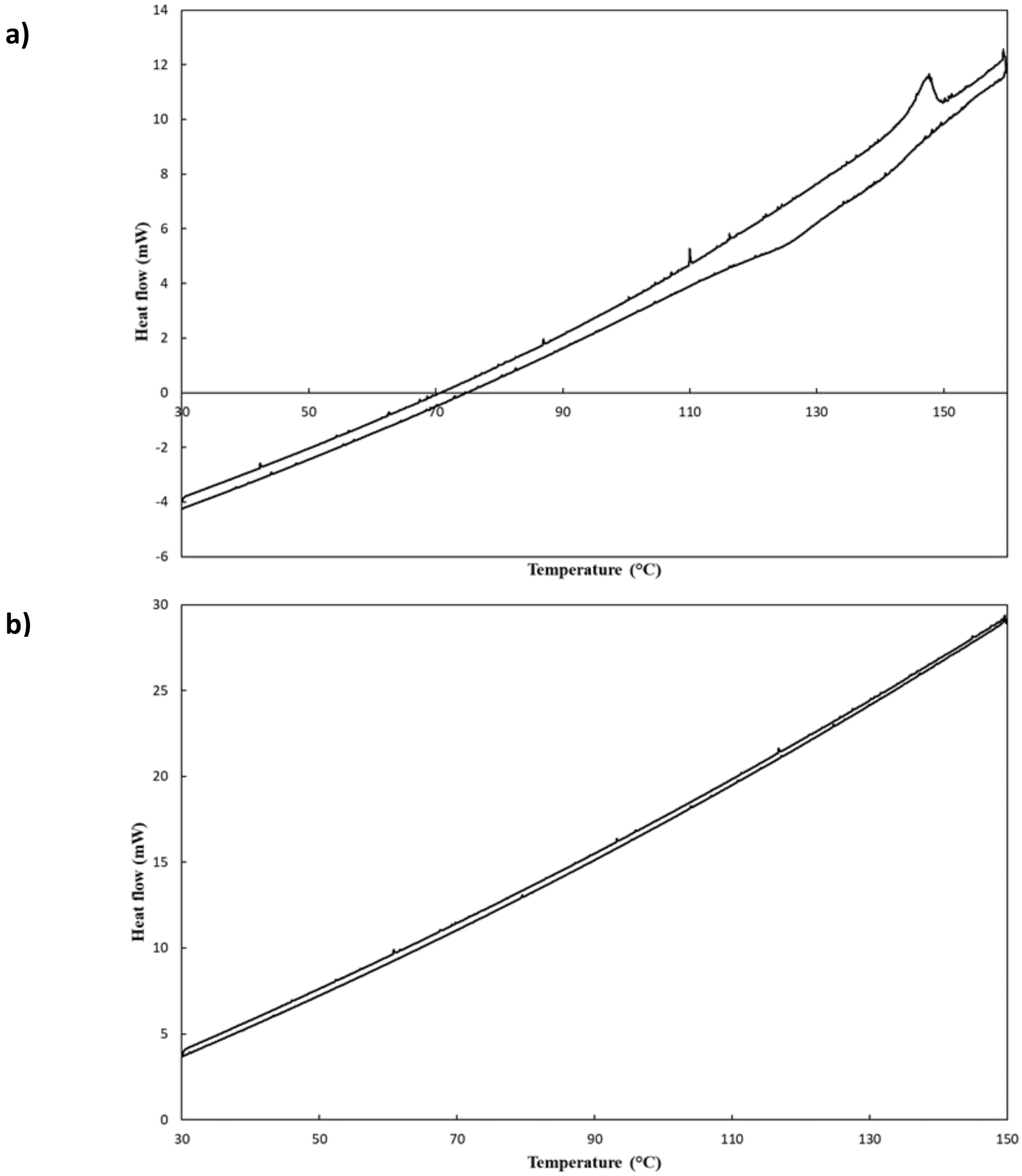

Figure 2.32 Second cycle DSC thermographs of (a) **61** and (b) **62**.

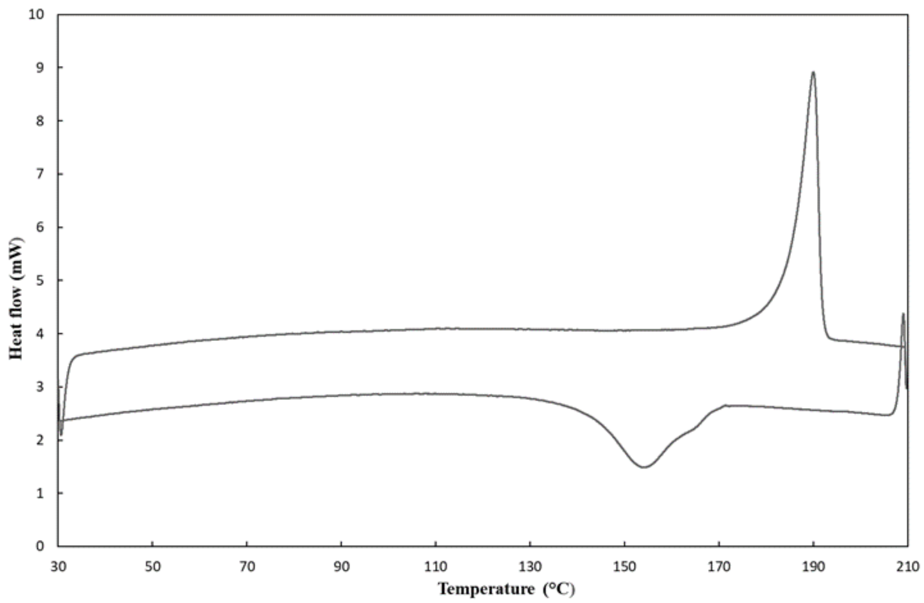

Figure 2.33 Second cycle DSC thermograph of **63** showing the melting and cooling transitions.

The DSC thermograph of **59** showed a single endothermic transition on the heating cycle, the melting transition (Cr-I), with an onset temperature of 81.6 °C and Δ_H = 39.7 kJ mol^{-1}. This corresponds to the observed melting point of 89-90 °C. On the cooling cycle, two exothermic transitions were observed, a lower energy exothermic step with an onset temperature of 71.5 °C followed by a more substantial exotherm at 60.6 °C. The Δ_H values of these transitions were -5.2 kJ mol^{-1} and -35.3 kJ mol^{-1} respectively. These values and that of the melting transition were reproducible over multiple heating and cooling cycles. **59** was then examined under polarised light at the same temperatures of the transitions as seen in DSC. On cooling from the isotropic melt, birefringent texture is observed following the first exothermic transition, characteristic of an ordered phase, as seen in Figure 2.34. When carrying out DSC

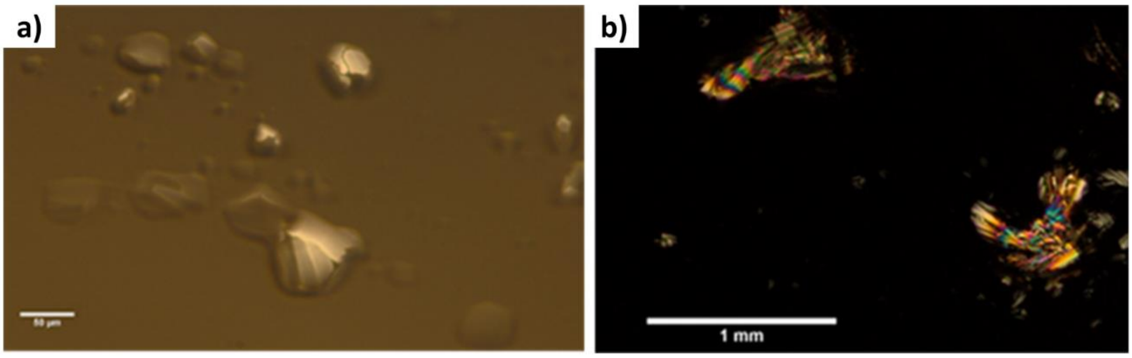

Figure 2.34 (a) Polarised optical microscopy of **59** at 72.9 °C, scale bar 50 µm and (b) polarised optical microscopy at 62.7 °C.

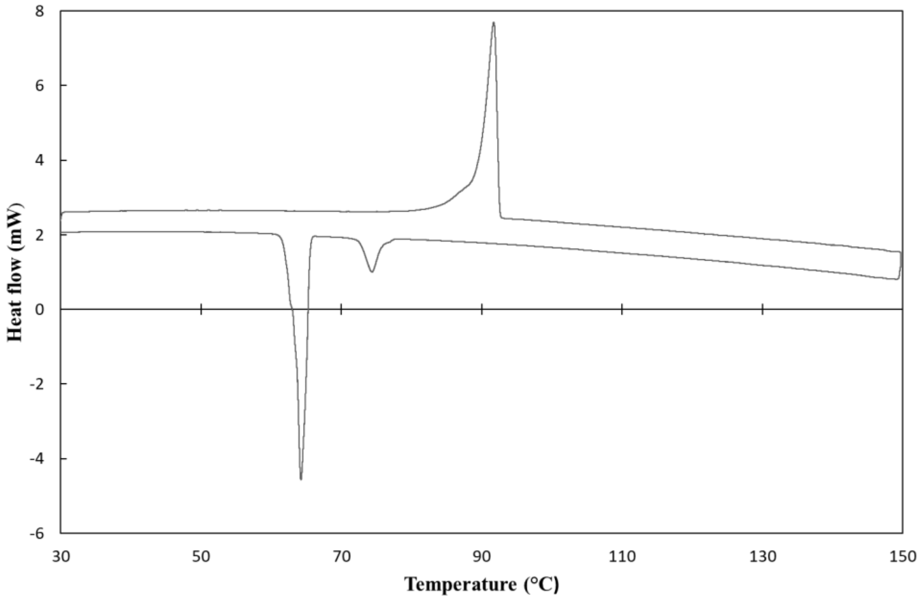

Figure 2.35 Second cycle DSC thermograph of **59** showing an endothermic transition at 81.6 °C and exothermic transitions at 71.5 and 60.6 °C.

investigations, it is standard practice to repeat the heating and cooling cycles multiple times and it is usual practice to report the second cycle.[44,137]

Furthermore, **58** was also subjected to DSC and POM analysis, with DSC revealing endothermic transition onsets at 59.3 °C, 75.1 °C and 95.5 °C, as seen in Figure 2.36. The transition enthalpies were calculated to be 9.4, 8.9 and 5.9 kJ mol^{-1} respectively. The first endothermic transition is thought to be a recrystallisation process in which the Cr1 low

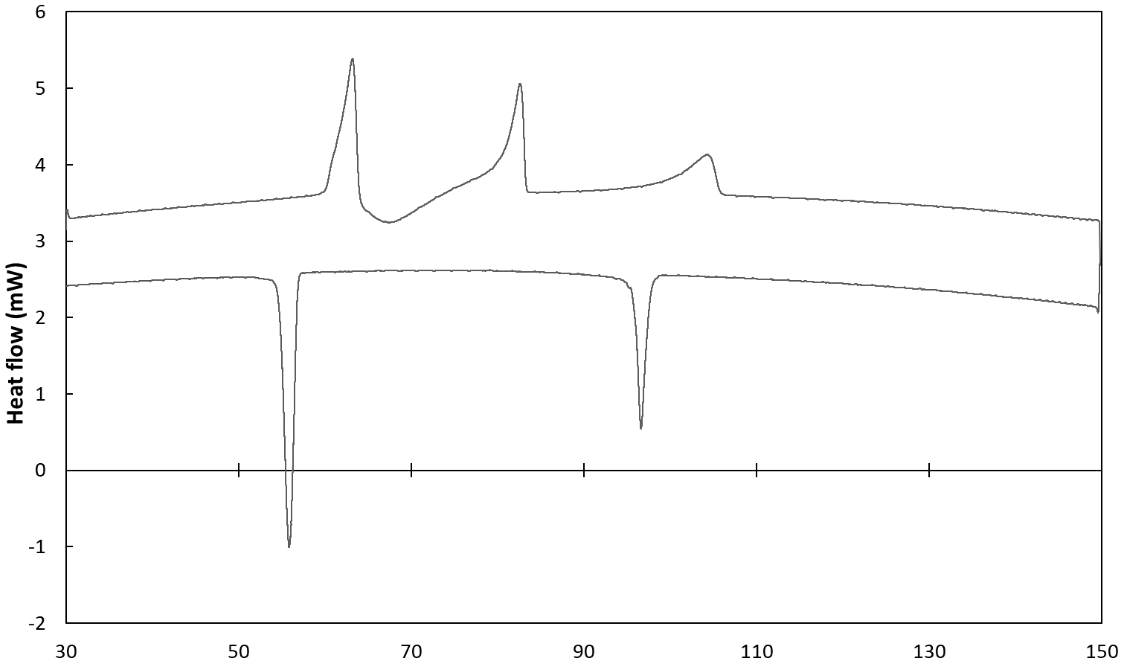

Figure 2.36 DSC thermograph of **58** showing endothermic transitions onset at 59.3, 75.1 and 95.5 °C and exothermic transitions at 98.6 and 57.2 °C

temperature crystalline phase is converted to a high-temperature crystalline phase. Figure 2.37 shows the effect of successive heating cycles in the range 30.0–74.0 °C, with the major endothermic peak centred at 63.0 °C diminishing, indicating eventual conversion to the high temperature crystalline phase without re-formation of the low temperature phase on cooling. Likewise, with **59**, optical microscopy of **58,** at temperatures corresponding to those of the transitions seen in the DSC thermographs, would suggest the presence of ordered phases, Figure 2.38. X-ray powder diffraction of this material after heating to 75 °C in air showed considerable changes in the positions and intensities of the major Bragg peaks compared to the diffraction pattern of a pristine sample. These results would suggest liquid crystal-like behaviour of **58** and **59**, however further experiments and more specialised equipment would be required to more accurately determine the liquid crystal type. The mesophase behaviour of the longer alkyl

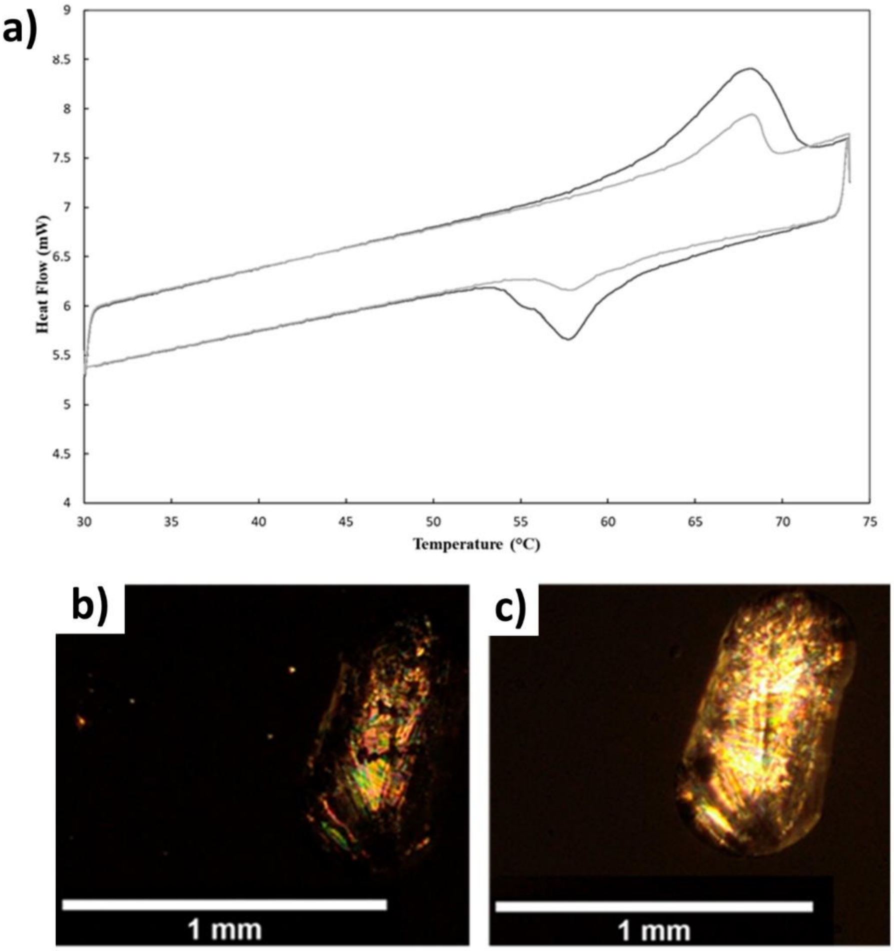

Figure 2.37 (a) DSC thermograph of compound **58** showing two sequential cycles 30–74 °C showing diminishing of the first phase transition on sequential heating and cooling cycles and polarised optical microscopy of **58** at 102.9 °C (b) and at 56 °C (c).

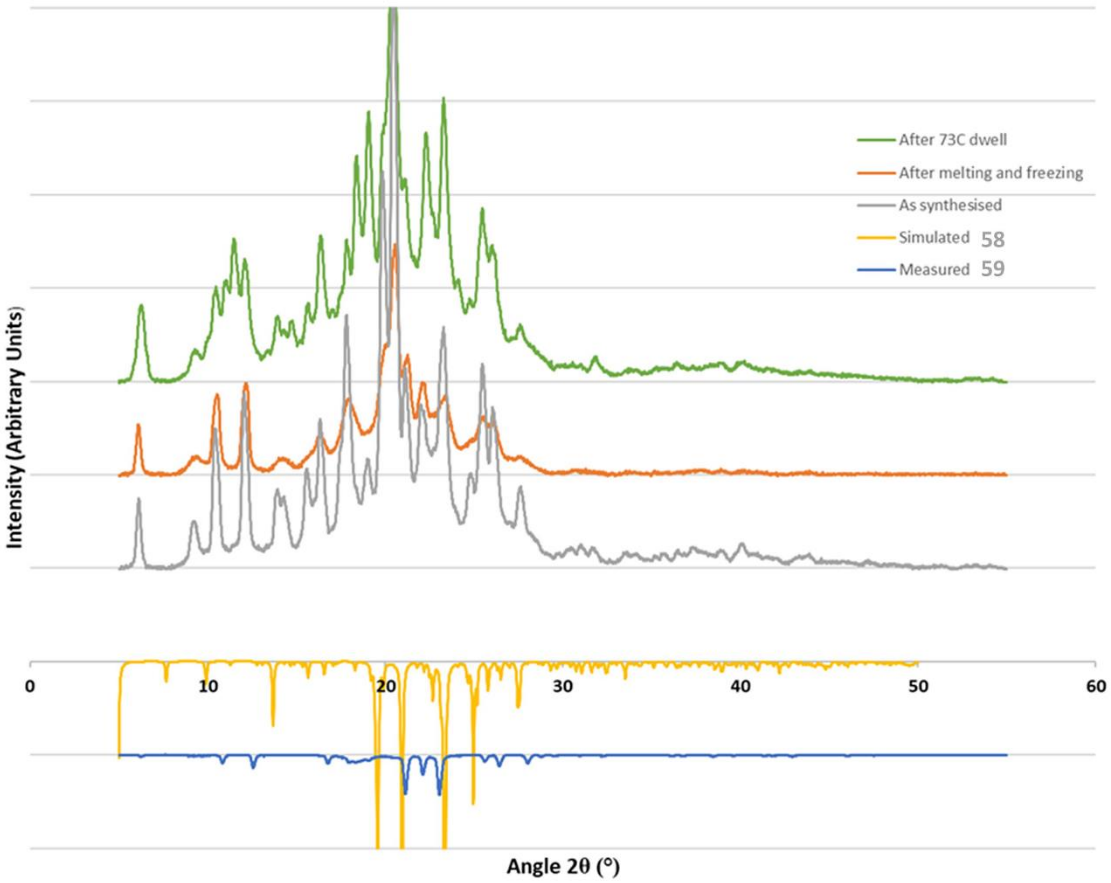

Figure 2.38. X-ray powder diffraction pattern for compound **58** (room temperature), showing the as-synthesised material consisting of multiple crystalline and polycrystalline phases (blue); the single, poorly-crystalline phase obtained by complete melting and freezing of the material (red); the mixture of at least two phases obtained by heating above the first phase transition temperature (green), and comparison with the simulated pattern for compound **58** (orange) and the measured pattern for compound **59** (purple).

chain derivatives **58** and **59**, but not observed for the shorter chain derivative **60** is not unexpected as it has been previously shown that the alkyl chains impart a soft region to facilitate phase separation thus leading to the formation of a mesophase.[135]

Following on from these structural, thermal and gelation studies, we decided to look at the mechanical properties of some of the **BTA** derivatives discussed to gain more insight into the strength of these materials. The materials chosen for this study are the strongest gelators, **61** and **63** and the AFM measurements of these materials will be discussed in the next section.

2.7 Preliminary Atomic force measurements

To further investigate the mechanical properties of some of the **BTA** derivatives, some preliminary atomic force microscopy measurements were carried out with the help of Dr Chiara Rotella and Prof. John Boland (School of Chemistry, Trinity College Dublin). AFM, unlike electron microscopy, is non-invasive and offers an accurate measurement of the height of the objects under study and can be used to calculate the Young's Modulus of the material under observation.[138,139] The Young's Modulus of a material, also known as the elastic modulus, is the ratio of stress to strain.[140] The Hertz model is one of the most common models used to calculate the Young's Modulus from the AFM force curves and is used in this case.[139] AFM operates by scanning a sharp tip at the end of a cantilever in the *X* and *Y* directions over a sample mounted on a piezo crystal. Any changes in the height (*Z* direction) due to the tip interacting with sample under investigation are usually optically detected, giving a topographical image of the substrate.[141] A schematic of the process for force measurements using AFM is shown in Figure 2.39.[142] There have been a couple of literature reports of AFM studies on **BTA** derivatives, with it being reported that the fragile **BTA** structures can be easily disrupted by the mechanical interactions with the AFM tip.[120] However, using AFM to determine the mechanical strenght of **BTA**-based systems seems to be currently relatively unexplored/

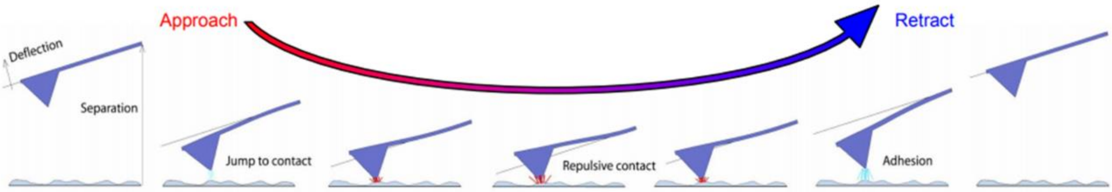

Figure 2.39 Schematic diagram of the vertical tip movement during the approach and retract parts of a force measurement**.** Image reproduced from reference 142.

The derivatives chosen for this study were the carboxylic acid derivatives **61** and **63**. These derivatives with the most and least robust gel fibres respectively and the aim was to measure the strength of the individual fibres and see if there was a difference between the two derivatives. To image the materials using AFM, a 5 μL sample of a dilute gel sample **61** was dropcast onto a silica wafer and dried under a stream of nitrogen. In the case of **63**, a dilute gel sample was used for the AFM experiment. SEM images of the samples used for the AFM studies are shown in Figure 2.41 and show the needle-like fibres of **61** and the mix of gel-like and crystalline-like fibres (right) in the sample of **63**. Shown in Figure 2.40 is the sample preparation method used for the AFM experiments.

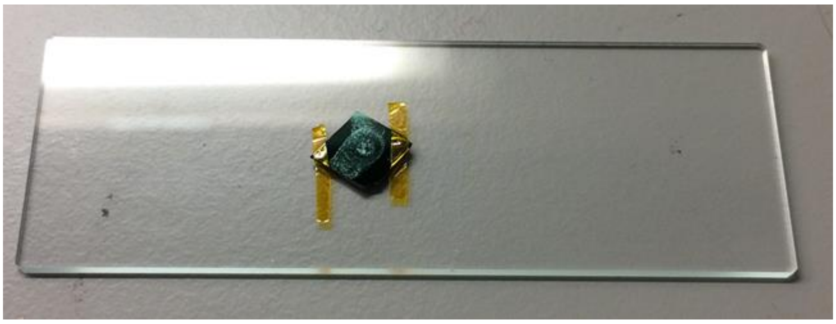

Figure 2.40 Sample preparation in which the sample is dropcasted onto a silica wafer which is then placed on a glass slide.

AFM is also used for imaging and for obtaining height profiles of the samples under observation, as can be seen in Figure 2.41. The sizes of the fibres of both **61** and **63** shown in Figure 2.41. are quite varied, with some of the **61** fibres shown to be quite thick, 500 nm-1 µm in size, while those of **63** are much smaller at approximately 200 nm. The images and height profiles were obtained using tapping mode, while the force curves were obtained using contact mode.

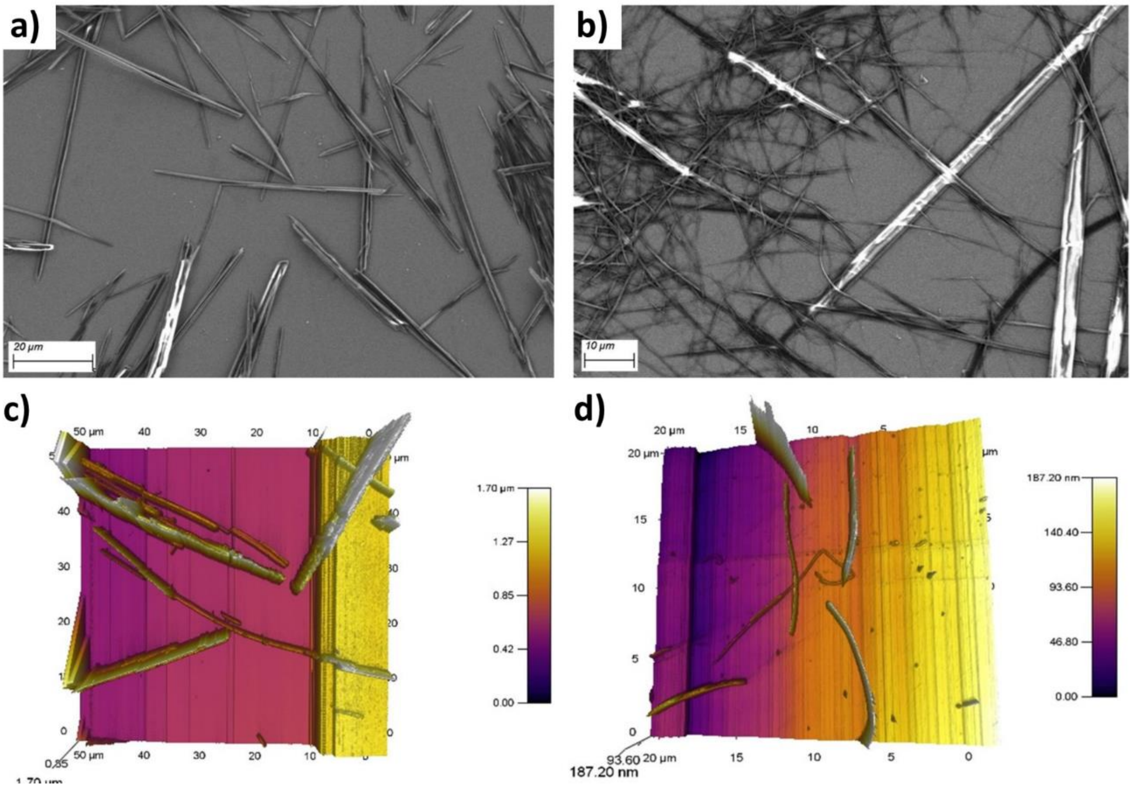

Figure 2.41 (a) SEM of the **61** samples used in the AFM studies, scale bar 20 µm; (b) **63**, gel sample, scale bar 10 µm; (c) AFM image of **61** showing some individual fibres of varying sizes and (d) **63** showing fibres of varying sizes.

The force curves obtained for **61** are shown in Figure 2.42, along with the calculated elastic moduli values for various points along the fibres. The Young's moduli values obtained for **61** would suggest that the fibres are quite strong, with the average value being approximately 1.6 GPa, which is stronger than cartilage (0.16 – 0.6) but weaker than tibial bone fibres or glass.[141] The slope of the curve as the tip approaches the sample is an indication of the stiffness of the sample, with the samples of greater stiffness having a greater angular coefficient of the slope.

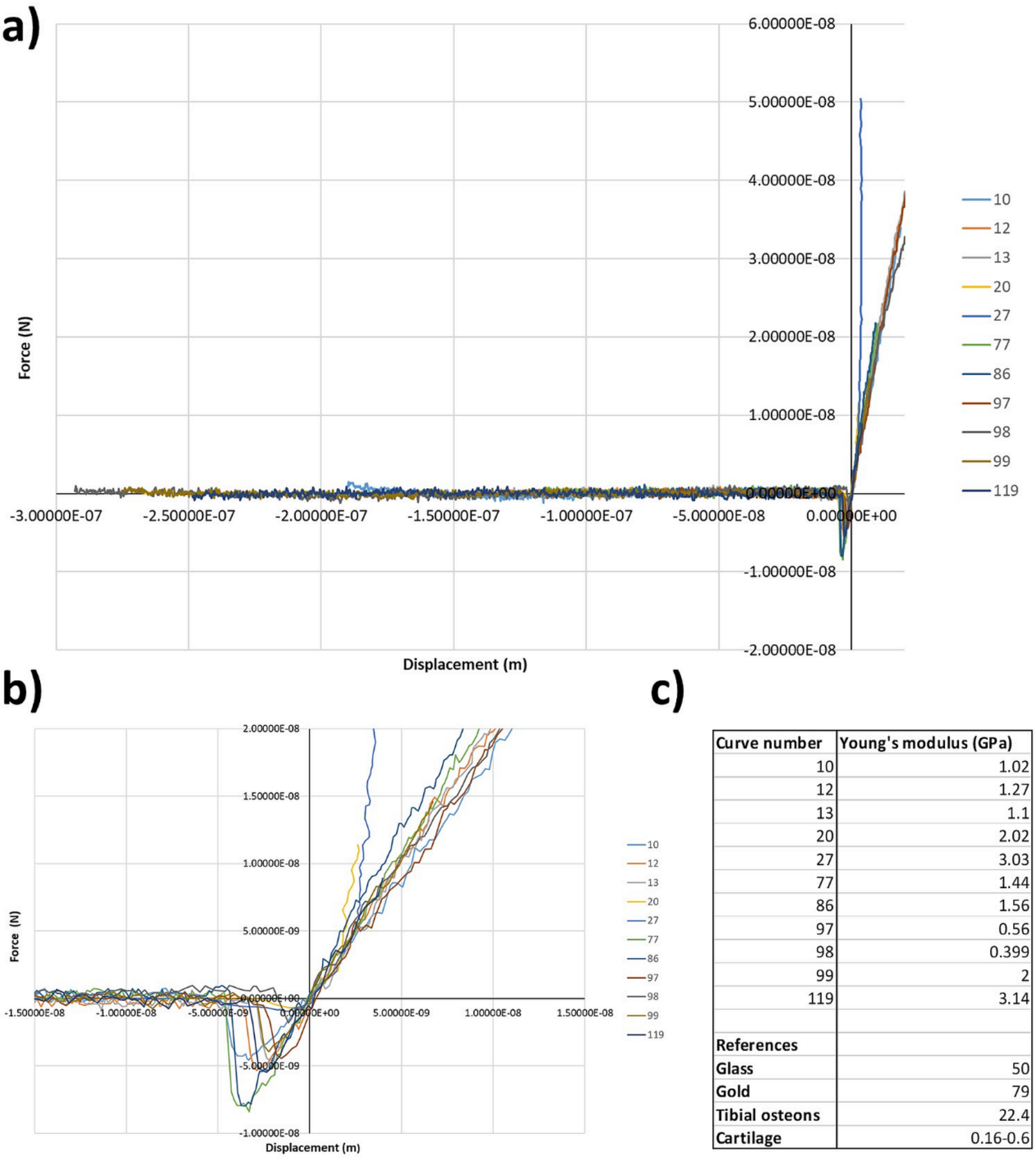

Curve number	Young's modulus (GPa)
10	1.02
12	1.27
13	1.1
20	2.02
27	3.03
77	1.44
86	1.56
97	0.56
98	0.399
99	2
119	3.14
References	
Glass	50
Gold	79
Tibial osteons	22.4
Cartilage	0.16-0.6

Figure 2.42 (a) Force curves of **61**; (b) force curve area of interest; (c) table containing the Young's Moduli values of the various curves and some reference values.[141]

The force curves and calculated values for the Young's Modulus at various points along the fibres of **63** are shown in Figure 2.43. The average value of the Young's Modulus is 1.2 GPa, slightly less than that of **61**. The behaviour of curve number 35 deviates from the behaviour of the others, this is due to the fibres sticking to the tip.

To conclude, the gel fibres of both **61**and **63** appear to be quite strong. Further work could be to investigate the differences in elastic moduli between the crystalline ester derivatives and the gel fibres of the carboxylic acid derivatives.

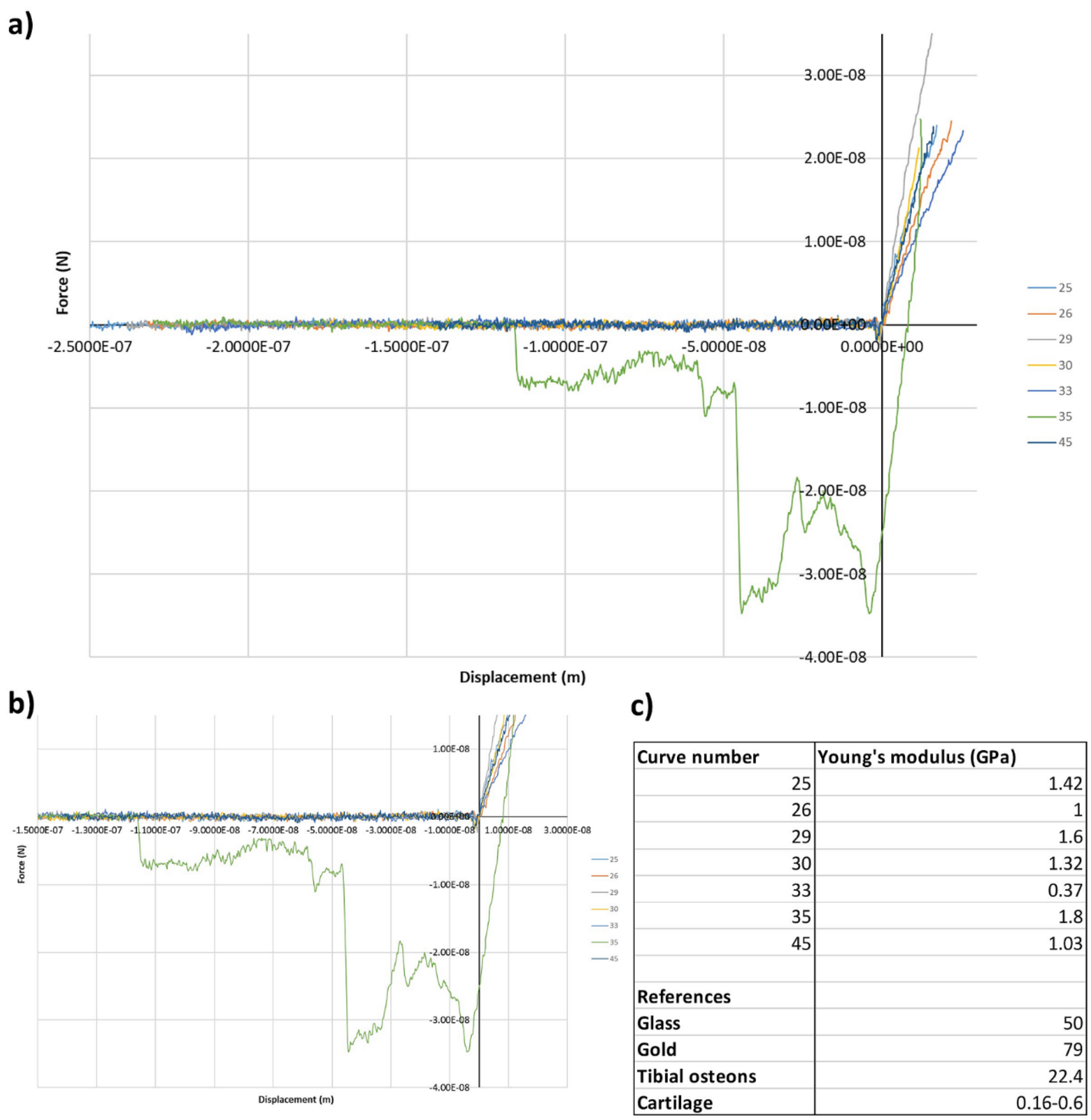

Curve number	Young's modulus (GPa)
25	1.42
26	1
29	1.6
30	1.32
33	0.37
35	1.8
45	1.03
References	
Glass	50
Gold	79
Tibial osteons	22.4
Cartilage	0.16-0.6

Figure 2.43 (a) Force curves of **63**; (b) force curve area of interest; (c) table containing the Young's Moduli values at various points along the fibres and some reference values.[141]

2.8 Conclusions and future perspectives

In this chapter, six **BTA** derivatives were synthesised, characterised and their self-assembly behaviour was assessed and compared to both the other derivatives and to other similar derivatives reported in the literature. It was deduced that very minor structural changes have a great influence on the structural and self-assembly properties of the derivatives.

The shorter chain derivatives tended more towards crystallisation and this tendency decreased as the alkyl chains lengthened, with it not being possible to obtain single crystals of the longest chain, carboxylic acid derivative **61**. Slight variations in the length of alkyl chain length greatly influence the structural features of the **BTA** derivatives, for example, in the case of the carboxylic acid derivatives, when n = 3 crystallisation dominates, whereas gelation occurs exclusively at n = 5, while n = 4 resulted in a mixture, depending on the conditions.

The ester derivative **59** displayed the typical triple helical-like arrangement of **BTA** compounds, while its carboxylic acid counterpart, **62**, did not. This is due to the carboxylic acid groups competing with the amide groups for hydrogen bonds, thus preventing the amide-amide hydrogen bonds necessary for the triple-helical arrangement. The importance of π-π interactions in these types of molecules and helical arrangements was shown recently by Anna Aletti, see appendix 8.7 for structure. In this case, the were no amides attached to the central core, but the extended structure still displayed a columnar type structure due to the π-π interactions. Thermal studies revealed the ester derivatives, **58** and **59**, to have mesophases, indicative of potential liquid crystal behaviour, however, the carboxylic acids derivatives did not have this behaviour. This is presumed to be due to the structural arrangement of the ester derivatives.

The carboxylic acid derivatives, **61** and **63**, were found to gelate under a variety of conditions, with the length of alkyl chain having an influence on the robustness of the material formed. The best gelation conditions for these derivatives were found to be in 2:1 H_2O/THF mixture, with gelation behaviour also observed in acid/base conditions. The longer alkyl chain derivative **61** formed a more robust gel than the shorter **63**, with the rheological studies confirming its gel-like behaviour and revealing it to be capable of returning to its original strength after shearing. Preliminary AFM measurements on the gel fibres showed the materials to be quite strong, however, further studies would be required to gain a better understanding of this strength.

Gas adsorption studies were carried out on the carboxylic acid derivatives **62** and **63** due to indications of pores in the crystal structures, however, both materials collapsed upon evacuation and lost their porous nature. Attempts were also made to obtain metal complexes of these derivatives, but these proved fruitless. Permanent porosity and the interaction of **BTA** compounds with metals will be discussed in Chapter 3.

‘The future is the home of our deepest fears and our wildest dreams.’

Grey’s Anatomy

3. Coordination chemistry of flexible benzene-1,3,5-tricarboxamide derived carboxylates; notable structural resilience and vaguely familiar packing motif

3.1 Introduction

As mentioned previously, the **BTA** motif is very useful for studying the correlation between structural features and the bulk properties of the resulting soft materials due to the ease of functionalising the **BTA** arms.[2,1,40,74] As such, **BTA** derivatives have been involved in a variety of applications, ranging from liquid crystalline displays and various biomedical applications to catalysis, as was summarised in Chapter 1.[74,76,79,143] In recent years, **BTA** derivatives have been used as ligands in coordination polymers, [17,102] with these derivatives made up of either rigid or amino acid based side chains. Relatively underexplored, however, is the use of both large bridging distances between the metal binding sites and inherent side-chain flexibility. In such systems, it would be expected that there would be a complex interplay of structure direction between the metal binding sites and the aggregation-prone **BTA** core, with sufficient spatial separation of the two key elements to allow for an extended structure dictated by two distinct synthons. Introducing some flexibility to the frameworks through the use of flexible ligands offers the potential to obtain some novel crystalline materials.[144]

This chapter will first discuss the synthesis and characterisation of two **BTA** derivatives, namely benzene-1,3,5-tricarboxamide tris phenylacetic acid **64** and the analogous trimethyl benzene-1,3,5-tricarboxamide tris acetate, **65**, as depicted in Figure 3.1. These two compounds have similar degrees of flexibility but have substantially different bridging distances and the presence of three additional aromatic rings for intermolecular interactions in **64**. The syntheses of these ligands, involving two to three steps, the reaction of the ligands with Cd(II) and the structural and physical properties of the resulting porous or non-porous constructs will be

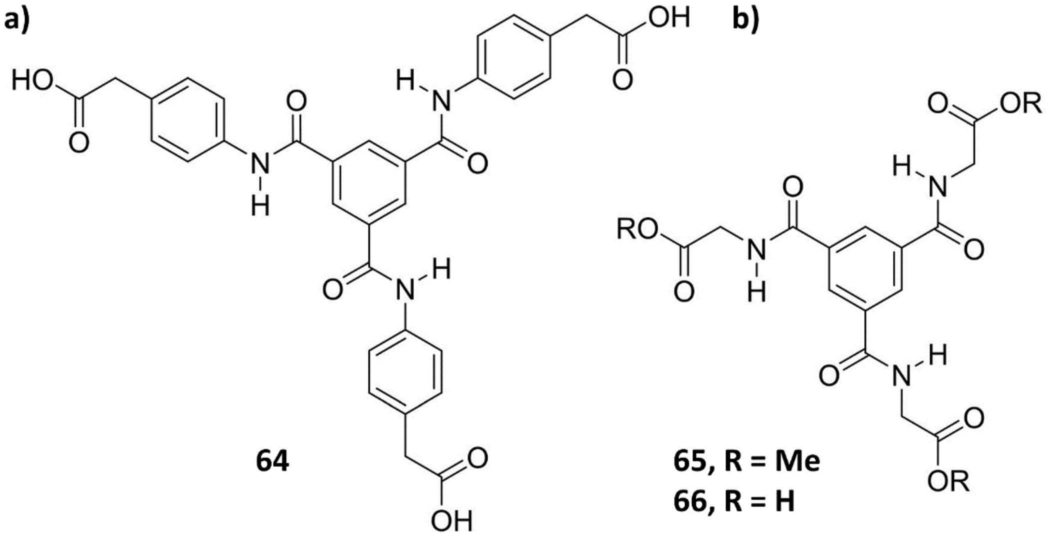

Figure 3.1 Structures discussed in the first part of this chapter, (a) **64** and (b) **65, 66**, where R = CH_3, H.

discussed in this chapter. Following this, the synthesis and self-assembly behaviour of amino acid extended derivatives of **64** will be discussed.

3.1.1 Design rationale

The compounds discussed in this chapter are ester and carboxylic acid derivatives with either an alkyl or aromatic spacer. The inspiration for this study came from previous studies on structurally similar compounds, for example the report on the reaction of **65** with Zn(II), Mn(II), Ni(II) and Co(II) resulting in the formation of 3D compact networks, though no adsorption studies were carried out on these materials.[145] Porous materials derived from amino acid based **BTA**s have also been reported, in which a tyrosine **BTA** analogue was found to adsorb N_2,[146] thus we decided to investigate the potential porous properties of a **BTA** derivatised with the simplest of amino acids, glycine, with metals other than that reported by Pan *et al.*[145] Many reports have been made on the structural and porous properties of an analogue of **64**,[83,89,102,146,147] **41**, shown in Figure 3.2, thus it was decided to slightly modify this structure in the hope of generating some structurally interesting and potentially porous materials.

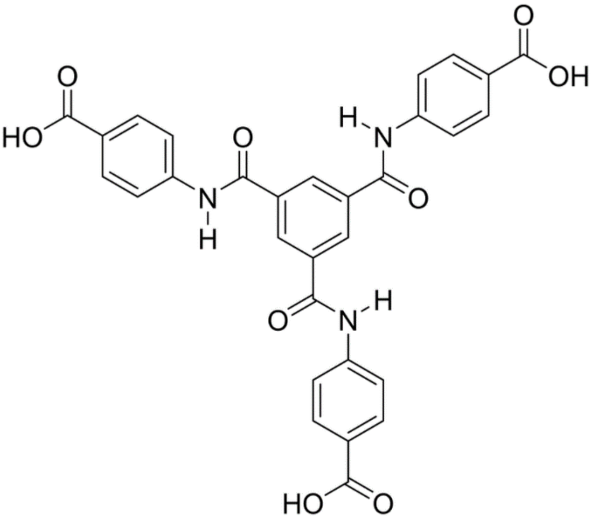

Figure 3.2 N, N', N''-bis-(4-carboxylate) trimesicamide, **41**, a structurally similar analogue to **64.**

In order to study the competitive influences of metal binding and the core hydrogen bonding on the extended frameworks containing **64** and **65**, Cd(II) was chosen as an appropriate metal ion for this study. Cd(II) has a good affinity for carboxylate donors in 6 to 8-coordinate bonding modes yet has no strong energetic preference for particular coordination geometries. These tendencies increase the likelihood of forming robust coordination frameworks where influences besides coordination geometry are likely to have a significant impact.

3.2 Synthesis and characterisation

3.2.1 Synthesis and characterisation of compounds 64 and 65

The syntheses of **64** and **65** were achieved using standard procedures for the symmetric tri-substitution of benzene-1,3,5-tricarbonyl trichloride, using methyl (4-aminophenyl) acetate and glycine methyl ester hydrochloride, respectively, Scheme 3.1.[14,148] Firstly, the methyl (4-aminophenyl) acetate was synthesised by stirring its corresponding methyl(aminophenyl) acetic acid derivative in MeOH and $SOCl_2$ at room temperature, followed by vacuum distillation to remove the MeOH and $SOCl_2$ revealing the ester as a yellow/orange solid in excellent yield (98%). The glycine methyl ester hydrochloride used was commercially obtained. **69** and **65**

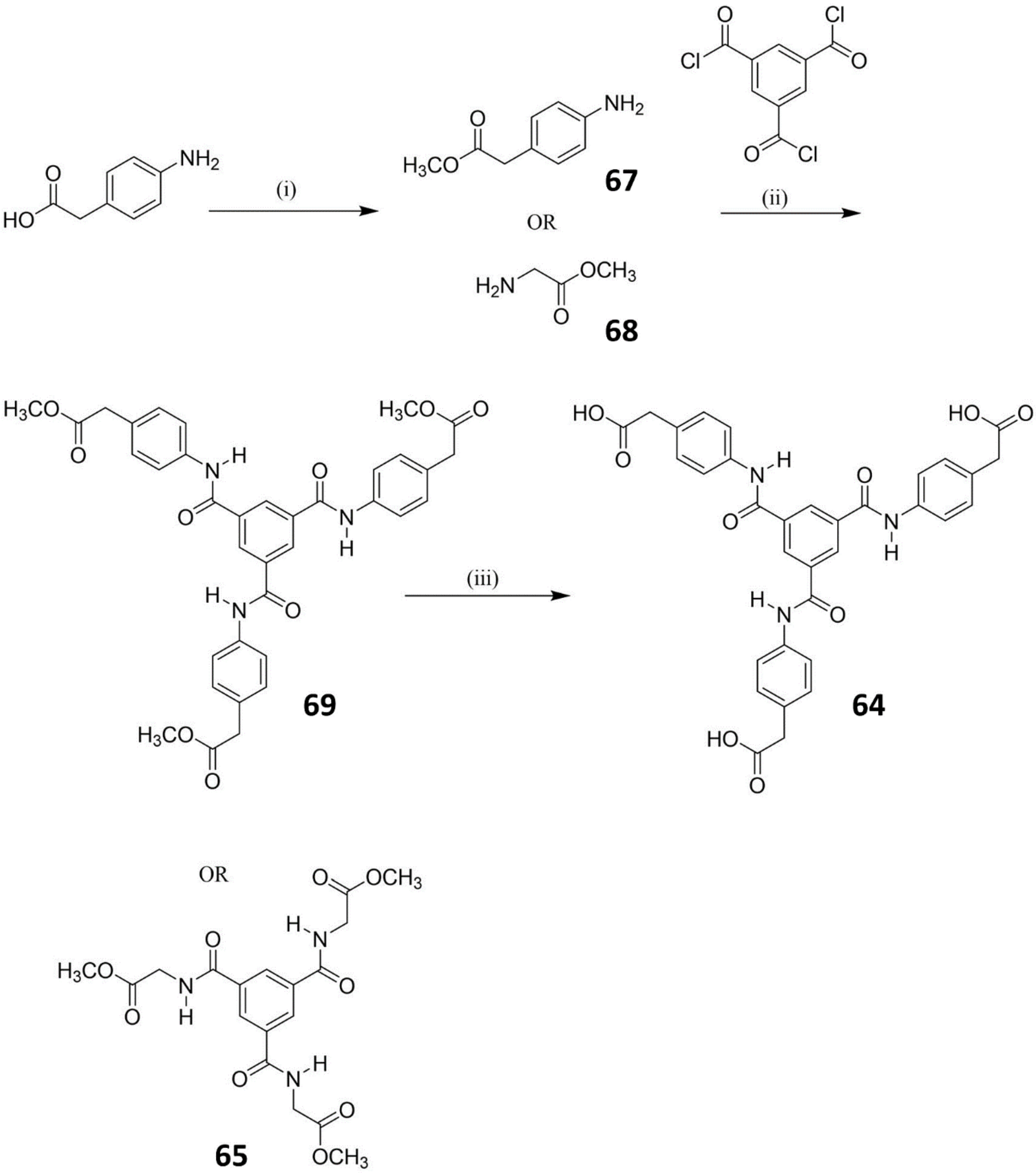

Scheme 3.1 Synthetic scheme for **69**, **65** and **64**, where (i) rt, $SOCl_2$, MeOH, 12 h, (ii) rt, DCM, Et_3N, 24 h and (iii) rt, NaOH, MeOH, 6 h.

were obtained by stirring the relevant amine in dry DCM, followed by addition of Et_3N and benzene-1,3,5-tricarbonyl to the mixture and left to stir at room temperature under an inert atmosphere for 24 h. Following this, the reaction mixture was washed with aqueous $NaHCO_3$ three times, then the organic layer was isolated and evaporated under reduced pressure to reveal white/yellow solids in 98 % and 51 % yields respectively. **69** required further purification in the form of stirring in a mixture of aqueous potassium hydroxide (KOH) and DCM, followed by separation and evaporation of the organic layer to reveal the compound as a pale yellow solid. **69** was converted to the corresponding carboxylic acid, **64**, by base hydrolysis, using aqueous NaOH and MeOH, followed by acidification to precipitate the neutral compound in 83 % yield. Each compound was fully characterised by ^1H and $^{13}C\{^1H\}$ NMR spectroscopy, IR spectroscopy and mass spectrometry to name a few techniques, with the results of such reported in the experimental section. An example of the stacked ^1H NMR spectra of **69**, **64** and **65** is shown in Figure 3.3, showing the characteristic **BTA** aromatic proton resonance as a sharp singlet at approximately 8.6 ppm in all cases.[108] In the case of **65**, isolation of the carboxylic acid derivative following base hydrolysis proved difficult due to water solubility, thus the subsequent coordination chemistry was more convenient using the methyl ester **65** as a feedstock. This ester then underwent an *in situ* hydrolysis reaction prior to coordination, a method often employed in solvothermal synthesis.[115,149,150] Solvothermal *in situ* synthesis has

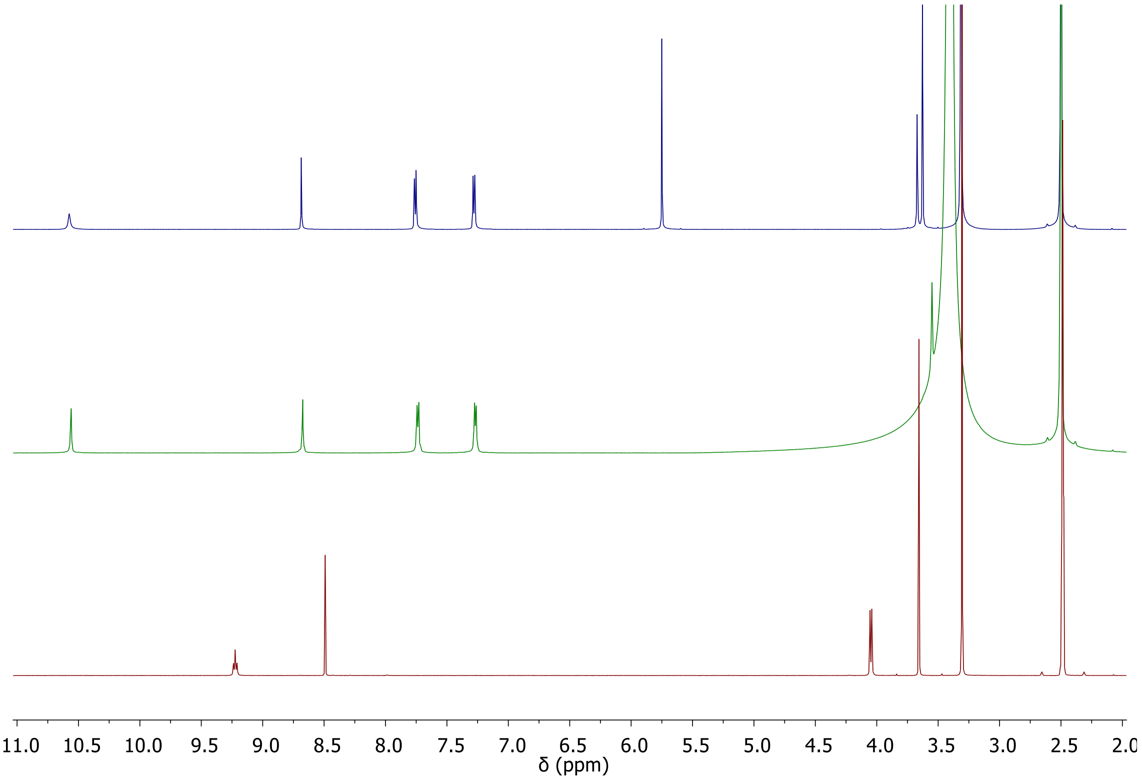

Figure 3.3 ^1H NMR of **69** (600 MHz, DMSO-d_6, top) **64** (600 MHz, DMSO-d_6, middle) and **65** (400 MHz, DMSO-d_6, bottom).

become a powerful approach in both crystal engineering of coordination complexes and organic synthesis.[149] *In situ* ligand synthesis is useful to prepare novel coordination complexes from metal ions and organic precursors that are not accessible from a direct reaction between the metal ion and ligand. Solvothermal reactions are carried out in sealed Teflon vials at high temperatures and pressures and is a valuable technique in preparing complexes with novel structures and properties, especially in growing crystals of complexes involving *in situ* ligand synthesis.[115,149] In this case, glass vials with Teflon seals in the lids were used and the reactions were carried out in a heat block. Single crystals of **65** were obtained from recrystallisation in water and will be discussed further in Section 3.4.1. Despite best efforts single crystals of quality suitable for diffraction, of both **64** and its ester precursor **69**, were not obtained, with further details of such found in the appendix.

3.2.2 Synthesis and characterisation of 64Cd and 65Cd

In the case of both coordination complexes, cadmium nitrate tetrahydrate (15 mg, 48 μmol) and the relevant ligand, **64** or **65** (10 mg), were dissolved in DMF/H_2O (1:1, 3 mL) in a sealed Teflon capped vial and heated to 100 °C in a heat block for 24 h. The resulting crystals were isolated by filtration and then characterised by X-ray powder diffraction, IR spectroscopy and elemental analysis. In both cases, the X-ray powder diffraction patterns were found to indicate phase purity, while the elemental analysis agreed with the expected values. These results are found in full in the experimental section.

3.3 Gelation attempts

Despite the propensity for symmetrical **BTA** derivatives to gelate, especially those with carboxylic acid termini,[14] there were no stable gels reliably formed from either **64** or its methyl ester precursor derivative, **69**, in a variety of different solvents and solvent mixtures. The poor gelation abilities of these derivatives most likely arises from their poor solubility in most common solvents. Also unsuccessful was the attempt to use the acid-base method, as mentioned in section 2.4 to gelate the carboxylic acid derivatives.[14] This resulted in the formation of precipitates rather than gel material. No gels were observed upon reaction of **64** with a variety of metals, unlike the reported metallogel behaviour of its structurally similar analogue in which **41** formed robust gels upon reaction with cadmium, copper, cobalt and zinc metal salts in water,[146] (Figure 3.2)This could be due to the poor solubility imparted by the aromatic linkers. The gelation properties of **65** were reported elsewhere, in which **65** was reported to not gelate ionic liquids or some organic solvents, while forming a partial gel in phosphate buffer,[92] thus further studies were not pursued in this thesis.[92,151] Instead we turned our attention to the structural studies of these derivatives, as will be discussed in the next section.

3.4 Structural studies

As was the case with in Chapter 2, the crystallography (single crystal experiments only, not X-ray powder diffraction) was carried out and the data solved and refined by Dr Chris Hawes (TCD, Keele University).

3.4.1 Structural study of 65·0.5H_2O

A single crystal of **65**, obtained from recrystallisation in water, was subjected to single crystal X-ray diffraction with the data obtained solved and the structural model refined in the monoclinic space group $P2_1/n$. The asymmetric unit was occupied by one complete molecule, along with two partial-occupancy H_2O sites (total occupancy 0.5) and is shown in Figure 3.4. There was minor disorder evident for one of the three methyl ester groups.

The **BTA** core, shown in Figure 3.4, exhibits approximate C_3 symmetry with each amide group assuming the typical *ca*.40° offset to the phenyl ring mean plane. This bonding arrangement leads to the common triple-helical hydrogen bonding of the adjacent molecules, which are aligned parallel to the *b* axis with three N-H···O hydrogen bonds between each unit. The interplanar distance between adjacent phenyl rings is 3.469(2) Å, which is half the length of the *b* unit cell edge. The adjacent phenyl rings are parallel and essentially co-axial, slipped by only 0.3 Å to one another. The methyl ester groups protrude from the helical stacks

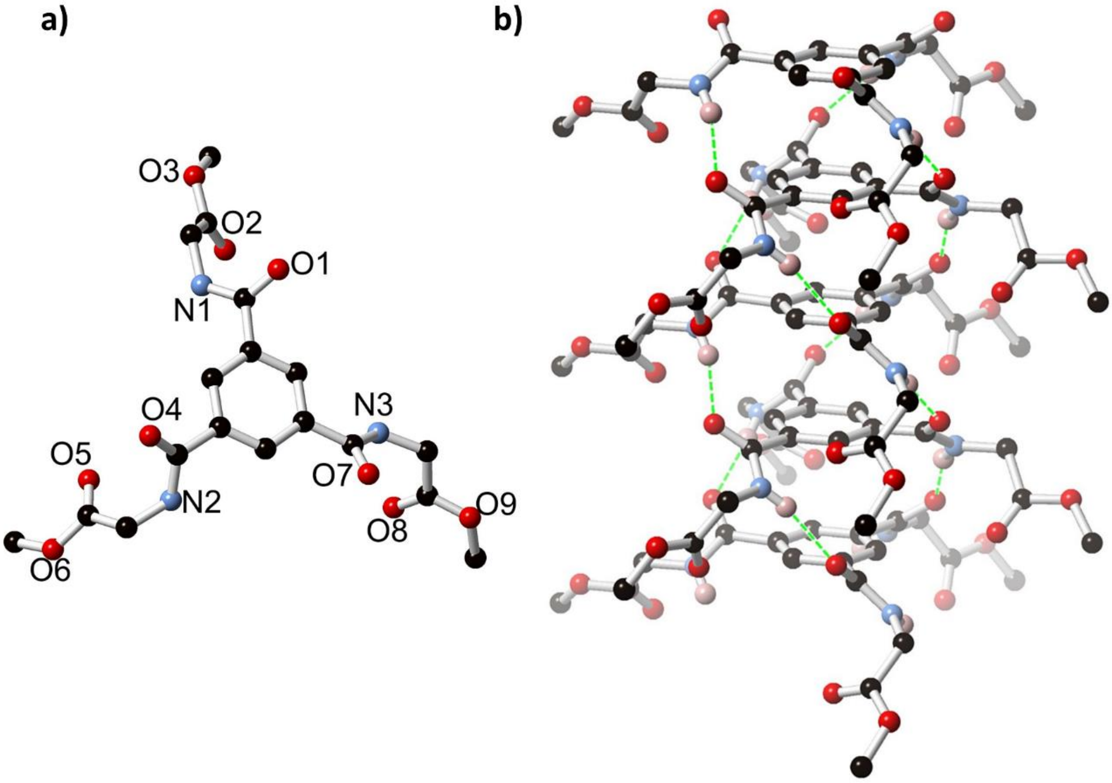

Figure 3.4 (a) Structure of **65** showing the molecular structure with heteroatom labelling scheme and (b) columnar stacking arrangement with triple-helical hydrogen bonding motif. Hydrogen bonds and ester disorder are omitted for clarity.

and were found to interdigitate between the adjacent columns, which align in a typical hexagonal rod packing motif. As mentioned in Chapter 2, X-ray powder diffraction is a useful method for both the characterisation of crystalline materials and for examining phase purity of a bulk sample.[124] Powder diffraction verified that the bulk sample contained a single phase and was phase pure, as evidenced by the matching patterns obtained from the measured and simulated experiments and is depicted in Figure 3.5. The structure of **65** confirms that the extended structure adopts the typical packing model of **BTA** compounds, similarly to **59**, when crystallised in the absence of any strongly competing hydrogen bonding or other intermolecular interactions. Yan and co-workers described the structure of the carboxylic acid derivative of **65,**[152] and showed it to form dimers that extend to sheets due to the hydrogen bonding interaction with H_2O molecules and did not form the helical stacks observed in the ester derivative, **65**. This difference in structural arrangement is due to the extra hydrogen bonding groups on the carboxylic acid compound interacting with neighbouring arms and highlights the effects small molecular changes and the addition of competing binding sites have on the overall structure. A similar effect was described in Chapter 2 for the middle length alkyl chain ester and carboxylic acid derivatives **59** and **62**.

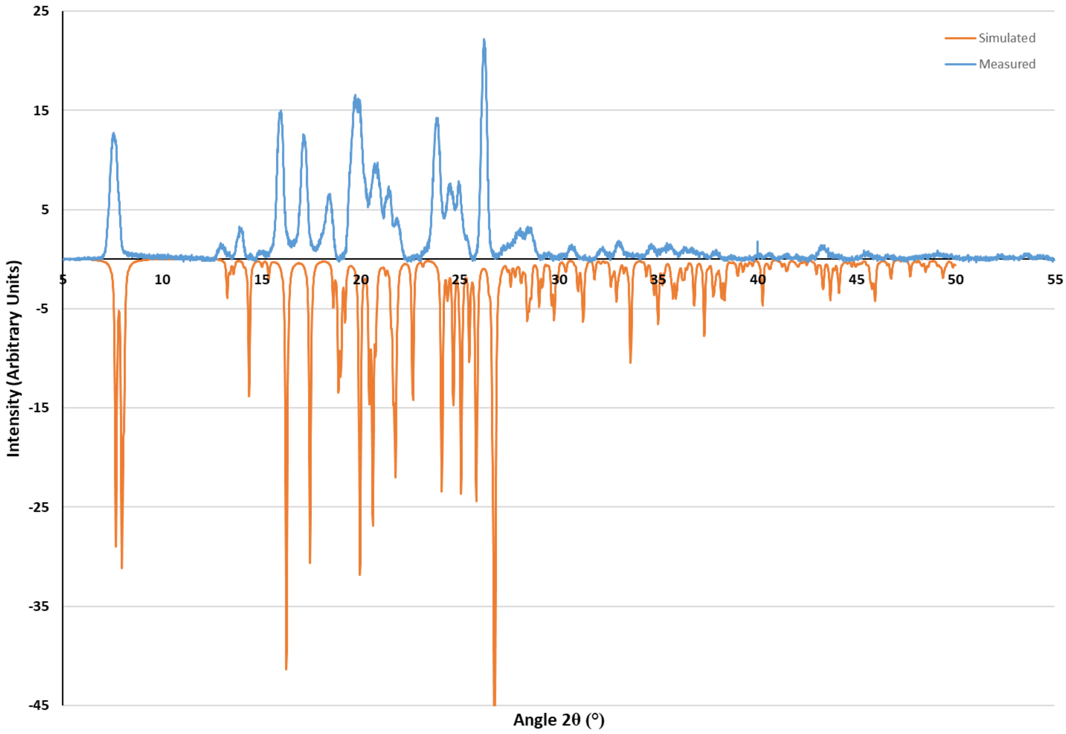

Figure 3.5 X-ray powder diffraction of **65** measured at room temperature (blue) compared to the simulated pattern from the single crystal data collected at 100 K (orange).

3.4.2 Structural study of [$Cd_3(64)_2(DMF)_2$]·$5H_2O$·2DMF

Single crystals of **64Cd** were grown in DMF/H_2O (1:1) using the solvothermal method described in 3.2.1 and 3.2.2. A single crystal of **64Cd** was analysed by single crystal X-ray diffraction at 100 K, with the data solved and the structural model refined in the triclinic space group *P*-1. The asymmetric unit contains three unique cadmium environments and two complete **64** species, with each of the carboxylates deprotonated. There was a small proportion of disorder present in the vicinity of cadmium sites Cd2 and Cd3, (further details in appendix). The coordination spheres of each of the three unique cadmium ions were filled by oxygen donors, either from **64** carboxylates or two unique DMF ligands, as depicted in Figure 3.6. The cadmium ion Cd1 adopts a 7-coordinate geometry, while Cd2 and Cd3 possess distorted octahedral 6-coordinate geometries. As is often the case for Cd-carboxylate systems, bridging coordination modes are widely adopted here; Cd1-Cd2 and Cd2-Cd3 are each bridged by three unique carboxylates, while Cd3-Cd1 are doubly bridged. A one-dimensional cadmium-carboxylate chain that extends parallel to the *a* axis results from this bridging.

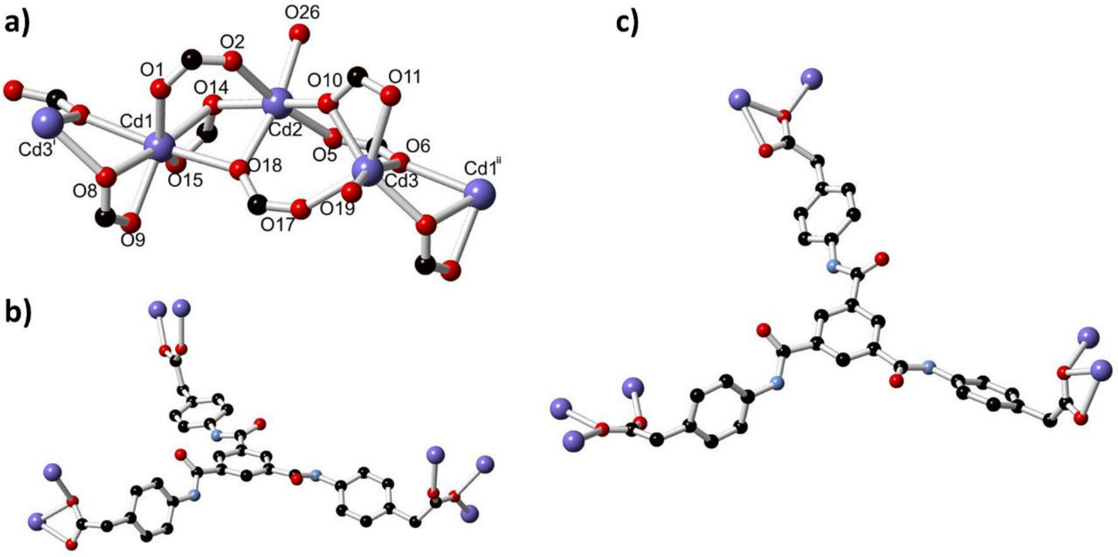

Figure 3.6 Connectivity and chemical environment of the three nodes in **64**; (a) Cadmium coordination geometry with heteroatom labelling scheme, where O26 corresponds to a coordinating DMF molecule; (b and c) Connectivity of the two crystallographically independent **64**molecules within the structure. Hydrogen atoms, framework disorder, lattice solvent molecules and selected atom labels are omitted for clarity.

The ligand species in the structure of **64Cd** adopts a splayed T-shaped conformation and the two crystallographically unique moieties alternate in a stack aligned parallel to the *a* axis and parallel to the cadmium-carboxylate chains. The two species exhibit similar conformations with the slight differences mainly manifested in variations in the orientation of the acetate fragments. The adjacent molecules align into slipped stacks, however, the traditional **BTA** hydrogen bonding mode is not observed between directly adjacent molecules; only three

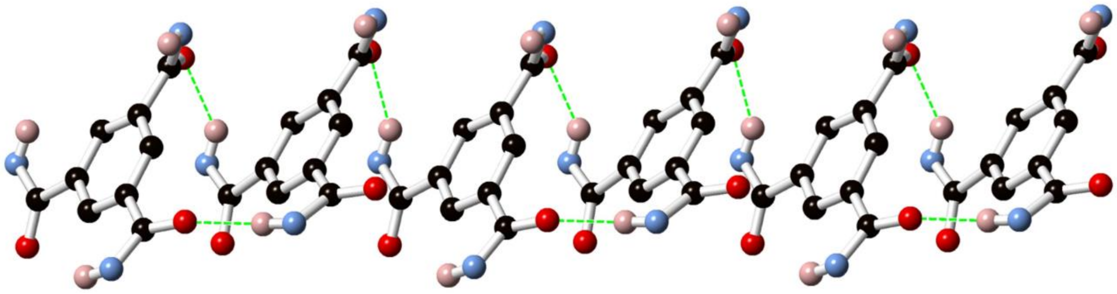

Figure 3.7 Hydrogen bonding interactions between alternating adjacent core units of **64Cd** molecules in the structure of complex **64Cd**, showing the slipped-stack packing arrangement.

of a possible six unique amide-amide hydrogen bonds are observed in each stack. The adjacent **BTA** ring planes are separated by *ca*. 3.2 Å in the direction of the plane normal vector, with the rings horizontally slipped by *ca*. 3.7 Å, thus differentiating this packing mode from the typical **BTA** helix, Figure 3.7. The remaining amide N-H groups that are not involved in amide-amide hydrogen bonding fulfil their bonding requirements by bonding to two lattice DMF molecules and a lattice water molecule.

The T-shaped conformation of the **64** molecules linking the one-dimensional cadmium carboxylate chains give rise to a corrugated double layer two-dimensional framework that is oriented parallel to the *ac* plane and shown in Figure 3.8. Two crystallographically independent, rectangular intra-layer solvent channels are present within each sheet, with maximum interatomic dimensions *ca.* 12.5 × 8 Å (omitting the solvent molecules). In total, 5 DMF (2 coordinating and 3 non-coordinating) sites were located in the crystallographic model, with a total occupancy of 4.2 DMF molecules per 3 cadmium ions, and three water sites with a total occupancy of 2.5 molecules per 3 cadmium ions. Further DMF sites are presumed to be present within the structure, associated with the 15 % disorder contribution of the two cadmium sites, however, this could not be sensibly modelled. Adjacent layers associate in the *b* direction through various π-π and C-H interactions, along with a defined hydrogen bonding interaction through lattice water molecules between cadmium-carboxylate chains of adjacent sheets. While all solvent molecules were included in the final refinement, removal of the lattice solvent from the model gave an estimate of 25 % solvent accessible volume. This solvent was mostly

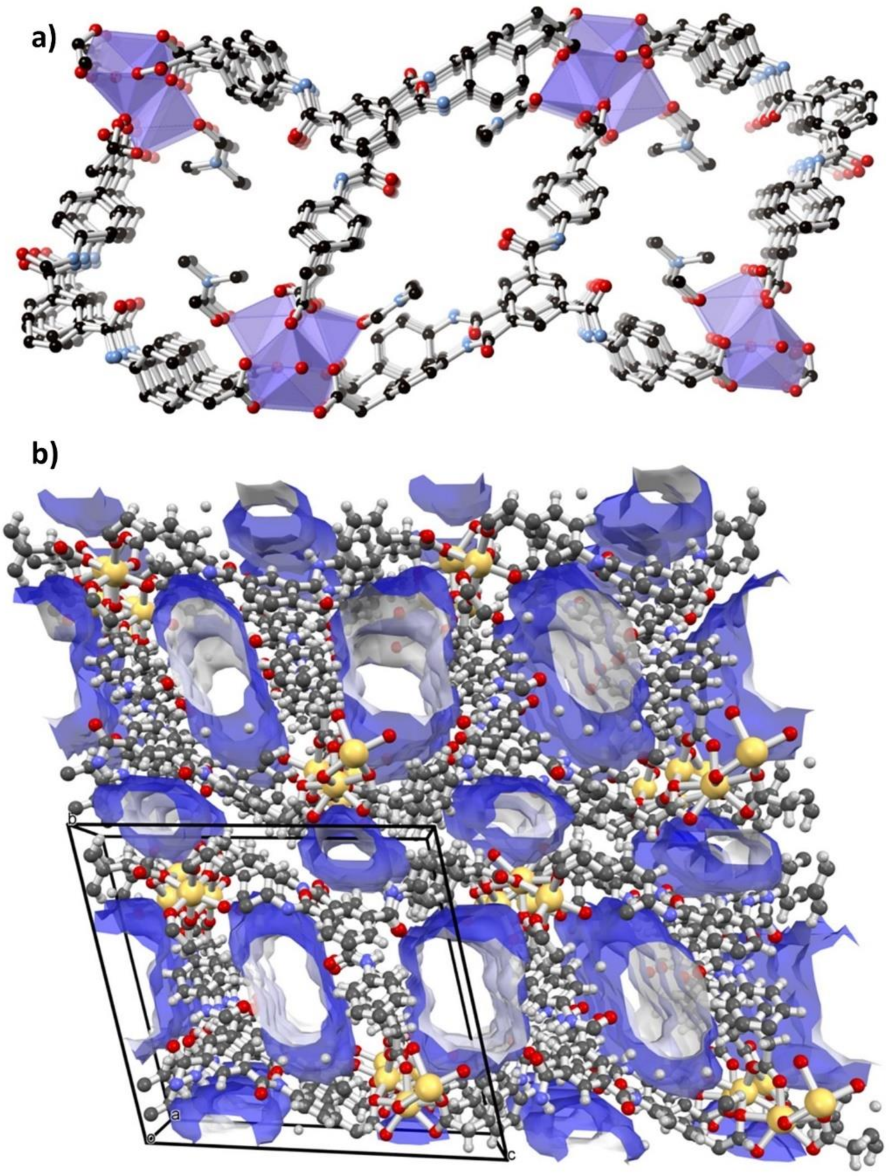

Figure 3.8 (a) structure of an individual network of **64Cd** showing the 1-dimensional intralayer solvent channels (non-coordinating solvent molecules omitted); (b) the 3-dimensional structure of **64Cd** showing the intralayer void volume and smaller interlayer pores.

localised in the intralayer channels with a small contribution from the narrow channels between the adjacent layers. Elemental analysis of a sample of **64Cd** revealed the presence of both H_2O and DMF molecules. The sample used for elemental analysis was freshly prepared and was not dried *in vacuo* before analysis. This was done in order to probe the presence of solvent molecules in the channels. Further details of the elemental analysis can be found in the experimental section. The presence of these solvent accessible channels probed further studies which will be discussed in 3.6.

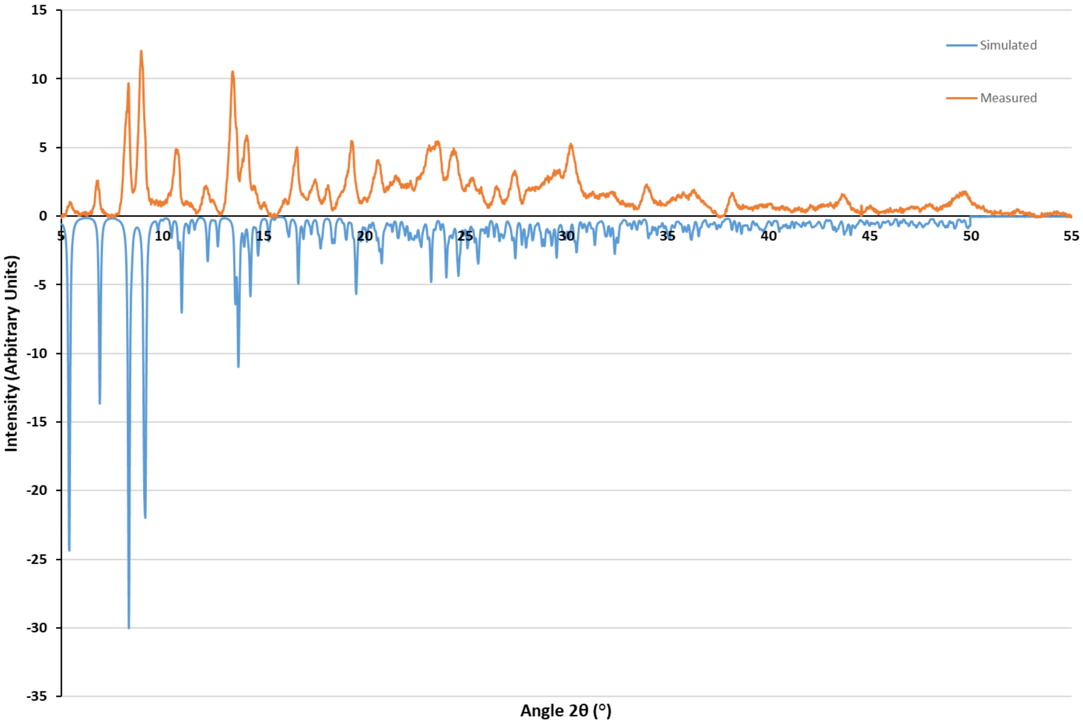

Figure 3.9 Measured (orange) and simulated (blue) X-ray powder diffraction pattern for **64Cd.**

The phase purity of a bulk sample of **64Cd** was confirmed using X-ray powder diffraction as shown in Figure 3.9, where the peaks of the measured pattern coincide with those of the simulated pattern derived from the single crystal data.

In a report by Zhao *et al.*, the coordination polymers formed upon the reaction of the analogue of **64**, **41**, with a variety of metals was discussed.[102] The authors reported that the zinc polymer had a layer type structure, while the coordination polymer generated from the reaction of the ligand with cobalt chloride displayed a doubly interpenetrated three-dimensional network. The reaction of the ligand with cadmium nitrate and cobalt nitrate resulted in isomorphous structures where a grid layered architecture in which the secondary building unit was a Cd3 cluster was observed. This study demonstrates the influence of the various metals on the structure of the resulting coordination polymers and also highlights the structural effects of incorporating an extra CH_2 group into **41**. As mentioned previously, one of the aims of this chapter was to investigate the effect of bridging distances and the presence of aromatic groups on two **BTA** derivatives with similar flexibility, thus the structure of coordination compound formed from the derivative without aromatic side arms will be discussed in the next section.

3.4.3 Structural study of $[Cd_3(65)_2(DMF)(H_2O)_3]\cdot 5(H_2O)$

A crystal of **65Cd** was subjected to single crystal X-ray diffraction, with the data solved and the structural model refined in the monoclinic space group $P2_1/c$. The asymmetric unit of **65Cd**, shown in Figure 3.10, contains three unique cadmium environments and two unique ligands within the asymmetric unit, and confirms that the *in situ* hydrolysis of the ester groups took place. The six independent carboxylate groups all undergo coordination to the cadmium ions, with the cadmium coordination spheres completed by one coordinating amide oxygen atom (O16), three unique aqua ligands and one DMF ligand. Each cadmium ion assumes a unique coordination number and geometry, with Cd1, Cd2 and Cd3 adopting 6-, 7- and 8-coordination geometries respectively. A trinuclear cluster mode best describes the metal coordination environment, where the metal centres are linked by four bridging carboxylate groups, as seen in Figure 3.10. Three of the bridging carboxylates adopt a μ_2-κO,O′:κO binding mode, with the remaining bridging carboxylate engaged in a triply bridging μ_3-κO:κO:κO′ coordination mode. The non-bridging carboxylates adopt purely chelating coordination modes. Around the periphery of the trinuclear cluster, numerous O- H···O hydrogen bonds (from the aqua ligands) and N-H···O hydrogen bonds from adjacent amide groups serve as further supports for the cluster geometry.

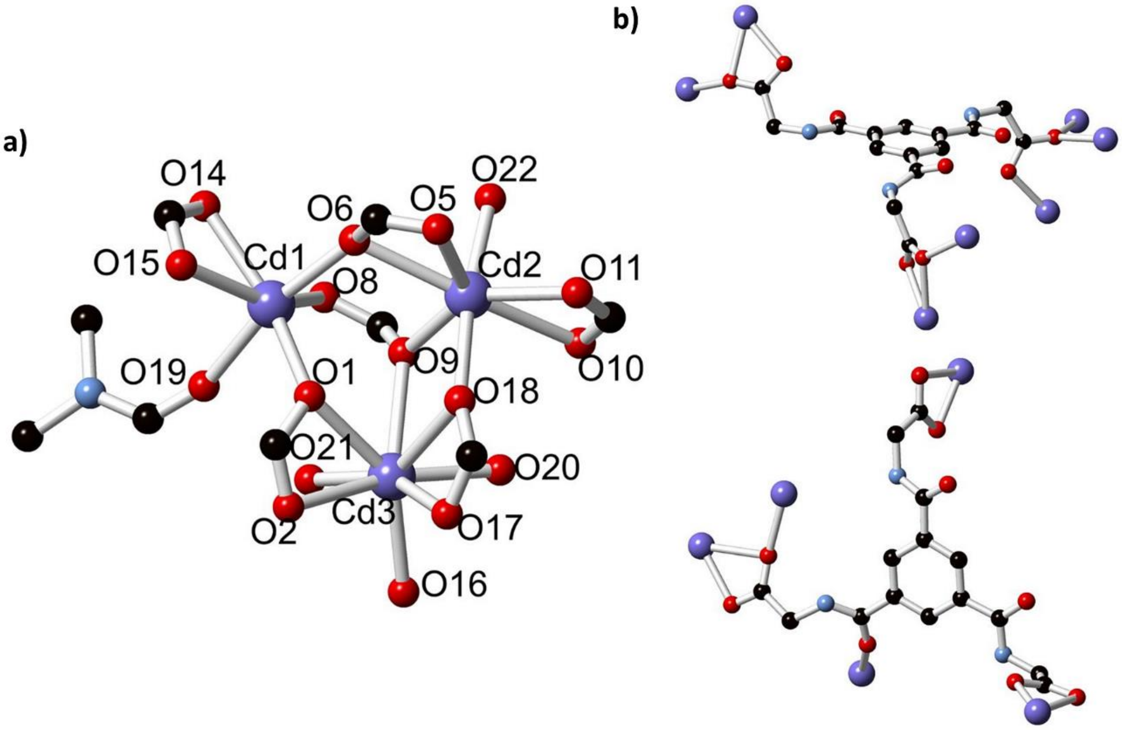

Figure 3.10 (a) the coordination sphere of the trinuclear cadmium node, with atom labelling scheme; (b) connectivity of the two unique **65** groups. Hydrogen atoms and atom labels are omitted for clarity.

The extended structure of **65Cd** is a densely connected three-dimensional coordination polymer. The connectivity of this polymer is quite complex and cannot be easily related to a known net; as seen in Figure 3.11. The complexity of this extended polymer is largely as a result of the coordination from the amide oxygen of one of the two unique ligand species, giving different connectivity to the two ligand nodes. Disregarding this interaction does not restore symmetry between the two nodes and fails to simplify the network description.

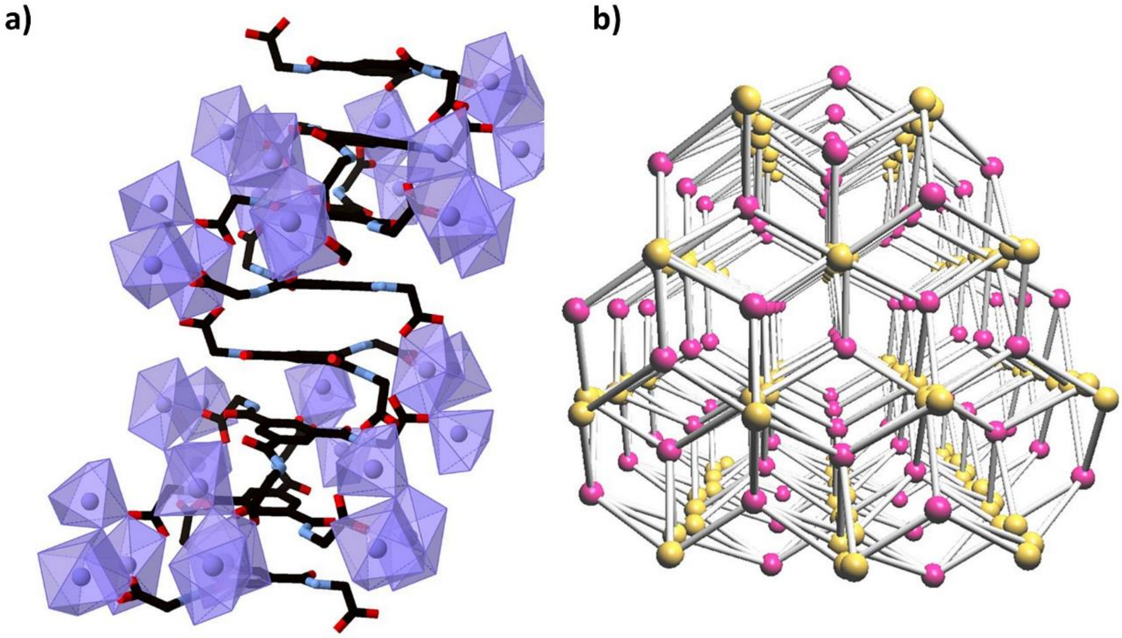

Figure 3.11 Extended structure of **65Cd**; (a) the linear stacks of **65** groups encircled by trinuclear cadmium clusters; (b) topological representation of the network viewed parallel to the stacks; yellow represents **65** nodes and pink represents cadmium clusters.

The structure of **65Cd** contains no amide-amide hydrogen bonding, unlike **64Cd** and other **BTA**-containing structures. In place of this, five N-H hydrogen bond donors are occupied in hydrogen bonds to carboxylate oxygen atoms, and one instance of an N-H···O hydrogen bond to a lattice water molecule is present. This is comparable behaviour to that encountered previously in the study of short-chain **BTA** carboxylate species,[148] discussed in Chapter 2, where competitive hydrogen bonding functionality is present. The **BTA** core groups, however, are still aligned in stacks in the structure of **65Cd** despite the absence of amide-amide interactions. The columns are aligned parallel to the *a* axis and proceed in an AABBAA fashion with respect to the two unique ligand molecules and these are supported by N-H···O (carboxylate) hydrogen bonds at their periphery. The aromatic cores are 3.66, 3.77 and 3.59 Å apart for the two symmetric and one unsymmetric pairings respectively, with the ring centroids slipped by 0.4-0.6 Å for the symmetric pairings and 1.6 Å for the unsymmetric pairing. By considering these columns as structural features, the extended network can be described as an approximately hexagonal rod packing motif, where each column is connected to one another through six sets of radially distributed cadmium cluster nodes, as depicted in Figure 3.11.

Besides the DMF and aqua ligands within the asymmetric unit, the structure of **65Cd** contains five lattice water molecules; minor crystallographic disorder required modelling these over a total of seven positions. These aqua ligands mainly take part in hydrogen bonding interactions with one another and the aqua ligands and carboxylate groups within the structure. These groups arrange to form narrow one-dimensional channels that are parallel to the crystallographic *c* axis and perpendicular to the propagation of the **BTA** stacks. These unbound water molecules account for an approximate solvent-accessible volume of 9%, increasing to 21% if the metal-bound solvent molecules are considered. Further investigations into the presence of solvent in these channels will be described in the next section. Phase purity was confirmed by x-ray powder diffraction and is shown in Figure 3.19 in 3.6.

As mentioned previously, in a study by Yan and co-workers,[145] they reported they reported the structures of **65** with zinc, manganese, nickel and cobalt. In each of these structures, each metal ion coordinates to three ligands and each ligand bridges three metal ions, as well as resulting in an infinite 2D anionic layer with honeycomb-like cavities. Two adjacent layers are staggered in such a way that non-interpenetrating double-layer structures are formed. These double layers are separated by a layer of hexaqua-metal cations through hydrogen bonds. Here it is reported that **65Cd** forms a 3D polymer and does not contain the anionic layer reported by Yan, thus highlighting the effects of different metals on the structures formed.

3.5 Thermal properties of 64Cd and 65Cd

As mentioned in section 3.4, both complexes **64Cd** and **65Cd** contain significant and continuous regions of lattice solvent, thus thermogravimetric analysis (TGA) was employed to ascertain to ideal conditions for desolvation and subsequent guest uptake studies. The analysis revealed that **64Cd** was found to exhibit a multi-step desolvation and decomposition profile, with a mass loss of approximately 30% below 70 °C and a further 10% below 150 °C. The graph then undergoes a gradual stabilisation before decomposition begins to occur at an onset temperature of 350 °C. The total volatile mass of approx. 40% corresponds to the combination of the crystallographically resolved DMF and H_2O guests, along with additional surface solvent from the freshly-isolated crystals. Soaking the crystals in acetonitrile (MeCN) for 48 hours allowed guest exchange, resulting in a phase that could be mostly desolvated at approx. room temperature, with the TGA curve shown to flatten above 100 °C, indicating the removal of all

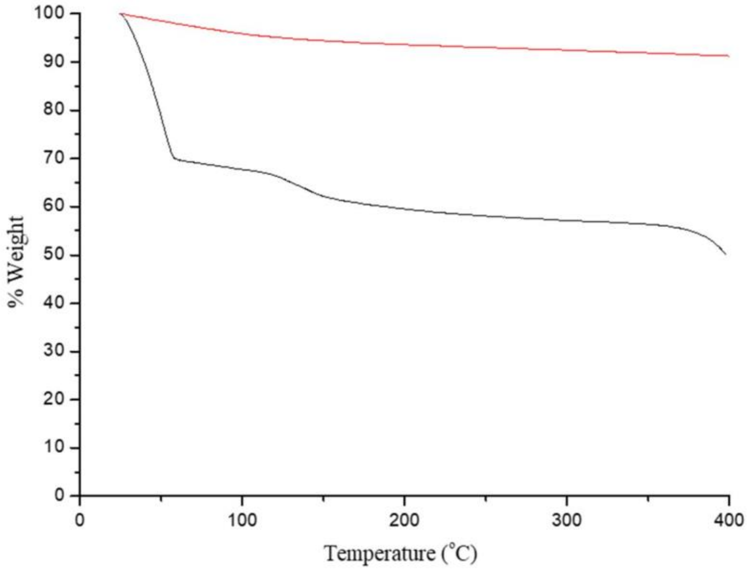

Figure 3.12 TGA trace for **64Cd** freshly isolated (black) and following MeCN exchange (red).

solvent molecules at this temperature, Figure 3.12. X-ray powder diffraction was then used to probe the solvent-exchanged and air-dried material, with this revealing that the material retained an equivalent structure to the as-synthesised material, as shown in Figure 3.17 in section 3.6.

In comparison to **64Cd**, TGA analysis of complex **65Cd** revealed a steep mass loss of about 25% before 100 °C, flattening before the onset of decomposition at approximately 300 °C, Figure 3.13. The tendency of complex **65Cd** to readily desolvate upon heating implied that solvent exchange was not necessary to achieve activation at moderate temperatures, thus solvent exchange was not necessary for the adsorption experiments on **65Cd**. The adsorption properties of **64Cd** and **65Cd** will be discussed in the next section.

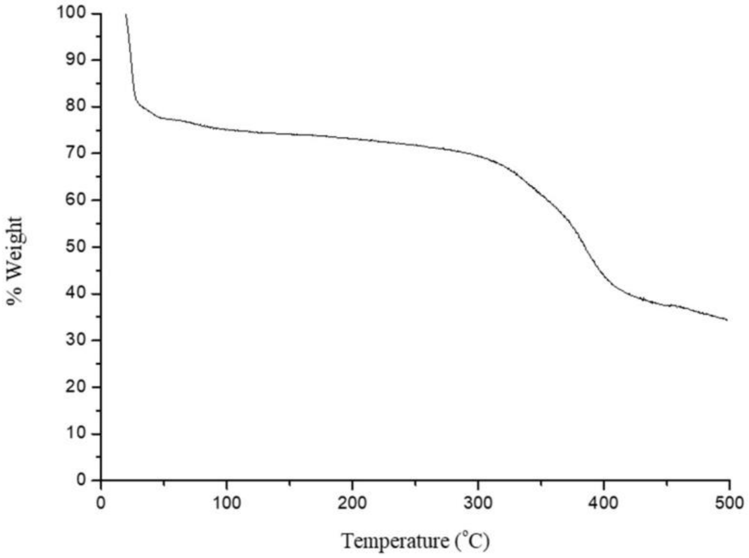

Figure 3.13 TGA of **65Cd** showing a mass loss of approximately 25% before 100 °C, followed by decomposition at about 300 °C.

3.6 Adsorption studies of 64Cd and 65Cd

In collaboration with Mr Kevin Byrne (of the Schmitt group, School of Chemistry, Trinity College Dublin) some gas adsorption studies of **64Cd** and **65Cd** were carried out. Following solvent exchange with MeCN, a sample of **64Cd** was activated under dynamic vacuum at 100 °C for 24 hours and the internal pore volume was characterised using CO_2 and N_2 as probe molecules. Relatively minor uptake of N_2 was observed at 77 K (ca. 6 cc(STP) per g) from microporous features in the pressure range P/P_o 0-0.01 followed by a shallow monotonic increase to $P = 0.99P_o$ up to a maximum loading of 14 cc(STP) per g, Figure 3.14. This low-capacity type I behaviour (with calculated BET surface area of *ca.* 5 m^2 g^{-1}, see Appendix) indicates poor affinity of the host for the N_2 probe molecule under these conditions. A type 1 isotherm is observed when adsorption is limited to, at most, a few molecular layers.[153] In physical adsorption, type 1 isotherms are encountered with microporous powders who have a pore size that does not exceed a few adsorbate molecule diameters. A gas molecule, when inside the pores, encounters the overlapping potential from the pore walls, enhancing the quantity of gas adsorbed at low relative pressures. At higher pressures, the pores are filled by adsorbed or condensed adsorbate leading to the plateau, thus indicating that little or no additional adsorption occurs once the pores are filled. Adsorption that results in a type 1 isotherm indicates that the pores are microporous and that the exposed surface resides almost exclusively within the pores and once filled with adsorbate, little or no external surface is available for additional adsorption.[153] BET analysis, obtained by applying the theory of Brunauer, Emmett and Teller,

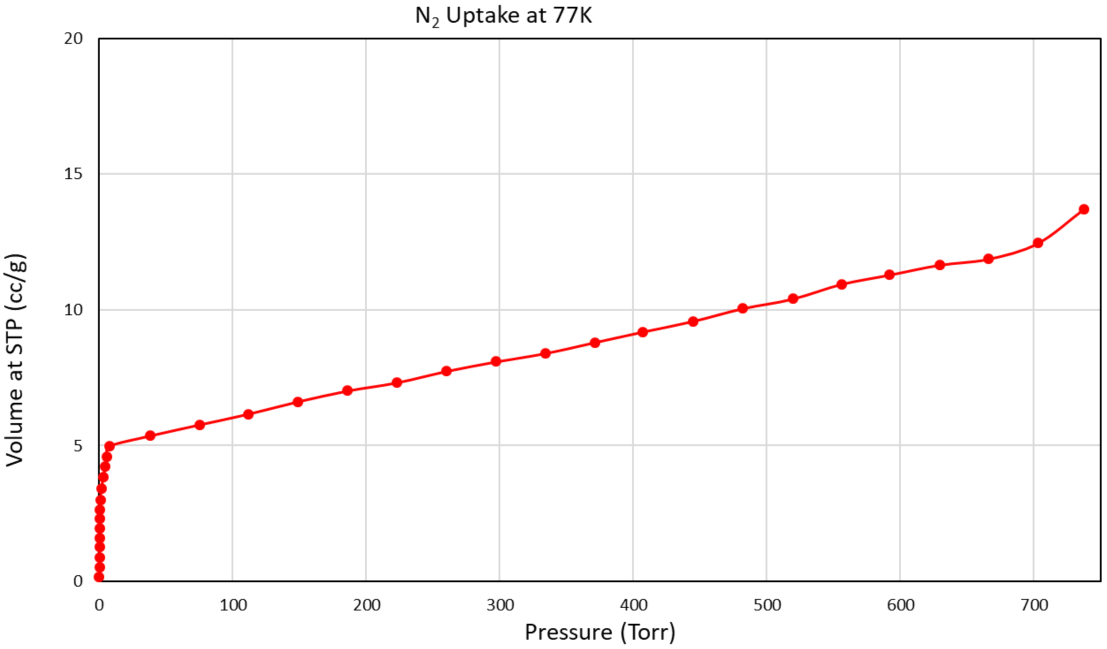

Figure 3.14 N_2 isotherm at 77 K for **64Cd**.

is the standard method for determining surface areas from nitrogen adsorption isotherms.[154] MOFs have been shown to display very large surface areas. The adsorption of CO_2 at 278 K displayed a much greater uptake, with a total adsorption capacity of 103 cc(STP) per g (17 wt%) at 1 bar, as seen in Figure 3.15. The Dubinin-Radushkevich (DR) method was used to calculate the surface area from these data, yielding a surface area at 278 K of 207 m^2 g^{-1}. This figure is more consistent with the microporous features apparent from the single crystal structure. The DR equation is widely used for describing the overall adsorption process of CO_2 in microporous materials, especially those of a carbonaceous origin. It has semi-empirical origins and is based on assumptions of a change in the potential energy between the gas and adsorbed phases and a characteristic energy of a given solid.[155] This selectivity for CO_2 is likely due to the relatively narrow and polar micropores present in **64Cd**, expected to favour the larger quadrupole of CO_2 compared to N_2. The smooth adsorption and desorption curves, with minor hysteresis, show no obvious indication of framework flexibility or reorganisation during the adsorption process.

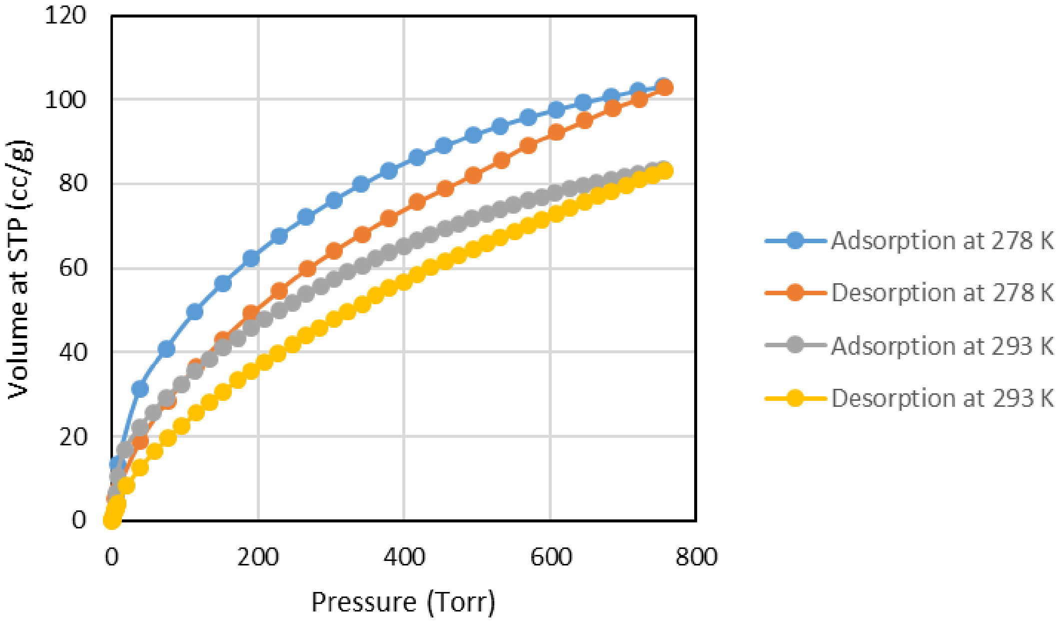

Figure 3.15 CO_2 adsorption and desorption for **64Cd** at 278 K and 293 K.

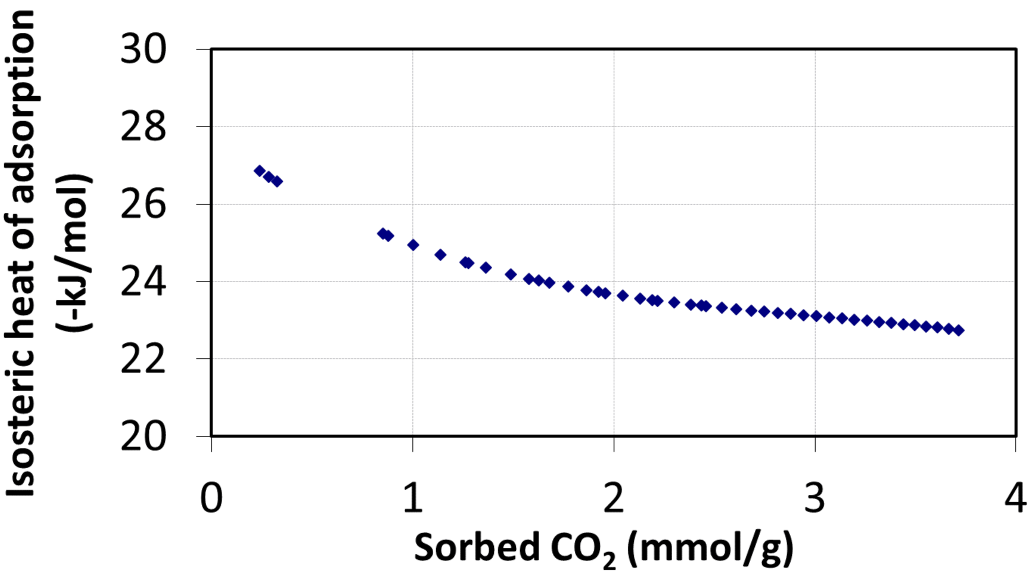

Figure 3.16 Estimated isosteric heat of adsorption for CO_2 in **64Cd** as a function of adsorbed quantity.

The adsorption cycle was repeated at 293 K and resulted in a similar curve with a maximum capacity of 83 cc(STP) per g at 1 bar. The datapoints from the two adsorption cycles were fitted using a virial-type model using the Clausius-Clapeyron relation and the enthalpy of adsorption across the loading range was estimated. Figure 3.16. shows the zero-loading enthalpy of adsorption for CO_2 is estimated at approximately -28 kJ mol^{-1}, reaching a plateau value of approximately -23 kJ mol^{-1} at higher loadings. These values are consistent with those

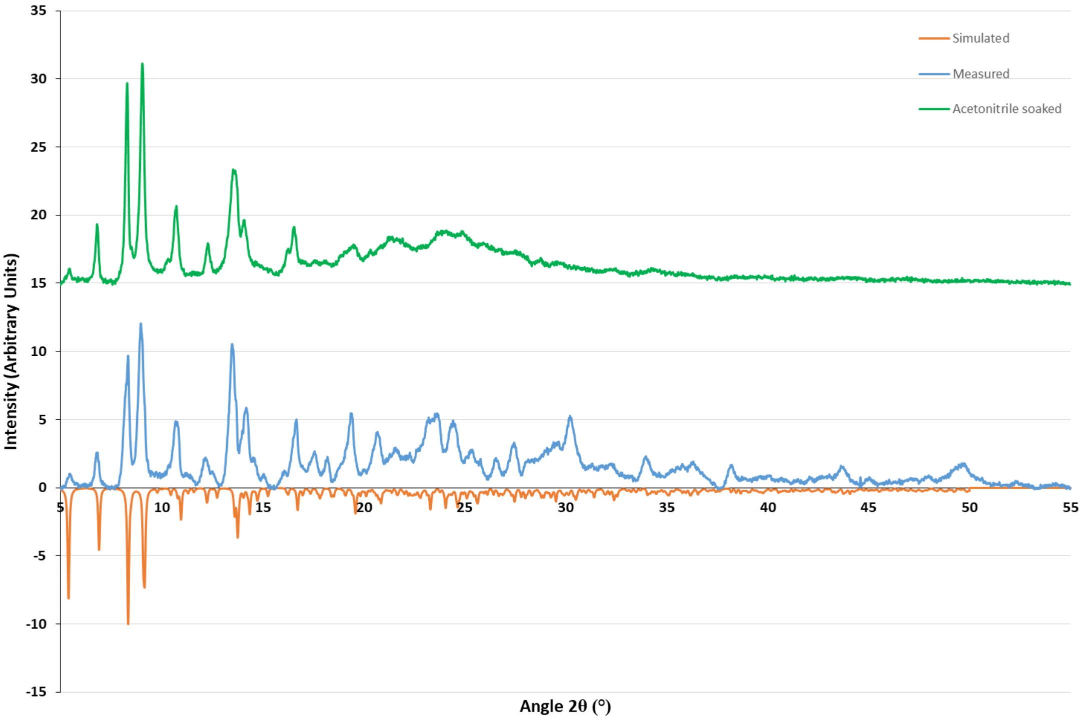

Figure 3.17 Offset X-ray powder diffraction of **64Cd** at room temperature (blue) and MeCN soaked sample of **64Cd** after adsorption experiment (green) compared to the simulated pattern of **64Cd** from the single crystal data collected at 100 K (orange) and (bottom).

typically observed for physisorption onto organic pore walls with modest polarity, suggesting little direct interaction from the metal sites or potential hydrogen bond donors in the adsorption process. Although the preferential adsorption of CO_2 at 278 K over N_2 at 77 K is not surprising for a microporous material, the CO_2 capacity displayed by **64Cd** under mild conditions is unusually high for a 2-dimensional framework showing only intralayer porosity; the capacity at 293 K/1 bar is comparable to that shown by well-known 3-dimensional materials including HKUST-1, MIL-53(Al) and UiO-66.[156]

Complex **65Cd** was also subject to gas uptake investigations, with evacuation of a freshly isolated sample carried out at 100 °C under dynamic vacuum overnight. In comparison to **64Cd**, both CO_2 (293 K) and N_2 (77 K) adsorption experiments showed negligible adsorption. The uptake of N_2 fell below the instrumental detection limit (see appendix), while CO_2 adsorption reached a maximum loading of *ca*. 17 cc(STP) per g at 1 bar with no obvious

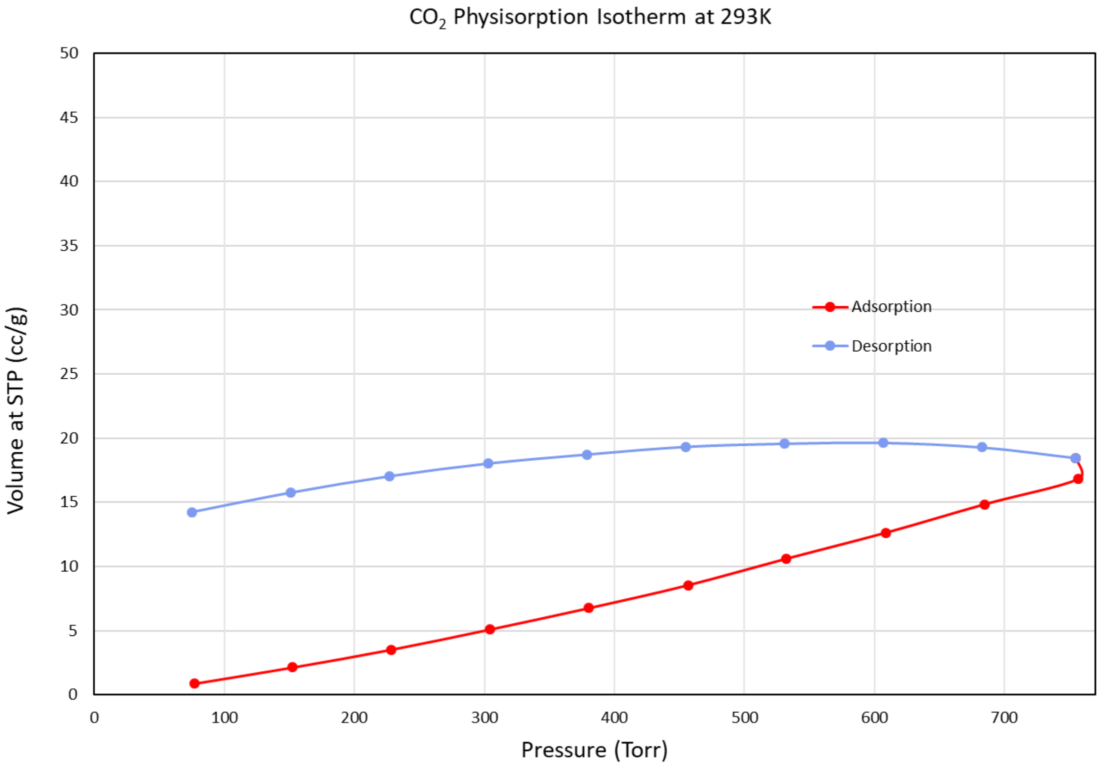

Figure 3.18 Adsorption and desorption of CO_2 at 293 K in **65Cd**.

inflection point in the absorption branch, both consistent with adsorption on the external particle surfaces only, Figure 3.18.

For both complexes **64Cd** and **65Cd**, X-ray powder diffraction following gas adsorption showed crystalline materials closely related in structure to the freshly synthesised compounds were recovered following exposure to air, as seen in Figure 3.17 and 3.19.

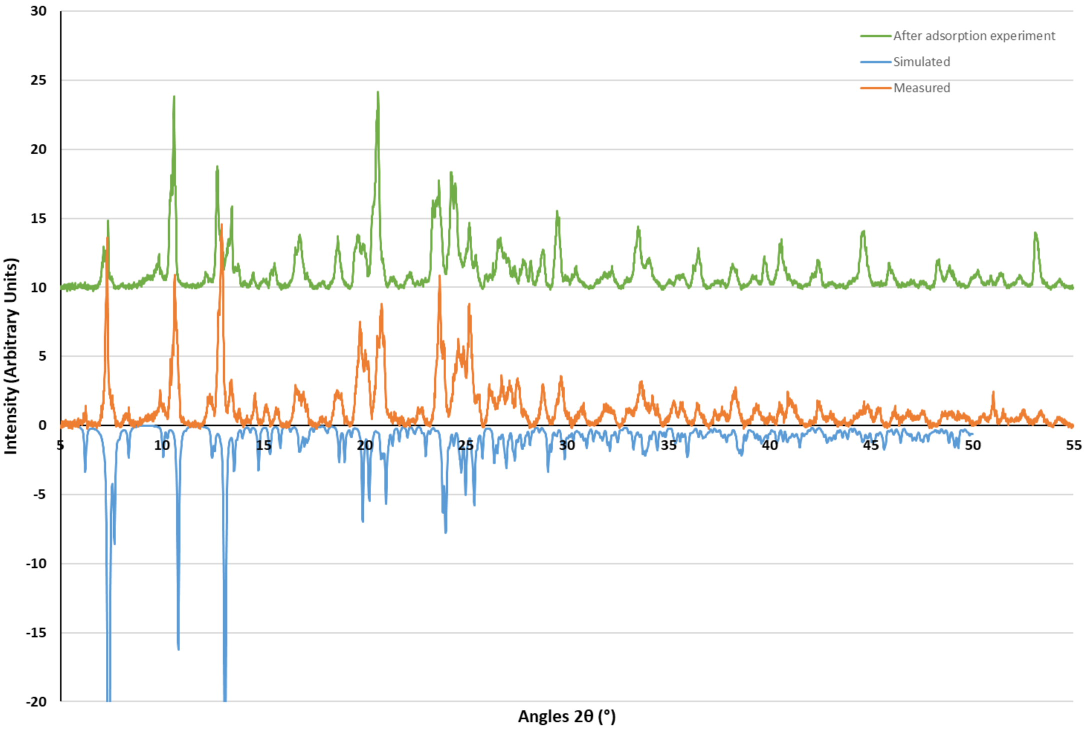

Figure 3.19 Offset X-ray powder diffraction of **65Cd** at room temperature (blue) and **65Cd** after adsorption experiment (green) compared to the simulated pattern of **65Cd** from the single crystal data collected at 100 K (orange).

To conclude this section, **64Cd** was found to be permanently porous, with an unusually high capacity for CO_2 for a two-dimensional material with intralayer porosity and retained its structure following the adsorption experiments. Many structurally similar compounds were subject to collapse upon evacuation,[69,144] thus indicating the structural resilience of the interconnected cadmium-carboxylate rod building units and the hydrogen bonding interactions present within the structure. **64Cd** also benefits from the extra π-π interactions on the **BTA** arms. On the other hand, **65Cd** did not display this permanent porosity, presumably due to a combination of factors, namely restricted pore size and greater ligand flexibility arising from the discrete cadmium-carboxylate cluster nodes, in comparison to the more inter-connected cadmium-carboxylate columns in **64Cd**.

3.7 Amino acid derivatives of 64

As the crystal structure or any reliable gelation behaviour was not observed for **64**, it was decided to further derivatise this compound with some simple amino acids to provide more hydrogen bonding units. Amino acid based **BTA**s have been reported to display both gelation and porous organic material behaviours.[3,17,92,151,157]. Glycine and alanine were the chosen amino acids and the structure of the compounds synthesised are shown in Scheme 3.2.

3.7.1 Synthesis and characterisation of 70-73

The synthesis of **70** and **72** was achieved using the same procedure as used in Chapter 2 for a coupling reaction between a carboxylic acid (**64**) and an amine (commercially available methyl ester protected amino acids alanine and glycine). This reaction involved the coupling reagents, EDC.HCl and DMAP and stirring at room temperature under an inert atmosphere for 72 h, Scheme 3.2. The reactions were carried out on a small scale and there were some difficulties in obtaining high purity samples of the ester derivatives in good yields, presumably due to both the poor solubility of the compounds and the difficulties in adding the amino acid to three arms.

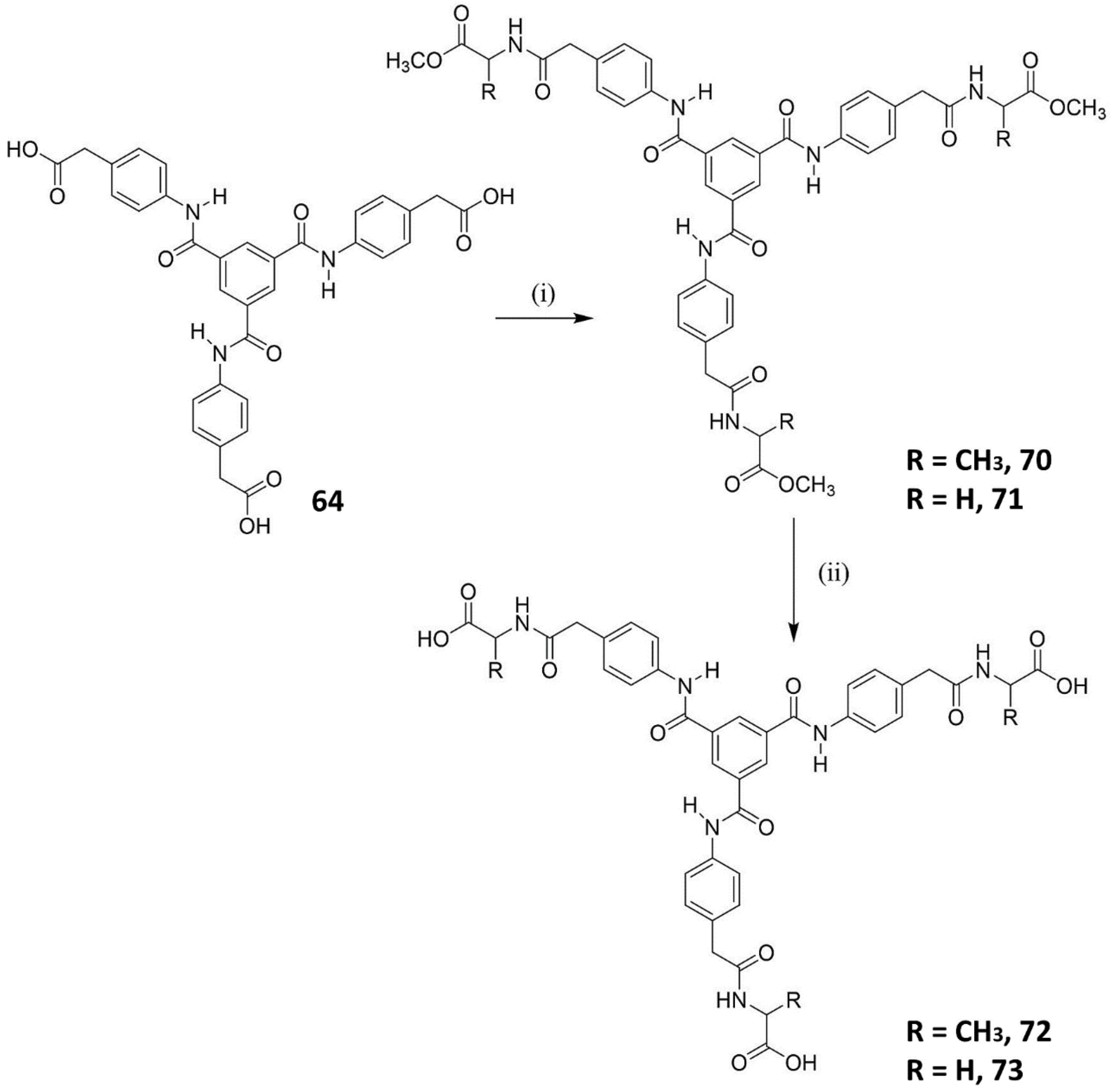

Scheme 3.2 Synthetic scheme for **70-73**, where (i) rt, DCM, EDC.HCl, DMAP, either alanine methyl ester hydrochloride or glycine methyl ester hydrochloride,72 h and (ii) rt, NaOH, MeOH, 6 h.

Despite the difficulties encountered during the synthesis, an adequate amount of the ester derivatives were generated to carry out some gelation and crystallisation studies. Base hydrolysis was then employed to convert the ester derivatives to their corresponding carboxylic acid. As described in Chapter 2, this involved stirring in NaOH and MeOH, followed by precipitation using an acid to reveal the carboxylic acid which was isolated by filtration. This was successful in the case of the glycine derivative with **72** being converted to **73**, however, it was less successful for the alanine derivative of **70**, with the ^{1}H NMR spectrum of **71** indicating that there was still a significant amount of the ester present. A comparison of the ^{1}H NMR spectrum obtained for **72** and **73** with its precursor **64** is shown in Figure 3.20, showing the appearance of the new NH shifts at approximately 8.5 and 8.25 ppm respectively. Purification of **71** proved rather difficult due to solubility issues, with washing, recrystallisation and column chromatography all proving unsuccessful. There was enough of **73** generated to carry out some gelation and crystallisation studies, however, there was not enough of **71** in sufficient yield and purity to carry out these studies. Full characterisation of these compounds, in the form of ^{1}H NMR spectroscopy, ^{13}C{^{1}H} NMR spectroscopy, IR spectroscopy and mass spectrometry can be found in the experimental section.

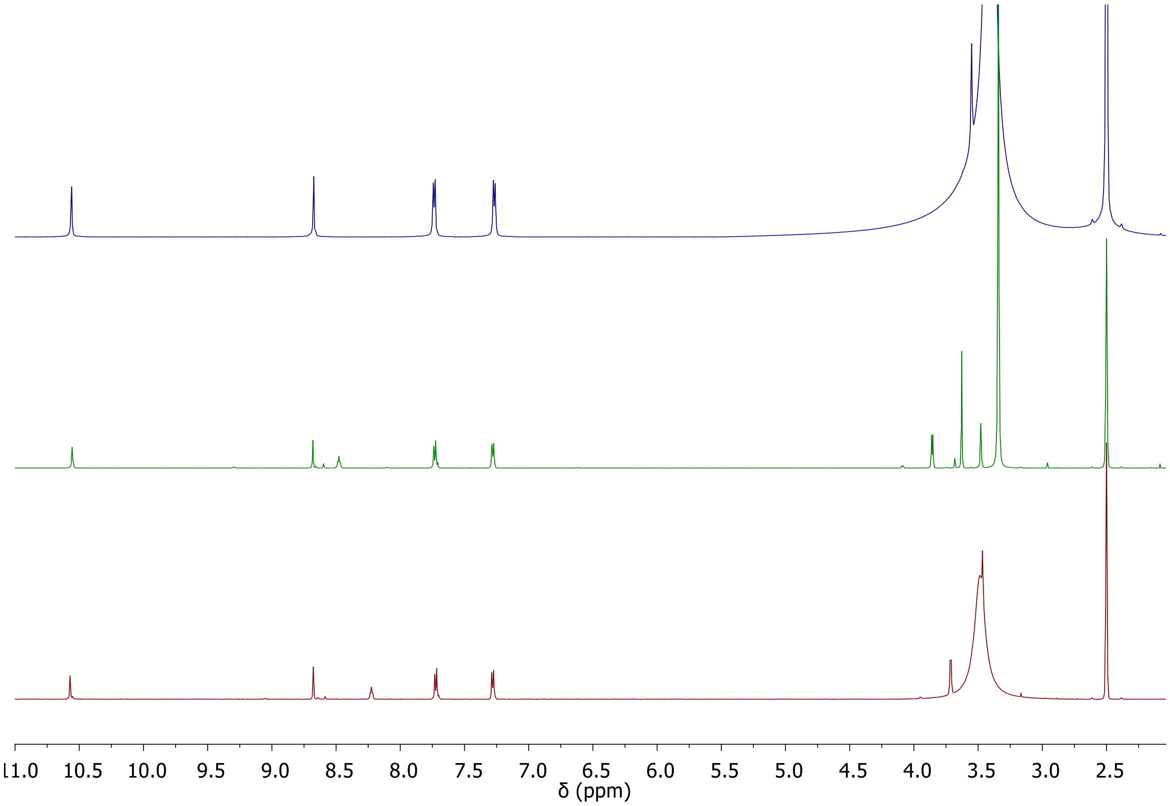

Figure 3.20 ^{1}H NMR spectra of **64** (600 MHz, DMSO-d_6, top), **72** (400 MHz, DMSO-d_6, middle) and **73** (600 MHz, DMSO-d_6, bottom).

3.8 Crystallisation attempts of 70, 72 and 73

With the aim of investigating the effect of extending the arms of the **BTA** with extra hydrogen bonding units on the structure and self-assembly behaviour of **64**, numerous crystallisation attempts of **70**, **72** and **73** were carried out. Various techniques were used, for example, slow evaporation from a variety of solvents, diffusion methods and solvothermal reactions. Unfortunately, these methods were not successful in generating single crystals of suitable quality for diffraction and instead resulted in amorphous solids. A number of attempts were also made to generate coordination polymers using the solvothermal technique described in 3.2.1. This was done using both the ester derivatives **70** and **72**, in the hopes of *in situ* hydrolysis of the ester as demonstrated for **65Cd** and the carboxylic acid derivative **73**. The reaction conditions, *i.e*. duration, solvents, metal salts, solvent ratios, ligand to metal ratio, were varied, however these attempts were unsuccessful. This would imply that extending the arms of the **BTA** to this extent or the degree of flexibility is too great to allow crystallisation to occur.

3.9 Investigations into the gelation of 70, 72 and 73

Given the unsuccessful attempts at obtaining crystals of **70**, **72** and **73**, we moved on to investigating the gelation potential of these compounds. Initially, some screening experiments involving a variety of conditions and solvents were carried .out. The ester derivative, **72**, was found to form a weak gel in MeOH, as seen in Figure 3.21. This material was not completely stable to inversion and TGA revealed the residual % weight to be quite high, approximately 3wt%, Figure 3.21. The morphology of this weak gel was probed by SEM and is shown in Figure 3.22. The morphology of this weak gel is quite different to that observed for the alkyl

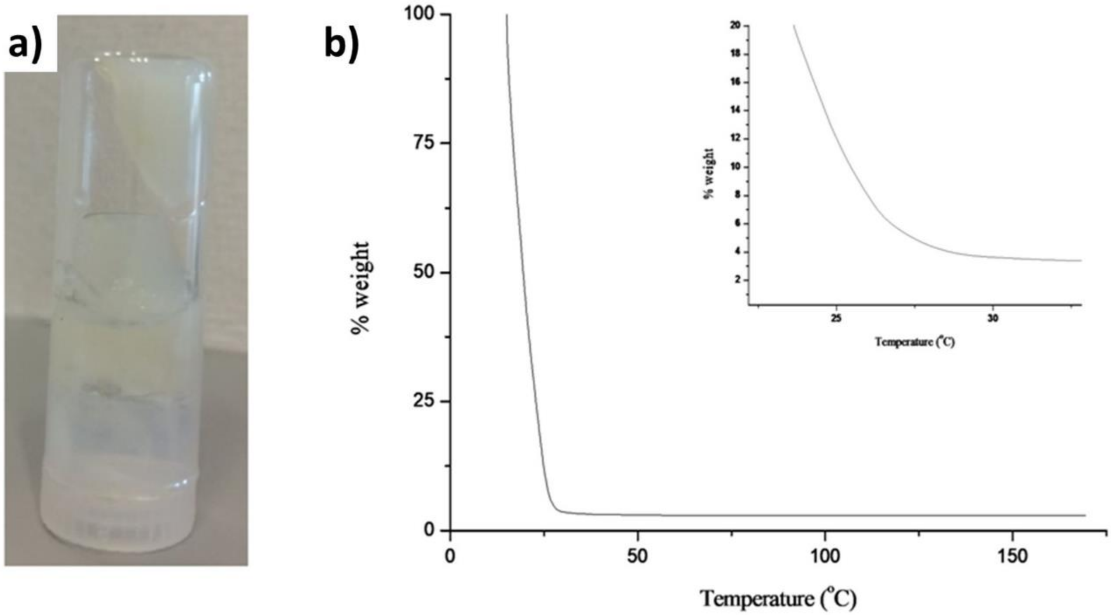

Figure 3.21 (a) Weak gel of **72** formed in MeOH and (b) TGA thermograph showing the w% to be approximately 3wt%.

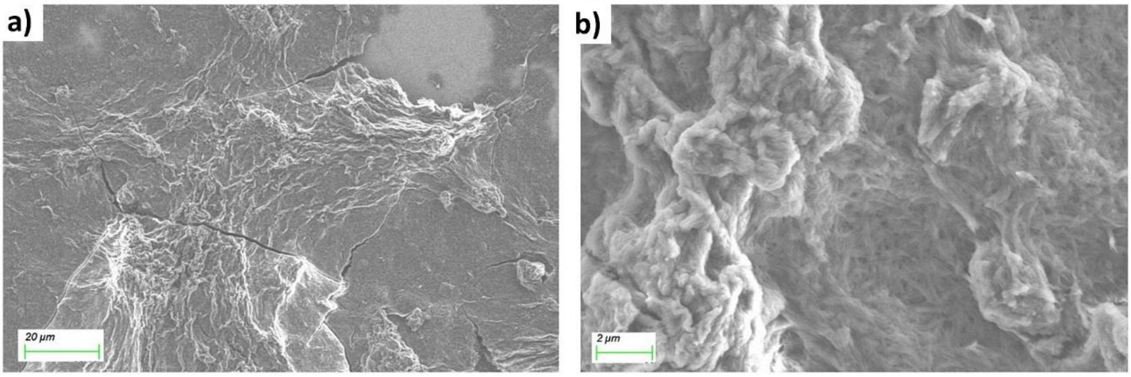

Figure 3.22 SEM images of xerogels of **72** (a, bar 20 µm, b, scale bar 2 µm).

chain derivatives discussed in Chapter 2. Here, the gel resembles a dried fibrous film as opposed to the individual, almost crystalline-like fibres observed for **61**, **62** and **63**.

Gelation screening of the ester derivative, **70**, in a variety of solvents was hindered by the poor solubility of the compound, however some gels were formed. **70** displayed a tendency to gelate in MeOH, however it was difficult to accurately determine the ideal conditions for this to occur, due to issues with solubility. **70** could be solubilised in MeOH upon heat and sonication, however at very low concentrations, only a weak gel was observed while upon increasing the concentration gelation occurred, but the compound was not completely soluble, as depicted in Figure 3.23. A crude TGA of this sample revealed the residual % weight to be approximately 1.75wt%. SEM studies on a dried gel sample of **70** formed in MeOH showed the

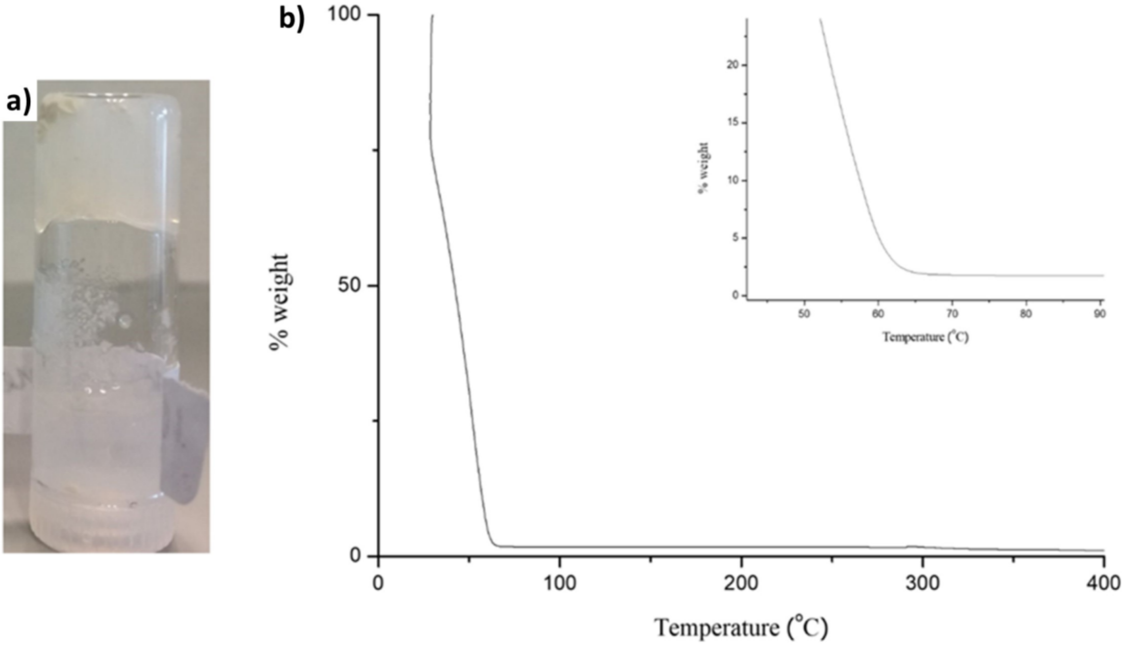

Figure 3.23 Gelation of **70** in MeOH, with some insoluble compound and TGA of **70** showing the %wt to be 1.75wt%.

presence of long, needle like fibres of varying diameters, approximately 0.2 -1.0 μm, Figure 3.24 and was not dissimilar to the morphology of the gels reported in Chapter 2.

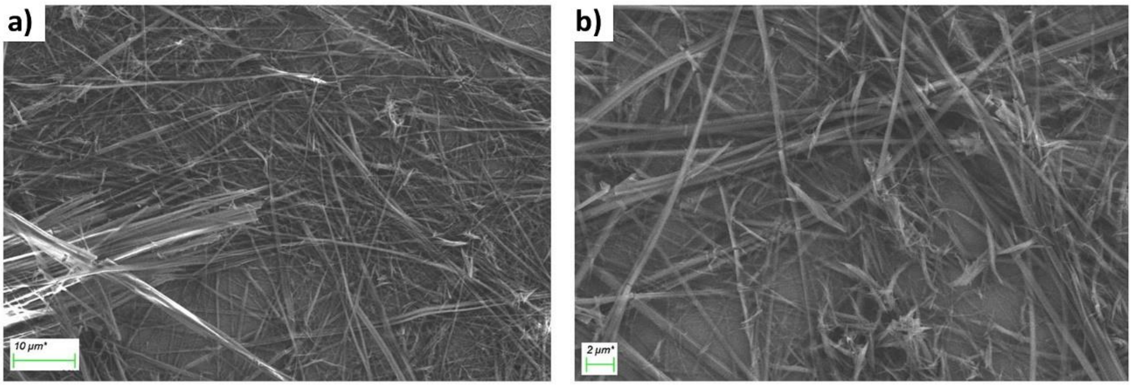

Figure 3.24 SEM of a xerogel sample of **70** in MeOH, (a) scale bar 10 μm, (b) scale bar 2 μm.

Gelation studies of the carboxylic acid **73** revealed the best conditions for gelation to be the acid/base method described in Chapter 2. 3 mg of **73** was dissolved in aqueous NaOH, followed by addition of HCl, this resulted in a milky solution which upon sitting for approximately two hours formed a gel, as seen in Figure 3.25. The gel was robust enough to survive inversion and TGA carried out on this sample showed the residual % weight to be quite high, at approximately 3.7 wt%.

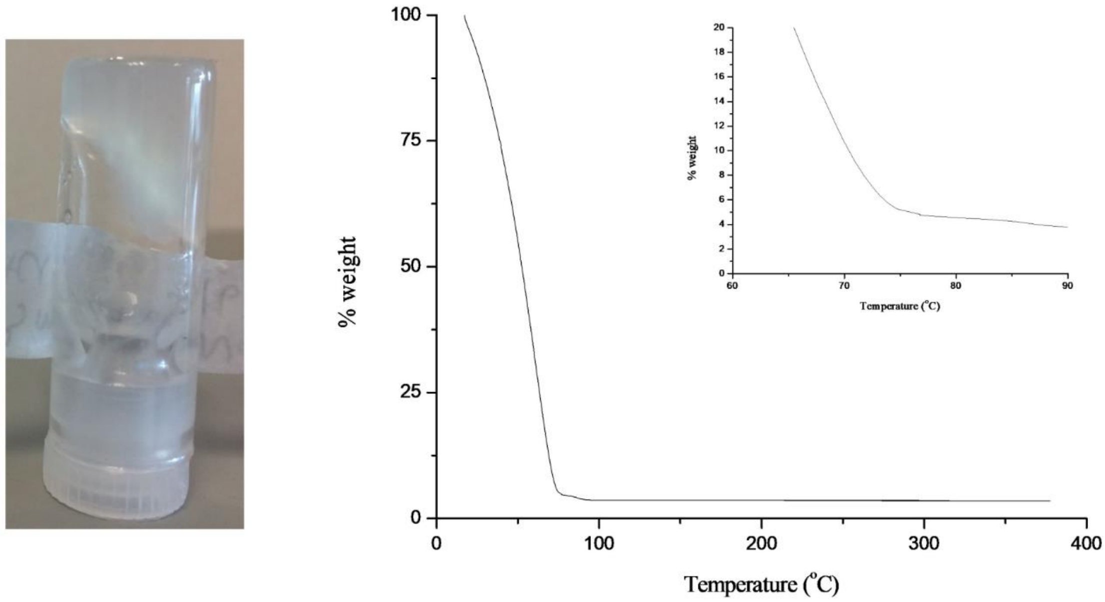

Figure 3.25 Inversion test of **73** generated using the acid/base method and TGA of the same gel showing the gel to be 3.7 wt%.

SEM images of the dried material are shown in Figure 3.26 and show the morphology of the gel to be similar to that observed for **72**, along with the presence of NaCl crystals which are circled in red.

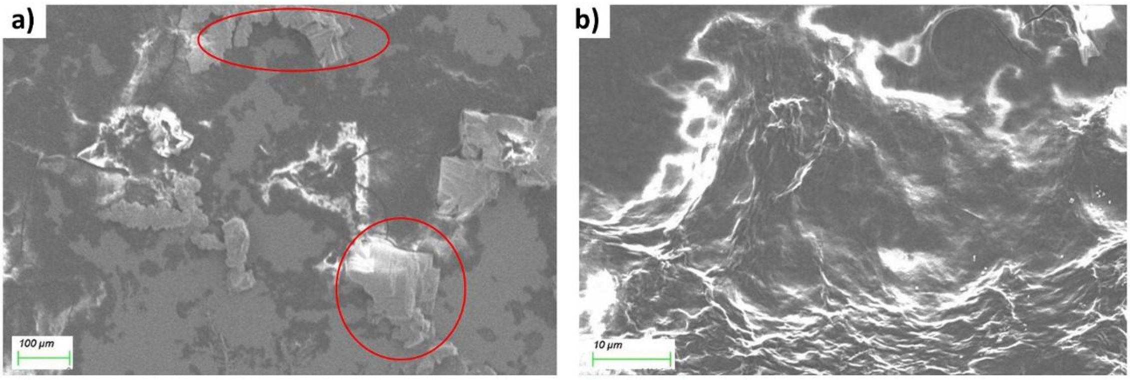

Figure 3.26 SEM of a dried sample of **73**, with some of the NaCl crystals circled in red (a) scale bar 100 μm and (b) SEM, scale bar 10 μm).

Previous studies by both the Gunnlaugsson group and others have shown that when various metals are added to organic gels, the materials can be strengthened to form more robust materials.[4,72,158] Addition of metals to form robust gels also opens the possibility to impart the properties of the metals on the gel, for example, magnetic, redox, catalytic, biological and sensing applications.[4,158,159] Given these successes, this approach was tested on **73** in an effort to obtain a more robust, less concentrated gelator. A similar method to that used by Kotova *et al.*, in which a solution of the chosen metal was added to a pre-formed gel sample and left to diffuse, was adopted here.[4] In this case, the metal used was a copper (II) chloride solution in MeOH and its effect on the gel structure and on the morphology is shown in Figure 3.28. In this case, the addition of metal solution to the weak gel did not result in a strengthening of the gel network, but rather, the opposite, as seen in Figure 3.27. The morphology of dried samples from these tests are also seen by SEM in Figure 3.28, with these images showing areas of fibrous material. These areas of seemingly dense fibrous material presumably occur during shrinkage

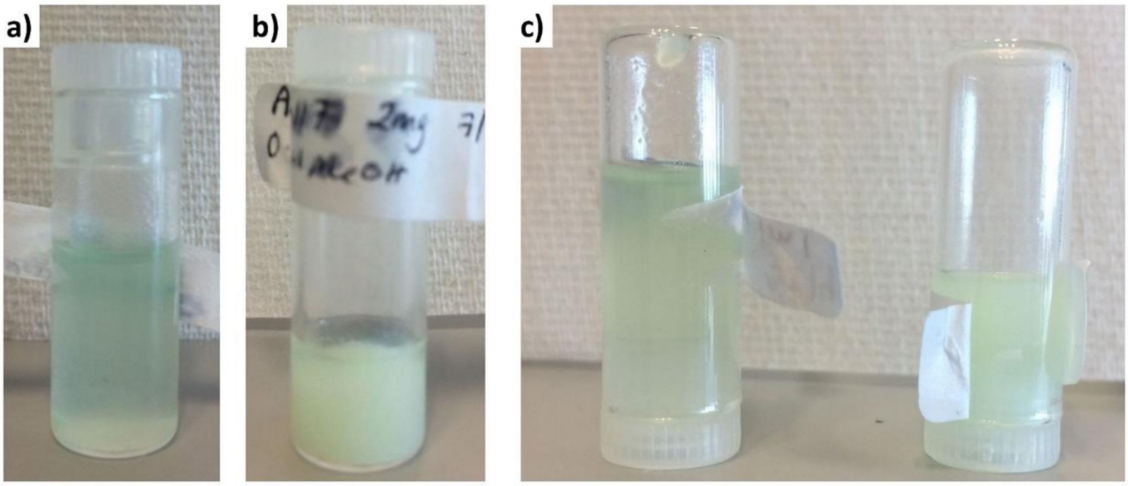

Figure 3.27 (a&b) Vials containing two different concentrations of **73** with $CuCl_2$ solution and (c) the failed inversion tests of these two materials.

of the material during the drying process required during SEM sample preparation, as there was little visual evidence of any gel formed in the sample vial, as the addition of metal seemed to destroy the gel network.

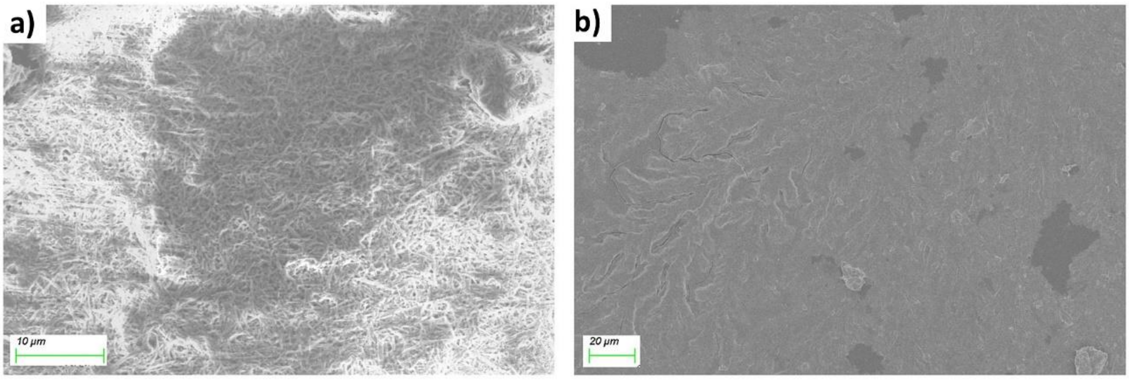

Figure 3.28 SEM of **73** and $CuCl_2$ showing some areas of gel-like materials formed upon concentration caused by drying.

Due to the difficulties in working with this family of amino acid compounds, *i.e.* solubility, yields and purification, further studies were not pursued. While the addition of the chosen amino acids to the end aromatic arm did improve the solubility and gelation potential of the compounds compared to that of **64**, it did not improve these properties significantly enough warrant further investigations. Crystallisation of these derivatives was not found to occur in the variety of conditions tested, indicating that the extension of the **BTA** arms may be imparting too much flexibility to the system, thus preventing crystallisation from occurring, thus also explaining the slight tendency towards gelation.[135]

3.10 Conclusions

Several **BTA** derivatives were presented in this chapter, mainly consisting of aromatic arms, and their structural and physical properties were probed. The gelation studies of **64** did not result in any gel material, despite several gelation techniques being carried out, with poor solubility hindering many of these attempts, thus our attention was then turned to structural studies. The glycine **BTA** derivative, **65**, was found to display the classical triple helical packing model, common for **BTA** structures and as demonstrated for the alkyl ester derivative **59** in Chapter 2. As was the case for **59**, it is presumed **65** adopts this structure due to the absence of any strongly competing hydrogen bonding or other intermolecular interactions. The effect of bridging distances and aromatic linkers on the resulting structural and porous properties were investigated in the case of **65Cd** and **64Cd**. It was found that **64Cd** displayed permanent porosity and an unusually high capacity for CO_2, while **65Cd** did not possess this permanent porosity. This is presumably due to the greater flexibility and more restricted pore size of **65Cd**.

The addition of some simple amino acids to the aromatic linkers in order to try to increase the gelation potential was only partly successful. The amino acids did slightly improve the solubility and the gelation abilities of the compounds, however, not enough to warrant further investigations and there were many difficulties involved in the synthesis and purification of these derivatives. For this particular family of **BTA** derivatives, it is clear that extending the side arms hinders the gelation and crystallisation potential.

‘Sure, if it was easy, we’d all do one.’

My dad on this PhD

4. Network polymers derived from BTA-amine based precursors

4.1 Introduction

As discussed in the introduction, polymers consist of monomeric units bonded together, with the bonds holding supramolecular polymers together being directional and reversible non-covalent interactions such as hydrogen bonding and hydrophobic interactions.[53-55] The supramolecular nature of these materials bestows them with unique modular and dynamic properties, while the non-covalent interactions allow for the tuning of the final properties of the aggregates. Supramolecular assemblies represent new and rapidly developing areas of polymer chemistry with potentially useful industrial applications, with evidence of their applicability seen in the formation of a spinout company, SupraPolix, based on the supramolecular polymer research from the laboratories of Meijer and Sijbesma at Eindhoven University.[53,57,88,96,106,160,161]

Taking this approach further, an approach to design two component cross-linked polymers was explored and will be discussed in this chapter. It was envisioned that this could be done using a printing type apparatus, in which two components are simultaneously injected into a reaction vessel and mixed to result in a covalently cross-linked polymer. The design of these structures was inspired by epoxy and alkyd resins which have been used as adhesives and coatings respectively.[162] Epoxy resins are oligomers that consist of two or more epoxide groups per molecule, while alkyd resins result from the polycondensation of multifunctional alcohols, with bifunctional acids or their anhydrides.[160,162]

Network polymers are formed when linear or branched polymer chains are joined together by covalent bonds, in a process called cross-linking.[160] Polymers that are not cross-linked and can usually be dissolved and, in most cases, can melt and flow are referred to as being thermoplastic.[160] After undergoing cross-linking, network polymers lose their ability to flow, and therefore cannot be moulded and these are referred to as being thermoset. These types of polymers are insoluble due to the cross-linking resulting in a great increase in molecular weight. These polymers can be swelled in the presence of a solvent as the solvent molecules can penetrate the network, resulting in a polymer-gel material. Uses of robust polymers include but are not limited to, engineering plastics, medical applications, conducting materials and optoelectronic materials.[93,160,163,164]

4.1.1 Design rationale

The group of Meijer have made great contributions to the field of supramolecular polymers, for example, one report was on a series of supramolecular polymers consisting of polyethylene glycol (PEG) end functionalised with four-fold hydrogen bonding ureidopyrimidone (UPy) moieties and alkyl spacers as shown in Figure 1.9 in the introduction. These were shown to be promising protein delivery carriers and could be administered by injection.[59] Another report by Meijer and co-workers detailed a series of **BTA** derivatives with amphiphilic ethylene glycol-based side chains, with the choice of side chain influencing the mechanical properties of the resulting hydrogel.[88] Meijer and co-workers have also reported a **BTA** decorated with aliphatic side chains, which shielded a central hydrogen-bonding unit from the surrounding water or other polar media, with hydrophilic ethylene glycol motifs at the periphery to ensure solubility.[165] This chapter will discuss attempts at generating supramolecular polymers using **BTA**-amino acids as the central core, with a variety of alkoxy amines as side chains. **BTA**s decorated with amino acids were chosen due to the inherent propensity of **BTA**s to

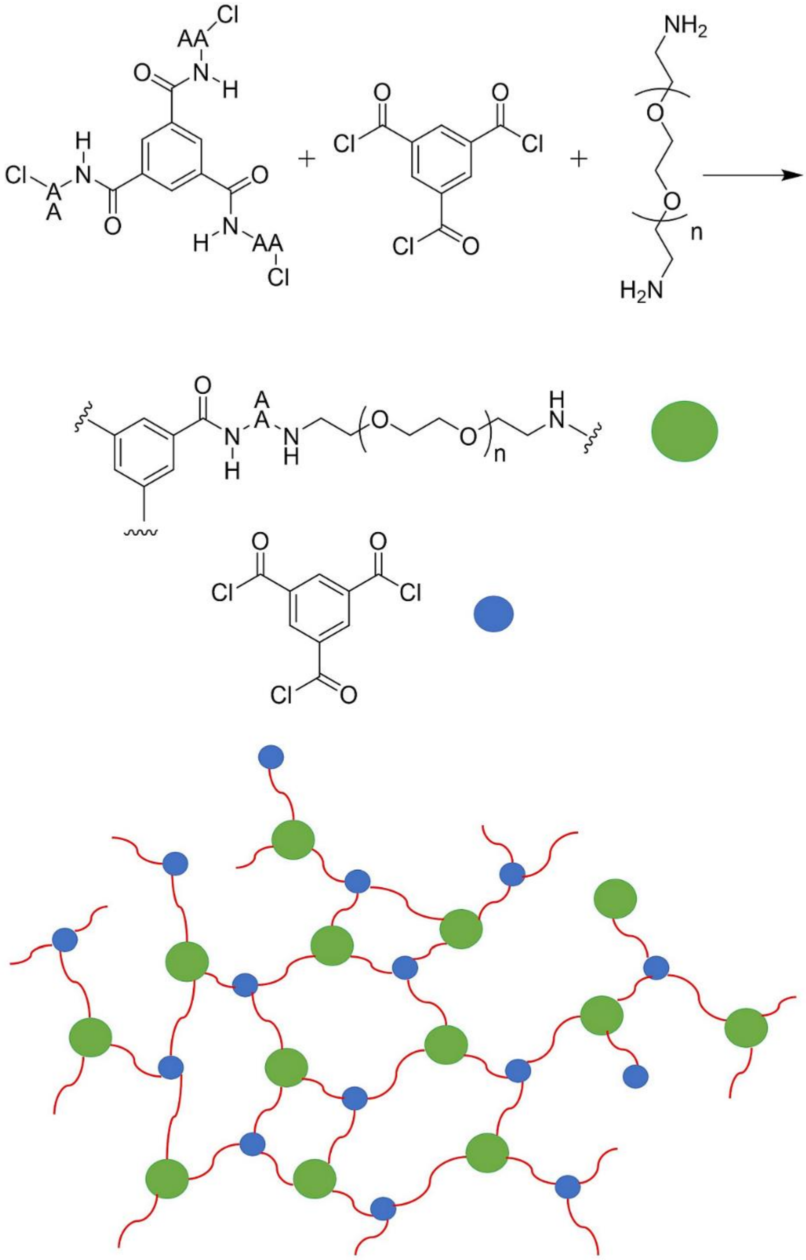

Scheme 4.1 Proposed scheme and design of the hyperbranched polymeric materials discussed in this section, similar to that reported by Chen and co-workers,[167] where the blue circles represent the additive, while the green circle represents the **BTA** unit and the red represents the cross-linking between the two units.

aggregate,[14,78,166] and in some cases, gelate.[92] The alkoxy side chains would impart some hydrophilicity to the system, similar to the systems used by Meijer and co-workers,[88,165] along with the terminal amine available for further reactions. For example, it was envisioned that the terminal amines could be covalently cross-linked using a reactive additive, giving rise to an extended, cross-linked polymer system, analogous to that reported by Chen and co-workers,[167] Scheme 4.1. It was envisioned that this could be done using a printing type apparatus, in which the two components are simultaneously injected into a reaction vessel and mixed to result in a covalently cross-linked polymer. The design of these structures were inspired by epoxy and alkyd resins which have been used as adhesives and coatings respectively.[168] Epoxy resins are oligomers that consist of two or more epoxide groups per molecule, while alkyd resins result from the polycondensation of multifunctional alcohols with bifunctional acids or their anhydrides.[160,168]

4.2 Synthesis of the amino acid BTA-based polymers

The synthesis and characterisation of amino acid-based **BTA** precursors used is shown below in Scheme 4.2. The amino acids chosen were phenylalanine methyl ester and the ethyl ester derivative, along with the alkyl ester **60** and its carboxylic acid derivative **63** described in Chapter 2. These were chosen due to their aggregation properties and previous reports of gelation behaviour.[92,166,169] The synthesis was achieved using the established conditions for the tri-substitution of benzene-1,3,5-tricarbonyl trichloride, using the ester protected amino acids in the presence of base. In this case, the reactions were carried out in dry DCM under an argon atmosphere in the presence of Et_3N and left to stir at room temperature for 24 h. Once complete

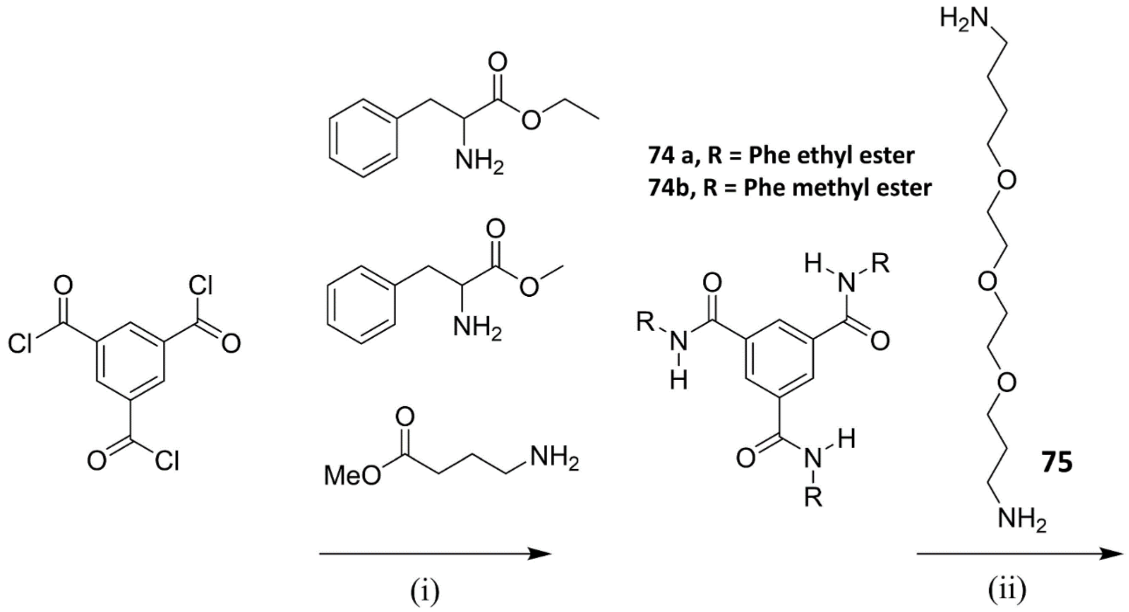

Scheme 4.2 Synthetic scheme for the **BTA** derivatives where (i) rt, dry DCM, Et_3N, argon, 24 h and (ii) MeCN or MeOH, reflux, 24 h.

and following an aqueous workup, the ester derivatives were recovered as white solids in good to excellent yields. **60** was hydrolysed to form the carboxylic acid derivative **63** by base hydrolysis as described in Chapter 2. The compounds were then fully characterised by ^{1}H and ^{13}C{^{1}H} NMR spectroscopy, IR spectroscopy, mass spectrometry and melting point and were consistent with the tri-substituted products. The ^{1}H NMR spectra of the **BTA** phenylalanine derivatives **74a** and **74b**, as with the derivatives discussed in Chapter 2, showed the aromatic protons to appear as a sharp singlet around 8.3 ppm, indicative of C_3 symmetry of the molecule, Figure 4.1.

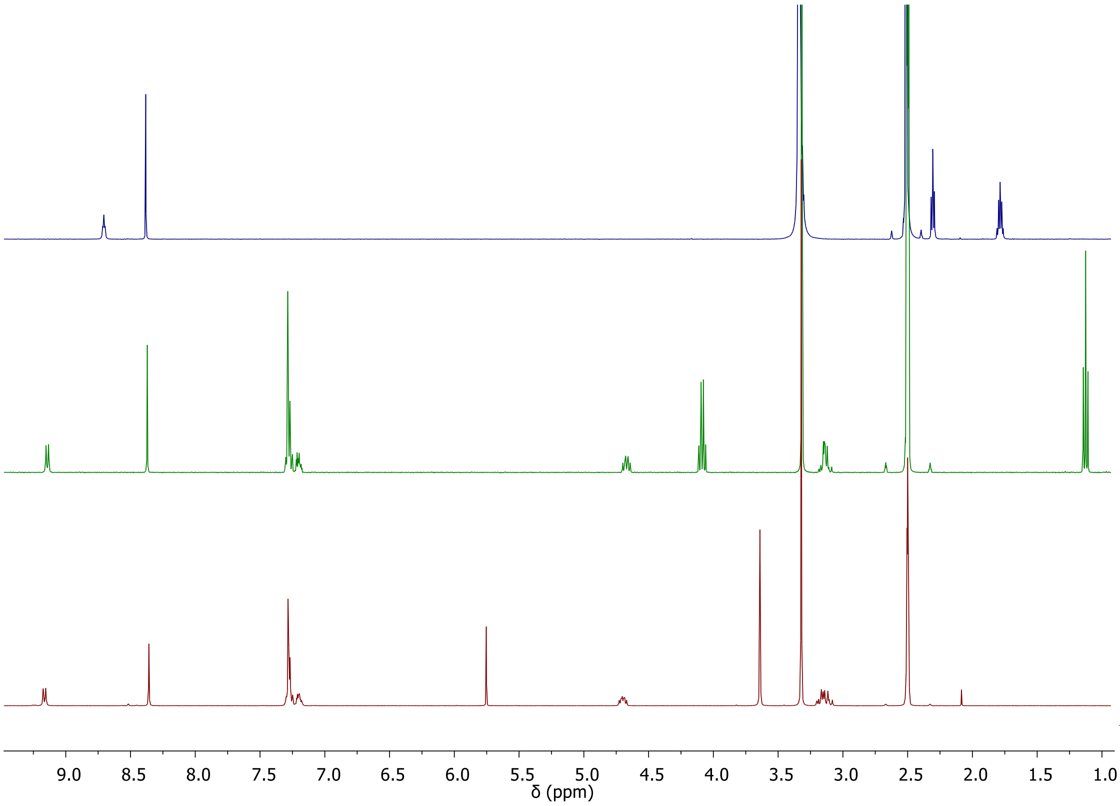

Figure 4.1 ^{1}H NMR (600 MHz and 400 MHz respectively, DMSO-d_6) of the three **BTA** derivatives used, **63** (top), **74b** (middle) and **74a** (bottom).

After the synthesis of the **BTA** derivatives, the attachment of the alkoxy amine chains was attempted using a variety of reaction conditions. Firstly, the phenylalanine derivative (3 equivalents) was dissolved in (i) MeCN or (ii) MeOH, followed by the addition of amine **75** (1 equivalent) to the respective reaction mixtures. The reactions were then refluxed for 24 h. The resulting reaction mixtures were analysed by TLC and indicated the presence of the free amine chain under the UV light after staining with ninhydrin, along with the presence of starting material, thus indicating that the reaction did not work or was very inefficient. This reaction was also carried out in neat, excess amine, however, this too proved unsuccessful.

Changing the approach slightly, it was decided to use a carboxylic acid derivative, **63,** and first convert it to its acyl chloride derivative using either oxalyl chloride or thionyl chloride, followed by reaction with the amine, as shown in Scheme 4.3. **63** was dissolved in $SOCl_2$ and with DMF as catalyst and left to stir at 50 °C for 24 h. The $SOCl_2$ and DMF were then removed by vacuum distillation to reveal a yellow-ish oil. Due to the reactivity of acid chlorides, this product was used without further purification. Six equivalents of the amine (assuming quantitative yield), was dissolved in dry MeCN and Et_3N, with the acid chloride (in dry MeCN) was added to this mixture over a one-hour period using a syringe pump, resembling a pseudo high dilution method in order to minimise di/trimerization and polymerisation.[170] This reaction mixture was then left to stir at room temperature for 48 h, after a yellow oil was recovered and analysed by ^{1}H NMR spectroscopy. The ^{1}H NMR spectrum did not show the presence of as many alkyl protons as would be expected and looked to show the presence of only one amine peak. One of the potential reasons for these reactions being unsuccessful could be due to the length of the chains and the increased steric bulk on each sequential amide formation making

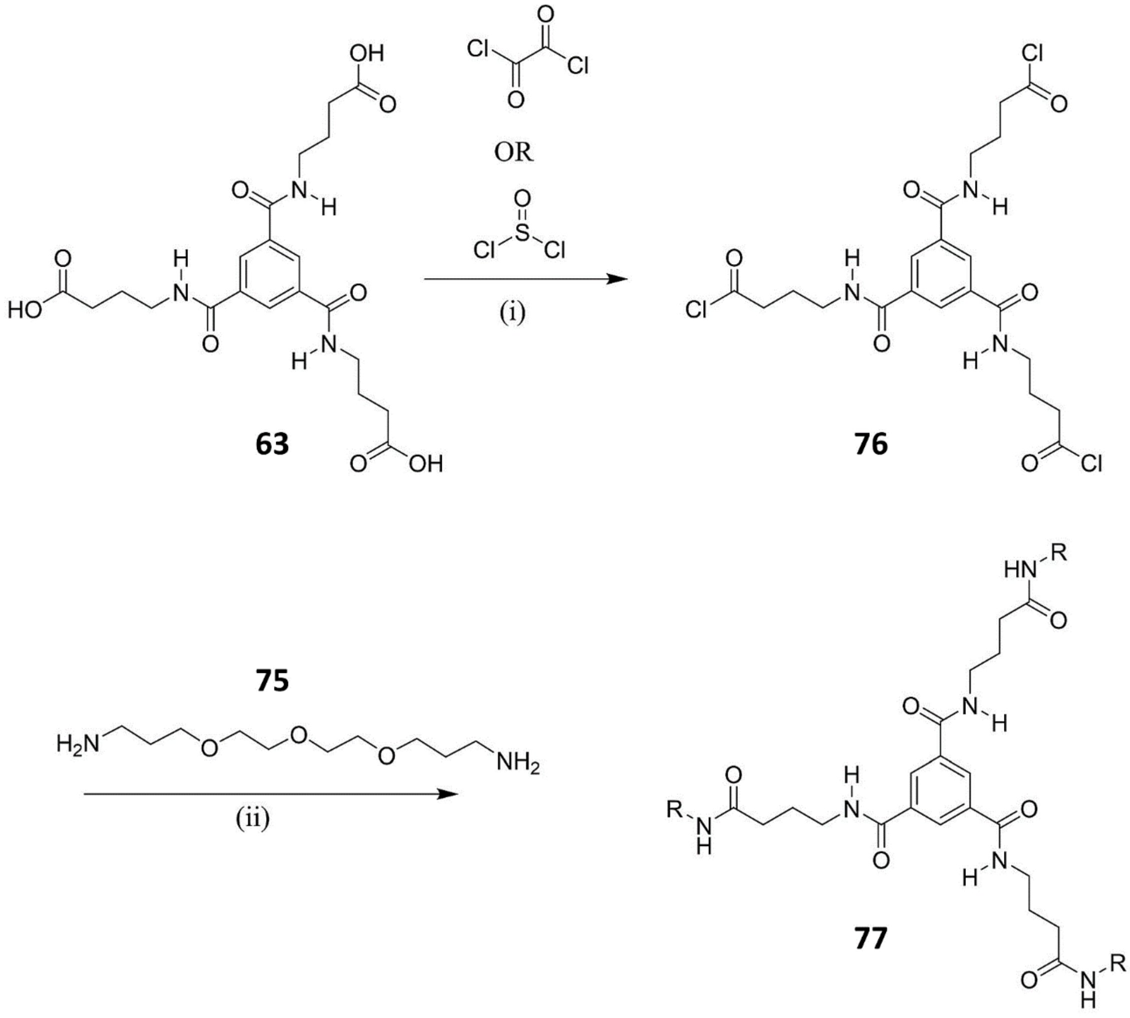

Scheme 4.3 Reaction of **63** with (i) thionyl chloride or oxalyl chloride to result in the acid chloride, followed by (ii) reaction with the amine.

the tri-substitution inefficient. Successful tri-substitution of a **BTA** core with bulky groups also proved difficult with some of the derivatives discussed in Chapters 2 and 3. Taking this into consideration, the approach was again modified and is reflected in Scheme 4.4. The amine was mono-protect one of the amine with a *tert*-butyloxycarbonyl (Boc) group as per a literature procedure, thus allowing the use of more forcing and varied conditions while preventing unselective or uncontrolled polymerisation.[162] This involved dissolving the amine in dry DCM, followed by addition of the Boc anhydride under an argon atmosphere at room temperature for 24 h. After 24 h, the organic layer was subject to aqueous workup, affording a pale-yellow oil. The ^{1}H NMR spectrum of the product was consistent with what was expected and with that reported in the literature.[162]

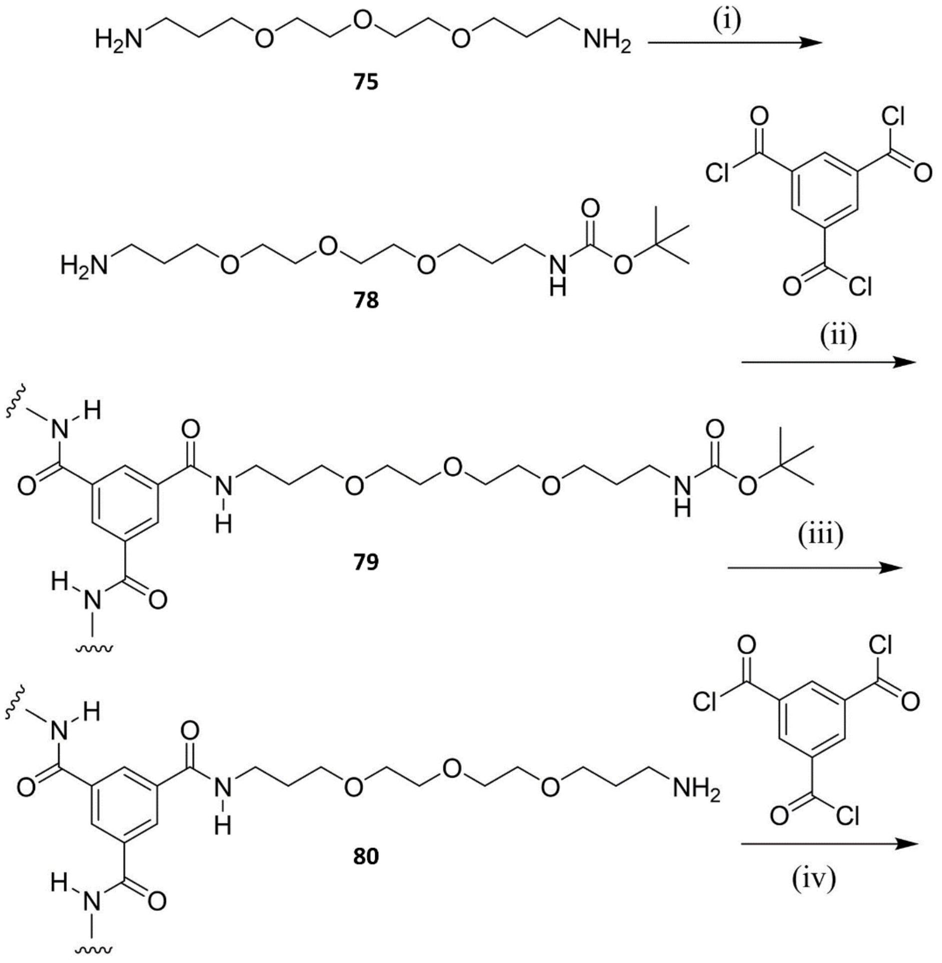

Scheme 4.4 Proposed reaction scheme for the generation of a cross-linked polymer system, where (i) di-*tert*-butyl dicarbonate, dry DCM, rt, 24 h.**,** (ii) dry DCM, Et_3N, rt, 72 h.

The next step in the reaction was to react the boc-protected amine with benzene-1,3,5-tricarbonyl trichloride, Scheme 4.4. The benzene-1,3,5-tricarbonyl trichloride was treated with 3.3 equivalents of Et_3N and **75** in dry DCM. This was then left to stir at room temperature for 72 h. The reaction mixture was then analysed by TLC which revealed the presence of a number of species which were separated by column chromatography on silica. One of the fractions was found to contain benzene-1,3,5-tricarboxylic acid, indicating the inefficiency of the reaction. Another component was isolated as a yellow oil, potentially the desired product and was analysed by NMR spectroscopy, Figure 4.2. Despite attempted purification by column chromatography, the NMR spectrum showed a number of impurities. For the successful tri-substitution of the core, it would be expected that the C_3 symmetry of the molecule would result in CH_2 protons that are symmetric and result in quite a simple NMR spectrum with one set of chemical shifts for the arms. In this case, however, there are more resonances in the aliphatic region that expected, indicating that the tri-substitution was not successful, and a mixture of asymmetric products was obtained. The aromatic region contained three prominent shifts which would be expected for the aromatic core protons and the two amides, however, it too contained a number of other smaller resonances, indicating the presence of other species. A similar observation was made for the $^{13}C\{^1H\}$ NMR, in which there was an excess of signals and can be seen in the appendix.

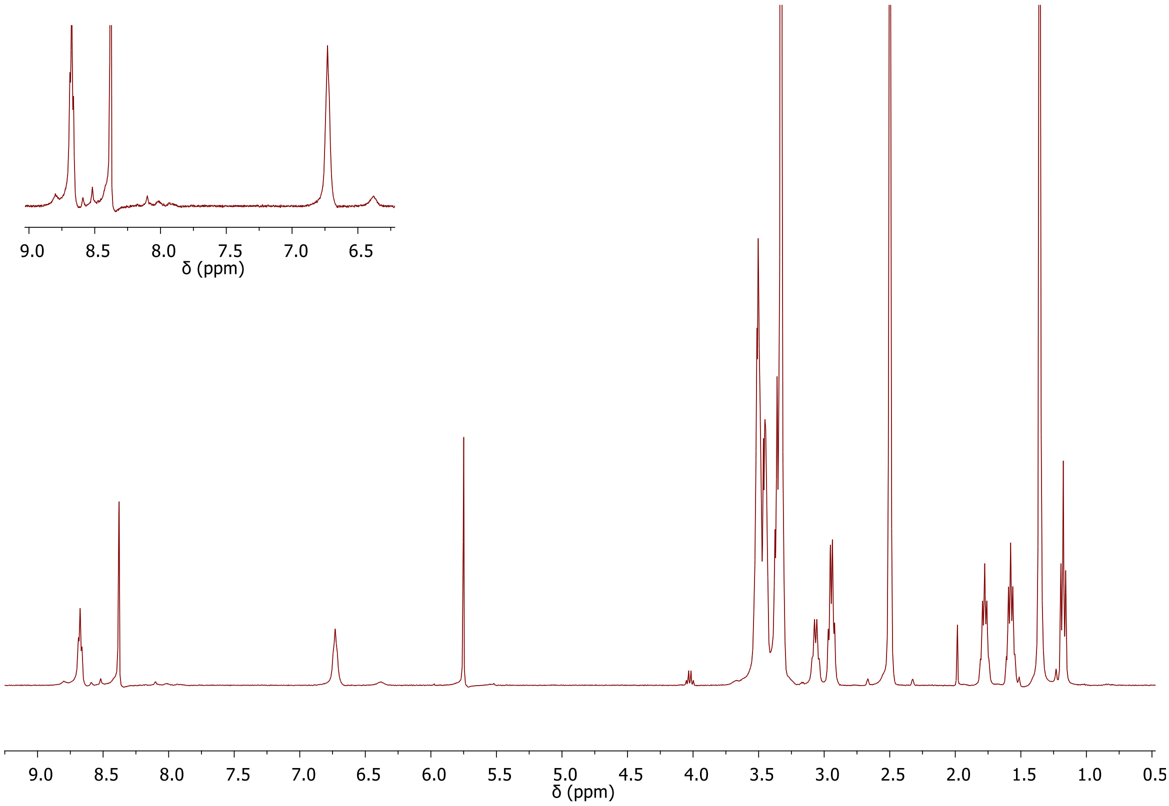

Figure 4.2 ^1H NMR (400 MHz, DMSO-d_6) of **79** showing the excess peaks in the aliphatic region and the inset showing the multiple aromatic peaks.

Taking these results into account, the approach was modified further and a shorter chain amine, 2,2(ethlenedioxy)bis(ethylamine), was used for the tri-substitution of a leucine functionalised **BTA** core, shown in Scheme 4.5. This was inspired by a report by Chen and co-workers in which they reported the synthesis of lysine-based, hyperbranched polymers that mimic the behaviour of endosomolytic cell-penetrating peptides for the purpose of drug delivery.[167] These polymers contained an aromatic core, decorated with lysine side chains and cross-linked with aromatic groups; the chains described here were more hydrophilic in nature. The first step in this approach was to mono-protect one of the amines of the chain, using the same procedure as for the **75**, Figure 4.4.[162] Once the reaction was complete, the product was analysed by NMR spectroscopy and mass spectrometry, with the ^{1}H NMR spectrum showing the appearance of the CH_3 of the Boc protecting group. The mono-protection was also confirmed by the mass spectroscopy, as detailed in 6.2.3. Following this, it was again attempted to attach this group to the leucine functionalised **BTA** core, using a coupling reaction, using the

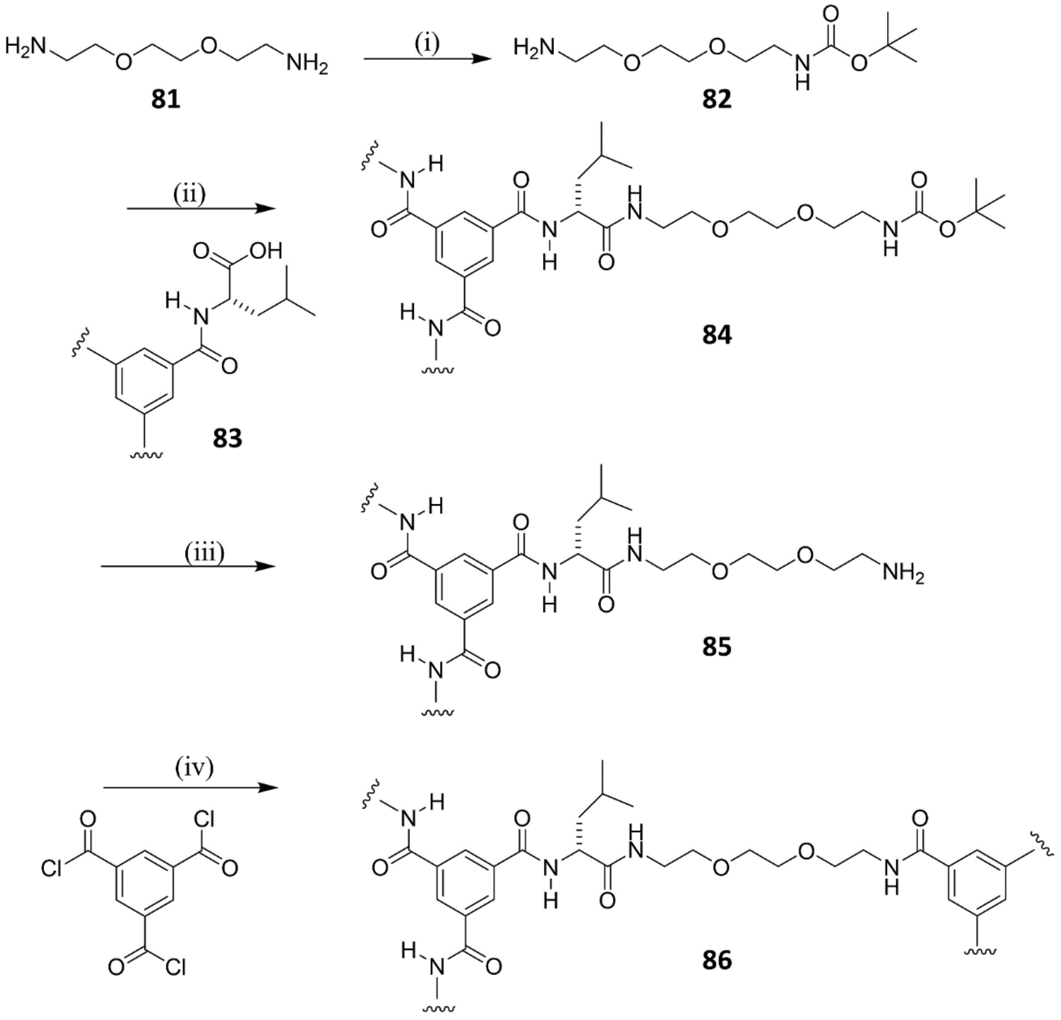

Scheme 4.5 Synthetic scheme for the synthesis of a leucine-based **BTA** polymer, **86**, where (i) di-*tert*-butyl dicarbonate, dry DCM, rt, 24 h, (ii) EDC.HCl, DMAP, dry DCM, rt, argon, 72 h, with (iii) and (iv) being the planned further steps.

same conditions as used previously in Chapters 2 and 3 for the coupling of an amine and carboxylic acid. Unfortunately, this reaction was unsuccessful, with the ^{1}H NMR of the material isolated after the reaction found to be the **BTA-**leucine starting material.

The last attempt made to generate an extended **BTA** polymer was to first couple a simple amino acid to the amine chain and then attempt to react this with benzene-1,3-5-tricarbonyl trichloride, as demonstrated in Scheme 4.6 to generate an extended polymer by reaction of both amines with the **BTA**-Cl. The first step was to protect the amine of the leucine which was carried out using a procedure reported by Adolfsson and co-workers.[171] This was then to be coupled to the mono-protected amine chain previously synthesised, using the standard coupling reaction conditions. This resulted in a white solid which was then subject to column chromatography. One of the fractions obtained appeared to contain the product by TLC analysis, thus this was evaporated to give a small amount of yellow oil. NMR studies, along with mass spectrometry indicated that the reaction was a success, however, the poor yield, the presence of impurities even after purification attempts and general inefficiency of the reaction,

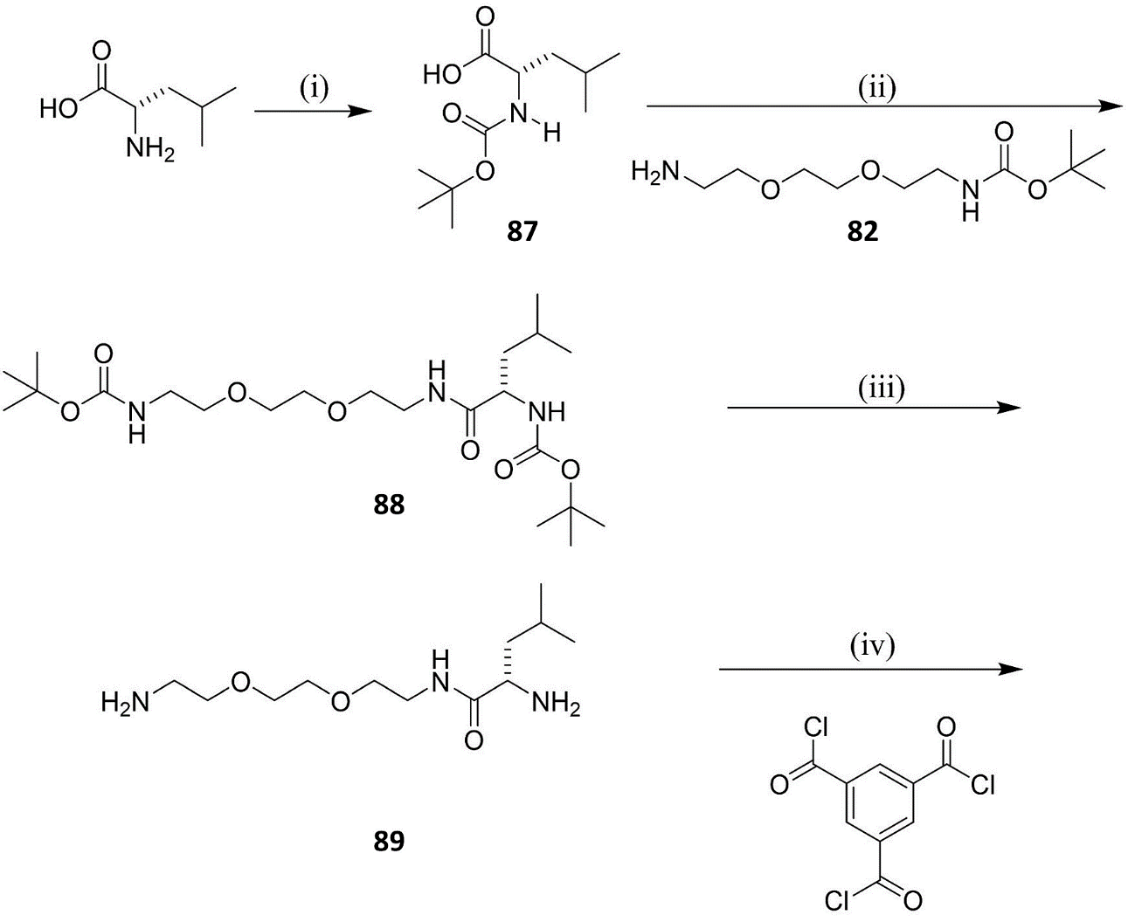

Scheme 4.6 Synthetic scheme for the polymer with the shorter chain where (i**)** di-*tert*-butyl dicarbonate, dry DCM, rt, 24 h, (ii) dry DCM, EDC.HCl, DMAP, argon, rt, 72 h, with (iii) and (iv) representing planned further steps.

prompted a change in focus to generating more dynamic polymers which will be discussed in the next section.

4.3 A Schiff-base cross-linked supramolecular polymer

The focus switched then switched from covalently linked polymers to non-covalent, more dynamic polymers. For this purpose, the **BTA** core was chosen due to its known aggregation properties,[14,108,157] with this functionalised with diiminophenol-based side chains, due to their well-established coordination chemistry.[172] As previously mentioned, the **BTA** core offers a readily modifiable core and it has been widely reported that the modification of the side chains can alter the bulk properties of the resulting materials.[86,103,173] Furthermore, metal coordination can further influence the nature of the materials and impart metal-centred functionalities, for example magnetic, photophysical or catalytic activities,[174] to the resulting materials. The reversible condensation between an amine and an aldehyde is one of the oldest and ubiquitous reactions in organic chemistry, with the product of this reaction known as ‘Schiff bases’.[175] The formation of an imine bond is an efficient reaction which involves the loss of H_2O when an amino and carbonyl group react to form a C=N bond either intra- or intermolecularly and can be catalysed using acid. The Schiff base linkage has been used in a wide variety of intricate molecular architectures,[176] for example helicates and metal-organic polyhedra,[177] while also being used as a linking element in the formation of covalent organic polymers and other extended organic systems.[178] Due to their well-established coordination chemistry and ready availability, 2,6-diiminophenol-derived synthons are ideal candidates as linking groups for functional organic polymers, readily from in solution and have the capacity for metal chelation. Taking all this into account, a functional Schiff base containing organic polymer, the combination of the **BTA** core motif with diiminophenol linkers and the physical and morphological properties of the resulting material and its interaction with Cu(II) ions will be discussed in the following section. The compounds studied are depicted in Scheme 4.7.

This project was carried out in collaboration with visiting student, Marcel Klein-Hitpaβ, while the X-ray crystallography was carried out, the data solved and refined by Dr Chris Hawes (TCD, Keele University).

4.3.1 Synthesis and characterisation of 90 and 91

The first step in the generation of the **BTA**-Schiff base polymer was the reaction of trimethyl-1,3,5-benzenetricarboxylate with ethylenediamine, Scheme 4.7, using a procedure previously reported by Xu and co-workers.[179] This reaction involved the addition of benzene-1,3,5-tricarboxylate to MeOH which was then added dropwise to the amine solution. The mixture was stirred at 0 °C for 30 min and then at room temperature for 24 h. Once the reaction was complete, the excess ethylenediamine was removed *in vacuo* and residual ethylenediamine removed by a toluene/MeOH azeotrope. The product was obtained as a white solid in excellent yield, 98% and fully characterised, with these results in agreement with both what was expected and reported in the literature.[179]

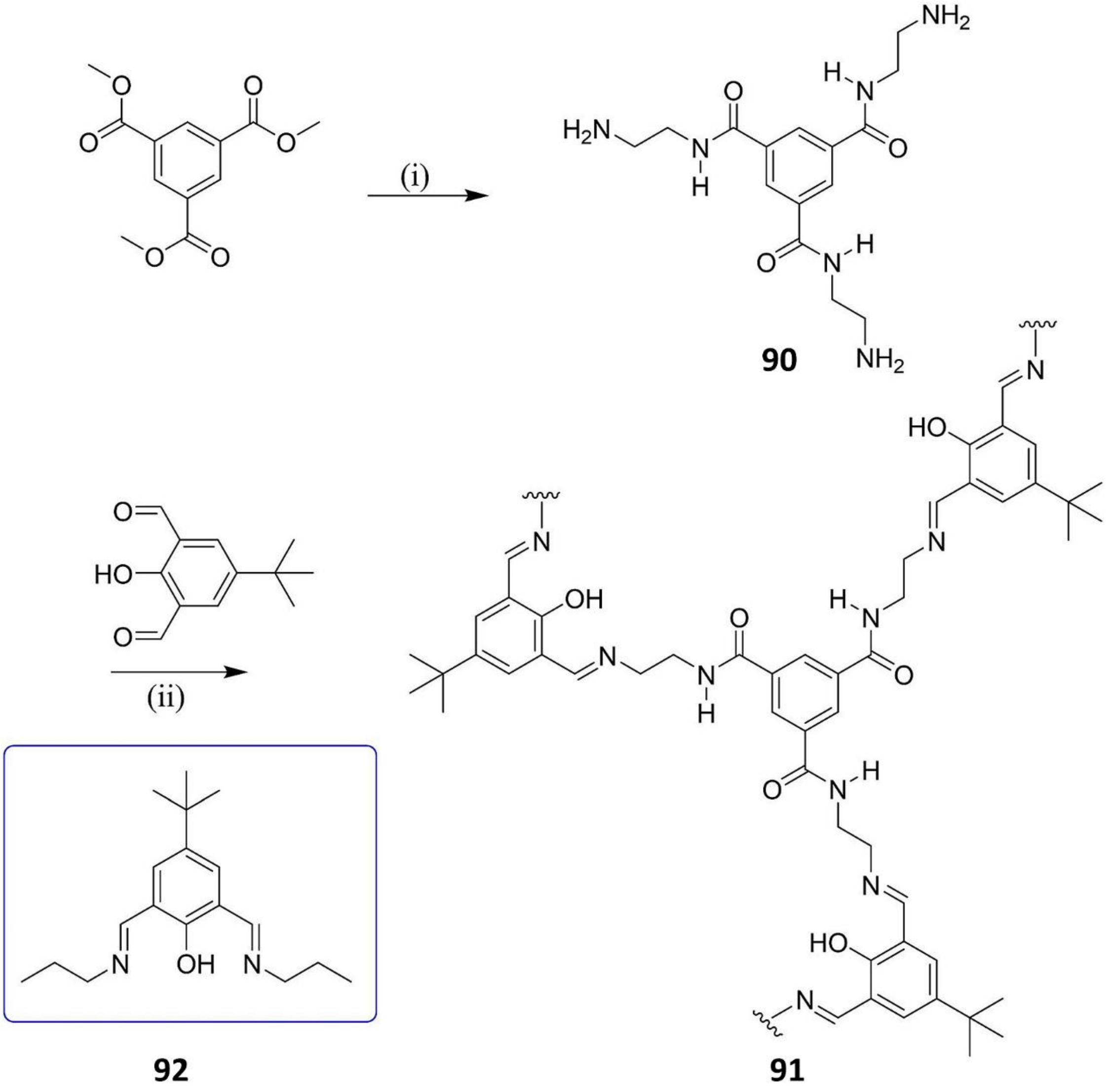

Scheme 4.7 The reaction scheme for the generation of the organic polymer, **91**, where (i) 1,2-ethylenediamine, MeOH, rt, 24 h and (ii) EtOH, rt, 18 h. Shown in the blue inset is the structure of the model compound, **92**.

Following this reaction, the triamine, **90**, was reacted with 4-tert-butyl-2,6-diformylphenol at room temperature in ethanol to generate the organic polymer, **91**. The product obtained was a yellow solid and was found to be insoluble in common NMR solvents such as DMSO-d_6, $CDCl_3$, MeCN-d_3 and MeOH-d_4, thus it was characterised using solid state NMR and X-ray powder diffraction. Solid-state $^{13}C\{^1H\}$ NMR was collected and compared to the solution-state spectra of the starting materials. The carbonyl signal of the dialdehyde precursor at 193 ppm disappears in the spectrum of the polymer, being replaced by a resonance characteristic of an imine, which overlapped with the amide and *ipso*-phenol signals in the 150-175 ppm region. The signal at approximately 60 ppm is consistent with the CH_2 group nearest the imine nitrogen atom, which undergoes a downfield shift following the formation of the Schiff base. The X-ray powder diffraction of the material revealed it to essentially amorphous in nature and is shown in the appendix.

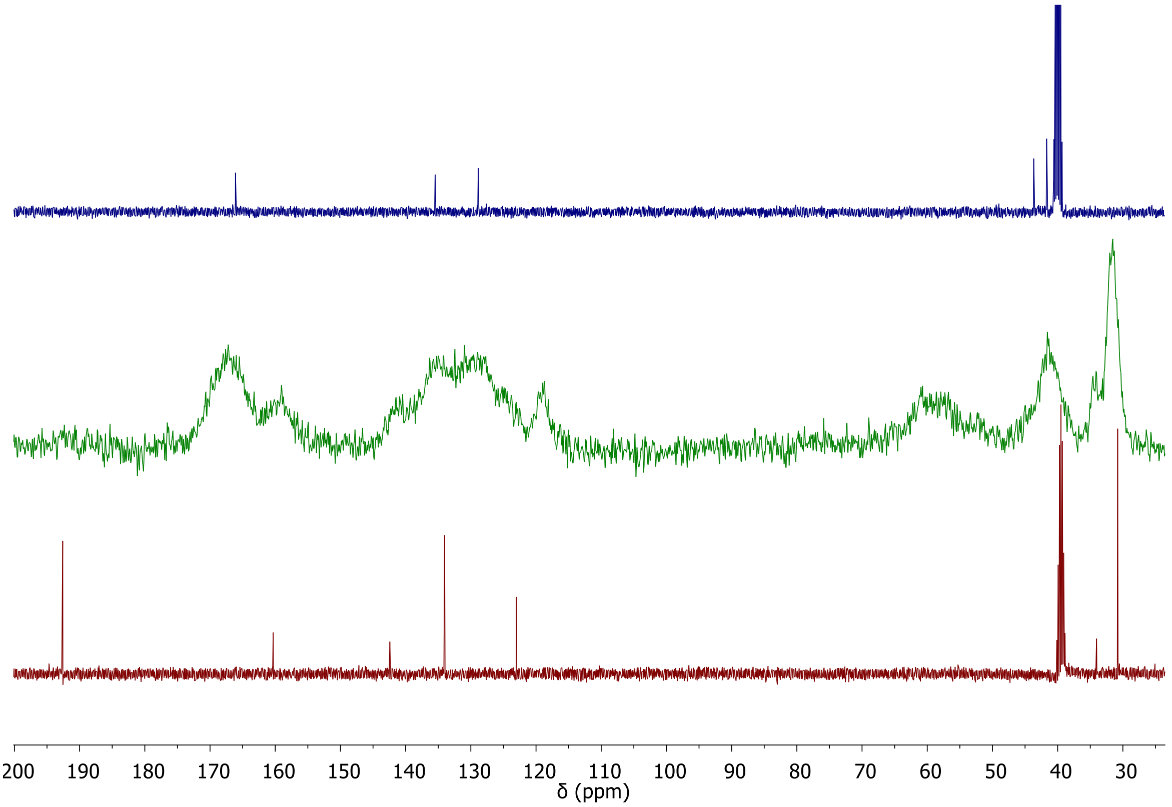

Figure 4.3 Comparison of ^{13}C NMR spectra for N, N´,N´´-tris(2-aminoethyl)benzene-1,3,5-tricarboxamide, **90** (d_6-DMSO, green), polymer **91** (CP-MAS, red) and 4-*tert*-butyl-2,6-diformylphenol, **92**, (d_6-DMSO, blue).

Thermogravimetric analysis of the polymer **91** is shown in Figure 4.4 and a steep mass loss of approximately 15% occurred between 25-50 °C which was followed by a gradual loss of a further 15% between 50-300 °C. A multi-step decomposition process was initiated at 325 °C, followed by a gradual mass loss up to 500 °C. the curve indicates that the presence of encapsulated volatile species. These are most likely solvent molecules and are consistent with

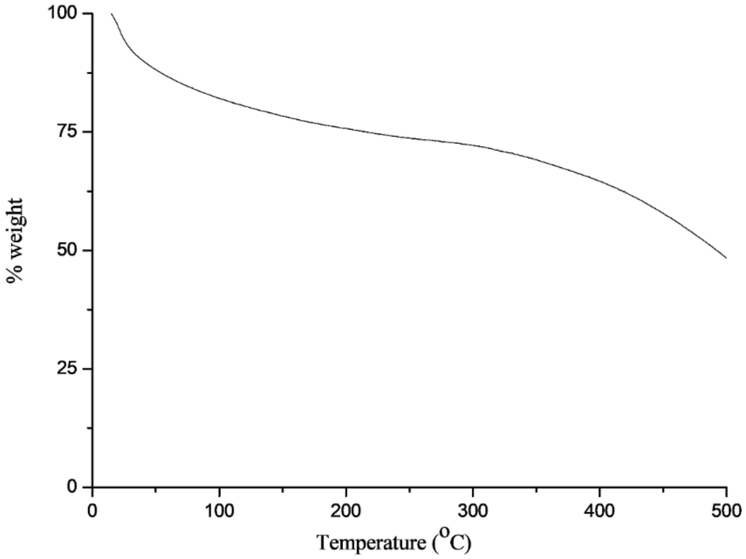

Figure 4.4 TGA of polymer **91** showing the initial weight loss of 15% below 50 °C, followed by a gradual loss of a further loss of 15% between 50-300 °C and then the onset of decomposition.

the results of the elemental analysis which indicated the presence of encapsulated water, which was most likely retained either after drying in vacuo or re-adsorbed from exposure from air.

The morphology of the polymer was studied by SEM. The sample was prepared by carrying out the condensation reaction with a silicon slide immersed in the reaction medium, with the adsorbed sample dried *in vacuo* before SEM analysis. The images obtained are shown in Figure 4.5 and show the polymer to consist of a tightly packed, dense network, with the individual particles having a smooth, approximately spherical shape. These particles appear to be fused to one another and form a thick layer on the silicon support.

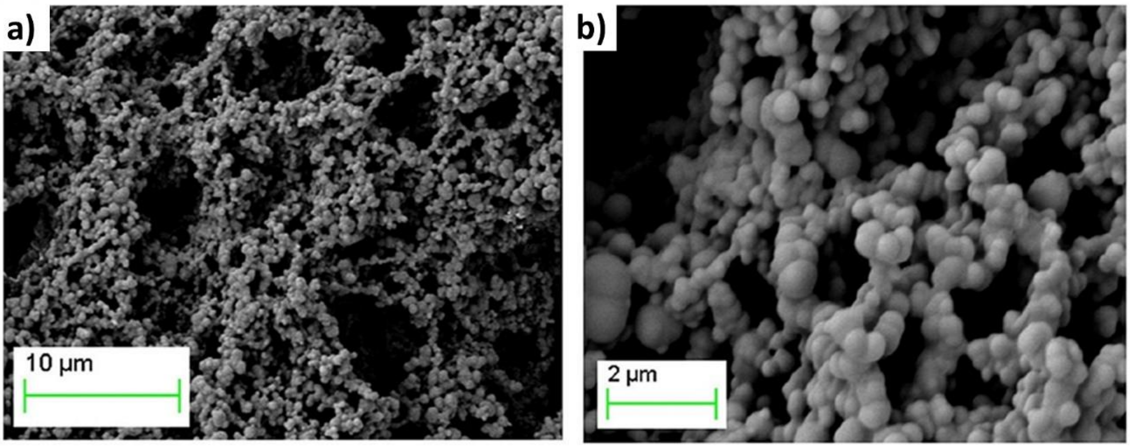

Figure 4.5 SEM images of the polymer **91** which was grown directly onto the silicon support, scale bars (a) 10µm and (b) 2 µm.

Following this, the potential porosity of the sample was examined using N_2 adsorption studies, carried out in collaboration with Mr Kevin Byrne (of Prof Wolfgang Schmitt’s group, School of Chemistry, Trinity College Dublin). The polymer was subject to N_2 adsorption studies which suggested that the material has a large pore size distribution and no significant microporosity. Surface area calculations are one of the most useful in characterising porous materials, with the BET analysis being one of the standard methods for determining the surface areas from the nitrogen adsorption data.[154] BET analysis relies on a number of assumptions, for example, it assumes that adsorption occurs by multilayer formation and the number of adsorbed layers is infinite at the saturation pressure. BET allows for a allows for a ranking of materials relevant to one another.[154] The BET surface area of this material was calculated and found to be *ca.* 12 m^2/g, indicative of no significant porosity, (see appendix).

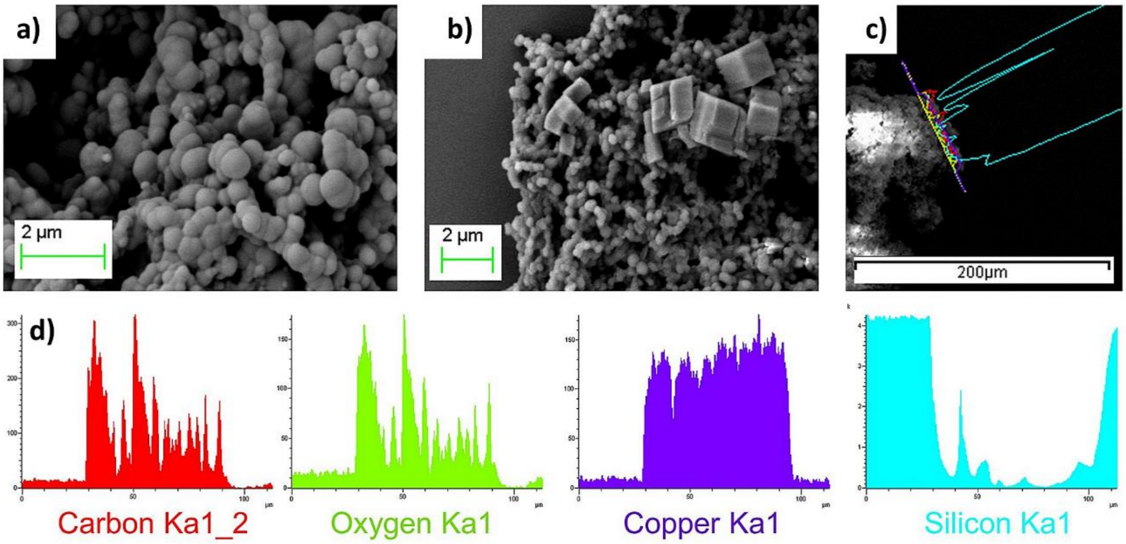

Figure 4.6 (a) SEM of the polymer, scale bar 2 µm, (b) SEM images of **91** after immersion in the copper solution, (c) area for the line mapping experiment of the immersed polymer and (d) the intensity profiles from the line mapping experiments showing the presence of (left to right) carbon, oxygen, copper and silicon.

Following the studies on the organic polymer, its interaction with Cu(II) ions in solution was investigated. The polymer was immersed in a solution of copper acetate in MeOH (5 mg/mL), with SEM analysis of the polymer after immersion in the copper solution is shown in Figure 4.6 and shows that the original morphology of the polymer is maintained but with the addition of small crystallites present on the surface of the particles. The nature of the surface coating was further investigated using EDX spectroscopy, which was carried out on both the polymer alone and the copper-soaked polymer. This analysis confirmed the presence of copper on the surface of the immersed polymer, while EDX on the polymer alone confirmed it to be purely organic in nature. A line mapping EDX experiment showed that the copper species was dispersed co-incident with the organic material and separate from any potential superficial copper coating artefacts present on the silicon support. The SEM and EDX would suggest that the copper salt is just present on the surface of the polymer, rather than coordinated to the polymer. The EDX experiment of the polymer alone can be found in the appendix.

4.3.2 Synthesis and characterisation of model compound 92

With the aim of gaining a more quantitative understanding of the possible modes of interaction between the copper ions and **91**, a model compound that contained a single diiminophenol binding site with *n*-propyl tails was prepared. The aim of this was to combine the X-ray structural data and FTIR data and to compare this to the copper-immersed polymer. The structure of the model compound is shown in Scheme 4.8. The model compound was prepared by the *in-situ* reaction of 4-*tert*-butyl-2,6-diformylphenol with two equivalents of *n*-propylamine in methanol at reflux. Once the product was obtained, attempts to crystallise metal complexes of this ligand directly from the reaction mixture or other alcohol solvents to imitate the soaking conditions of **91** were unsuccessful and thus, MeCN was then used instead. The yellow MeOH solution of the ligand was evaporated and gave a yellow oil which was then taken up in MeCN and combined with a solution of Cu(II) acetate hydrate in MeCN. The resulting green solution was left to stand for 48 h to yield dark green crystals, which were then isolated by filtration and subject to single crystal X-ray diffraction.

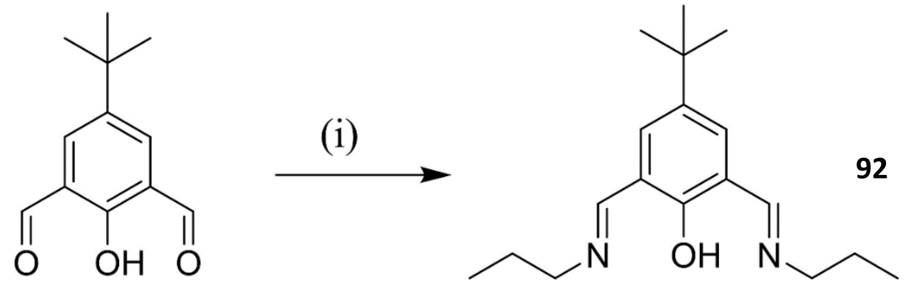

Scheme 4.8 Synthesis of the model **92** where (i) C_3H_9N, MeOH, reflux.

The diffraction data for the copper complex were solved and the structural model refined in the monoclinic space group $P2_1/c$. The asymmetric unit was found to contain the molecule in its entirety and no associated solvent molecules or guests. The complex consists of a tetrahedral Cu_4O centre, surrounded by four acetato ligands that each bridge between two pairs of copper ions as shown in Figure 4.7. The remaining coordination sites are occupied by two ligand molecules that each bridge two copper ions. The six unique Cu–Cu distances fall in the range 3.0154(14) – 3.1983(14) Å and are typical of [Cu_4O] cores.[180] The overall structure of the model compound is quite similar to those derived from other 4-substituted 2,6-diformylphenols and various alkylamines under similar reaction conditions,[181,182] and can also be considered as being typical for acyclic diiminophenol ligands in general, thus demonstrating the suitability of this compound as a model for **91**. This is shown in Figure 4.8, in which the structures reported by Banerjee and co-workers are very structurally similar to that of the model compound **92**.[181]

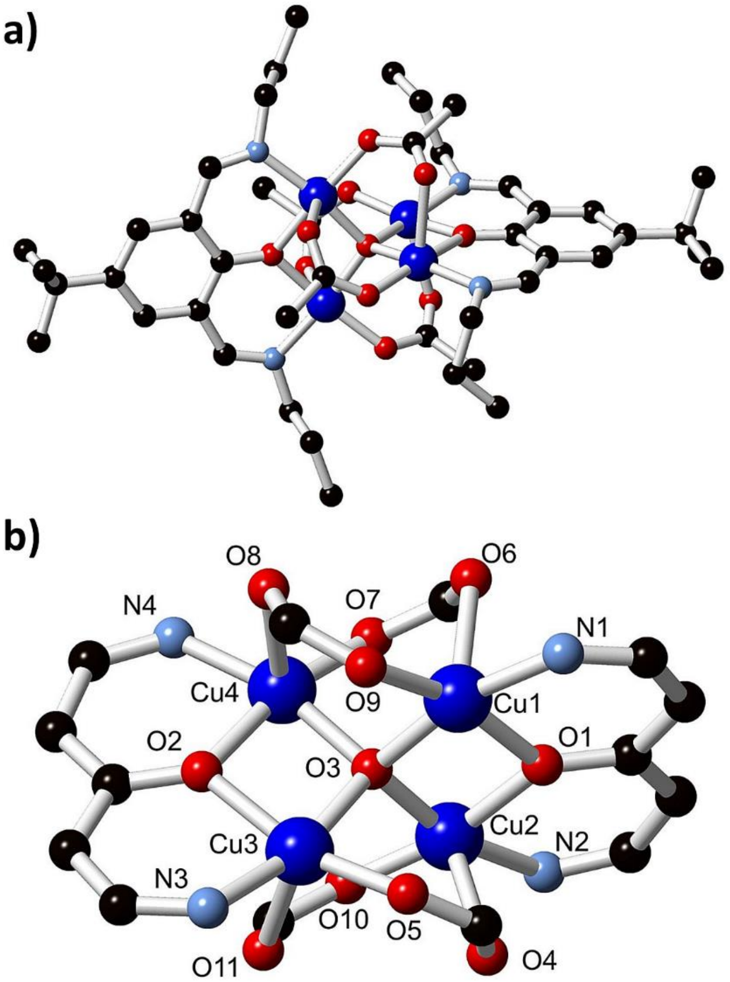

Figure 4.7 X-ray crystal structure of the model compound, **92**, showing (a) the structure of the complete complex and (b) the core connectivity with labelling scheme. Hydrogen atoms are omitted for clarity.

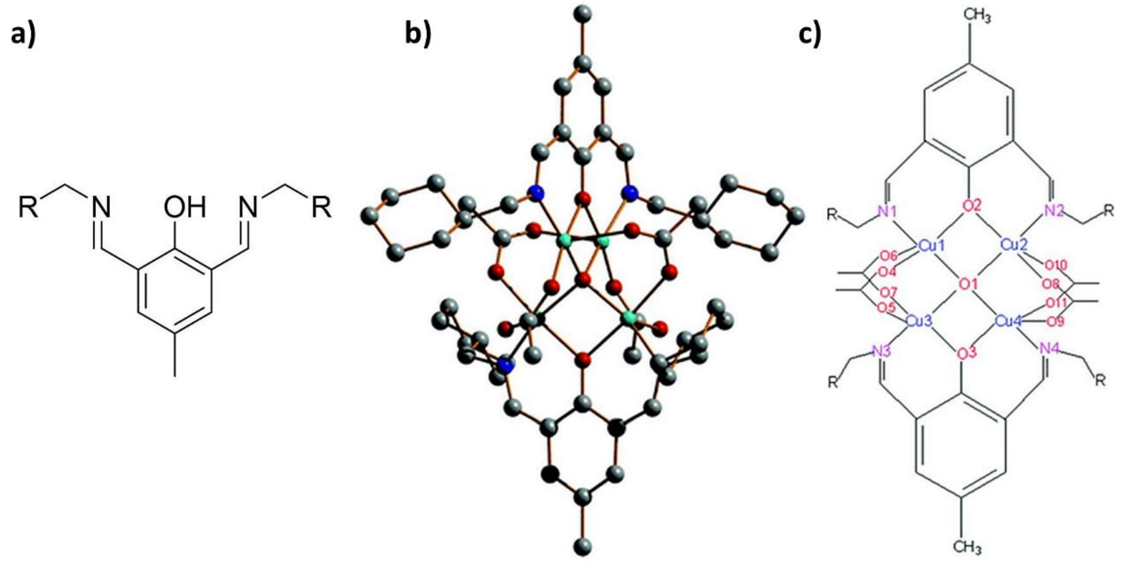

Figure 4.8 (a) Structure reported by Banerjee and co-workers where R = a variety of phenyl groups. (b) a perspective view of the one of the reported copper complexes and (c) the metal and donor connectivities for the reported complexes. Images reproduced from reference 31.

Further structural comparisons between the model compound and the polymer **91** were made using FTIR in an attempt to ascertain the nature of the copper binding that occurs on the surface of the polymer **91**. The IR spectra of **91**, Cu polymer **91**, model compound **92** and Cu(II) acetate hydrate were measured and are shown in Figure 4.9. The majority of the organic functional group absorbances are retained upon addition of Cu(II) acetate to ligand **91**, for example, the overlapping amide C=O and imine C=N stretching bands (maxima at 1637 cm^{-1}) and the aromatic C–C stretch at 1527 cm^{-1}. The addition of copper to **91** gave rise to new stretches at 1585, 1447-1423, 1067, 677 and 619 cm^{-1} with these bands assigned to the acetate/acetato species, thus confirming the inclusion of these species in addition to the polymer

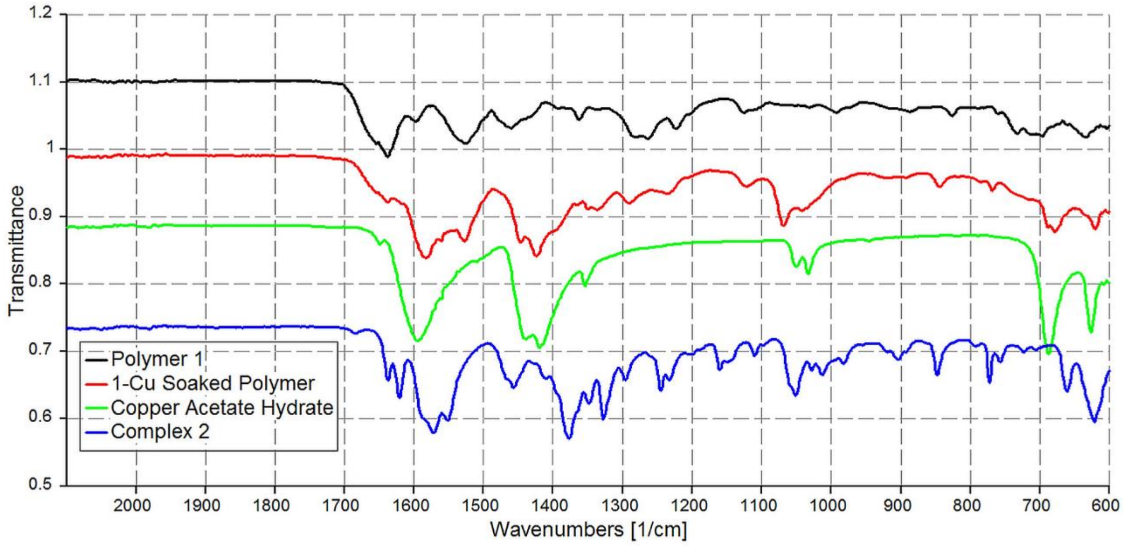

Figure 4.9 Offset FTIR spectra of **91** (black), Cu polymer **91** (red), Cu (II) acetate hydrate (green) and complex **92** (blue).

species (confirmed by EDX spectroscopy, Figure 4.6). By comparing the acetato stretches, it would appear that the Cu polymer **91** strongly resembles the sum of the spectra of ligand **91** and pure Cu (II) acetate hydrate. The carboxylate ν_{asym} and ν_{sym} bands of both are in close agreement, with the difference between the two being approximately 165 cm^{-1} for polymer **91**, the difference, Δ, for Cu(II) acetate is 175 cm^{-1}.This parameter is known to be indicative of the mode of carboxylate binding, with a Δ of < 100 cm^{-1} for chelating carboxylates, ~160 cm^{-1} for ionic carboxylates and fully symmetric bridging while the Δ for monodentate or unsymmetrically bridging carboxylates can be > 300 cm^{-1}.[183] Thus, this would indicate that the carboxylates in polymer **91** are symmetrical, unlike those in **92** in which Δ is 200 cm^{-1}, suggesting a lower symmetry character in the bridging mode of **92** compared to Cu(II) acetate and **91**. This lower symmetry character is corroborated by the X-ray crystal structure in which each of the four unique carboxylate groups coordinates to one axial and one equatorial site of the square pyramidal copper ion. The Cu–O bond distances for each acetate differ by on average 15-20% of the average Cu–O bond length. Further evidence of this asymmetry is evident when the carbon-oxygen bond lengths are examined, with the more weakly bound oxygen atom showing a greater carbon-oxygen double bond character, with the bond distances falling, on average, 0.06(2) Å shorter than those of the more strongly bound oxygen atom for each of the four ligands.

The sum of the spectroscopic observations would suggest that there is a strong relationship between the structure of the bound copper ions in polymer **91** to the paddle-wheel structure of Cu(II) acetate and its solvates,[184] rather than the diiminophenolate-chelated species that is observed in **92** and related complexes.

Further investigations of the interaction of **91** with d-block metals ions were carried out in equivalent soaking experiments to that used for copper, *i.e.*, soaking the polymer in methanolic solutions of Co(II) acetate tetrahydrate and Zn acetate dihydrate. The cobalt-soaked polymer gave an IR spectrum that appears to be the sum of the free polymer and the metal salt, shown in Figure 4.10, thus indicating that the metal salt is not interacting with the polymer. On the other hand, soaking the polymer in the zinc solution resulted in a broadening and reduction in intensity of the ν_{sym} (COO) absorbances and variations in the positions and intensities of the CH_3 rocking modes compared to the pure zinc metal salt, thus indicating some degree of interaction between the two species, Figure 4.10. The implication of a more significant interaction between Zn(II) and the polymer in comparison to the interaction between the Cu(II) and the polymer, is in keeping with the chemical properties of the two metal salts. Zinc has less of a tendency to form rigid paddlewheel-type coordination behaviour and there are a wider range of possible coordination geometries for this particular case.

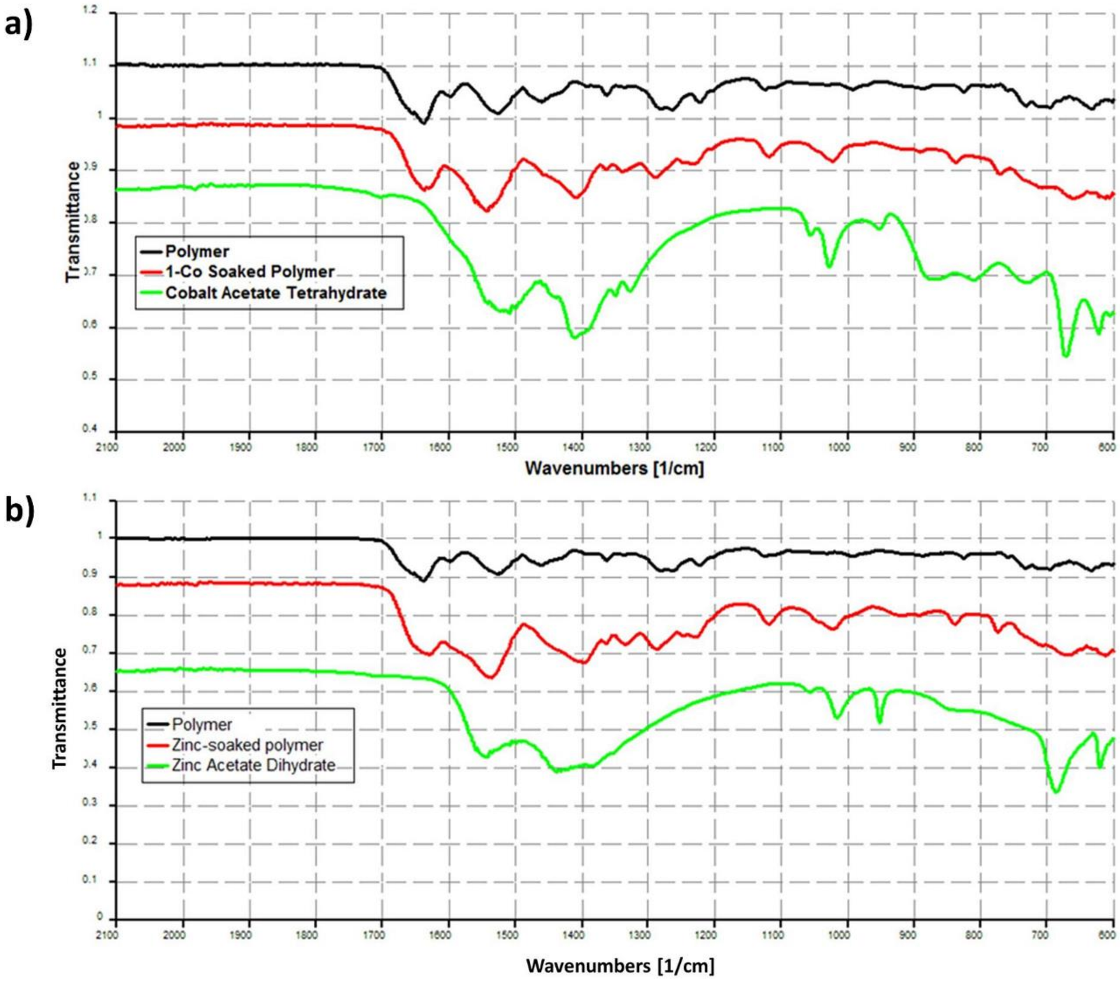

Figure 4.10 (a) Offset FTIR spectra for the polymer **91** (black), cobalt-soaked polymer (red) and cobalt acetate tetrahydrate (green) and (b) offset spectra for the polymer (black), zinc-soaked polymer (red) and zinc acetate dehydrate.

In summary, ligand **91** has a granular, spherical morphology and was found to be amorphous by X-ray powder diffraction and acts as a substrate for the deposition of copper acetate from an alcohol solution. The presence of copper on the surface was confirmed using EDX spectroscopy and was further probed using FTIR. The IR studies involved a comparison between the **91**, the soaked polymer of **91**, Cu(II) acetate hydrate and the model complex **92**, which revealed the soaked polymer to be more like the paddlewheel structure of the Cu(II) acetate rather than the model complex. This implied that the mechanism of adsorption was based on nucleation of a copper acetate on the surface of the polymer, rather than binding within the Schiff-base compartments of the polymer itself. The experiments with Co(II) revealed a similar behaviour to that of Cu(II), while the Zn(II) ions displayed more of a tendency for chemical transformation on the polymer surface.

4.4 Conclusions and future perspectives

In summary, two different approaches were investigated to generate polymeric materials based on **BTA** amine-based precursors. The first approach was to generate a covalently linked system, which resulted in a number of synthetic challenges. Unfortunately, the target molecule was not obtained in sufficient yield and purity to warrant further study. The synthetic difficulties are thought to be due to a number of factors including the difficulties in achieving efficient tri-substitution of the core with bulky side chains and the solubility similarities between the mono-, di and tri-substituted products. Further modification of the target molecule, for example a modification in hydrophilicity and chain length, may result in a more efficient synthesis and should be the subject of future study.

The second section of this chapter discussed the synthesis and characterisation of a non-covalent, more dynamic polymer. This polymer contained a **BTA** core and was functionalised with diiminophenol-based side chains to form a Schiff-base linked organic polymer, **91**. The morphological and physical properties of this material and its interactions with a variety of metals were probed using a variety of techniques, for example, X-ray powder diffraction, SEM, EDX and IR spectroscopy. It was found that the polymer interacts with Cu ions through a nucleation or seeding mechanism rather than via chemisorption within the diiminophenol binding pockets, with Co ions displaying a similar effect, while Zn ions appear to display a different binding mode. Further work in this area could include modification of the organic polymer to allow for to incorporation of transition metals into the binding pockets.

The area of supramolecular polymers and materials is a rapidly developing field, with these materials offering many advantages over existing technologies, for example, in the areas of sensing, plastics, medical devices and optoelectronics.[40,56,61,93,163,185] The **BTA** motif offers a readily modifiable core, known for its aggregation properties and is an ideal candidate for the basis of many of these potential materials and applications, however, much work is still required in order to better tune the synthesis and predict the behaviours of its materials.

‘That’ll do pig, that’ll do.’

Ending scene, Babe

5. Structural studies of a series of pyridine-3,5-dicarboxamides

5.1 Introduction to the pyridine-3,5-dicarboxamide motif and recent related examples in this field within the Gunnlaugsson group

Moving away from the **BTA** core unit, we decided to investigate the effect of side chain on the self-assembly of conceptually related core, the pyridine-3,5-dicarboxamide motif. In this case, there are two sites available for side arm functionality, along with the pyridine nitrogen available for metal coordination. The aim of this work was to study the effect of functionalising this pyridine core with the same side arm groups as were used in the **BTA** work and some simple amino acids and then investigate the structural features of the resulting materials. Previous work within the Gunnlaugsson group has focused on the pyridine-2,6-dicarboxamide motif,[16,73,186,187,188,189,190] with a variety of derivatives and applications reported. For example, Lincheneau and co-workers reported the formation of two complexes based on a tryptophan-based pyridyl amide ligand and the lanthanides europium and terbium.[190] In this work, both enantiomers were synthesised, and the crystal structures were obtained, followed by solution studies of the complexes formed by the ligands and europium or terbium. These solution studies revealed the exclusive formation of a 2:1 ligand/metal complex in the case of both metals, while the expected 3:1 stoichiometry was not formed suggesting that steric hindrance or α-amino ester participation is preventing the 3:1 complex from forming.

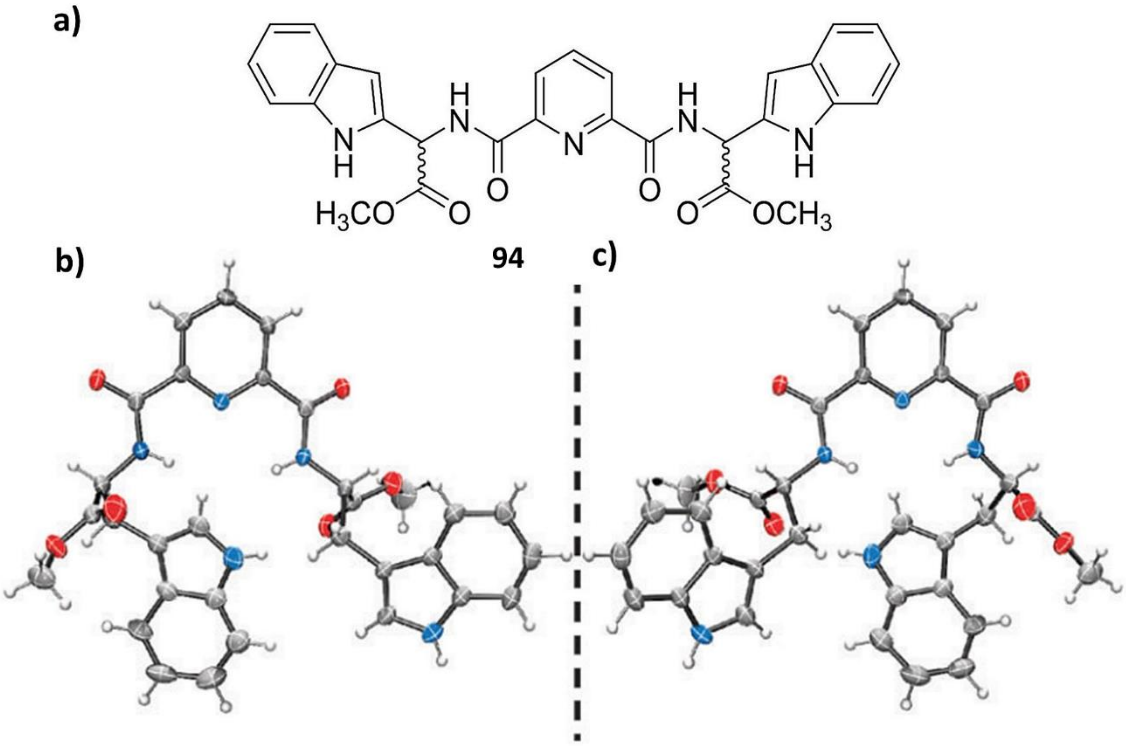

Figure 5.1 (a) Tryptophan-based pyridyl amide ligand synthesised by Lincheneau and (b&c) the X-ray crystal structures of the (S,S) and (R,R). Image reproduced from reference 190.

Another example from the group involved the study of the ligands shown below in Figure 5.2 in which the pyridine core was functionalised with naphthyl ethylamide groups.[186] Here, the single crystal X-ray structures of the ligands were reported and showed that the two ligands adopt the same overall arrangement in which the amide NH protons are oriented in such a way that they point inwards towards the pyridyl nitrogen atom, thus allowing for two hydrogen bonds to one carbonyl oxygen acceptor on the neighbouring molecule. Single crystals of the europium complexes were also obtained and revealed that the Eu(III) centres were coordinated by three ligands, through each of the pyridyl nitrogen atoms and the adjacent

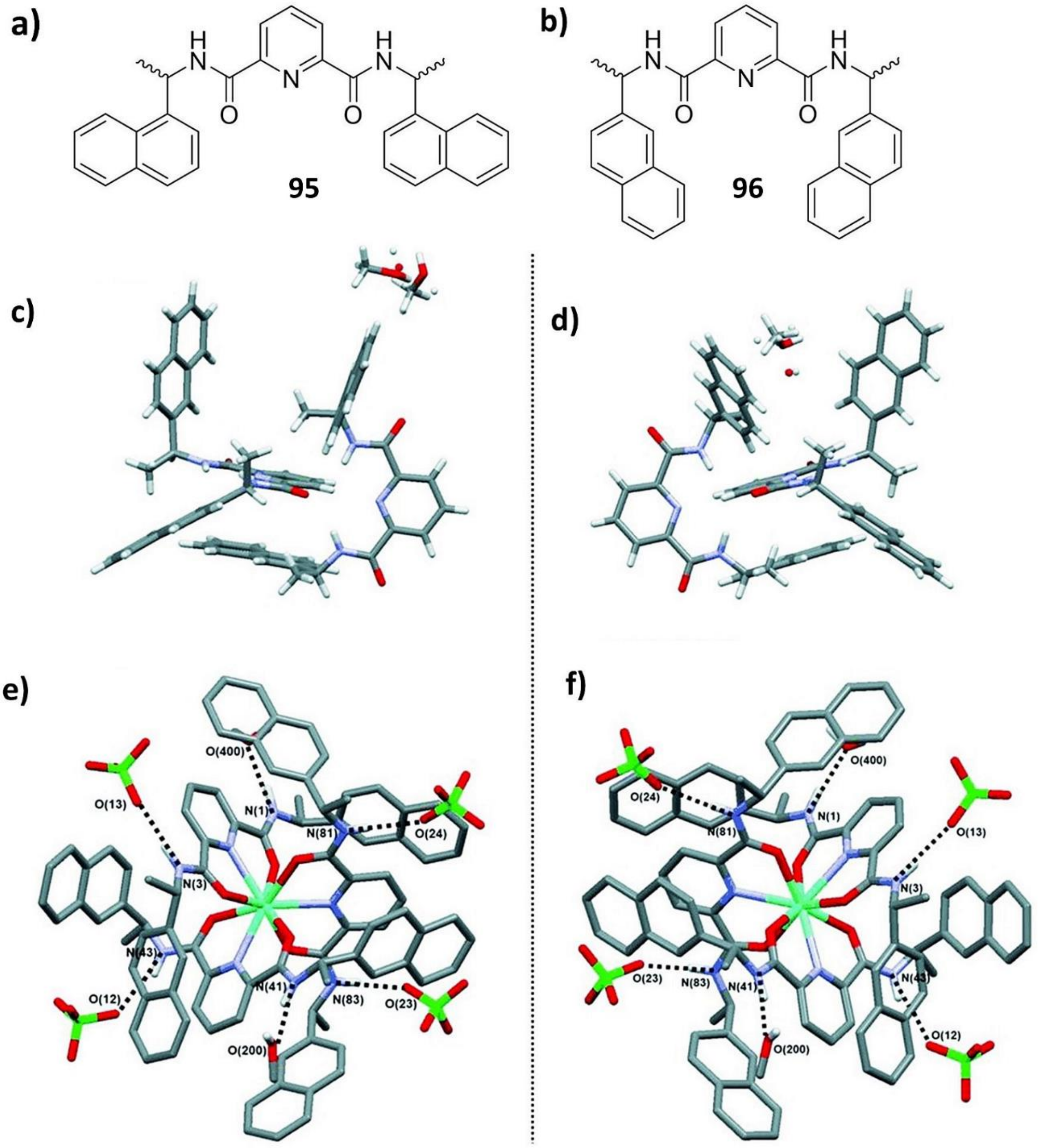

Figure 5.2 (a&b) Structure of **95** and **96**, (c&d) perspective view of the asymmetric units of **95** and **96** and (e&f) the Eu(III) complexes of **95** and **96** showing the hydrogen bonding involving all six amide protons. Interstitial water molecule and hydrogen atoms other than NH and OH protons are omitted for clarity in the Eu structures Images reproduced from reference 186.

carbonyl oxygen atoms, resulting in an overall nine-coordinate tri-capped trigonal prismatic geometry. The ligands are arranged in a helical fashion around the Eu(III) centre. There are some differences in the complexes of ligand **95** and ligand **96**, for example there are no well-defined pores generated through the crystal packing in the case of **96**, thus indicating that this structural change can have a major effect on the overall packing interactions. X-ray crystal structural data for the Eu(III) complexes of **95(*S*,*S*)** and **96(*R*,*R*)** confirmed the chirality of the complexes and indicated that the ion is more tightly packed than for those made from **95′(*S*,*S*)** or **96′(*R*,*R*)** due to increased π···π stacking between the naphthalene and pyridyl groups compared to the more flattened and open structure of 2-naphthyl series in **95′(*S*,*S*)** or **96′(*R*,*R*)**. This work demonstrated the formation of new, highly symmetrical, coordination-driven lanthanide self-assemblies or bundles dubbed the ‘trinity sliotar’, an example of which is shown in Figure 5.3.

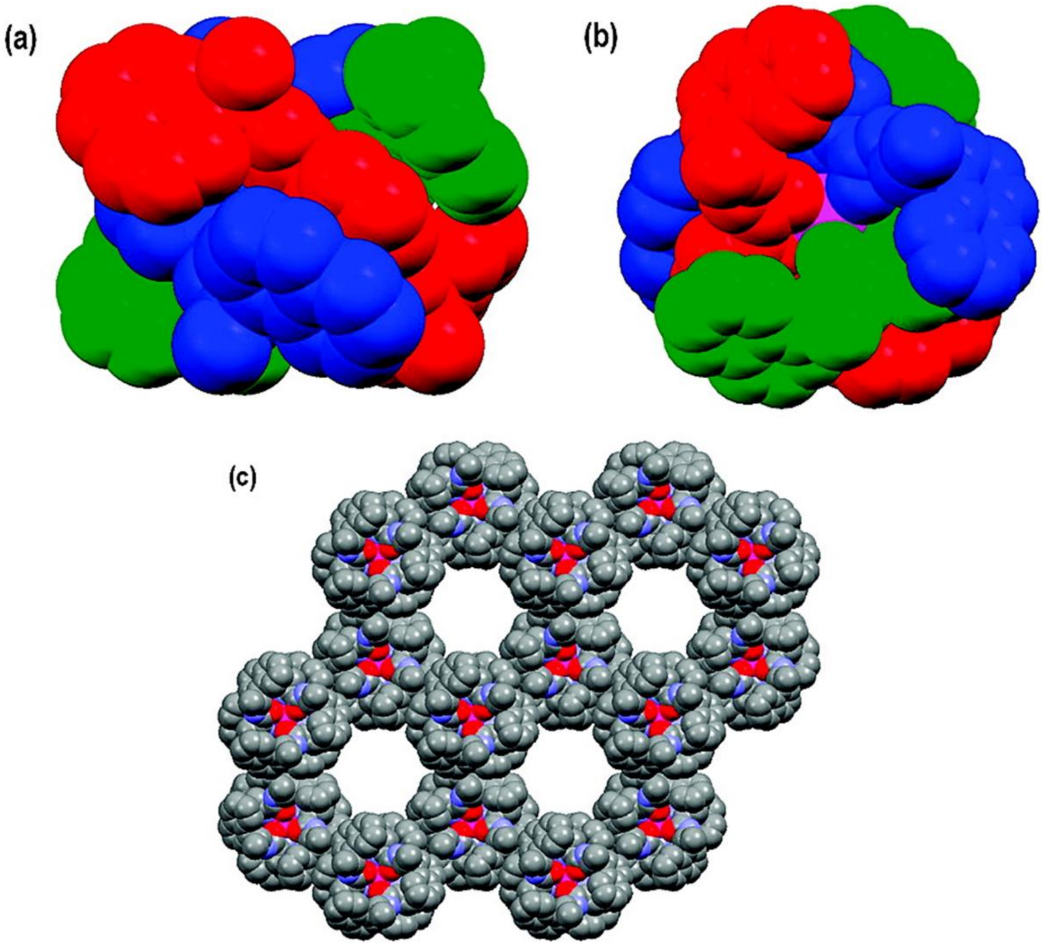

Figure 5.3 An example of the X-ray crystal structure of **95** (R, R)-Tb showing the ‘helical’ arrangement of the three ligands around the Tb(III) (pink) as viewed (a) down the *a*-axis, (b) down the *c*-axis and (c) the packing diagram viewed down the *c*-axis showing the channels. Hydrogen atoms, solvent molecules and counter-ions are omitted for clarity. Images reproduced from reference 186.

Another use of pyridine-based lanthanide complexes by the Gunnlaugsson group was in the development of Langmuir Blodgett films.[189] The Langmuir-Blodgett (LB) technique is an elegant method for the fabrication of well-defined layered structures with molecular level precision. During the LB process, an insoluble monolayer of amphiphilic molecules is spread on the surface of a water phase, followed by compression of the monolayer into a highly condensed state. This can then be transferred onto a solid support in a layer-by-layer manner.[191] Incorporation of lanthanides into these potentially functional nanostructures opens up the possibility for possible applications in the areas of molecular recognition, sensing, imaging and for use in optical devices.[192] In the reports by the Gunnlaugsson group, the formation of a number of chiral luminescent lanthanide amphiphilic complexes and their use in the generation of LB films was discussed. The ligands used and an X-ray crystal structure of one of these ligands is depicted in Figure 5.4. The ligand was found to crystallise in the chiral monoclinic space group $P2_1$ and contained two crystallographically independent molecules in the asymmetric unit. One molecule adopted a relatively *trans* coplanar chain configuration or ‘straight chain’ while the other formed a somewhat square shape through ‘kinks’ in the chain. The two molecules packed into dimers through classical NH···O hydrogen bonding and offset face to face π-π stacking, with the pyridyl group of the straight chain compound sitting into the square of the bent chain compound. Eu(III) complexes of both ligands were prepared and crystallised with the properties of the complexes then evaluated. It was found that reaction between the ligands and Eu(III) resulted in the formation of 3:1 ligand to metal complexes. The self-assembling properties of these complexes at the water-air interface by forming Langmuir-Blodgett films, as before this study, only a small number of reports of LB films made from

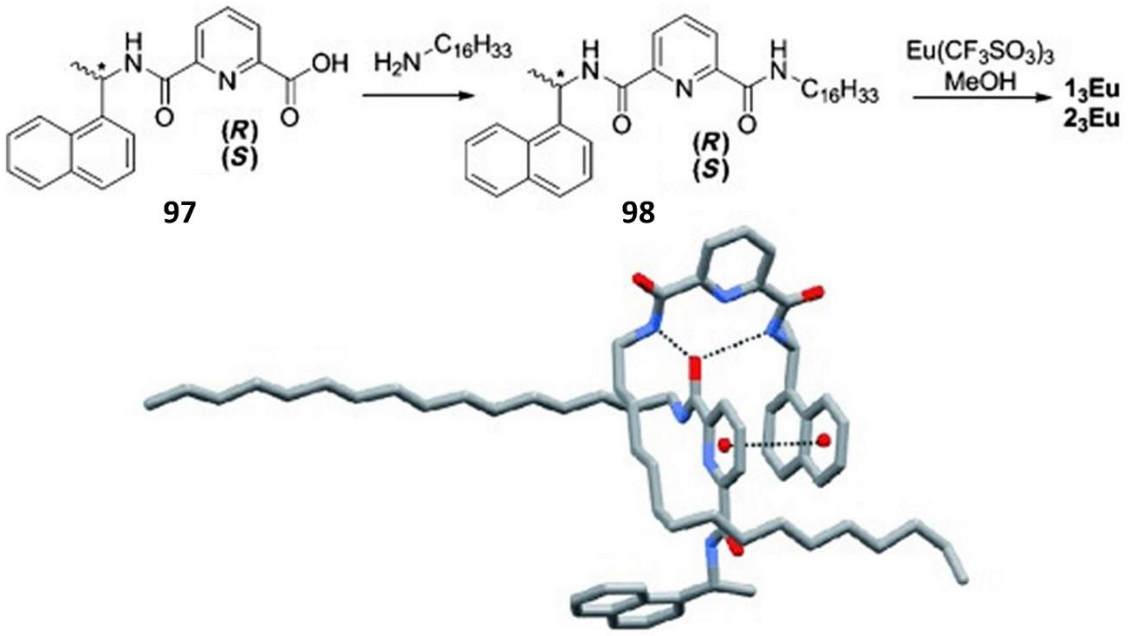

Figure 5.4 Synthetic scheme for the synthesis of **98R** and **98S**, along with their Eu(III) complexes. Perspective view of the crystal structure of **98R**, with the dashed lines representing intermolecular interactions. Hydrogen atoms are omitted for clarity. Image reproduced from reference 191.

kinetically and thermodynamically stable lanthanide complexes had been made. LB films of both complexes were prepared and transferred onto quartz slides and the photophysical properties were then evaluated. It was found that the UV/Vis absorption and the fluorescence emission of the films matched well with the results obtained for the complexes in solution and the films were stable under ambient conditions for several months. The chiral emission of these films was also probed using circularly polarised luminescence (CPL) spectroscopy and these investigations revealed both films to give rise to Eu(III)-centred CPL, confirming the chirality of the films. This report was one of the first in the area of lanthanide CPL emitting amphiphilic self-assemblies.

The use of a pyridine based ligand in the formation of a catenane has also been reported by the Gunnlaugsson group.[193] The synthetic strategy for this work is depicted in Figure 5.5, in which the initial self-assembly of pyridyl di-amide ligands containing polyethoxy spacers and terminal alkene groups with a lanthanide ion would result in preorganisation of the alkene groups in a manner that could allow catenation or 'closing' by 'triple clipping' of adjacent alkenes using ring-closing metathesis (RCM), in the presence of a second generation Grubbs catalyst. Catenation, resulting in both [2]- and [3]catenanes was confirmed using a number of NMR and mass spectrometry experiments and these were reported to be the first examples of lanthanide templated [2] and [3]catenanes. Other advances and potential applications of structures based on the pyridine dicarboxamide motif in supramolecular chemistry have also been made by other research groups and some of these will be discussed in the next section.

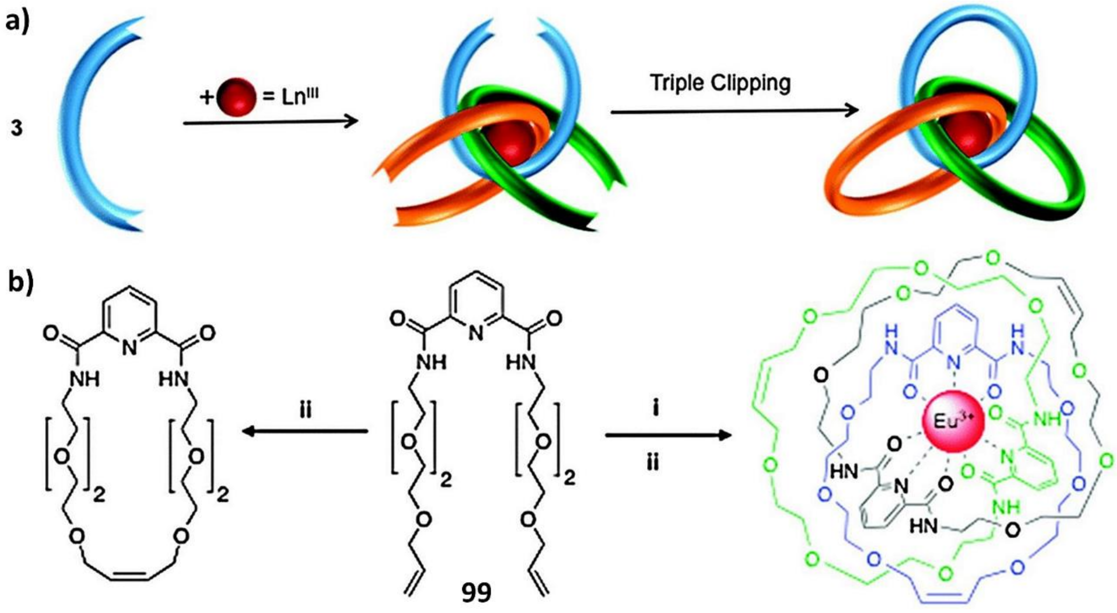

Figure 5.5 (a)The synthetic strategy for the lanthanide-directed synthesis of the [3]catenane, involving 1:3 (M:L) self-assembly formation between the **99** and the Ln(III) to give Ln·**99**$_3$ and catenation by 'triple clipping' to result in cat·Ln·**99**$_3$. (b) The synthesis of **99.99b** and cat·Ln·**99**$_3$. Image reproduced from reference 193.

5.2 Other advances based on the pyridine dicarboxamide motif

An interesting use of pyridine-2,6-dicarboxamide ligands is the report of its use as a G-quadruplex binding ligand.[194-196] G-quadruplex binding ligands are of interest due to their potential as anti-cancer agents. In normal and healthy cells, telomeres are shortened each time DNA replication occurs, with apoptosis occurring after approximately 30-40 replications. In cancer cells, telomerase, the enzyme that maintains the telomeres, is often overexpressed and it is thought that this is responsible for unlimited cell proliferation.[194] G-quadruplex binding ligands are thought to inhibit telomerase activity through stabilising the folding of the of the telomeric G-rich single-stranded overhang into a four-stranded DNA structure called the G-quadruplex.[194] The structures reported in these studies are shown in Figure 5.6 and are known as **100** and its dimer **101**. **100** has been shown to display good selectivity for G4 structures compared with double-stranded DNA and was shown to preferentially localise at telomeres in human living cells. It was also found to inhibit proliferation and induced apoptosis of telomerase-positive glioma cell lines.[194,196] It was recently shown that the dimer form, **101**, is more efficient than its monomer form at impairing the formation and for inducing the dissociation of the complex formed between a replication protein and human telomeric DNA.

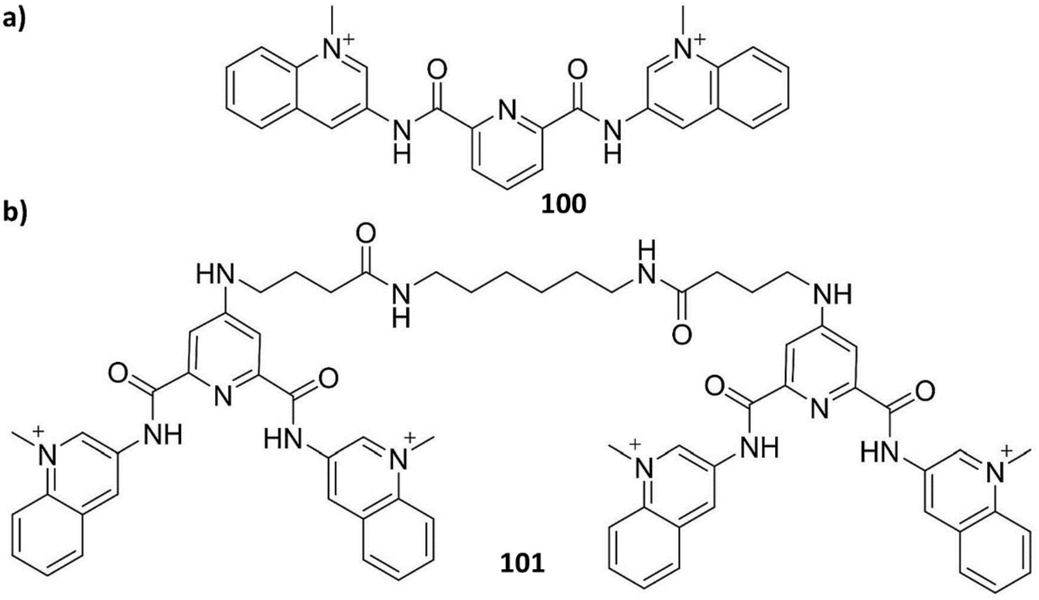

Figure 5.6 (a) The compound known as **100** and (b) its dimer form known as **101**.

A more common application of pyridine dicarboxamide based materials, particularly pyridine-2,6-dicarboxamide, is in the generation of coordination polymers.[197,198] Another reported use of pyridine-2,6-dicarboxamides has been as a building block in the synthesis of rotaxanes.[199]

Gupta and co-workers reported the synthesis and catalytic properties of a number of coordination polymers based on a pyridine-2,6-dicarboxamide derivative containing thiazoline rings.[197] A cobalt metalloligand was first synthesised, shown in Figure 5.7 and the appended thiazoline rings were found to be uncoordinated. This metalloligand was then reacted further with Zn(II), Cd(II) and Hg(II) salts to result in heterometallic coordination polymers, with the crystallographic studies showing the coordination polymers to be infinite one-dimensional chain structures. These secondary metals were then used as catalytic sites for reusable heterogeneous catalysis for ring opening reactions of oxiranes and thiiranes, Knoevenagel condensation of benzaldehydes and benzo-thialdehydes and the cyanation reactions of aldehydes and carbo-thialdehydes, reactions that have been shown to be carried out effectively in the presence of a suitable Lewis acidic metal.[200] Here Gupta and co-workers demonstrated that the size and Lewis acidity of secondary metals potentially controls the catalytic outcome *via* a preferential interaction with the substrates, with the Hg-based coordination polymer found to be the best catalyst. The authors proposed that this was due to the high affinity of the Hg(II) ion to interact with the soft sulphur atom as the primary reason for its better performance.

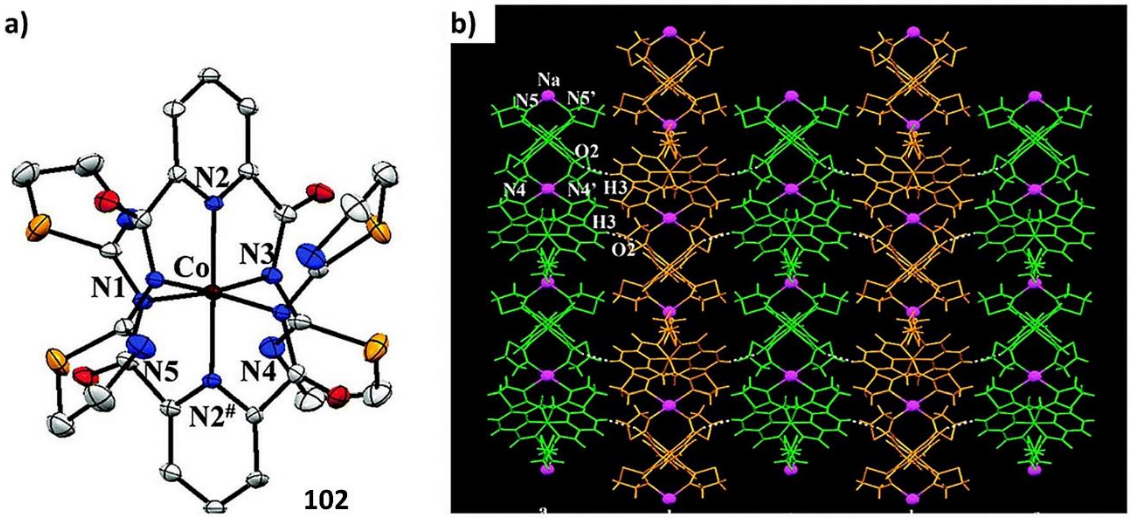

Figure 5.7 (a) Thermal ellipsoid representation of the metalloligand, with the thermal ellipsoids drawn at 30% probability level, while the Na^+ ion and hydrogen atoms have been omitted for clarity and (b) a packing view along the *b* axis with the complex anions shown in green and orange whereas the Na^+ ions are shown in magenta. Images reproduced from reference 197.

Bai and co-workers reported the synthesis of a MOF synthesised by a solvothermal reaction between a pyridine-3,5-dicarboxamide based ligand, shown in Figure 5.9, and zinc nitrate and reported the gas uptake of the resulting material.[201] The X-ray analysis of the MOF showed that each Zn(II) centre is four-coordinate, binding two oxygen atoms from the pyridine ligand with monodentate coordination mode, one nitrogen atom from a third pyridine ligand and one oxygen atom from a water molecule. The two kinds of zinc atom centres connect with

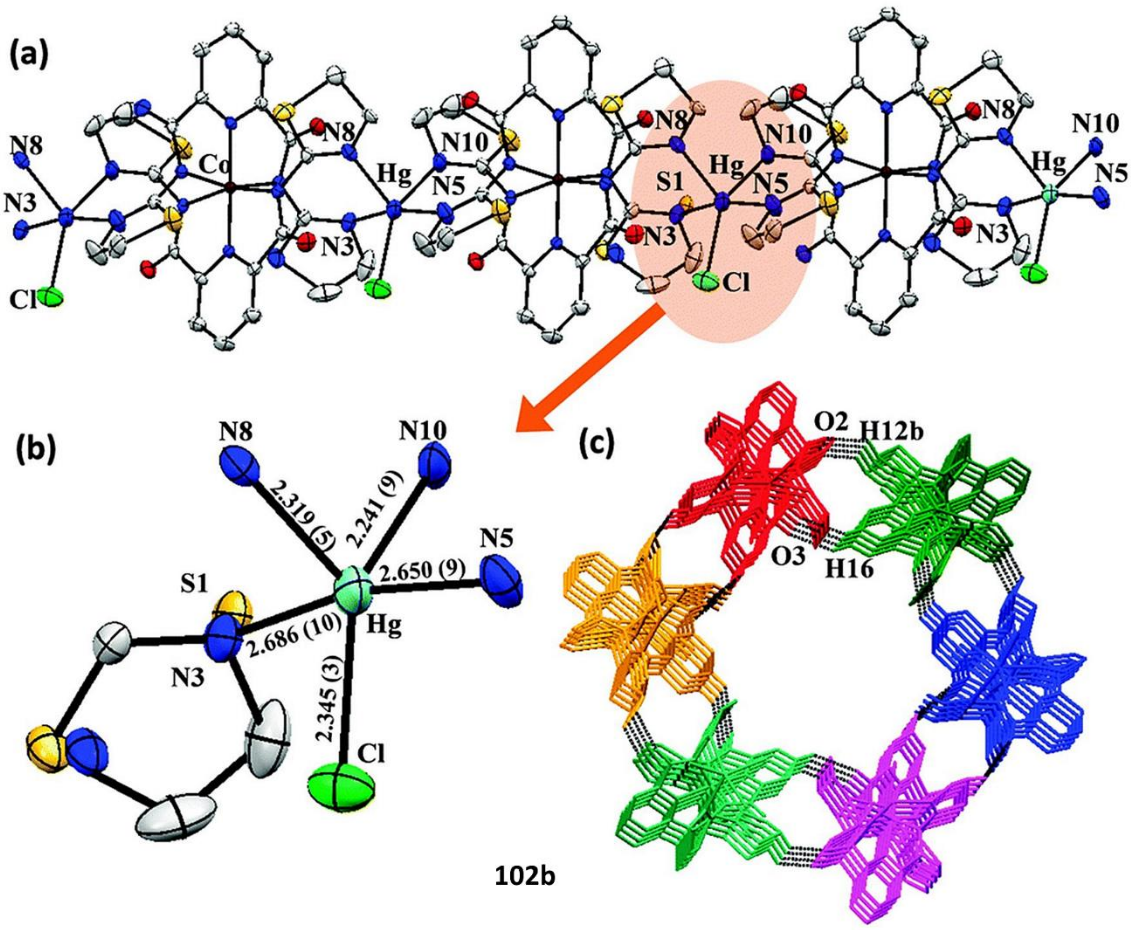

Figure 5.8 (a) Thermal ellipsoid representation of the Hg-coordination polymer, **102b**, with the thermal ellipsoids drawn at 30% probability level and the hydrogen atoms are omitted for clarity; (b) coordination sphere of the Hg(II) ion with bond distances including rotationally disordered thiazoline ring with both N and S atoms; (c) honeycomb structure generated due to the weak interactions between the 1D chains. Images reproduced from reference 197.

ligands of the same shape to generate a large cage type structure, which further assembles to form a three-dimensional network. To investigate the permanent porosity of the MOF, the sample was subject to a number of gas adsorption experiments, with the material found to take up a significant amount of N_2 and possessed a large surface area.

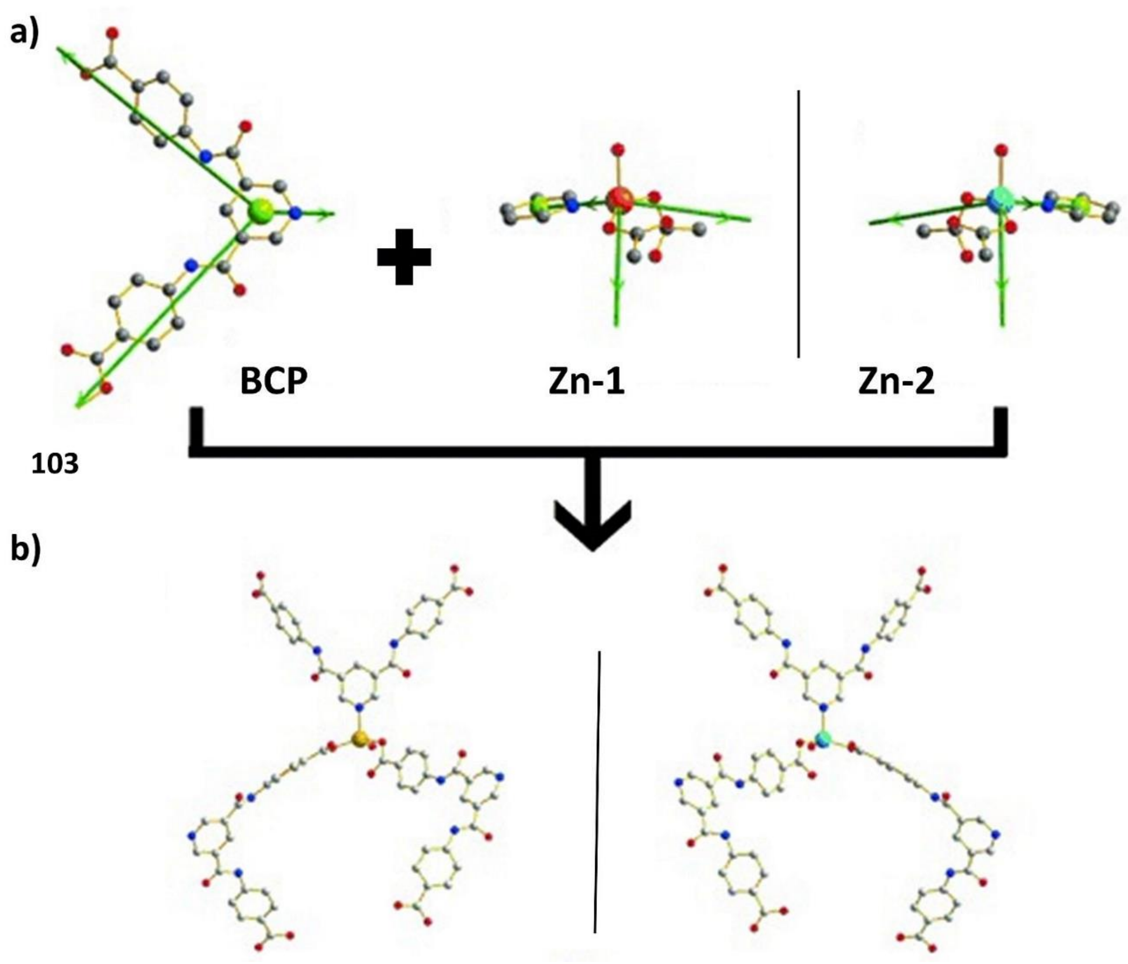

Figure 5.9 (a) Structure of the pyridine ligand used by Bai and co-workers; (b) a pair of zinc centres, each coordinated to three pyridine-based ligands. Images reproduced from reference 201.

Another report of pyridine-3,5-dicarboxamide ligands as MOF building blocks include the report by Qu and co-workers of the hydrothermal reaction of $CoCl_2$ with a pyridine-3,5-dicarboxamide ligand and a benzene-1,3,5-tricarboxylic acid to result in two novel polynuclear cobalt cluster-based MOFs, with one of the complexes displaying excellent photocatalytic activity for dye degradation under UV light.[202]

Taking these examples into account, we decided to investigate the effect of side arm functionality on a pyridine-3,5-dicarboxamide core and study the materials formed from a variety of these derivatives. This will be discussed in the following section.

5.3 Design rationale for the compounds that will be discussed in this chapter

Pyridine-3,5-dicarboxamide was chosen as the central motif for this chapter due to a number of reasons, namely, it has a structurally similar core to **BTA** but with a greater potential for metal coordination and would be relatively easily derivatised with a number of side arms. Given that various pyridine-2,6-dicarboxamides were the subject of previous research within the Gunnlaugsson group and that there are much fewer examples of pyridine-3,5-dicarboxamides in the literature, it was decided that this motif would be a suitable core molecule for this study. It was also chosen as pyridine-2,6-dicarboxamides tend to chelate, while the 3,5 isomer should have three independent binding sites, which is comparable to **BTA** derivatives discussed in previous chapters. A number of side chains were used in for this study, ranging from some simple amino acids to the derivatives used in the **BTA** studies, with these derivatives discussed in this section are shown in Scheme 5.1.

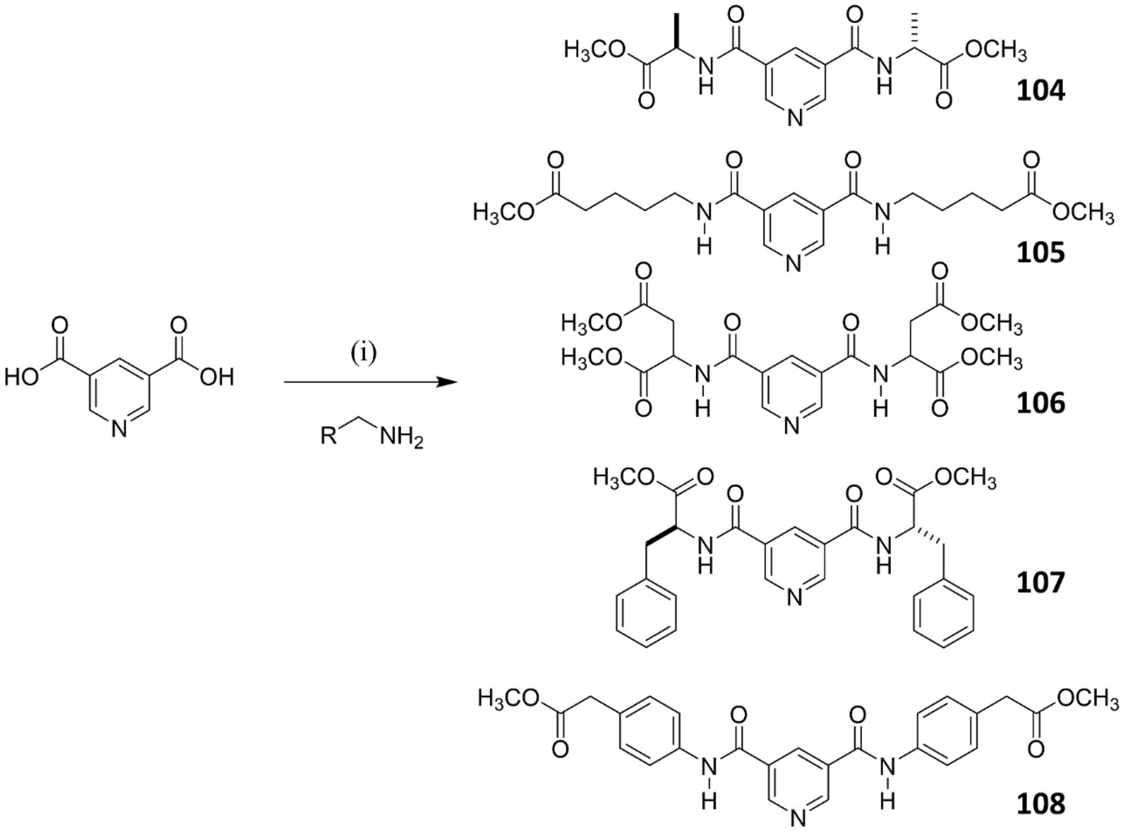

Scheme 5.1 Synthetic scheme for the pyridine derivatives discussed in this chapter where (i) EDC.HCl, DMAP, DCM, argon, rt, 72 h.

5.3.1 Synthesis and characterisation of the pyridine derivatives

The synthetic scheme for the pyridine derivatives is shown in Scheme 5.1 and involved just one step, a coupling reaction between pyridine-3,5-dicarboxylic acid and the respective amino ester side arm. This reaction was achieved by dissolving the carboxylic acid in dry DCM, cooled in ice followed by the addition of the peptide coupling reagents, EDC.HCl and DMAP, and then the addition of the amine, with the reaction mixture left to stir at room temperature in an inert atmosphere for 72 h. The reaction solvent was removed under reduced pressure to reveal white/yellow oils in all cases, with the resultant oils dried *in vacuo* before the addition of water causing the precipitation of white/yellow solids which were isolated by filtration and dried *in vacuo*. The yields for these reactions varied from approximately 37 % to 65 %. The compounds

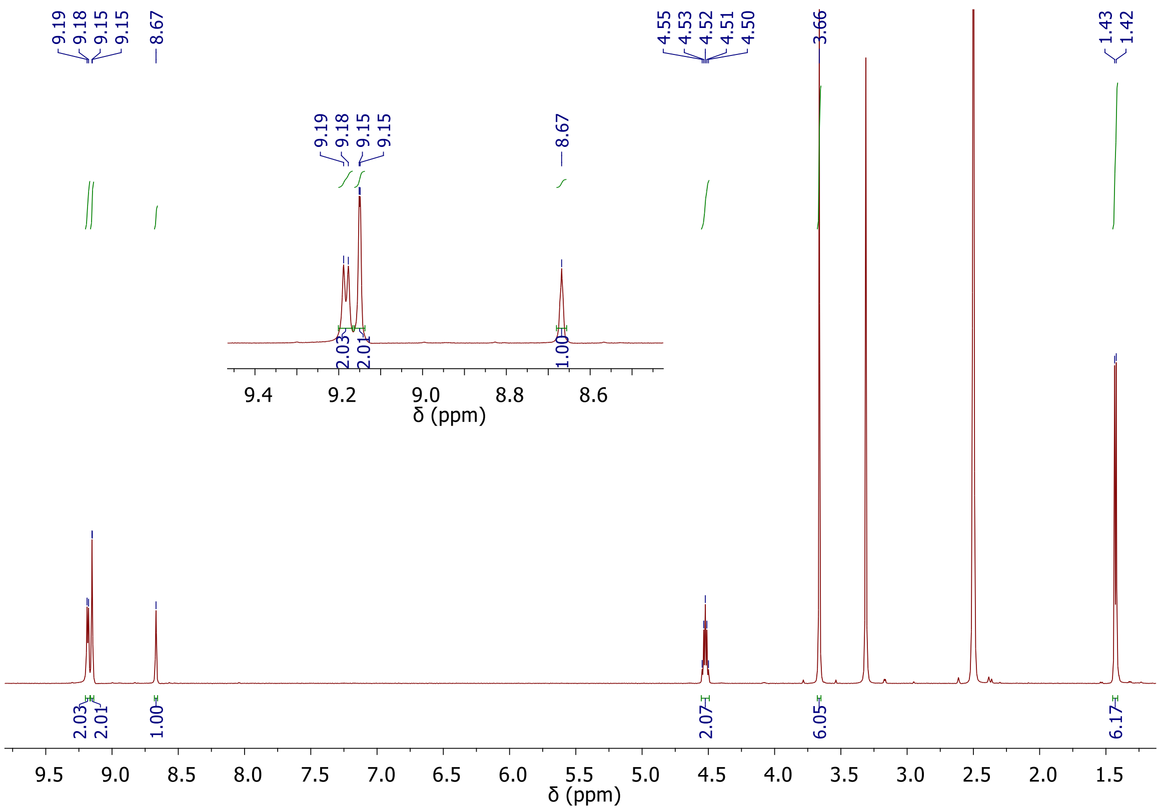

Figure 5.10 ^{1}H NMR (600 MHz, DMSO-d_6) spectrum of **104** showing the characteristic aromatic and amide protons.

were all fully characterised, with these data available in the experimental and appendix sections. An example of a ^{1}H NMR spectrum for one of these derivatives, **104**, is shown in Figure 5.10, with the characteristic pyridine aromatic protons between approximately 8 and 9 ppm and amide proton shifts, the most downfield for all the derivatives, between 9 and 10 ppm shown in the inset. Once isolated, the derivatives were subject to a number of crystallisation attempts which will be discussed in the next section.

5.3.2 Attempts to hydrolyse the ester derivatives

A number of attempts to hydrolyse the pyridine ester derivatives were carried out in order to obtain the carboxylic acid compounds. The objective of this was to make a thorough comparison between the families of **BTA**-based ligands and pyridine-based ligands and to study the influence of side group functionality on the properties of both. The same method used in previous chapters, base hydrolysis using aqueous NaOH and MeOH, was first attempted, however isolation of the carboxylic acid derivative was not achieved. This is likely due to the protonation of the pyridine nitrogen during the acidic work-up of the reaction. Attempts were made to adjust the pH of the reaction mixture, and then extract the desired product, however, these too were unsuccessful. Moving on from this approach, it was decided to couple the benzyl ester protected alanine onto the pyridine-3,5-dicarboxylic acid core with the hope that this could

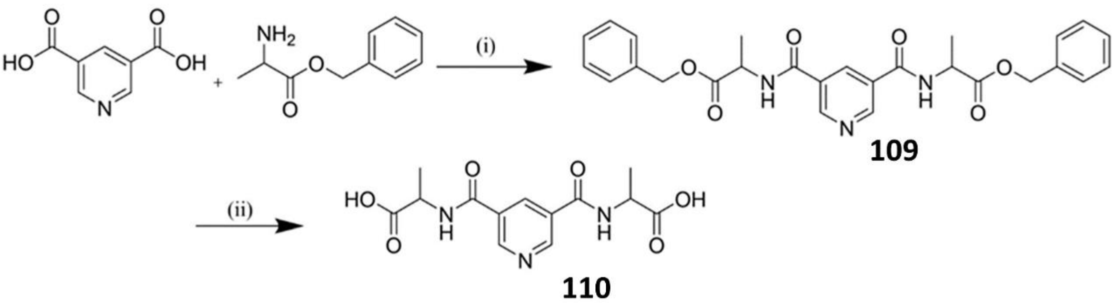

Scheme 5.2 Proposed synthetic scheme for the synthesis of carboxylic acid terminated pyridine derivative **110**, where (i) Et3N, HOBt, EDC.HCl, dry DCM, argon atmosphere, 72 h, (ii) TES, MeOH, Pd/C, 24 h.

then be de-protected to reveal the alanine derivative of **104**, Scheme 5.2. Despite a number of attempts to de-protect **109**, isolation of the carboxylic acid derivative in a good yield and purity using the procedure previously reported by Kotova *et al.*[188] was not successful. ^{1}H NMR spectra from these attempts revealed the presence of a number of impurities and are shown below, in comparison with the methyl ester alanine derivative. An almost identical spectrum, minus the CH_3 resonance, would be expected, however this was not the case. The spectrum of **110** shown in Figure 5.11 displayed a number of impurities, particularly in the aliphatic region, most likely containing triethylsilane. Despite several purification attempts, it was not possible to isolate the pure product. Future work should focus on optimising this synthesis to result in a pure compound. After these unsuccessful attempts, the syntheses of the carboxylic acid derivatives

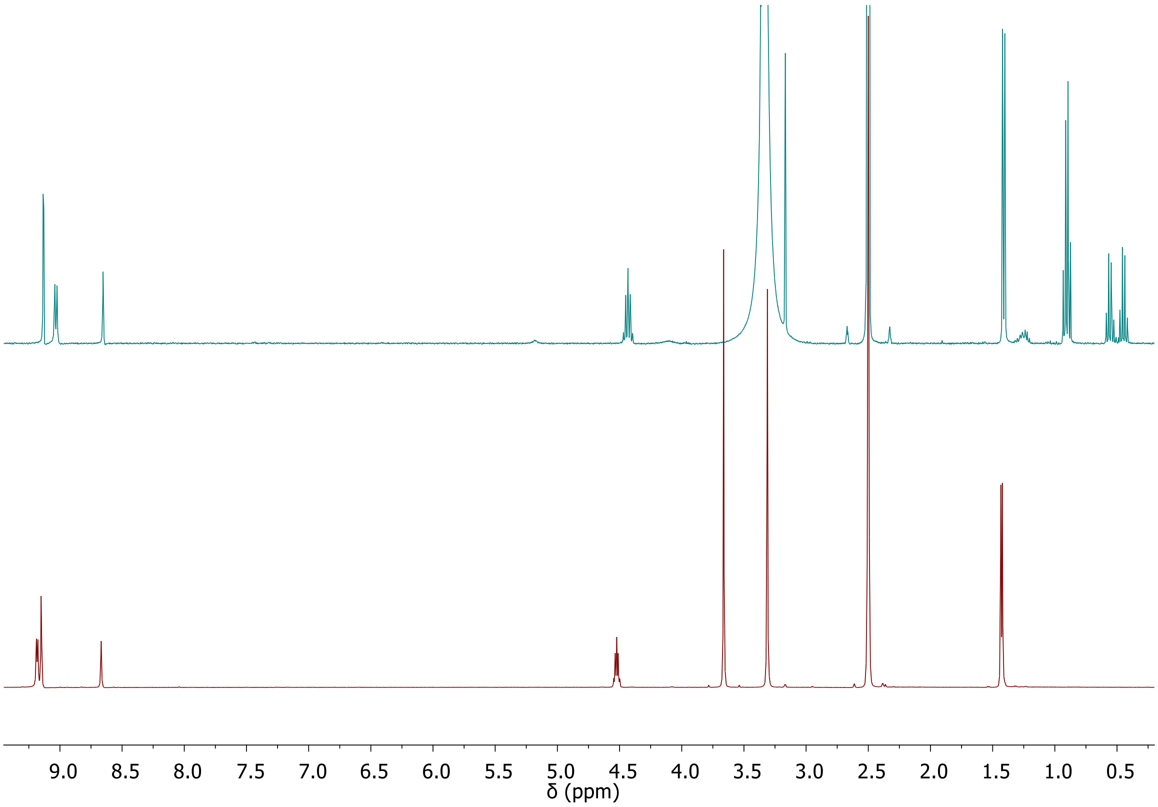

Figure 5.11^{1}H NMR (400 MHz, DMSO-*d*$_6$) spectra of **110** (top) and **104** (bottom).

were abandoned and instead the focus of the remainder of this chapter was on the ester derivatives and their structural properties, which will be discussed in the next section.

5.4 Structural studies of the pyridine derivatives

After a variety of screening attempts employing a several crystallisation techniques and conditions, a number of single crystals suitable for diffraction were obtained. Details of the various conditions and techniques are summarised in Table 5.1 below. The crystallography in this chapter was carried out and the data solved and refined by Dr Chris Hawes, (TCD, Keele University) and June Lovitt (TCD). As far as can be determined, there are very few reported X-ray crystal structures of simple pyridine-dicarboxamides, particularly pyridine-3,5-dicarboxamides, thus these compounds are a novel area of study.[203]

Table 5.1 Table detailing the crystallisation attempts for the pyridine derivatives, where Y indicates that the method was attempted, while N indicates that the method was not tested. Successful crystallisations are indicated by the conditions that were successful.

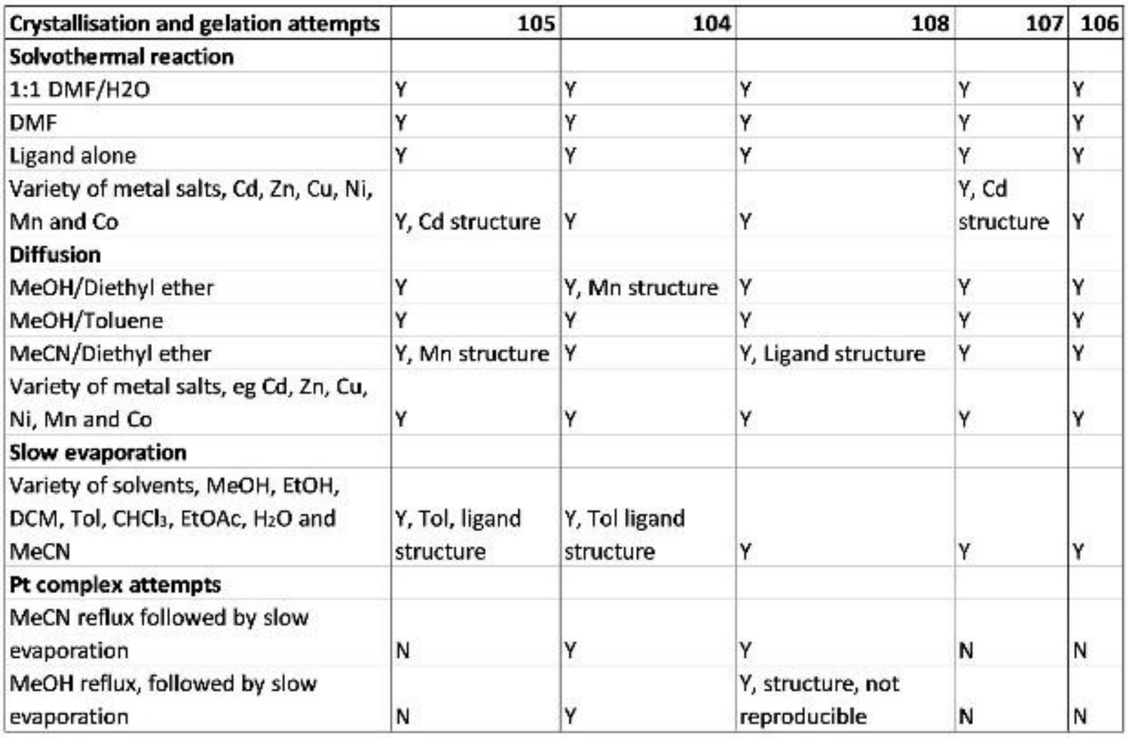

Crystallisation and gelation attempts	105	104	108	107	106
Solvothermal reaction					
1:1 DMF/H2O	Y	Y	Y	Y	Y
DMF	Y	Y	Y	Y	Y
Ligand alone	Y	Y	Y	Y	Y
Variety of metal salts, Cd, Zn, Cu, Ni, Mn and Co	Y, Cd structure	Y	Y	Y, Cd structure	Y
Diffusion					
MeOH/Diethyl ether	Y	Y, Mn structure	Y	Y	Y
MeOH/Toluene	Y	Y	Y	Y	Y
MeCN/Diethyl ether	Y, Mn structure	Y	Y, Ligand structure	Y	Y
Variety of metal salts, eg Cd, Zn, Cu, Ni, Mn and Co	Y	Y	Y	Y	Y
Slow evaporation					
Variety of solvents, MeOH, EtOH, DCM, Tol, $CHCl_3$, EtOAc, H_2O and MeCN	Y, Tol, ligand structure	Y, Tol ligand structure	Y	Y	Y
Pt complex attempts					
MeCN reflux followed by slow evaporation	N	Y	Y	N	N
MeOH reflux, followed by slow evaporation	N	Y	Y, structure, not reproducible	N	N

5.4.1 Structural studies of 104

The ligand **104** contains alanine ester side chains and a single crystal of this derivative was obtained from a toluene evaporation with the data solved and refined in the monoclinic space group $P2_1$. The asymmetric unit, shown in Figure 5.12, was found to contain the entire molecule with no associated guest or solvent molecules. The extended structure formed a 2D polymer, Figure 5.12, with the interactions between the neighbouring molecules consisting solely of

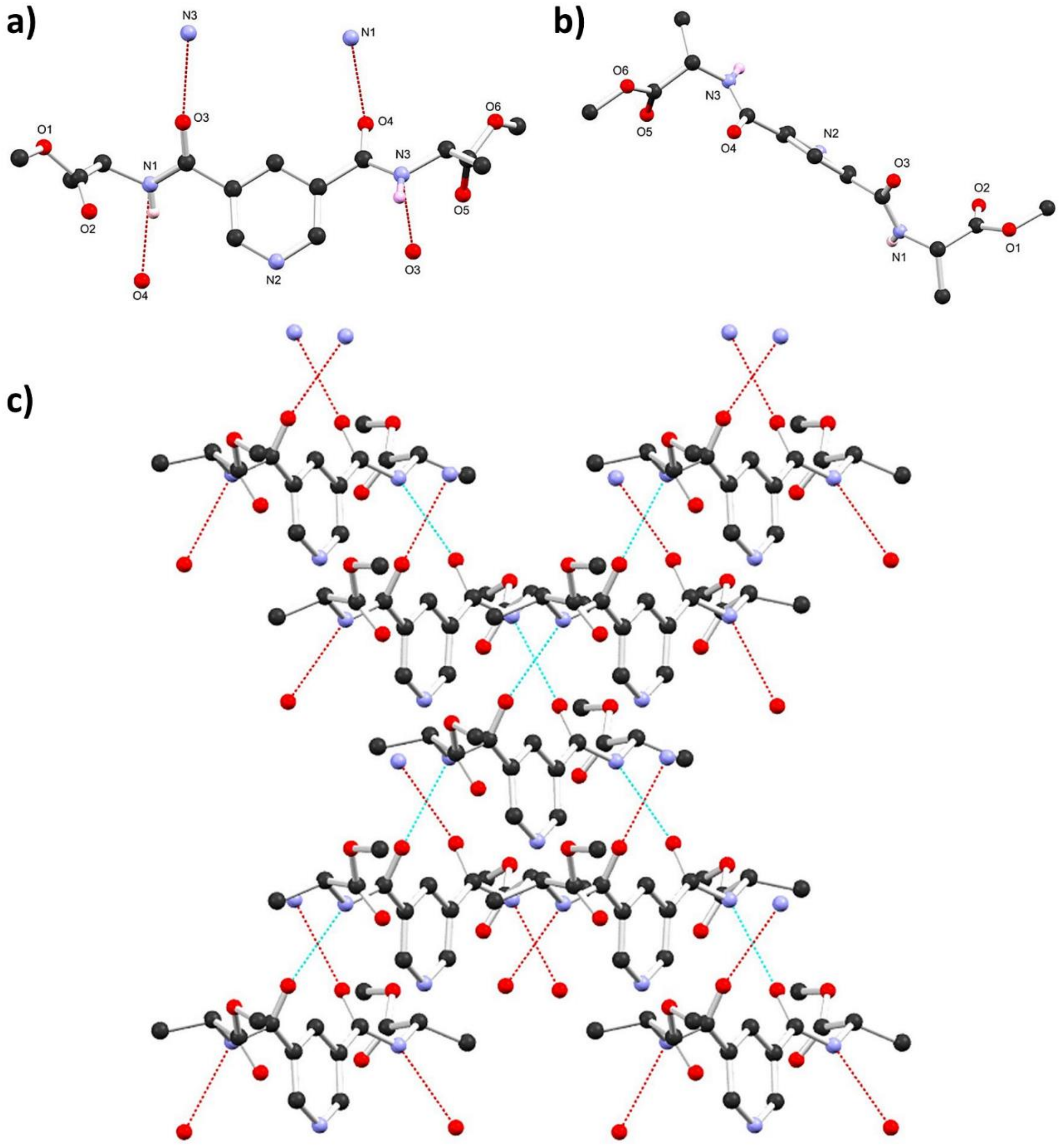

Figure 5.12 (a) Asymmetric unit of **104** with heteroatom labelling scheme; (b) view along the *b* axis showing the orientation of the alanine side arms and (c) extended structure viewed along the *c* axis of **104**. In all cases, selected hydrogen atoms are omitted for clarity.

hydrogen bonding interactions. Each molecule interacts with four other molecules. O3 and O4 each accept a hydrogen bond from a NH on a neighbouring molecule, but a neighbour in the opposite direction. Likewise, N1 and N3 each donate a hydrogen bond to neighbouring CO groups (distances 2.948(2) and 2.937(3) Å). The ester groups of this derivative do not take part in any bonding between the molecules, nor were there any π-π interactions present.

The phase purity of this sample was then investigated using powder diffraction, with the experimental pattern compared to that predicted from the single crystal data and this is shown in Figure 5.13. The bulk sample was prepared in the same way as that used for the single crystal sample, recrystallisation from toluene which was then dried and grinded into a fine

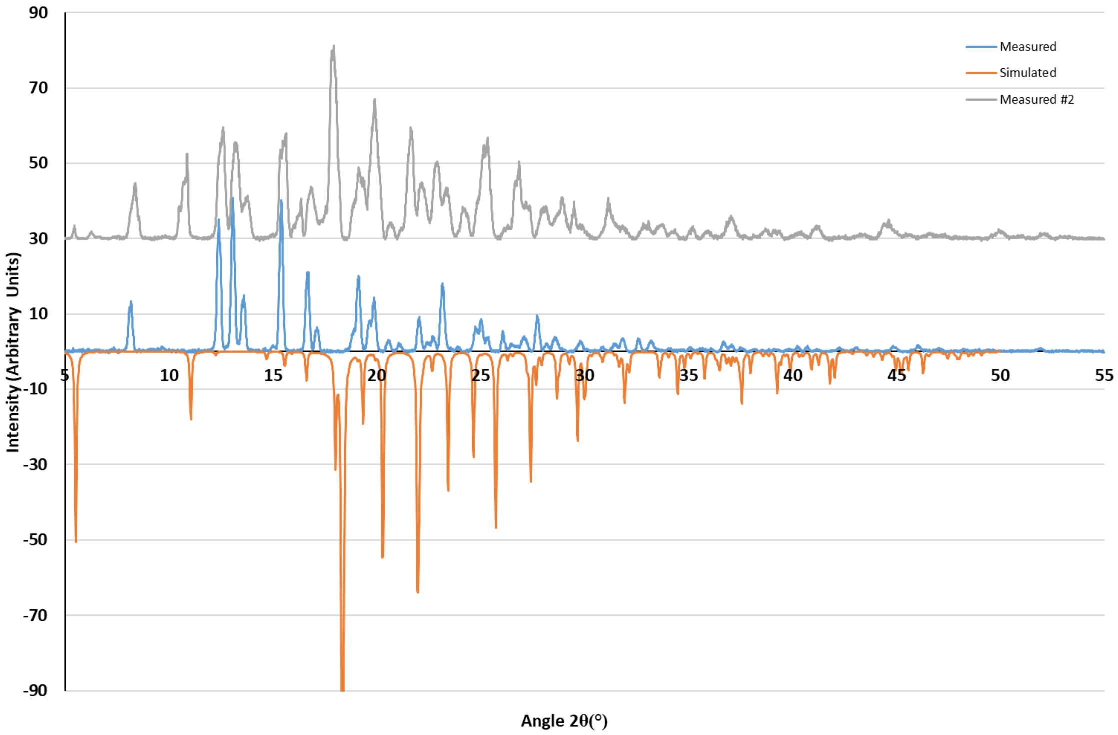

Figure 5.13 X-ray powder diffraction pattern for **104** (room temperature, blue and grey) and comparison with the pattern simulated from the single crystal data (100 K, orange) obtained for **104**.

powder suitable for powder diffraction. As seen in Figure 5.13, the measured pattern does not match that simulated from the single crystal data, which suggests that the dry bulk sample consists of a different polymorph to that subject to single crystal diffraction. A second sample was also measured, however, this too did not agree with that predicted and instead closely resembled the first measured sample, Figure 5.13, thus indicating the polymorphous nature of the crystals. Many attempts were made to isolate single crystals of this phase, however, these attempts were not successful. Following this, we decided to attempt to generate some coordination polymers using transition metals and these attempts will be discussed in the next section.

5.4.2 Structural studies of 104Mn

A single crystal of **104Mn** was obtained by diffusion of diethyl ether into a methanolic solution of the ligand and $MnCl_2 \cdot 4H_2O$, with the data solved and refined in the monoclinic space group

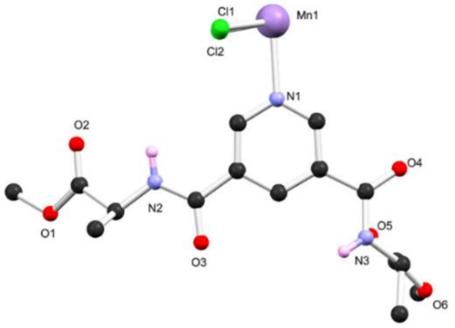

Figure 5.14 Asymmetric unit of **104Mn** with heteroatom labelling scheme viewed along the *b* axis. Selected hydrogen atoms are omitted for clarity.

P2_1.In this structure, the Mn ion is octahedral with each Mn having four Cl in the equatorial plane, along with one pyridine nitrogen and one amide oxygen atom in the axial plane. The extended structure forms a 2D polymer, with each Cl bridging two Mn and each ligand bridging two Mn, forming a chain structure, shown in Figure 5.15. Hydrogen bonding interactions in this structure are between N3 of the uncoordinated amide and Cl2 of one of the chains, while the N2 of the coordinating amide hydrogen bonds to O5 of one of the ester groups.

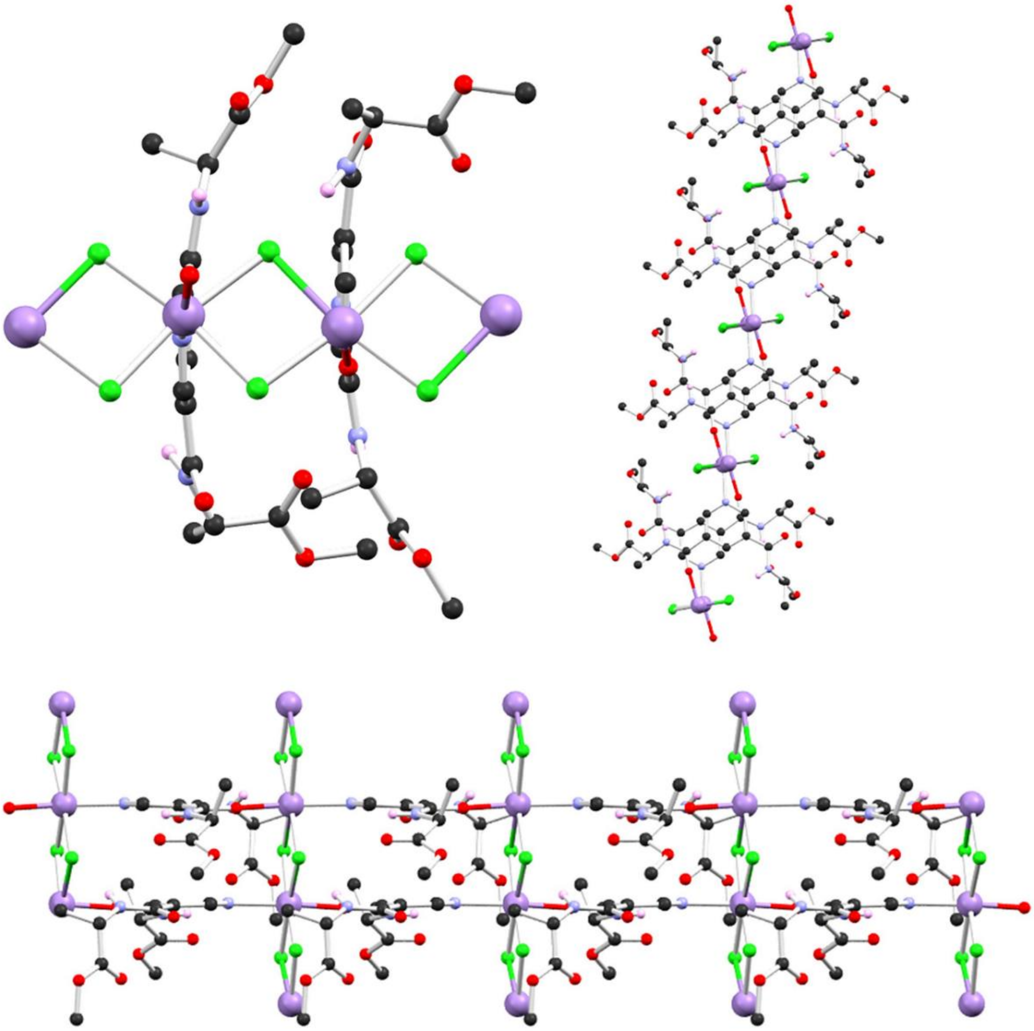

Figure 5.15 Extended structure of **104Mn**, showing the chain-like structure, viewed along the *a*, *b* and *c* axes respectively. Selected hydrogen atoms are omitted for clarity.

A bulk sample of **104Mn** was prepared for X-ray powder diffraction in order to assess the bulk purity of the sample. The sample was prepared on a large scale by dissolving the ligand and $MnCl_2$ in MeOH, followed by the addition of diethyl ether which caused the precipitation of a crystalline solid. The pattern, Figure 5.16, from the bulk sample was found to have corresponding peaks to that for of the pattern simulated from the single crystal data thus indicating phase purity and the reproducibility of crystallisation. There is a slight difference in peak position due the difference in temperature that the powder diffraction and single crystal

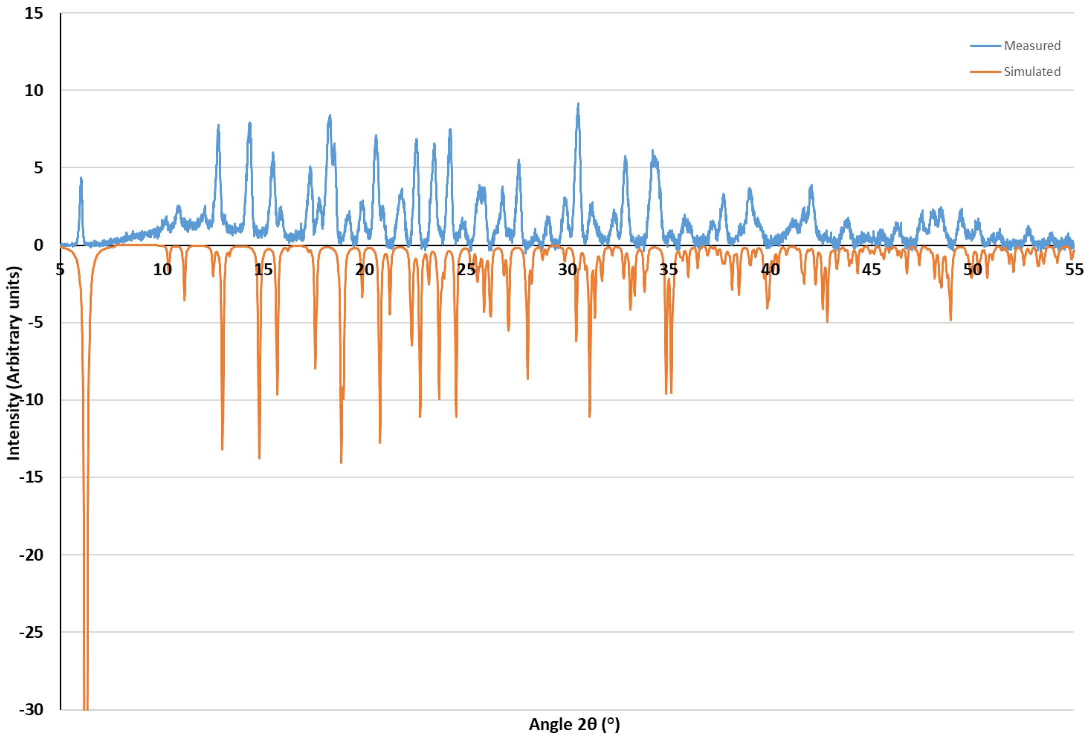

Figure 5.16 X-ray powder diffraction for **104Mn** (room temperature, blue) and comparison with the simulated pattern from the single crystal data (100 K, orange) obtained for **104Mn**.

experiments were carried out at. Further attempts were made to obtain coordination polymers with other transition metals, to investigate the effect of the metal on the structure and these attempts will be discussed in the next section.

5.4.3 Reactions of 104 with other transition metals

Multiple attempts were made to obtain coordination polymers of **104** with other transition metals in order to make structural comparisons, with many of these attempts only affording amorphous solids or precipitates. One of these examples is shown in Figure 5.17, obtained from a diethyl ether diffusion into a MeCN solution of **104** and $CoCl_2{\cdot}6H_2O$ resulted in a fibrous-like material. A dried sample of this material was subject to SEM and Energy-Dispersive X-ray (EDX) spectroscopy, as seen in Figure 5.17. EDX is a technique that is used in conjunction with SEM in which the x-rays emitted from a sample during bombardment by an electron beam are detected. The X-ray energy that is emitted is characteristic of the element from which it is emitted, thus can be used to determine the elemental composition of the sample under analysis.[204] Figure 5.17 shows the vial containing the material formed along with the SEM images and EDX spectra. Also shown is the energy dispersive spectrum. From the SEM image, we can see that the sample has a needle-like morphology, while the EDX elemental maps show that the sample contains oxygen, cobalt and chlorine, along with the presence of silicon from the wafer used in the sample preparation. The energy dispersive spectrum obtained also shows the presence of these elements. This indicates the presence of cobalt in the sample, but further investigations would be required to determine if the cobalt is coordinated to the ligand or whether it is coating the sample, but not bound.

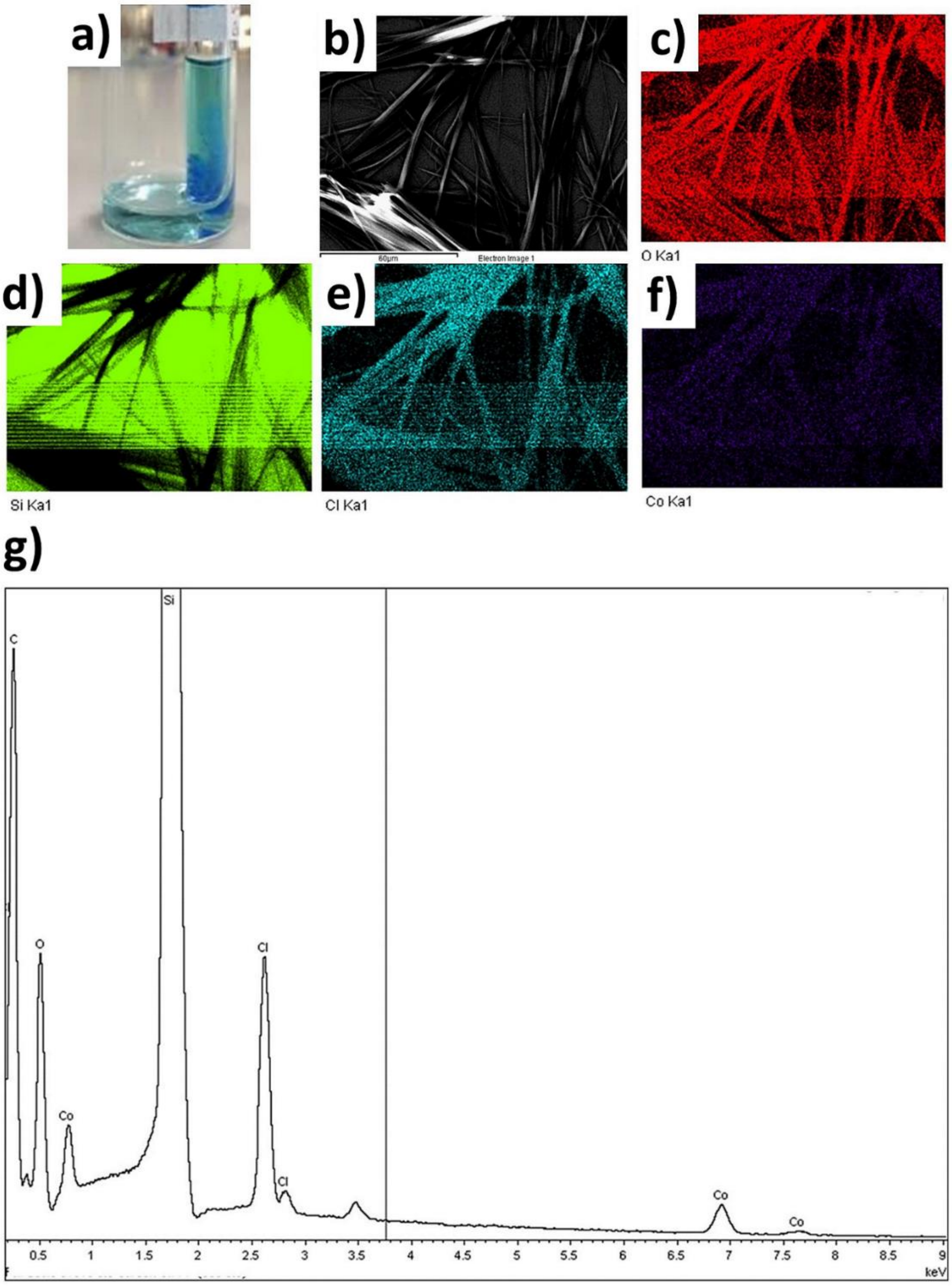

Figure 5.17 (a) Vial containing the material formed from **104** and $CoCl_2$, (b) SEM image of the dried sample of **104Co**, (c) elemental map showing the presence of oxygen, (d) elemental map showing the presence of silicon, (e) elemental map showing the presence of chlorine and (f) elemental map showing the presence of cobalt and (g) the energy dispersive spectrum for the sample.

5.4.4 Structural studies of 105

A single crystal of **105**, the pyridine derivative contained the same side arm functionality as the **BTA** derivative **59**, was obtained from the slow evaporation of a MeCN solution of the ligand. The data were solved and refined in the monoclinic space group $P2_1/c$. The experiment was run using the molybdenum source and at room temperature as opposed to the more usual 100 K. X-ray diffraction experiments are commonly carried out at lower temperatures and it is generally accepted that the structural information obtained is of better quality than that obtained at room temperature.[205] Room temperature was used as the crystals displayed unusual phase behaviour at 100 K, which will be further discussed later. The asymmetric unit of **105** contains the molecule in its entirety and is shown in Figure 5.18.

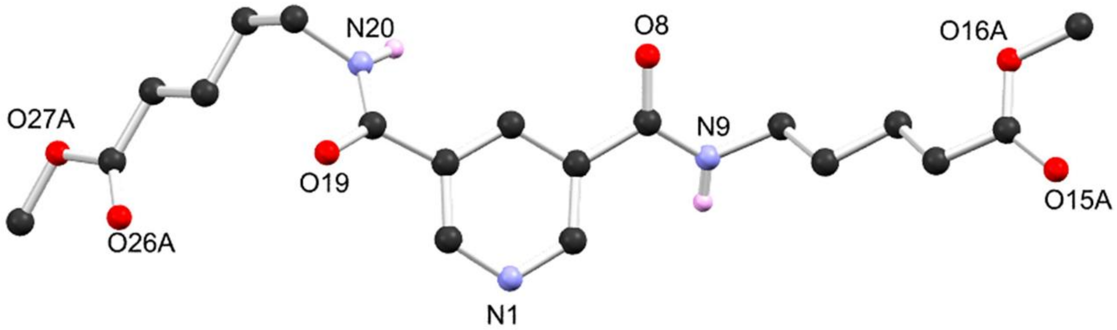

Figure 5.18 Asymmetric unit of **105** with heteroatom labelling scheme. Selected hydrogen atoms are omitted for clarity.

The extended structure of **105** displays the same behaviour as that observed for **104** a 2D polymer connected through hydrogen bonding interactions between the amide groups (N···O distances 2.782(2) Å and 2.829(2) Å, angle N–H···O 150 (5) As with **104**, each of the hydrogen bonding units interact with a different ligand, leading to the same cross type structure

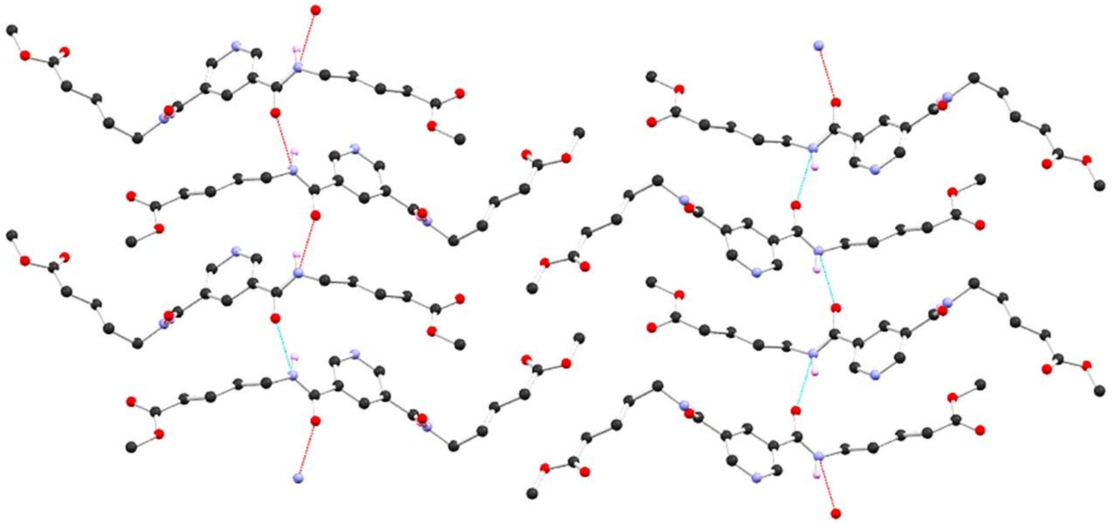

Figure 5.19 Extended structure of **105** viewed along the *a* axis**.** Selected hydrogen atoms are omitted for clarity.

seen in **104**. The ester groups do not participate in any bonding interactions, nor are there any π-π interactions present, just as in **104**. However, the terminal ester groups displayed positional disorder with the ester group originating from C14 modelled over two positions split at 0.36 and 0.64 occupancy, while the ester group originating from C25 modelled over two positions split at 0.83 and 0.17 occupancy. As with the other crystalline samples, powder diffraction was carried out to establish phase purity, Figure 5.20. The measured pattern agreed closely to that calculated from the single crystal data, with some differences in intensity, potentially due to the needle-like nature of the crystals, thus the bulk sample appears pure.

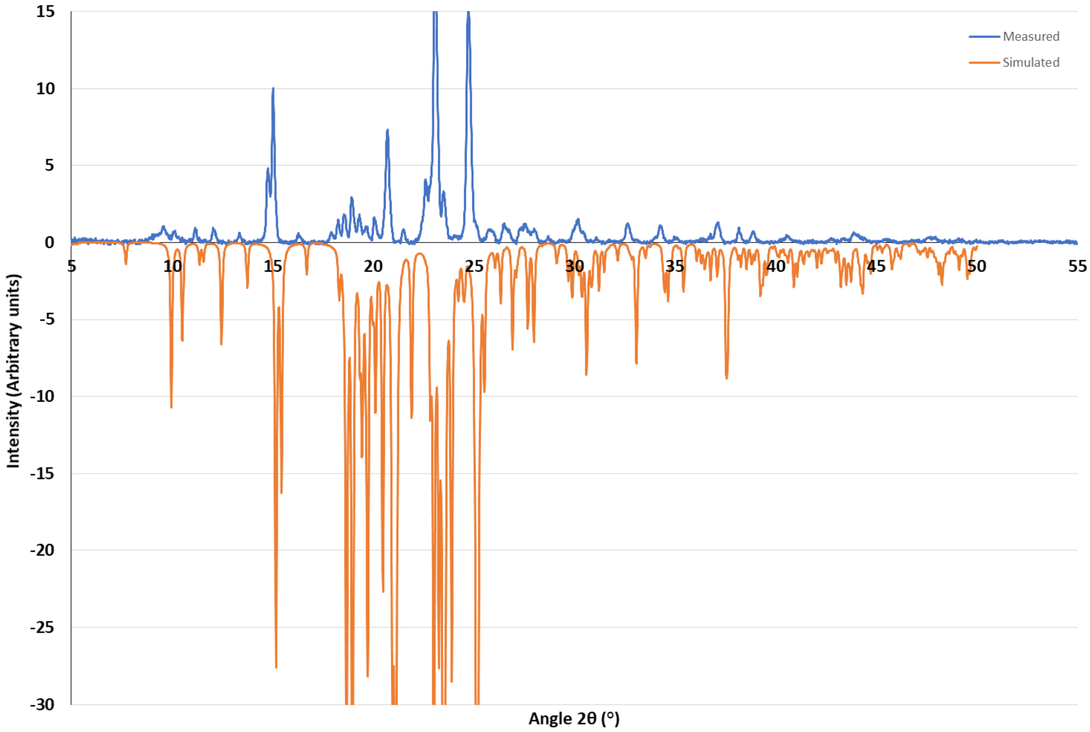

Figure 5.20 X-ray powder diffraction for **105** (room temperature, blue) and comparison to the pattern obtained from the single crystal data (room temperature, orange).

Due to the phase transition on cooling in the cryostream observed during the first single crystal experiment at 100 K, we decided to investigate the phase behaviour of **105** using differential scanning calorimetry, as described in Chapter 2. The DSC apparatus available for this study was capable of accurately cooling to approximately -80°C or 193.15 K, thus not quite as low a temperature as the X-ray diffractometer, however it was hoped that it might give us some insight into the phase behaviour. As is common practice, the second heating and cooling cycle is reported, and this shown in Figure 5.21.[44,137] The DSC thermograph showed only one transition on the heating and cooling cycles respectively, with the onset of the crystalline to isotropic liquid (Cr-I) transition occurring at 107 °C, while the onset of the isotropic liquid to crystalline (I-Cr) transition occurred at 97 °C. This suggests that any other phase transitions are limited to temperatures outside of the range of the DSC, thus no further studies were pursued.

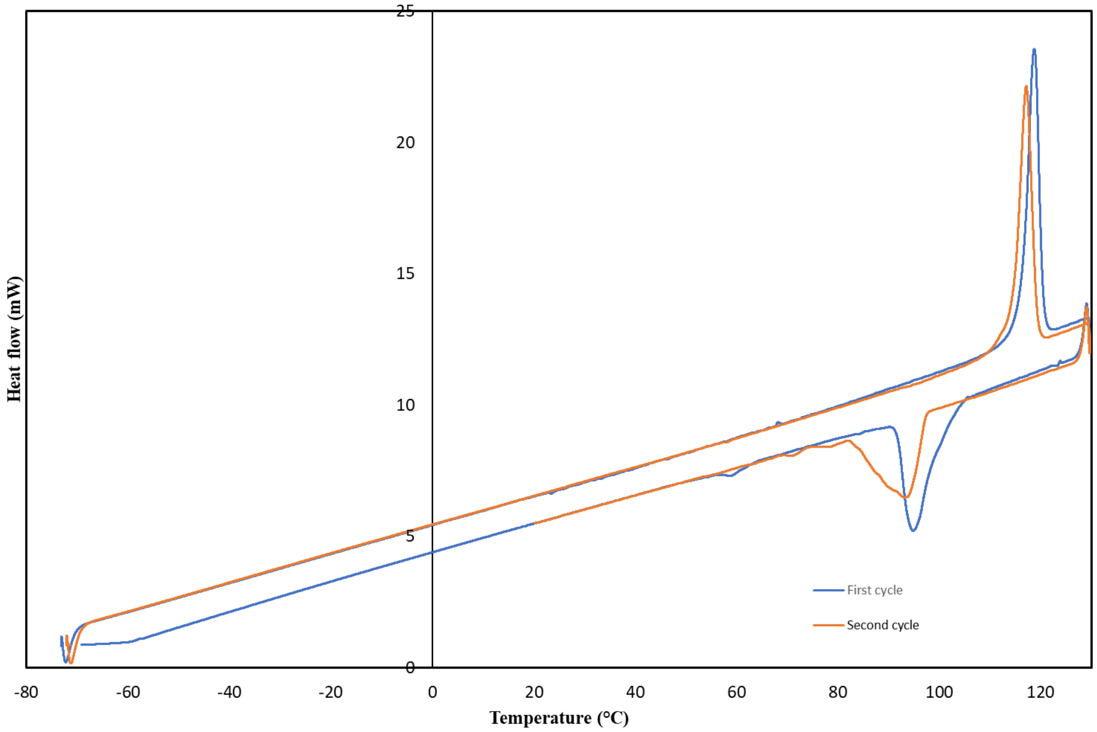

Figure 5.21 First (blue) and second cycle (orange) DSC thermograph of **105** showing the melting and cooling transition.

Likewise for the **BTA** derivatives, **59** and **65**, discussed in Chapters 2 and 3, the alanine ester and four carbon chain amino ester pyridine derivatives also display the same solid state structure. This is due to the interactions that occur in the structure are hydrogen bonds between the amide groups near the core aromatic unit and no interactions take place between the peripheral ester groups, thus the length of alkyl chain for these derivatives does not greatly affect the solid-state structure of the ligands. There does seem to be an influence of chain length on thermal properties of the derivatives, however, as evidenced by the phase transition of **105** upon cooling to 100 K. In the next section, the addition of some transition metals to the ligands and their effect on structure will be discussed.

5.4.5 Structural studies of 105Mn

A single crystal of **105Mn** was obtained from a diethyl ether diffusion into an acetonitrile-solution of the ligand and $MnCl_2$ and the data was solved and refined in the triclinic space group *P*-1. The asymmetric unit of this structure contains the ligand and two crystallographically unique coordinating Mn ions and is shown in Figure 5.22. There are also bridging chlorido ligands present. In this structure, the ligand coordinates to Mn1 through the pyridine nitrogen N1 and to Mn2 through one of the amide oxygen atoms, O3 to form a two-dimensional coordination polymer. There are also some hydrogen bonds between the amides and the aqua

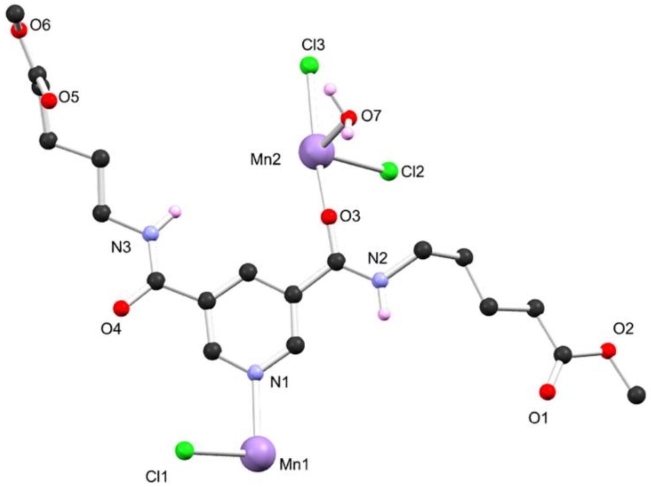

Figure 5.22 Asymmetric unit of **105Mn** with heteroatom labelling scheme, selected hydrogens are omitted for clarity.

ligand, for example O4 to O7, however there is no amide-amide interactions present. Both Mn1 and Mn2 are octahedral, though they have slightly different coordination environments. Mn1 has four bridging chlorido ligands in the equatorial plane, along with two nitrogens in the axial plane. The equatorial plane of Mn2 is occupied by three Cl ligands, along with O7 from the aqua ligand. The coordination environments of both Mn are shown in Figure 5.23. The interactions between this ligand and Mn are quite similar to that observed for the coordination polymer of the alanine methyl ester derivative, **105Mn**.

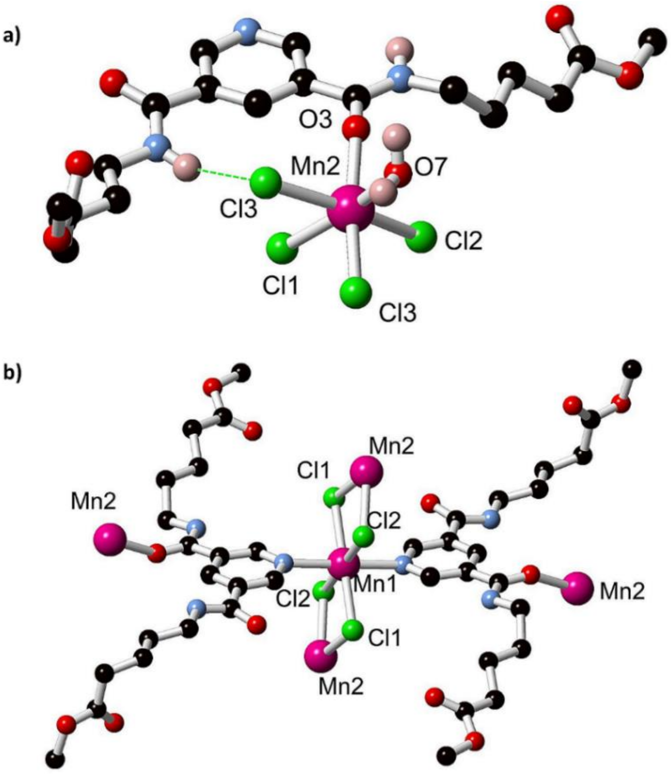

Figure 5.23 (a) Coordination environment of Mn2 in **105Mn** and (b) coordination environment of Mn1. Selected hydrogens are omitted for clarity.

A bulk sample of **105Mn** was prepared by dissolving the ligand and $MnCl_2$ in MeCN followed by the addition of ether which caused the precipitation of a solid which was filtered, dried and subject to X-ray powder diffraction. The pattern obtained was found to contain the same peaks to that calculated from the single crystal data obtained for **105Mn** and is shown in Figure 5.24. There are some small shifts in the peak positions which may be explained by the differences in the temperatures that the experiments were carried out at and the amount of solvent present in the two samples may also have an influence.

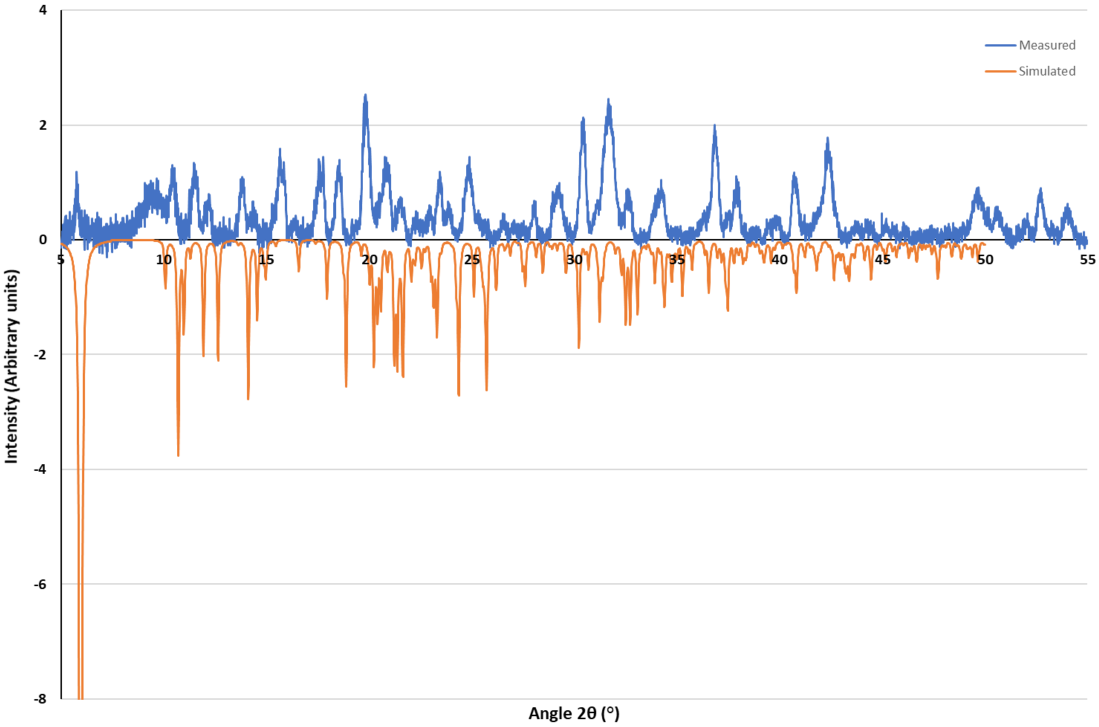

Figure 5.24 X-ray powder diffraction of **105Mn** (blue, room temperature) in comparison to the simulated pattern (orange, 100 K).

5.4.6 Structural studies of 105Cd

A second 2D polymer was obtained from the solvothermal reaction between **105** and $Cd(NO_3)_2$ in 1:1 DMF/H_2O and the data were solved and refined in the triclinic space group *P*-1. The solvothermal technique was previously described in Chapter 3. The asymmetric unit consists of two ligands and two metals, along with a number of H_2O molecules and is shown in Figure 5.25. The Cd1 is coordinated through one pyridine nitrogen atom, N2, two aqua molecules and to the carboxylate oxygens, O7, O8, O11, and O12. Similarly, Cd2 is coordinated though a pyridine nitrogen atom, N5, two aqua molecules, and the carboxylate oxygens O1, O2, O5 and O6. The coordination environments of both metal ions are shown in Figure 5.25. There was no π-π stacking present in the structure, while there are some hydrogen bonding interactions between the amide oxygen and nitrogen atoms and the aqua molecules.

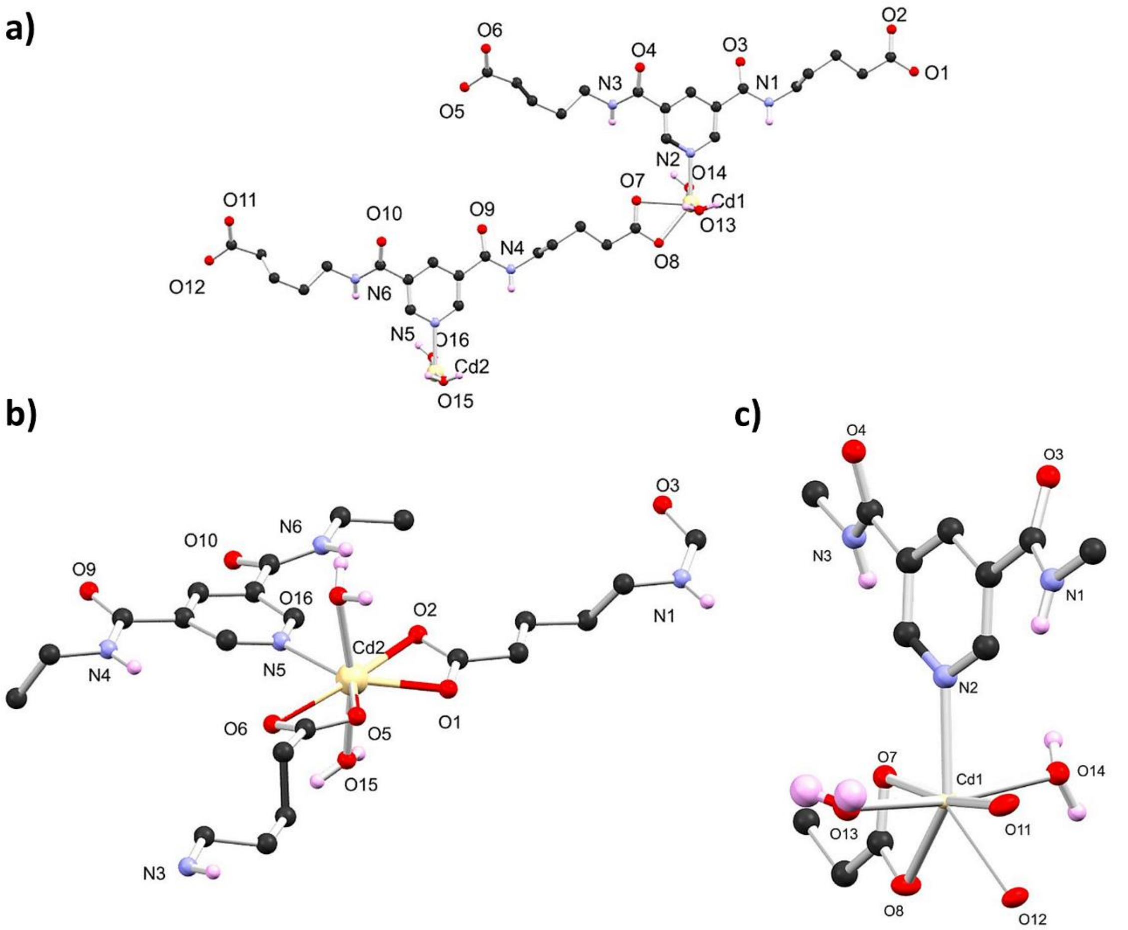

Figure 5.25 (a) Asymmetric unit of **105Cd** with heteroatom labelling scheme; (b) coordination environment of Cd2 and (c) Cd1. Selected hydrogen atoms and H_2O molecules are omitted for clarity.

The bulk purity of **105Cd** was analysed using X-ray powder diffraction as is common practice. There were some difficulties in obtaining enough sample for the diffraction experiment, however, after many attempts enough solid sample was obtained in order to carry out the experiment. The difficulties in obtaining adequate sample were due to the difficulties in synthesising a large quantity of phase pure crystals. The pattern obtained was not a match to the simulated pattern calculated from the single crystal data, thus the experiment was repeated using another batch of sample. This too did not agree with the simulated pattern, but rather resembled an amorphous solid, with an example shown of this shown in Figure 5.26. This would indicate that the sample used for the powder diffraction experiment was not the same phase as the sample run in the single crystal experiment, thus the sample was polymorphous. Many attempts were made to obtain single crystals of this other phase of suitable quality for diffraction, however, these attempts were unsuccessful. Moving on from the simple alkyl chain derivatives, we then moved on to investigating the structural properties of the aromatic pyridine derivatives which will be discussed in the next section.

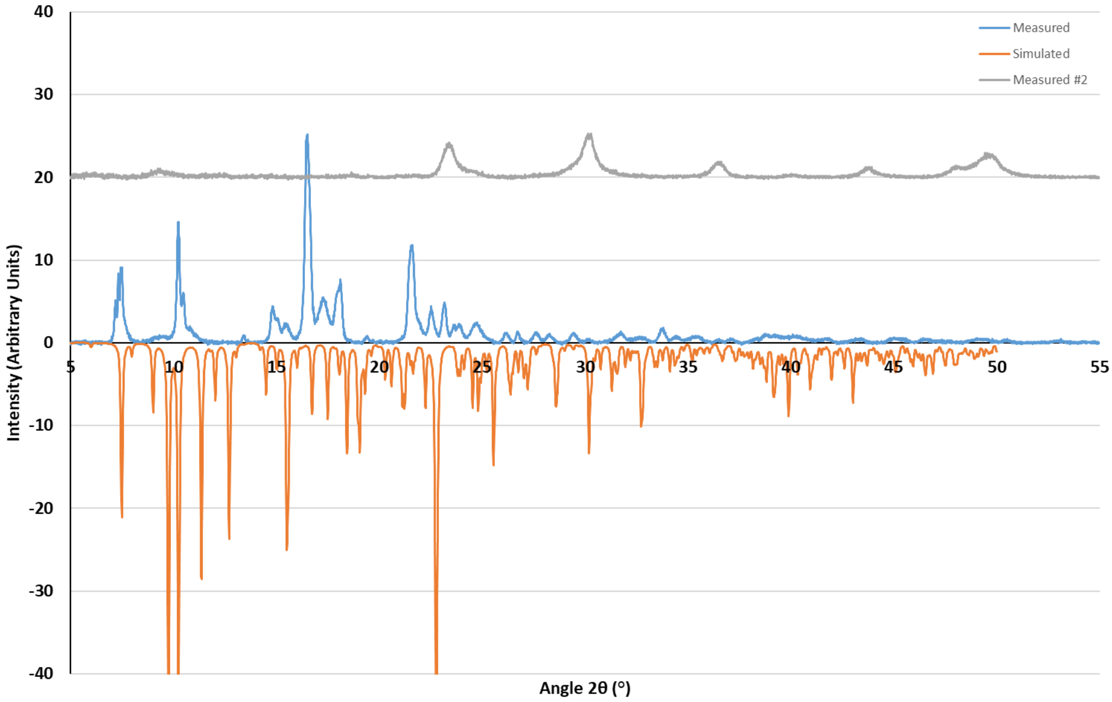

Figure 5.26 X-ray powder diffraction pattern of the measured sample of **105Cd** (room temperature, blue), second measured sample (room temperature, grey) in comparison to the pattern obtained from the single crystal data (100 K, orange).

5.4.7 Structural studies of 107Cd

Many attempts using a variety of conditions were made to obtain single crystals of diffraction quality of the aromatic derivative, **107**, however these were not successful. Moving on from these attempts, we decided to attempt to crystallise the ligand in the presence of transition metals, with one of these attempts being successful. A solvothermal reaction of **107** and

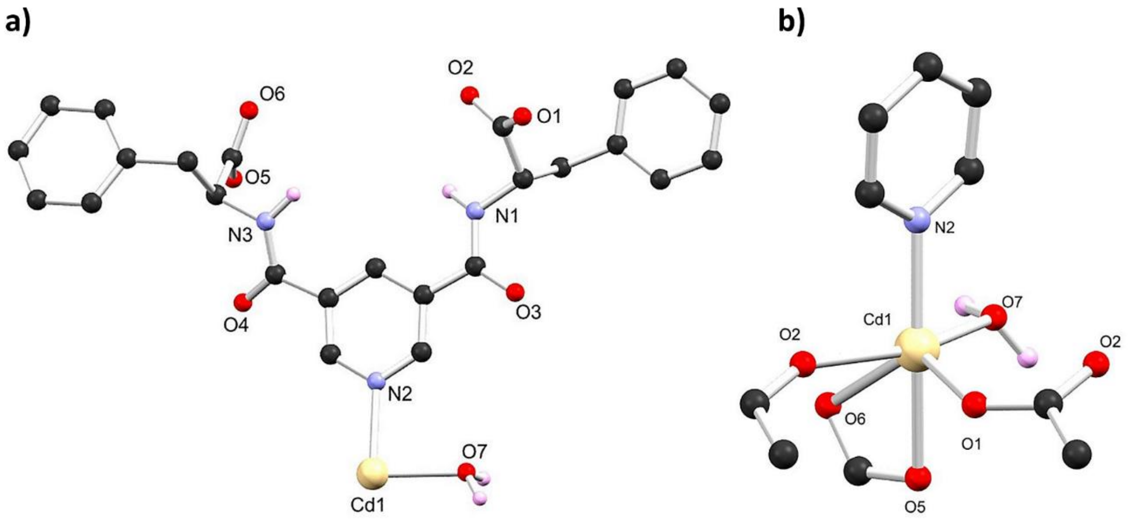

Figure 5.27 (a) Asymmetric unit of **107Cd** with heteroatom labelling scheme, selected hydrogens are omitted for clarity; (b) coordination environment of Cd1.

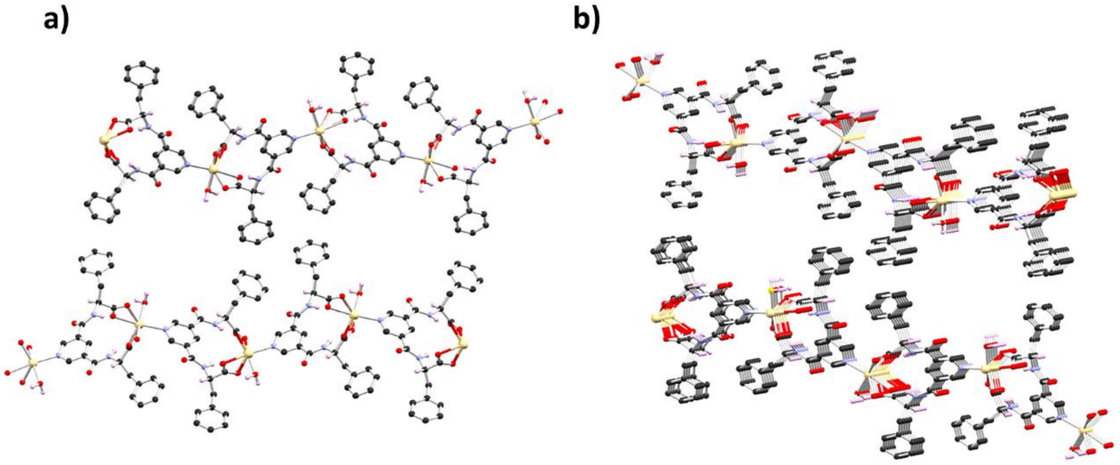

Figure 5.28 Extended structure of **107Cd.**

$Cd(NO_3)_2$ in a 1:1 DMF/H_2O mixture for 24 h resulted in single crystals of suitable quality for diffraction and the data obtained were solved and refined in the orthorhombic space group $P2_12_12_1$. The asymmetric unit, shown in Figure 5.26, contains the ligand in its entirety along with the coordinated Cd ion and an aqua molecule. There is some positional disorder present in the structure, with the aromatic group originating from C17 modelled over two positions split at 0.33 and 0.66 occupancy for C26-C32 and C19-C25 respectively, see appendix. The extended structure forms a 2D sheet, Figure 5.28, with the significant interactions being hydrogen bonding between H1, O1, N3 and O5. There are no significant stacking interactions within the structure and there are no interactions holding the sheets together. There are some channels present, however, given the weak interactions holding the structure together, these would most likely fall apart if the sample were subject to evacuation and porosity investigations. In this structure, the Cd is six coordinate and coordinates to one chelating carboxylate group, O5 and O6, one water molecule, O7 and to two monodentate carboxylates, O1 and O2 that each bridge two Cd. The coordination environment of the Cd is shown in Figure 5.26. There was a number of water molecules, estimated to be 15% of the mass from the SQUEEZE, present within the structure and their presence was accounted for using the SQUEEZE routine in PLATON,[129] with the exact water content further analysed by elemental analysis and TGA. TGA was carried out on a freshly isolated sample and a dried sample and the results of such are shown below in Figure 5.29. The freshly isolated sample (black) showed a mass loss of approximately 30% before 40 °C followed by a further loss of 5% before 80 °C, with these losses accounting for the loss of surface and channel solvent. There was no further mass loss until 360 °C at which point the mass decreased to 20 % and remained relatively stable up until 500 °C. The sample dried *in vacuo* on the other hand showed a mass loss of only about 10% up to 100 °C and

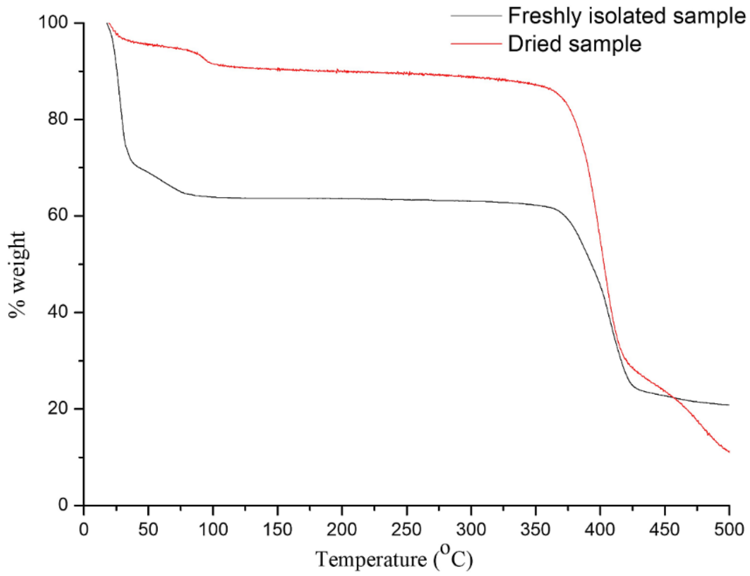

Figure 5.29 TGA of a freshly isolated and dried sample of **107Cd**.

remained stable up until approximately 360 °C when the onset of decomposition began. These clear differences in mass losses before 100 °C clearly indicate the presence of a significant amount of surface and channel solvent in the freshly isolated sample, and even a small amount of solvent, presumably in the channels, present in the dried sample. Elemental analysis showed there to be 1.25 H_2O molecules per molecule of **107Cd** (see experimental for more details).

Powder diffraction was also carried out on **107Cd** and is shown in Figure 5.30. The measured pattern is in agreement to that simulated from the single crystal data, with the

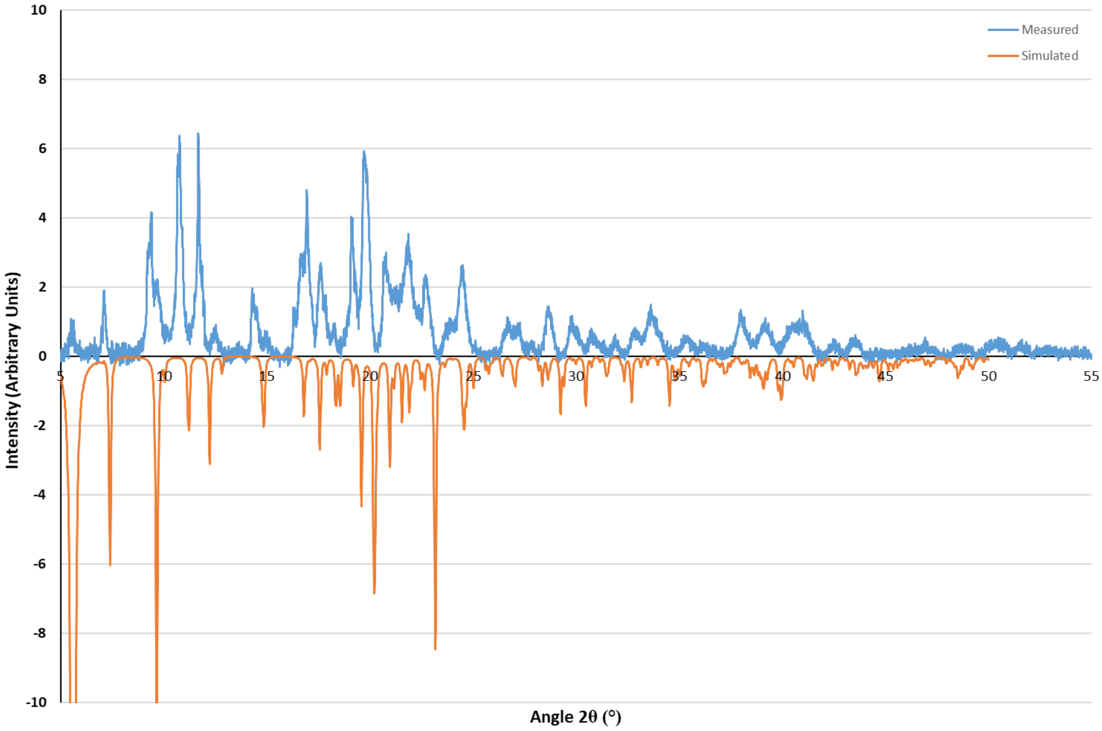

Figure 5.30 X-ray powder diffraction of the measured sample of **107Cd** (room temperature, blue) in comparison to that simulated from the single crystal data (100 K, orange).

positions of the peaks coinciding, thus the sample appears to phase pure and indicates the reproducibility of the crystallisation process. Moving on from this derivative, we decided to synthesise and investigate the structural features of a similar derivative with the aromatic arms used in Chapter 3 for **64Cd.**

5.4.8 Structural studies of 108

A single crystal of **108** was obtained from an acetonitrile-diethyl ether diffusion and the data was solved and refined in the monoclinic space group *C*2/*c*. The crystals isolated were needle-like and somewhat flexible which will be discussed in a further section. The asymmetric unit is shown in Figure 5.31 and was found to contain the molecule in its entirety. The extended structure of **108** forms a one-dimensional polymer and contains some weak π-π stacking interactions and is shown in Figure 5.31. This was the only ligand structure to display π-π stacking interactions.

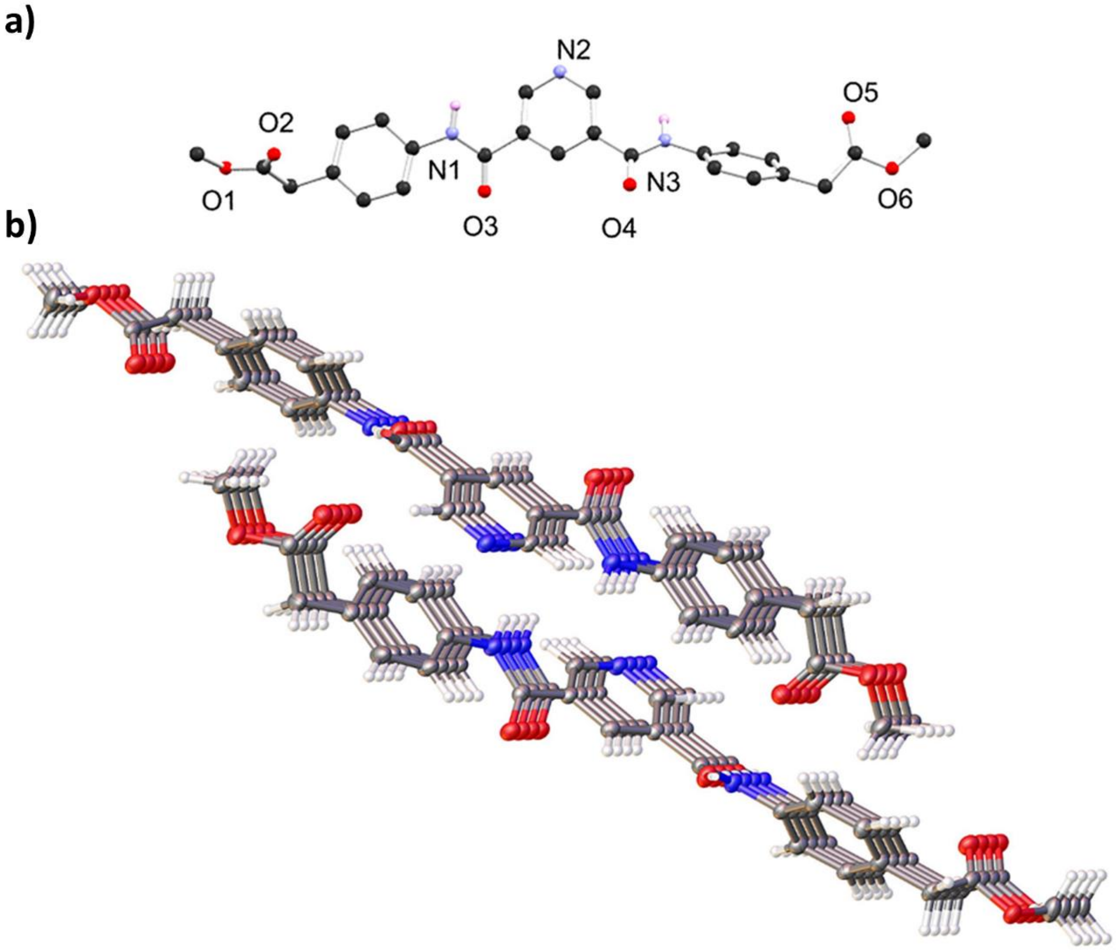

Figure 5.31 (a) Asymmetric unit of **108** with heteroatom labelling scheme. Selected hydrogen atoms are omitted for clarity; (b) extended structure of **108**.

A bulk sample was prepared by dissolving the ligand in acetonitrile, followed by the addition of ether which caused the precipitation of a crystalline solid which was used for powder diffraction. As was the case for **63** in Chapter 2, the crystals of **108** were needle-like, thus this was taken into account by applying the March-Dollase parameter (0.65) for preferred orientations to the simulated powder pattern of **108**.[130] The pattern obtained from the diffraction experiment showed the material to be phase pure and is shown in Figure 5.32.

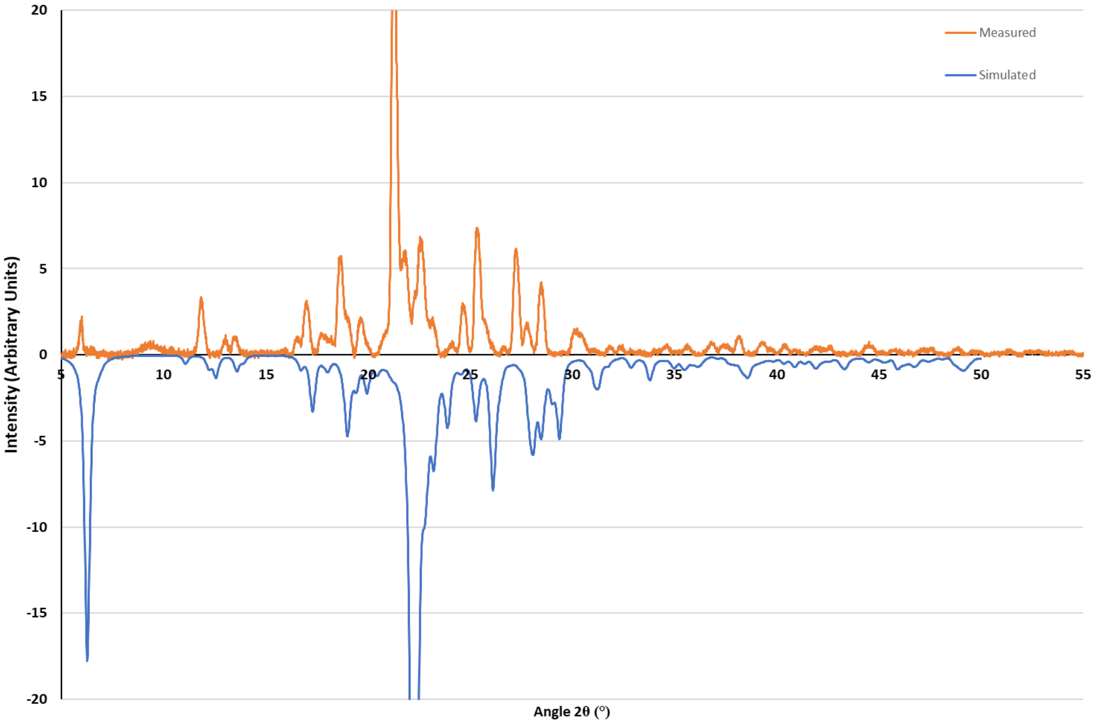

Figure 5.32 X-ray powder diffraction pattern of the measured sample of **108** (room temperature, blue) in comparison with the pattern simulated from the single crystal data (100 K, orange).

A number of attempts were made to obtain coordination compounds of **108** as detailed in Table 5.1, however, these were mostly unsuccessful. A single crystal of suitable quality for diffraction was obtained from the reflux of **108** with $PtCl_2(DMSO)_2$ in MeOH for 6 h. The solvent was evaporated and the solid re-dissolved in MeCN and left to slowly evaporate to result in a small number of single crystals. The asymmetric unit was found to contain the ligand, one Pt, two cis chlorido ligands and a DMSO that coordinates through the sulfur. There was some weak hydrogen bonding observed in the structure between the amide groups and the O atom of DMSO and Cl. Attempts were made to re-synthesise these crystals, however the reaction was not reproducible, and no further characterisation or investigations were possible. This structure will therefore not be discussed further in this chapter, but the structure can be found in the appendix.

5.5 AFM studies of 108

Given the flexible-like nature of **108**, it was decided to investigate the hardness and elasticity of these materials using AFM. Typically, single crystals are brittle and inelastic, thus these mechanical properties limit their use in applications such as flexible electronics and optical devices.[206] It has been reported that crystals with the potential to be reversibly and repeatedly bent are attractive for engineering applications that require materials that can be tuned through external stimuli. [207]

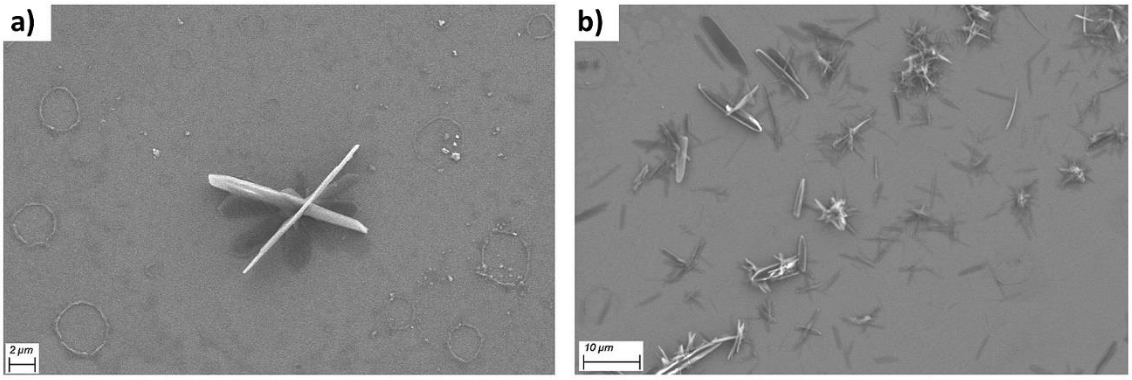

Figure 5.33 (a) SEM of a dried sample of **108**, scale bar 2 μm and (b) scale bar 10 μm.

Crystals of **108** were prepared using the same procedure as described above, and the size and morphology of the resulting crystals was analysed using SEM as shown in Figure 5.33 and optical microscopy which can be found in the appendix. The needle-like crystals were found to be approximately 1 μm in diameter and found to aggregate in bundles. This size was determined to be suitable for the AFM apparatus available. AFM was carried out in collaboration with Dr Chiara Rotella and Prof. John Boland (School of Chemistry, Trinity College Dublin). As for the samples in Chapter 2, the AFM samples were prepared by dropcasting 5 μL of the sample in MeCN onto a silica wafer, followed by drying under a stream of nitrogen. The AFM analysis of the fibre diameter was in agreement with the SEM analysis, approximately 1 μm and the height profile showed the heights to range from 150 nm to 630 nm,

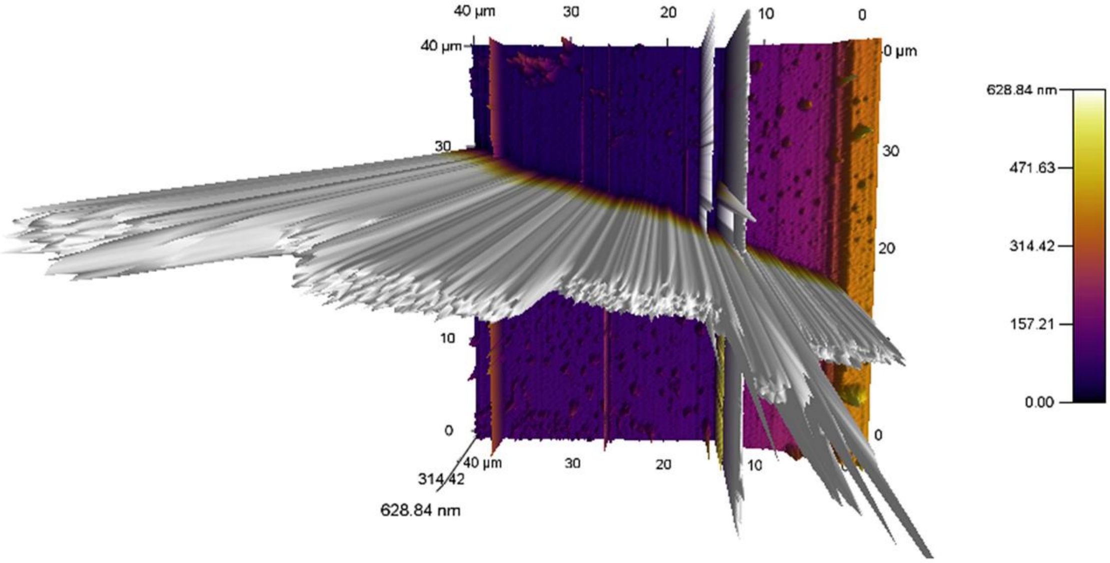

Figure 5.34 AFM image of **108** showing the height and sizes of the needle-like crystals.

Figure 5.34. The fibres were also found to aggregate as was previously shown in the SEM analysis. Following this, force measurements were attempted, with a crude force curve obtained shown in Figure 5.35. Force measurements for this sample proved difficult due to the difficulties in obtaining an isolated single crystal to measure. The Young's modulus calculated for the force curve shown was found to be 2.67 GPa, which would indicate that the material is quite strong in comparison with the reported Young's Modulus of other materials, for example, glass was 50 GPa and cartilage has a value of 0.16-0.6 GPa.[141] It is also a larger value than that obtained for the **BTA** derivatives, **61** and **63**, in Chapter 2 which had Young's moduli values of 1.6 and 1.2 GPa respectively. Further studies into the mechanical properties of **108** and other similar derivatives should be carried out to gain a better understanding of their behaviours and to determine if they have future applications in the field of elastic crystals.

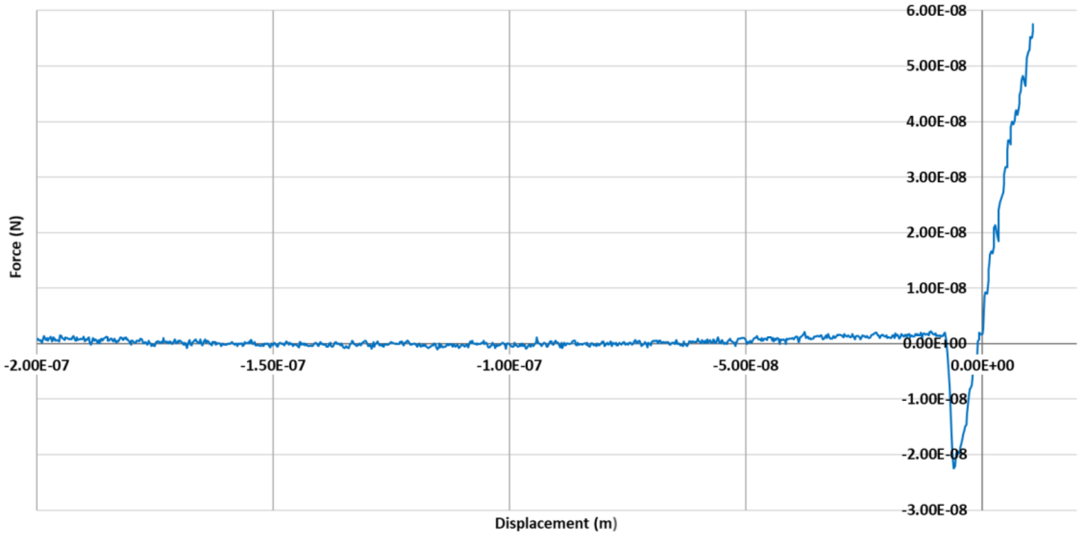

Figure 5.35 Force curve for **108**.

5.6 Conclusions and future perspectives.

To conclude, the synthesis and characterisation of a number of pyridine-3,5-dicarboxamide derivatives was reported and their interactions with metal salts was investigated. The X-ray structures obtained for the ligands **105** and **104** revealed them to arrange into 2D polymers with the main interaction within the polymer being intramolecular hydrogen bonding between the amides, similarly to the **BTA** derivatives reported in Chapters 2 and 3. The larger, aromatic side chain derivative **108** was the only ligand structure to display π-π interactions and appeared to possess some elastic crystal properties, however, further mechanical studies are required in this area to determine their potential. The reaction of the ligands with various metal salts resulted in the formation of a number of 2D coordination polymers, with hydrogen bonding playing a major role in these structures. Unlike the **BTA** derivative **64Cd** reported in Chapter 3, none of the mentioned pyridine coordination polymers display potential as permanently porous materials due to the weak intramolecular interactions between them, for example in the case of **107Cd**.

In comparison to the similarly derivatised **BTA** compounds reported in this thesis, the pyridine-3,5-dicarboxamide derivatives had a greater tendency towards crystallisation, which is partly intuitive due to the greater rotational freedom imparted by the third arm, thus making crystallisation more challenging. These derivatives also reacted with metals more readily to generate 2D coordination polymers, unlike the **BTA** derivatives, with the pyridine nitrogen greatly aiding this coordination. Many of the structures reported were phase pure and reproducible as evidenced by the powder diffraction experiments, though there were some issues with a small number of the structures exhibiting polymorphous behaviour.

Single crystals of the ligand of **106** or coordination polymers containing **106** were not obtained. This would suggest the that the side arm groups are preventing crystallisation from occurring, potentially due to the extra hydrogen bond acceptors present or the increased flexibility. Crystallisation attempts of the **BTA** derivative containing this side arm functionality were also unsuccessful.

To make a more detailed comparison to the corresponding **BTA** derivatives, the reaction to generate the carboxylic acid derivatives should be optimised in the future, with particular attention paid to the gelation potential of the compounds. The carboxylic acid derivatives could also be of interest with respect to coordination chemistry, with the extra coordination and hydrogen bonding potential of the carboxylic groups It would also be interesting to investigate if there would be competitive hydrogen bonding interactions arising from the carboxylic acid groups, as was seen with the **BTA** derivatives. Unlike the **BTA** derivatives, the pyridine compounds should give rise to metallogels due to the greater potential for metal coordination.

5.7 Final Summary

The structural versatility of a number of **BTA**-based derivatives was demonstrated throughout this thesis. The introduction provided an overview of **BTA**-based systems, which were found to form a variety of different materials with a number of potential applications, ranging from microcapsules capable for drug delivery,[82] to porous materials capable of gas adsorption,[17,103] to MRI contrast agents.[86] While it has been reported that the nature of side chain greatly influences the self-assembly of **BTA**-based materials, the majority of these reports involved significantly different structures, thus the variety in behaviour is relatively unsurprising. The aim of this thesis was to study the effect of small structural changes on self-assembly behaviour and function, by looking at some relatively simple **BTA** derivatives and building them up to more structurally complex derivatives.

Chapter 2 mainly focused on ester and carboxylic acid terminated derivatives of various alkyl chain length and investigated the influence of small structural changes on structural properties and function. For example, it was demonstrated that the ester derivatives had a greater tendency towards crystallisation and in some cases formed the helical structure typical of **BTA** derivatives. However, this was limited by the length of the alkyl chain influencing the formation of the helix, with the longest derivative, **58**, containing a pentyl spacer not displaying this arrangement. The corresponding carboxylic acid derivatives had a greater tendency towards gelation with the length of alkyl chain again influencing this behaviour, with the pentyl derivative **61** forming the most robust material. The materials formed from these structures were also subject to a variety of different experiments to further assess their behaviour. Interestingly, the ester derivatives displayed mesophases, indicative of liquid crystal properties, while the carboxylic acid derivatives did not. Preliminary AFM studies on the gel fibres of the carboxylic acid derivatives, **61** and **63**, indicated that the fibres were quite strong. As far as can be determined, there have been only a small number of reports of AFM studies of **BTA**-based materials, thus this is a relatively unexplored area of investigation.[120] Gas adsorption experiments on **62** and **63** revealed that the materials collapsed upon evacuation, thus these derivatives do not possess permanent porosity or gas adsorption properties. The vast array of properties found in this structurally similar family of compounds indicates the significant effect of small variations in structure on the form and function of **BTA**-based materials and again, demonstrates the subtleties in predicting or tuning the behaviour of **BTA**-based compounds.

Chapter 3 discussed the synthesis, characterisation and evaluation of gas adsorption properties for two **BTA**-based coordination polymers with a similar degree of flexibility but different bridging distances, along with the presence of aromatic rings in the side chains of one of the derivatives, **64**. The crystal structure of **65** was also obtained and found to display the classical helical arrangement common for **BTA** derivatives in the absence of competing hydrogen bonding interactions. The solvothermal reaction of the ligands **64** and **65** with $Cd(NO_3)_2$ resulted in the formation of coordination polymers which were subject to gas adsorption studies. Polymer **64Cd** was found to display permanent porosity and a high capacity for CO_2, while **65Cd** did not. This is presumably due to the greater flexibility and more restricted pore size of **65Cd**. The extension of **64** with simple amino acids and studies on the resulting materials implied that further structural expansion and addition of more hydrogen bonding groups hindered both gelation and crystallisation abilities.

Two different approaches to generate polymeric materials based on **BTA**-amine based precursors were reported in Chapter 4. The first approach attempted to generate a covalently linked system, however, this approach was hindered by a number of synthetic challenges and the target polymer was not obtained. Further modification of the target molecule and synthetic route in the future could result in an interesting polymeric system and remain of current interest and importance within the field, as evidenced by the formation of a spinout company, Suprapolix, based on research of similar polymeric systems by Meijer and Sijbesma, along with a number recent of high-impact articles .[53 55,88,106,164,167] The second part of this chapter discussed the synthesis and characterisation of a non-covalent, dynamic polymer based on a **BTA** core and functionalised with diiminophenol-based side chains to result in a Schiff-base linked organic polymer. The properties of the organic polymer and its interactions with metals were probed using a variety of techniques, with Cu(II) ions found to interact through a nucleation or seeding mechanism rather than through chemisorption within the diiminophenol binding pockets.

Overall these three chapters have shown the variety and versatility of the materials formed by structurally-related **BTA** derivatives and have demonstrated the challenges in tuning and predicting the behaviour of such.

Chapter 5 discussed the synthesis, characterisation and structural properties of a number of pyridine-3,5-dicarboxamide derivatives functionalised with similar chains to those used in the formation of the **BTA** materials above. Similarly to the **BTA** family of compounds, these structures were investigated the influence of the side chains on the materials formed by these compounds. A variety of techniques were employed to study these derivatives, such as X-ray crystallography, DSC and SEM. The ester-terminated derivatives had a much greater tendency towards crystallisation and metal interaction than their **BTA** counterparts, partly due to lower degree of flexibility imparted by the two side chains compared to the three of the **BTA** and the pyridine nitrogen, respectively. Future work should focus on the synthesis of the carboxylic acid terminated derivatives in order to make a thorough comparison to the **BTA** family of derivatives reported.

‘Everything happens for a reason.’

My mom, on everything

6. Experimental

6.1 General materials and methods

All solvents and chemicals were purchased from commercial sources and used without further purification. All chemicals were purchased from Sigma-Aldrich, Ireland Ltd. or TCI Ltd. unless otherwise stated and used without further purification. Flash chromatography was carried out using a TeledyneIsco CombiFlash Rf 200 automated purification system; pre-packed normal phase, amine or C18 silica cartridges used were supplied by TeledyneIsco RediSep® or Grace Technologies. Thin-layer chromatography (TLC) was conducted using MerckMillipore Kiesegel 60 F254 silica or alumina plates and visualised under λ = 254 nm; amine containing compounds were visualised using Ninhydrin in EtOH. Melting points were determined using an Electrothermal IA9000 digital melting point apparatus.

6.1.2 NMR spectroscopy

Deuterated solvents used for NMR analysis ($CDCl_3$, $(CD_3)_2SO$) were purchased from Apollo Scientific. The ^{1}H NMR spectra were recorded at 400 MHz using a Bruker Spectrospin DPX-400 instrument and the ^{13}C{^{1}H} NMR spectra were recorded at 100 MHz using a Bruker Spectrospin DPX-400 instrument. NMR spectra were also recorded using a Bruker AV-600 instrument operating at 600.1 MHz for ^{1}H NMR and 150.9 MHz for ^{13}C{^{1}H} NMR. Chemical shifts are reported in commercially available deuterated solvents; δ in ppm relative to $SiMe_4$ (= 0 ppm) referenced relative to the internal solvent signals: Data were processed with MestReNova 6.0.2. Multiplicities are abbreviated as follows: singlet (s), doublet (d), triplet (t), quartet (q), pentet (p), multiplet (m) and broad singlet (br s): *J* in Hz. All NMR spectra were carried out at 293 K.

6.1.3 Mass spectrometry

Mass spectrometry was carried out using HPLC grade solvents. Electrospray mass spectra were determined on a Micromass LCT spectrometer and high resolution mass spectra were determined relative to a standard of leucine enkephaline. Maldi-Q-TOF mass spectra were carried out on a MALDI-Q-TOF-Premier (Waters Corporation, Micromass MS technologies, Manchester, UK) and high-resolution mass spectrometry was performed using Glu-Fib with an internal reference peak of *m/z* 1570.6774.

6.1.4 Infrared Spectroscopy

Infrared spectra were recorded on a Perkin Elmer Spectrum One FT-IR spectrometer equipped with universal ATR sampling accessory.

6.1.5 X-ray Crystallography

Unless otherwise stated, X-ray data were collected on a Bruker APEX-II DUO diffractometer using microfocus Cu Kα (λ = 1.5405 Å) or graphite-monochromated Mo Kα (λ = 1.5405 Å) radiation. All data collections were carried out using standard ω and φ scans at 100 K with temperature control provided by a Cobra cryostream. The data were reduced and multi-scan absorption corrections applied using SADABS[208] within the Bruker APEX3 software suite.[209] Phase purity of crystalline materials was confirmed with X-ray powder diffraction patterns recorded with a Bruker D2 Phaser instrument using Cu Kα (λ = 1.5405 Å) radiation. Samples were finely ground and applied to a quartz sample holder. Data were measured at room temperature in the 2θ range 5-55° in 0.01° increments with concurrent rotation in φ of 1 RPM. Additional X-ray powder diffraction data for 101 was collected at 100 K on a Bruker Apex-II Duo instrument using Cu Kα radiation in the 2θ range 2-55°, and was converted to θ vs intensity data by integration of Debye rings obtained from the area detector data. Raw data were compared with the simulated patterns from the single crystal data collections carried out at 100 K.

6.1.6 Scanning Electron Microscopy

Microscopy analysis of gel/aggregate/crystalline samples by Scanning Electron Microscopy (SEM) was carried out using the facilities of the Advanced Microscopy Laboratory (AML) in Trinity College Dublin. Samples were prepared by a drop-casting methodology onto clean silicon wafers. The manually drop cast samples were dried overnight in ambient conditions and under high vacuum for 2 hours prior immediately to their imaging. In some cases, samples were coated with a conductive Pd/Au layer using a Cressington 208Hr high resolution sputter coater, in order to improve contrast where static charging interfered with the imaging. Low kV SEM was carried out using the Zeiss ULTRA Plus using an SE2 detector. EDX measurements were carried out using a Carl Zeiss Ultra SEM that was equipped with an Oxford Instruments Inca System EDX setup. The samples used for EDX analysis were uncoated.

6.1.7 Polarised Optical Microscopy

A (BX53) cross polarising microscope equipped with an XC50 camera and Linkam scientific instruments LTS420 temperature-controlled stage equipped with Stream Basic software was used for the polarised optical microscopy images.

6.1.8 Atomic Force Microscopy

AFM was carried out in collaboration with Dr Chiara Rotella of Prof. John Boland's research group, School of Chemistry, Trinity College Dublin. All mechanical measurements were performed using an Asylum MFP-3D Atomic Force Microscope using a Nanosensors SSS-NCH-10 tip. This tip was made from doped silicon, with force constant range 10-130 N/m. This tip was used for both the non-contact and tapping modes. Argyle software was used to view the obtained images.

6.1.9 Thermal Analysis

Thermal gravimetric analysis was performed on a Perkin Elmer Pyris 1 TGA equipped with an ultra-micro balance with a sensitivity of 0.1 microgram. Samples were spread on alumina crucibles and heated under a nitrogen purge flow of 20 ml min^{-1} at a heating rate of 5 °C min^{-1}. Elemental analysis was carried out on an Exeter Analytical CE440 elemental analyser at the microanalysis laboratory, School of Chemistry and Chemical Biology, University College Dublin. The thermal phase transitions of each compound were examined using a Perkin Elmer Diamond Differential Scanning Calorimeter (DSC). Samples were prepared in crimped aluminium sample pans of 50 μL capacity, with equivalent reference pans. Heating and cooling cycles were carried out at heating/cooling rates of 2 °C min^{-1} in the appropriate temperature range, with 5 minute equilibration times at the end of each temperature scan. All data are shown with endotherms upwards.

6.1.10 Gas adsorption studies

Gas adsorption isotherms were carried out in collaboration with Mr. Kevin Byrne of Prof Wolfgang Schmitt's group in SNIAMS, School of Chemistry, TCD and were measured using a Quantachrome Autosorb IQ gas sorption analyser. Chemically pure (CP, N4.5) grade He, N_2, H_2 and CO_2 gases were used for the measurements.

6.1.11 Rheological measurements

Rheological measurements were carried out with the help of Dr Benjamin Haffner and Prof. Matthias E. Möbius in SNIAMS, School of Physics, TCD and were measured with a Anton Paar MCR 301 rheometer with a 50 mm parallel plate geometry.

6.2 Synthetic procedures

Synthetic procedures are presented in order of their discussion.

6.2.1 Synthesis of compounds discussed in Chapter 2

5-Nitro-1,10-phenanthroline (110)

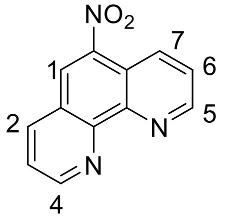

Phenanthroline (5 g, 27.7 mmol) was dissolved in conc. H_2SO_4 (30 mL), then nitric acid (15 mL, 65%) was added drop-wise, and the reaction mixture was set to reflux at 160 °C for 3 h. NaOH was added drop-wise to neutralise the reaction and the mixture was filtered, then washed with H_2O and dried in *vacuo* resulting in an orange solid (2.24 g, 9.94 mmol, 38%). m.p. 198-200 ˚C (lit.[210] m.p. 198-200 ˚C). ^{1}H NMR (DMSO-d_6, 400 MHz, δ) 9.29-9.27 (m, 1H, 4), 9.24-9.22 (m, 1H, 5), 9.03 (s, 1H, 1), 8.89 (d, 1H, *J* = 8.6 Hz, 2), 8.78 (d, 1H, *J* = 8.1 Hz, 7), 7.95-7.91 (m, 2H, 3, 6). ^{13}C{^{1}H} NMR (DMSO-d_6, 100 MHz, δ) 151.7 (C-N), 150.5 (C-N), 144.1

(C-N), 141.7 (C-N), 134.8 (C-C), 134.6 (C-C), 126.3 (C-C), 125.7 (C-C), 125.6 (C-C), 121.2 (C-C). HRMS-ESI+ (*m/z*): $[M+H]^+$ calculated for $C_{12}H_8N_3O_2$ 226.0538; found 226.0612. IR v_{max} (cm^{-1}): 3406, 1589, 1503, 1446, 1419, 1384, 1342, 1144, 1106, 984, 905, 830, 804, 732.

5 Amino-1,10-phenanthroline (67)

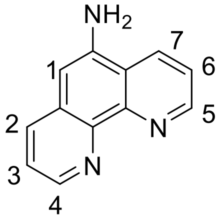

A mixture of 5-Nitro-1,10-phenanthroline (1.2 g, 5.33 mmol) and 5% Pd/C (0.3 g) was put under reflux in EtOH (50 mL) for 1 h at 90 °C. $N_2H_4{\cdot}H_2O$ (2.6 mL, 53.3 mmol, 10 equivalents) was slowly added to the mixture and left at reflux for 4 h. The hot solution was then filtered through celite and concentrated under reduced pressure. Resultant brown solid was washed with H_2O, then filtered to reveal the purified yellow-brown product (0.92 g, 4.71 mmol, 88%). m.p. 245 ˚C decomposed. ^1H NMR (DMSO-d_6, 600 MHz, δ) 9.05 (dd, 1H, *J* = 4.2, 1.6 Hz, 5), 8.68-8.65 (m, 2H, 4,7), 8.04 (dd, 1H, *J* = 8.1, 1.6 Hz, 2), 7.73 (dd, 1H, *J* = 8.3, 4.2 Hz, 6), 7.50 (dd, 1H, *J* = 8.1, 4.2 Hz, 3), 6.86 (s, 1H, 1), 6.1 (s, 2H, NH_2). $^{13}C\{^1H\}$ NMR (DMSO-d_6, 150 MHz, δ) 149.3 (C-N), 146.2 (C-N), 144.8(C-N), 142.7(C-N), 140.3 (C-NH_2), 132.7, 130.8, 130.6, 123.2, 120, 101.8 (C-C). HRMS-ESI+ (*m/z*): $[M+H]^+$ calculated for $C_{12}H_{10}N_3$ 196.0875, found 196.0875. IR v_{max} (cm^{-1}): 3416, 3321, 1635, 1611, 1593, 1488, 1427, 1303, 1106, 1033, 884, 841, 812, 735, 625.

N^1, *N*^{3}, *N*^{5}-tris(phenanthroline-5-butanamido) benzene-1,3,5-tricarboxamide (68)

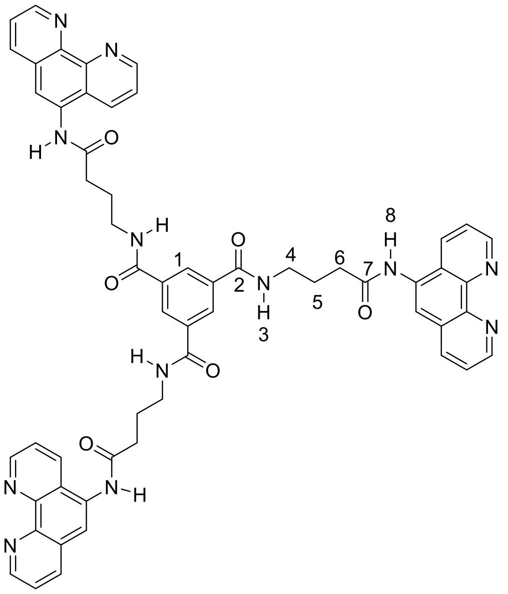

63 (1 equivalent) was added to dry DCM in a sealed reaction vial under an argon atmosphere and left to stir at room temperature for 5 minutes before being cooled on ice. EDC.HCl (2.5 eq.) and DMAP (1 eq.) were then added and stirred for 5 min before the addition of the relevant amine (2.5 eq.) The reaction mixture was then left to stir under an argon atmosphere at room temperature for 72 h. The reaction solvent was removed under reduced pressure to reveal orange oil. This resultant oil was dried in vacuo before the addition of water causing the precipitation of an orange solid, which was then washed with MeCN which was then filtered and dried *in vacuo* to give the solid in 23% yield. ^1H NMR (DMSO-d_6, 400 MHz, δ) 10.19 (s, 3H, H1), 9.11-9.09 (m, 3H, H_{phen}), 9.03-9.01 (m, 3H, H_{phen}), 8.79 (bs, 3H, H3), 8.64 (bd, 3H *J* = 8.36 Hz, H_{phen}), 8.47 (s, 3H, H_{BTA}), 8.43-8.41 (m, 3H, H_{phen}), 8.16 (s, 3H, H_{phen}), 7.82-7.78

(m, 3H, H$_{phen}$), 7.74-7.71 (m, 3H, H$_{phen}$), 3.45-3.43 (m, 6H, H4), 2.67-2.63 (m, 6H, H6), 2.06-1.97 (m, 6H, H5). ^{13}C{^{1}H} NMR (DMSO-d_6, 150 MHz, δ) 172.1, 165.6, 149.8, 149.3, 145.8, 143.8, 135.8, 134, 131.8, 131.7, 128.5, 128.1, 124.9, 123.5, 122.8, 119.7, 40, 33.5, 25.2. IR ν_{max} (cm^{-1}): 3248, 1654, 1528, 1443, 1284, 1175, 881, 801, 737, 575, 557.

***N*-(2, 2′; 6′, 2″)Terpyridin-4′-yl-propane-1,3-diamine (64)**

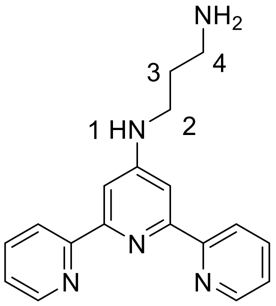

4’-chloro-2,6’:6’,2’’-terpyridine was dissolved in 1,3-diaminopropane (3.52 g, 4 mL, 47 mmol) and refluxed at 125 ˚C for 24 h. After cooling to room temperature, the solution was added to ice-water, causing a white precipitate to form. This was separated by centrifugation, with the white solid then dissolved in DCM and washed with H_2O three times. The organic layer was then dried over Na_2SO_4, filtered and the solvent was removed under reduced pressure to yield a white solid (0.25 g, 0.8 mmol, 57%). m.p. 144 ˚C (lit.[211] mp 147 ˚C). ^{1}H NMR (CDCl$_3$, 400 MHz, δ) 8.67-8.64 (m, 2H, CH$_{tpy}$), 8.62 (d, J = 8 Hz, 2H, CH$_{tpy}$), 7.83 (m, 2H, CH$_{tpy}$), 7.66 (s, 2H, CH$_{tpy}$), 7.3 (dd, J = 7.5, 4.8 Hz, 2H, CH$_{tpy}$), 5.07 (bs, 1H, H1), 3.47-3.37 (m, 2H, H2), 2.91 (t, J = 6.5 Hz, 2H, H3), 1.83 (p, J = 6.5 Hz, 2H, H4), 1.26 (s, 1H, NH$_2$).[121]

***N*^{1},*N*^{3},*N*^{5}–Tris((S,S,S)-1-(3-(2,6-di(pyridine-2-yl)pyridine-4-ylamino)propylcarbamoyl)ethyl)-1,3,5-tricarboxamide (66)**

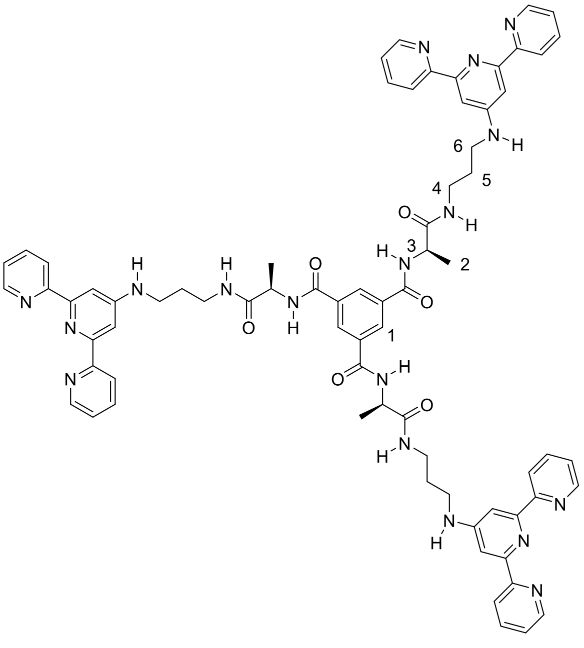

Compound **64** (0.22 g, 0.72 mmol) was dissolved in DMF (1 mL) and dry DCM (3 mL) and cooled on ice. EDC.HCl (0.14 g, 0.72 mmol) was then added and the reaction mixture was stirred under argon at 0 ˚C for 30 min, followed by 30 min at room temperature. HOBt (0.1 g, 0.72 mmol) was then added and stirred for a further 1 h. *(S, S, S)*–Tris-alanine benzene-1,3,5-tricarboxamide (0.84 g, 0.2 mmol) was then added and the resulting mixture was stirred under argon at room temperature for 24 h. The mixture was added to DCM and the organic layer was washed with a saturated solution of aqueous $NaHCO_3$ solution three times and organic layer was separated, dried and then the solvent was evaporated under reduced pressure to reveal an off-white/yellow solid. Yield 60%. ^{1}H NMR (DMSO-d_6, 400 MHz, δ) 8.71

(m, 3H, NH), 8.65 (d, J = 3.9 Hz, 6H, CH$_{\text{tpy}}$), 8.54 (d, J = 7.9 Hz, 6H, CH$_{\text{tpy}}$), 8.48 (s, 3H, H1), 8.12 (bs, 3H, NH), 7.93 (t, J = 11, 4.2 Hz, 6H, CH$_{\text{tpy}}$), 7.67 (s, 6H, CH$_{\text{tpy}}$), 7.427.40 (m, 6H, CH$_{\text{tpy}}$), 6.87 (t, J = 4.9 Hz, 3H, NH), 4.52-4.48 (m, 3H, C3), 3.26-3.19 (m, 12H, C4, C6), 1.81-1.73 (m, 6H, C5), 1.35 (d, J = 7 Hz, 9H, C2). ^{13}C{^{1}H} NMR (DMSO-d_6, 150 Hz, δ) 172.2, 165.3, 155.9, 155.5, 154.9, 148.9, 137, 134.3, 129.3, 123.8, 120.6, 49.2, 36.5, 28.5, 18.2. HRMS-MALDI (*m/z)*: [M+H]$^+$ calculated for $C_{72}H_{73}N_{18}O_6$, 1285.5960, found 1285.5962.[121]

General procedure for the synthesis of methyl 4-aminobutanoate (111), methyl 5-aminopentanoate (112) and methyl 6-aminohexanoate (113).

The appropriate amino acid (21 mmol) was dissolved in 100 mL of CH_3OH and cooled on ice, before addition of 5 equivalents of $SOCl_2$ dropwise. The mixture was stirred for 12 h at room temperature. $SOCl_2$ and CH_3OH were removed by vacuum distillation to reveal a powdery white solid in each case, which was dried *in vacuo.*

Methyl 4-aminobutanoate, (111)

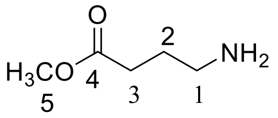

Compound **111** was obtained in 94% yield; m.p. 118 ˚C (lit.[212] m.p. 118.5-122 ˚C). ^{1}H NMR (DMSO-d_6, 400 MHz, δ) 7.98 (s, 2H, NH_2), 3.6 (s, 3H, H5), 2.83-2.75 (m, 2H, H1), 2.44 (t, J = 7.5 Hz, 2H, H3), 1.84-1.76 (m, 2H, H2) ^{13}C{^{1}H} NMR (DMSO-d_6, 100 Hz, δ) 172.8 (C4), 51.5 (C5), 38 (C1), 30.2 (C3), 22.4 (C2). IR v_{max} (cm^{-1}): 3024, 2951, 1734, 1597, 1574, 1517, 1474, 1420, 1385, 1345, 1270, 1192, 1149, 1054, 1021, 983, 949, 899, 882.

Methyl 5-aminopentanoate, **(112)**

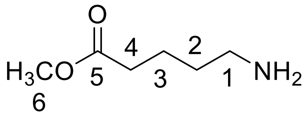

Compound **112** was obtained in 86% yield; m.p. 132-136 ˚C (lit.[212] m.p. 132-137 ˚C). ^{1}H NMR (DMSO-d_6, 400 MHz, δ) 7.95 (s, 2H, NH_2), 3.59 (s, 3H, H6), 2.76 (m, 2H, H1), 2.39-2.28 (m, 2H, H4), 1.52-1.48 (m, 4H, H2, H3). ^{13}C{^{1}H} NMR (DMSO-d_6, 150 Hz, δ) 173.1 (C5), 51.3 (C6), 38.4 (C1), 32.7 (C4), 26.4 (C2), 21.4 (C3). HRMS-ESI$^+$ (m/z): [M+H]$^+$ calculated for $C_6H_{14}NO_2$, 132.1025, found 132.1030. IR v_{max} (cm^{-1}): 3024, 2931, 1734, 1597, 1575, 1518, 1474, 1443, 1420, 1385, 1345, 1270, 1192, 1149, 1149, 1054, 1022, 982, 949, 899, 882, 747, 700, 586.

Methyl 6-aminohexanoate, **(113)**

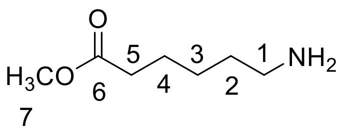

Compound **113** was obtained in 98% yield; m.p. 80-84 ˚C (lit.[213] m.p. 81-82 ˚C) ^{1}H NMR (DMSO-d_6, 400 MHz, δ) 7.92 (s, 2H, NH_2), 3.58 (s, 3H, H7), 2.78-2.70 (m, 2H, H1), 2.30 (t, J = 7.3 Hz, 2H, H5), 1.58-1.49 (m, 4H, H2, H4), 1.3 (q, J = 8.0 Hz, 2H, H3). ^{13}C{^{1}H} NMR (DMSO-d_6, 150 Hz, δ) 173.2 (C6), 51.2 (C7), 38.5 (C1), 33.0 (C5), 26.6 (C2), 25.3 (C4), 23.9 (C3). HRMS-ESI$^+$ (m/z): $[M+H]^+$ calculated for $C_7H_{16}NO_2$, 146.1103, found 146.1171. IR ν_{max} (cm^{-1}): 3019, 2927, 2865, 1726, 1627, 1603, 1583, 1496, 1425, 1395, 1363, 1313, 1228, 1192, 1143, 1094, 1045, 977, 949, 931, 832, 812, 731, 703, 611.

General procedure for the synthesis of 58, 59 and 60

The appropriate alkylamino-ester (3 equivalents) was dissolved in anhydrous DCM (50 mL) and cooled on ice, before addition of Et_3N (3 equivalents) dropwise. The solution was stirred under argon and allowed reach room temperature before addition of benzene-1,3,5-tricarbonyl trichloride (1 equivalent). The mixture was stirred for 24 h at room temperature under an argon atmosphere. Solution was washed with a saturated aqueous solution of $NaHCO_3$ solution in H_2O three times, with organic layer collected and evaporated to reveal a white solid which was dried *in vacuo*. Product was purified by silica column chromatography (gradient DCM/MeOH (90:10)).

***N^1*, *N^3*, *N^5*-tris(trimethoxybutanoyl)-benzene-1,3,5-tricarboxamide (60),** Compound **60** was obtained in 85% yield; m.p. 100 ˚C. ^{1}H NMR (DMSO-*d*$_6$, 600 MHz, δ) 8.7 (t, *J* = 5.6 Hz, 3H, NH), 8.37 (s, 3H, H6), 3.59 (s, 9H, H5), 3.29 (overlapping with H_2O signal, 6H, H1), 2.39 (t, *J* = 7.4 Hz, 6H, H3), 1.81 (quin, *J* = 7.2 Hz, 6H, H2). ^{13}C{^{1}H} NMR (DMSO-*d*$_6$, 150 Hz, δ) 173.6 (C4), 166.1 (C6), 135.5 (Aromatic), 128.9 (C7), 51.7 (H5), 39.2 (C3), 31.3 (C1), 24.9 (C2). HRMS-ESI$^+$ (*m/z)*: $[M+H]^+$ calculated for $C_{24}H_{34}N_3O_9$, 508.2295, found 505.2296. IR ν_{max} (cm^{-1}): 3234, 3065, 2955, 1735, 1629, 1555, 1430, 1375, 1347, 1295, 1280, 1208, 1166, 1093, 1058, 992, 901, 864, 901, 864, 808, 723, 690, 659, 586, 566.

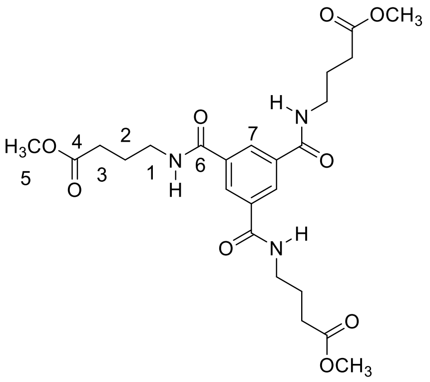

***N^1*, *N^3*, *N^5*-tris(trimethoxypentanoyl)-benzene-1,3,5-tricarboxamide (59)**, Compound **59** was obtained in 77% yield; m.p. 89-90 ˚C. ^{1}H NMR (DMSO-*d*$_6$, 600 MHz, δ) 8.68 (t, *J*= 5.5 Hz, 3H, NH), 8.36 (s, 3H, H9), 3.58 (s, 9H, H7), 3.31-3.26 (m, 6H, H1), 2.35 (t, *J*= 7.1 Hz, 6H, H4), 1.59-1.53 (m, 12H, H2, H3). ^{13}C{^{1}H} NMR (DMSO-*d*$_6$, 150 Hz, δ) 173.3 (C6), 163.4 (C8), 135.1 (Aromatic), 128.3 (C9), 51.2 (C7), 32.9 (C4), 28.4 (C1), 21.9 (C2, C3). Found C, 58.98, H, 7.18, N, 7.64, calculated for $C_{27}H_{39}N_3O_9$: C, 59.0, H, 7.15, N,

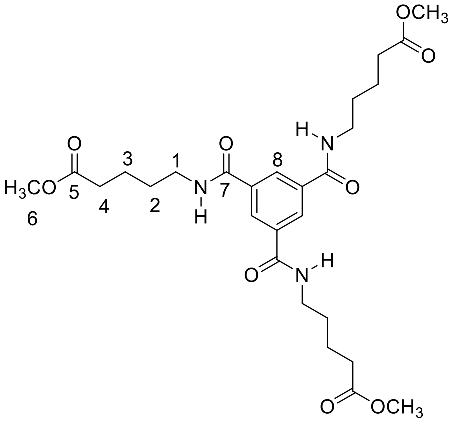

7.64%. HRMS-ESI$^+$ (*m/z)*: $[M+H]^+$ calculated for $C_{27}H_{40}N_3O_9$, 550.2686, found 550.2767. IR ν_{max} (cm^{-1}): 3224, 3066, 2955, 2875, 1736, 1636, 1561, 1470, 1434, 1414, 1384, 1327, 1311, 1245, 1166, 1106, 1084, 1028, 977, 882, 744, 664, 597.

***N*^{1}*, N*^{3}*, N*^{5}-tris(trimethoxyhexanoyl)-benzene-1,3,5-tricarboxamide (58)**, Compound **58** was obtained in 80% yield; m.p. 84 ˚C. ^{1}H NMR (DMSO-*d*$_6$, 600 MHz, δ) 8.67 (s, 3H, NH), 8.35 (s, 3H, H9), 3.57 (s, 9H, H7), 3.31-3.22 (m, 6H, H1), 2.31 (t, 6H, *J* = 7.6 Hz, H5), 1.55 (dd, 12H, *J* = 15.1, 7.6 Hz, H2, H4), 1.35-1.27 (m, 6H, H3). $^{13}C\{^1H\}$ NMR (DMSO-*d*$_6$, 150 Hz, δ) 173.4 (C6), 165.4 (C8), 135.1 (Aromatic), 128.3 (C9), 51.2 (C7), 33.2 (C1), 28.7 (C5), 25.9 (C2, C4), 24.2 (C3). Found C, 60.98, H, 7.73, N, 7.11, calculated for $C_{30}H_{45}N_3O_9$: C, 60.88, H, 7.67, N, 7.10%. HRMS-ESI$^+$ (*m/z)*: $[M+H]^+$ calculated for $C_{30}H_{46}N_3O_9$, 592.3156, found 592.3325. IR ν_{max} (cm^{-1}): 3232, 3069, 2939, 2865, 1736, 1636, 1560, 1464, 1435, 1417, 1373, 1292, 1233, 1188, 1164, 1107, 1008, 907, 883, 794, 732, 589, 579, 566.

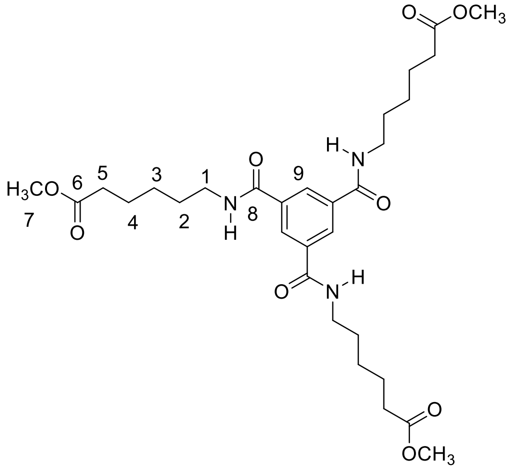

General procedure for the synthesis of 61, 62 and 63

The corresponding ester derivative (1.9 mmol in the case of **63**, **62** and 0.7 mmol in the case of **61**) was dissolved in 5 mL CH_3OH, cooled on ice and 5 equivalents of NaOH was added dropwise. The resulting solution was left to stir at room temperature for 4 h. Acetic acid was added dropwise until the formation of a white precipitate occurred. This was then filtered and washed with H_2O, with the resulting white solid dried in vacuo. The synthesis of **61** was previously reported using a similar method.[214]

***N*^{1}*, N*^{3}*, N*^{5}-tris(1-hydroxybutanoyl)-benzene-1,3,5-tricarboxamide (63)**, Compound **63** was obtained in 87% yield; m.p. 185 °C. ^{1}H NMR (DMSO-*d*$_6$, 600 MHz, δ) 12.08 (s, 1H, OH), 8.71 (t, *J* = 5.3 Hz, 3H, NH), 8.38 (s, 3H, H7), 3.31 (overlapping with H_2O signal, C1), 2.31 (t, *J* = 7.3 Hz, 6H, C3), 1.79 (quin, *J* = 7.3 Hz, 6H, C2). $^{13}C\{^1H\}$ NMR (DMSO-*d*$_6$, 150 Hz, δ) 174.7 (C4), 166.1 (C6), 135.5 (Aromatic), 128.9 (C7), 39.3 (C3), 31.6 (C1), 24.9 (C2). Found: C, 52.21; H, 6.09; N, 8.56, calculated for $C_{21}H_{27}N_3O_9 \cdot 1.2H_2O$: C, 52.18; H, 6.04; N, 8.70%. HRMS-ESI$^+$ (m/z): $[M+H]^+$ calculated for

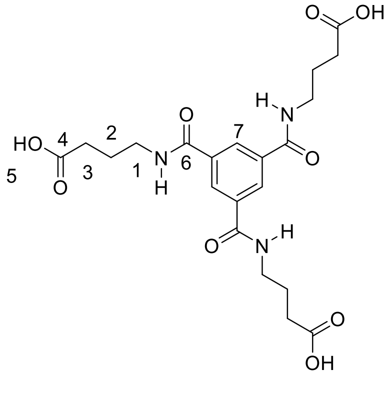

$C_{21}H_{27}N_3O_9Na$, 488.1645, found 488.1633. IR ν_{max} (cm^{-1}): 3366, 2967, 1722, 1707, 1635, 1556, 1531, 1477, 1407, 1339, 1288, 1261, 1177, 1094, 936, 857, 736, 720, 605, 578.

***N^1*, *N^3*, *N^5*-tris(1-hydroxypentanoyl)-benzene-1,3,5-tricarboxamide (62)**, Compound 62 was obtained in 77% yield; m.p. 158 °C. ^{1}H NMR (DMSO-*d*$_6$, 600 MHz, δ) 12.01 (s, 3H, OH), 8.67 (t, *J* = 5.1 Hz, 3H, NH), 8.36 (s, 3H, H8), 3.29 (overlapping with H_2O signal, 6H, H1), 2.25 (apparent s, 6H, H4), 1.55 (apparent s, 12H, H2, H3). $^{13}C\{^1H\}$ NMR (DMSO-*d*$_6$, 150 Hz, δ) 174.9 (C5), 165.9 (C7), 135.6 (Aromatic), 128.8 (C8), 33.8 (4), 29 (C1), 22.5 (C2, C3). Found: C, 55.81; H, 6.63; N, 8.13, calculated for $C_{24}H_{33}N_3O_9\cdot0.4\,H_2O\cdot0.25\,CH_3OH$: C, 55.80; H, 6.64; N, 8.14%. HRMS-ESI$^+$ (m/z): $[M+H]^+$ calculated for $C_{24}H_{34}N_3O_9$, 508.2295, found 508.2286. IR ν_{max} (cm^{-1}): 3345, 2929, 1711, 1612, 1588, 1541, 1460, 1428, 1411, 1311, 1299, 1269, 1241, 1220, 1186, 1101, 1069, 1034, 928, 915, 839, 777, 747, 693, 640, 566.

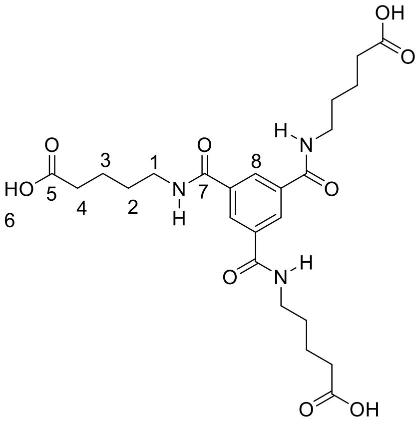

***N^1*, *N^3*, *N^5*-tris(1-hydroxyhexanoyl)-benzene-1,3,5-tricarboxamide (61)**, Compound **61** was obtained in 94% yield; m.p. 144 °C. ^{1}H NMR (DMSO-*d*$_6$, 600 MHz, δ) 11.98 (s, 3H, OH), 8.65 (t, 3H, *J* = 5.5 Hz, NH), 8.36 (s, 3H, aromatic), 3.27 (overlapping with H_2O signal, 6H, H1), 2.21 (t, 6H, *J* = 7.4 Hz, H5), 1.55-1.53 (m, 12H, H2, H4), 1.32 (m, 6H, H3). $^{13}C\{^1H\}$ NMR (DMSO-*d*$_6$, 150 Hz, δ) 174.43 (C6), 165.4 (C8), 135.1 (C9), 128.27 (C6), 33.59 (C5), 28.75 (C1), 26.0 (C2, C4), 24.2 (C3). Found: C, 57.89; H, 7.22; N, 7.38, calculated. for $C_{27}H_{39}N_3O_9\cdot0.66\,H_2O$: C, 57.76; H, 7.24; N, 7.48%. HRMS-ESI$^-$ (m/z): $[M-H]^-$ calculated for $C_{27}H_{38}N_3O_9$, 548.2608, found 548.2599. IR ν_{max} (cm^{-1}): 3364, 3317, 2946, 1697, 1636, 1587, 1540, 1461, 1410, 1342, 1273, 1236, 1187, 1107, 1064, 874, 789, 715, 654, 611, 580.

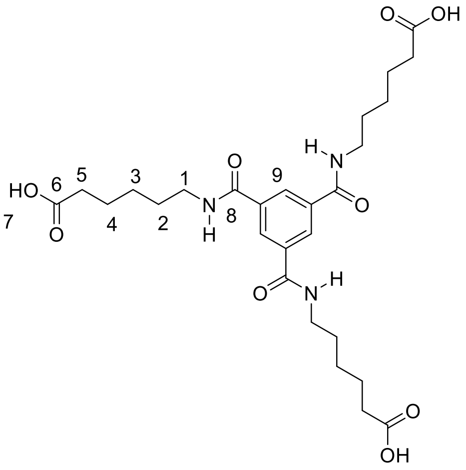

6.2.2 Synthesis of the compounds discussed in Chapter 3

Methyl 2-(4-aminophenyl)acetate (67)

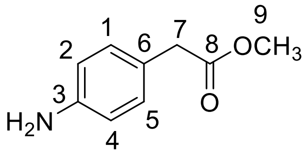

4-Aminophenylacetic acid (3 g, 19.8 mmol) was dissolved in 100 mL of CH_3OH, then cooled on ice before the dropwise addition of $SOCl_2$ (7.06 g, 4.2 mL, 59.4 mmol). Solution was left to stir for 12 h at room temperature. $SOCl_2$ and CH_3OH were then removed by vacuum distillation to yield a yellow solid which was dried *in vacuo* (3.3 g, 19.5 mmol, 98%); m.p. decomposed > 185 °C. ^{1}H NMR (DMSO-d_6, 600 MHz, δ) 7.35 (d, *J* = 8.3 Hz, 2H, H1, H5), 7.28 (d, *J* = 8.2 Hz, 2H, H2, H4), 3.71 (s, 2H, H7), 3.61 (s, 3H, H9). ^{13}C{^{1}H} NMR (DMSO-d_6, 150 Hz, δ) 171.4 (RCOOCH$_3$), 171.4 (C8) 133.6 (C1, C5), 131.6(C3),130.7 (C6), 122.5 (C2, C4), 51.8 (C9), 39.6 (C7, overlapping DMSO) HRMS-ESI$^+$ (*m/z*): [M+H]$^+$ calculated for $C_9H_{11}NO_2$, 166.0868, found 166.0869. IR ν_{max} (cm^{-1}): 2769, 2584, 1772, 1614, 1565, 1515, 1436, 1357, 1218, 1172, 995, 950, 901, 810, 772, 719, 684.

***N^1, N^3, N^5*-tris(4-(methoxyacetyl)phenyl)-benzene-1,3,5-tricarboxamide (69)**

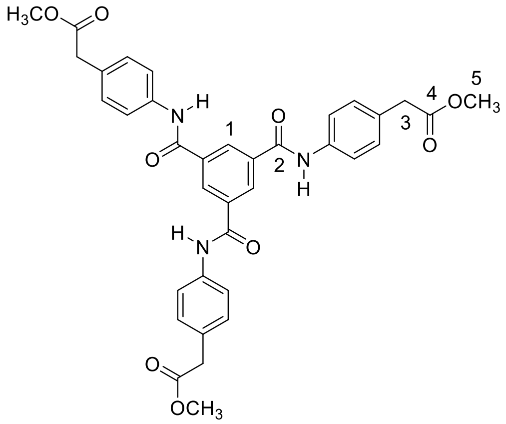

67 (0.3 g, 1.7 mmol) was dissolved in dry DCM (20 mL), then cooled in ice before the addition of Et$_3$N (0.34 g, 0.45 mL, 2.5 mmol). Benzene-1,3,5-tricarbonyl trichloride was dissolved in dry DCM (10 mL) and added to the solution of methyl 2-(4-aminophenyl)acetate and Et$_3$N, with the resulting mixture stirred under argon at room temperature for 24 h. Solution was washed with saturated aqueous NaHCO$_3$ solution in H$_2$O three times, with the organic layer collected and the solvent evaporated to reveal a yellow solid. To purify, the solid was dissolved in 40 mL KOH solution (1 M) and 40 mL DCM and stirred at room temperature for 3 h. The organic layer was then separated and washed with water, with the DCM then evaporated to reveal a pale yellow solid (0.15 g, 0.23 mmol, 45%); m.p. 188-197 °C; ^{1}H NMR (DMSO-d_6, 600 MHz, δ) 10.58 (s, 3H, NH), 8.69 (s, 3H, H1), 7.76 (d, *J* = 8.4 Hz, 6H, Aromatic), 7.29 (d, *J* = 8.4 Hz, 6H, Aromatic), 3.67 (s, 6H, H3), 3.63 (s, 9H, H5). ^{13}C{^{1}H} NMR (DMSO-d_6, 150 Hz, δ) 171.7 (C4), 165.5 (C2), 137.7 (Aromatic), 135.5 (Aromatic), 129.9 (C1), 129.6 (Aromatic), 120.4 (Aromatic), 51.2 (C5) 39.6 (overlapping DMSO, C3). HRMS-ESI$^+$ (m/z): [M+Na]$^+$ calculated for

$C_{36}H_{33}N_3O_9Na$, 674.2106, found 674.2114. IR ν_{max} (cm^{-1}): 3348, 2942, 2853, 1729, 1643, 1601, 1514, 1434, 1411, 1315, 1255, 1196, 1152, 1093, 1011, 917, 846, 797, 698.

N^1, N^3, N^5-tris(4-(hydroxyacetyl)phenyl)-benzene-1,3,5-tricarboxamide (64)

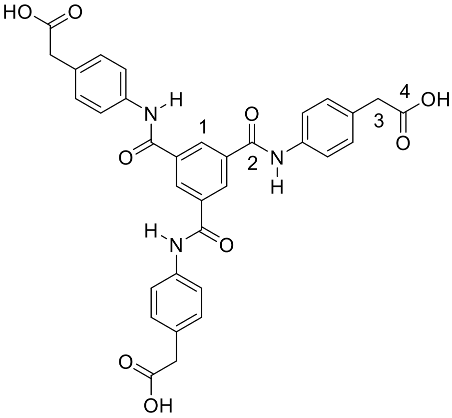

The corresponding ester derivative **69** was dissolved in 5 mL CH_3OH, cooled on ice and 1M NaOH solution was added dropwise. The resulting solution was left to stir at room temperature for 6 h. Acetic acid was added dropwise until the formation of a beige precipitate occurred. This was then filtered and washed with H_2O, with the resulting white solid dried *in vacuo*, 83%; m.p. 250-260 °C. ^1H NMR (DMSO-d_6, 600 MHz, δ) 10.56 (s, 3H, NH), 8.67 (s, 3H, H1), 7.74 (d, *J* = 8.4 Hz, 6H, Aromatic), 7.27 (d, *J* = 8.4 Hz, 6H, Aromatic), 3.53 (s, overlapping with H_2O signal, C3). $^{13}C\{^1H\}$ NMR (DMSO-d_6, 150 Hz, δ) 172.9 (C2), 164.6 (C4), 137.6 (Aromatic), 135.6 (Aromatic), 130.8 (Aromatic), 129.7 (Aromatic), 120.5 (Aromatic), 40.1 (C3). HRMS-ESI$^-$ (*m/z)*: [M-H]$^-$ calculated for $C_{33}H_{27}N_3O_9$, 608.1669, found 608.1663. IR ν_{max} (cm^{-1}): 3316, 3070, 1707, 1647, 1603, 1533, 1513, 1412, 1322, 1221, 1192, 1168, 1020, 905, 809, 662.

N^1, N^3, N^5-tris(4-methoxyacetyl)-benzene-1,3,5-tricarboxamide (65)

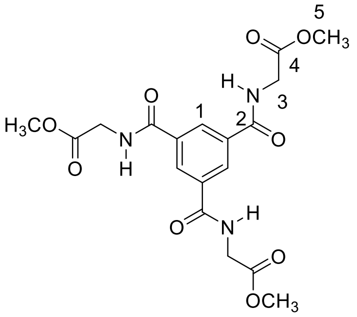

Glycine methyl ester hydrochloride (1.67 g, 13 mmol) was dissolved in dry DCM (50 mL), then cooled on ice before the addition of Et_3N (2.52 g, 3.3 mL, 18 mmol). Benzene-1,3,5-tricarbonyl trichloride (1 g, 3.7 mmol) was added to the mixture and it was then stirred under argon at room temperature for 24 h. Solution was washed with saturated aqueous $NaHCO_3$ solution in H_2O three times, with the organic layer collected and the solvent evaporated to reveal a pale off-white/yellow solid (0.79 g, 1.9 mmol, 50%); m.p. 182-186 °C; ^1H NMR (DMSO-d_6, 400 MHz, δ) 9.22 (t, *J* = 5.7 Hz, 3H, NH), 8.48 (s, 3H, H1), 4.04 (d, *J* = 5.8 Hz, 6H, H3), 3.64 (s, 9H, H5). $^{13}C\{^1H\}$ NMR (DMSO-d_6, 100 Hz, δ) 170.2 (C4), 165.8 (C2), 134.4 (Aromatic), 129 (Aromatic), 51.8 (C5), 41.3 (C3). HRMS-ESI$^-$ (*m/z)*: [M-H]$^-$ calculated for $C_{18}H_{20}N_3O_9$, 422.12, found 422.1192. IR ν_{max} (cm^{-1}): 3245, 3069, 2951, 1752, 1641, 1563, 1436, 1400, 1362, 1310, 1203, 1091, 1027, 973, 920, 796, 689.

$[Cd_3(64)_2(DMF)_2]\cdot 5H_2O\cdot 4DMF$ (64Cd)

Cadmium nitrate tetrahydrate (15 mg, 48 μmol) and **64** (10 mg, 16 μmol) were dissolved in DMF/H_2O (1:1, 3 mL), The reaction was sealed in a Teflon capped vial and heated at 100 °C for 24 h. The resulting crystals were isolated by filtration to give **64Cd**. m.p. (decomposed) > 300 °C; Found C, 48.47; H, 4.06; N, 7.24, Calculated. for $C_{66}H_{48}Cd_3N_6O_{18}\cdot5H_2O\cdot4DMF$: C, 48.47; H, 4.49; N, 7.25 %. IR ν_{max} (cm^{-1}): 3267, 2928, 1652, 1603, 1564, 1531, 1513, 1437, 1384, 1319, 1281, 1254, 1202, 1095, 1061, 1022, 927, 861, 815, 794, 751, 735, 715, 698, 679, 658. Phase purity was established by X-ray powder diffraction.

Synthesis of $[Cd_3(65)_2(DMF)]\cdot5(H_2O)$ (65Cd), Cadmium nitrate tetrahydrate (15 mg, 48 μmol) and **65** (10 mg, 24 μmol) were dissolved in DMF/H_2O (1:1, 3 mL), The reaction was sealed in a Teflon capped vial and heated at 100 °C for 24 h. The resulting crystals were isolated by filtration to give **65Cd**. m.p. decomposed > 300 °C; Found C, 30.2; H, 3.19; N, 7.3, calculated for $C_{33}H_{47}Cd_3N_7O_{27}$: C, 30.23; H, 3.61; N, 7.48 %. IR ν_{max} (cm^{-1}): 3327, 2938, 1652, 1593, 1531, 1430, 1390, 1288, 1269, 1092, 1003, 931, 904, 711, 664, 560. Phase purity was established by X-ray powder diffraction.

General procedure for the synthesis of 72 and 70

64 (1 equivalent) was added to dry DCM in a sealed reaction vial under an argon atmosphere and left to stir at room temperature for 5 minutes before being cooled on ice. EDC.HCl (3.5 eq.) and DMAP (3.5 eq.) were then added and stirred for a further 5 minutes before the addition of the relevant amino acid (alanine methyl ester hydrochloride or glycine methyl ester hydrochloride). The reaction mixture was left stirring at room temperature under an argon atmosphere for 72 h. The reaction solvent was removed under reduced pressure to reveal a pale-yellow oil in both cases which was dried *in vacuo*. Water was then added to this oil to cause precipitation of beige solids in both cases which were isolated by filtration and dried *in vacuo*.

***N*^{1}, *N*^{3}, *N*^{5}-tris-(4-methyl-Gly-acetylphenyl)-benzene-1,3,5-tricarboxamide (72)**,

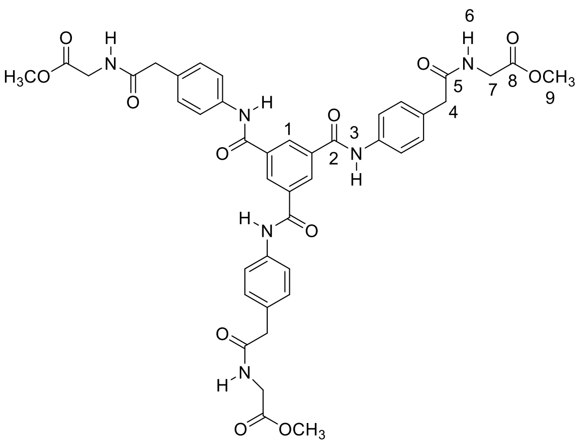

Compound **72** was obtained in 58% yield; m.p. 185-192 °C. ^{1}H NMR ((DMSO-d_6, 400 MHz, δ) 10.55 (s, 3H, H3), 8.68 (s, 3H, H1), 8.48 (t, *J* = 5.82 Hz, 3H, H6), 7.72 (d, *J* = 8.52 Hz, 6H, Aromatic), 7.29 (d, *J* = 8.52 Hz 6H, Aromatic), 3.86 (d, *J* = 4.8 Hz, 6H, H7), 3.63 (s, 9H, H9), 3.48 (s, 6H, H4). $^{13}C\{^{1}H\}$ NMR (DMSO-d_6, 150 Hz, δ) 170.8 (C5), 170.4 (C8), 164.4 (C2), 137.3 (Aromatic) 135.5 (Aromatic), 131.7 (Aromatic), 129.7 (C1), 129.3 (Aromatic), 120.4

(Aromatic), 51.7 (C9), 41.4 (C4), 40.7 (C7). HRMS (m/z) (MALDI$^+$) calculated for [M+Na]$^+$ $C_{42}H_{42}N_6O_{12}Na$, 845.2758, found 845.2774. IR $v_{\max}$ (cm^{-1}): 3287, 1735, 1648, 1648, 1602, 1513, 1411, 1318, 1211, 1034, 806, 706.

N^1, N^3, N^5-tris-(4-(methyl-Ala)-acetylphenyl)-benzene-1,3,5-tricarboxamide (70),

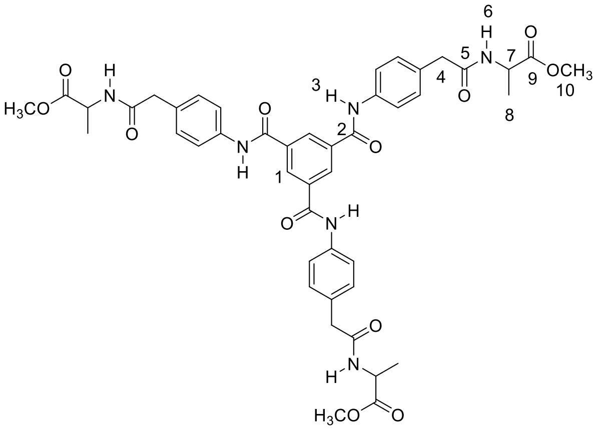

Compound 70 was obtained in 22% yield. m.p. 240-245 °C. ^{1}H NMR (DMSO-d_6, 400 MHz, δ) 10.56 (s, 3H, H3), 8.67 (s, 3H, H1), 8.56 (d, 3H, J = 6.96 Hz, H6) 7.73 (d, J = 8.36 Hz, Aromatic) 7.27 (d, J = 8.36 Hz, Aromatic), 4.26 (p, 3H, J = 7.16 Hz, H7), 3.61 (s, 9H, H10), 3.45 (overlapping with H_2O, H4), 1.28 (d, 9H, J = 7.28 Hz, H9). ^{13}C{^{1}H} NMR (DMSO-d_6, 150 Hz, δ) 173.2 (C9), 170.1 (C5), 164.5 (C2), 137.3 (Aromatic), 135.5 (Aromatic), 129.3 (Aromatic), 120.4 (Aromatic), 51.9 (C10), 47.7 (C7), 41.3 (C4), 17 (C8). HRMS-ESI$^-$ (*m/z)*: [M-H] calculated for $C_{45}H_{47}N_6O_{12}$, 863.3257, found 863.3233. IR $v_{\max}$ (cm^{-1}): 3286, 1735, 1648, 1603, 1512, 1411, 1318, 1210, 1033, 806.

N^1, N^3, N^5-tris-(4-(Gly-acetyl)phenyl)-benzene-1,3,5-tricarboxamide (73)

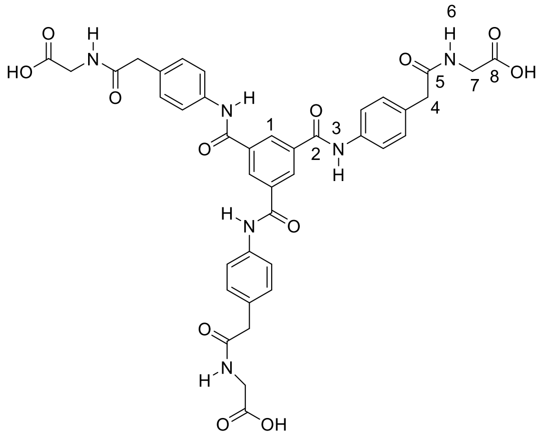

The corresponding ester derivative **72** was dissolved in 5 mL CH_3OH, cooled on ice and 5 equivalents of NaOH was added dropwise. The resulting solution was left to stir at room temperature for 6 h. Acetic acid was added dropwise until the formation of a beige precipitate occurred. This was then filtered and washed with H_2O, with the resulting white solid dried *in vacuo*. m.p. 165-170 °C. ^{1}H NMR (DMSO-d_6, 600 MHz, δ) 10.56 (s, 3H, H3), 8.68 (s, 3H, H1), 8.22 (bs, 3H, H6), 7.74 (d, 6H, J = 8.34 Hz, Aromatic), 7.29 (d, 6H, J = 8.34 Hz, Aromatic), 3.72 (d, 6H, J = 5.64 Hz, H7), 3.3 (s, overlapping with H_2O, 6H, H4). ^{13}C{^{1}H} NMR (DMSO-d_6, 150 Hz, δ) 171.4 (C5), 170.5 (C8), 164.5 (C2), 137.3 (Aromatic), 135.5 (Aromatic), 131.9 (Aromatic), 129.8 (Aromatic), 129.4 (C1), 120.4 (Aromatic), 41.6 (C7), 41.2 (C4). IR $v_{\max}$ (cm^{-1}): 3283, 2950, 1735, 1647, 1603, 1514, 1411, 1213, 1033, 914, 808, 706, 588.

6.2.3 Synthesis of the compounds discussed in Chapter 4

Synthesis of N-Boc-4,7,10-trioxa-1,13-tridecanediamine, **(78)**

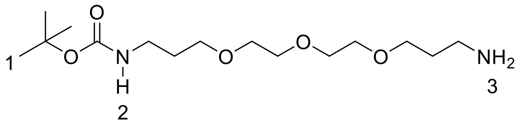

4,7,10-Trioxa-1,13-tridecanediamine, **75**, (4.02 g, 18 mmol) was added to 20 mL of dry DCM and cooled on ice under an argon atmosphere. Di-*tert*-butyl decarbonate (0.88 g, 4 mmol) was dissolved in dry DCM and added dropwise to the amine solution. The reaction mixture was left to stir at room temperature for 24 h. Once the reaction was complete, the organic mixture was washed three times with an aqueous solution of $NaHCO_3$, the organic layer was separated, dried over Na_2SO_4 and evaporated under reduced pressure to reveal the product as a pale-yellow oil. ^{1}H NMR ($CDCl_3$, 400 MHz, δ) 5.09 (bd, 1H, H2), 3.62 (bs, 4H, CH_2) 3.58 (bs, 4H, CH_2), 3.54-3.51 (m, 4H, CH_2), 3.22 (bd, 2H, *J* = 5.72 Hz, H3), 2.79 (t, 1H, *J* = 6.68 Hz), 1.76-1.70 (m, 3H, CH_2), 1.42 (s, 9H, H1).

Synthesis of N-Boc-2,2-(ethylenedioxy)diethylamine (82)

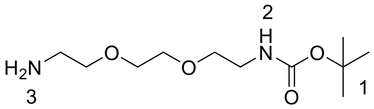

2,2-(ethylenedioxy)bis(ethylamine), **81**, (4g, 0.027 mol) was added to dry DCM and cooled on ice under an argon atmosphere. Di-*tert*-butyl decarbonate (1.2 g, 0.0058 mol) was dissolved in dry DCM and added dropwise to the amine solution. The reaction mixture was left to stir at room temperature for 24 h under an argon atmosphere. Once complete, a precipitate had formed which was removed by filtration, with the organic filtrate then washed with a saturated aqueous $NaHCO_3$ solution three times. The organic layer was separated and dried over $MgSO_4$ and evaporated under reduced pressure to reveal the product as a colourless oil. ^{1}H NMR (DMSO-*d*$_6$, 400 MHz, δ) 6.65 (s, 1H, H2), 3.2 (td, *J* = 5.8 Hz, 1.32 Hz, CH_2), 2.9 (q, *J* = 5.76 Hz, CH_2), 2.36 (bd., *J* = 1.56 Hz, CH_2) 1.64 (s, 2H, H3), 1.2 (s, 9H, H1).[215] HRMS-ESI$^+$ (*m/z)*: $[M+H]^+$ calculated for $C_{11}H_{25}N_2O_4$, 249.1808, found 249.1805.

General procedure for the synthesis of 74a, 74b and 114

The appropriate ester protected amino acid (3 equivalents) was dissolved in anhydrous DCM (50 mL) and cooled on ice, before addition of Et_3N (3 equivalents) dropwise. The solution was stirred under argon and allowed to reach room temperature before addition of benzene-1,3,5-tricarbonyl trichloride (1 equivalent). The mixture was then stirred for 24 h at room temperature under an argon atmosphere. Solution was washed with a saturated aqueous $NaHCO_3$ solution three times, with organic layer collected and the solvent evaporated to reveal a white solid which was dried *in vacuo*.

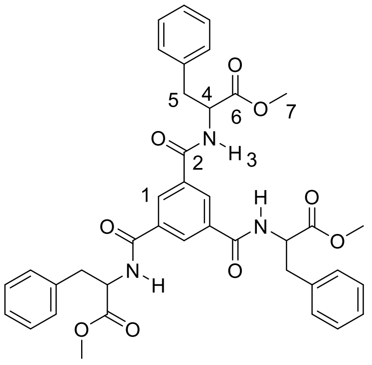

***N^1*, *N^3*, *N^5*-tris(methyl-Phe)-benzene-1,3,5-tricarboxamide (74b)** Compound **74b** was obtained in yield 72%, m.p. 188-193 °C. ^{1}H NMR (DMSO-d_6, 400 MHz, δ) 9.18 (d, *J* = 6.9 Hz, 3H, H3), 8.36 (s, 3H, H1), 7.29-7.18 (m, 15H, Aromatic), 4.73-4.67 (m, 3H, H4), 3.64 (s, 9H, H7), 3.2-3.1 (m, 6H, H5). ^{13}C{^{1}H} NMR (DMSO-d_6, 100 Hz, δ) 172.0 (C6), 165.6 (C2), 137.6 (Aromatic), 134.2 (Aromatic), 129.3 (Aromatic), 128.3 (Aromatic), 126.5 (Aromatic), 54.4 (C4), 52.0 (C7), 36.2 (C5). HRMS (m/z) (MALDI$^+$) calculated for [M+Na]$^+$ $C_{39}H_{39}N_3O_9Na$, 716.2584, found 716.2565. IR ν_{max} (cm^{-1}): 3225, 3030, 2951, 1744, 1638, 1541, 1497, 1422, 1310, 1215, 1169, 1101, 1030, 991, 911, 841, 742, 699.

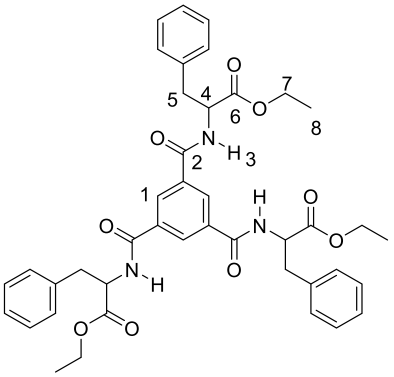

***N^1*, *N^3*, *N^5*-tris(ethyl-Phe)-benzene-1,3,5-tricarboxamide** (**74a**), Compound **74a** was obtained in 33% yield. mp. 208.5-210 °C. ^{1}H NMR (DMSO-d_6, 400 MHz, δ) 9.15 (d, *J* = 7.6 Hz, 3H, H3), 8.37 (s, 3H, H1), 7.30-7.27 (m, 12H, Aromatic), 7.22-7.18 (m, 3H, Aromatic), 4.69 (q, *J* = 8.8 Hz, 3H, H4), 4.11 (q, *J* = 7.10 Hz , 6H, H7), 3.19-3.09 (m, 6H, H5), 1.13 (t, *J* = 7.10 Hz, 9H, H8). ^{13}C{^{1}H} NMR (DMSO-d_6, 100 Hz, δ) 171.5 (C6), 165.6 (C2), 137.5 (Aromatic), 134.2 (Aromatic), 129.2 (Aromatic), 129.0 (Aromatic), 128.3 (Aromatic), 126.5 (Aromatic), 60.6 (C7), 54.5 (C4), 36.3 (C5), 14.0 (C8). HRMS (m/z) (MALDI$^+$) calculated for [M+Na]$^+$ $C_{42}H_{45}N_3O_9Na$, 758.3054, found 758.3058. IR ν_{max} (cm^{-1}): 3230, 3062, 2982, 1741, 1637, 1552, 1496, 1455, 1443, 1375, 1311, 1195, 1100, 1027, 914, 860, 739, 699, 562.

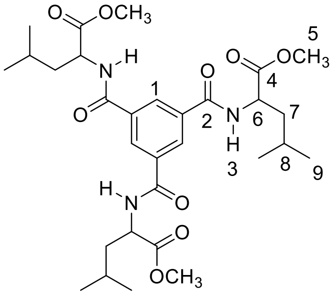

***N^1*, *N^3*, *N^5*-tris(methyl-Leu)-benzene-1,3,5-tricarboxamide (114)**, Compound **114** was obtained in 26% yield. m.p. 270 °C. ^{1}H NMR (DMSO-d_6, 400 MHz, δ) 9.12 (d, 3H, *J* = 7.56 Hz, H3), 8.48 (s, 3H, H1), 4.56-4.50 (m, 3H, H6), 3.66 (s, 9H, H5), 1.85-1.55 (m, 9H, H7, H8), 0.92 (dd, 18H, *J* = 14.44 Hz, 6.52 Hz, H9). ^{13}C{^{1}H} NMR (DMSO-d_6, 100 Hz, δ) 172.9 (C4), 165.9 (C2), 134.3 (Aromatic), 129.4 (Aromatic), 51.9 (C5), 51.1 (C6), 24.4 (C7), 22.9 (C8), 21.1 (C9). HRMS-ESI$^+$ (m/z): [M+H]$^+$ calculated for $C_{30}H_{45}N_3O_9Na$, 614.3054, found 614.3059. IR ν_{max} (cm^{-1}):3233, 3059, 2956, 2871, 1745, 1638, 1536, 1468, 1368, 1296, 1271, 1226, 1199, 1155, 1093, 1019, 911, 854, 716, 691, 551.

N^1, N^3, N^5-tris(Leu)-benzene-1,3,5-tricarboxamide, (83)

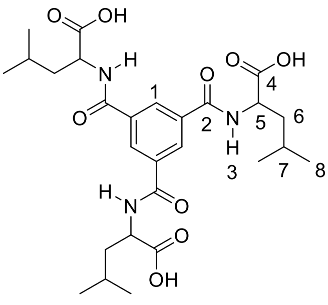

114 was dissolved in 5 mL CH_3OH, cooled on ice and 1M NaOH solution was added dropwise. The resulting solution was left to stir at room temperature for 4 h. Acetic acid was added dropwise until the formation of a white precipitate occurred. This was then filtered and washed with H_2O, with the resulting white solid dried *in vacuo* (48.5%). m.p. decomposed > 275 °C. ^{1}H NMR (DMSO-d_6, 400 MHz, δ) 8.93 (d, 3H, J = 7.8 Hz, H3), 8.45 (s, 3H, H1), 4.48 (m, 3H, H5), 1.82-1.67 (m, 6H, H6), 1.62-1.56 (m, 3H, H7), 0.92 (dd, 18H, J = 12.16 Hz, 6.4 Hz, H8). ^{13}C{^{1}H} NMR (DMSO-d_6, 100 Hz, δ) 174.0 (C4), 165.9 (C2), 134.6 (Aromatic), 129.2 (Aromatic), 51.0 (C5), 24.5 (C6), 23.0 (C7), 21.1 (C8). HRMS-ESI$^+$ (m/z): [M+H]$^+$ calculated for $C_{27}H_{40}N_3O_9$, 550.2759, found 550.2756. IR v_{max} (cm^{-1}): 3294, 2958, 1722, 1645, 1543, 1469, 1436, 1400, 1368, 1633, 1296, 1203, 1161, 1125, 1093, 1014, 971, 943, 912, 861, 818, 778, 748, 670, 582.

Synthesis of 2-[(tert-butoxycarbonyl)amino]-4-methylpentanoic acid (87)

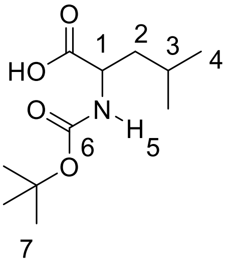

Leucine was dissolved in a 1:1 THF/H_2O (80 mL) mixture before the addition of 2 equivalents of NaOH. Di-*tert*-butyl decarbonate (1.1 equivalents) was then added to the mixture and was left to stir at room temperature for 48 h. Upon completion of the reaction the THF was evaporated under reduced pressure, followed by extraction of the aqueous layer using DCM. The aqueous layer was adjusted to pH 4, then extracted with DCM. The DCM was separated and dried over Na_2SO_4, and evaporated under reduced pressure to give a clear oil. ^{1}H NMR (DMSO-d_6, 400 MHz, δ) 7.03 (d, 1H, J = 8.24, H5), 3.87 (m, 1H, H1), 1.64 (m, 1H, H3), 1.49-1.37 (m, 2H, H2), 1.35 (s, 9H, H7), 0.84 (dd, 6H, J = 12 Hz, 6.64 Hz, H4).

N^1, N^3, N^5-tris(2-aminoethyl)-benzene-1,3,5tricarboxamide (90)

The procedure used was adapted from that reported by Luo and co-workers.[179] Under an argon atmosphere, ethylenediamine (EDA) (20 mL) was added to a flask. Trimethyl benzene-1,3,5-tricarboxylate (0.51 g, 2.02 mmol) was dissolved in CH_3OH (20 mL) and added dropwise to the solution of EDA under an argon atmosphere at 0 °C. The solution was stirred at 0 °C for 30 min and then at room temperature for 24 h. The excess ethylenediamine was removed *in vacuo*, and the residue was dissolved in a mixture of toluene/methanol (10:1) and the

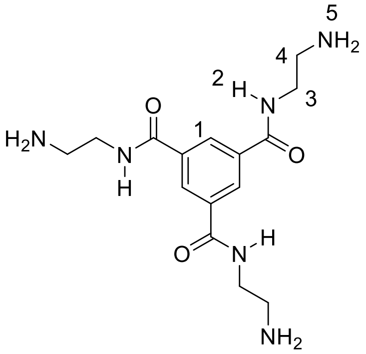

solvent was again removed under vacuum to remove the residual ethylenediamine. This process was repeated three times and the product was obtained as a sticky yellow solid (0.67 g, 2 mmol, 98%). ^{1}H NMR (DMSO-d_6, 400 MHz, δ) 8.61 (t, J = 5.6 Hz, 3H, H2), 8.39 (s, 3H, H1), 3.29 (q, J = 6.2 Hz, overlapping with water peak, H3), 2.70 (t, J = 6.5 Hz, 6H, H4). ^{13}C{^{1}H} NMR (DMSO-d_6, 100 Hz, δ) 165.7, 135.1, 128.4, 43.2, 41.3. HRMS-ESI^{+} (m/z): [M+H]$^{+}$ calculated for $C_{15}H_{25}N_6O_3^{+}$ 337.1983. IR ν_{max} (cm^{-1}): 3278, 3064, 2932, 2870, 1639, 1589, 1534, 1430, 1387, 1287, 1186, 1108, 1071, 1035, 913, 852, 821, 703.[216]

4-tert-Butyl-2,6-diformylphenol-polymer (91)

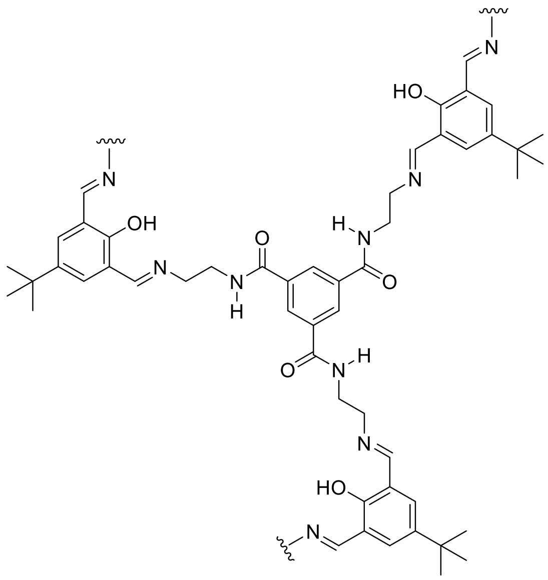

4-tert-Butyl-2,6-diformylphenol (37 mg, 178 µmol) was dissolved in EtOH (5 mL). N^{1}, N^{3}, N^{5}-tris(2-aminoethyl)-benzene-1,3,5-tricarboxamide, **90**, (40 mg, 119 µmol, 0.66 eq.) was dissolved in EtOH (2 mL) before being added to the solution of 4-tert-Butyl-2,6-diformylphenol in EtOH. A yellow precipitate immediately formed, and the mixture was stirred at room temperature for 18 h. The solution was filtered, and the precipitate was washed with ethanol before drying *in vacuo*, with the product obtained as a yellow solid. (27 mg, 22.8 µmol 35%); m.p. > 300 °C; Found C, 61.39; H, 6.40; N, 12.60; Calculated for $C_{66}H_{78}N_{12}O_9 \cdot 6H_2O$ C, 61.38; H, 7.02; N, 13.01. SS-CP-MAD (101 MHz, δ) 167.2, 141.5, 136.3, 132.5, 131.0, 118.8, 60.8, 41.6, 34.1, 31.6. IR ν_{max} (cm^{-1}): 3287, 2957, 2865, 1637, 1597, 1527, 1459, 1363, 1265, 1223, 1124, 992, 825, 733, 696, 633.[216]

6.2.4 Synthesis of the compounds discussed in Chapter 5

General procedure for the synthesis of 105, 104, 107, 108 and 106

3,5-Pyridinedicarboxylic acid (1 equivalent) was added to dry DCM in a sealed reaction vial under an argon atmosphere and left to stir at room temperature for 5 minutes before being cooled on ice. EDC.HCl (2.5 eq.) and DMAP (1 eq.) were then added and stirred for 5 min before the addition of the relevant amine (2.5 eq.) The reaction mixture was then left to stir under an argon atmosphere at room temperature for 72 h. The reaction solvent was removed under reduced pressure to reveal colourless/ yellow oils in all cases. These resultant oils were dried *in vacuo* before the addition of water causing the precipitation of white/pale yellow solids which were then filtered and dried *in vacuo*.

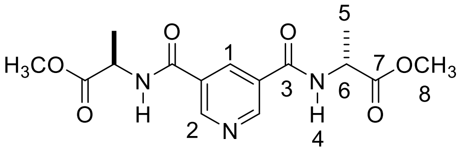

***N^3*, *N^5*,-(methyl-Ala)-3,5-pyridinedicarboxamide (104)**, Compound **104** was obtained in 49% yield. m.p. 100-106 °C. ^{1}H NMR (DMSO-*d_6*, 600 MHz, δ) 9.19 (d, *J* = 6.7 Hz, 2H, H4), 9.15 (s, 2H, H2), 8.67 (s, 1H, H1), 4.55-4.50 (m, 2H, H6), 3.66 (s, 6H, H8), 1.42 (d, *J* = 7.3 Hz, 6H, H5). ^{13}C{^{1}H} NMR (DMSO-*d_6*, 150 Hz, δ) 172.8 (C7), 164.3 (C3), 150.8 (C2), 134.4 (C1), 129.0 (Aromatic), 52.0 (C8), 48.4 (C6), 16.6 (C5). Found C, 54.61; H, 5.75; N, 11.94, calculated. for $C_{15}H_{19}N_3O_6\cdot0.12C_7H_8$: C, 54.64; H, 5.77; N, 12.05 %. HRMS-ESI$^+$ (m/z): $[M+H]^+$ calculated for $C_{15}H_{19}N_3O_6$, 338.1344, found 338.1347. IR ν_{max} (cm^{-1}): 3279, 2954, 1736, 1676, 1634, 1535, 1439, 1377, 1356, 1268, 1221, 1197, 1158, 1027, 980, 950, 924, 877, 853, 702, 660, 580.

104Mn, A methanolic solution of **104** and $MnCl_2\cdot4H_2O$ was added to a diethyl ether diffusion to result in single crystals suitable for diffraction**.** Phase purity was established by powder diffraction**.** m.p. decomposed > 250 °C.

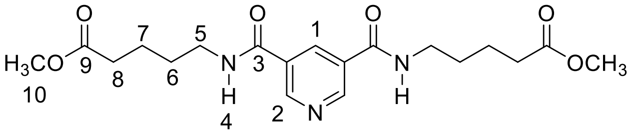

***N^3*, *N^5*,-(methoxypentanoyl)-3,5-pyridinedicarboxamide (105)**,Compound **105** was obtained in 64% yield. m.p. 112-114 °C; ^{1}H NMR (DMSO-*d_6*, 600 MHz, δ) 9.08 (s, 2H, H2), 8.77 (t, *J* = 5.2 Hz, 2H, NH), 8.57 8.55 (m, 1H, H1), 3.58 (s, 6H, H10), 3.28 (overlapping H_2O, 4H, H5), 2.35 (t, *J* = 6.84 Hz, 4H, H8), 1.57-1.55 (m, 8H, H6, H7). ^{13}C{^{1}H} NMR (DMSO-*d_6*, 150 Hz, δ) 173.3 (C9), 164.2 (C3), 150.2 (C2), 133.8 (C1), 129.8 (Aromatic, 51.2 (C10), 38.8 (C5), 32.3 (C8), 28.4 (C6), 21.9 (C7). Found C, 57.35; H, 6.57; N, 10.43, calculated for $C_{38}H_{54}N_6O_{12}\cdot0.5H_2O$: C, 57.35; H, 6.96; N, 10.56 %. HRMS-ESI$^+$ (m/z): $[M+Na]^+$ calculated for $C_{19}H_{27}N_3NaO_6$, 416.1792, found 416.1791. IR ν_{max}(cm^{-1}): 3274, 2953, 1732, 1632, 1554, 1438, 1384, 1361, 1329, 1289, 1269, 1243, 1196, 1166, 1103, 1079, 1025, 996, 947, 912, 728, 707, 675, 560.

105Cd, Cadmium nitrate tetrahydrate (15 mg, 48 μmol) and **105** (10 mg, 24 μmol) were dissolved in DMF/H_2O (1:1, 3 mL), The reaction was sealed in a Teflon capped vial and heated at 100 °C for 24 h. The resulting crystals were isolated by filtration to give **105Cd.** m.p. Decomposition > 280 °C. IR ν_{max} (cm^{-1}): 3307, 3074, 2928, 1658, 1557, 1497, 1382, 1155, 1105, 858, 703.

105Mn, A solution of **105** and $MnCl_2\cdot4H_2O$ in MeCN was subjected to a diethyl ether diffusion to result in single crystals suitable for diffraction. m.p Decomposition at 250 °C.

***N*^{3}, *N*^{5},-(methyl-Phe)-3,5-pyridinedicarboxamide (107)**, Compound **107** was obtained in 58% yield. m.p. 147.5-148.5 °C, ^{1}H NMR (DMSO-*d*$_6$, 600 MHz, δ) 9.25 (d, *J* = 7.74 Hz , 2H, H4), 9.02 (d, *J* = 2.16 Hz, 2H, H2), 8.5 (t, *J* = 2.1 Hz, 1H, H1), 7.30-7.26 (m, 8H, Aromatic), 7.21-7.18 (m, 2H, Aromatic) , 4.72-4.68 (m, 2H, H5), 3.64 (s, 6H, H7), 3.20-3.17 (m, 2H, H8), 3.10-3.06 (m, 2H, H8). ^{13}C{^{1}H} NMR (DMSO-*d*$_6$, 150 Hz, δ) 172.3 (C6), 164.9 (C3), 151.1 (C2), 137.9 (Aromatic), 134.8 (C1), 129.5 (Aromatic), 128.8 (Aromatic), 127.1 (Aromatic), 54.8 (C5), 52.5 (C7), 36.7 (C8). Found C 64.07, H 5.31, N 8.81, calculated for $C_{27}H_{27}N_3O_6 \cdot 0.9H_2O \cdot 0.2MeCN$: C 64.10, H 5.76, N 8.79 %. HRMS-ESI$^+$ (m/z): [M+H]$^+$ calculated for $C_{27}H_{28}N_3O_6$, 490.1973, found 490.1978. IR *v*$_{max}$ (cm^{-1}):3317, 1740, 1650, 1526, 1216, 1096, 985, 700, 644.

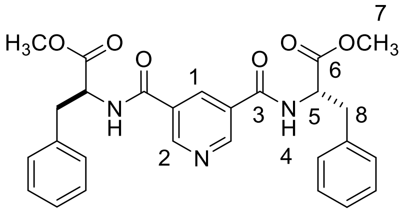

107Cd, Cadmium nitrate tetrahydrate (15 mg, 48 μmol) and **107** (10 mg, 20 μmol) were dissolved in DMF/H_2O (1:1, 3 mL), The reaction was sealed in a Teflon capped vial and heated at 100 °C for 24 h. The resulting crystals were isolated by filtration to give **107Cd.** m.p. (decomposed) > 300 °C. Found C 48.99; H 3.72; N 6.91, calculated for $C_{25}H_{23}CdN_3O_7 \cdot 1.25H_2O$: C 49.03; H 4.19; N 6.86 %. IR *v*$_{max}$ (cm^{-1}): 3235, 3059, 2957, 1735, 1641, 1541, 1438, 1212, 1165, 1111, 993, 872, 722, 693. Phase purity was established by powder diffraction.

***N*^{3}, *N*^{5},-(methoxyacetylphenyl)-3,5-pyridinedicarboxamide (108)**, Compound **108** was obtained in 65% yield. m.p. decomposed at 230 °C; ^{1}H NMR (DMSO-*d*$_6$, 600 MHz, δ) 10.6 (s, 2H, NH), 9.26 (d, *J* = 2.1 Hz, 2H, H2), 8.81 (t, *J* = 2.1 Hz, 1H, H1), 7.74-7.73 (m, 4H Aromatic), 7.29-7.27 (m, 4H, Aromatic), 3.67 (s, 4H, H4), 3.62 (s, 6H, H6). ^{13}C{^{1}H} NMR (DMSO-*d*$_6$, 150 Hz, δ) 171.7 (C5), 163.4 (C3), 151.0 (C2), 137.5 (Aromatic), 134.7 (C1), 130.2 (Aromatic), 130.1 (Aromatic), 129.7 (Aromatic), 120.4 (Aromatic), 51.7 (C6), overlapping DMSO (C4). HRMS-ESI$^+$ (m/z): [M+H]$^+$ calculated for $C_{25}H_{24}N_3O_6$, 462.1660, found 462.1662. IR *v*$_{max}$ (cm^{-1}): 3275, 3125, 2953, 1730, 1603, 1646, 1519, 1434, 1412, 1327, 1310, 1222, 1160, 1002, 958, 916, 894, 830, 807, 793, 719, 684.

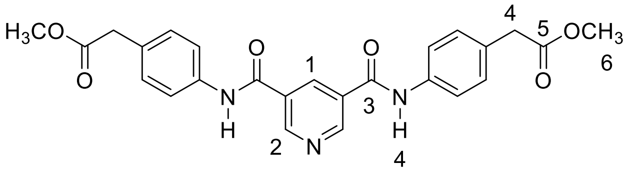

108-cr, A solution of **108** in MeCN was added to a diethyl ether diffusion for a number of days to result in single crystals of suitable quality for diffraction. Found C 64.57, H 4.9, N 8.99, calculated for $C_{25}H_{23}N_3O_6 \cdot 0.2H_2O$, C 64.57, H 5.17, N 9.04 %. Phase purity was confirmed by powder diffraction.

N^3, N^5,-(methyl-Asp)-3,5-pyridinedicarboxamide (106)

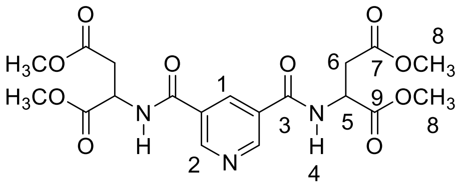

Compound **106** was obtained in 37% yield. m.p. 93-94.5 °C. ^{1}H NMR (DMSO-d_6, 600 MHz, δ) 9.34 (d, *J* = 7.52 Hz, 2H, H4), 9.13 (d, *J* = 2.1 Hz, 2H, H2), 8.62 (t, *J* = 2 Hz, 1H, H1), 4.90-4.85 (m, 2H, H5), 3.66 (s, 6H, H8), 3.63 (s, 6H, H8), 2.97-2.86 (m, 4H, H6). ^{13}C{^{1}H} NMR (DMSO-d_6, 150 Hz, δ) 170.9 (C7/C9), 170.4 (C7/C9), 164.3 (C3), 150.9 (Aromatic), 134.3 (Aromatic), 128.9 (Aromatic), 52.4 (C8), 51.8 (C8), 49.3 (C5), 35.2 (C6). HRMS-ESI$^-$ (*m/z)*: [M-H]$^-$ calculated for $C_{19}H_{22}N_3O_{10}$, 452.1311, found 452.1315. IR v_{max} (cm^{-1}): 3302, 2956, 1747, 1731, 1681, 1668, 1640, 1599, 1536, 1441, 1430, 1405, 1346, 1303, 1268, 1220, 1201, 1165, 1102, 1070, 1028, 983, 932, 887, 807, 779, 749, 705, 635, 580.

7. References

1. I. V. Kolesnichenko and E. V. Anslyn, *Chem. Soc. Rev.*, 2017, **46**, 2385-2390.
2. T. R. Canrinus, F. J. R. Cerpentier, B. L. Feringa and W. R. Browne, *Chem. Commun.*, 2017, **53**, 1719-1722.
3. M. de Loos, J. H. van Esch, R. M. Kellogg and B. L. Feringa, *Tetrahedron*, 2007, **63**, 7285-7301.
4. O. Kotova, R. Daly, C. M. G. dos Santos, P. E. Kruger, J. J. Boland and T. Gunnlaugsson, *Inorg. Chem.*, 2015, **54**, 7735-7741.
5. R. Daly, O. Kotova, M. Boese, T. Gunnlaugsson and J. J. Boland, *ACS Nano*, 2013, **7**, 4838-4845.
6. A. J. Savyasachi, O. Kotova, S. Shanmugaraju, S. J. Bradberry, G. M. Ó'Máille and T. Gunnlaugsson, *Chem*, 2017, **3**, 764-811.
7. J. M. Lehn, *Angew. Chem. Int. Ed.*, 1988, **27**, 89-112; J. M. Lehn, *Chem. Soc. Rev.*, 2007, **36**, 151-160; J.-M. Lehn, *Chem. Soc. Rev.*, 2017, **46**, 2378-2379.
8. G. M. Whitesides and B. Grzybowski, *Science*, 2002, **295**, 2418-2421.
9. G. Whitesides, J. Mathias and C. Seto, *Science*, 1991, **254**, 1312-1319.
10. G. M. Whitesides and M. Boncheva, *Proc. Natl. Acad. Sci. U. S. A.*, 2002, **99**, 4769-4774.
11. M. B. Baker, L. Albertazzi, I. K. Voets, C. M. A. Leenders, A. R. A. Palmans, G. M. Pavan and E. W. Meijer, *Nat. Commun.*, 2015, **6**, 6234.
12. Y. Sang, P. Duan and M. Liu, *Chem. Commun.*, 2018, **54**, 4025-4028.
13. W. Xibo, W. Daoliang, C. Mingming, W. Chengsha, W. Shenghui, H. Ningdong, L. Liangbin and Z. Guobing, *Chem. Eur. J.*, 2015, **21**, 15388-15394.
14. R. C. T. Howe, A. P. Smalley, A. P. M. Guttenplan, M. W. R. Doggett, M. D. Eddleston, J. C. Tan and G. O. Lloyd, *Chem. Commun.*, 2013, **49**, 4268-4270.
15. K. Pandurangan, J. A. Kitchen, S. Blasco, F. Paradisi and T. Gunnlaugsson, *Chem. Commun.*, 2014, **50**, 10819-10822.
16. M. Martínez-Calvo, O. Kotova, M. E. Möbius, A. P. Bell, T. McCabe, J. J. Boland and T. Gunnlaugsson, *J. Am. Chem. Soc.*, 2015, **137**, 1983-1992.
17. P. Jana, A. Paikar, S. Bera, S. K. Maity and D. Haldar, *Org. Lett.*, 2014, **16**, 38-41.
18. P. S. Mukherjee, N. Das and P. J. Stang, *J. Org. Chem.*, 2004, **69**, 3526-3529; S. Hasegawa, S. Horike, R. Matsuda, S. Furukawa, K. Mochizuki, Y. Kinoshita and S. Kitagawa, *J. Am. Chem. Soc.*, 2007, **129**, 2607-2614.
19. Z. Shen, T. Wang and M. Liu, *Angew. Chem. Int. Ed.*, 2014, **53**, 13424-13428.
20. E. R. Draper, L. L. E. Mears, A. M. Castilla, S. M. King, T. O. McDonald, R. Akhtar and D. J. Adams, *RSC Adv.*, 2015, **5**, 95369-95378.
21. H. Qian and I. Aprahamian, *Chem. Commun.*, 2015, **51**, 11158-11161.
22. G. Yu, X. Yan, C. Han and F. Huang, *Chem. Soc. Rev.*, 2013, **42**, 6697-6722.
23. N. M. Sangeetha and U. Maitra, *Chem. Soc. Rev.*, 2005, **34**, 821-836.
24. J. W. Steed, *Chem. Commun.*, 2011, **47**, 1379-1383.
25. A. Dawn and H. Kumari, *Chem. Eur. J.*, 2018, **24**, 762-776.
26. J. R. Engstrom, A. J. Savyasachi, M. Parhizkar, A. Sutti, C. S. Hawes, J. M. White, T. Gunnlaugsson and F. M. Pfeffer, *Chem. Sci.*, 2018, **9**, 5233-5241.
27. A. Y. Y. Tam and V. W. W. Yam, *Chem. Soc. Rev.*, 2013, **42**, 1540-1567.
28. E. R. Draper and D. J. Adams, *Chem. Soc. Rev.*, 2018, **47**, 3395-3405.
29. D. K. Chattopadhyay and D. C. Webster, *Prog. Polym. Sci.*, 2009, **34**, 1068-1133.
30. C. D. Jones and J. W. Steed, *Chem. Soc. Rev.*, 2016, **45**, 6546-6596.
31. J. W. Steed, *Chem. Soc. Rev.*, 2010, **39**, 3686-3699.
32. S. M. Ramalhete, K. P. Nartowski, N. Sarathchandra, J. S. Foster, A. N. Ward, J. Angelo, G. O. Lloyd and Y. Z. Zhumyak, *Chem. Eur. J.*, 2017, **23**, 8014-8024; C. Ma, Y. Shi, D. A. Pena, L. Peng and G. Yu, *Angew. Chem. Int. Ed.*, 2015, **54**, 7376-7380.

33. E. J. Howe, B. O. Okesola and D. K. Smith, *Chem. Commun.*, 2015, **51**, 7451-7454.
34. D. E. Clarke, E. T. Pashuck, S. Bertazzo, J. V. M. Weaver and M. M. Stevens, *J. Am. Chem. Soc.*, 2017, **139**, 7250-7255.
35. N. Sreenivasachary and J. M. Lehn, *Proc. Natl. Acad. Sci. U. S. A.*, 2005, **102**, 5938-5943.
36. M. Zhang, A. Vora, W. Han, R. J. Wojtecki, H. Maune, A. B. Le, L. E. Thompson, G. M. McClelland, F. Ribet, A. C. Engler and A. Nelson, *Macromolecules*, 2015, **48**, 6482-6488; B. Escuder, F. Rodriguez-Llansola and J. F. Miravet, *New J. Chem.*, 2010, **34**, 1044-1054; M. O. M. Piepenbrock, G. O. Lloyd, N. Clarke and J. W. Steed, *Chem. Rev.*, 2010, **110**, 1960-2004.
37. J. Li, L. Geng, G. Wang, H. Chu and H. Wei, *Chem. Mater.*, 2017, **29**, 8932-8952.
38. L. E. Buerkle, H. A. von Recum and S. J. Rowan, *Chem. Sci.*, 2012, **3**, 564-572.
39. J. A. Foster, M. O. M. Piepenbrock, G. O. Lloyd, N. Clarke, J. A. K. Howard and J. W. Steed, *Nat. Chem.*, 2010, **2**, 1037-1043.
40. D. B. Amabilino, D. K. Smith and J. W. Steed, *Chem. Soc. Rev.*, 2017, **46**, 2404-2420.
41. C. Colquhoun, E. Draper, R. Schweins, M. Marcello, L. Serpell, D. Vadukul and D. Adams, *Soft Matter*, 2017, **13**, 1914-1919.
42. P. Dechambenoit, S. Ferlay, B. Donnio, D. Guillon and M. W. Hosseini, *Chem. Commun.*, 2011, **47**, 734-736.
43. B. Hugo, I. Verónica, B. Joaquín, S. J. Luis, E. Anabel and G. Raquel, *Chem. Eur. J.*, 2016, **22**, 4924-4930.
44. D. Gao, J. Andeme Edzang, A. K. Diallo, T. Dutronc, T. S. Balaban, C. Videlot-Ackermann, E. Terazzi and G. Canard, *New J. Chem.*, 2015, **39**, 7140-7146.
45. I. Paraschiv, M. Giesbers, B. van Lagen, F. C. Grozema, R. D. Abellon, L. D. A. Siebbeles, A. T. M. Marcelis, H. Zuilhof and E. J. R. Sudhölter, *Chem. Mater.*, 2006, **18**, 968-974.
46. J. Jensen, S. C. Grundy, S. L. Bretz and C. S. Hartley, *J. Chem. Educ.*, 2011, **88**, 1133-1136.
47. K. Binnemans, *Handbook on the Physics and Chemistry of Rare Earths*, Elsevier, 2005.
48. T. Kato, T. Kutsuna, K. Hanabusa and M. Ukon, *Adv. Mater.*, 1998, **10**, 606-608; S. Sergeyev, W. Pisula and Y. H. Geerts, *Chem. Soc. Rev.*, 2007, **36**, 1902-1929.
49. M. O'Neill and S. M. Kelly, *Adv. Mater.*, 2003, **15**, 1135-1146.
50. Y. Gao, J. M. Slattery and D. W. Bruce, *New J. Chem.*, 2011, **35**, 2910-2918.
51. J. A. M. Lugger, D. J. Mulder, S. Bhattacharjee and R. P. Sijbesma, *ACS Nano*, 2018, **12**, 6714-6724.
52. S. I. Kawano, Y. Ishida and K. Tanaka, *J. Am. Chem. Soc.*, 2015, **137**, 2295-2302.
53. T. F. A. De Greef, M. M. J. Smulders, M. Wolffs, A. P. H. J. Schenning, R. P. Sijbesma and E. W. Meijer, *Chem. Rev.*, 2009, **109**, 5687-5754.
54. O. J. G. Goor, S. I. S. Hendrikse, P. Y. W. Dankers and E. W. Meijer, *Chem. Soc. Rev.*, 2017, **46**, 6621-6637.
55. M. H. Bakker, C. C. Lee, E. W. Meijer, P. Y. W. Dankers and L. Albertazzi, *ACS Nano*, 2016, **10**, 1845-1852.
56. S. I. Stupp and L. C. Palmer, *Chem. Mater.*, 2014, **26**, 507-518.
57. L. N. Neumann, M. B. Baker, C. M. A. Leenders, I. K. Voets, R. P. M. Lafleur, A. R. A. Palmans and E. W. Meijer, *Org. Biomol. Chem.*, 2015, **13**, 7711-7719.
58. K. Petkau-Milroy, D. A. Uhlenheuer, A. J. H. Spiering, J. A. J. Vekemans and L. Brunsveld, *Chem. Sci.*, 2013, **4**, 2886-2891.
59. P. Y. W. Dankers, T. M. Hermans, T. W. Baughman, Y. Kamikawa, R. E. Kieltyka, M. M. C. Bastings, H. M. Janssen, N. A. J. Sommerdijk, A. Larsen, M. J. A. v. Luyn, A. W. Bosman, E. R. Popa, G. Fytas and E. W. Meijer, *Adv. Mater.*, 2012, **24**, 2703-2709.

60. J. Liu, C. S. Y. Tan, Z. Yu, N. Li, C. Abell and O. A. Scherman, *Adv. Mater.*, 2017, **29**, 1605325.
61. S. Bähring, L. Martín-Gomis, G. Olsen, K. A. Nielsen, D. S. Kim, T. Duedal, A. Sastre-Santos, J.O. Jeppesen and J. L. Sessler., *Chem. Eur. J.*, 2016, **22**, 1958-1967.
62. T. R. Cook, Y.-R. Zheng and P. J. Stang, *Chem. Rev.*, 2013, **113**, 734-777.
63. S. Kitagawa, R. Kitaura and S. I. Noro, *Angew. Chem. Int. Ed.*, 2004, **43**, 2334-2375.
64. B. Moulton and M. J. Zaworotko, *Chem. Rev.*, 2001, **101**, 1629-1658.
65. H. Deng, S. Grunder, K. E. Cordova, C. Valente, H. Furukawa, M. Hmadeh, F. Gándara, A. C. Whalley, Z. Liu, S. Asahina, H. Kazumori, M. O’Keeffe, O. Terasaki, J. F. Stoddart and O. M. Yaghi, *Science*, 2012, **336**, 1018-1023.
66. P. A. Kobielska, A. J. Howarth, O. K. Farha and S. Nayak, *Coord. Chem. Rev.*, 2018, **358**, 92-107; L. E. Kreno, K. Leong, O. K. Farha, M. Allendorf, R. P. Van Duyne and J. T. Hupp, *Chem. Rev.*, 2012, **112**, 1105-1125; Y. Shuai, F. Liang, W. Kecheng, P. Jiandong, B. Matheiu, L. Christina, S. Yujia, Q. Junsheng, Y. Xinyu, Z. Peng, W. Qi, Z. Lanfang, Z. Yingmu, Z. Liangliang, F. Yu, L. Jialuo and Z. Hong-Cai, *Adv. Mater.*, 2018, **0**, 1704303; D. Farrusseng, S. Aguado and C. Pinel, *Angew. Chem. Int. Ed.*, 2009, **48**, 7502-7513.
67. C. Orellana-Tavra, R. J. Marshall, E. F. Baxter, I. A. Lázaro, A. Tao, A. K. Cheetham, R. S. Forgan and D. Fairen-Jimenez, *J. Mater. Chem. B*, 2016, **4**, 7697-7707.
68. C. Orellana-Tavra, S. Haddad, R. J. Marshall, I. Abánades Lázaro, G. Boix, I. Imaz, D. Maspoch, R. S. Forgan and D. Fairen-Jimenez, *ACS Appl. Mater. Interfaces*, 2017, **9**, 35516-35525.
69. C. S. Hawes, N. F. Chilton, B. Moubaraki, G. P. Knowles, A. L. Chaffee, K. S. Murray, S. R. Batten and D. R. Turner, *Dalton Trans.*, 2015, **44**, 17494-17507.
70. S. Nandi, D. Chakraborty and R. Vaidhyanathan, *Chem. Commun.*, 2016, **52**, 7249-7252.
71. T. Gunnlaugsson, *Nat Chem*, 2016, **8**, 6-7.
72. E. P. McCarney, J. P. Byrne, B. Twamley, M. Martinez-Calvo, G. Ryan, M. E. Mobius and T. Gunnlaugsson, *Chem. Commun.*, 2015, **51**, 14123-14126.
73. S. J. Bradberry, A. J. Savyasachi, R. D. Peacock and T. Gunnlaugsson, *Faraday Discuss.*, 2015, **185**, 413-431.
74. S. Cantekin, T. F. A. de Greef and A. R. A. Palmans, *Chem. Soc. Rev.*, 2012, **41**, 6125-6137.
75. A. Desmarchelier, B. G. Alvarenga, X. Caumes, L. Dubreucq, C. Troufflard, M. Tessier, N. Vanthuyne, J. Ide, T. Maistriaux, D. Beljonne, P. Brocorens, R. Lazzaroni, M. Raynal and L. Bouteiller, *Soft Matter*, 2016, **12**, 7824-7838; M. A. J. Veld, D. Haveman, A. R. A. Palmans and E. W. Meijer, *Soft Matter*, 2011, **7**, 524-531.
76. P. J. M. Stals, J. F. Haveman, R. Martin-Rapun, C. F. C. Fitie, A. R. A. Palmans and E. W. Meijer, *J. Mater. Chem.*, 2009, **19**, 124-130.
77. A. Paikar, A. Pramanik and D. Haldar, *RSC Adv.*, 2015, **5**, 31845-31851.
78. T. Shikata, D. Ogata and K. Hanabusa, *J. Phys. Chem. B*, 2004, **108**, 508-514.
79. Y. Matsunaga, N. Miyajima, Y. Nakayasu, S. Sakai and M. Yonenaga, *Bull. Chem. Soc. Jpn.*, 1988, **61**, 207-210.
80. P. J. M. Stals, M. M. J. Smulders, R. Martín-Rapún, A. R. A. Palmans and E. W. Meijer, *Chem. Eur. J.*, 2009, **15**, 2071-2080.
81. M. Kristiansen, P. Smith, H. Chanzy, C. Baerlocher, V. Gramlich, L. McCusker, T. Weber, P. Pattison, M. Blomenhofer and H. W. Schmidt, *Cryst. Growth Des.*, 2009, **9**, 2556-2558.
82. K. E. Broaders, S. J. Pastine, S. Grandhe and J. M. J. Frechet, *Chem. Commun.*, 2011, **47**, 665-667.

83. A. Bernet, R. Q. Albuquerque, M. Behr, S. T. Hoffmann and H. W. Schmidt, *Soft Matter*, 2012, **8**, 66-69.
84. N. E. Shi, H. Dong, G. Yin, Z. Xu and S. H. Li, *Adv. Funct. Mater.*, 2007, **17**, 1837-1843.
85. C. F. C. Fitié, I. Tomatsu, D. Byelov, W. H. de Jeu and R. P. Sijbesma, *Chem. Mater.*, 2008, **20**, 2394-2404.
86. P. Besenius, J. L. M. Heynens, R. Straathof, M. M. L. Nieuwenhuizen, E. Terreno, S. Aime, G. J. Strijkens, K. Nicolay and E. W. Meijer, *Contrast Media Mol. Imaging*, 2012, **7**, 356-361.
87. M. Blomenhofer, S. Ganzleben, D. Hanft, H. W. Schmidt, M. Kristiansen, P. Smith, K. Stoll, D. Mäder and K. Hoffmann, *Macromolecules*, 2005, **38**, 3688-3695.
88. C. M. A. Leenders, T. Mes, M. B. Baker, M. M. E. Koenigs, P. Besenius, A. R. A. Palmans and E. W. Meijer, *Mater. Horiz.*, 2014, **1**, 116-120.
89. S. Seibt, S. With, A. Bernet, H. W. Schmidt and S. Förster, *Langmuir*, 2018, **34**, 5535-5544.
90. X. J. Kuang, A. Wajahat, W. T. Gong, M. K. Dhinakaran, X. H. Li and G. I. Ning, *Soft Matter*, 2017, **13**, 4074-4079.
91. C. Li, *Chem. Commun.*, 2014, **50**, 12420-12433; Z. Huacheng and Z. Yanli, *Chem. Eur. J.*, 2013, **19**, 16862-16879; T. Li-Li, L. Haiwei, T. Yanchun, Z. S. Xiao-An, W. Bo and Y. Ying-Wei, *Adv. Mater.*, 2014, **26**, 7027-7031; T. Ogoshi, R. Sueto, K. Yoshikoshi and T.-a. Yamagishi, *Chem. Commun.*, 2014, **50**, 15209-15211.
92. Y. Ishioka, N. Minakuchi, M. Mizuhata and T. Maruyama, *Soft Matter*, 2014, **10**, 965-971.
93. L. Yang, X. Tan, Z. Wang and X. Zhang, *Chem. Rev.*, 2015, **115**, 7196-7239.
94. D. van der Zwaag, T. de Greef and E. W. Meijer, *Angew. Chem. Int. Ed.*, 2015, **54**, 8334-8336.
95. G. M. ter Huurne, L. N. J. de Windt, Y. Liu, E. W. Meijer, I. K. Voets and A. R. A. Palmans, *Macromolecules*, 2017, **50**, 8562-8569; D. van der Zwaag, T. F. A. de Greef and E. W. Meijer, *Angew. Chem. Int. Ed.*, 2015, **54**, 8334-8336.
96. M. H. Bakker, C. C. Lee, E. W. Meijer, P. Y. W. Dankers and L. Albertazzi, *ACS Nano*, 2016, **10**, 1845-1852.
97. C. F. C. Fitié, W. S. C. Roelofs, P. C. M. M. Magusin, M. Wübbenhorst, M. Kemerink and R. P. Sijbesma, *J. Phys. Chem. B*, 2012, **116**, 3928-3937.
98. C. Invernizzi, C. Dalvit, H. Stoeckli-Evans and R. Neier, *Eur. J. Org. Chem.*, 2015, **2015**, 5115-5127.
99. Y. J. Choi, D. Y. Kim, M. Park, W. J. Yoon, Y. Lee, J. K. Hwang, Y. W. Chiang, S. W. Kuo, C. H. Hsu and K. U. Jeong, *ACS Appl. Mater. Interfaces*, 2016, **8**, 9490-9498.
100. L. Jia, N. Tang and J. J. Vittal, *J. Mol. Struct.*, 2009, **920**, 14-17.
101. D. Moon, S. Kang, J. Park, K. Lee, R. P. John, H. Won, G. H. Seong, Y. S. Kim, G. H. Kim, H. Rhee and M. S. Lah, *J. Am. Chem. Soc.*, 2006, **128**, 3530-3531; J. Park, S. Hong, D. Moon, M. Park, K. Lee, S. Kang, Y. Zou, R. P. John, G. H. Kim and M. S. Lah, *Inorg. Chem.*, 2007, **46**, 10208-10213.
102. Y. Zhang, Q. Wang, Y. J. Xiao, J. Han and X. L. Zhao, *Polyhedron*, 2012, **33**, 127-136.
103. L. Rajput, V. V. Chernyshev and K. Biradha, *Chem. Commun.*, 2010, **46**, 6530-6532.
104. P. Besenius, G. Portale, P. H. H. Bomans, H. M. Janssen, A. R. A. Palmans and E. W. Meijer, *Proc. Natl. Acad. Sci. U.S.A.*, 2010, **107**, 17888-17893.
105. C. W. Cairo, J. E. Gestwicki, M. Kanai and L. L. Kiessling, *J. Am. Chem. Soc.*, 2002, **124**, 1615-1619; F. Fernandez-Trillo, L. M. Grover, A. Stephenson-Brown, P. Harrison and P. M. Mendes, *Angew. Chem. Int. Ed.*, 2017, **56**, 3142-3160; F. Hong, F. Zhang, Y. Liu and H. Yan, *Chem. Rev.*, 2017, **117**, 12584-12640.

106. S. P. W. Wijnands, W. Engelen, R. P. M. Lafleur, E. W. Meijer and M. Merkx, *Nat. Commun.*, 2018, **9**, 65.
107. W. Engelen, S. P. W. Wijnands and M. Merkx, *J. Am. Chem. Soc.*, 2018, **140**, 9758-9767.
108. O. Kotova, R. Daly, C. M. G. dos Santos, M. Boese, P. E. Kruger, J. J. Boland and T. Gunnlaugsson, *Angew. Chem. Int. Ed.*, 2012, **51**, 7208-7212.
109. C. A. Volkert and A. M. Minor, *MRS Bull.*, 2007, **32**, 389-399.
110. K. Pandurangan, J. A. Kitchen, S. Blasco, E. M. Boyle, B. Fitzpatrick, M. Feeney, P. E. Kruger and T. Gunnlaugsson, *Angew. Chem. Int. Ed.*, 2015, **54**, 4566-4570.
111. J. P. Byrne, J. A. Kitchen, O. Kotova, V. Leigh, A. P. Bell, J. J. Boland, M. Albrecht and T. Gunnlaugsson, *Dalton Trans.*, 2014, **43**, 196-209.
112. J. I. Lovitt, C. S. Hawes, A. D. Lynes, B. Haffner, M. E. Mobius and T. Gunnlaugsson, *Inorg. Chem. Front.*, 2017, **4**, 296-308.
113. C. S. Hawes, K. Byrne, W. Schmitt and T. Gunnlaugsson, *Inorg. Chem.*, 2016, **55**, 11570-11582.
114. S. Shanmugaraju, C. S. Hawes, A. J. Savyasachi, S. Blasco, J. A. Kitchen and T. Gunnlaugsson, *Chem. Commun.*, 2017, **53**, 12512-12515.
115. H. L. Dalton, C. S. Hawes and T. Gunnlaugsson, *Cryst. Growth Des.*, 2017, **17**, 4365-4376.
116. E. P. McCarney, C. S. Hawes, J. A. Kitchen, K. Byrne, W. Schmitt and T. Gunnlaugsson, *Inorg. Chem.*, 2018, **57**, 3920-3930.
117. A. Desmarchelier, M. Raynal, P. Brocorens, N. Vanthuyne and L. Bouteiller, *Chem. Commun.*, 2015, **51**, 7397-7400; S. Lee, S. Oh, J. Lee, Y. Malpani, Y. S. Jung, B. Kang, J. Y. Lee, K. Ozasa, T. Isoshima, S. Y. Lee, M. Hara, D. Hashizume and J. M. Kim, *Langmuir*, 2013, **29**, 5869-5877.
118. V. Nagarajan and V. R. Pedireddi, *Cryst. Growth Des.*, 2014, **14**, 1895-1901.
119. E. Huerta , B. van Genabeek , B. A. G. Lamers, M. M. E. Koenigs, E. W. Meijer and A. R. A. Palmans, *Chem. Eur. J.*, 2015, **21**, 3682-3690.
120. M. A. Beuwer, M. F. Knopper, L. Albertazzi, D. van der Zwaag, W. G. Ellenbroek, E. W. Meijer, M. W. J. Prins and P. Zijlstra, *Polym. Chem.*, 2016, **7**, 7260-7268.
121. A. J. Savyasachi, PhD Thesis, Trinity College Dublin, 2017.
122. R. B. P. Elmes, K. N. Orange, S. M. Cloonan, D. C. Williams and T. Gunnlaugsson, *J. Am. Chem. Soc.*, 2011, **133**, 15862-15865.
123. A. M. Nonat, A. J. Harte, K. Senechal-David, J. P. Leonard and T. Gunnlaugsson, *Dalton Trans.*, 2009, 4703-4711.
124. D. M. Poojary and A. Clearfield, *Acc. Chem. Res.*, 1997, **30**, 414-422.
125. L. B. McCusker and C. Baerlocher, *Chem. Commun.*, 2009, 1439-1451.
126. A. R. A. Palmans, J. A. J. M. Vekemans, H. Fischer, R. A. Hikmet and E. W. Meijer, *Chem. Eur. J.*, 1997, **3**, 300-307.
127. H. Wang, B. Li, H. Wu, T. L. Hu, Z. Yao, W. Zhou, S. Xiang and B. Chen, *J. Am. Chem. Soc.*, 2015, **137**, 9963-9970.
128. H. Li, M. Eddaoudi, T. L. Groy and O. M. Yaghi, *J. Am. Chem. Soc.*, 1998, **120**, 8571-8572.
129. A. L. Spek, *Acta Crystallogr Sect C.: Struct. Chem*, 2015, 9-18.
130. H. Sitepu, *Powder Diffr.*, 2009, **24**, 315-326.
131. J. M. Poolman, J. Boekhoven, A. Besselink, A. G. L. Olive, J. H. van Esch and R. Eelkema, *Nat. Protoc.*, 2014, **9**, 977.
132. N. E. Shi, H. Dong, G. Yin, Z. Xu and S. H. Li, *Adv. Funct. Mater.*, 2007, **17**, 1837-1843.

133. C. Colquhoun, E. R. Draper, R. Schweins, M. Marcello, D. Vadukul, L. C. Serpell and D. J. Adams, *Soft Matter*, 2017, **13**, 1914-1919.
134. D. J. Abdallah and R. W. Weiss, *Adv. Mater.*, 2000, **12**, 1237-1247.
135. T. Ishi-i, T. Hirayama, K. I. Murakami, H. Tashiro, T. Thiemann, K. Kubo, A. Mori, S. Yamasaki, T. Akao, A. Tsuboyama, T. Mukaide, K. Ueno and S. Mataka, *Langmuir*, 2005, **21**, 1261-1268.
136. Perkin Elmer DSC 8000, http://www.perkinelmer.com/product/dsc-8000-lab-system-n5340511, (accessed 30/7/18); Perkin Elmer DSC Beginner's guide, http://www.perkinelmer.com/CMSResources/Images/46-74542GDE_DSCBeginnersGuide.pdf, (accessed 30/7/18).
137. S. J. Lee, C. R. Park and J. Y. Chang, *Langmuir*, 2004, **20**, 9513-9519.
138. C. F. Josep, C. Eugenio, F. A. Alicia and P. C. Elena, *Nanotechnology*, 2014, **25**, 395703.
139. H. Brochu and P. Vermette, *Langmuir*, 2008, **24**, 2009-2014.
140. J. J. Licari and D. W. Swanson, in *Adhesives Technology for Electronic Applications (Second Edition)* J. J. Licari and D. W. Swanson, William Andrew Publishing, Oxford, 2011, DOI: https://doi.org/10.1016/B978-1-4377-7889-2.10007-5, pp. 345-377.
141. A. Vinckier and G. Semenza, *FEBS Lett.*, 1998, **430**, 12-16.
142. A practical guide to AFM spectroscopy and data analysis https://www.jpk.com/app-technotes-img/AFM/pdf/jpk-tech-force-spectroscopy.14-2.pdf, (accessed 30/7/18).
143. C. A. Jiménez, J. B. Belmar, L. Ortíz, P. Hidalgo, O. Fabelo, J. Pasán and C. Ruiz-Pérez, *Cryst. Growth Des.*, 2009, **9**, 4987-4989.
144. Z. J. Lin, J. Lu, M. Hong and R. Cao, *Chem. Soc. Rev.*, 2014, **43**, 5867-5895.
145. R. Sun, Y. Z. Li, J. Bai and Y. Pan, *Cryst. Growth Des.*, 2007, **7**, 890-894.
146. S. Banerjee, N. N. Adarsh and P. Dastidar, *Soft Matter*, 2012, **8**, 7623-7629.
147. L. Rajput, D. Kim and M. S. Lah, *CrystEngComm*, 2013, **15**, 259-264.
148. A. D. Lynes, C. S. Hawes, E. N. Ward, B. Haffner, M. E. Mobius, K. Byrne, W. Schmitt, R. Pal and T. Gunnlaugsson, *CrystEngComm*, 2017, **19**, 1427-1438.
149. X. M. Zhang, *Coord. Chem. Rev.*, 2005, **249**, 1201-1219.
150. O. R. Evans, R. G. Xiong, Z. Wang, G. K. Wong and W. Lin, *Angew. Chem. Int. Ed.*, 1999, **38**, 536-538; G. B. Hix, B. M. Kariuki, S. Kitchin and M. Tremayne, *Inorg. Chem.*, 2001, **40**, 1477-1481; K. E. Knope and C. L. Cahill, *Inorg. Chem.*, 2008, **47**, 7660-7672.
151. S. H. Jung, K. Y. Kim, A. Ahn, M. Y. Choi, J. Jaworski and J. H. Jung, *ACS Appl. Mater. Interfaces*, 2016, **8**, 14102-14108.
152. B. Gong, C. Zheng and Y. Yan, *J. Chem. Crystallogr.*, 1999, **29**, 649-652.
153. J. E. S. Lowell, *Powder surface area and porosity*, Chapman and Hall London, New York Second edn., 1984.
154. K. S. Walton and R. Q. Snurr, *J. Am. Chem. Soc.*, 2007, **129**, 8552-8556.
155. F. Carrasco-Marin, M. V. Lopez-Ramon and C. Moreno-Castilla, *Langmuir*, 1993, **9**, 2758-2760; C. Nguyen and D. D. Do, *Carbon*, 2001, **39**, 1327-1336.
156. K. Sumida, D. L. Rogow, J. A. Mason, T. M. McDonald, E. D. Bloch, Z. R. Herm, T. H. Bae and J. R. Long, *Chem. Rev.*, 2012, **112**, 724-781; G. E. Cmarik, M. Kim, S. M. Cohen and K. S. Walton, *Langmuir*, 2012, **28**, 15606-15613; J. M. Simmons, H. Wu, W. Zhou and T. Yildirim, *Energy Environ. Sci.*, 2011, **4**, 2177-2185.
157. P. P. Bose, M. G. B. Drew, A. K. Das and A. Banerjee, *Chem. Commun.*, 2006, 3196-3198.
158. F. Fages, *Angew. Chem. Int. Ed.*, 2006, **45**, 1680-1682.
159. S. C. Grindy and N. Holten-Andersen, *Soft Matter*, 2017, **13**, 4057-4065.

160. M. P. Stevens, *Polymer Chemistry, an introduction* Oxford University Press New York, 3rd edn., 1999.
161. C. M. A. Leenders, M. B. Baker, I. A. B. Pijpers, R. P. M. Lafleur, L. Albertazzi, A. R. A. Palmans and E. W. Meijer, *Soft Matter*, 2016, **12**, 2887-2893.
162. W. Zhao, J. Hu and W. Gao, *ACS Appl. Mater. Interfaces*, 2017, **9**, 23528-23535.
163. T. F. A. de Greef and E. W. Meijer, *Nature*, 2008, **453**, 171.
164. J. Lee and J. Y. Chang, *Langmuir*, 2018, **34**, 11843-11849.
165. C. M. A. Leenders, L. Albertazzi, T. Mes, M. M. E. Koenigs, A. R. A. Palmans and E. W. Meijer, *Chem. Commun.*, 2013, **49**, 1963-1965.
166. G. Srinivasulu, B. Sridhar, K. Ravi Kumar, B. Sreedhar, V. Ramesh, R. Srinivas and A. C. Kunwar, *J. Mol. Struct.*, 2011, **1006**, 180-184.
167. S. Wang and R. Chen, *Chem. Mater.*, 2017, **29**, 5806-5815.
168. H.-G. Elias, *An introduction to polymer science* VCH Publishers Weinheim, Germany and New York , USA, 1st edn., 1997.
169. S. Dinda, M. Ghosh and P. K. Das, *Langmuir*, 2016, **32**, 6701-6712; W. Chen, G. Qing and T. Sun, *Chem. Commun.*, 2017, **53**, 447-450.
170. *Macromolecular design of polymeric materials*, Marcel Dekker, New York 1997.
171. I. M. Pastor, P. Västilä and H. Adolfsson, *Chem. Eur. J.*, 2003, **9**, 4031-4045.
172. D. Chandra, A. Dutta and A. Bhaumik, *Eur. J. Inorg. Chem.*, 2009, **2009**, 4062-4068.
173. M. P. Lightfoot, F. S. Mair, R. G. Pritchard and J. E. Warren, *Chem. Commun.*, 1999, 1945-1946; C. Kulkarni, E. W. Meijer and A. R. A. Palmans, *Acc. Chem. Res.*, 2017, **50**, 1928-1936.
174. J. Zhang and C. Y. Su, *Coord. Chem. Rev.*, 2013, **257**, 1373-1408.
175. M. E. Belowich and J. F. Stoddart, *Chem. Soc. Rev.*, 2012, **41**, 2003-2024.
176. H. Vardhan, A. Mehta, I. Nath and F. Verpoort, *RSC Adv.*, 2015, **5**, 67011-67030; A. J. McConnell, C. S. Wood, P. P. Neelakandan and J. R. Nitschke, *Chem. Rev.*, 2015, **115**, 7729-7793.
177. R. A. Bilbeisi, T. K. Ronson and J. R. Nitschke, *Angew. Chem. Int. Ed.*, 2013, **52**, 9027-9030; D. Pelleteret, R. Clérac, C. Mathonière, E. Harté, W. Schmitt and P. E. Kruger, *Chem. Commun.*, 2009, 221-223; A. D. Faulkner, R. A. Kaner, Q. M. A. Abdallah, G. Clarkson, D. J. Fox, P. Gurnani, S. E. Howson, R. M. Phillips, D. I. Roper, D. H. Simpson and P. Scott, *Nat. Chem.*, 2014, **6**, 797.
178. P. Pandey, A. P. Katsoulidis, I. Eryazici, Y. Wu, M. G. Kanatzidis and S. T. Nguyen, *Chem. Mater.*, 2010, **22**, 4974-4979; S. Kandambeth, A. Mallick, B. Lukose, M. V. Mane, T. Heine and R. Banerjee, *J. Am. Chem. Soc.*, 2012, **134**, 19524-19527.
179. F. Xu, J. W. Xu, B. X. Zhang and L. Yan Ling, *AlChE J.*, 2015, **61**, 35-45.
180. M. Sarkar, R. Clérac, C. Mathonière, N. G. R. Hearns, V. Bertolasi and D. Ray, *Inorg. Chem.*, 2011, **50**, 3922-3933; X. Wang, K.-Q. Zhao, M. R. J. Elsegood, T. J. Prior, X. Liu, L. Wu, S. Sanz, E. K. Brechin and C. Redshaw, *RSC Adv.*, 2015, **5**, 57414-57424.
181. P. Roy, M. Nandi, M. Manassero, M. Riccó, M. Mazzani, A. Bhaumik and P. Banerjee, *Dalton Trans.*, 2009, 9543-9554.
182. A. K. Ghosh and D. Ray, *Polyhedron*, 2013, **52**, 370-376; R. Shakya, P. H. Keyes, M. J. Heeg, A. Moussawel, P. A. Heiney and C. N. Verani, *Inorg. Chem.*, 2006, **45**, 7587-7589.
183. G. B. Deacon and R. J. Phillips, *Coord. Chem. Rev.*, 1980, **33**, 227-250.
184. J. N. Van Niekerk and F. R. L. Schoening, *Nature*, 1953, **171**, 36.
185. K. Petkau-Milroy, M. H. Sonntag and L. Brunsveld, *Chem. Eur. J.*, 2013, **19**, 10786-10793.
186. O. Kotova, J. A. Kitchen, C. Lincheneau, R. D. Peacock and T. Gunnlaugsson, *Chem. Eur. J.*, 2013, **19**, 16181-16186; J. P. Leonard, P. Jensen, T. McCabe, J. E. O'Brien, R.

D. Peacock, P. E. Kruger and T. Gunnlaugsson, *J. Am. Chem. Soc.*, 2007, **129**, 10986-10987.

187. S. J. Bradberry, J. P. Byrne, C. P. McCoy and T. Gunnlaugsson, *Chem. Commun.*, 2015, **51**, 16565-16568; O. Kotova, S. Comby, C. Lincheneau and T. Gunnlaugsson, *Chem. Sci.*, 2017, **8**, 3419-3426; R. M. Duke, T. McCabe, W. Schmitt and T. Gunnlaugsson, *J. Org. Chem.*, 2012, **77**, 3115-3126; C. Lincheneau, C. Destribats, D. E. Barry, J. A. Kitchen, R. D. Peacock and T. Gunnlaugsson, *Dalton Trans.*, 2011, **40**, 12056-12059.
188. O. Kotova, S. Blasco, B. Twamley, J. O'Brien, R. D. Peacock, J. A. Kitchen, M. Martinez-Calvo and T. Gunnlaugsson, *Chem. Sci.*, 2015, **6**, 457-471.
189. D. E. Barry, J. A. Kitchen, M. Albrecht, S. Faulkner and T. Gunnlaugsson, *Langmuir*, 2013, **29**, 11506-11515; J. A. Kitchen, D. E. Barry, L. Mercs, M. Albrecht, R. D. Peacock and T. Gunnlaugsson, *Angew. Chem. Int. Ed.*, 2012, **51**, 704-708.
190. C. Lincheneau, J. P. Leonard, T. McCabe and T. Gunnlaugsson, *Chem. Commun.*, 2011, **47**, 7119-7121.
191. K. Ariga, Y. Yamauchi, T. Mori and J. P. Hill, *Adv. Mater.*, 2013, **25**, 6477-6512.
192. K. Binnemans, *Chem. Rev.*, 2009, **109**, 4283-4374; J. C. G. Bünzli and C. Piguet, *Chem. Soc. Rev.*, 2005, **34**, 1048-1077; S. Pandya, J. Yu and D. Parker, *Dalton Trans.*, 2006, 2757-2766; S. V. Eliseeva and J. C. G. Bünzli, *Chem. Soc. Rev.*, 2010, **39**, 189-227.
193. C. Lincheneau, B. Jean-Denis and T. Gunnlaugsson, *Chem. Commun.*, 2014, **50**, 2857-2860.
194. G. Pennarun, C. Granotier, L. R. Gauthier, D. Gomez, F. Hoffschir, E. Mandine, J. F. Riou, J. L. Mergny, P. Mailliet and F. D. Boussin, *Oncogene*, 2005, **24**, 2917.
195. A. Rajendran, M. Endo, K. Hidaka, P. L. Thao Tran, M. P. Teulade-Fichou, J. L. Mergny and H. Sugiyama, *RSC Adv.*, 2014, **4**, 6346-6355.
196. C. Saintomé, P. Alberti, N. Guinot, P. Lejault, J. Chatain, P. Mailliet, J. F. Riou and A. Bugaut, *Chem. Commun.*, 2018, **54**, 1897-1900.
197. D. Bansal, S. Pandey, G. Hundal and R. Gupta, *New J. Chem.*, 2015, **39**, 9772-9781.
198. X. L. Wang, N. L. Chen, G. C. Liu, H. Y. Lin and J. W. Zhang, *Eur. J. Inorg. Chem.*, 2015, **2015**, 1924-1940; D. Wang, S. V. Lindeman and A. T. Fiedler, *Eur. J. Inorg. Chem.*, 2013, **2013**, 4473-4484.
199. N. Fu, J. M. Baumes, E. Arunkumar, B. C. Noll and B. D. Smith, *J. Org. Chem.*, 2009, **74**, 6462-6468.
200. A. Mishra, A. Ali, S. Upreti and R. Gupta, *Inorg. Chem.*, 2008, **47**, 154-161; A. Mishra, A. Ali, S. Upreti, M. S. Whittingham and R. Gupta, *Inorg. Chem.*, 2009, **48**, 5234-5243.
201. R. Yun, Z. Lu, Y. Pan, X. You and J. Bai, *Angew. Chem. Int. Ed.*, 2013, **52**, 11282-11285.
202. X. Wang, J. Huang, L. Liu, G. Liu, H. Lin, J. Zhang, N. Chen and Y. Qu, *RSC Adv.*, 2013, **3**, 13944-13952.
203. I. L. Karle, D. Ranganathan and S. Kurur, *J. Am. Chem. Soc.*, 1999, **121**, 7156-7157.
204. Energy Dispersive X-ray spectroscopy https://www.mee-inc.com/hamm/energy-dispersive-x-ray-spectroscopyeds/, (accessed 11/8/18, 2018).
205. A. E. Goeta and J. A. K. Howard, *Chem. Soc. Rev.*, 2004, **33**, 490-500.
206. A. Worthy, A. Grosjean, M. C. Pfrunder, Y. Xu, C. Yan, G. Edwards, J. K. Clegg and J. C. McMurtrie, *Nat. Chem.*, 2017, **10**, 65; S. Takamizawa and Y. Miyamoto, *Angew. Chem. Int. Ed.*, 2014, **53**, 6970-6973; S. Krause, V. Bon, I. Senkovska, U. Stoeck, D. Wallacher, D. M. Többens, S. Zander, R. S. Pillai, G. Maurin, F. X. Coudert and S. Kaskel, *Nature*, 2016, **532**, 348; S. Saha and G. R. Desiraju, *J. Am. Chem. Soc.*, 2017, **139**, 1975-1983.
207. P. Commins, I. T. Desta, D. P. Karothu, M. K. Panda and P. Naumov, *Chem. Commun.*, 2016, **52**, 13941-13954.

208. SADABS, *Bruker-AXS Inc*, 2016, , Madison, WI.
209. APEX-3, *Bruker-AXS Inc*, 2016, Madison, WI
210. G. F. Smith and F. W. Cagle, *J. Org. Chem.*, 1947, **12**, 781-784.
211. S. H. Jung, J. Jeon, H. Kim, J. Jaworski and J. H. Jung, *J. Am. Chem. Soc.*, 2014, **136**, 6446-6452.
212. N. G. Delaney, *EP 0136883*, 1985.
213. L. Gros, S. O. Lorente, Jimenez, V. Yardley, L. Rattray, H. Wharton, S. Little, S. L. Croft, L. M. Ruiz-Perez, D. Gonzalez-Pacanowska and I. H. Gilbert, *J. Med. Chem.*, 2006, **49**, 6094-6103.
214. M. A. Ashraf, J. K. Notta and J. S. Snaith, *Tetrahedron Lett.*, 2003, **44**, 9115-9119.
215. J. Lohbeck and A. K. Miller, *Bioorg. Med. Chem. Lett.*, 2016, **26**, 5260-5262.
216. M. Klein-Hitpaß, A. D. Lynes, C. S. Hawes, K. Byrne, W. Schmitt and T. Gunnlaugsson, *Supramol. Chem.*, 2018, **30**, 93-102.

8. Appendix

8.1 ^{1}H and ^{13}C{^{1}H} NMR Spectra

8.1.1 Spectra of compounds discussed in Chapter 2

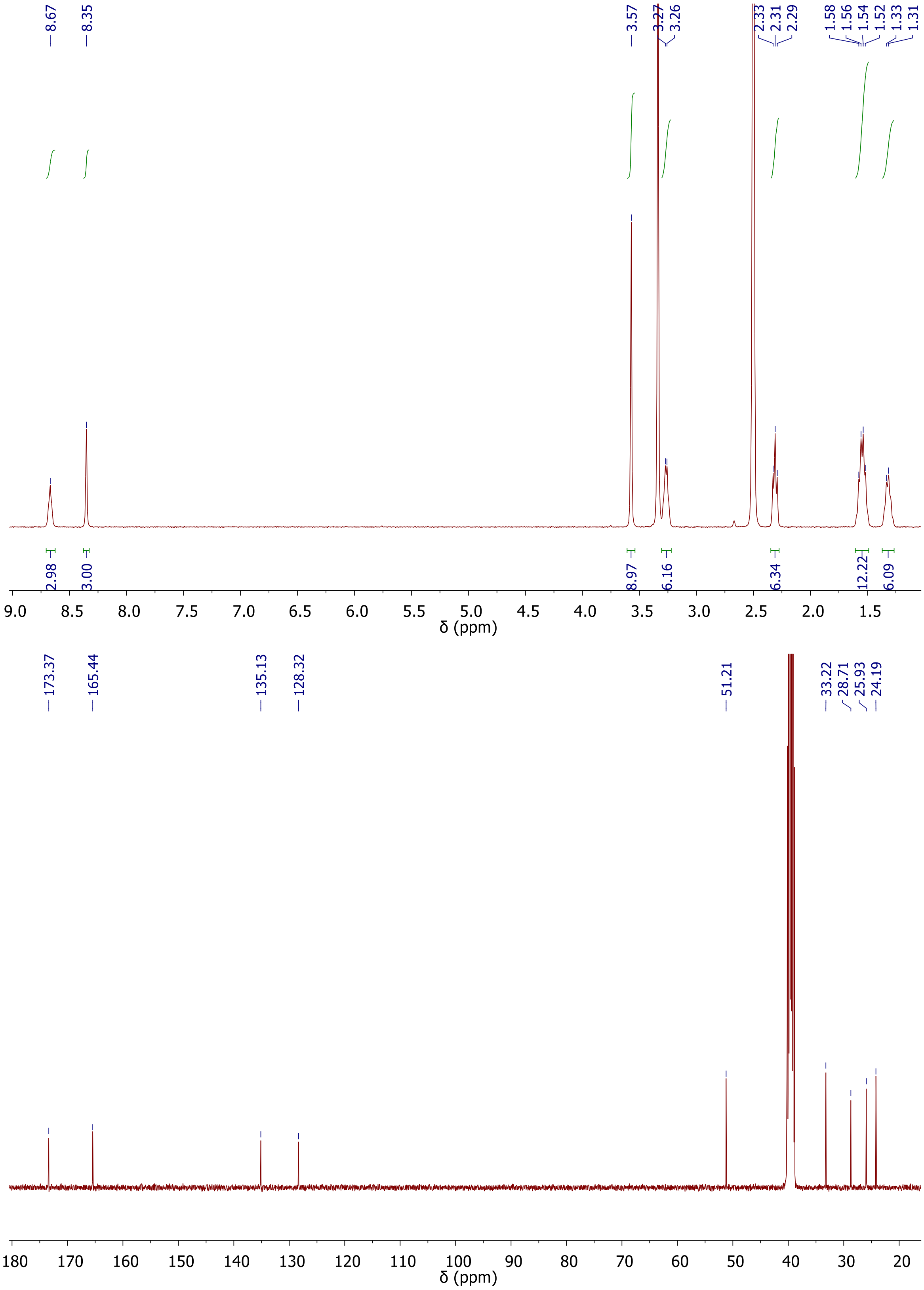

Figure 8.1 ^{1}H NMR (600 MHz, DMSO-d_6) and ^{13}C{^{1}H} NMR (150 MHz, DMSO-d_6) spectra of **58**.

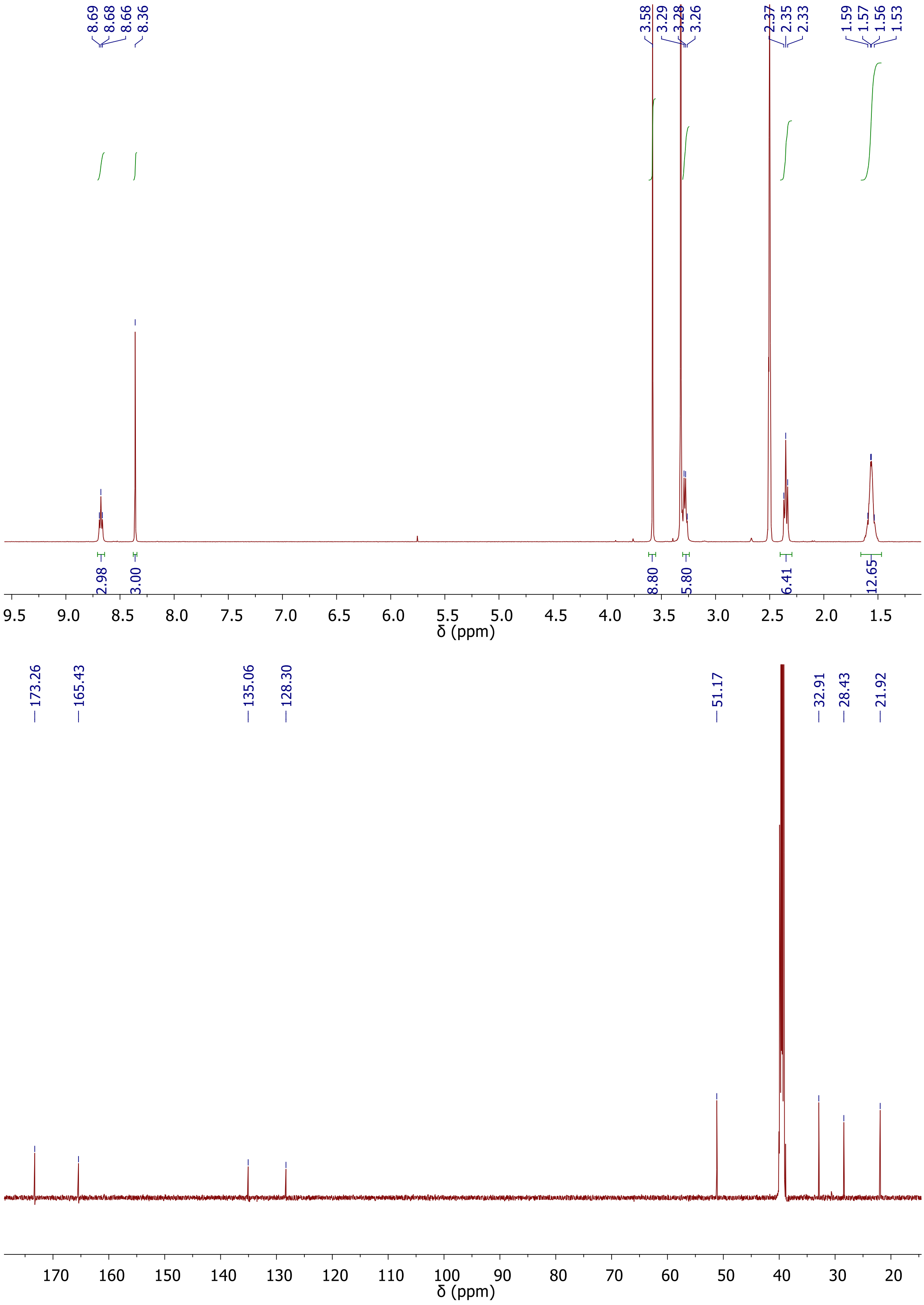

Figure 8.2 ^{1}H NMR (600 MHz, DMSO-d_6) and ^{13}C{^{1}H} NMR (150 MHz, DMSO-d_6) spectra of **59**.

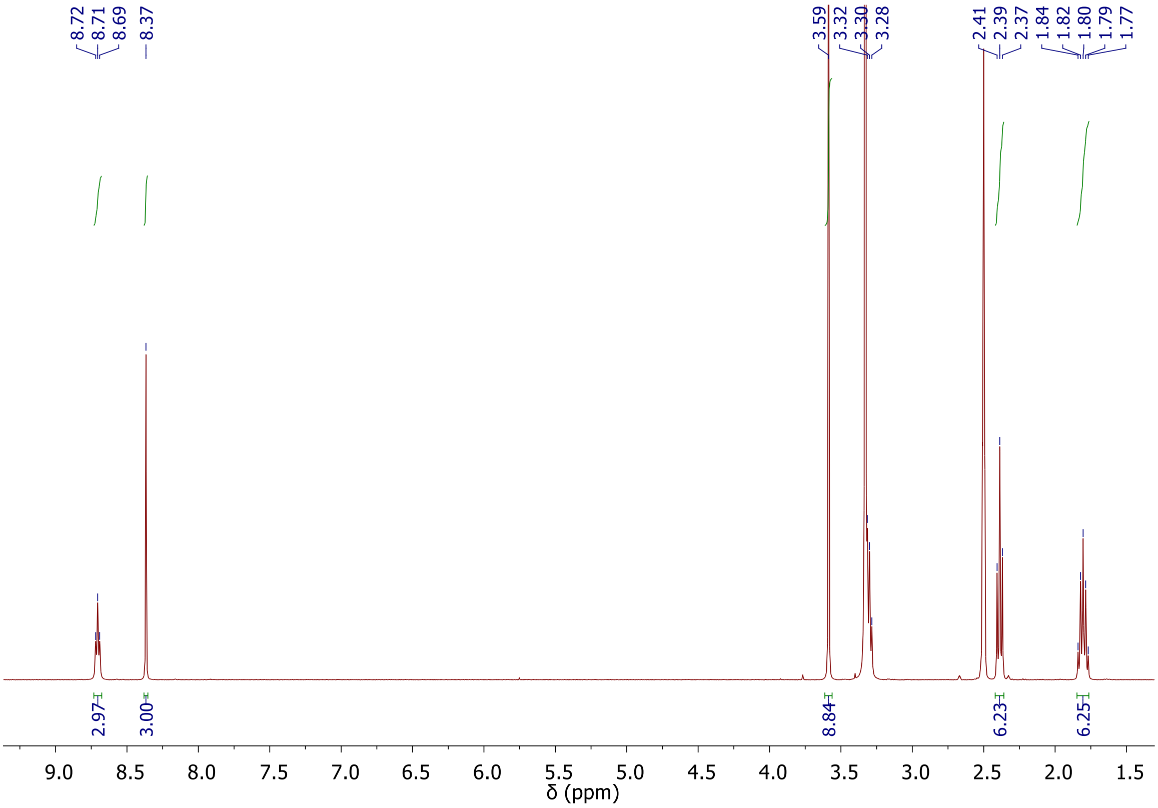

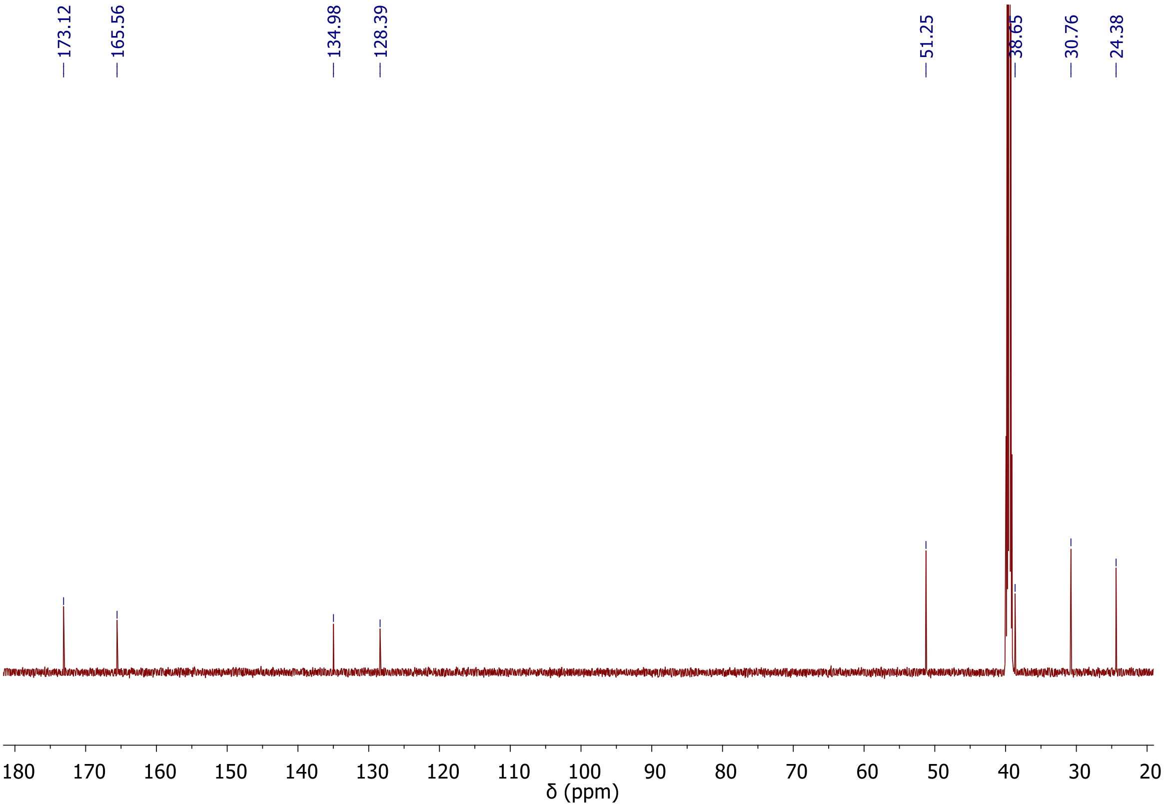

Figure 8.3 ^{1}H NMR (600 MHz, DMSO-d_6) and ^{13}C{^{1}H} NMR (150 MHz, DMSO-d_6) spectra of **60**.

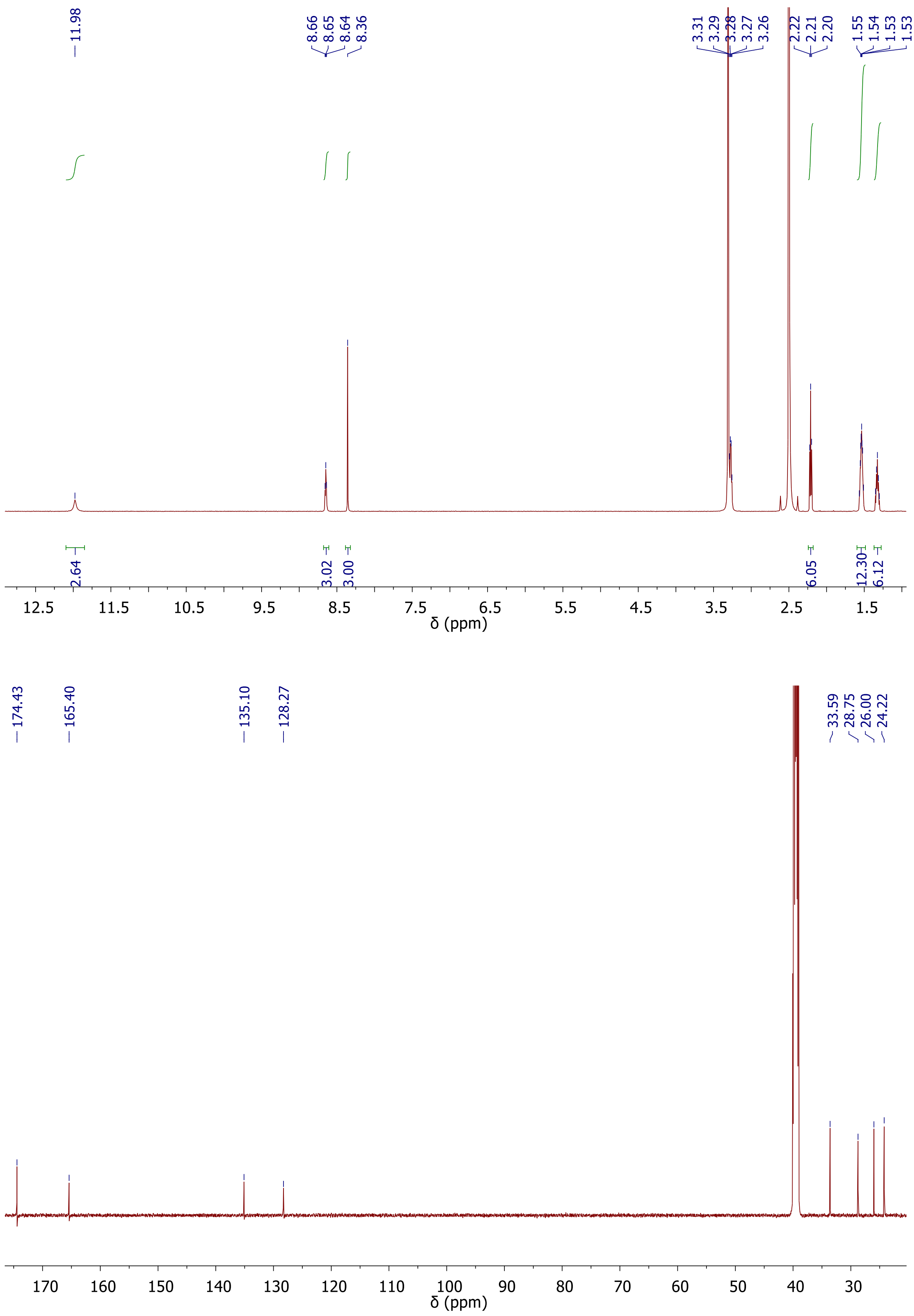

Figure 8.4 ^{1}H NMR (600 MHz, DMSO-d_6) and ^{13}C{^{1}H} NMR (150 MHz, DMSO-d_6) spectra of **61**.

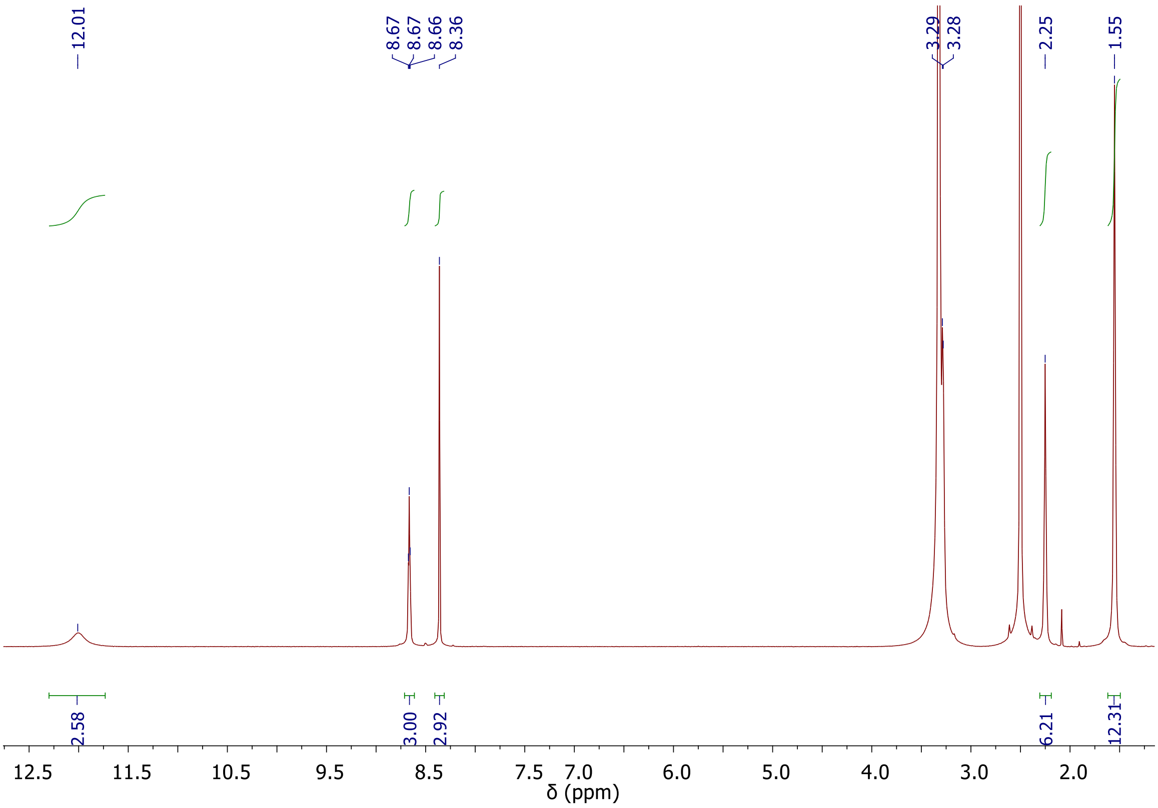

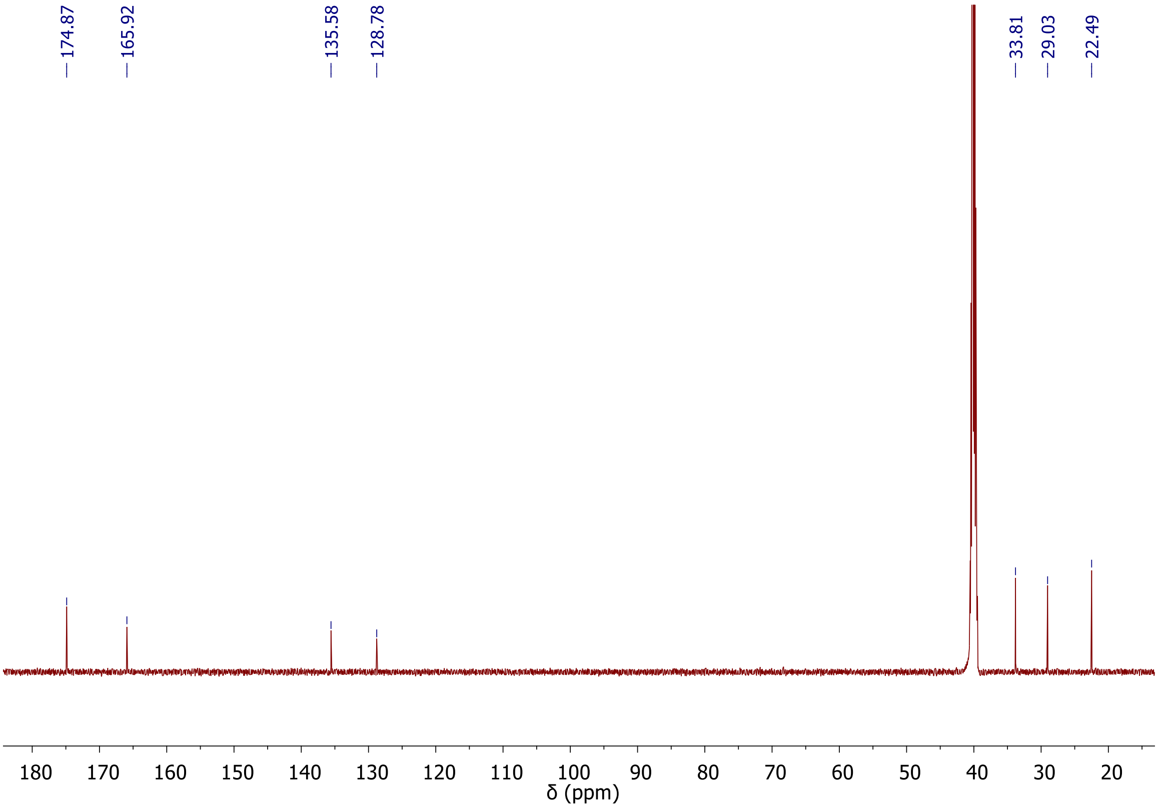

Figure 8.5 ^{1}H NMR (600 MHz, DMSO-d_6) and ^{13}C{^{1}H} NMR (150 MHz, DMSO-d_6) spectra of **62**.

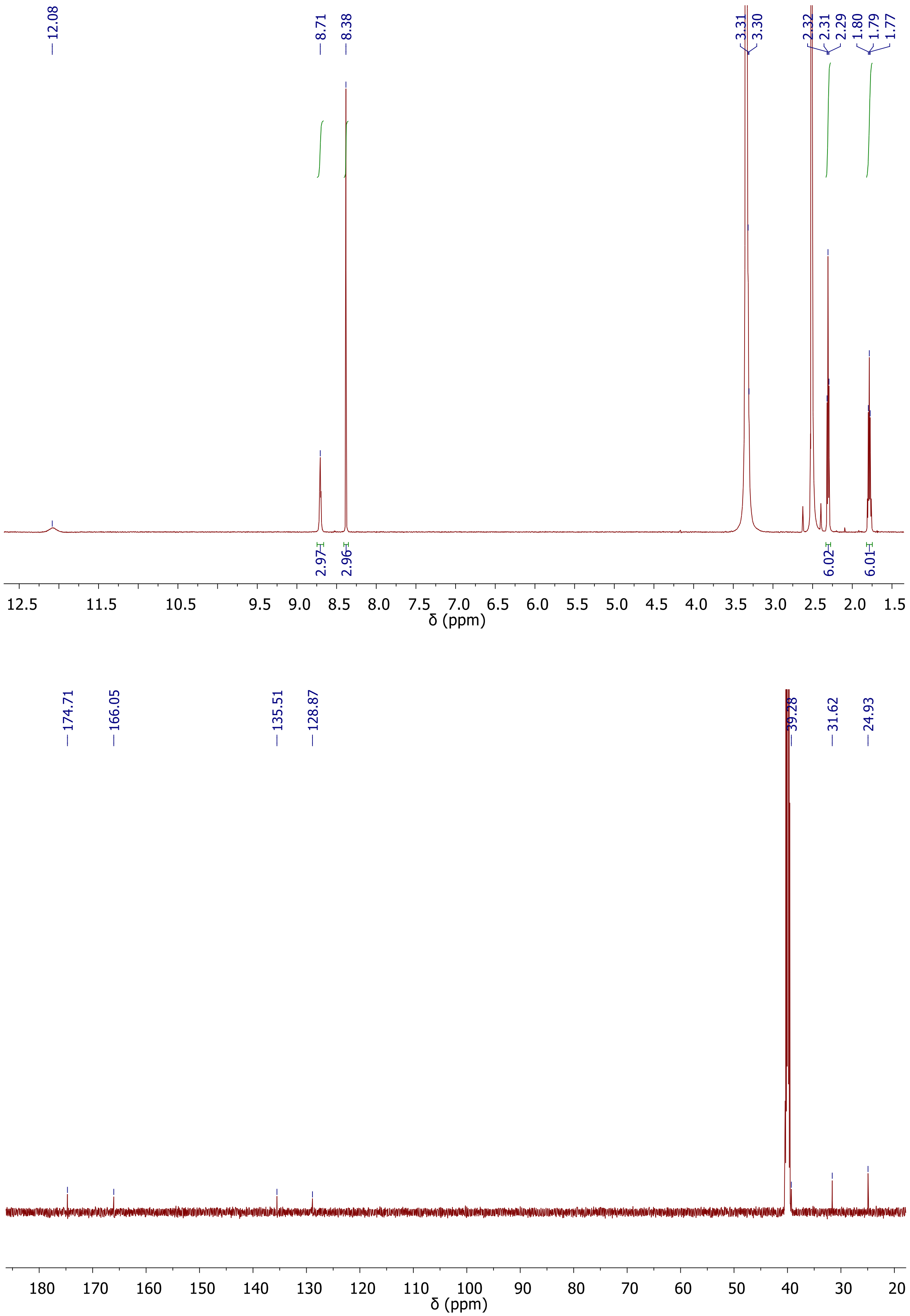

Figure 8.6 ^{1}H NMR (600 MHz, DMSO-d_6) and ^{13}C{^{1}H} NMR (150 MHz, DMSO-d_6) spectra of **63**.

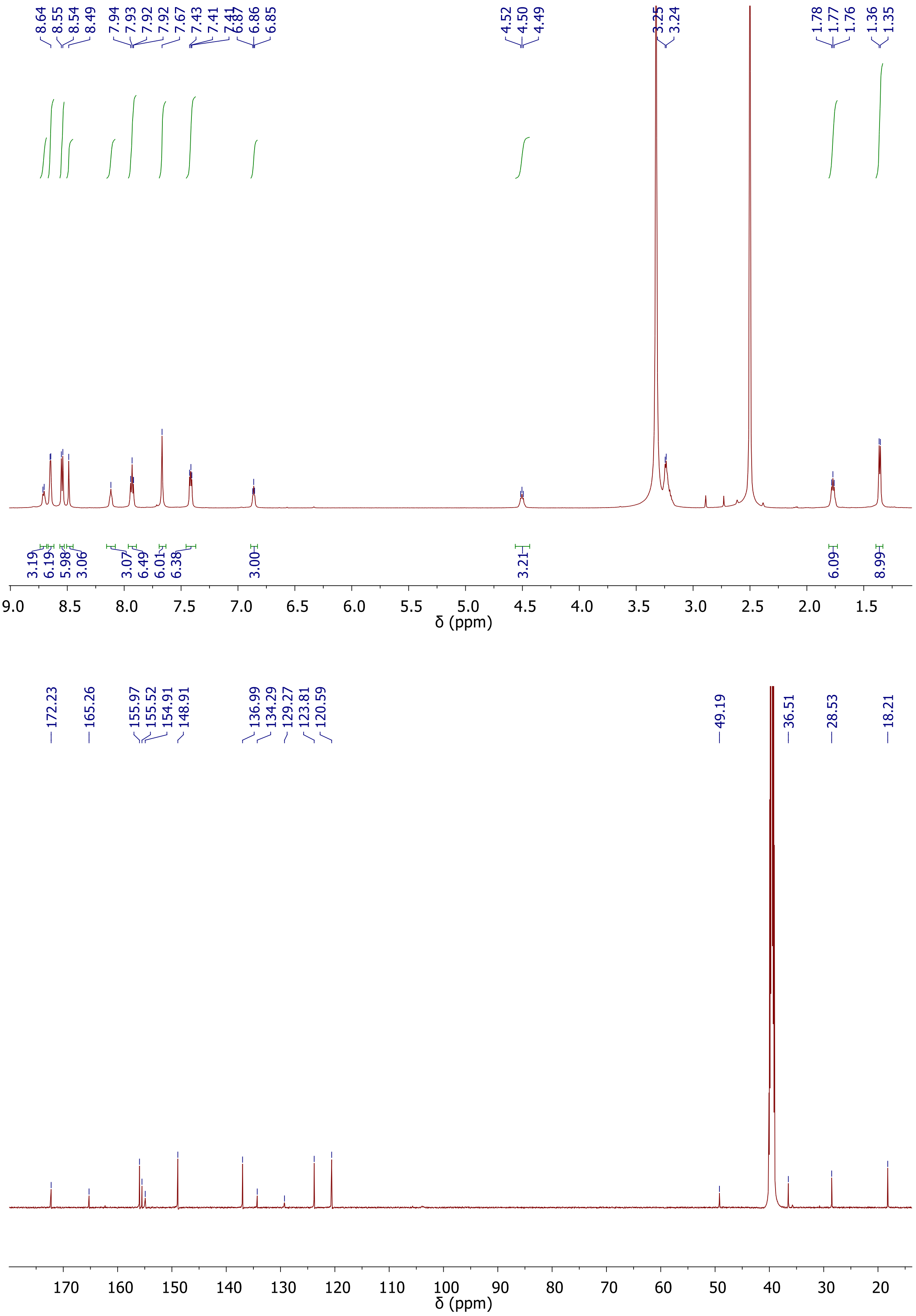

Figure 8.7 ^{1}H NMR (400 MHz, DMSO-d_6) and ^{13}C{^{1}H} NMR (150 MHz, DMSO-d_6) spectra of **66**.

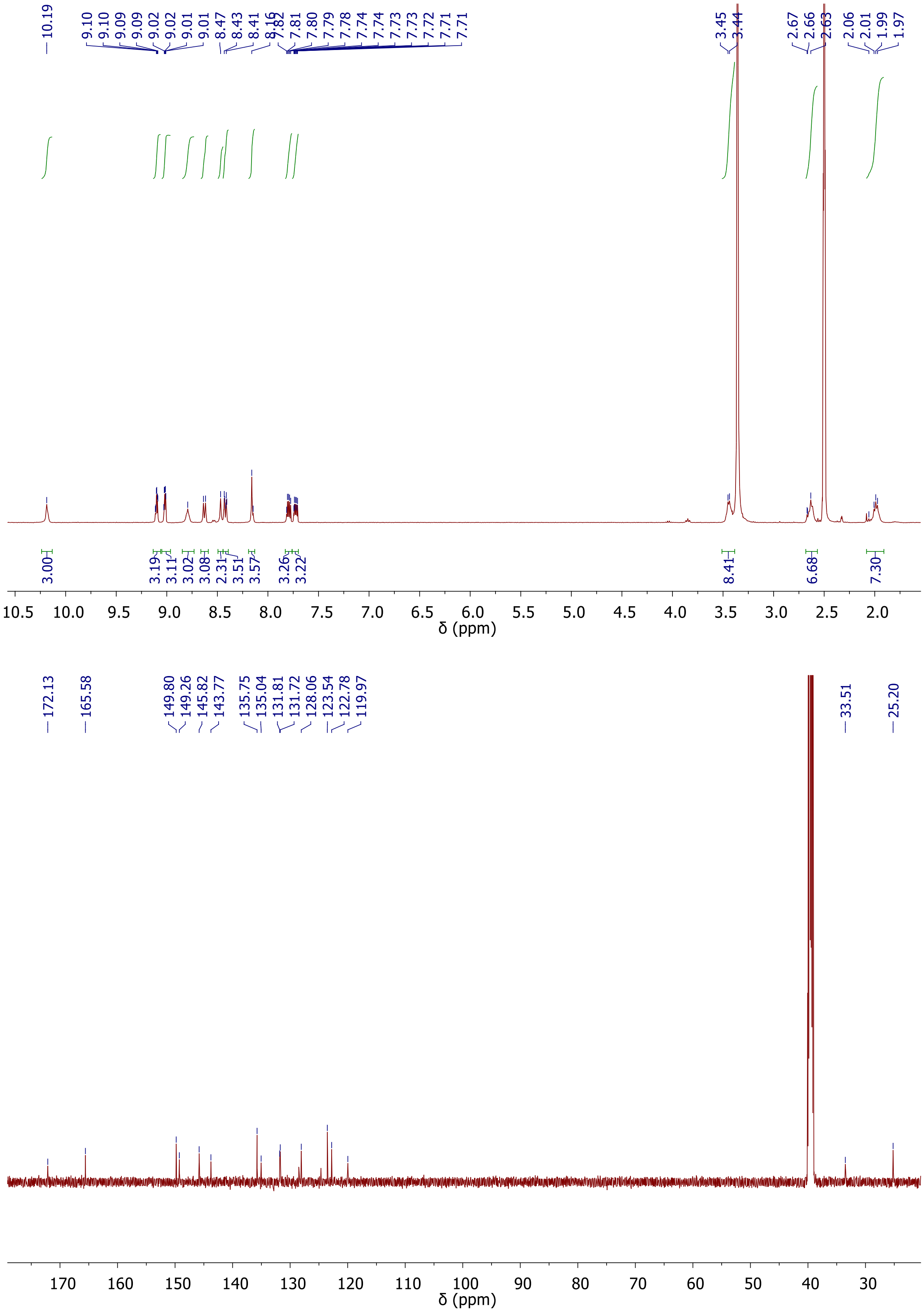

Figure 8.8 ^{1}H NMR (400 MHz, DMSO-d_6) and ^{13}C{^{1}H} NMR (150 MHz, DMSO-d_6) spectra of **68**.

8.1.2 Spectra of compounds discussed in Chapter 3

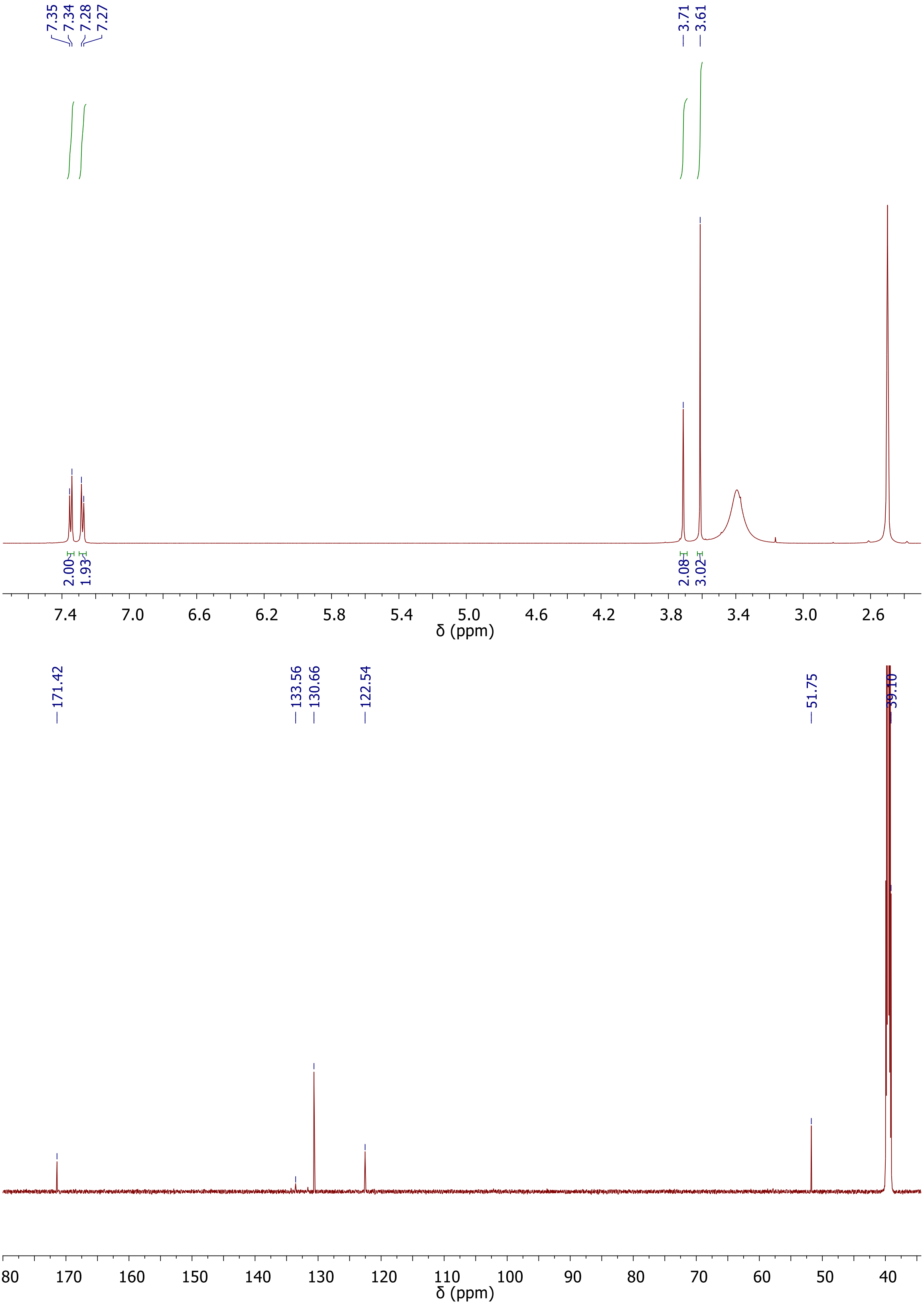

Figure 8.9 ^{1}H NMR (600 MHz, DMSO-d_6) and $^{13}C\{^{1}H\}$ NMR (150 MHz, DMSO-d_6) spectra of **67**.

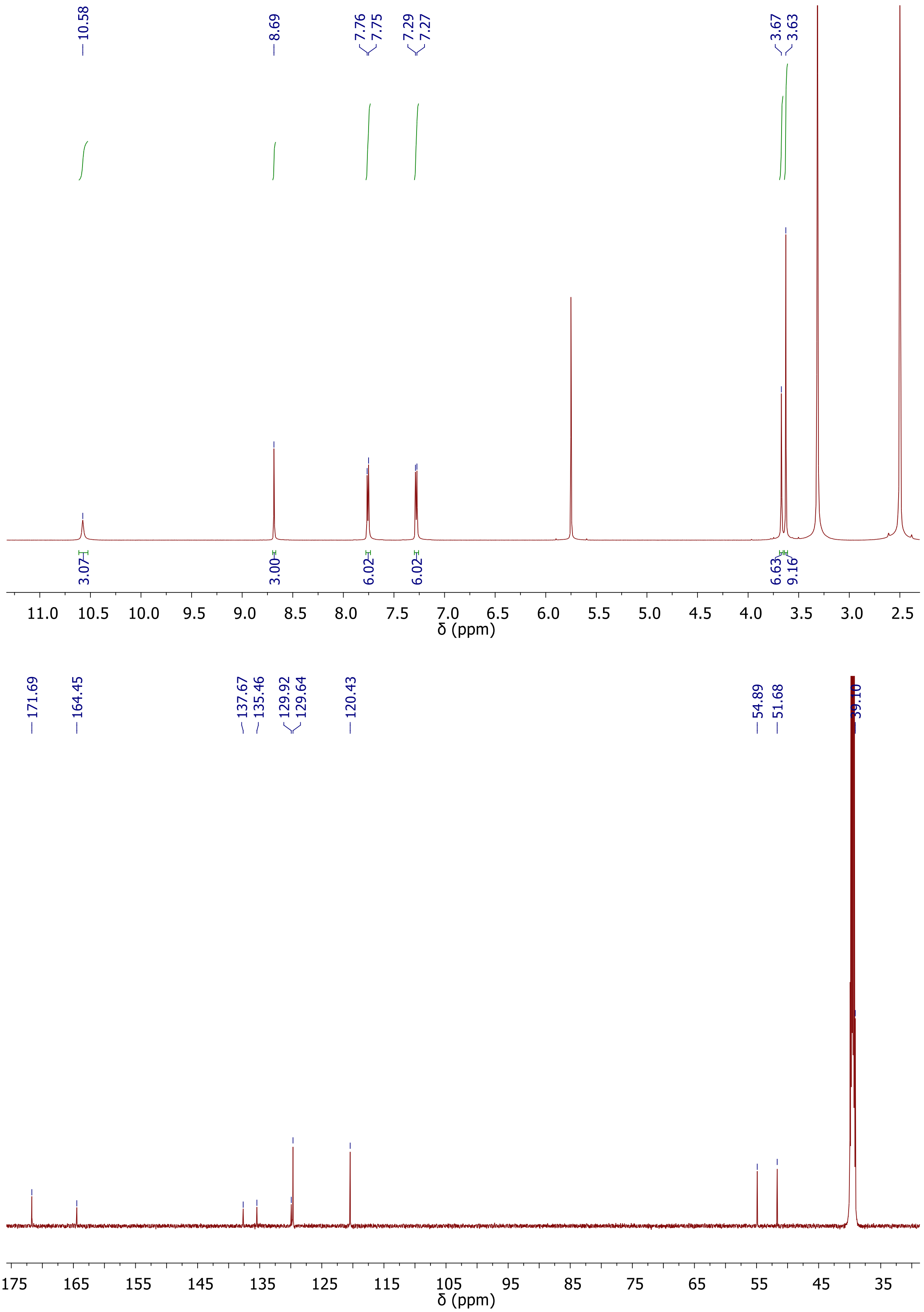

Figure 8.10 ^{1}H NMR (600 MHz, DMSO-d_6) and ^{13}C{^{1}H} NMR (150 MHz, DMSO-d_6) spectra of **69**.

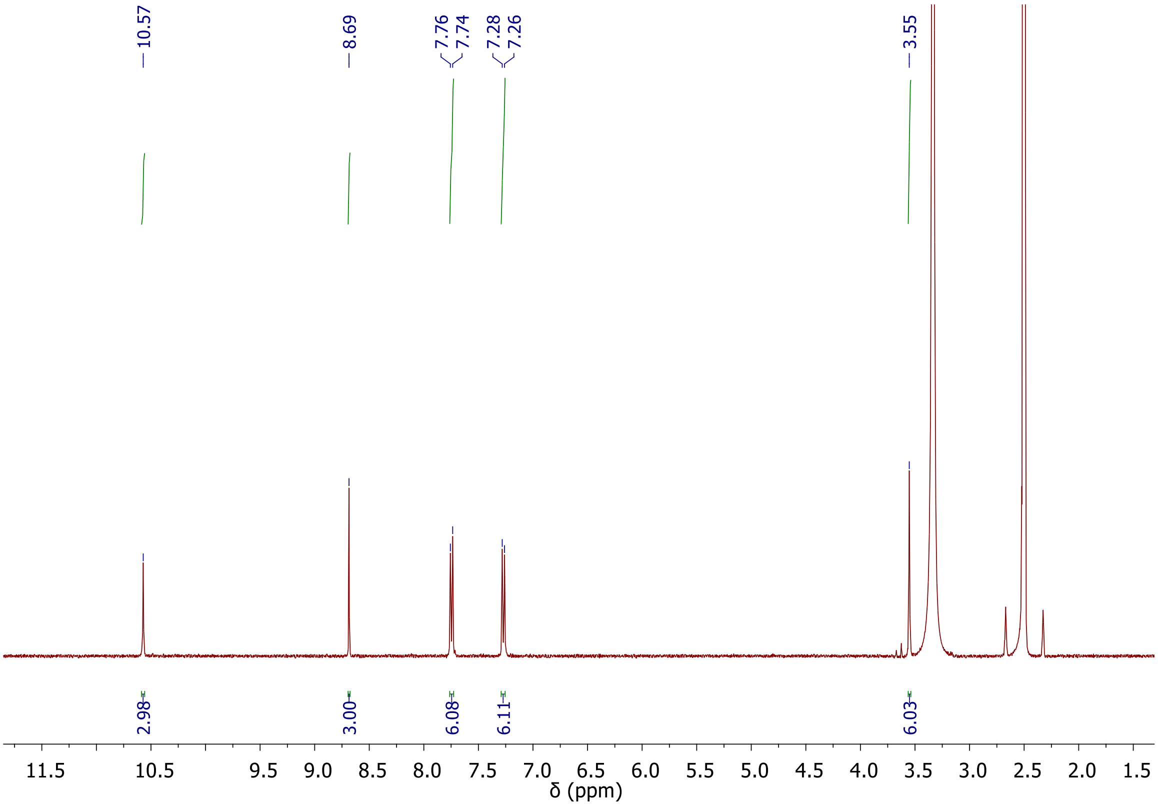

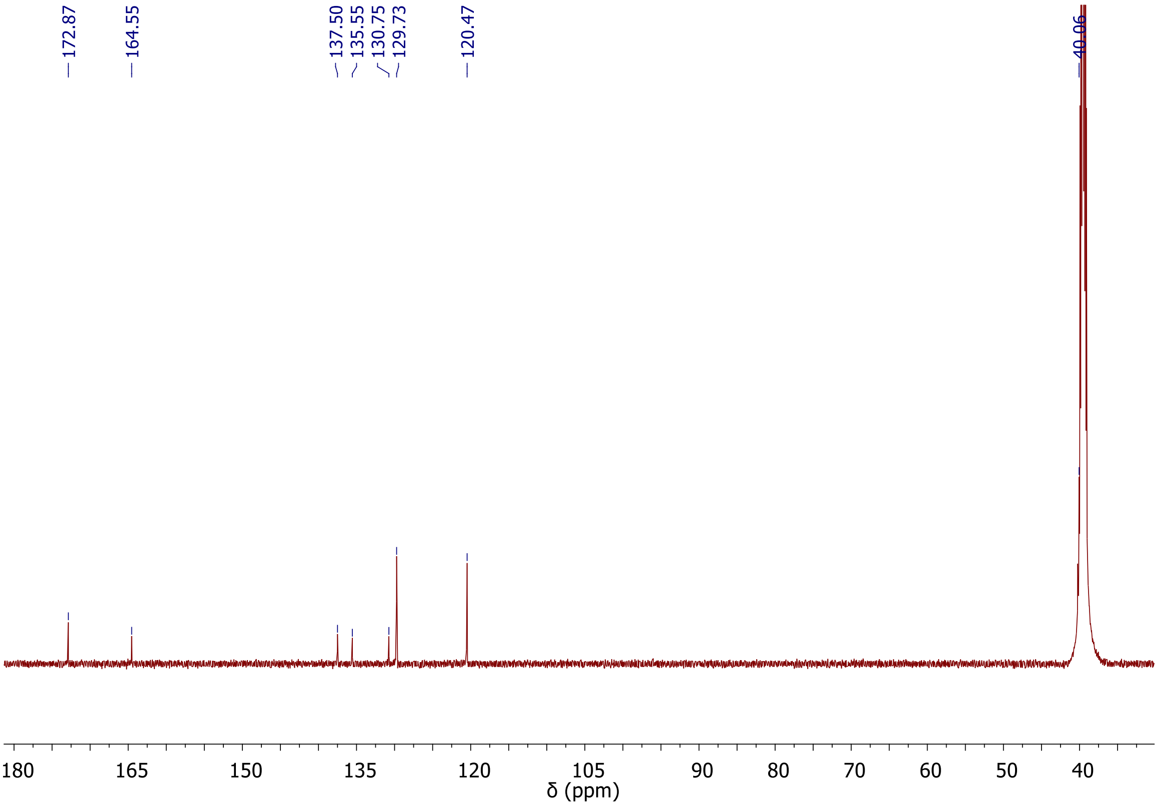

Figure 8.11 ^{1}H NMR (600 MHz, DMSO-d_6) and ^{13}C{^{1}H} NMR (150 MHz, DMSO-d_6) spectra of **64**.

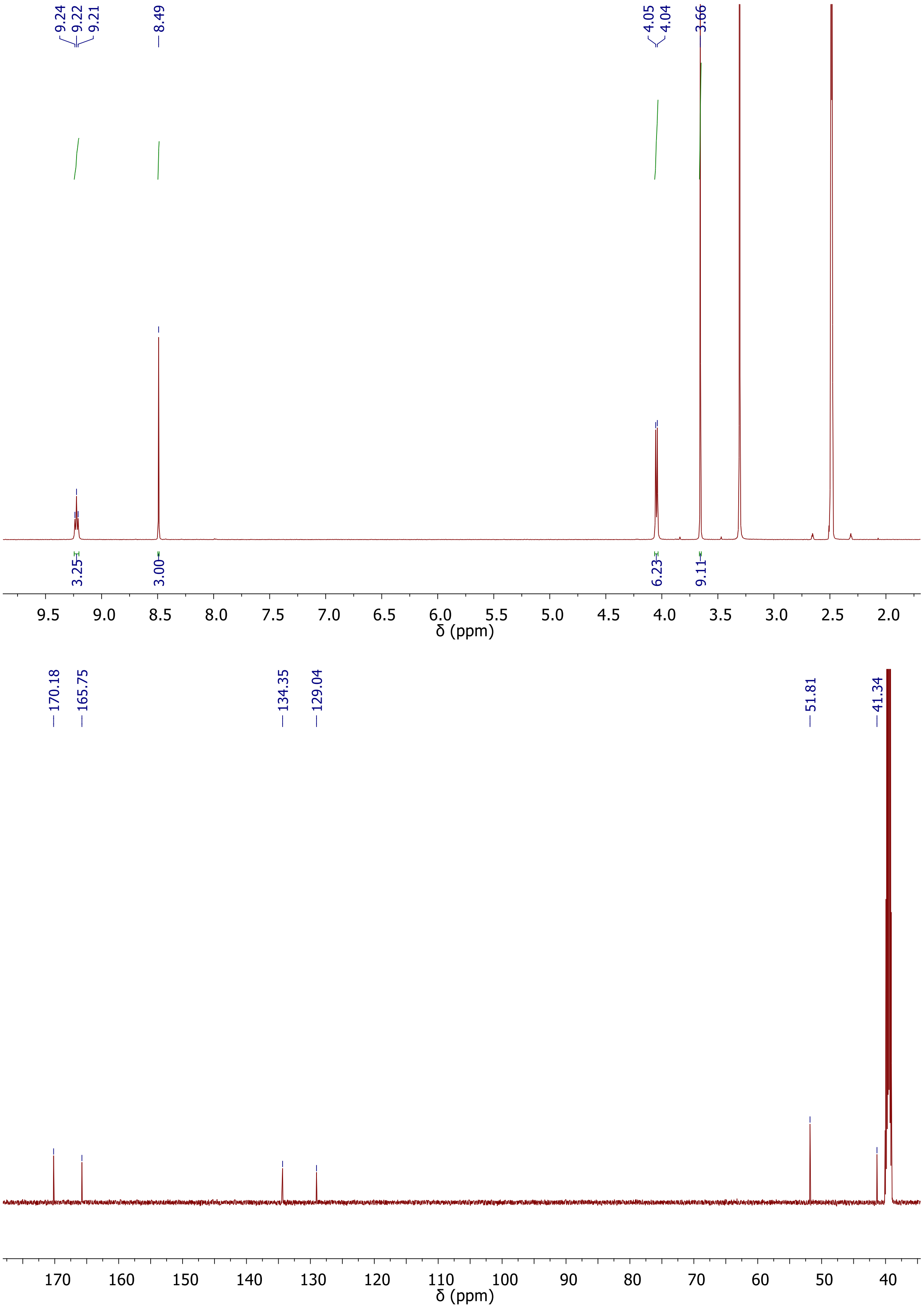

Figure 8.12 ^{1}H NMR (400 MHz, DMSO-d_6) and ^{13}C{^{1}H} NMR (100 MHz, DMSO-d_6) spectra of **65**.

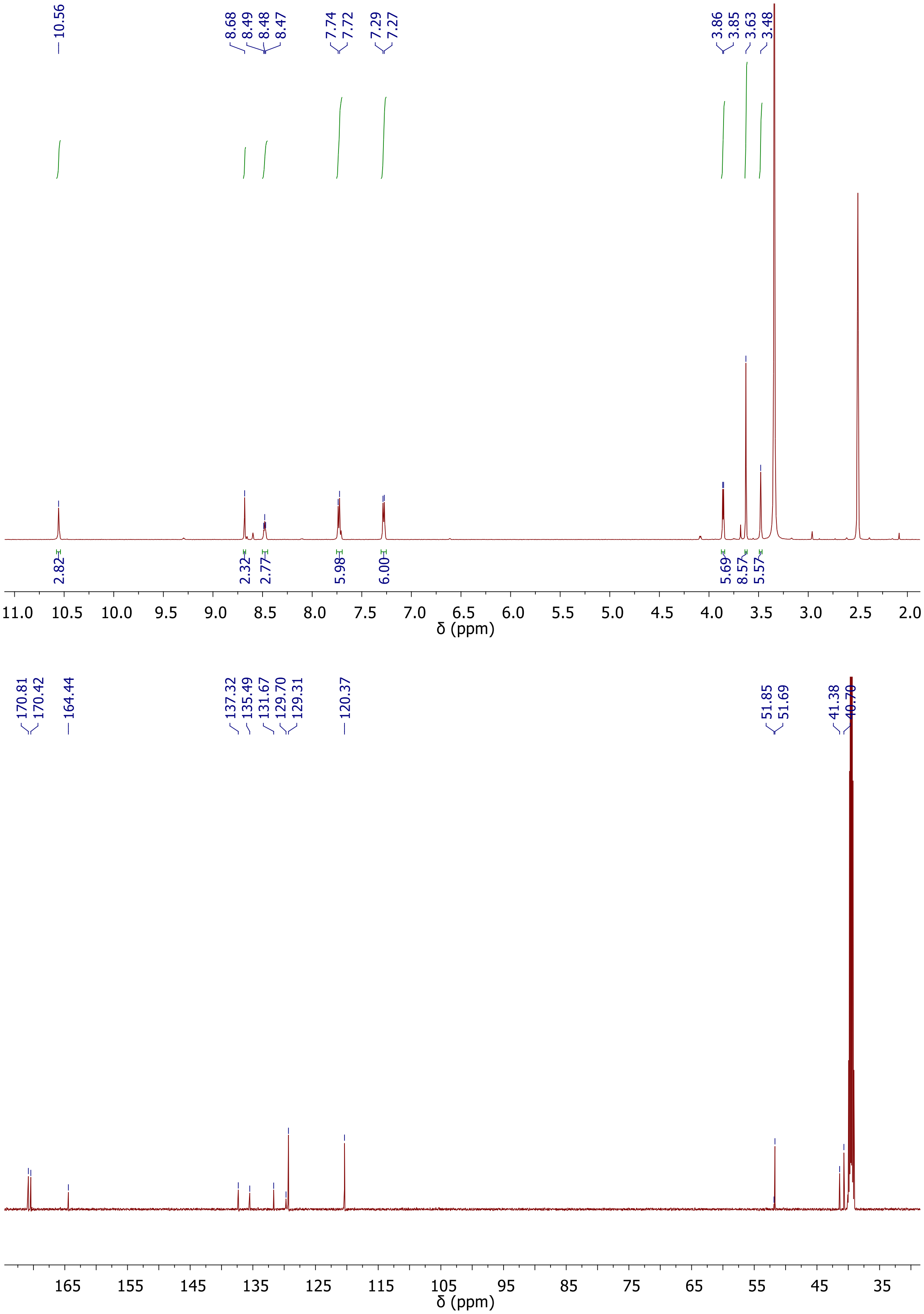

Figure 8.13 ^{1}H NMR (400 MHz, DMSO-*d*$_{6}$) and ^{13}C{^{1}H} NMR (150 MHz, DMSO-*d*$_{6}$) spectra of **72**.

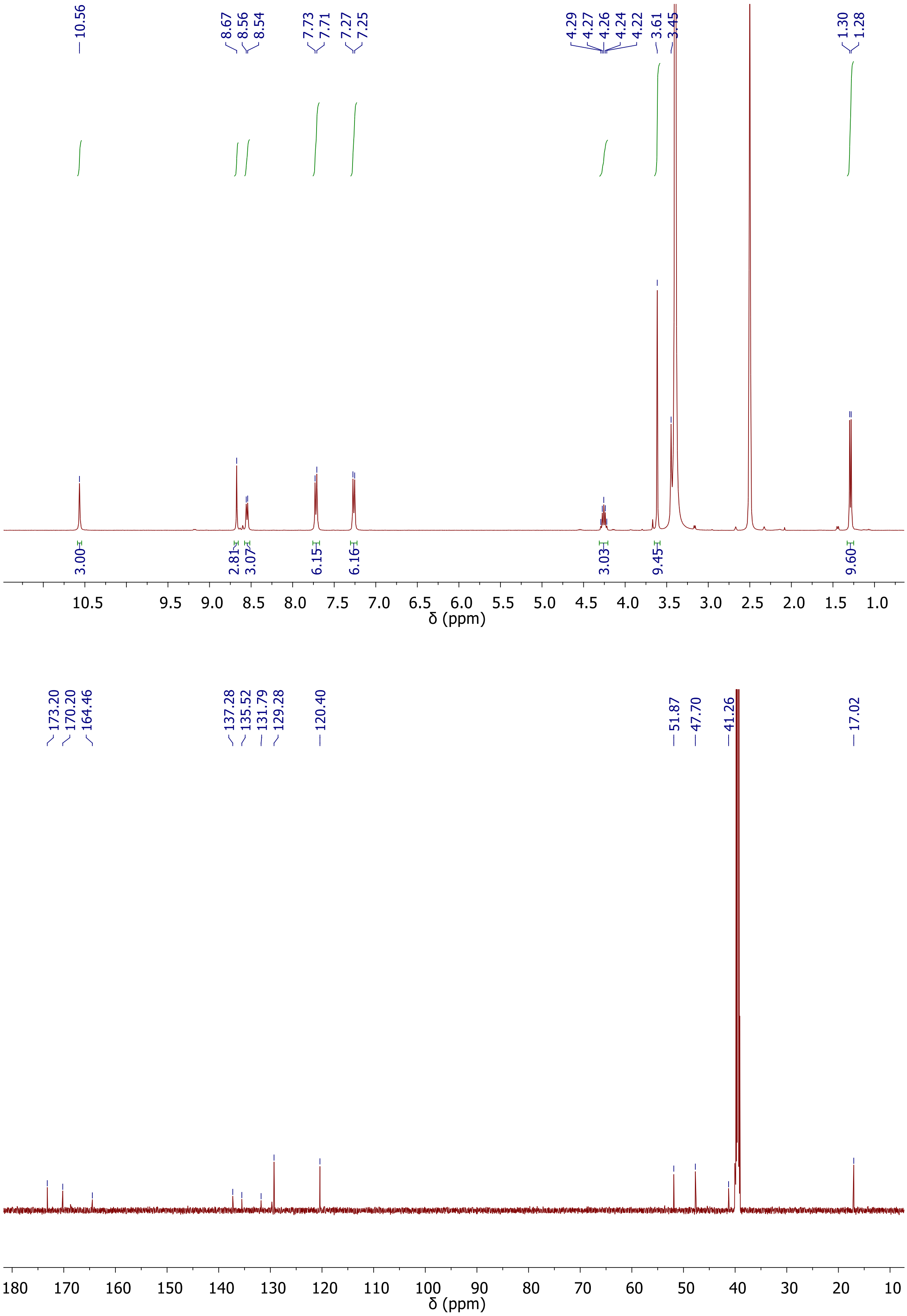

Figure 8.14 ^{1}H NMR (400 MHz, DMSO-d_6) and ^{13}C{^{1}H} NMR (150 MHz, DMSO-d_6) spectra of **70**.

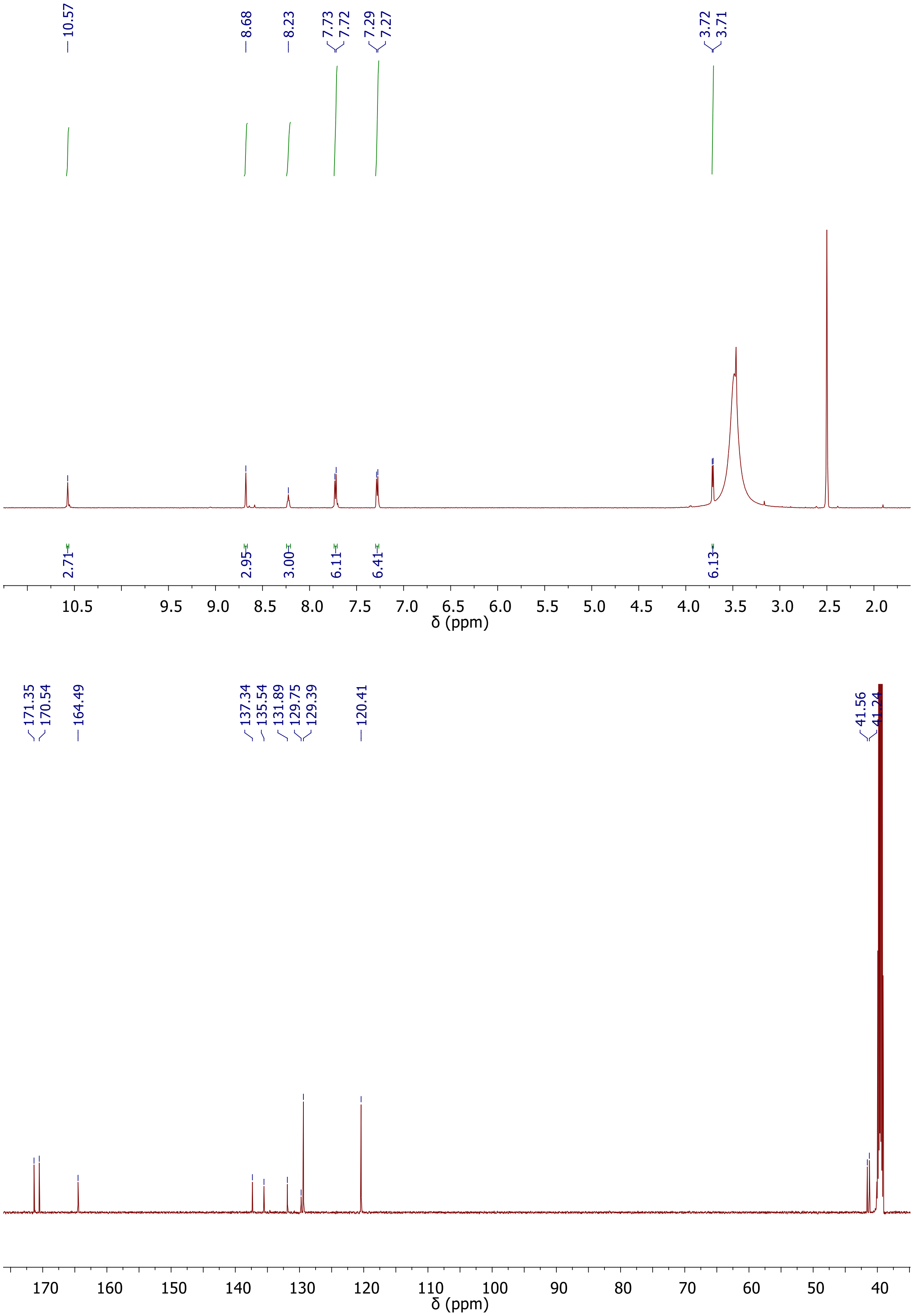

Figure 8.15 ^{1}H NMR (600 MHz, DMSO-d_6) and ^{13}C{^{1}H} NMR (150 MHz, DMSO-d_6) spectra of **73**.

8.1.3 Spectra of compounds discussed in Chapter 4

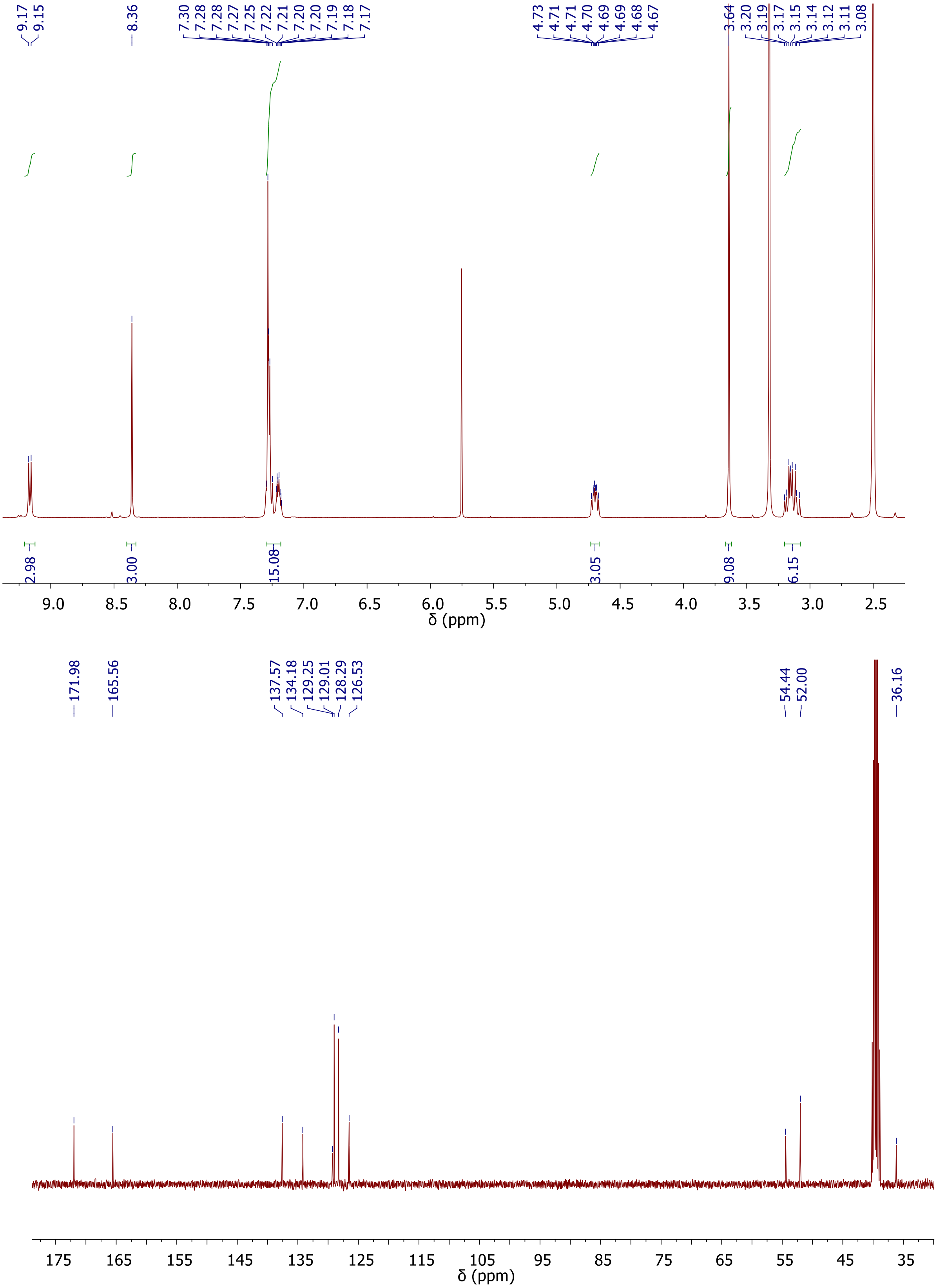

Figure 8.16 ^{1}H NMR (400 MHz, DMSO-*d*$_6$) and ^{13}C{^{1}H} NMR (100 MHz, DMSO-*d*$_6$) spectra of **74b**.

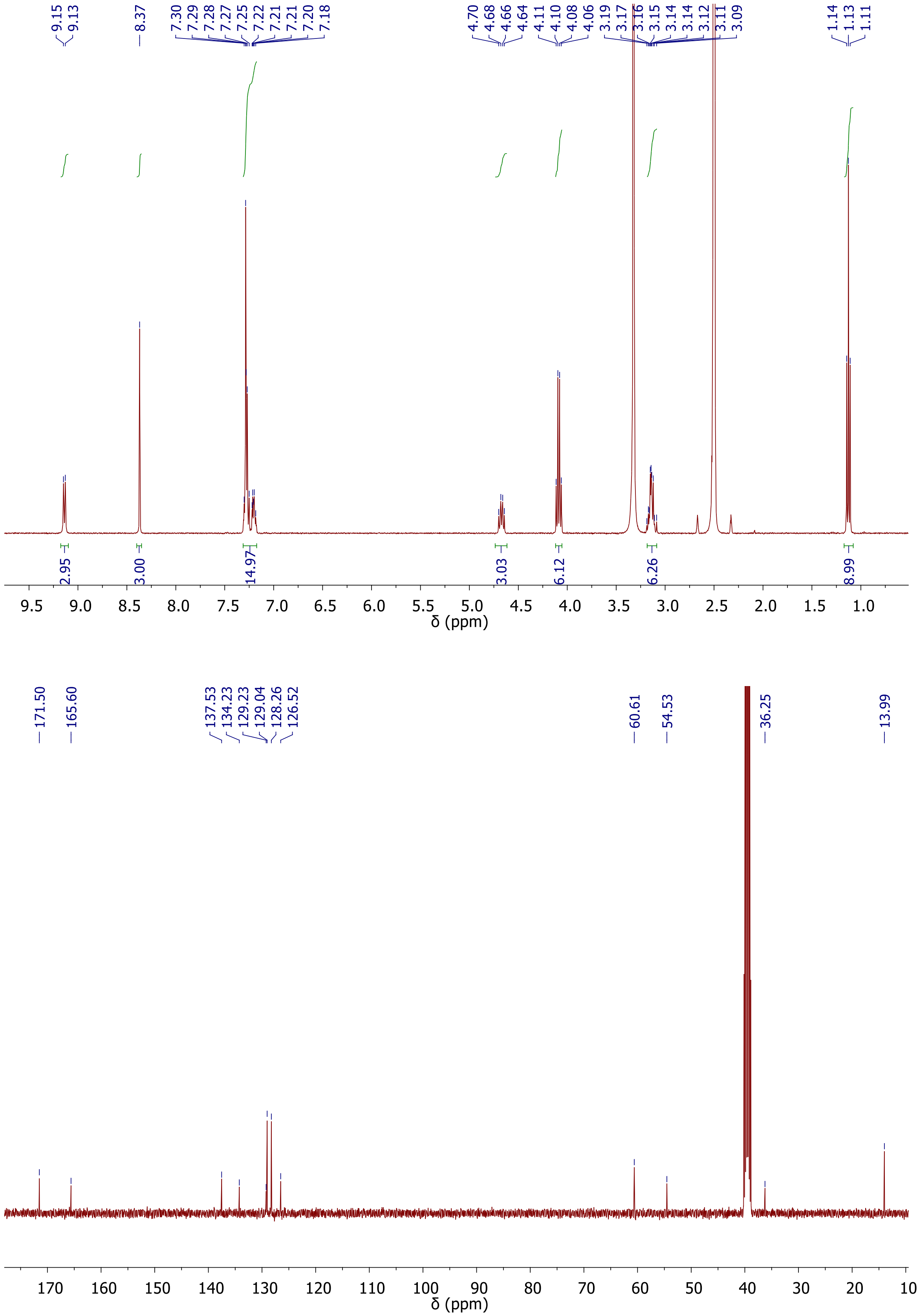

Figure 8.17 ^{1}H NMR (400 MHz, DMSO-d_6) and ^{13}C{^{1}H} NMR (100 MHz, DMSO-d_6) spectra of **74a**.

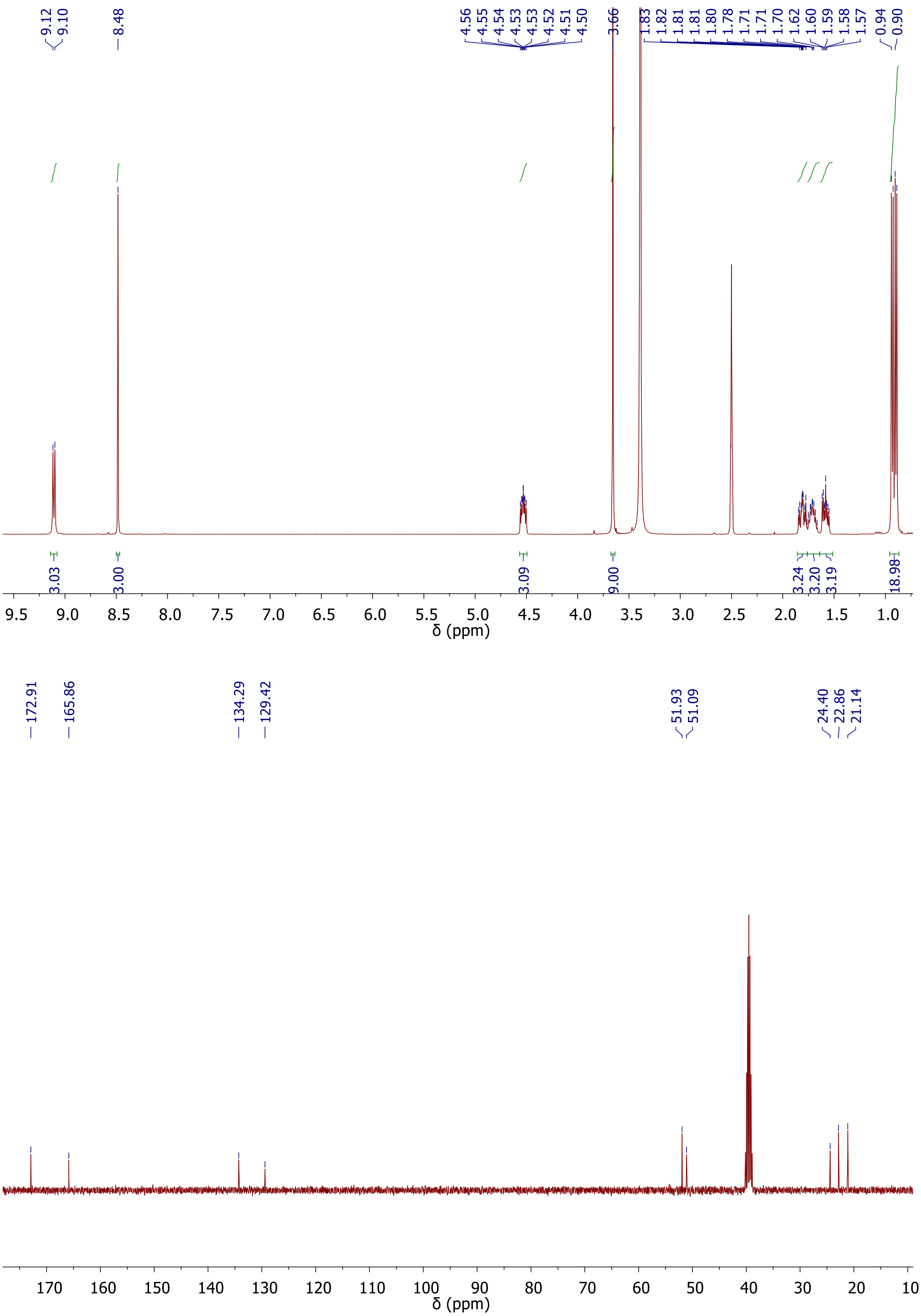

Figure 8.18 ^{1}H NMR (400 MHz, DMSO-d_6) and ^{13}C{^{1}H} NMR (100 MHz, DMSO-d_6) spectra of **114**.

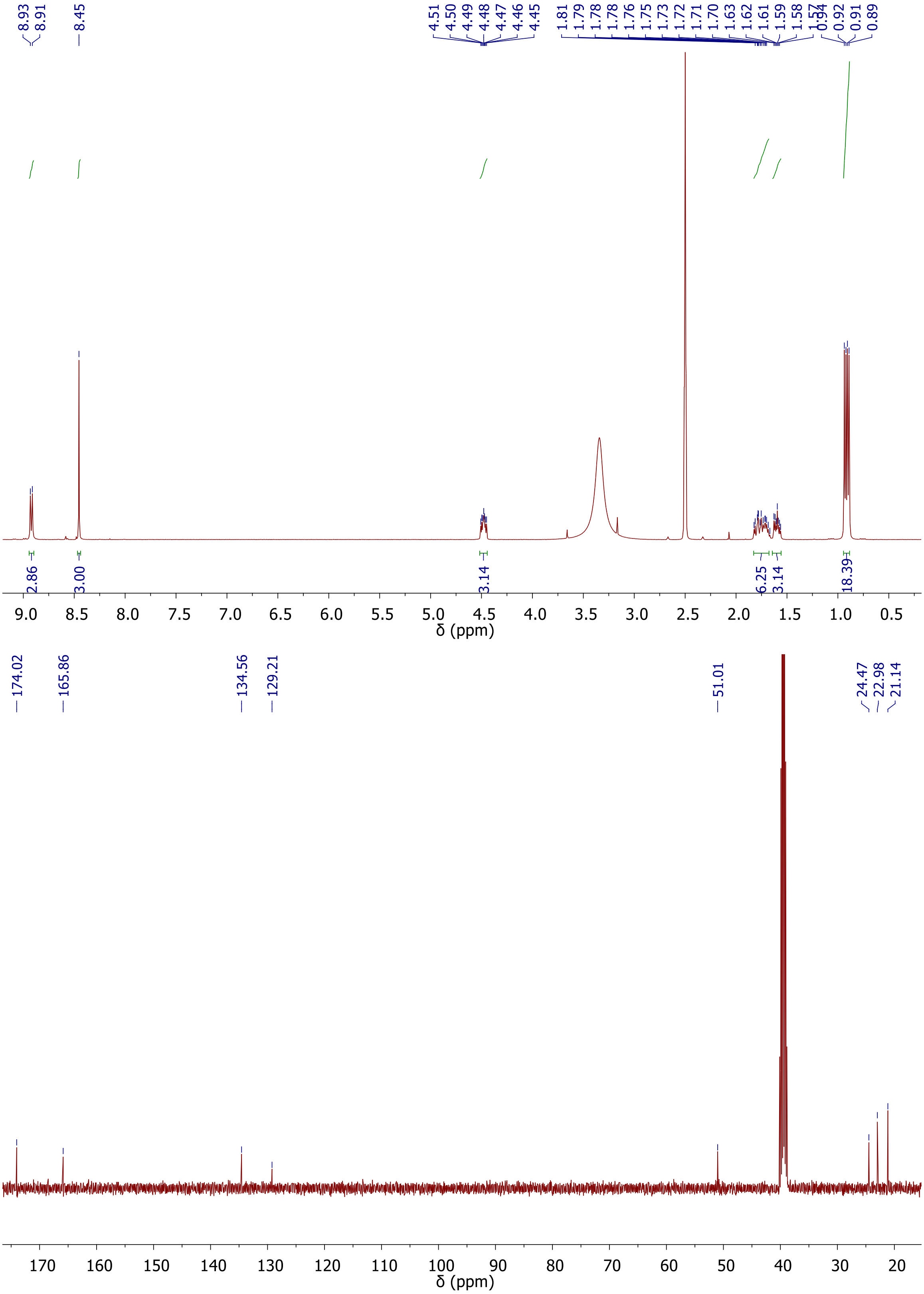

Figure 8.19 ^{1}H NMR (400 MHz, DMSO-d_6) and $^{13}C\{^{1}H\}$ NMR (100 MHz, DMSO-d_6) spectra of **83**.

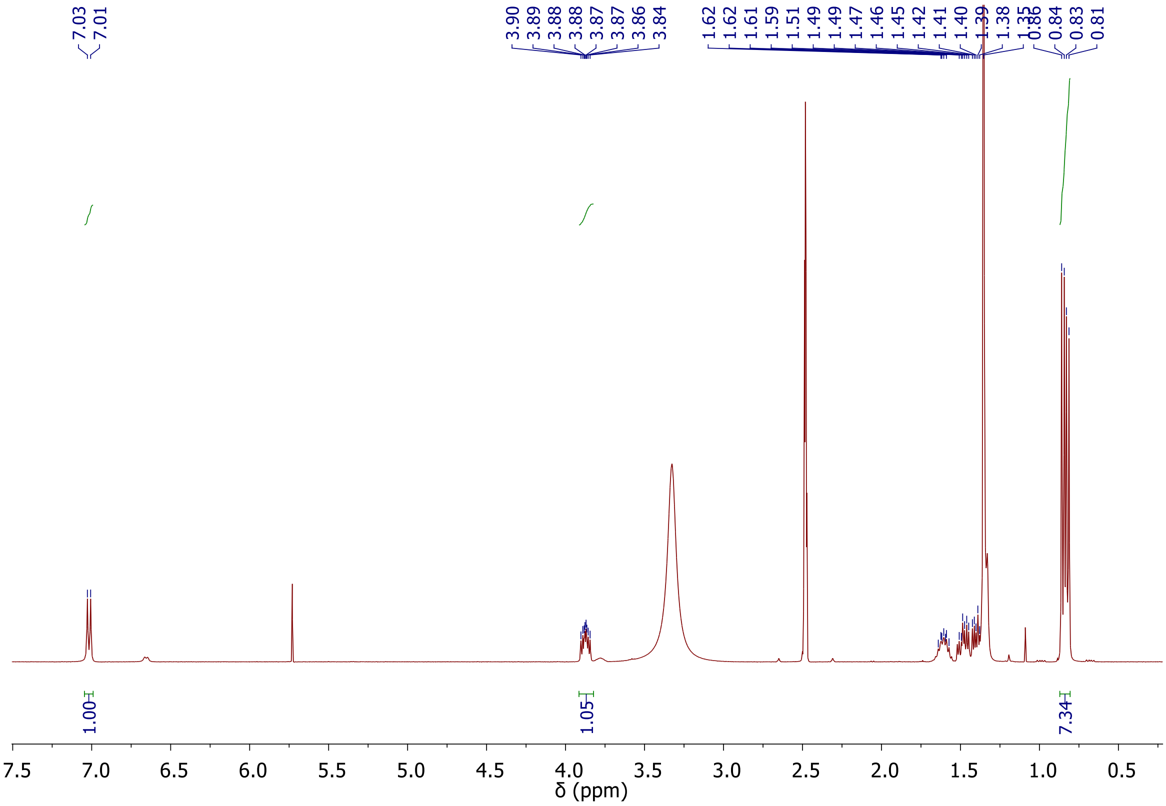

Figure 8.20 ^{1}H NMR (400 MHz, DMSO-d_6) spectrum of **87**.

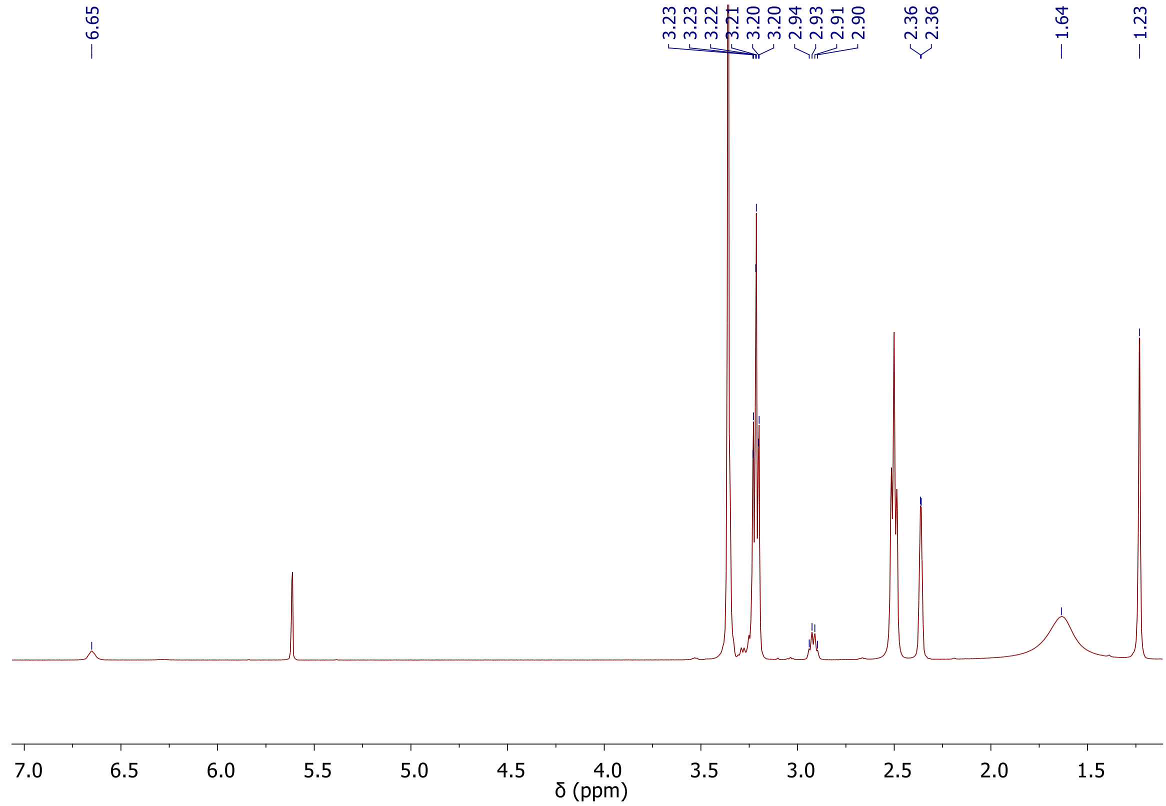

Figure 8.21 ^{1}H NMR (400 MHz, DMSO-d_6) spectrum of **82**.

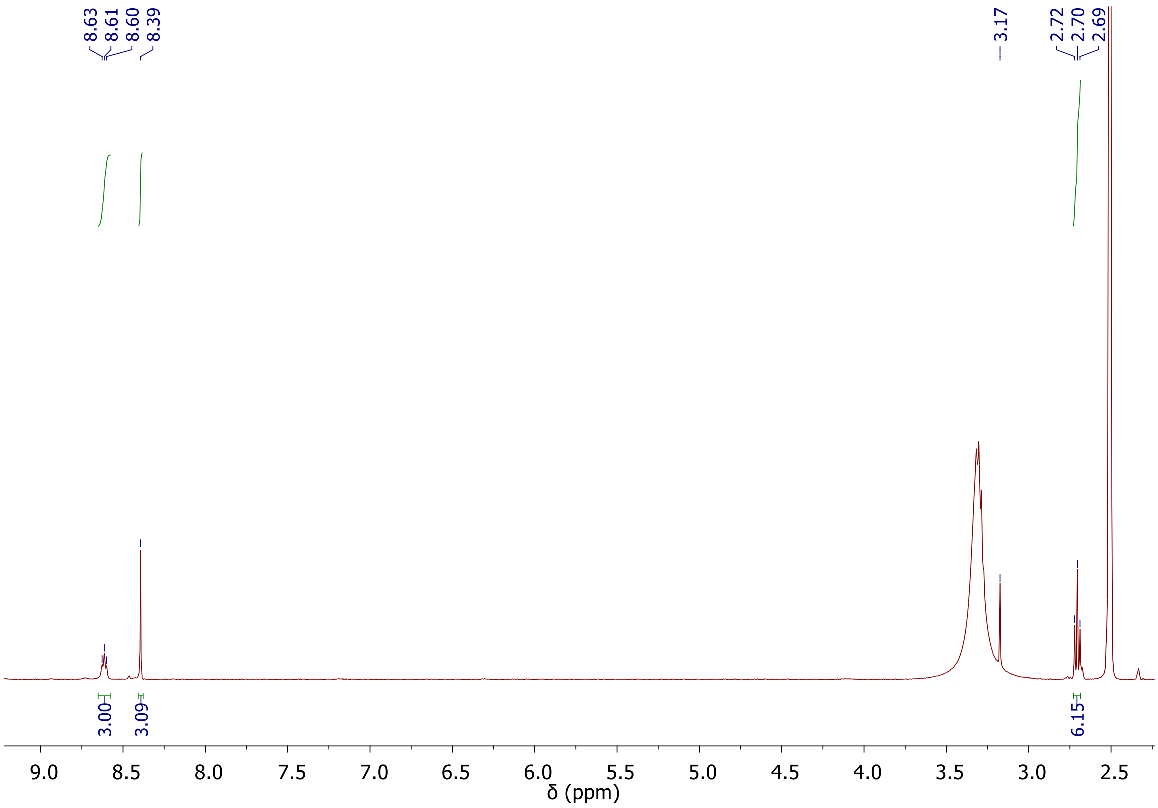

Figure 8.22 ^{1}H NMR (400 MHz, DMSO-d_6) spectrum of **90**.

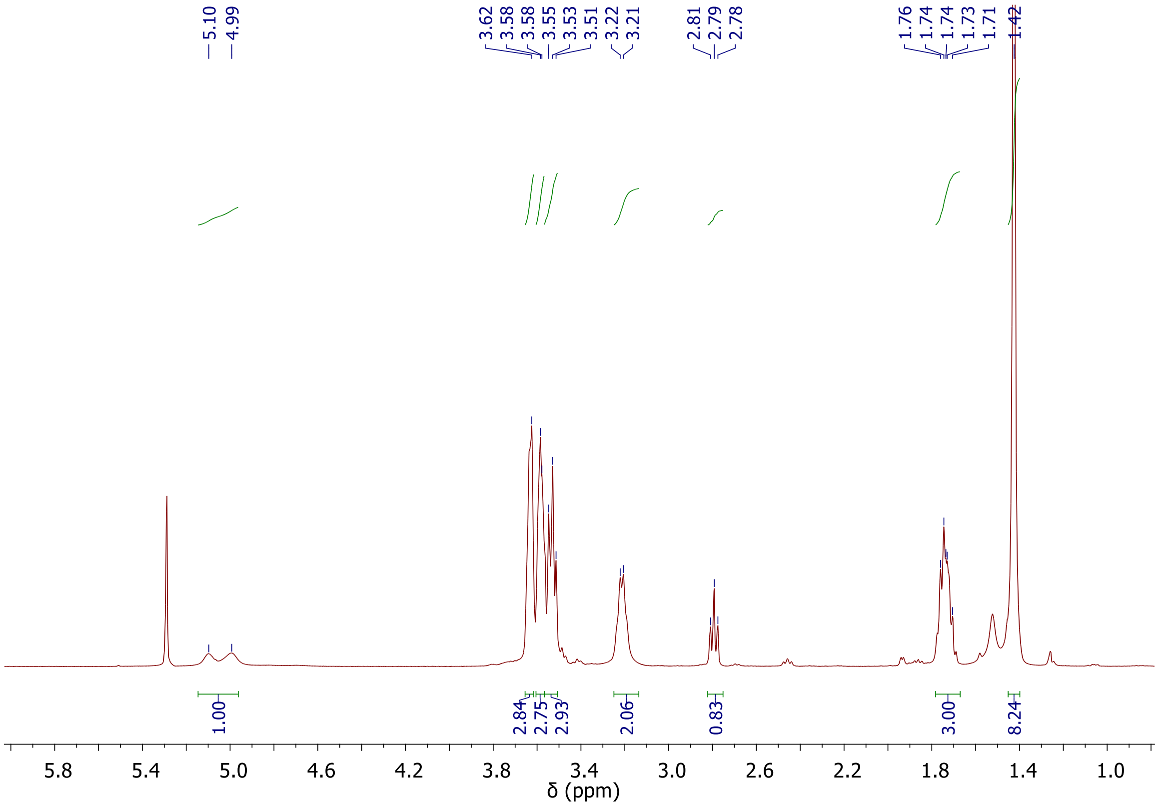

Figure 8.23 ^{1}H NMR (400 MHz, CDCl$_3$) spectrum of **78**.

8.1.5 Spectra of compounds discussed in Chapter 5

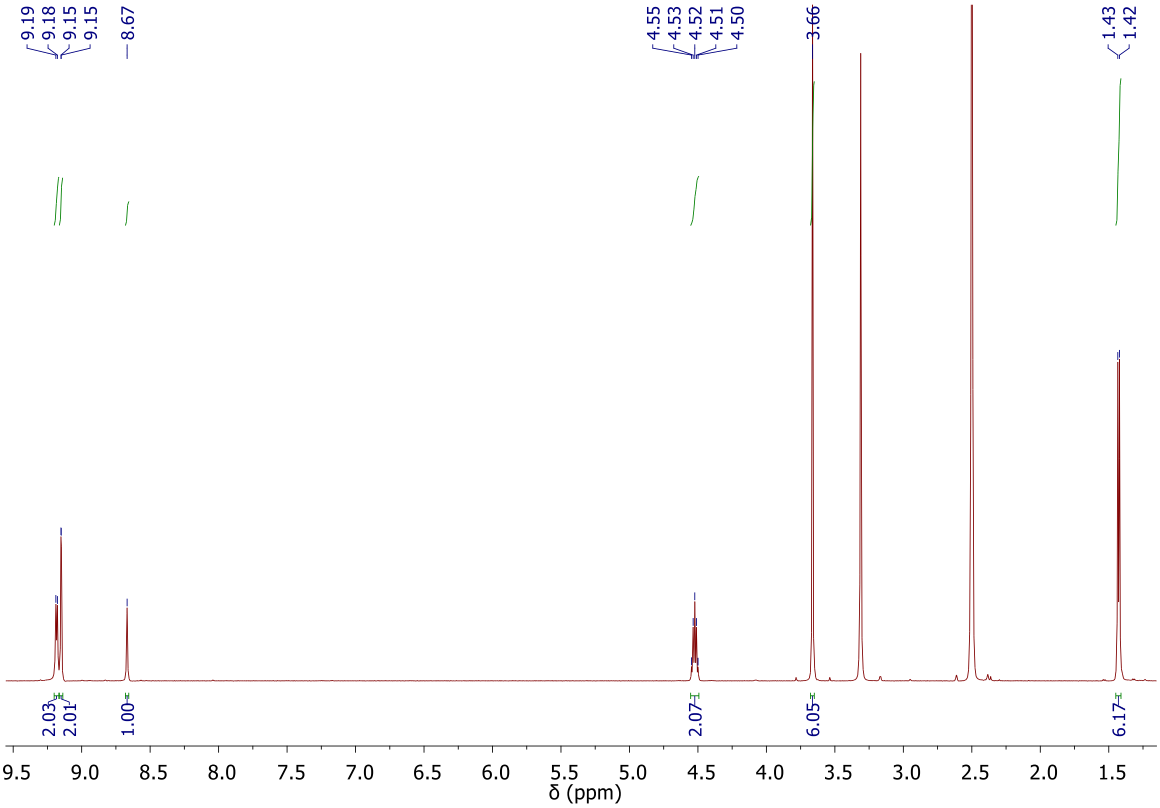

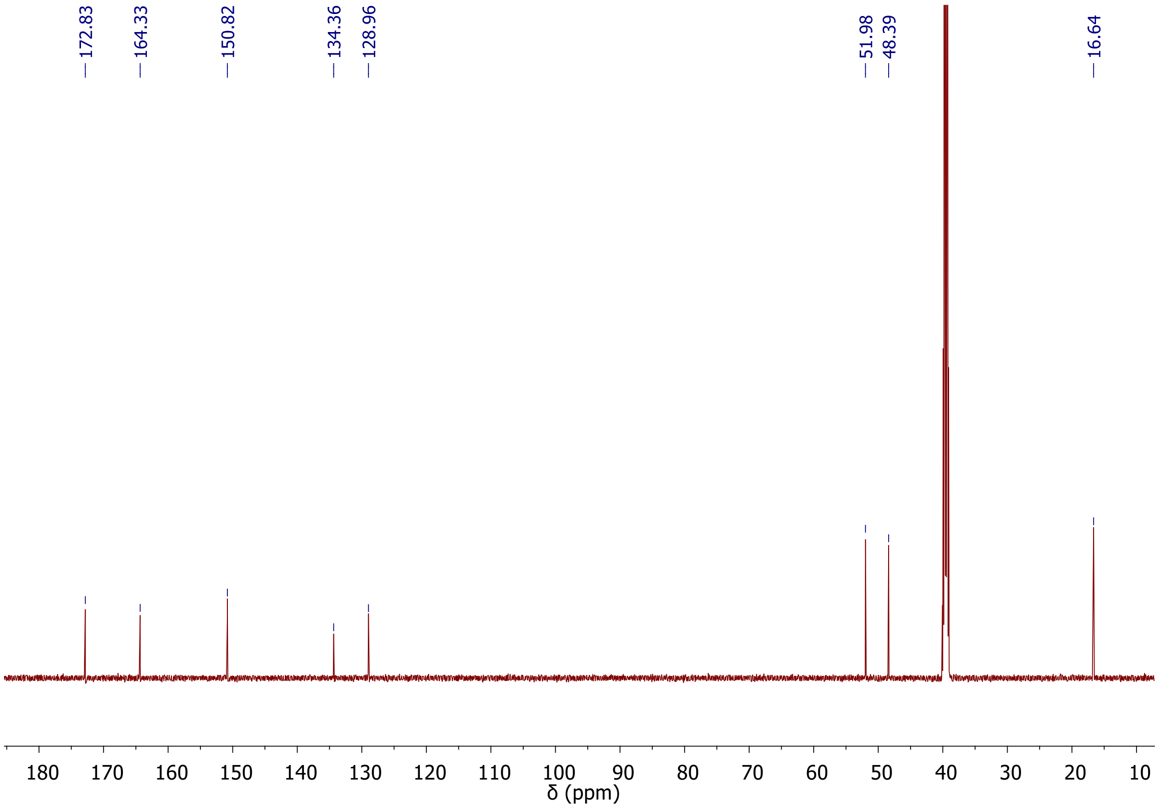

Figure 8.24 ^{1}H NMR (600 MHz, DMSO-d_6) and ^{13}C{^{1}H} NMR (150 MHz, DMSO-d_6) spectra of **104**.

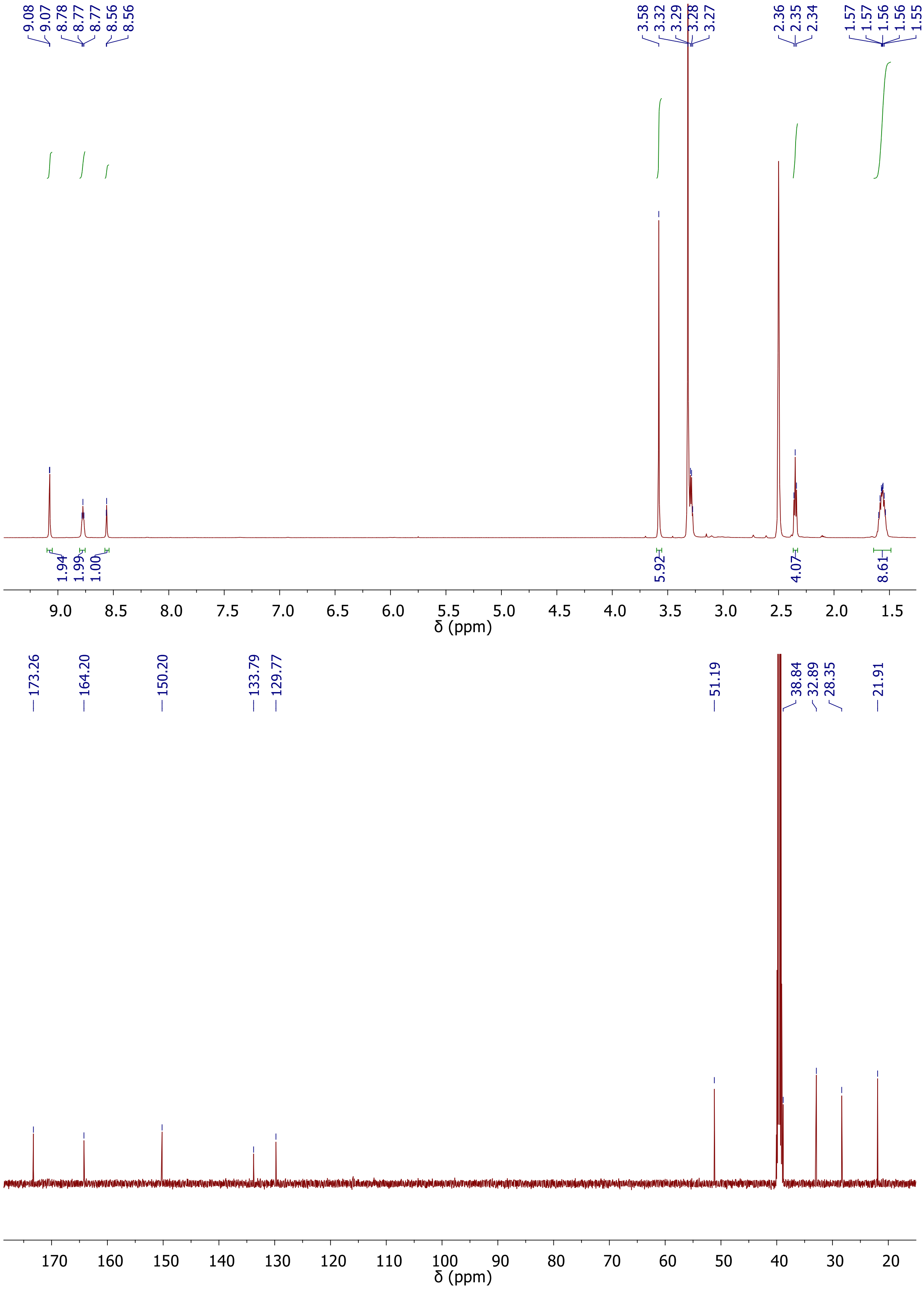

Figure 8.25 ^{1}H NMR (600 MHz, DMSO-d_6) and ^{13}C{^{1}H} NMR (150 MHz, DMSO-d_6) spectra of **105**.

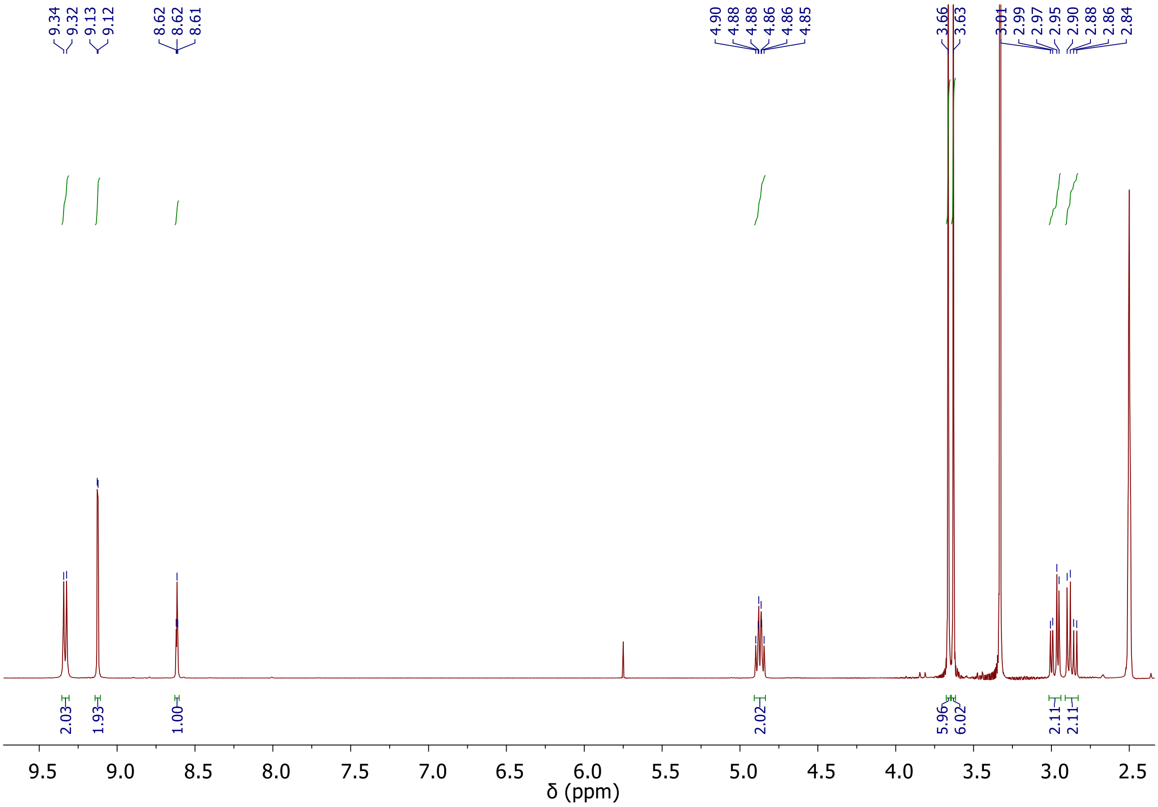

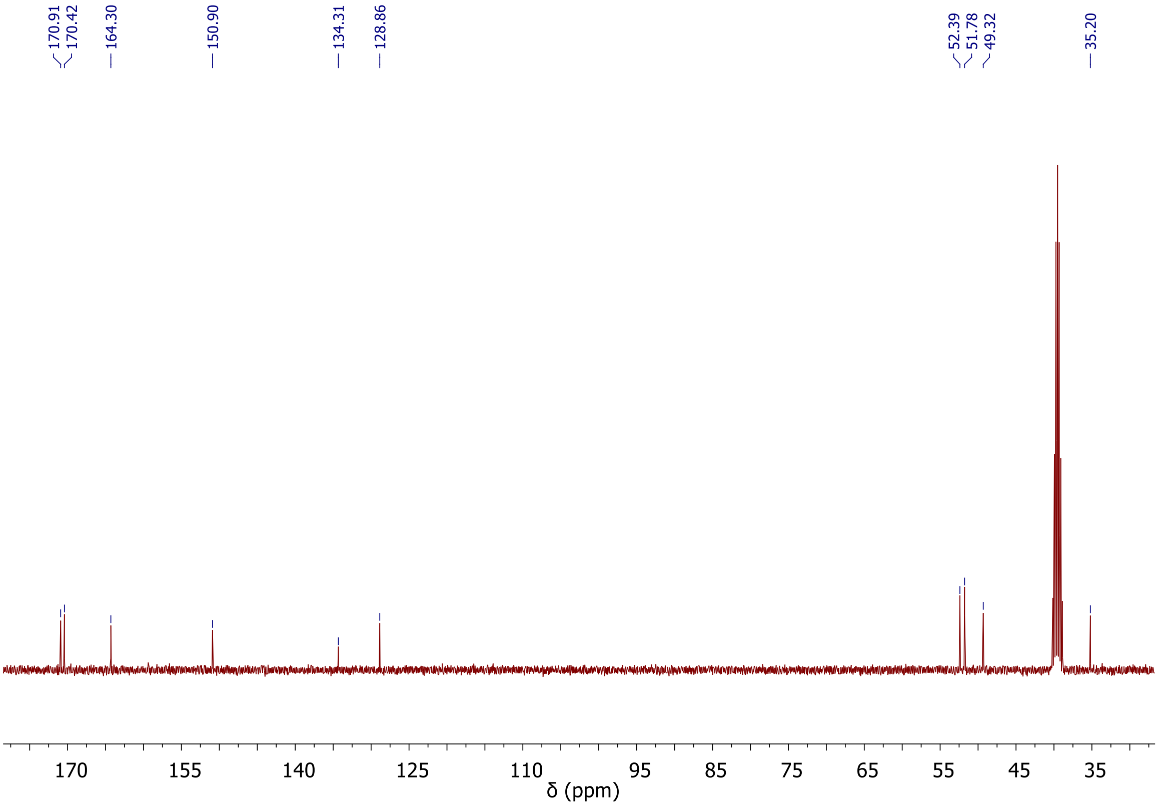

Figure 8.26 ^{1}H NMR (600 MHz, DMSO-d_6) and ^{13}C{^{1}H} NMR (150 MHz, DMSO-d_6) spectra of **106**.

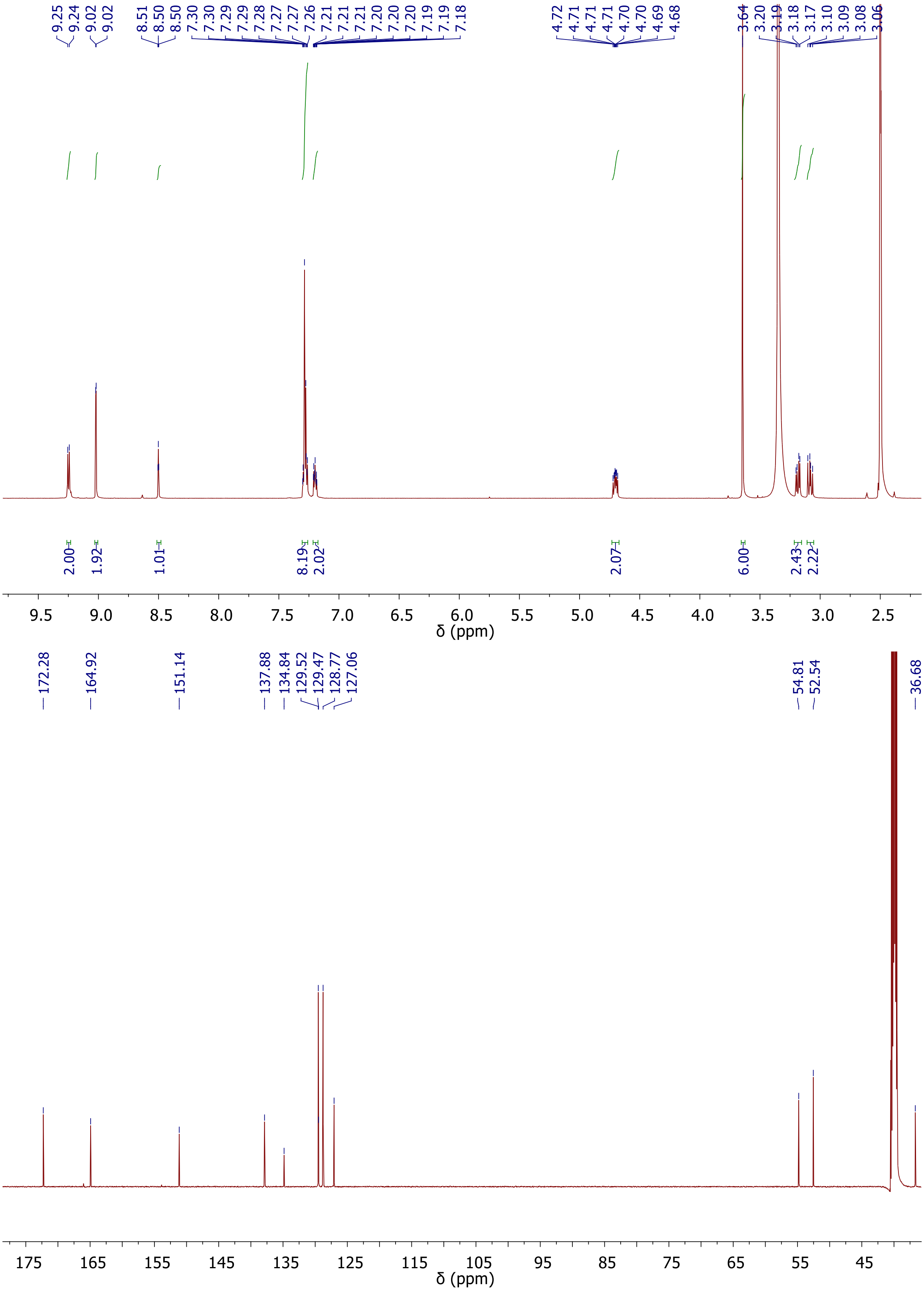

Figure 8.27 ^{1}H NMR (600 MHz, DMSO-d_6) and ^{13}C{^{1}H} NMR (150 MHz, DMSO-d_6) spectra of **107**.

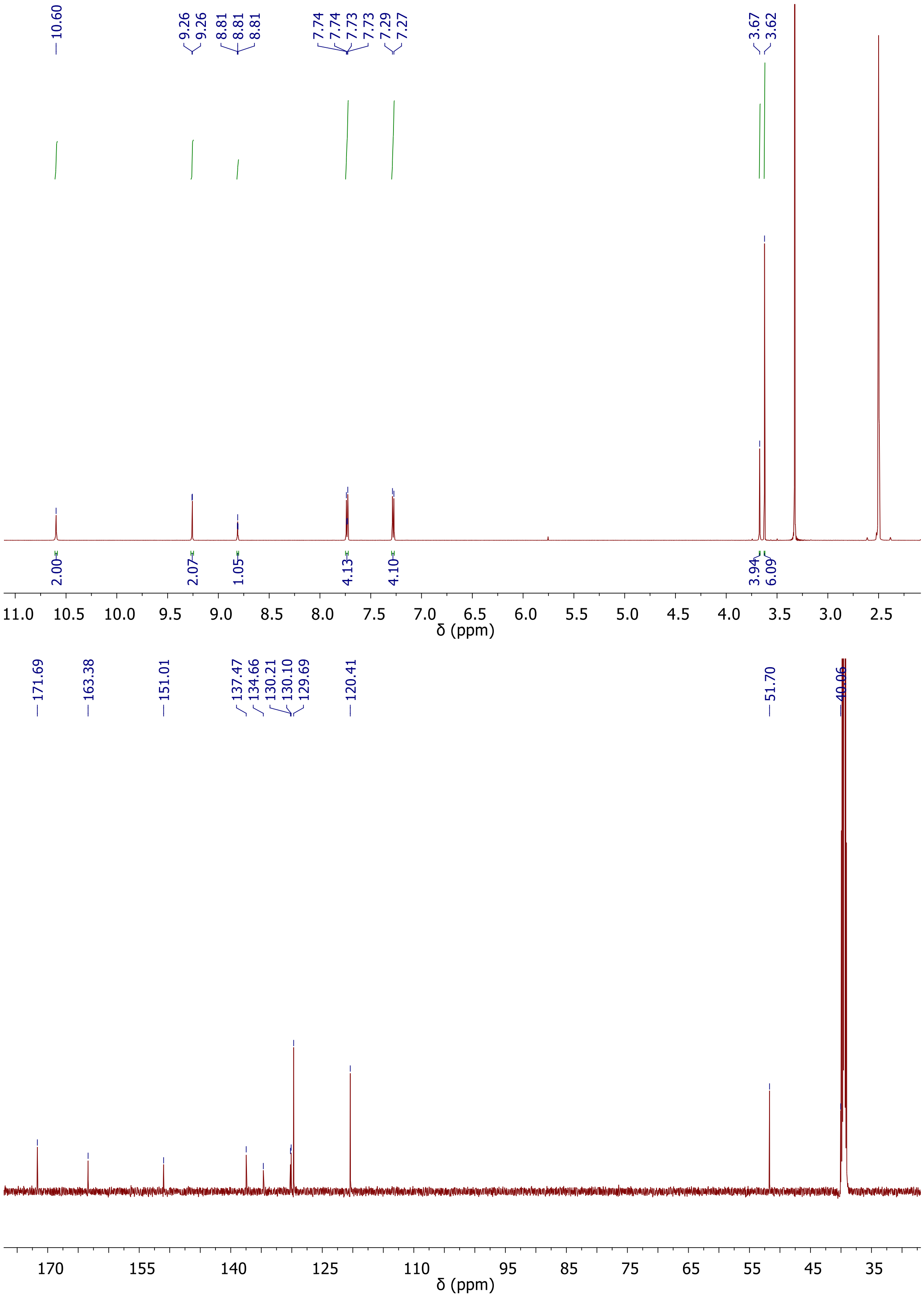

Figure 8.28 ^{1}H NMR (600 MHz, DMSO-d_6) and ^{13}C{^{1}H} NMR (150 MHz, DMSO-d_6) spectra of **108**.

8.2 Crystallography

8.2.1 X-ray table of compounds 60, 57, 58 and 55 discussed in Chapter 2

Identification code	63	59	62	58
Empirical formula	$C_{21}H_{27}N_3O_9$	$C_{27}H_{39}N_3O_9$	$C_{24}H_{43}N_3O_{14}$	$C_{30}H_{45}N_3O_9$
Formula weight	465.45	549.61	597.61	591.69
Temperature/K	100	99.99	99.99	100
Crystal system	triclinic	hexagonal	monoclinic	monoclinic
Space group	P-1	$P6_3/m$	P2/n	$P2_1/c$
a/Å	4.9042(2)	15.5682(6)	24.6517(13)	19.627(2)
b/Å	16.9098(6)	15.5682(6)	4.7182(3)	7.3150(10)
c/Å	17.0515(7)	6.8268(3)	25.6558(12)	23.510(3)
α/°	77.472(3)	90	90	90
β/°	87.209(4)	90	96.827(4)	114.567(8)
γ/°	83.111(3)	120	90	90
Volume/Å^3	1370.06(9)	1432.93(13)	2962.9(3)	3069.9(7)
Z	2	2	4	4
ρ_{calc}g/cm^3	1.128	1.274	1.34	1.28
μ/mm^{-1}	0.753	0.797	0.94	0.779
F(000)	492	588	1280	1272
Crystal size/mm^3	0.1 × 0.08 × 0.02	0.3 × 0.03 × 0.02	0.25 × 0.03 × 0.01	0.15 × 0.11 × 0.02
Radiation	CuKα (λ = 1.54178)	CuKα (λ = 1.54178)	CuKα (λ = 1.54178)	CuKα (λ = 1.54178)
2Θ range for data collection/°	5.388 to 133.542	6.556 to 136.63	4.7 to 136.732	4.95 to 136.482
Index ranges	$-5 \le h \le 5, -19 \le k \le 20, -19 \le l \le 20$	$-18 \le h \le 12, -17 \le k \le 18, -8 \le l \le 8$	$-28 \le h \le 29, -5 \le k \le 5, -30 \le l \le 27$	$-23 \le h \le 23, -8 \le k \le 5, -26 \le l \le 28$
Reflections collected	10762	5499	26640	16636
Independent reflections	4771 [R_{int} = 0.0406, R_{sigma} = 0.0591]	956 [R_{int} = 0.0554, R_{sigma} = 0.0382]	5443 [R_{int} = 0.0766, R_{sigma} = 0.0970]	5625 [R_{int} = 0.1111, R_{sigma} = 0.1318]
Data/restraints/parameters	4771/6/322	956/1/113	5443/17/418	5625/68/450
Goodness-of-fit on F^2	1.045	1.064	1.026	0.969
Final R indexes [I>=2σ (I)]	R_1 = 0.0581, wR_2 = 0.1507	R_1 = 0.0533, wR_2 = 0.1608	R_1 = 0.0547, wR_2 = 0.1396	R_1 = 0.0884, wR_2 = 0.2088
Final R indexes [all data]	R_1 = 0.0854, wR_2 = 0.1651	R_1 = 0.0615, wR_2 = 0.1674	R_1 = 0.0729, wR_2 = 0.1547	R_1 = 0.2020, wR_2 = 0.2795
Largest diff. peak/hole / e Å^{-3}	0.24/-0.25	0.17/-0.15	0.32/-0.30	0.46/-0.27
CCDC Deposition No.	1503992	1503993	1503994	1503995

8.2.2 X-ray table for compounds 66Cd, 67 and 67Cd discussed in Chapter 3

Identification code	**64Cd**	**65**	**65Cd**
Empirical formula	$C_{79.5}H_{80}Cd_3N_{10.5}O_{25.16}$	$C_{18}H_{21.42}N_3O_{9.59}$	$C_{33}H_{47}Cd_3N_7O_{27}$
Formula weight	1922.38	433.29	1310.97
Temperature/K	100.01	99.98	100.01
Crystal system	triclinic	monoclinic	monoclinic
Space group	P-1	P21/n	P21/c
a/Å	9.3062(3)	13.0286(4)	15.0689(6)
b/Å	20.1158(6)	6.9850(2)	22.3544(9)
c/Å	22.2589(7)	22.2051(6)	14.3047(6)
α/°	101.9120(10)	90	90
β/°	101.2140(10)	93.3610(10)	109.6750(10)
γ/°	98.7420(10)	90	90
Volume/Å3	3918.4(2)	2017.29(10)	4537.3(3)
Z	2	4	4
ρcalcg/cm3	1.629	1.427	1.919
μ/mm-1	0.895	1.005	1.495
F(000)	1952	909	2616
Crystal size/mm3	0.25 × 0.09 × 0.02	0.17 × 0.08 × 0.06	0.4 × 0.24 × 0.05
Radiation	MoKα (λ = 0.71073)	CuKα (λ = 1.54178)	MoKα (λ = 0.71073)
2Θ range for data collection/°	3.184 to 52.116	7.976 to 136.696	2.87 to 57
Index ranges	-11 ≤ h ≤ 11, -24 ≤ k ≤ 24, -27 ≤ l ≤ 27	-15 ≤ h ≤ 15, -8 ≤ k ≤ 8, -26 ≤ l ≤ 26	-20 ≤ h ≤ 20, -30 ≤ k ≤ 30, -19 ≤ l ≤ 19
Reflections collected	68542	20803	132473
Independent reflections	15474 [Rint = 0.0719, Rsigma = 0.0683]	3693 [Rint = 0.0349, Rsigma = 0.0218]	11504 [Rint = 0.0325, Rsigma = 0.0148]
Data/restraints/parameters	15470/45/1126	3693/31/338	11504/28/675
Goodness-of-fit on F2	1.014	1.067	1.119
Final R indexes [I>=2σ (I)]	R1 = 0.0504, wR2 = 0.1162	R1 = 0.0483, wR2 = 0.1364	R1 = 0.0324, wR2 = 0.0810
Final R indexes [all data]	R1 = 0.0884, wR2 = 0.1317	R1 = 0.0516, wR2 = 0.1410	R1 = 0.0384, wR2 = 0.0855
Largest diff. peak/hole / e Å-3	1.24/-0.87	0.57/-0.32	1.62/-1.03

8.2.3 X-ray table for compound 96 discussed in Chapter 4

Id+A1:B28entification code	**92**
Empirical formula	$C_{44}H_{66}Cu_4N_4O_{11}$
Formula weight	1081.16
Temperature/K	100
Crystal system	monoclinic
Space group	$P2_1/c$
a/Å	12.4474(7)
b/Å	26.4033(15)
c/Å	15.8247(9)
α/°	90
β/°	110.345(2)
γ/°	90
Volume/Å^3	4876.4(5)
Z	4
ρ_{calc}g/cm^3	1.473
μ/mm^{-1}	1.78
F(000)	2248
Crystal size/mm^3	0.15 × 0.14 × 0.12
Radiation	MoKα (λ = 0.71073)
2Θ range for data collection/°	3.084 to 50.998
Index ranges	$-15 \le h \le 12$, $-31 \le k \le 31$, $-19 \le l \le 17$
Reflections collected	49627
Independent reflections	9036 [R_{int} = 0.0676, R_{sigma} = 0.0589]
Data/restraints/parameters	9036/0/582
Goodness-of-fit on F^2	1.085
Final R indexes [I>=2σ (I)]	R_1 = 0.0713, wR_2 = 0.1920
Final R indexes [all data]	R_1 = 0.1029, wR_2 = 0.2084
Largest diff. peak/hole / e Å^{-3}	1.39/-0.94

8.2.4 X-ray tables for compounds 104, 104Mn, 105, 105Mn, 105Cd, 107Cd and 108 discussed in Chapter 5

Identification code	**104**	**104Mn**	**105**
Empirical formula	$C_{15}H_{19}N_3O_6$	$C_{15}H_{19}Cl_2MnN_3O_6$	$C_{38}H_{54}N_6O_{12}$
Formula weight	337.33	463.17	786.87
Temperature/K	100.01	99.99	295(2)
Crystal system	monoclinic	monoclinic	monoclinic
Space group	$P2_1$	$P2_1$	$P2_1/c$
a/Å	6.2417(3)	8.6821(10)	4.9533(5)
b/Å	8.0860(3)	7.5087(10)	45.885(5)
c/Å	16.0975(7)	14.3282(18)	9.3644(10)
α/°	90	90	90
β/°	96.642(2)	100.038(4)	105.158(4)
γ/°	90	90	90
Volume/Å^3	806.99(6)	919.8(2)	2054.3(4)
Z	2	2	2
ρ_{calc}g/cm^3	1.388	1.672	1.272
μ/mm^{-1}	0.918	1.047	0.095
F(000)	356	474	840
Crystal size/mm^3	0.22 × 0.13 × 0.03	0.13 × 0.04 × 0.01	0.5 × 0.08 × 0.04
Radiation	CuKα (λ = 1.54178)	MoKα (λ = 0.71073)	MoKα (λ = 0.71073)
2Θ range for data collection/°	11.066 to 136.756	4.764 to 52.134	5.738 to 52.994
Index ranges	-7 ≤ h ≤ 7, -9 ≤ k ≤ 9, -19 ≤ l ≤ 19	-10 ≤ h ≤ 10, -9 ≤ k ≤ 9, -17 ≤ l ≤ 17	-6 ≤ h ≤ 6, -57 ≤ k ≤ 56, -11 ≤ l ≤ 11
Reflections collected	9438	9710	21518
Independent reflections	2920 [R_{int} = 0.0534, R_{sigma} = 0.0544]	3637 [R_{int} = 0.0955, R_{sigma} = 0.1397]	4216 [R_{int} = 0.0416, R_{sigma} = 0.0365]
Data/restraints/parameters	2920/3/227	3637/82/248	4216/150/312
Goodness-of-fit on F^2	1.045	0.939	1.046
Final R indexes [I>=2σ (I)]	R_1 = 0.0359, wR_2 = 0.0949	R_1 = 0.0505, wR_2 = 0.0682	R_1 = 0.0561, wR_2 = 0.1543
Final R indexes [all data]	R_1 = 0.0382, wR_2 = 0.0963	R_1 = 0.1138, wR_2 = 0.0816	R_1 = 0.0730, wR_2 = 0.1684
Largest diff. peak/hole / e Å^{-3}	0.15/-0.19	0.41/-0.51	0.28/-0.16
Flack parameter	-0.17(12)	0.05(5)	

Identification code	105Mn	105Cd	108Pt
Empirical formula	$C_{38}H_{58}Cl_6Mn_3N_6O_{14}$	$C_{34}H_{76}Cd_2N_6O_{29}$	C27H29Cl2N3O7PtS
Formula weight	1200.42	1257.8	805.58
Temperature/K	99.99	100.01	100
Crystal system	triclinic	triclinic	monoclinic
Space group	P-1	P-1	P21/c
a/Å	8.9760(3)	10.2353(3)	14.3036(7)
b/Å	9.4524(3)	14.7931(4)	10.5503(5)
c/Å	15.0764(4)	18.7753(5)	19.8346(10)
α/°	90.686(2)	92.1030(10)	90
β/°	100.683(2)	105.1260(10)	105.589(4)
γ/°	96.159(2)	95.5870(10)	90
Volume/Å^3	1249.06(7)	2725.56(13)	2883.1(3)
Z	1	2	4
ρ_{calc}g/cm^3	1.596	1.533	1.856
μ/mm^{-1}	9.606	0.87	11.924
F(000)	617	1300	1584
Crystal size/mm^3	0.09 × 0.09 × 0.02	0.37 × 0.22 × 0.03	0.07 × 0.01 × 0.01
Radiation	CuKα (λ = 1.54178)	MoKα (λ = 0.71073)	CuKα (λ = 1.54178)
2Θ range for data collection/°	5.968 to 136.588	2.772 to 61.158	6.416 to 136.67
Index ranges	-10 ≤ h ≤ 10, -11 ≤ k ≤ 8, -18 ≤ l ≤ 18	-14 ≤ h ≤ 14, -21 ≤ k ≤ 21, -26 ≤ l ≤ 26	-17 ≤ h ≤ 17, -12 ≤ k ≤ 12, -23 ≤ l ≤ 23
Reflections collected	12698	101318	22740
Independent reflections	4544 [R_{int} = 0.0432, R_{sigma} = 0.0448]	16703 [R_{int} = 0.0377, R_{sigma} = 0.0280]	5281 [Rint = 0.1064, Rsigma = 0.1007]
Data/restraints/parameters	4544/4/318	16703/10/683	5281/0/374
Goodness-of-fit on F^2	1.023	1.018	1.016
Final R indexes [I>=2σ (I)]	R_1 = 0.0376, wR_2 = 0.0970	R_1 = 0.0331, wR_2 = 0.0744	R1 = 0.0652, wR2 = 0.1550
Final R indexes [all data]	R_1 = 0.0429, wR_2 = 0.0999	R_1 = 0.0552, wR_2 = 0.0827	R1 = 0.0901, wR2 = 0.1708
Largest diff. peak/hole / e Å^{-3}	0.41/-0.66	2.27/-1.21	3.05/-1.69
Flack parameter			

Identification code	**107Cd**	**108**
Empirical formula	$C_{25}H_{23}CdN_3O_7$	$C_{25}H_{23}N_3O_6$
Formula weight	589.9	461.46
Temperature/K	99.98	99.99
Crystal system	orthorhombic	monoclinic
Space group	$P2_12_12_1$	C2/c
a/Å	5.01040(10)	31.2927(12)
b/Å	18.2930(4)	5.2243(2)
c/Å	31.4687(8)	28.9595(11)
α/°	90	90
β/°	90	115.871(3)
γ/°	90	90
Volume/Å^3	2884.27(11)	4259.9(3)
Z	4	8
ρ_{calc}g/cm^3	1.358	1.439
μ/mm^{-1}	6.436	0.865
F(000)	1192	1936
Crystal size/mm^3	0.16 × 0.02 × 0.01	0.26 × 0.14 × 0.01
Radiation	CuKα (λ = 1.54178)	CuKα (λ = 1.54178)
2Θ range for data collection/°	5.588 to 136.67	6.278 to 136.434
Index ranges	$-5 \le h \le 6, -21 \le k \le 18, -37 \le l \le 37$	$-37 \le h \le 37, -6 \le k \le 6, -34 \le l \le 24$
Reflections collected	24995	13841
Independent reflections	5230 [R_{int} = 0.0518, R_{sigma} = 0.0463]	3895 [R_{int} = 0.0514, R_{sigma} = 0.0517]
Data/restraints/parameters	5230/107/392	3895/2/315
Goodness-of-fit on F^2	1.07	1.031
Final R indexes [I>=2σ (I)]	R_1 = 0.0527, wR_2 = 0.1373	R_1 = 0.0501, wR_2 = 0.1296
Final R indexes [all data]	R_1 = 0.0542, wR_2 = 0.1384	R_1 = 0.0668, wR_2 = 0.1404
Largest diff. peak/hole / e Å^{-3}	1.86/-0.60	0.27/-0.27
Flack parameter	0.049(15)	

8.2.5 Disorder of 66Cd

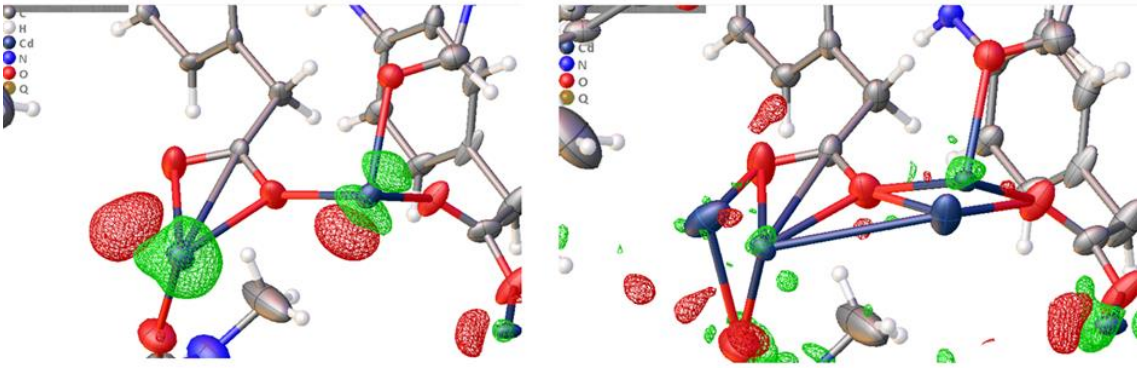

Figure 8.29 Residual electron density maps for complex **1** before (left, rendered at +/- 1.4 e·Å^3) and after (right, rendered at +/- 0.9 e·Å^3) modelling the disorder around cadmium sites Cd2 and Cd3.

8.2.6 Disorder of 107Cd

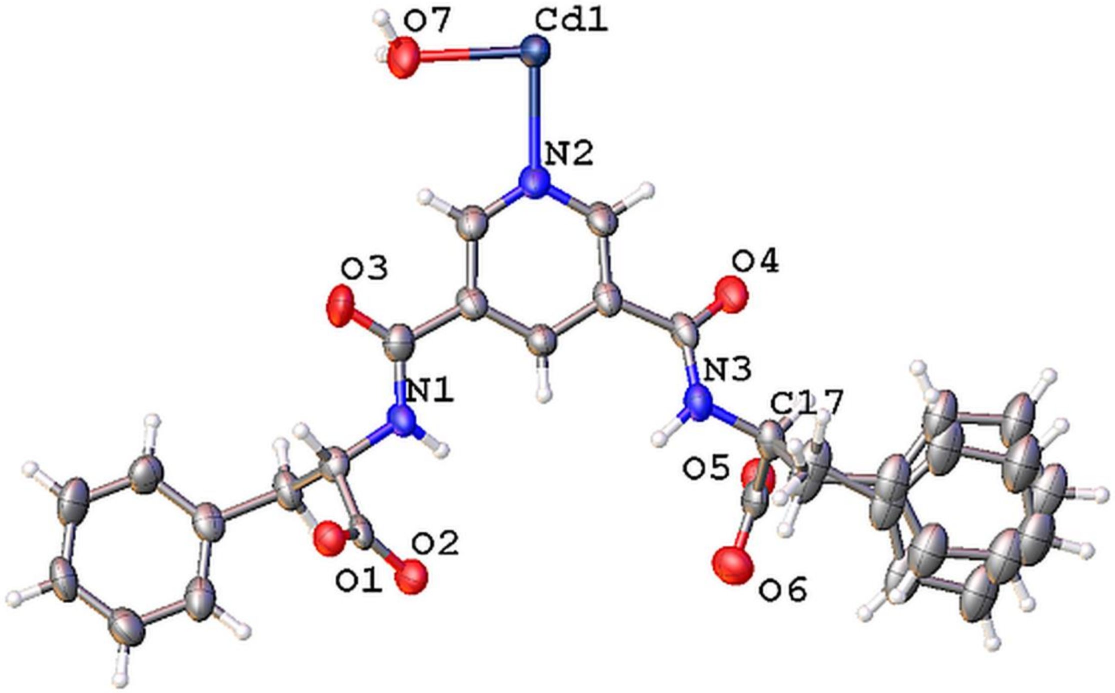

Figure 8.30 Disorder of the aromatic group originating from C17.

8.2.7 Structure of 108Pt

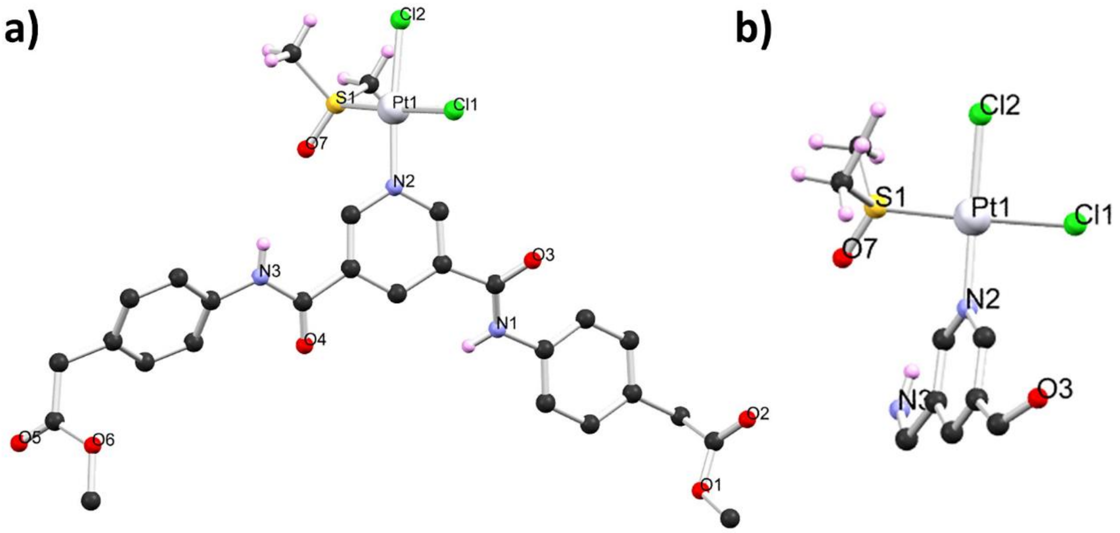

Figure 8.31 (a) Asymmetric unit of **108Pt** with heteroatom labelling scheme and (b) coordination environment of the Pt centre. Selected hydrogen atoms are omitted for clarity.

8.2.8 Powder diffraction

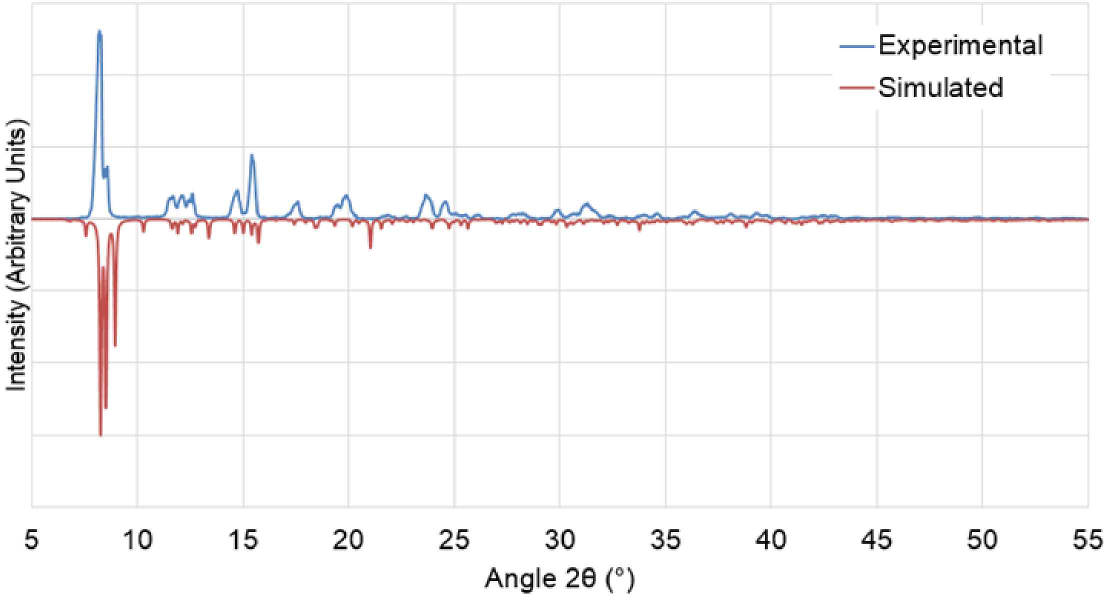

Figure 8.32 X-ray powder diffraction pattern for **92** (blue, room temperature) compared with the simulated pattern from the X-ray structural model (red, 100K).

8.3 Optical microscopy

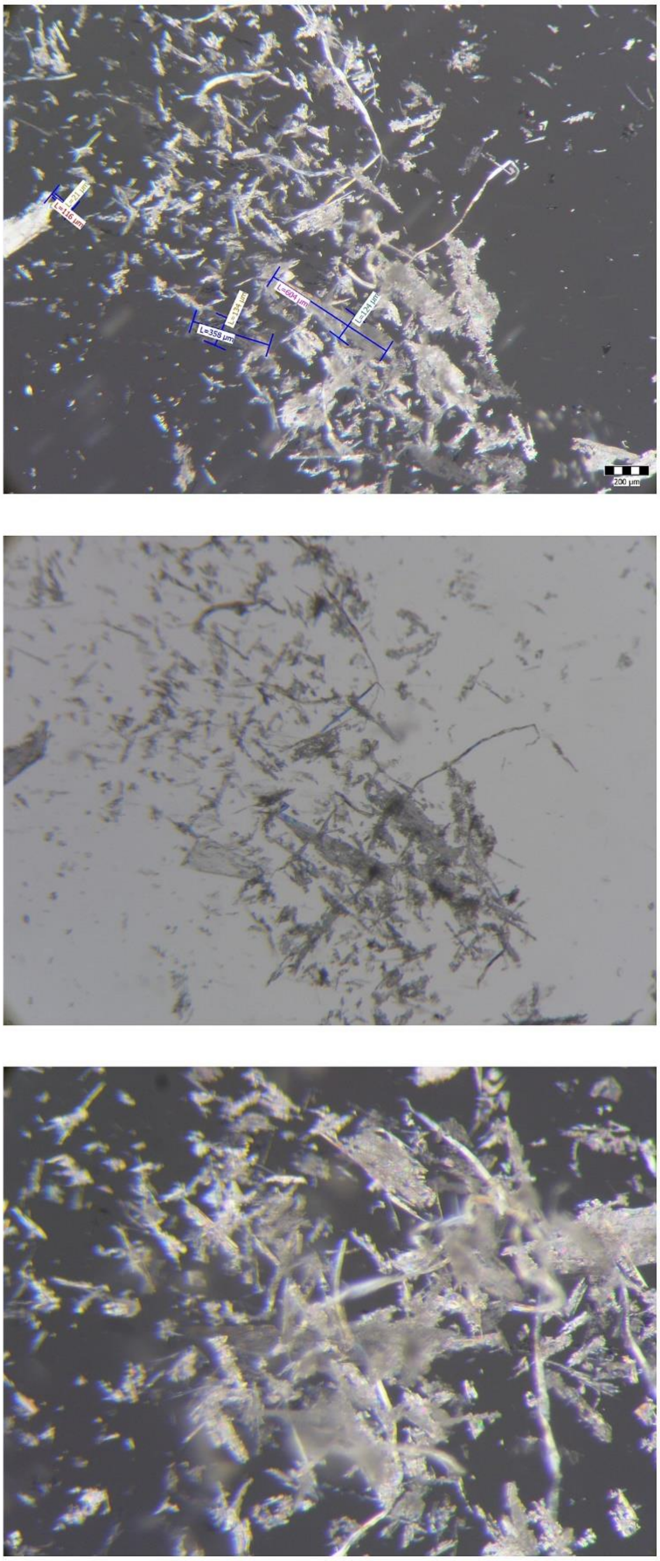

Figure 8.33 POM of the crystals of **108**, top scale bar 200 µm, with measurements of crystals ranging in length and diameter, from approximately116-600 µm in diameter and 21-135 µm.

8.4 Adsorption Data

8.4.1 64Cd

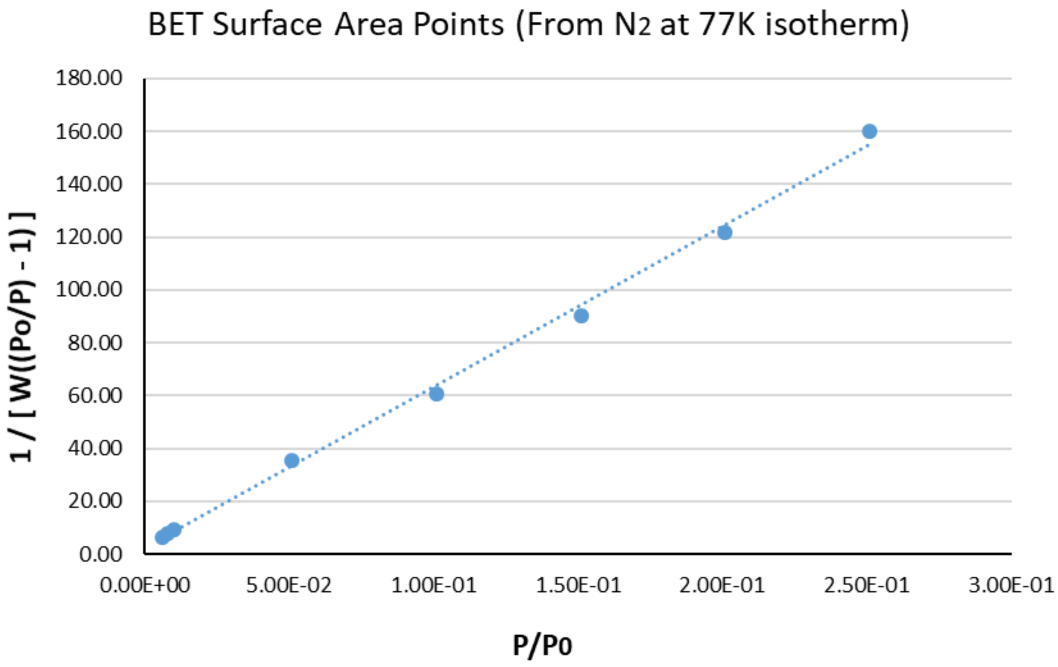

Slope = 608.320

Intercept = 2.235e+00

Correlation coefficient, r = 0.998621

C constant= 273.134

Surface Area = 5.704 m^2/g

Figure 8.34 BET surface area points of **64Cd** and calculation of surface area.

8.4.2 65Cd

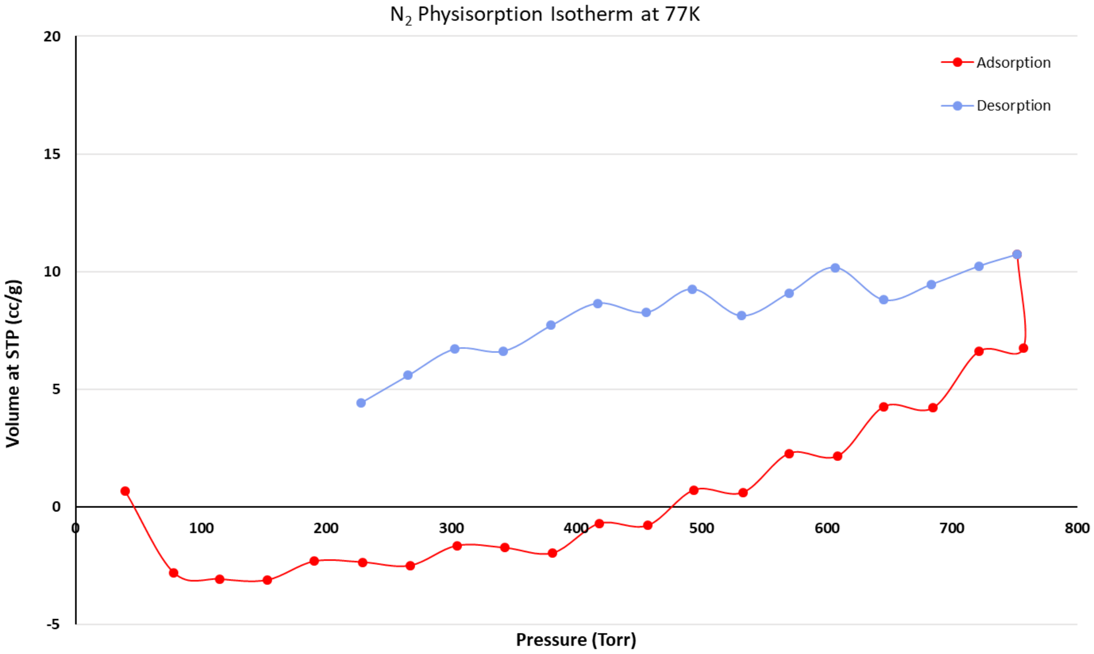

Figure 8.35 N_2 isotherm for **65Cd** at 77 K

8.4.3 91

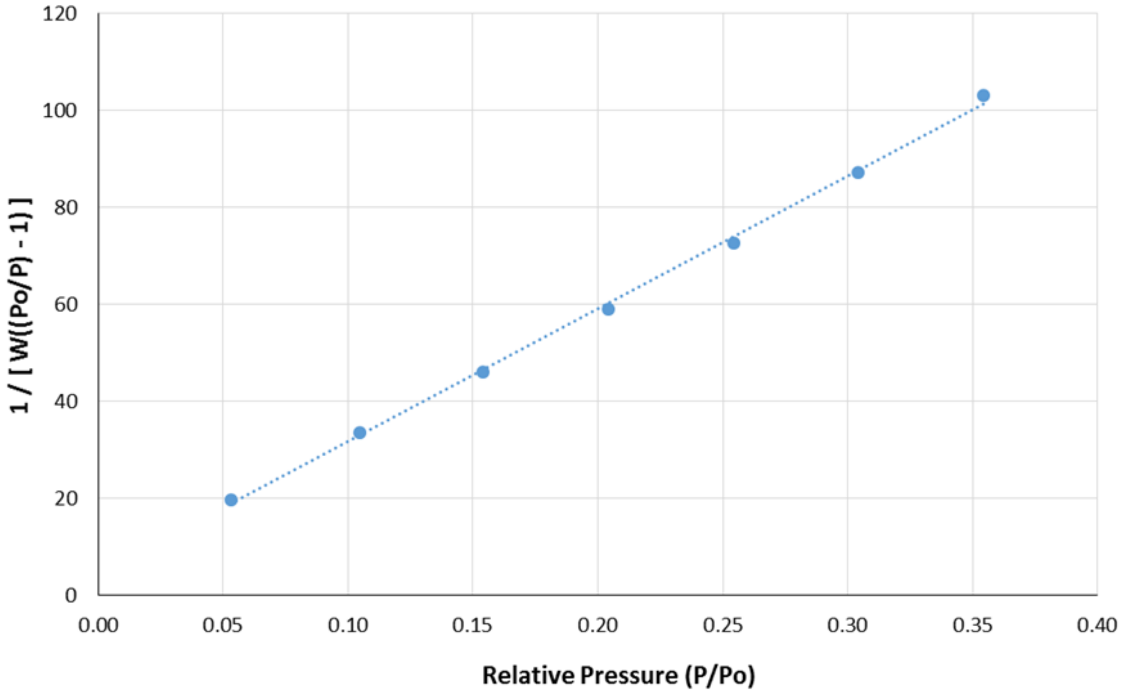

Slope = 273.868
Intercept = 4.31e+00
Correlation coefficient, 0.999231
C constant = 64.546
Surfface Area 12.519 m²/g

Figure 8.36 Brunauer-Emmett-Teller (BET) transformed isotherm plot for 91 (N_2, 77K).

8.5 EDX

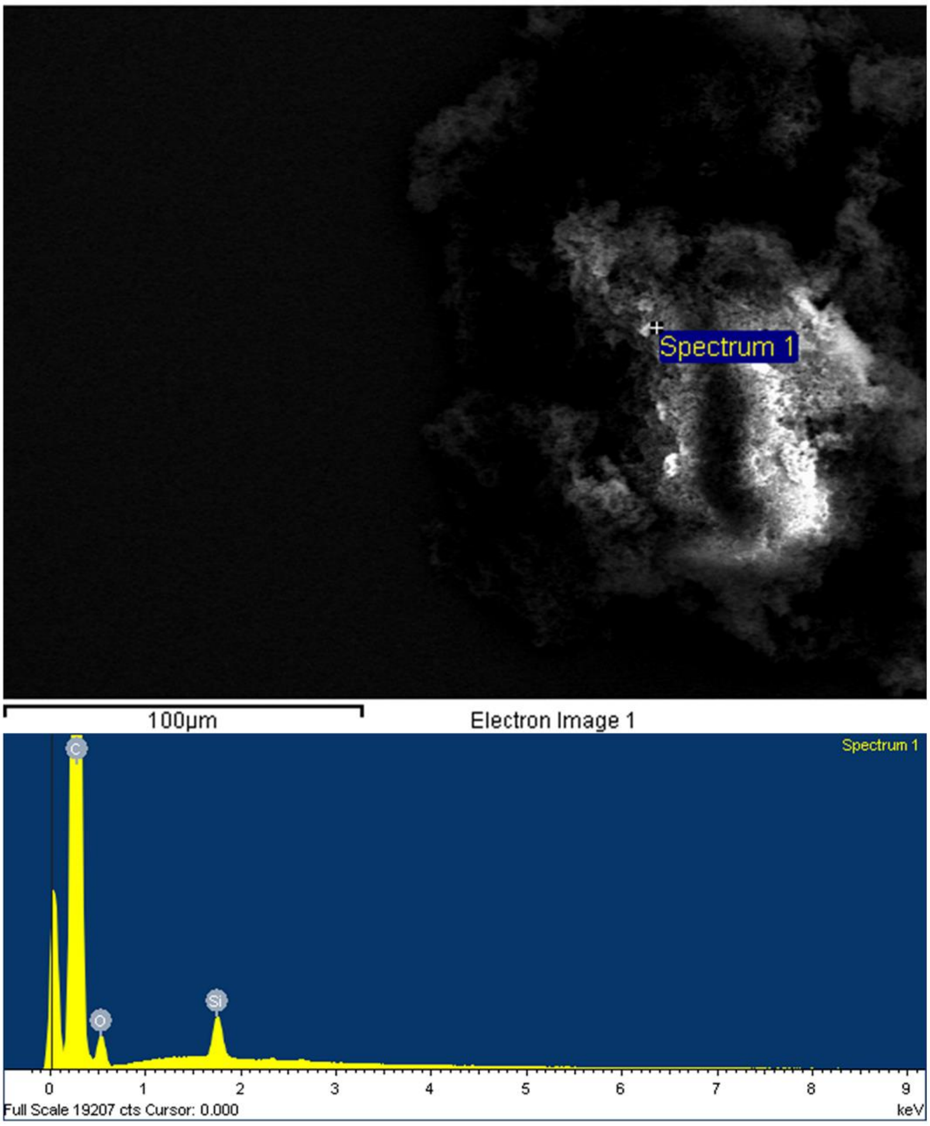

Figure 8.37 EDX output for the organic polymer **91** discussed in Chapter 4.

8.6 Crystallisation and Gelation attempts for the compounds discussed in Chapters 2 and 3

Crystallisation and gelation attempts	**58**	**59**	**61**	**62**	**63**
Solvothermal reaction					
1:1 DMF/H2O	Y	Y	Y	Y	Y
DMF	Y	Y	Y	Y	Y
Ligand alone	Y	Y	Y	Y	Y
Variety of metal salts, Cd, Zn, Cu, Ni, Mn and Co	Y	Y	Y	Y	Y
Diffusion					
MeOH/Diethyl ether	Y	Y	Y	Y	Y
MeOH/Toluene	Y	Y	Y	Y	Y
MeCN/Diethyl ether	Y	Y	Y	Y	Y
Variety of metal salts, eg Cd, Zn, Cu, Ni, Mn and Co	Y	Y	Y	Y	Y
Slow evaporation					
Variety of solvents, MeOH, EtOH, DCM, Tol, $CHCl_3$, EtOAc, H_2O and MeCN	Y, 2:1 H_2O/THF	Y, 1:1 MeOH/H_2O	Y	Y, 1:1 MeOH/H_2O	Y
Acid/base gelation attempts	N	N	Y, weak gel	Y, weak	Y, very weak
Gelation tests in a variety of solvents	Y	Y	Y, gel 2:1 H_2O/THF	Y, weak	Y, weak gel, 2:1 H_2O/THF

Crystallisation and gelation attempts	**69**	**64**	**65**
Solvothermal reaction			
1:1 DMF/H2O	Y	Y	Y
DMF	Y	Y	Y
Ligand alone	Y	Y	Y
Variety of metal salts, Cd, Zn, Cu, Ni, Mn and Co	Y	Y, Cd structure	Y, Cd structure
Diffusion			
MeOH/Diethyl ether	Y	Y	Y
MeOH/Toluene	Y	Y	Y
MeCN/Diethyl ether	Y	Y	Y
Variety of metal salts, eg Cd, Zn, Cu, Ni, Mn and Co	Y	Y	Y
Slow evaporation			
Variety of solvents, MeOH, EtOH, DCM, Tol, $CHCl_3$, EtOAc, H_2O and MeCN	Y	Y	Y, L structure from H_2O
Acid/base gelation attempts	N	Y	N
Gelation tests in a variety of solvents	Y	Y	N

8.7 X-ray crystal structure obtained by Anna Aletti

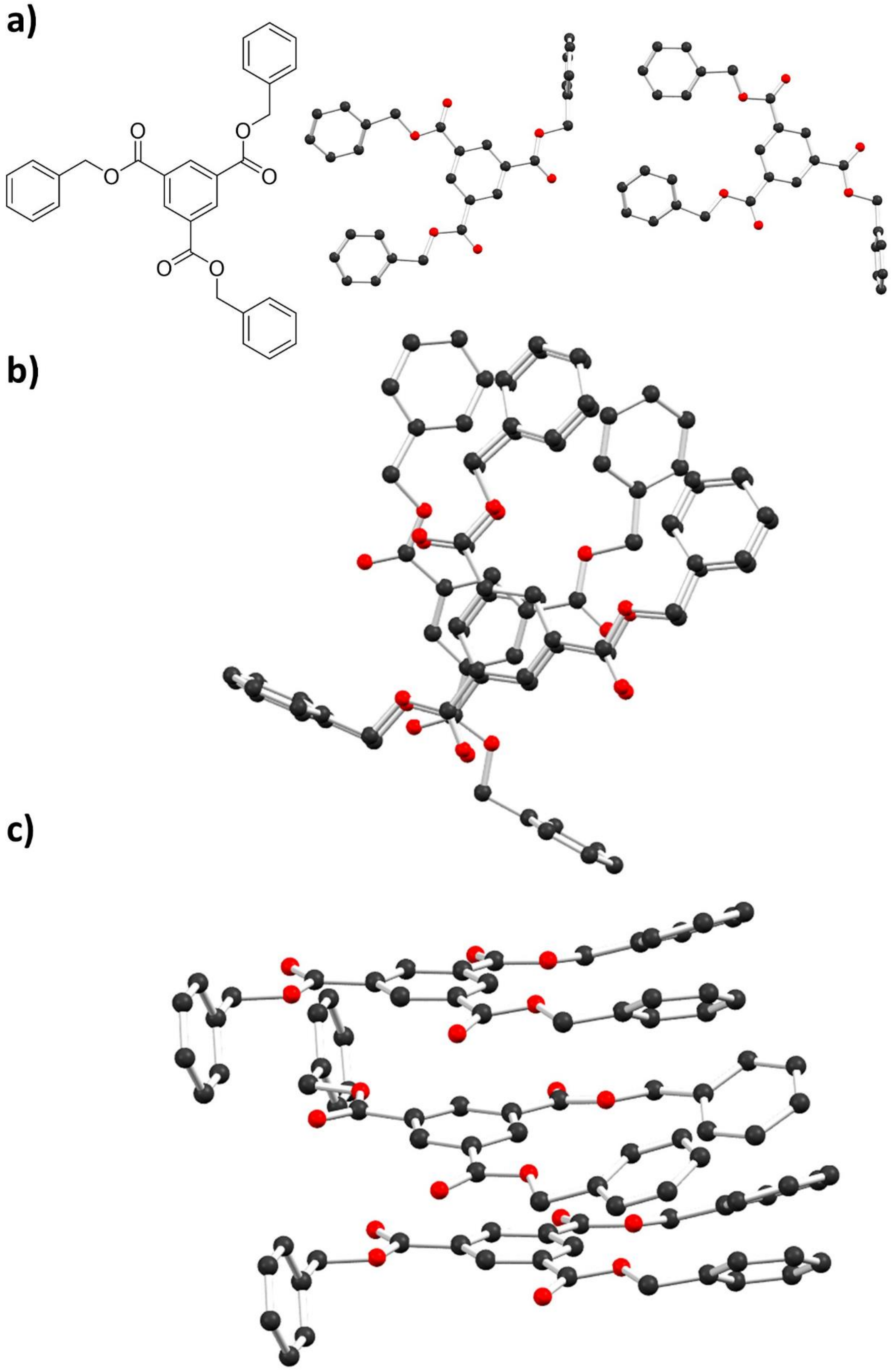

Figure 8.38 (a) Structure and asymmetric unit of the compound obtained by Anna Aletti and (b&c) extended packing of the ligand.